Karlsruher Institut für Technologie

Synthesis of *Cage*-shaped Polymers by Topological Conversion

Zur Erlangung des akademischen Grades eines

DOKTORS DER NATURWISSENSCHAFTEN

(Dr. rer. nat.)

von der KIT-Fakultät für Chemie und Biowissenschaften

des Karlsruher Instituts für Technologie (KIT)

genehmigte

DISSERTATION

von

M.Sc. Martin GAUTHIER-JAQUES

aus

BOUDEVILLIERS (NE), SCHWEIZ

1. Referent: Prof. Dr. Patrick THÉATO
2. Referent: Prof. Dr. Stefan BRÄSE

Tag der mündlichen Prüfung: 16.07.2021

Dédié à Eliane, Gilles & Anne

Die vorliegende Arbeit wurde im Zeitraum von Januar 2018 bis Juni 2021 am Institut für Technische Chemie und Polymerchemie (ITCP) und am Institut für Biologische Grenzflächen 3 (IBG-3) am Karlsruher Institut für Technologie (KIT) – Universitätsbereich unter der Betreuung von Prof. Dr. Patrick THÉATO angefertigt.

Hiermit versichere ich, dass ich die Arbeit selbstständig angefertigt, nur die angegebenen Quellen und Hilfsmittel benutzt und mich keiner unzulässigen Hilfe Dritter bedient habe. Insbesondere habe ich wörtlich oder sinngemäß aus anderen Werken übernommene Inhalte als solche kenntlich gemacht. Die Satzung des Karlsruher Instituts für Technologie (KIT) zur Sicherung wissenschaftlicher Praxis habe ich beachtet. Des Weiteren erkläre ich, dass ich mich derzeit in keinem laufenden Promotionsverfahren befinde, und auch keine vorausgegangenen Promotionsversuche unternommen habe. Die elektronische Version der Arbeit stimmt mit der schriftlichen Version überein und die Primärdaten sind gemäß Abs. A (6) der Regeln zur Sicherung guter wissenschaftlicher Praxis des KIT beim Institut abgegeben und archiviert.

Karlsruhe, den 09.06.2021

_____

Martin GAUTHIER-JAQUES

Publications

Publications arising from this Dissertation

[1] M. Gauthier-Jaques, P. Theato, Synergy of Macrocycles and Macromolecular Topologies: An Efficient [3_4] Triazolophane-Based Synthesis of *Cage*-Shaped Polymers. *ACS Macro Lett.* **2020**, *9*, 700–705.

[2] A. J. Butzelaar, M. Gauthier-Jaques, K. L. Liu, G. Brunklaus, M. Winter, P. Theato, The Power of Architecture – *Cage*-shaped PEO and its Application as Polymer Electrolyte. *Polym. Chem.* **2021**, *12*, 4326–4331.

Other Publications

[1] M. Gauthier-Jaques, H. Mutlu, H. Gaballa, P. Theato, Synthesis and Application of Reactive Polymers via RAFT Polymerization. In: G. Moad (ed.), E. Rizzardo (ed.), RAFT Polymerization: Methods, Synthesis and Applications. *Wiley-VCH*, **2021**, ISBN: 978-3-527-34495-6.

Conference Contributions

[1] ‘’*Synergy of Macrocycles and Macromolecular Topologies: An Efficient [3_4]Triazolophane-Based Synthesis of Cage-Shaped Polymers.*’’ Poster presented on September 28th-29th 2020 at the online poster session of the Macrosymposium 2020 "100 Years Macromolecular Chemistry" conference.

Abstract

The very existence of a causal link between the topology and the thermo-mechanical properties of polymers is a unique aspect of polymer science with no equivalent in the world of small organic molecules. Since the birth of modern polymer chemistry 100 years ago, polymer chemists competed ingeniously to produce ever more numerous and sophisticated polymer topologies. Among them, *cage*-shaped polymers stand out by their polycyclic architecture and the absence of polymer chain-ends. Although the synthesis of *cage*-shaped polymers turned out to be particularly tedious and constituted a major challenge to polymer chemists, several synthesis strategies with their own strengths and weaknesses were developed over the past 20 years. With one notable exception, the topological conversion of acyclic polymer precursors was particularly employed. However, the usual complex nature of these precursors, the common necessity to work in high-dilution and the frequent low yields of the topological conversion step made *cage*-shaped polymers difficult to obtain beyond the 100-milligram-scale and in a reproducible manner.

It is in this context that, within this work, a new methodology to generate *cage*-shaped polymers was conceptualized and developed. Starting from *star*-shaped polymer precursors, the topological conversion was envisaged to occur by $(AB)_n$ *n*-oligomerization of *n* bifunctional end-groups present at each arm of the polymer into a chemically inert macrocyclic structure. To do so, the chemistry involved in the $(AB)_n$ *n*-oligomerization was carefully chosen to fulfil a strict list of prerequisites in order to be viable, namely *inter alia* to be orthogonally initiated by a specific trigger as well as to irreversibly proceed with a high conversion and a high kinetic rate. As a result, CuAAC (copper-catalyzed azide-alkyne cycloaddition) click chemistry was selected and the syntheses of several potential AB end-groups examined. The first efforts to produce *star*-shaped polymer precursors were focused on the syntheses of *star*-shaped RAFT (reversible addition−fragmentation chain-transfer) agents, that were designed to directly bear the bifunctional end-groups. The synthesis of *cage*-shaped polymers was then intended to be achieved in only two steps, which were the RAFT polymerization itself and the topological conversion without the need of further post-polymerization modification in between. However, the synthesis of end-functionalized *star*-shaped RAFT agent proved to be more difficult than anticipated and the following polymerization suffered from side-reactions between the CTAs (chain transfer agents) and the end-group functionalities. In consequence, the *star*-shaped polymers were envisioned to be obtained by proton-catalyzed ROP (ring-opening

polymerization) of ε-caprolactone from multifunctional initiators. Meanwhile, the core idea of this work, namely the topological conversion of *star*-shaped polymers into polymer cages by $(AB)_n$ *n*-oligomerization, was greatly strengthened by the reports of D_{2h}-[3_4]triazolophane macrocycles in the scientific literature. While D_{2h}-[3_4]triazolophanes cannot be strictly speaking obtained by $(AB)_4$ tetramerization, their unreported D_{4h} regioisomer owns all prerequisites to do so from *m*-azidoethynylbenzene units. Thus, a well-defined four-arm *star*-shaped poly(ε-caprolactone) was synthetized and quantitively end-functionalized with a *m*-azidoethynylbenzene carboxylic acid derivative. From this point, a first 50-milligram-scale synthesis of *cage*-shaped polymer was achieved in high dilution condition. Motivated by these results, the kinetic of the intramolecular topological conversion was optimized by progressive reduction of the reaction time. Subsequently, the polymer concentration was gradually increased to examine its impact on the undesired intermolecular cross-linking reactions. Once these preliminary studies were completed, the influence of the polymer size on the synthesis yield and thermo-mechanical properties of the *cage*-shaped polymers was thoroughly considered. To do so, four *star*-shaped poly(ε-caprolactone)s varying in molecular weights were synthetized, end-functionalized and converted into their respective polymer cages at the 50-miligram-scale. The core of this work was later published in detail. Afterwards, the upscaling of the topological conversion from a known poly(ε-caprolactone) was examined by using a semi-batch process. From this point onwards, the robustness of the procedure was challenged by varying the nature of the polymer substrate and increasing the topological conversion yield beyond the gram-scale to finally envisage a concrete application for *cage*-shaped polymer materials. Accordingly, a *cage*-shaped poly(ethylene oxide) polymer was produced up to the 1.5-gram-scale and its ability to be used as a polymer electrolyte for lithium-ion batteries was later examined in the framework of a collaboration. Thanks to the particular topology of its polymer, purely amorphous poly(ethylene oxide) electrolytes were obtained with minimal lithium-salt loading ratios. The ionic conductivity being highly favored by the presence of non-crystalline phases within the polymer lattice, the *cage*-shaped polymer electrolytes widely outperformed the ionic conductivity values recorded for standard poly(ethylene oxide) electrolytes below their crystallization temperature. The results of this collaboration are in the process of being published.

Zusammenfassung

Die Existenz eines kausalen Zusammenhangs zwischen der Topologie und den thermomechanischen Eigenschaften von Polymeren ist ein einzigartiger Aspekt der Polymerwissenschaft, der keine Entsprechung in der Untersuchung kleiner organischer Moleküle hat. Seit der Geburtsstunde der modernen Polymerchemie vor 100 Jahren wetteiferten Polymerchemiker mit Erfindungsreichtum, um immer zahlreichere und komplexere Polymertopologien herzustellen. Unter ihnen stechen die käfigförmigen Polymere durch ihre polyzyklische Architektur und das Fehlen von Polymerkettenenden hervor. Obwohl sich die Synthese von käfigförmigen Polymeren als besonders langwierig erwies und eine große Herausforderung für Polymerchemiker darstellte, wurden in den letzten 20 Jahren mehrere Synthesestrategien mit ihren eigenen Stärken und Schwächen entwickelt. Mit einer bemerkenswerten Ausnahme war die topologische Umsetzung von azyklischen Polymervorstufen besonders verwendet. Die übliche Komplexität dieser Vorstufen, die häufige Notwendigkeit in hoher Verdünnung zu arbeiten, und die oftmals geringen Ausbeuten des topologischen Konversionsschrittes machten es jedoch schwierig, käfigförmige Polymere jenseits des 100-Milligramm-Maßstabs und in reproduzierbarer Weise zu erhalten.

Vor diesem Hintergrund wurde im Rahmen dieser Arbeit eine neue Methodik zur Herstellung käfigförmiger Polymere konzipiert und entwickelt. Ausgehend von sternförmigen Polymervorstufen wurde die topologische Umwandlung durch $(AB)_n$ *n*-Oligomerisierung von *n* bifunktionellen Endgruppen, die an jedem Arm des Polymers vorhanden sind, in eine chemisch inerte makrozyklische Struktur vorgesehen. Dazu wurde die Chemie der $(AB)_n$ *n*-Oligomerisierung sorgfältig ausgewählt, um eine Liste strenger Voraussetzungen zu erfüllen, nämlich u.a. Irreversibilität der Reaktion, hoher Umsatz, hohe kinetische Rate und eine mögliche Initiation durch einen spezifischen Auslöser.Als Ergebnis wurde die CuAAC (Kupfer-katalysierte Alkin-Azid-Cycloaddition) Click-Chemie gewählt und die Synthesen mehrerer potentieller AB-Endgruppen untersucht. Die ersten Bemühungen zur Herstellung sternförmiger Polymervorstufen konzentrierten sich auf die Synthesen sternförmiger RAFT (Reversible Additions-Fragmentierungs Kettenübertragungspolymerisation)-Agenzien, welche direkt bifunktionelle Endgruppen tragen sollten. Die Synthese von käfigförmigen Polymeren sollte dann in nur zwei Schritten erfolgen, nämlich der RAFT-Polymerisation selbst und der topologischen Umwandlung. Die Synthese der endfunktionalisierten sternförmigen

RAFT-Agenzien erwies sich jedoch als problematisch und die anschließende Polymerisation litt unter Nebenreaktionen zwischen den Kettenübertragungsagenzien und den Endgruppenfunktionalitäten. Als Konsequenz sollten die sternförmigen Polymere durch protonenkatalysierte ROP (ringöffnende Polymerisation) von ε-Caprolacton aus multifunktionalen Initiatoren gewonnen werden. Der Kerngedanke dieser Arbeit, nämlich die topologische Umwandlung sternförmiger Polymere in Polymerkäfige durch $(AB)_n$-*n*-Oligomerisierung, wurde indes durch die Existenz von D_{2h}-[3*4*]Triazolophan-Makrozyklen in der wissenschaftlichen Literatur stark verstärkt. Während D_{2h}-[3*4*]Triazolophane streng genommen nicht durch $(AB)_4$-Tetramerisierung erhalten werden können, besitzt das bis dahin literaturunbekannte D_{4h}-Regioisomer alle Voraussetzungen, um aus *m*-Azidoethinylbenzol-Einheiten erhalten zu werden. So wurde ein wohldefiniertes vierarmiges sternförmiges Poly(ε-caprolacton) synthetisiert und quantitativ mit einem *m*-Azidoethynylbenzol-Carbonsäurederivat endfunktionalisiert. Von diesem Punkt aus wurde eine erste Synthese von käfigförmigem Polymer im 50-Milligramm-Maßstab unter Hochverdünnungsbedingungen erreicht. Ausgehend von diesen Ergebnissen wurde die Kinetik der intramolekularen topologischen Umsetzung durch schrittweise Verkürzung der Reaktionszeit optimiert. Anschließend wurde die Polymerkonzentration schrittweise erhöht, um deren Einfluss auf die unerwünschten intermolekularen Vernetzungsreaktionen zu untersuchen. Nach Abschluss dieser Vorstudien wurde der Einfluss der Polymergröße auf die Syntheseausbeute und die thermomechanischen Eigenschaften der käfigförmigen Polymere eingehend betrachtet. Dazu wurden vier sternförmige Poly(ε-caprolactone) mit unterschiedlichen Molekulargewichten synthetisiert, endfunktionalisiert und im 50-Milligramm-Maßstab in ihre jeweiligen Polymerkäfige überführt. Anschließend wurde die Aufskalierung der topologischen Umsetzung aus einem bekannten Poly(ε-caprolacton) im Semi-Batch-Verfahren untersucht. Von diesem Zeitpunkt an wurde die Robustheit des Verfahrens durch Variation der Beschaffenheit des Polymersubstrats und Erhöhung der topologischen Umsatzausbeute über den Gramm-Maßstab hinaus gestestet, um schließlich eine konkrete Anwendung für käfigförmige Polymermaterialien ins Auge zu fassen. So wurde ein käfigförmiges Poly(ethylenoxid)-Polymer im 1,5-Gramm-Maßstab hergestellt und im Rahmen einer Kooperation auf seine Eignung als Polymerelektrolyt für Lithium-Ionen-Batterien untersucht. Dank der besonderen Topologie des Polymers konnten rein amorphe Poly(ethylenoxid)-Elektrolyte mit minimalen Lithium-Salz-Beladungsverhältnissen erhalten werden. Da die Ionenleitfähigkeit durch das Vorhandensein nicht-kristalliner Phasen innerhalb

des Polymergitters stark begünstigt wird, übertrafen die käfigförmigen Polymerelektrolyte die für Standard-Poly(ethylenoxid)-Elektrolyte bekannten Werte der Ionenleitfähigkeit unterhalb ihrer Kristallisationstemperatur deutlich.

Table of Contents

1 Introduction

Since Staudinger published his first seminal work on macromolecules in 1920,[1] many generations of researchers have dedicated their efforts to polymer chemistry and allowed over the past 100 years the creation of a wide choice of complex and precise macromolecular architectures.[2,3] Among them, cyclic topologies benefit from their absence of terminal chains and of their singular structure to minimize their hydrodynamic volume in solution, increase their chemical stability against degradation, limit their conformations that they can adopt as well as reduce their propensity to crystallize in bulk compared to their acyclic counterparts. In this context, *cage*-shaped polymers – consisting of at least two cyclic chains covalently interconnected through two junction points – hold a very special place among them, although their synthesis turned out to constitute a worthy challenge for polymer chemists over the past two decades. Nonetheless, the design of *cage*-shaped architectures is not restricted to polymer science and nano-capsules made out of gold,[4] silica,[5] DNA,[6,7] protein,[8,9,10,11] or discrete metal organic framework (MOF)[12,13] nanostructures were *inter alia* reported and their potential applications as drug carrier, supramolecular catalytic flasks, host-guest recognition analytic devices as well as molecular machines have aroused the interest in a broad range of scientific disciplines.[14,15] Despite this apparent diversity however, only few synthetic methodologies exist that allow the efficient synthesis of polymeric cage architectures.

Hence, novel routes for the generation of *cage*-shaped polymers by means of topological conversion of *star*-shaped polymers will be investigated in the current thesis. In order to enable a better understanding of the present work, the following theoretical background will focus on a) a brief introduction on key concepts relative to polymer chemistry; b) an overview of the past advances that enabled the synthesis of macrocyclic molecules and cyclic polymers; c) an in-depth discussion on the current state-of-art of the *cage*-shaped polymer syntheses and applications. At last, the driving motivation leading to this work will be stated and the key aspects of the present approach to produce polymer cages provided.

2 Theoretical Background

2.1 General Introduction to Polymer Science

2.1.1 Polymer topology

The study, design, and production of polymeric materials with specific physical properties is one of the primordial objectives of polymer science. Although the polymer composition is of great importance, the influence of topology on the physical properties is not to be neglected. For example, poly(ethylene) – the most produced polymer worldwide – is available with a wide range of mechanical properties fitting each specific application.[16,17] These properties depend on the degree of crystallinity present in the polymer and therefore on the abundance of branching within their structure. Thus, crystalline high-density poly(ethylene)s consisting mostly of linear polymer chains result to rigid materials while amorphous low-density poly(ethylene)s display softer properties and are used when flexibility is needed. In a similar manner, most polymers produced at the industrial scale are obtained by free radical polymerization and usually possess a certain branching degree. This branching results from high radical concentration leading to termination and chain transfers reactions. In particular, the hydrogen abstractions of the propagating radical to random parts of the polymer chains lead to the transfer of the propagating unit along the polymer chain.[18] By tuning the branching ratio to follow exponential trends, hyperbranched polymer can even be obtained.[19]

By further variation of the polymerization and post-polymerization modification procedures, more complex architectures can be achieved.[20] **(Scheme 1)** For instance, lateral polymer chains can be incorporated by several grafting methods, yielding so-called graft polymers.[21] Thus, previously synthesized polymer chains can be ‘’grafted onto’’ the central polymer by direct trapping of the propagating chains onto functionalized polymers or by post-polymerization modification methods, ‘’grafted from’’ by initiating secondary polymerization from a preexistent polymer chain, or finally ‘’grafted through’’ by direct polymerization of macromonomers bearing large side chains. By analogy, polymer stars can be obtained by a ‘’core-first’’ method, which involves the polymerization from a multivalent initiator, or by an ‘’arm-first’’ method, using the aggregation of multiple polymer chains by multivalent small molecular cores.[22] In case of interconnected polymer structures,

tridimensional polymer networks can be formed, and thus changing drastically the mechanical properties of the materials compared to the parent, linear polymers.

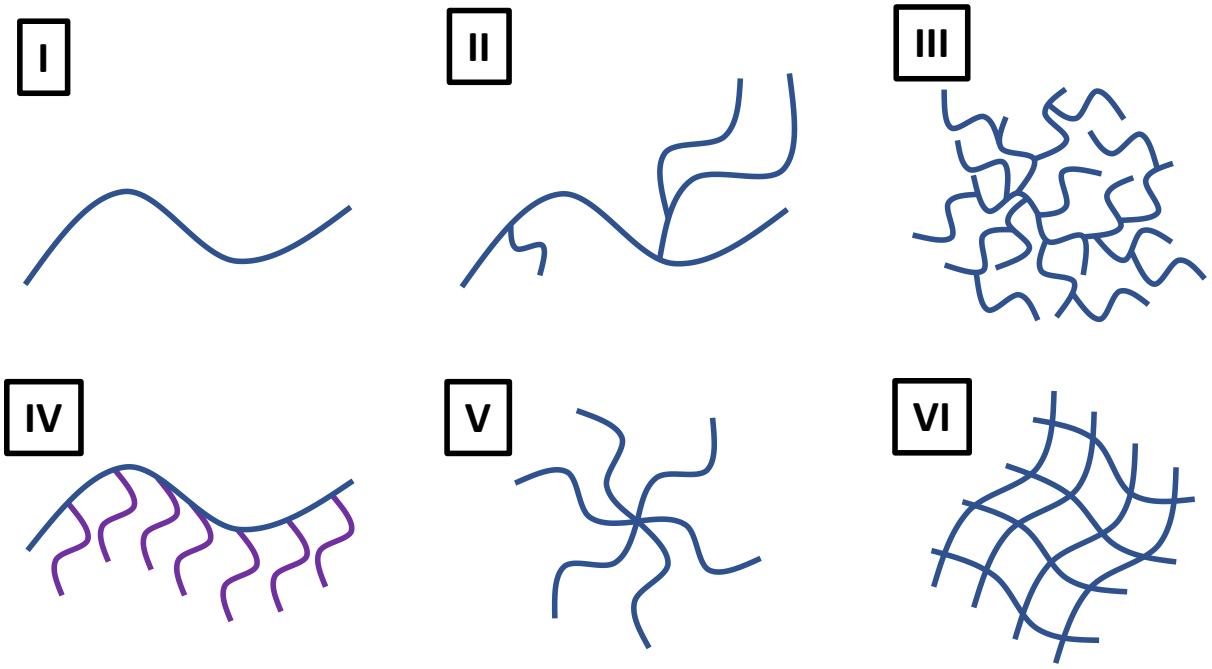

Scheme 1: Common linear (**I**), branched (**II**), hyperbranched (**III**), graft (**IV**), star (**V**) and network (**VI**) polymer topologies.

2.1.2 Living Chain-growth Polymerizations

In order to be able to produce highly complex polymer architectures, precise and defect-free polymerization methodologies are fundamental.[23] In this regards, well-defined polymers can be obtained by living chain-growth polymerization or polymerization methods approaching this behavior, *inter alia* the living anionic and cationic polymerizations as well as the reversible-deactivation radical polymerizations. To be considered ‘’living’’, a chain-growth polymerization must thoroughly fulfill a specific list of criteria. Foremost, living polymerizations are characterized by a strict absence of side reactions, which can occur during the polymerization combined with the simultaneous initiation and growth of all chains. **(Scheme 2, I–III)** Thus, in absence of termination or chain transfer reactions, all propagating chains remain active even when all monomers are consumed, yielding ideally dispersity below 1.05 and following a monodisperse Gaussian distribution focused on a precise degree of polymerization (DP) as well as nearly defect-free polymer structure with high end-group fidelity. **(Scheme 2, IV)** The formation of block copolymers by subsequent addition of distinct

monomer(s) on living chains constitute another major feature brought by living polymerizations.

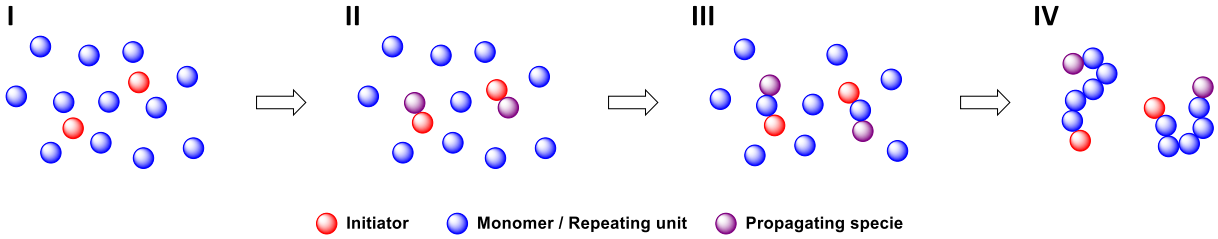

Scheme 2: Schematic view of a living chain-growth polymerization.

The anionic polymerization of vinyl monomers bearing electron-withdrawing groups is usually considered as the first[24] and closest example of a flawless living polymerization at the cost of a low functional group and impurity tolerance.[25,26] Famously, the anionic polymerization of styrene can be initiated by the combination of alkali metal and naphthalene can also lead to linear polymer bearing two propagating chains located at both chain ends. In these conditions, alkali metal and naphthalene are first reacted together to form reactive alkali naphthalenide radical anions, which can subsequently react by single electron transfer with vinyl monomers. Once the radical anions formed on the monomer, the formed unstable radicals immediately dimerize, forming telechelic anionic propagating chains. **(Scheme 3, I)** Alternatively, the nucleophilic addition of a strong organometallic base like *n*-butyllithium on a first styrene molecule can be used to directly initiate the propagating anion. **(Scheme 3, II)**

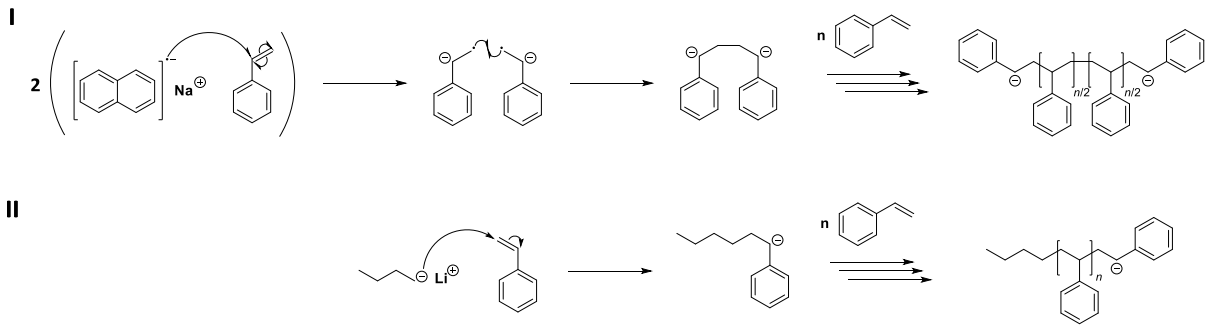

Scheme 3: Mechanisms of styrene living anionic polymerization initiated by alkali naphthalenide (**I**) or *n*-butyllithium (**II**).

In addition, the anionic (AROP) and cationic (CROP) ring-opening polymerizations can also display under appropriate conditions some characteristics of living polymerizations.[27] Unlike the polymerization techniques mentioned above, the actual nature and number of chemical bonds in the polymers does not vary from the monomers. Therefore, the ring-opening

polymerizations are thermodynamically-driven by the release of ring-strain. Hence, AROPs are initiated by formation of a propagating nucleophilic anion in presence of cyclic monomers bearing an electrophile functional group (i.e. ester, amide, carbonate). As each step yields the next propagating anion, AROP results in strictly linear polymers with narrow dispersity and does not terminate in absence of protic impurities. **(Scheme 4, I)** On the contrary, CROPs require Brønsted or Lewis acids as catalysts to enhance the reactivity of the monomer electrophile group. **(Scheme 4, II)**

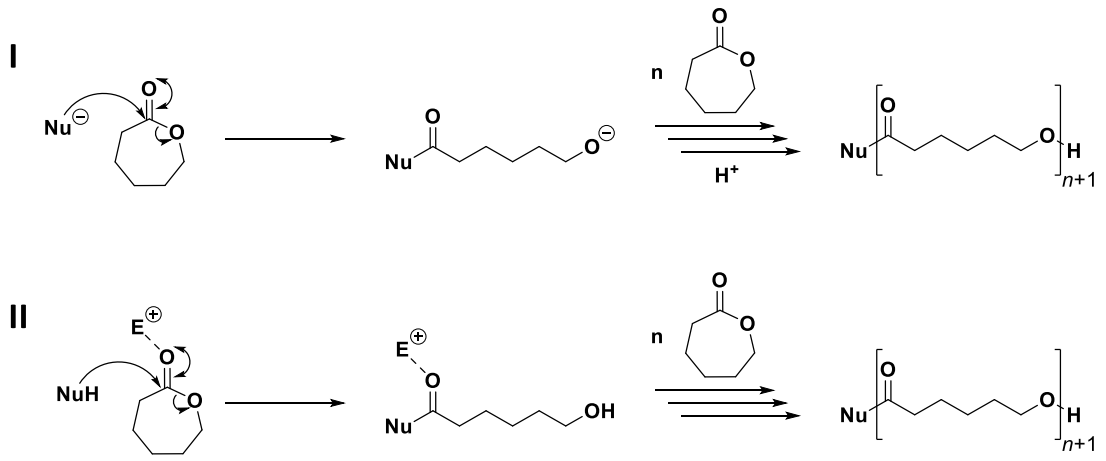

Scheme 4: Examples of anionic and cationic ring-opening polymerization mechanisms using ε-caprolactone as monomer.

At last, cationic[28] and radical[29] polymerizations can also exhibit – in some extent – some living character. Although living cationic polymerizations will not be further discussed herein, a closer look will be taken at living radical polymerization methods. Unlike free radical polymerization (FRP), the group of the reversible-deactivation radical polymerizations (RDRP) allow radical polymerizations to acquire living character by lowering the instantaneous radical concentration in the polymerization medium. To do so, two distinct strategies based on reversible equilibrium with a dormant species (NMP, ATRP) or a chain-transfer agent (RAFT) were developed during the two last decades of the 20th century.

The oldest of the current three main RDRPs – the nitroxide mediated polymerization (NMP)[30] – was developed by Rizzardo, Moad and Solomon in the late 1980s[31] by taking advantage of the unreactive nature of nitroxide radicals to induce a thermal equilibrium between propagating radicals and dormant species. **(Scheme 5, I)** Unlike typical radicals, neither hydrogen abstraction, polymerization initiation, nor dimerization occurs with nitroxide radicals due to the delocalization of the unpaired electron within their π-orbitals located between the oxygen and

nitrogen atoms. Even so, nitroxide radicals conserve the capacity to pair with unstable carbon-centered radicals by forming alkoxyamine groups. Besides the reaction temperature, the alkoxyamine recombination-dissociation equilibrium is influenced by the monomers reactivity and nitroxide structures. Thus, the chemical structure of the nitroxide and more precisely the electronic and steric hindrance effects induced by its substituents define the equilibrium constant of a polymerization at given monomers and temperature. Thus, commercially available nitroxide radicals like TEMPO can efficiently control the polymerization of styrenic monomers at temperatures usually above 100 °C. On the contrary, acyclic nitroxide radicals produce less stable alkoxyamine and therefore allow the use of lower polymerization temperatures as well as other monomers like acrylic esters or acrylamides. Nevertheless, at the exception of the commercially available TEMPO and of some of its derivatives, the synthesis of most of the complex nitroxide radicals remains challenging and time consuming. At last, as TEMPO compatibility with monomers and functional group tolerance at high polymerization temperatures is restricted, the industrial application of NMP remains detrimental in comparison to the other two RDRP techniques and more generally to all FRP methods.

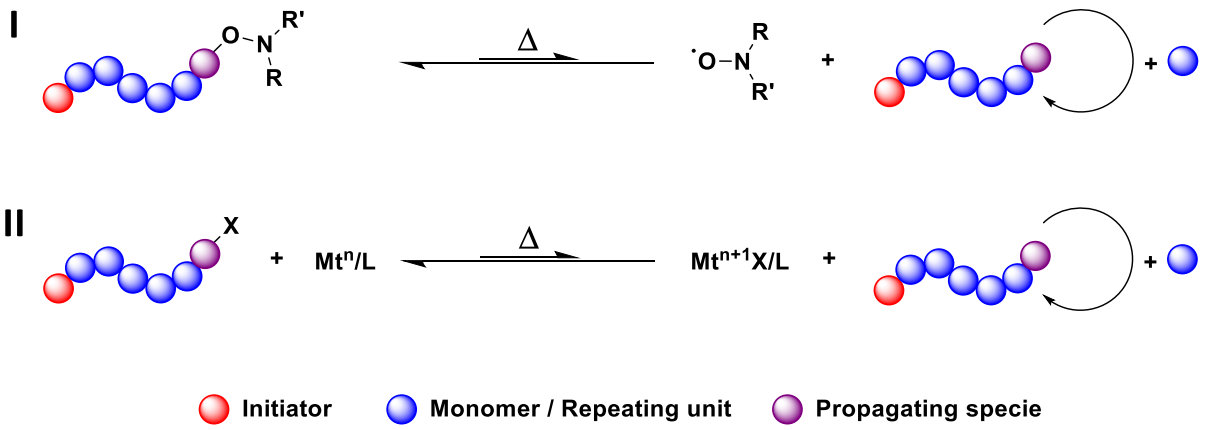

Scheme 5: Overview of the (**I**) NMP and (**II**) ATRP mechanisms, including the equilibrium taking place between propagating and dormant species.

On the contrary, the atom transfer radical polymerization (ATRP)[32] was independently and simultaneously reported by Sawamoto[33] and Matyjaszewski[34] in 1995. Similar to NMP, its mechanism is based on an equilibrium taking place between a predominant dormant species and a propagating radical. **(Scheme 5, II)** Thus, the dormant species, usually an alkyl halide, can be activated by a transition metal complex *via* reversible one-electron transfer mechanism with no need of an additional radical source. Moreover, as each alkyl halide has equal probability to react in the equilibrium, each chain can grow in parallel while keeping a low

instantaneous radical concentration in the medium. Although many transition metals are available as ATRP catalysts, copper(I) remains by far the most popular one due to its ease of use combined with its large functional group tolerance. Furthermore, the controlled polymerization of a wide range of monomers is made possible by simple variation of the transition metal ligand, making ATRP a very versatile, easy-to-use, and inexpressive technique for the synthesis of well-defined polymers. However, no polymerization technique is exempted of drawbacks. Thus, in the present case, the transition metal catalyst often needs to be removed post-polymerization either due to the inherent metal toxicity or due to the dyeing of the polymer, depending on the final application.

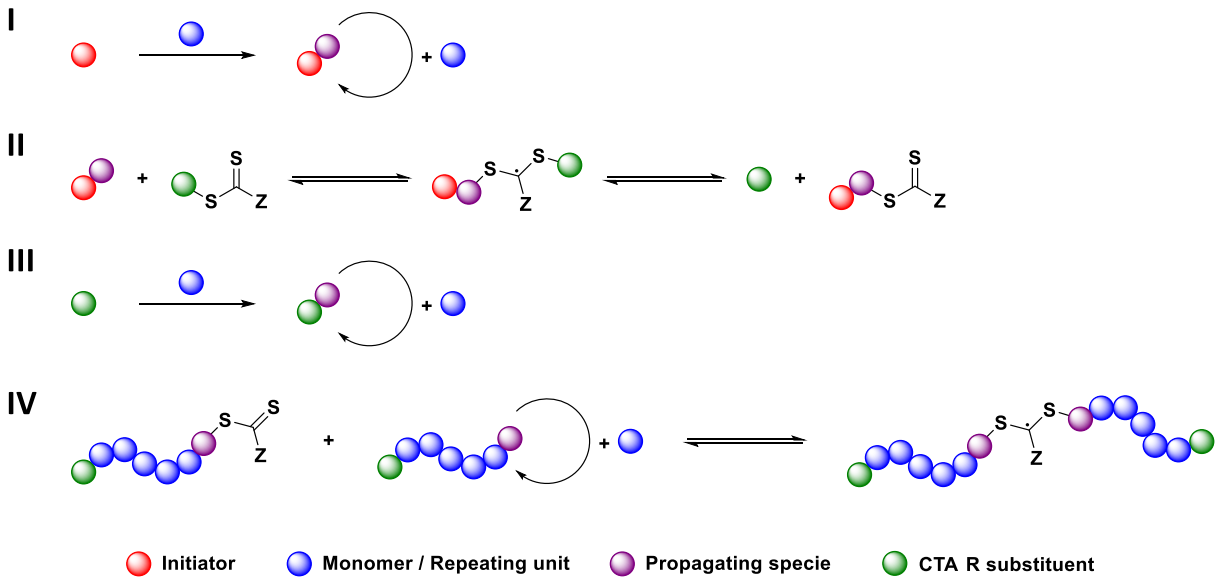

Scheme 6: Simplified mechanism of RAFT polymerization, consisting in (**I**) Initiation and propagation of polymer chains from an external radical source; (**II**) RAFT pre-equilibrium; (**III**) Re-initiation and propagation of new radical species issued from the RAFT pre-equilibrium; (**IV**) RAFT main equilibrium and further polymerization.

Finally, the last and most recent of the three main RDRP methods, the Reversible Addition Fragmentation chain Transfer (RAFT), was reported in the late 1990s.[35] Unlike NMP and ATRP techniques, which are based on a reversible equilibrium between a dormant and an active species, RAFT allows a substantial reduction of the radical initiator equivalent by a factor of at least 10. Indeed, the very fast equilibrium taking place between the few propagating chains and the chain-transfer agents (CTA) allows a simultaneous growth of all polymer chains present in the polymerization medium.[36] In term of mechanism, the RAFT process can be subdivided in four distinct steps. Foremost, the initiation and propagation of a small amount of polymer chains occurs from an external radical source (usually 5 to 10 mol% to the CTA). **(Scheme 6, I)** Then,

a pre-equilibrium is almost instantaneously established by capture of the propagating radicals to the CTA, leading to the random release of one of the CTA leaving substituents. **(Scheme 6, II)** Subsequently, the radical species released from the RAFT pre-equilibrium can further reinitiate chain-growth polymerization. **(Scheme 6, III)** From this point, all polymer chains are allowed to virtually grow simultaneously as the CTA exchange kinetic remains faster than the propagation rate. **(Scheme 6, IV)** Among its qualities, the RAFT process allows the preparation of a large range of polymers featuring low dispersity in a broad temperature range by adapting the CTA structure. Additionally, the high end-group fidelity and high tolerance to functional groups, water and impurities makes RAFT a versatile and reliable polymerization method in many application domains.[37]

2.2 From Macrocycles to Cyclic Polymers

Since the first postulate of the cyclic nature of benzene by Kekulé in 1865,[38,39] chemists have never stopped marveling at the extremely rich architectural diversity that cyclic – and later macrocyclic – molecules could offer. Hence, the first synthesis and isolation of covalently or supramolecularly bonded macrocycles were progressively reported from the end of the 19th century to nowadays, each possessing their own set of properties and possible applications in host-guest supramolecular chemistry as well as in materials science.[40] Despite this, the International Union of Pure and Applied Chemistry (IUPAC) does not actually give any quantitative description of the ‘’macrocycle’’ terminology but rather describes them simply as ‘’cyclic macromolecules or macromolecular cyclic portions of a macromolecule’’.[41] However, cyclic molecules contending at least 10–15 atoms participating to the cycle are commonly described as macrocycles in the scientific literature. While the earliest reports of macrocycle synthesis were derived from thermodynamically-driven reactions, most common and recent synthesis strategies rely on favoring the kinetic products by working in highly diluted concentrations. In this regard, it is worthwhile to take a closer look at a non-exhaustive series of named and unnamed macrocyclic structures that have marked their research field back at their times in order to better follow the evolution of macrocycles to cyclic polymers.

2.2.1 Synthesis of Macrocyclic Molecules

Among most prominent thermodynamically-driven macrocyclic products, cyclodextrins consist in a series of cyclic oligosaccharides industrially produced by enzymatic intramolecular trans-glycosylation reactions from helical amylose (i.e. starch partial constituent, poly[(1→4)-*α*-*D*-glucopyranan]).[42] While cyclodextrins were discovered in the late 19th century[43] and formally characterized in the 1940s by X-ray crystallography,[44] their use at large scale in the pharma-, food-, textile- and cosmetic industrial processes was only initiated from the second half of the 20th century.[45,46] The three main most abundant cyclodextrins constituted of six, seven and eight glucose units – namely α-, β-, and γ-cyclodextrins – respectively are well-known to possess their own set of physicochemical and biological properties while keeping a low oral toxicity.[47] **(Scheme 7)** In this regard, taking advantage of the lipophilic character of their conic internal cavity coupled to their more hydrophilic outer surface, supramolecular host-guest interactions of various guests with different polarity and size were reported and used *inter alia* for drug delivery applications and analytical methodologies

by enhancing the guest chemical stability and solubility.[48] In particular, their cavity diameter is known to be directly related to the cyclodextrin size and therefore vary from a range of 4.7-5.3 Å for α-cyclodextrin, to 6.0–6.5 Å for β-cyclodextrin, and finally 7.5–8.3 Å for γ-cyclodextrin.[49] Furthermore, cyclodextrins own the possibility to be functionalized three times per glucose unit at each of their primary/secondary alcohol, yielding 18 to 24 substitutions from α-cyclodextrin to γ-cyclodextrin.

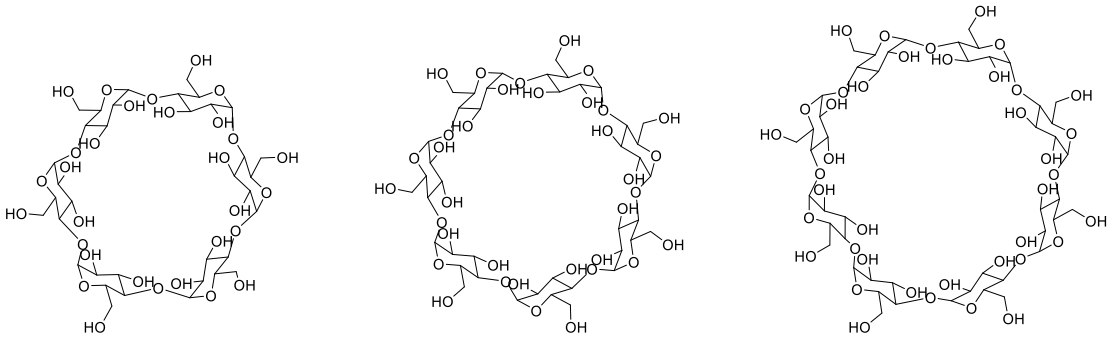

Scheme 7: Structures of α-, β-, and γ-cyclodextrins constituted of six, seven and eight glucose units, respectively.

Apart from cyclodextrins, a series of thermodynamically-driven macrocyclic products, which did not reach the same industrial success, can be mentioned. Thus, under the term of calix[n]arenes[50] is gathered a family of *para*-substituted phenols condensed at their *ortho*-positions by formaldehyde units in basic condition. While the existence of calix[n]arenes was reported since the 1940s[51,52] and the industrial interest for related Bakelite polymer,[53] their structures remained mainly unambiguous until the 1980-90s and Gutsche's work.[54] Etymologically, the calix[n]arenes took their names from the singular cup shape (*calix* meaning cup in Latin) adopted by the iconic calix[4]arene **(Scheme 8, I)** obtained from the condensation of four para-(*tert*-butyl)phenol and formaldehyde units. Although the permanent *cup*-shaped conformation results from the four *tert*-butyl groups bulkiness, larger calix[6]arenes and calix[8]arenes do not usually share the same conformation. In general, calix[n]arenes are synthetized in a single step in good yields up to the multigram-scale and without any prior dilution requirement. Nonetheless, while calix[4]arenes tend to be thermodynamically favored, calix[6]arenes and calix[8]arenes kinetical products are synthetized by further optimizing the temperature and the reaction time. In term of applications, calix[4]arenes are particularly used in supramolecular chemistry to act as an efficient host to encapsulate a wide range of apolar molecular guests in polar solvents due to their lipophilic internal cavity.[55] By further

functionalizing the phenol positions, larger structures made from calix[n]arene dimers were later transformed into large spherical cavities enabling thermal host-guest equilibrium (i.e. hemicarcerand) or irreversible (i.e. carcerand) encapsulation of large molecular guests[56,57] next to miscellaneous spherand[58,59] and other cavitand[60,61] macrostructures. In a similar manner, veratrole alcohol trimerization by acid-catalyzed condensation leading to cyclotriveratrylene macrostructures **(Scheme 8, II)** were formally characterized in 1965.[62] In analogy to the (hemi)carcerand carriers made out of calix[n]arenes dimers, cyclotriveratrylene dimerization led to similar macromolecular cavities (i.e. (hemi)cryptophane) enabling host-guest supramolecular chemistry.[63,64] Furthermore, the condensation of glycolurils (usually five to ten units) and formaldehyde molecules taking place under acidic conditions and yielding pumpkin-shaped (i.e. cucurbitaceae) macrocycles, named accordingly cucurbit[n]urils. While their existences was first reported in 1905[65], the cucurbit[n]uril structures were only formally established in 1981[66] and led to a large range of host-guest supramolecular chemistry applications.[67] Further examples of *cup*-shaped macrocyclic structures were also published. Thus, resorcinol and pyrogallol condensation with aldehydes in acidic condition led to the respective formation of resorc[4]arenes[68] **(Scheme 8, III)** and pyrogallol[4]arenes **(Scheme 8, IV)** and were in both cases further employed as supramolecular carriers for the complexation of guests by the formation of large hydrogen-bonded molecular capsules.[69,70,71,72]

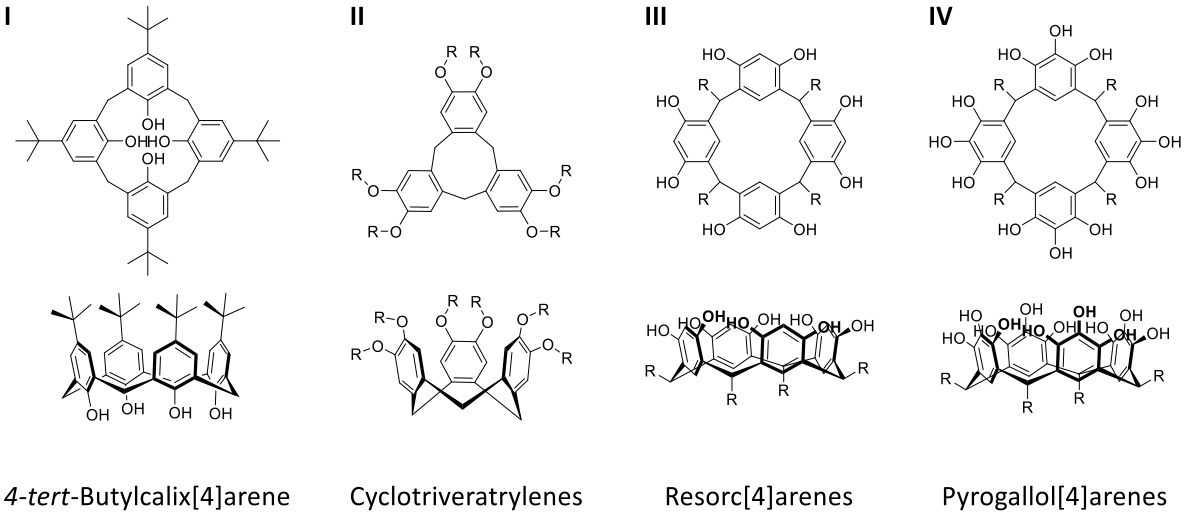

Scheme 8: A series of thermodynamically-favored macrocyclic products.

Unlike previous examples, most recent macrocycles are not thermodynamically favored and therefore necessitate specific conditions during their synthesis to yield the desired products. Thus, cyclic ethylene oxide oligomers – commonly known as crown ethers due to the

resemblance their conformations share with crowns once complexed to cations – are a family of multidentate chelating ligands developed in the 1960s, notably by C. J. Pedersen, which display high and size-selective complexation equilibriums, notoriously for alkali metal cations in low polar solvents.[73,74] **(Scheme 9, I–III)** Crown ethers are cataloged according to the macrocycle size and by the oxygen atom number present in the cycle. Thus, the most common 12-crown-4, 15-crown-5 and 18-crown-6 ethers are known to preferably bind respectively lithium, sodium and potassium cations by matching their effective ionic radius with their cavity size.[75] However, the structural diversity of crown ether-like structures does not limit itself to these examples and further substitution of oxygen atoms by other heteroatoms and variation of the structures led to many singular macrocycles. For instance, ethylene imine oligomers – referred as aza-crown ethers – chelating abilities were recognized for their transition metal complexation abilities.[76] Further enhancement of binding constants and selectivity were achieved by having resort to tridimensional macromolecules as proposed by J. M. Lehn and J. P. Sauvage in 1967.[77,78] Taking their name from the metaphor of an ion trapped in a crypt, these cryptands expanded the ion recognition toolbox by obtaining higher selectivity and higher chelating constants than their two-dimensional crown ether counterparts could ever offer.[79] In particular, the [2.2.2]-cryptand **(Scheme 9, IV)** – referring to the number of oxygens present on each chain – was found to outmatch 18-crown-6 for the complexation of potassium cations in terms of selectively and binding constants by several orders of magnitude. In a more general way, cryptands were widely reported to efficiently coordinate not only cations but also anions by producing amine-rich cryptands at low pH.[80]

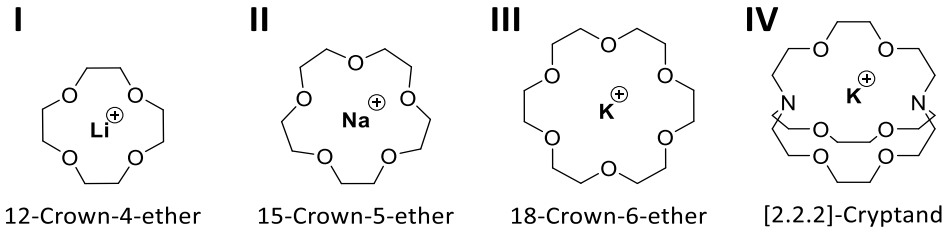

Scheme 9: Most common crown ethers and cryptand known to selectively bind lithium, sodium and potassium cations, respectively.

On the contrary, the synthesis of cyclocholate[81] and cyclocholamide[82] macrocycles in high dilution and sharing steroid oligomers as linear building blocks were successfully employed to serve as supramolecular hosts for ionic or polar guests.[83] In this regard, the rigid steroid structure strongly restrains the macrostructure conformations, leading to the formation of outer lipophilic and internal hydrophilic parts created by the presence of the steroidal polar

substituents directed towards the cavity center. Finally, in terms of advantages, the use of cholic acid and more generally of any steroid bile acids – secreted from the liver of vertebrate animals for the digestion of lipides – allow a high availability and a low cost of enantiomerically pure starting materials. Finally, a large variety of artificial conjugated macrocycles like annulenes or bearing benzene, acetylene, thiophene, pyridine or even porphyrin patterns greatly enriched the conjugated macrocycles diversity in the last decades thanks to their unique mechanical, optical and electronic properties.[84,85,86,87]

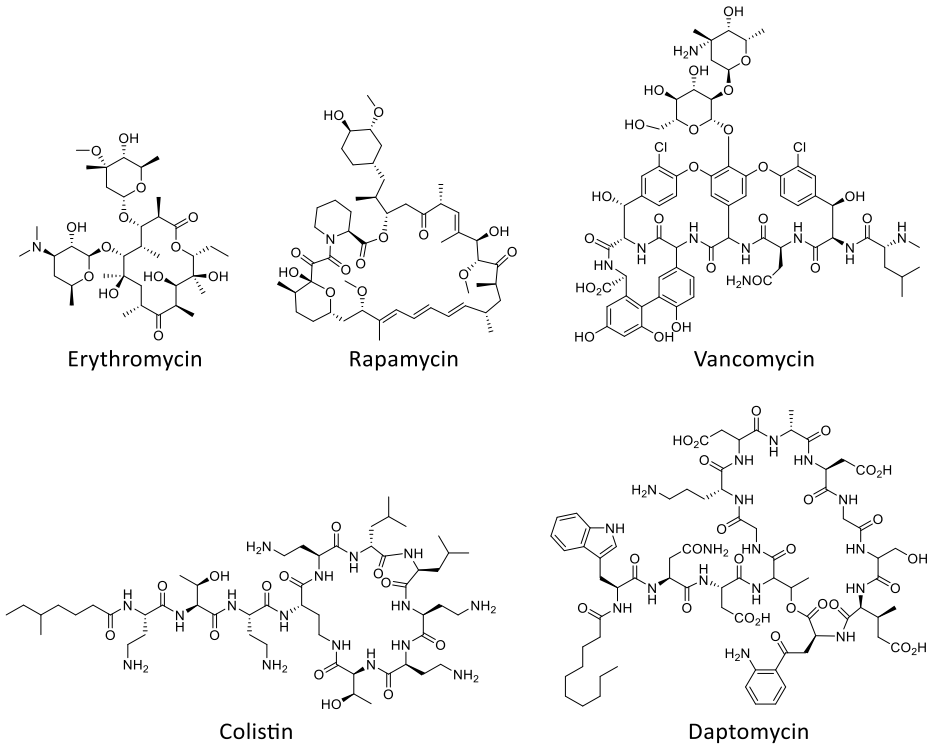

Scheme 10: Examples of macrocyclic molecules isolated from bacteria or fungi, that exhibit antibiotic properties.

In addition of being worth of interest for materials science and supramolecular chemistry,[88] the study of cyclic macromolecules also shines when their properties are devoted to biological processes like the fundamental roles of porphyrin derivatives *inter alia* for the photosynthesis (i.e. chlorophylls) and blood oxygen transport (i.e. hemes)[89] as well as for medicals applications as drug delivery carriers or active substances.[90,91,92] In this sense, peptides hold a very particular place and, compared to their linear counterparts, cyclic peptides can count on a higher conformal preorganization while keeping a certain flexibility, which allow a higher selectivity and host-guest binding constant with the biological target in living organisms without strongly affecting their solubility in water.[93] Furthermore, their cyclic topology

reduces the overall polarity of the macromolecule, allowing a better distribution of the medication though cell membrane permittivity in the body, as well as increasing their chemical stability in biological organisms and expanding the lifetime of active substance *in vivo*.[94] Thus, several natural occurring cyclic peptides isolated from bacteria or fungi were reported to exhibit antibiotic properties (erythromycin,[95] rapamycin,[96] vancomycin,[97] colistin,[98] daptomycin[99]) **(Scheme 10)** but also to act as immunosuppressive (cyclosporin[100]), anti-cancer (epothilone,[101] dactinomycin[102]) and antifungal drugs (caspofungin[103]), or on the contrary as deadly toxins. For instance, some cyclic cyanotoxins (microcystins,[104] nodularins,[105]), **(Scheme 11)** which are produced by cyanobacteria known for the blue-green tides observed time to time in oceans, are known for their high toxicity towards humans and more generally for all animals.[106] Additionally, in recent years several synthetic macrocyclic drugs were produced by biochemical peptide synthesis to offer synthetic substitutes to biological counterparts.[107,108] For instance, some artificial cyclic peptides (octreotide,[109] lanreotide,[110] pasireotide[111]) were synthetized and investigated as substitutes for somatostatin growth hormone, which further acts in the regulation of most hormones in the human body.[112]

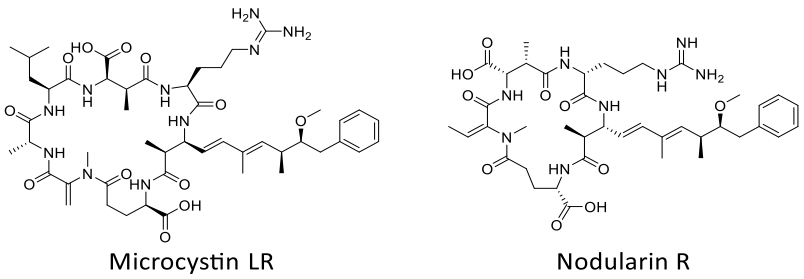

Scheme 11: Microcystin LR and Nodularin R; two highly toxic macrocyclic cytotoxins secreted by cyanobacteria known for the blue-green tides.

Compared to the extraction from living organisms and to the biochemical peptide synthesis, the examples of cyclic non-repetitive peptide-like structures with biological active motifs obtained by chemical synthesis suffered from low yields, high time- and resource-investment as well as from the necessity to perform the cyclization step in high dilution conditions to avoid unwanted oligomerization reactions. Despite the high synthetical challenges, several reports of cyclization of peptide-like structures were still published.[113,114] By analogy with the peptide structure, most common examples involved the formation of amide bonds (peptide coupling) or ester bonds (macro-lactonization). However, both reactions cannot be simply achieved in mild conditions without former chemical activation and therefore require coupling agents to mimic the enzymatic processes taking place in the ribosomes of the living cells. In this sense, several

known ester and amide coupling procedures, most of which exhibit accurate toxicity for living organisms, were employed for the cyclization of linear peptides. Thus, the Mitsunobu reaction[115,116,117] as well as other miscellaneous EDC/HOBt,[118,119] BOP,[120,121,122] DPPA[123,124] and PFP[125,126] coupling agents were employed for this purpose. While most common approaches mimic the peptide coupling by processing though intramolecular amidation or esterification, the use of more exotic chemistry was also abundantly reported. For instance, the reductive amination, which is also widely employed in industrial drug synthesis processes, was used in this precise purpose.[127,128] Furthermore, reports of intramolecular bimolecular (S_N2)[129,130,131] and aromatic (S_NAr)[132,133,134] nucleophilic substitutions, ring-closing metathesis (RCM),[135,136,137] disulfide bond formation,[138] CuAAC click chemistry,[139] thiol-ene chemistry,[140] and palladium catalyzed cross-coupling reactions (i.e. Stille,[141,142,143] Sonogashira,[144] Heck,[145] Suzuki,[146,147] Buchwald-Hartwig,[148] Tsuji-Trost,[149] Trost's enyne[150]) were also reported.

However, all of the aforementioned cyclization reactions remain unable to induce structural patterns within the macrocycle structures by their own, but rather rely on the synthesis steps coming before or after the cyclization step. For this reason, the use of multicomponent reactions (MCR) as macrocyclization reactions was also deeply investigated.[151] Multicomponent reactions regroup a series of reactions allowing the synthesis of highly diverse and complex products by one pot reactions in high yield and from three or more – possibly simple – precursors. In particular, these reactions are also known to possess an excellent atom economy and more importantly a high substrate selectivity.[152] Among all MCRs, the Ugi four-components reaction (Ugi-4CR) occurring between a primary amine, a carbonyl group (aldehyde or ketone), a carboxylic acid and an isocyanate and in a lesser extent the Passerini three-component reaction (Passerini-3CR) occurring in absence of a primary amine were particularly appreciated for the macrocyclization step.[153,154,155]

2.2.2 Introduction to Cyclic Polymers – Stockmayer's Equation

Considering the wide diversity of macrocyclic structures, it is all natural that polymer chemists also joined their efforts to produce polymers sharing cyclic architectures. Taking up advantages already noticed for non-polymeric macrocycles – namely an increased chemical stability towards degradation due to the lack of chain-ends – additional benefits specific to polymers were observed. Thus, a reduction of the hydrodynamic volume combined with the limitation of

structural conformations were reported to impact the ability of polymers to crystalize or to make chain entanglements. However, cyclic polymers suffer even more from low macrocyclization kinetics than their non-polymeric counterparts as the polymer size increases. While non-thermodynamically favored macrocycle syntheses already suffered from a loss of efficiency and the need for more dilute conditions, the increased spacing of the intramolecular reactive sites within polymers exacerbate that initial issue.

In this regard, according to the Stockmayer's equation published in 1950[156] **(Equation 1)** some observations can be made on the parameters that influence the probability of intramolecular cyclization (P_c) and of intermolecular oligomerization (P_L) for a given linear precursor. In the present equation, the $\langle r^2 \rangle$ term designate the mean-square distance between the two ends groups of the polymer and ν_s the volume within the end-group are reactive while M_n, c and N_A designate the molecular weight, the polymer concentration and the Avogadro's number, respectively.

$$P_c = \left(\frac{3}{2\pi}\right)^{3/2} \cdot \frac{\nu_s}{\langle r^2 \rangle^{3/2}} \quad (\mathbf{1}) \qquad\qquad P_L = \frac{2N_A c}{M_n} \cdot \nu_s \quad (\mathbf{2})$$

Equation 1: Stockmayer's Equation for (**1**) the probability of intramolecular cyclization (P_c) and (**2**) the probability of intermolecular oligomerization (P_L).

In the special case a polymer with defined end-groups is considered, the Stockmayer's equation can bring some qualitative observation of their effects on the probability of intramolecular cyclization (P_c) and the probability of intermolecular cross-linking (P_L). **(Equation 2)**

$$P_c = const. \cdot \frac{1}{\langle r^2 \rangle^{3/2}} \quad (\mathbf{1})' \qquad\qquad P_L = const. \cdot \frac{c}{M} \quad (\mathbf{2})'$$

Equation 2: (**1**)′ and (**2**)′ as simplified version of the Stockmayer's Equations (**1**) and (**2**).

First, it can be noticed from equation **(1)'** that the probability of cyclisation (P_c) is inversely proportional to the mean-square distance between the two ends groups of the polymer, inducing that the bigger the polymer chain will be, the smaller will be the probability of cyclization. Secondly, we can observe from equation **(2)'** that the probability of intermolecular cross-linking (P_L) is proportional to the polymer concentration and inversely proportional to the polymer molecular weight. These observations lead to the conclusion that in order to maximize the cyclization probability, the polymer chain length will have to stay as short as possible while the

concentration of linear polymers will have to remain low to minimize the cross-linking probability.

2.2.3 Cyclic Polymers Synthesis

Historically, the first examples of synthetic cyclic polymers were achieved in the 1960s by ring-chain equilibrium.[157] However, the linear byproducts were highly predominant and cyclic polymers had to be isolated by preparative SEC, typically resulting in anecdotical yields. Nowadays, cyclic polymers can be obtained by two main strategies, namely the topological conversion of telechelic linear polymers and the ring-expansion of a preexisting low-molecular weight macrocycle.[158,159,160] **(Scheme 12, IV)** The topological conversion of telechelic polymers can be further subdivided into closing reactions occurring intramolecularly between two end-groups in high dilution **(Scheme 12, I–III)** or intermolecularly *via* a bimolecular set of polymers bearing each their own set of complementary functionalities (A_2+B_2). **(Scheme 12, I)**

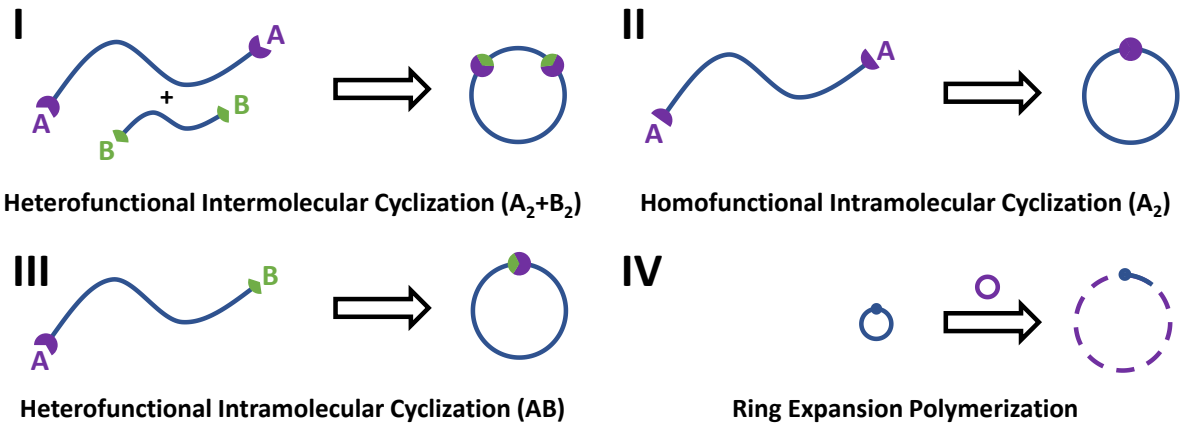

Scheme 12: Overview of the four main strategies used to obtain cyclic polymers.

2.2.3.1 Heterofunctional Intermolecular Cyclization (A_2+B_2)

Among the topological conversion methods, the intermolecular heterofunctional approach (A_2+B_2) suffers from most drawbacks, including the challenge to conserve an equimolar stochiometric ratio between the two telechelic building blocks as well as the difficulty to optimize the reaction kinetics as the intermolecular reactions are needed and need to be avoided at the same time during the reaction to obtain the desired cyclic architecture while avoiding undesired building block oligomerization. **(Scheme 13; Scheme 14, I)**

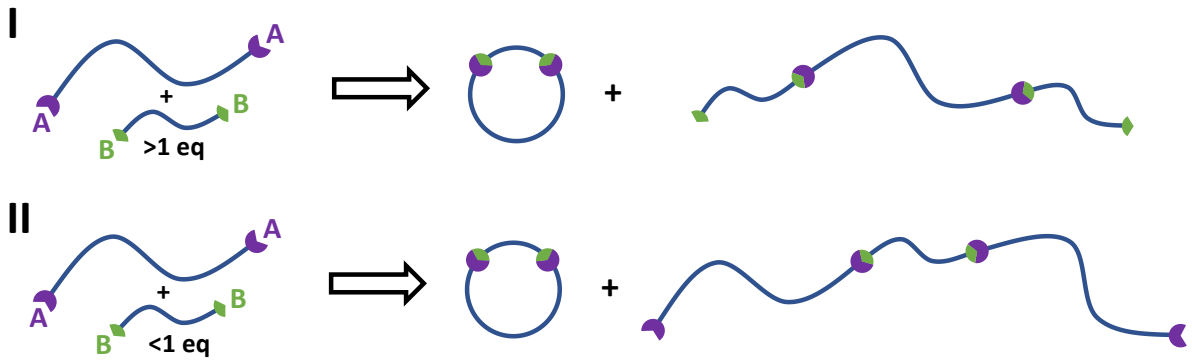

Scheme 13: Representation of both cases of non-equimolar stochiometric ratio issued from a pair of telechelic species.

The first intermolecular cyclizations were achieved in 1980 by quenching of α,ω-dianionic polystyrene (PS) chains – obtained *via* naphthalene-sodium initiated styrene anionic polymerization – with bifunctional halide linkers *via* S_N2 mechanism.[161,162,163] Examples of extremely large cyclic PS polymers bearing molecular weights up to 450 kg mol^{-1} were later reported,[164] however cyclization yields for similar closing strategy remained below 50%.[165] Subsequent yield improvements were achieved by preorganization of the chain-ends prior to the cyclization step. For instance, in direct relation with the preceding examples, the addition of an excess of bifunctional halide linkers followed by a biphasic S_N2 reaction with diaminoalkanes at the toluene-water interface resulted in topological conversion yields above 80%.[166] Further examples of thiol-ene chemistry[167], and activated amide formation[168] were also reported. At last, examples of cyclic poly(tetrahydrofuran) (PTHF)[169] and PS[170] polymers achieved by electrostatic preassembly of acyclic precursors (Electrostatic Self-Assembly and Covalent Fixation, ESA-CF[171,172]) were reported by Tezuka. The ESA-CF based itself on the intermolecular electrostatic preorganization in high dilution of a mixture of macromolecules and low-molecular weight linkers, which create an electrostatic template for the future formation of covalently-linked complex topologies. Once the polymer salt dissolved in a liquid medium, large electrostatic networks are kinetically favored. However, due to the dynamic exchange taking place between the solvated ionic species, the intermolecular connections within the network constantly reorganize themselves. Coupled with the diffusion resulting from the Brownian motion, the charged species progressively diffuse homogenously through the liquid until, below a critical polymer concentration limit, the formation of discreet electrostatic complexes becomes thermodynamically favored. Ultimately, once the equilibrium

is reached, the covalent fixation of the electrostatic templates can be initiated by thermal treatment, yielding the desired topology.

2.2.3.2 Homofunctional Intramolecular Cyclization (A_2)

On the contrary, hetero- and homofunctional intramolecular approaches are by many aspects more efficient to obtain cyclic polymers due to their concentration-independent reaction kinetic, allowing the reduction of their polymer concentration to minimize the undesired intermolecular reaction without consequence on their intramolecular cyclization kinetic. **(Scheme 14, II–III)**

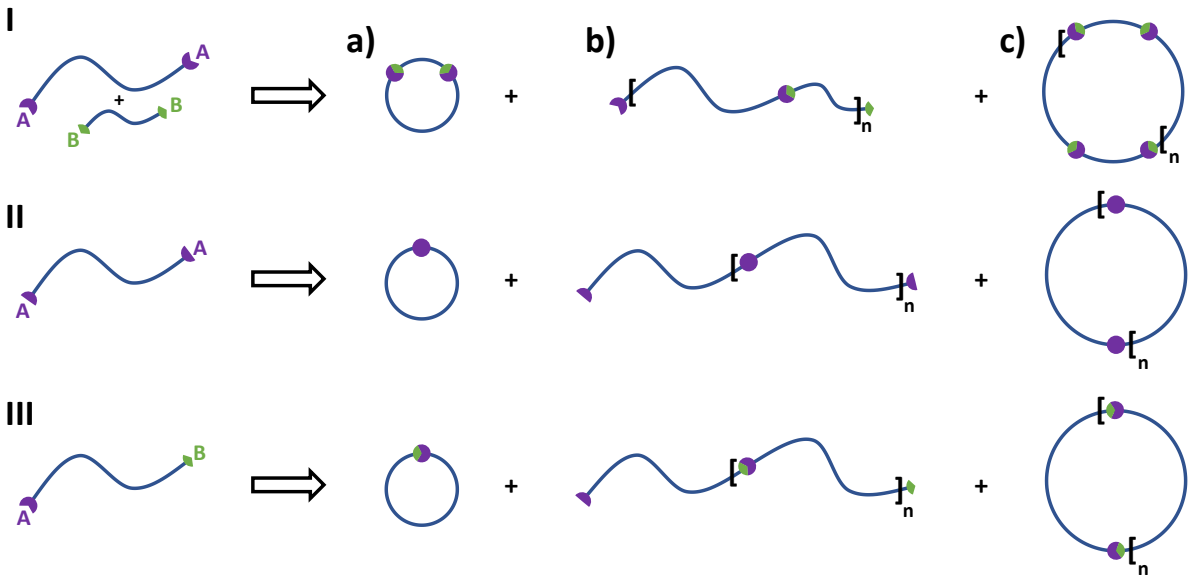

Scheme 14: a) Intramolecular cyclization; **b**) Intermolecular oligomerization; and **c**) Intermolecular oligomerization followed by Intramolecular cyclization products issued from the topological conversion of telechelic polymers.

Both approaches usually require post-polymerization modifications before the topological conversion. However, while the intramolecular heterofunctional approaches (AB) cyclization step was reported with a wide scope of distinct reactions, examples of intramolecular homofunctional cyclization (A_2) remained unusual. Nonetheless, ring-closing metathesis (RCM) of alkene end-functionalized poly(isobutene),[173] PTHF,[174,175] PS[176] and PMA[177] telechelic chains in high dilution condition led to the respective cyclic polymers. Another example involving the formation of disulfide bonds was brought up by Monteiro and coworkers. Starting from difunctional reversible addition-fragmentation chain transfer (RAFT) agents, styrene polymerization and dithiocarbonate cleavage were achieved, resulting in telechelic PS chains end-functionalized with thiol, which could then be oxidized by iron (III) chloride in high

dilution condition to yield cyclic PS by disulfide bond formation.[178] Additional examples of intramolecular homofunctional cyclization involving disulfide bond chemistry[179] and Glaser coupling[180] were also reported.

2.2.3.3 Heterofunctional Intramolecular Cyclization (AB)

In early 1990s, Schappacher and Deffieux reported the living cationic HI/I_2 polymerization of vinyl ethers end-functionalized with a styrenic unit, which was cyclized by abstraction of the terminal iodide by tin(IV) chloride addition. The resulting carbocation then reacted with the styrene end-group to form – after quenching of the carbocation with methanol – stable cyclic poly(vinyl ether).[181] A similar cyclization strategy was subsequently applied to the living anionic polymerization of styrene. The styrene and the iodide functional end-groups were this time introduced to the polymer *via* polymerization quenching and post-polymerization modification, respectively.[182] Subsequent work on cyclic PS polymers by the same authors was achieved by acid-catalyzed transacetalization reaction from a α,ω-acetal-diol-PS substrate.[183] Furthermore, the cyclization of telechelic PS chains bearing carboxylic acid and primary amine end-groups was achieved thought activated amidation by Kubo and coworkers.[184,185] Styrene polymerization by NMP from hydroxy-TEMPO and azo radical initiator bearing carboxylic acid groups led – after activated esterification – also to a cyclic polymer topology.[186] Naturally, the combination of CuAAC click chemistry with ATRP,[187,188,189,190] RAFT polymerization,[191,192] and NMP[193] were not left aside. More unusual reports of strain promoted azide-alkyne cycloaddition (SPAAC) reactions triggering cyclization by UV-light irradiation,[194] atom transfer radical cross-coupling (ATRC),[195] enyne metathesis[196] as well as tosyl[197,198,199] and halide[200] S_N2 reactions were also additionally published. Finally, Diels-Alder cycloadditions were conducted between maleimide and furan,[201] anthracene[202] linear dienyl[203] as well as between orthoquinodimethane and acrylate[204] or a dithiobenzoate RAFT chain transfer agent.[205]

2.2.3.4 Ring Expansion Polymerization

Beside topological conversion methods, the use of ring expansion polymerization (REP) methods constitute a valuable alternative for the synthesis of cyclic polymers from low-molecular weight cyclic initiators. In particular, ring expansion mechanisms, which do not require an equilibrium between cyclic dormant and linear propagating species, are ideal to synthetize high-molecular weight ring-shaped polymers. Hence, high-dilution conditions can

be avoided, allowing more efficient gram-scaled syntheses of high molecular weight cyclic polymers. In the past decades, REP methods were widely reported in the scientific literature.[206] For instance, the viability of RDRP methods like RAFT[207] or NMP[208] starting from cyclic initiator is no longer to be demonstrated. Among to the olefin metathesis field, ring-expansion metathesis polymerization (REMP) led to a library of covalently-bound cyclic polymers though back-biting elimination of modified ruthenium catalyst.[209,210,211,212] Similarly, cyclic polymers were obtained by alkyne metathesis though tungsten catalysts.[213] Moreover, the coordination and insertion of lactide or lactone monomers into cyclic tin[214,215,216,217] or aluminum oxide[218] initiators by ring opening polymerization (ROP) led to the corresponding cyclic polymers. While the metal catalyst usually remains in the polymer structures, making them particularly prone to hydrolysis, a series of post-polymerization modifications strongly enhanced the chemical stability of the products without compromising their cyclic topology.[219,220,221,222] Further example of cationic REP of vinyl ethers from a cyclic initiator were conducted.[223] Additionally, examples of nucleophilic and electrophilic zwitterionic ring-opening polymerizations (NZROP and EZROP) were also published. Thus, electrostatic NZROP of lactone and lactide monomers co-catalyzed by a zinc complex paired with amines or phosphines[224] as well as catalyzed by *N*-heterocyclic carbenes,[225,226,227,228] isothioureas,[229] pyridine[230] and imidazole[231] were achieved. On the contrary, although being less common, the EZROP of epoxide monomers though borane complex as Lewis acid catalyst[232] was also successfully conducted. Finally, more confidential reports of ethylene sulfide REP initiated by cyclic thiocarbamate,[233,234] methylene C1 polymerization from cyclic borane precursor by Shea[235] and lipase-mediated REP of lactone[236] were published.

2.2.4 Miscellaneous Cyclic Polymer Topologies

Besides simple ring-shaped polymers, a wide diversity of mono- and polycyclic polymer architectures have been reported over the last few decades. Whether by topological conversion or ring-expansion polymerization methods, these topologies were achieved though the same chemistries already employed to produce ring-shaped polymers. Thus, examples of grafted polymer rings connected with linear polymer chains **(Scheme 15, I)** were produced by CuAAC,[237,238,239,240] ESA-CF,[241] esterification,[242,243] S_N2 reaction,[244] REMP[245,246,247,248] and NZROP[249] while spiro polycyclic polymer **(Scheme 15, II)** were produced by REP,[250,251] RCM,[252,253] CuAAC,[254,255,256,257] Glaser coupling,[258] amidation[259] and ESA-CF.[169,260,261] Further examples of bridged polycyclic polymer topologies with linear chains **(Scheme 15, III)**

were achieved *via* ESA-CF[169,261,262] by simple variation of the nature and number of the ionic functionalities present in each precursor. At last, syntheses of fused polycyclic polymers including strictly two **(Scheme 15, IVa)** or more **(Scheme 15, IVb)** junction points within their architecture were published. While miscellaneous fused polycyclic structures **IVb** remain restricted to a few syntheses *via* a combination of CuAAC, RCM and ESA-CF reactions,[263,264] the synthesis of the **IVa** structures – commonly referred as polymer cages – turned out to be much more diversified. Consequently, the various strategies applied for their synthesis will be discussed in detail in the upcoming chapter.

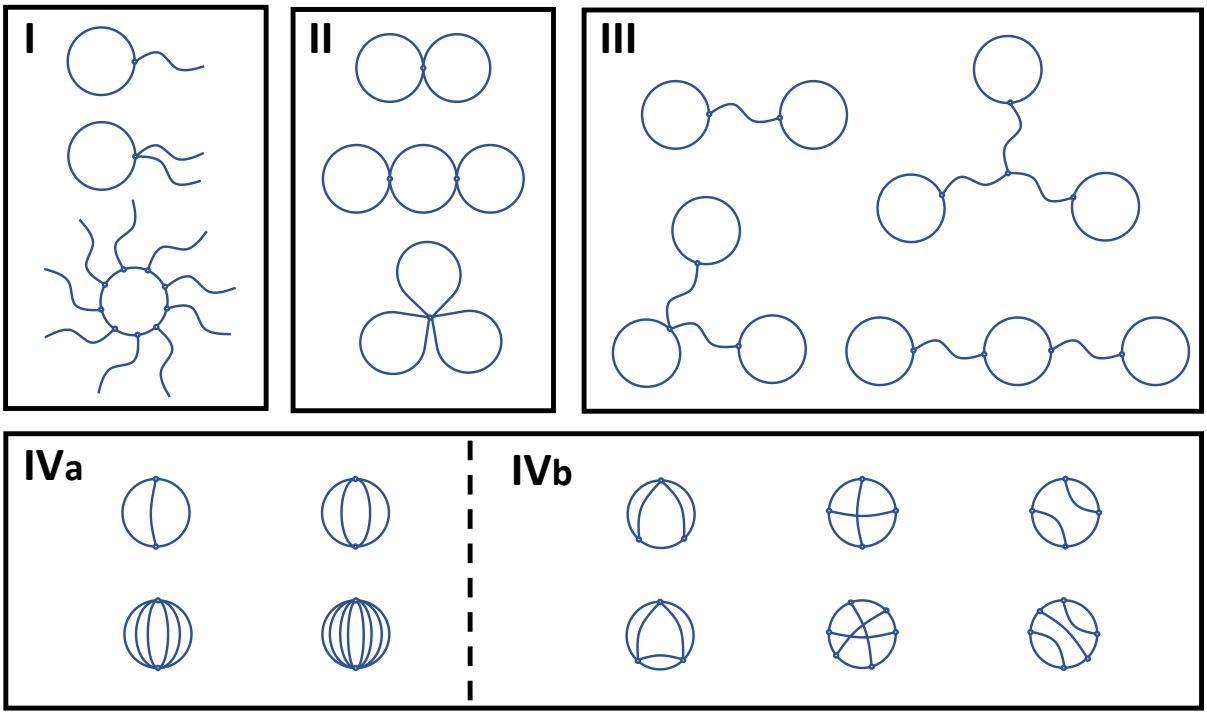

Scheme 15: Examples of (poly)cyclic polymer topologies (**I**) grafted with linear polymer chains, (**II**) grafted with additional cyclic polymers, (**III**) bridged with cyclic polymers through linear chains, and (**IV**) fused with additional polymer chains.

2.3 Synthesis of *Cage*-shaped Polymers*

As shown in the previous chapter, the synthesis of cyclic polymers can be realized either by topological conversion of an acyclic polymer substrate *via* post-polymerization modification or by ring-extension polymerization of a preexisting low-molecular cyclic initiator. By analogy, the synthesis of covalently-bound polymer cages were expected to follow the same scheme. However, while several examples of polymer cage formations by topological conversion were reported since the beginning of the 20th century, only one example of a polymer cage obtained through the arm-expansion of low-molecular polycyclic precursors was reported so far. In fact, the generation of polymer cages was found, in comparison to the monocyclic polymer synthesis, to be much more challenging, to enforce more synthetical restrictions and to suffer from an additional high predisposition to cross-link into networks. As a result, the diversity of synthesis approaches is so far still very much limited. In this regard, it is crucial to critically look back at what has been accomplished so far before stepping forward. To do so, previous approaches will be categorized in five subchapters, as summarized in **Scheme 16**.

*Parts of this subchapter – including the text, figures, tables and schemes – might/will be subsequently published within a perspective review discussing the various approaches reported over the last 20 years to produce *cage*-shaped polymers as well as the related developments that might arise in a near future.

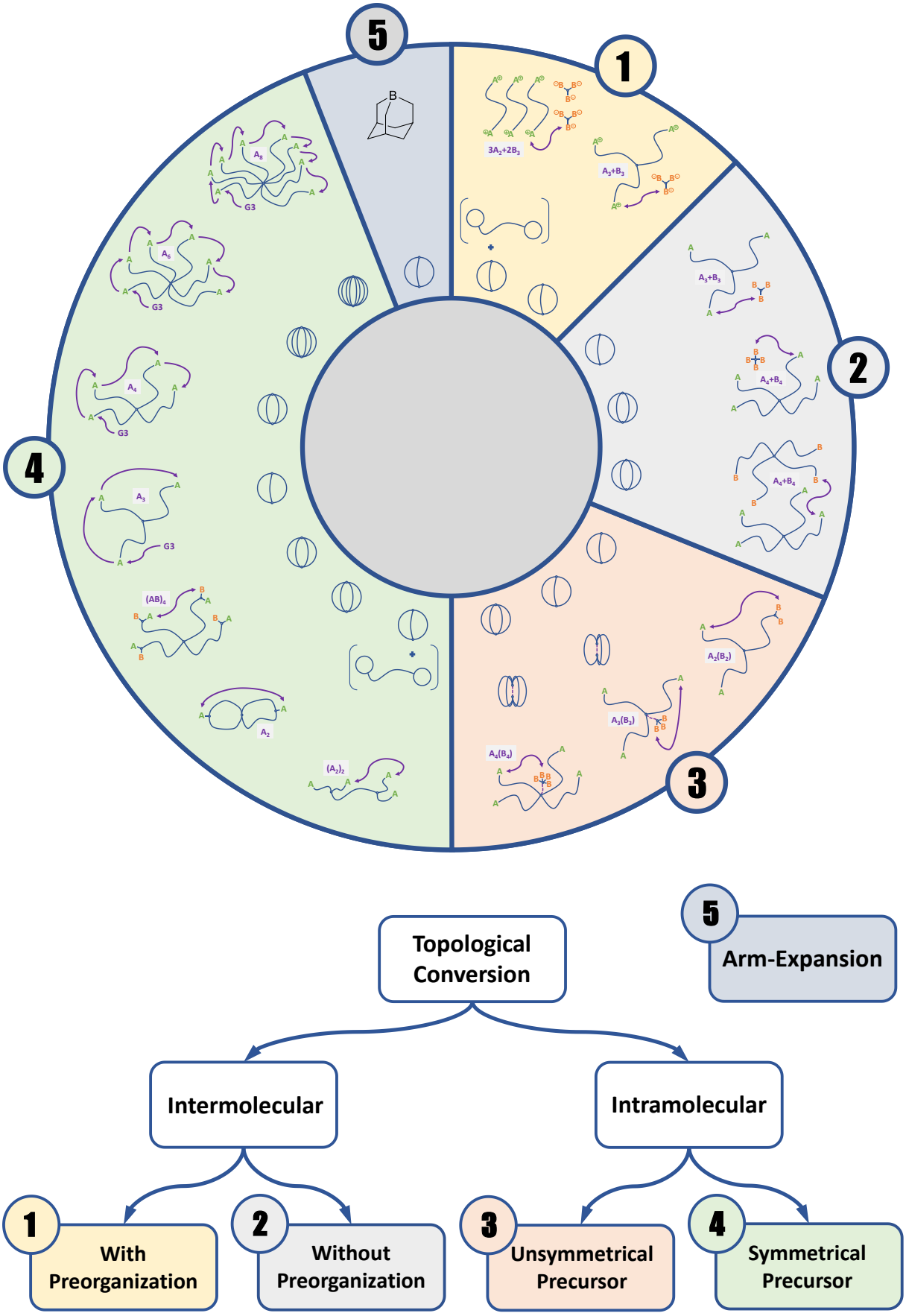

Scheme 16: Classification of all *cage*-shaped polymer synthesis methods in five subcategories.

2.3.1 Intermolecular Topological Conversion with Preorganization

Historically, the first examples of isolated three-arm *cage*-shaped polymers were reported by Tezuka and Oike in the early 2000s. Thus, three-arm polymer cages were assembled by ESA-CF from three-arm *star*-shaped polytetrahydrofuran bearing cyclic quaternary amine end-groups and trifunctional carboxylate linkers. Once the thermodynamic equilibrium reached in high dilution, the A_3+B_3 pairs were covalently bound and the isolated yields were comprised between 40 and 52%.[169,265] **(Table 1, Entry 1b–2; Scheme 17, I)** A second approach for the generation of three-arm polymer cages based on the same chemistry was reported shortly after from the same authors.[169] **(Table 1, Entry 1a; Scheme 17, II)** The thermodynamic equilibrium took place between three telechelic linear polymer-chains and two trifunctional linkers in a $3A_2$+$2B_3$ intermolecular system. However, the reaction resulted in 67% yield of a topological mixture constituted of 78% intramolecularly favored *barbell*-shaped polymer and only of 22% three-arm polymer cages, yielding an extrapolated low 15% yield for cage polymers. Nevertheless, although being restricted to the milligram-scale and necessitating some synthetical efforts to produce the ionic species in high purity, the ESA-CF methodology shines by its unique ability to produce – beyond polymer cages – a large library of complex cyclic topologies.[171,172]

Table 1: Intermolecular topological conversions with preorganization

Entry	Closing system	Polymer type Closing reaction	N° arm	Isolated yield / %	Isolated mass / mg	$M_{n,^1H\text{-}NMR}$ / kg mol^{-1}	$Đ_{SEC}$
1a	$3A_2$+$2B_3$	PTHF / ESA-CF	3	15 *	*n/a*	13	1.11 *
1b	A_3+B_3	PTHF / ESA-CF	3	52	*n/a*	14	1.06
2	A_3+B_3	PTHF / ESA-CF	3	49	11.0	7.3	1.10
	A_3+B_3	PTHF / ESA-CF	3	40	9.0	9.6	1.16
	A_3+B_3	PTHF / ESA-CF	3	42	9.4	11.9	1.07

** Value extrapolated from an isolated mixture of both cage- and barbell-shaped topologies.*

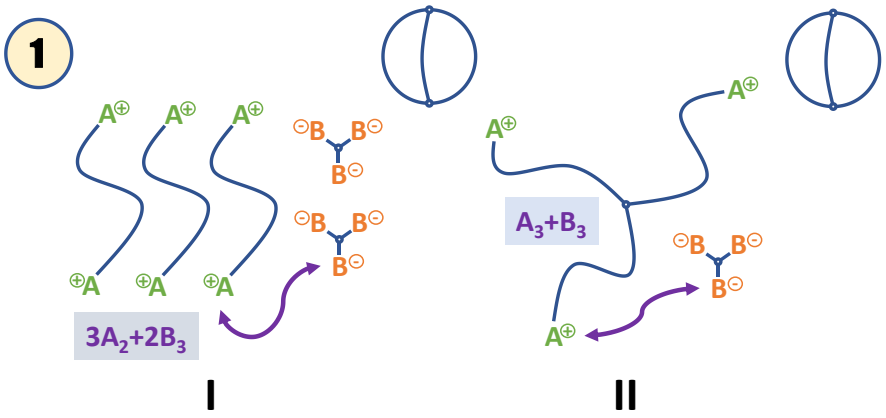

Scheme 17: Schematic overview of all intermolecular topological conversions with preorganization.

2.3.2 Intermolecular Topological Conversion without Preorganization

Unlike previously discussed examples, the syntheses of polymer cages that involve an intermolecular step without any kind of preorganization strongly suffer from undesired competitive cross-linking, which ultimately leads to network formation. Thus, the topological conversion of two distinct four-arm *star*-shaped poly(ethylene oxide) (PEO) polymers, end-functionalized respectively with NHS activated esters and primary amines, into an expected large four-arms cage was reported recently by Matsushita and colleagues.[266] **(Table 2, Entry 3; Scheme 18, III)** While the purification procedure taking advantage of the interaction of α-cyclodextrin and chain-end PEOs was worth of interest, the A_4+B_4 intermolecular topological conversion resulted in an extremely low 0.5% yield, i.e. circa 10 mg product for 1.8 gram of starting material. This particular example illustrates well the limitation of intermolecular systems, which do not include any preorganization to reduce network formation as intermolecular reactions are needed and have to avoid at the same time to yield the desired product. A few years earlier, intermolecular coupling between azide end-functionalized three-[267] **(Table 2, Entry 4; Scheme 18, I)** and four-arm[268,269,270] **(Table 2, Entry 5–7; Scheme 18, II)** PS stars and trifunctional alkyne linkers were reported by Paik and coworkers. However, out of the 17% yield reported for a three-arm polymer,[267] no information on the isolated yields were given. Instead, the yields were extrapolated from size-exclusion chromatography (SEC) analysis. Considering the natural propensity of this kind of topological conversion to yield networks, it has to be feared that only the weakly crosslinked and discreet topologies might be able to eluate through the SEC column. In this regard, these

kinds of values should not be considered sufficient to determine the efficiency of the topological conversion. In addition, the topological purity not only impacts the reaction yield but also the quality of the obtained material, and therefore only the characterizations obtained from a previously isolated topology should be taken into account. Finally, all given molecular weights were only estimated either by SEC or light-scattering, and the values of dispersity for the *cage*-shaped polymers were almost never mentioned, making any comparison with other polymer cage synthesis difficult.

Table 2: Intermolecular topological conversion without preorganization.

Entry	Closing system Closing reaction	Polymer type	N° arm	Isolated yield / %	Isolated mass / mg	M_n / kg mol^{-1}	$Đ_{SEC}$
3	A_4+B_4	PEO / NHS ester	4	0.5 *	10	20.6 **	1.08
4	A_3+B_3	PS / CuAAC	3	17 *	166	6.3 **	*n/a*
	A_3+B_3	PS / CuAAC	3	30 **	*n/a*	4.2 **	*n/a*
5	A_4+B_4	PS / CuAAC	4	81 **	*n/a*	6.7 **	1.01
6	A_4+B_4	PS / CuAAC	4	65 **	*n/a*	6.8 **	*n/a*
	A_4+B_4	PS / CuAAC	4	51 **	*n/a*	7.2 **	*n/a*
7	A_4+B_4	PS / CuAAC	4	63 **	*n/a*	6.0 ***	*n/a*

** Isolated yield, ** Estimated by SEC, *** Estimated by LS*

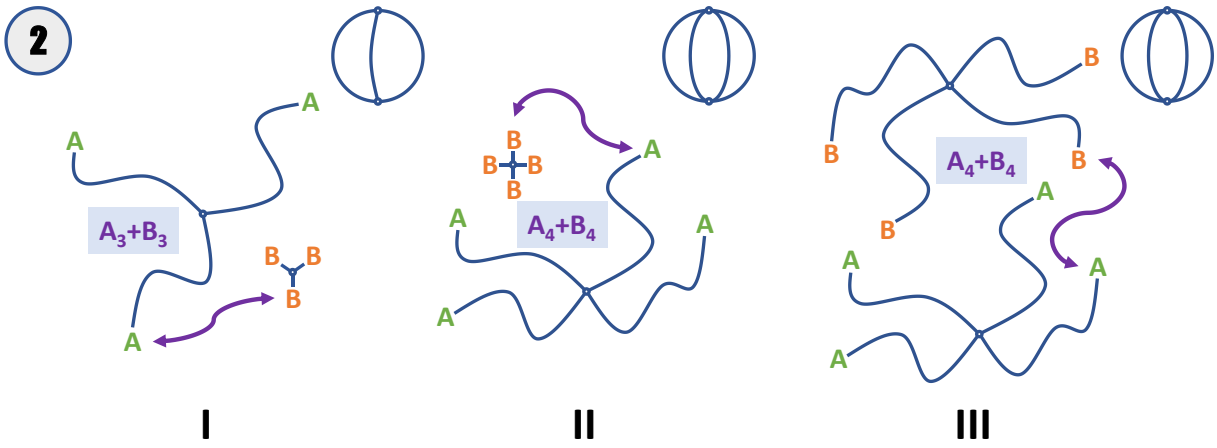

Scheme 18: Schematic overview of all intermolecular topological conversion without preorganization.

2.3.3 Intramolecular Topological Conversion from an Asymmetrical Precursor

To overcome the intermolecular drawbacks, strictly intramolecular topological conversions, which occur within a unique precursor, were investigated. Taking advantage of their concentration-independent kinetics, unimolecular topological conversions were employed in high dilution condition to suppress the undesired intermolecular side-reactions without impacting their intramolecular reaction rate. While their synthesis suffered from being usually more complex and challenging than their intermolecular analogues, the intramolecular closing systems were further subdivided regarding to their complexity in two distinct groups. Thus, if the use of low or non-symmetrical precursors tends to be easier to conceptualize, their synthesis turns out to be usually particularly challenging. On the contrary, the synthesis of precursors with a high degree of symmetry in their structure are less resource- and time-demanding, but require more care in their conception to ensure an efficient topological conversion. The unsymmetrical intramolecular precursors are discussed in more detail below while the symmetrical ones will be subsequently addressed. The pioneering example of unsymmetrical precursors that reacted intramolecularly to deliver polymer cages was reported in 2009 by Pan and Shi.[271] **(Table 3, Entry 8; Scheme 19, I)** This specific example was based on the synthesis of a series of four different three-arms A_2B miktoarm *star*-shaped polymers decorated with one poly(ε-caprolactone) (ε-PCL) and two PS arms respectively obtained by ATRP and ROP. The intramolecular topological conversion occurred by CuAAC in a $A_2(B_2)$ manner *via* the slow addition of the polymer into the reaction medium. It is particularly interesting to note that the term of *theta*-shaped polymer was preferred to the one of *cage*-shaped by the authors, due to the independent length of the PS and ε-PCL arms, respectively. However, the authors failed to report yields for the higher molecular weight *theta*-shaped polymers, and the absence of any network removal measures before the given isolated 70% yield along the monomodal SEC trace raises doubts about the reaction workup. Alternatively, an intramolecular approach involving unsymmetrical precursors was later proposed by Satoh in 2016.[272] **(Table 3, Entry 9; Scheme 19, II–III)** Tri- and tetra-functional ROP initiators bearing respectively three and four azide groups separated by a benzyl linker were achieved. Subsequently, ROP and the introduction of terminal alkynes at each arm chain ends by post-polymerization modification were performed. The intramolecular topological conversions of the respective three and four-arm star polymers into *trefoils*- and *quatrefoils*-shaped polymers were achieved by CuAAC. This first topological conversion was directly followed by the cleavage of the initiators center by palladium-catalyzed

hydrogenation of the benzyl linker to finally form three- and four-arm polymer cages, respectively. This initial work was expanded in 2021 with the analysis of three polymer cages made of block, diblock and triblock copolymer chain-arms, respectively.[273] **(Table 3, Entry 10; Scheme 19, II)** Nevertheless, although both approaches are elegant in their conception, the particularly high number of preliminary steps prior to their *cage*-shaped synthesis makes further development in this direction particularly arduous.

Table 3: Intramolecular topological conversions from asymmetrical precursor.

Entry	Closing system	Polymer type Closing reaction	N° arm	Isolated yield / %	Isolated mass / mg	M_n / kg mol^{-1}	$Đ_{SEC}$
8	$A_2(B_2)$	PS-*co*-PCL / CuAAC	3	70	70	9.4 *	1.12
	$A_2(B_2)$	PS-*co*-PCL / CuAAC	3	*n/a*	*n/a*	16.5 *	1.10
	$A_2(B_2)$	PS-*co*-PCL / CuAAC	3	*n/a*	*n/a*	19.2 *	1.09
	$A_2(B_2)$	PS-*co*-PCL / CuAAC	3	*n/a*	*n/a*	27.0 *	1.09
9	A_3B_3	PBO / CuAAC	3	48	78	3.3 **	1.04
	A_3B_3	*** / CuAAC	3	72	511	22.9 **	1.03
	A_4B_4	PBO / CuAAC	4	78	359	3.8 **	1.02
	A_4B_4	*** / CuAAC	4	61	336	23.4 **	1.02
10	A_3B_3	*** / CuAAC	3	66	592	22.6 **	1.02
	A_3B_3	*** / CuAAC	3	31	337	22.6 **	1.02
	A_3B_3	*** / CuAAC	3	69	719	22.6 **	1.03

** Estimated by SEC, ** Estimated by ^{1}H-NMR, *** Poly(n-decyl glycidyl ether)–block–poly[2-(2-(2-methoxyethoxy)ethoxy)ethyl glycidyl ether]*

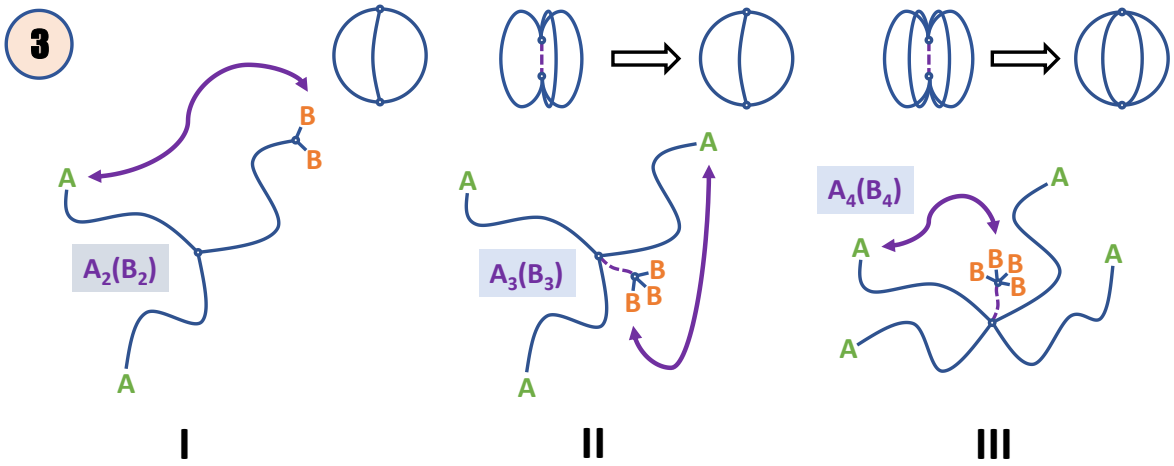

Scheme 19: Schematic overview of all intramolecular topological conversions from asymmetrical precursors.

2.3.4 Intramolecular Topological Conversion from Symmetrical Precursors

As previously mentioned, not all precursors require high synthetical investment due to the introduction of a higher degree of symmetry within their structure. In this regard, the first two examples of polymer cages obtained by intramolecular conversion of symmetrical precursors were published both by Tezuka and colleagues in 2005.[262,274] **(Table 4, Entry 11–12; Scheme 20, I)** The synthesis of the *H*- and *eight*-shaped PTHF precursors bearing four and two terminal alkene groups respectively were achieved by ESA-CF, before being intermolecularly converted into three- and four-arm polymer cages by ring-closing metathesis (RCM) in high dilution conditions. While the *eight*-shaped polymer topological conversion resulted in a good 67% yield, the *H*-shaped precursor approach suffered from the competitive formation of *barbell*-shaped polymers as the major product, negatively impacting the reaction yield to 20% and the product isolation by preparative SEC. However, none of these two examples reached the simplicity and efficiency expected for symmetrical precursors.

Table 4: Intramolecular topological conversion from symmetrical precursor.

Entry	Closing system	Polymer type Closing reaction	N° arm	Isolated yield / %	Isolated mass / mg	$M_{n,^1H\text{-}NMR}$ / kg mol^{-1}	$Đ_{SEC}$
11	A_2	PTHF / RCM	4	67	20.2	10.6	1.18
12	A_4	PTHF / RCM	3	20	14	14.7	*n/a*
13	A_3	ε-PCL / ROMO	3	92	27.6	6.1	1.09
	A_3	ε-PCL / ROMO	3	80	24.0	8.0	1.09
	A_3	ε-PCL / ROMO	3	84	25.2	10.7	1.09
	A_4	ε-PCL / ROMO	4	97	29.1	6.1	1.08
	A_4	ε-PCL / ROMO	4	94	28.2	8.9	1.08
	A_4	ε-PCL / ROMO	4	91	27.3	10.4	1.08
	A_6	ε-PCL / ROMO	6	91	27.3	6.1	1.08
	A_6	ε-PCL / ROMO	6	99	29.7	9.5	1.09
	A_6	ε-PCL / ROMO	6	91	27.3	11.9	1.07
	A_8	ε-PCL / ROMO	8	98	29.4	7.4	1.06
	A_8	ε-PCL / ROMO	8	98	29.4	9.6	1.08
	A_8	ε-PCL / ROMO	8	85	25.5	13.2	1.06
14	A_3	ε-PCL / ROMO	3	68	74.5	10.6	1.08

In fact, it was only recently that the intramolecular topological conversion from simple and symmetrical precursor truly matured when Satoh and coworkers proposed the intramolecular closing step by ring-opening metathesis oligomerization (ROMO) of norbornene end-functionalized ε-PCL stars in 2019 and 2021.[275,276] **(Table 4, Entry 13-14; Scheme 20, II–V)** While the addition of the 3rd generation Grubbs catalyst on the first arm is strictly speaking an intermolecular process, the kinetic of the following oligomerization was found to be fast enough to make a second catalyst addition unlikely. Thus, once the stoichiometric ratio between polymer and catalyst was optimized to [1:6], the reaction proceeded with an intramolecular-like kinetic in a strict oxygen-free atmosphere. Not only three-, four-, but also six-, and eight-arm ε-PCL cages with various molecular weights were obtained in very high isolated yields comprised between 80% and 99%. This major breakthrough work is not only the first and only example of cages possessing more than four arms until now, but constitute also an efficient way to synthetize polymer cages with virtually any number of arms.

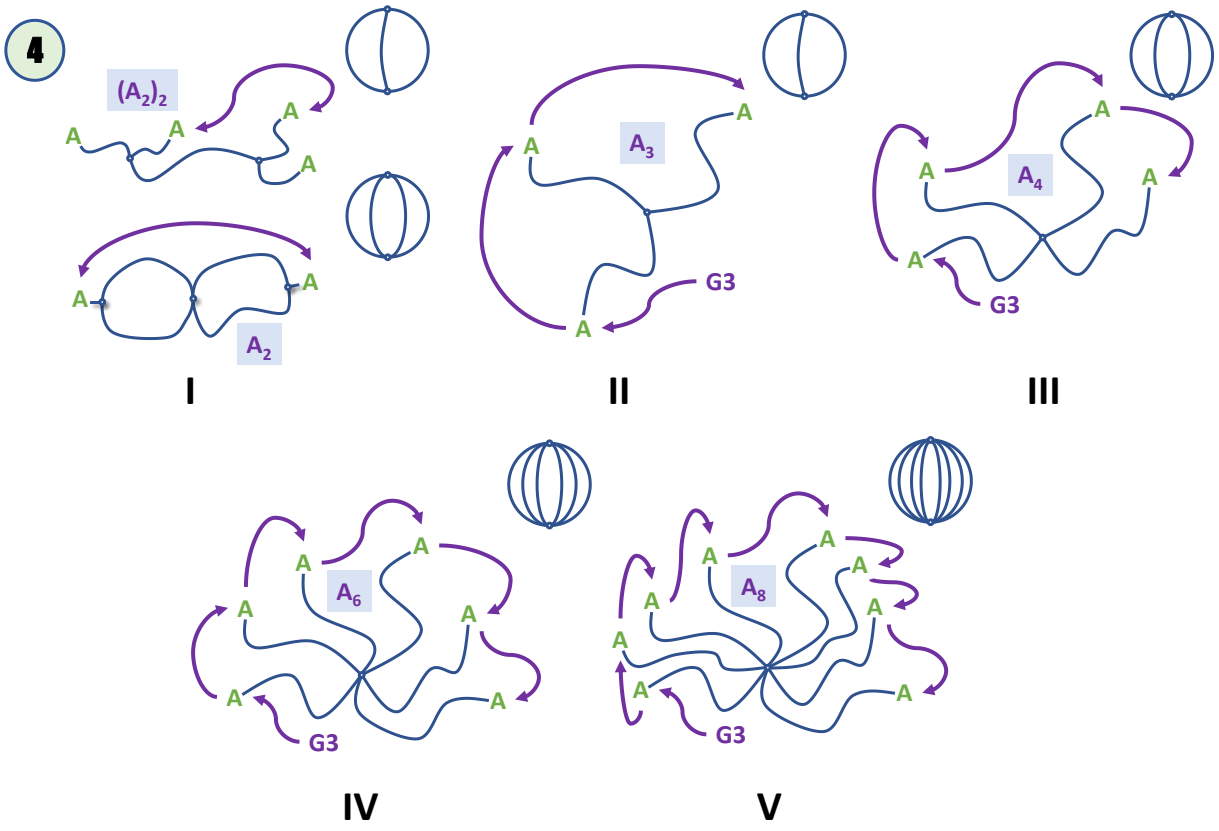

Scheme 20: Schematic overview of all intramolecular topological conversions from symmetrical precursor.

Therefore, only the prerequisite to obtain defect-free polymer stars as well as end-functionalization fidelity might limit this number. Furthermore, as long as the end-functionalization with norbornene remains effective, the functional tolerance of the 3rd generation Grubbs catalyst ensures a large scope of polymer composition and functionalization. Thenceforth, a critical question has been raised to the synthesis of polymer cage within the milligram-scale could have reached an optimal efficiency through the ROMO approach. On the contrary, once aiming for larger scales, the necessity to quench the living oligomers to prevent further cage oligomerization prior to any further precursor addition suppress the possibility to run the reaction in semi-batch mode, making any gram-scale material synthesis and subsequent tangible application unlikely.

2.3.5 *Cage*-shaped Polymer Synthesis by Arm Expansion

Beside topological conversion methods, the use of arm expansion methods might constitute a valuable alternative to efficient gram-scaled synthesis of high-molecular weight polymer cages by analogy with what has been done for the synthesis of polymer rings, as discussed previously. However, most of these mechanisms could not simply be transferred to polymer cage synthesis due to their inability to elongate three or more polymer chains simultaneously from a single reactive center. In this context, the only report of polymer three-arm cage synthesis achieved though arm-expansion was published, at best of our knowledge, by Shea and coworkers in 2003.[277] **(Table 5, Entry 15; Scheme 21)** Taking advantage of C1 methylene insertion-polymerization from a borane-adamantane precursor, high-molecular weight three-arm poly(ethylene) cages over 35 kg mol^{-1} were obtained.

Table 5: *Cage*-shaped polymers obtained through arm-expansion.

Entry	Closing system	Polymer type Polymerization method	N° arm	M_n / kg mol^{-1}	$Đ_{SEC}$
15	Arm-Exp.	PE / C1 methylene insertion	3	2.4 *	1.06
	Arm-Exp.	PE / C1 methylene insertion	3	5.6 *	1.09
	Arm-Exp.	PE / C1 methylene insertion	3	10.5 *	1.08
	Arm-Exp.	PE / C1 methylene insertion	3	19.6 *	1.08
	Arm-Exp.	PE / C1 methylene insertion	3	21.7 **	1.12
	Arm-Exp.	PE / C1 methylene insertion	3	35.4 **	1.12

** Estimated by SEC, ** Estimated by LS, *** Estimated by ^{1}H-NMR*

The mechanism of the homopolymerization consisted in the migration insertion of a methylene group to a trialkyl borane center. While the migration reaction did not require any particular dilution to avoid the network formation as the cage integrity was never compromised, the unstable nature of the trialkyl borane in presence of dioxygen or water strongly restricted the scope of analytical characterization, and hence the application of this specific system. Furthermore, besides the well-known low solubility issue of poly(ethylene) in organic solvents, two-third of the borane-adamantane precursors were reported to be kinetically trapped at low degree of polymerization due to the robability to lead to sterically hindered conformations. Nevertheless, the use of similar arm-expansion methods could constitute an interesting alternative to the synthesis of covalently stable *cage*-shaped polymers at the multigram-scale, and therefore might open the way to applications for polymer cages.

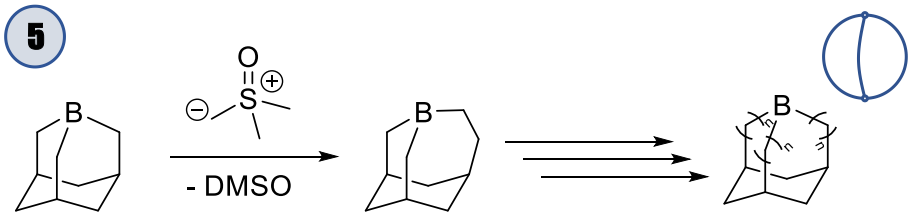

Scheme 21: Schematic overview of C1 methylene insertion-polymerization from a borane-adamantane precursor.

3 Motivation

As discussed in the last part of the theoretical background, several strategies have been developed over the past two decades to synthetize polymer cages in a milligram-scale. However, the transition from academic curiosities to applied materials science until now remains compromised by both its synthetic complexity and its restriction to be scaled up.

Hence, this thesis intends to propose an efficient and rationalized novel synthesis of *cage*-shaped polymers that could be obtained with minimal synthetical effort at the gram-scale. In order to achieve this objective, a new intramolecular topological conversion strategy will be investigated within this work. The present approach was conceptualized on the use of AB bifunctional end-groups, which under specific conditions, are allowed to react and to self-closing themselves into $(AB)_n$ thermodynamically and kinetically favored macrocyclic structures. **(Scheme 22)**

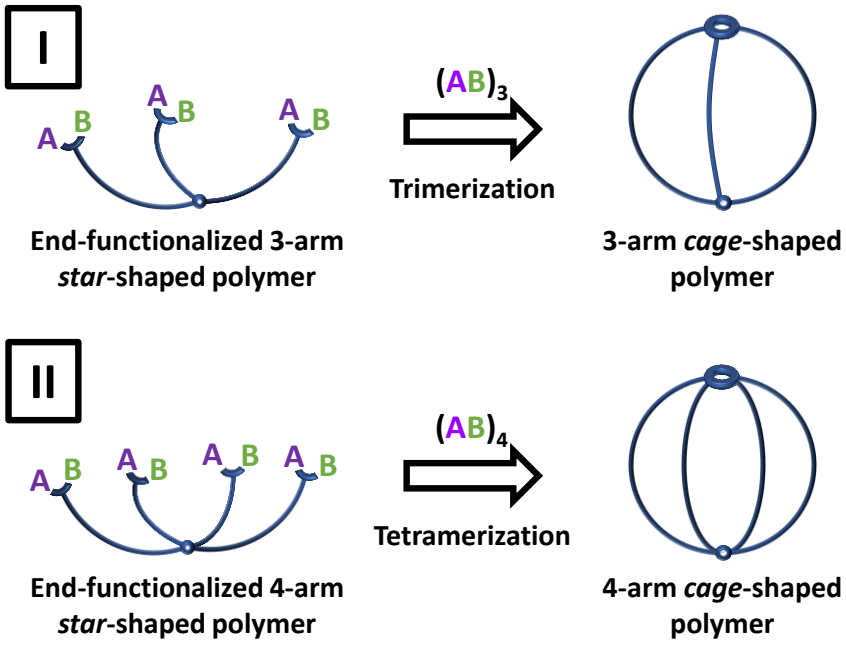

Scheme 22: Schematic representation of the $(AB)_n$ strategy that will be investigated within this work including (**I**) the $(AB)_3$ trimerization for the synthesis of three-arm polymer cages, and (**II**) the $(AB)_4$ tetramerization for the synthesis of four-arm polymer cages.

Compared with most previous topological conversion strategies, the use of a single kind of end-group located at each arm ends of *star*-shaped polymers ensures the accessibility of the

precursor while the intramolecular nature of the topological conversion allows polymer concentration-independent reaction kinetics and therefore no specific need of polymer concentration optimization. **(Scheme 23)** Furthermore, as each arm owns the opportunity to react without distinction with any other arm, the impact on the reaction kinetics of the meeting of two end-groups might be greatly minimized than in the case of asymmetrical end-groups. At last, the *in-situ* formation of chemically inert closing systems might constitute a great opportunity to upscale the synthesis of *cage*-shaped polymers *via* semi-batch processes.

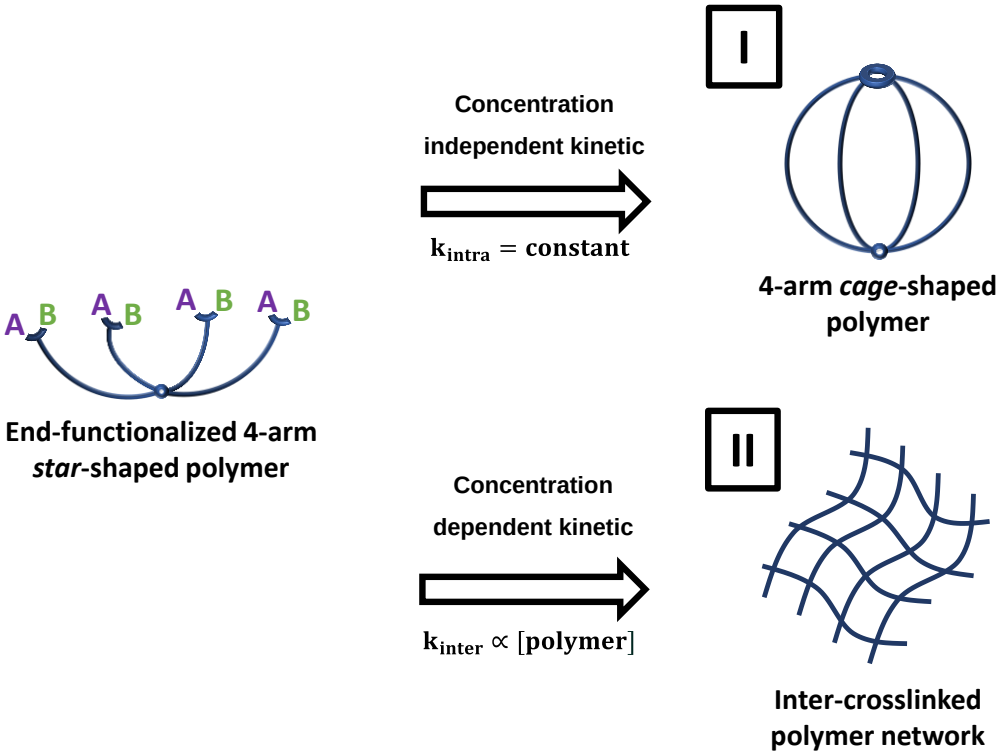

Scheme 23: Representation of **(I)** the intramolecular concentration independent kinetic of the $(AB)_4$ tetramerization reaction leading to *cage*-shaped polymer versus (**II**) the concentration independent kinetic nature of the intermolecular reactions leading to crosslinked polymer networks.

That said, such an approach requires a reaction that fulfils a strict list of specifications, such as a high orthogonality to preliminary synthesis step conditions as well as a high conversion and a high kinetic rate. The reaction initiation also needs to be strictly controlled by a specific trigger like the addition of a catalyst or a physical stimulus. Furthermore, only the expected macrostructure corresponding to the polymer arm number has to be thermodynamically favorited. At last, the synthesis of the polymer precursor, including the end-group synthesis and the polymer end-functionalization have syntheses accessible enough to allow the approach to be viable.

4 Project Part I – Early Attempts of *Cage*-shaped Polymer Synthesis

4.1 Project Part I – Introduction

Before being able to investigate the synthesis of polymer cages by topological conversion of polymer stars through $(AB)_n$ *n*-oligomerization of bifunctional end-groups, two practical choices had to be made. First of all, the choice of the chemistry employed in the formation of a $(AB)_n$ macrocycle has to be defined. When looking back at the diversity of chemistries used to produce macrocyclic structures **(See Theoretical Background, Part II)** a non-negligible number of candidates can be envisioned at first. However, due to the extended list of restrictions, the list of reasonable choices shrinks rapidly. Even so, one well established click reaction – the copper(I)-catalyzed azide-alkyne cycloaddition (CuAAC)[278] – was found to own the potential to fulfill all prerequisites listed as follows: a) a high orthogonality and a strict monitoring of the reaction *via* Cu(I) catalysis; b) a high conversion and a kinetic rate occurring even in high dilution conditions; c) the formation of rigid triazole rings as product, that could potentially self-assemble into an larger stable and unreactive macrocyclic structure; and d) an accessible synthesis of end-groups including both azide and terminal alkyne functional groups by various reaction pathways. Nevertheless, literature describing rigid macrocycles with triazole motifs within their structures was lacking at first sight. Therefore, within this first part of the results chapter, several syntheses of potential azide-alkyne end-groups featuring different lengths and rigidity between both functional groups were examined.

Secondly, the polymerization technique used to produce well-defined *star*-shaped polymers had to be defined. Considering the high end-group fidelity and narrow dispersity of polymers produced by reversible-deactivation radical polymerizations (RDRP) from a broad range of vinylic monomers, ATRP, NMP and RAFT polymerization methods were considered. ATRP was disqualified because of its incompatibility with any $(AB)_n$ end-groups based on CuAAC chemistry as the presence of traces Cu(I) issued from the polymerization could have led to the crosslinking of the polymer material prior to its high-dilution requested to avoid intermolecular reactions. In a lesser extent, the most common and efficient end-functionalization of ATRP polymers consisting in the S_N2 reaction of the terminal secondary halide with sodium azide

would have also altered the reactions orthogonality, as CuAAC would have been used for both the end-functionalization and the topological conversion steps. On the contrary, NMP suffers from the lack of accessibility of its nitroxide synthesis, particularly in the case of *star*-shaped initiators bearing multiple nitroxides within a single molecular structure and specific end-groups on all nitroxides. As a consequence, the core-first synthesis of polymer star from regioselective *star*-shaped RAFT chain-transfer agents was chosen. To suppress the use of post-polymerization modifications prior of the topological conversion, the RAFT chain transfer agent was also planned to directly include the end-groups within its structure. At last, the Z-group approach of *star*-shaped polymer synthesis by RAFT was privileged to minimize the occurrence of star-star coupling by radical recombination or disproportionation. Despite limiting the molecular weight upper limit, this choice allowed the propagating radicals to remain linear and near the central part of the polymer stars thank to the fast chain-transfer equilibrium.[279] **(Scheme 24)**

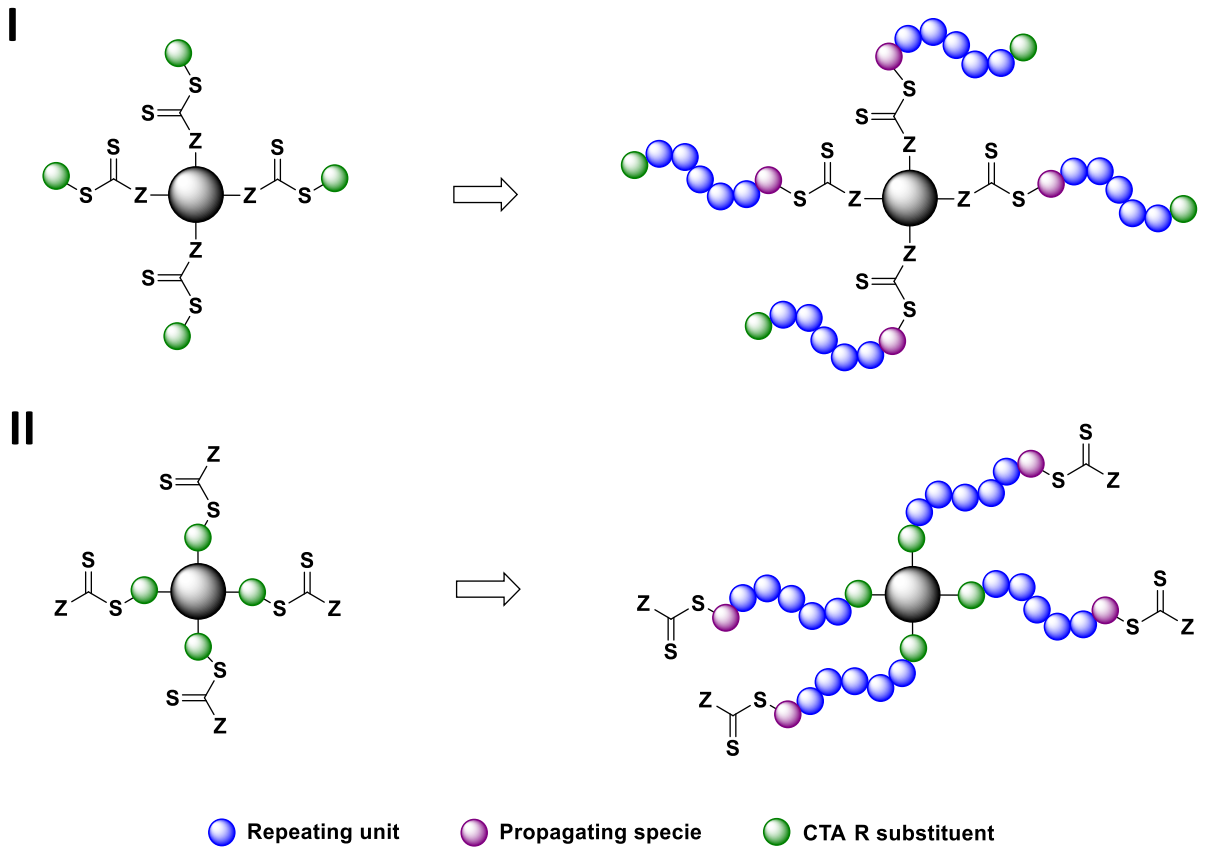

Scheme 24: (**I**) Z-group and (**II**) R-group approach of core-first synthesis of polymer stars obtained from *star*-shaped RAFT agents.

4.2 Project Part I – Results and Discussion

4.2.1 Linear CTA as a Model for *Star*-shaped RAFT Agent

In order to investigate the synthesis of a *star*-shaped RAFT agent and its compatibility with different monomers and polymerization conditions, the synthesis of a linear RAFT agent sharing an equivalent molecular structure was initially devised. In terms of structural restrictions, both sides of the linear CTA had to be adjustable, as one side would later bear the end-group and the other one the center of the regioselective CTA. At last, the linear RAFT agent ability to reach high yields was estimated essential to ensure the viability of the synthesis of *star*-shaped RAFT agents bearing multiple CTAs. As a consequence of these considerations, the linear RAFT agent **R01** was synthetized. **(Scheme 25)** The first synthesis step consisted in the equilibrium reaction of thiolactic acid with carbon disulfide and triethylamine as an organic base in order to form the thiocarbonate anions, which were further reacted with benzyl bromide *via* S_N2 mechanism. The resulting crude product was then esterified without preliminary purification by EDC/DMAP coupling with benzyl alcohol as nucleophile, resulting in **R01** isolated in 82% yield over two steps. While the benzyl bromide was planned to constitute later the center of the *star*-shaped RAFT agent, the benzyl alcohol was expected to be replaced by functionalized end-groups to achieve – directly following the polymerization – the topological conversion to *cage*-shaped polymers.

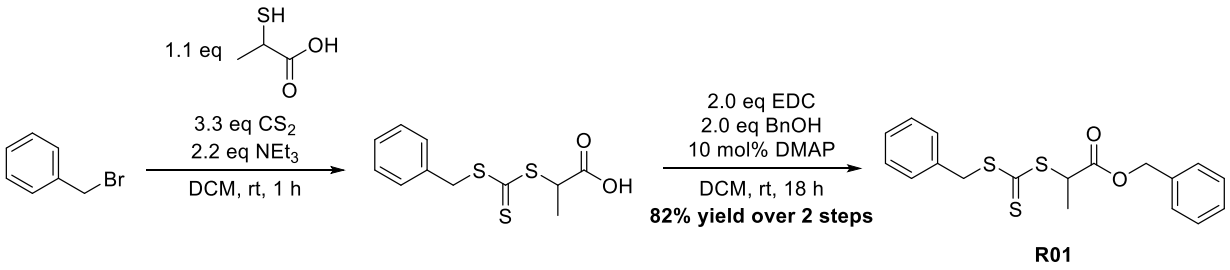

Scheme 25: Two-step synthesis of linear RAFT agent **R01** obtained in overall 82% yield.

Foremost, the ability of RAFT agent **R01** to control styrene polymerization was estimated. To test this assumption, a styrene polymerization **P01** was conducted at 80 °C in bulk with 10 mol% AIBN relative to the CTA and samples were taken after 1, 2 and 4 hours. **(Scheme 26, I; Table 6, Entry 1–3)** The CTA was found to control the polymerization efficiently, though

with a relatively slow propagation rate (i.e. a $M_{n,^1H\text{-}NMR}$ of 4.8 kg mol^{-1} after 4 hours polymerization).

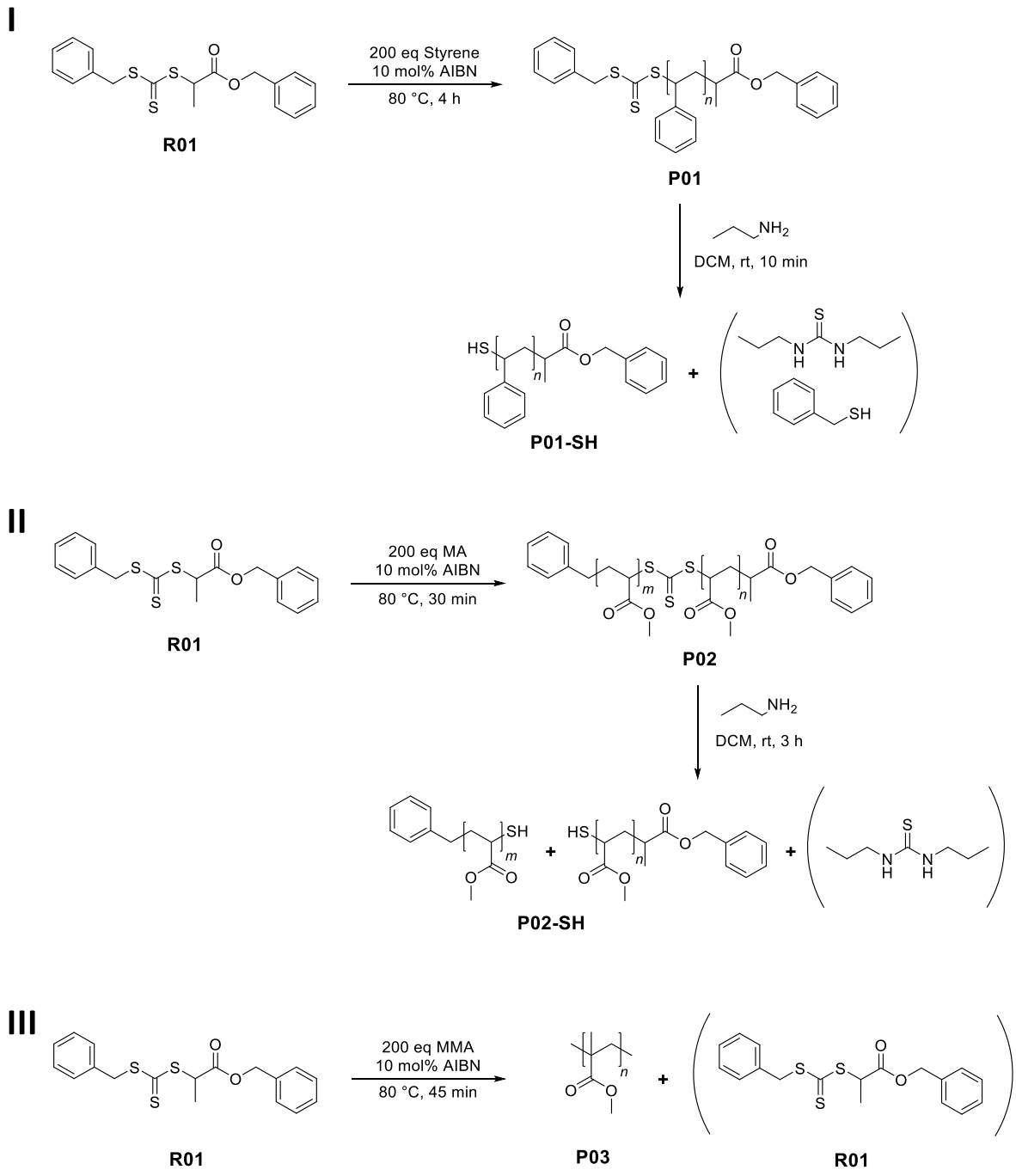

Scheme 26: (**I**) RAFT polymerization **P01** of styrene by RAFT agent **R01** followed by its aminolysis to obtain thiol end-functionalized **P01-SH** PS. (**II**) Non-regioselective RAFT polymerization of MA **P02** followed by the CTA aminolysis yielding **P02-SH**; (**III**) Free radical polymerization of MMA to PMMA **P03** caused by the inability of the RAFT agent **R01** to achieve an efficient chain transfer with MMA radicals.

Thus, according to the SEC analysis, a $M_{n,SEC}$ value of 4.9 kg mol^{-1} with a relatively low dispersity of 1.17 was reached after 4 hours. To ensure the regioselectivity of **R01** CTA with styrene, **P01** samples were cleaved at the trithiocarbonate position by aminolysis with *n*-propylamine to obtain the respective thiol terminated **P01-SH** polymers. **(Scheme 26, I; Table 6, Entry 4–6)** Each of the **P01-SH** samples were characterized by SEC_{THF} analysis, systematically leading to monodisperse SEC traces. The number of repeating units per polymer chain (degree of polymerization, DP) was additionally estimated from **P01** and **P01-SH** $M_{n,SEC}$ and **P01** $M_{n,^1H\text{-}NMR}$ data. All methods led to similar DP values at the exception of the sample taken after 4 hours, suggesting – at least to some extent – the regioselectivity of **R01** CTA polymerization with styrene. **(Figure 1)**

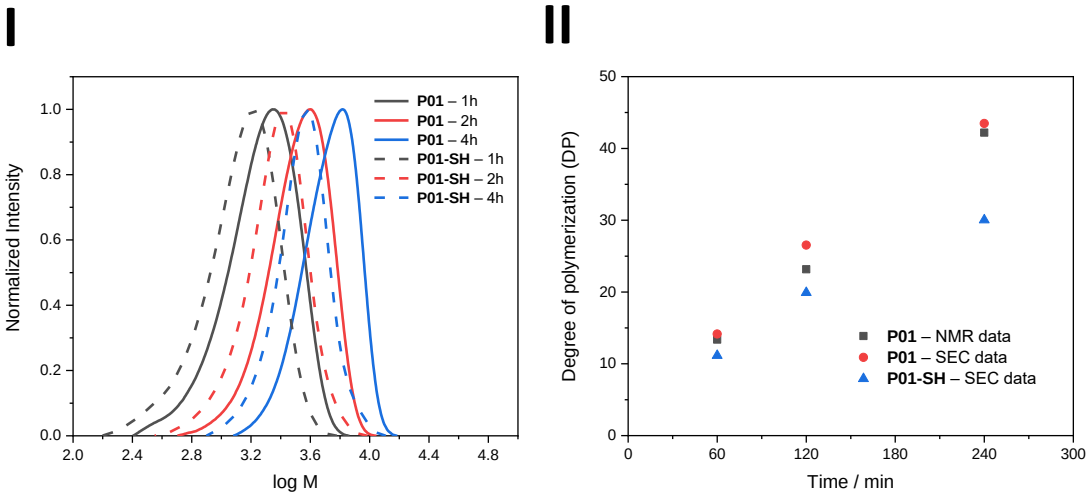

Figure 1: (**I**) SEC traces of **P01** and **P01-SH** polymer samples; (**II**) Degree of polymerization reached at 1, 2 and 4 hours of polymerization and calculated from **P01** and **P01-SH** $M_{n,SEC/THF}$ as well as **P01** $M_{n,^1H\text{-}NMR}$ data.

Secondly, the control induced by the **R01** CTA was investigated for the polymerization of methyl acrylate (MA) at 80 °C with 10 mol% AIBN relative to the CTA. After 30 minutes, the reaction was interrupted due to its high viscosity, yielding poly(methyl acrylate) (PMA) **P02** exhibiting a $M_{n,SEC}$ of 14.0 kg mol^{-1} and a dispersity of 1.11. **(Scheme 26, II; Table 6, Entry 7)** The CTA aminolysis of **P02** led to a monodisperse distribution **P02-SH** with an estimated $M_{n,SEC}$ value of 8.1 kg mol^{-1} and a dispersity of 1.13. **(Scheme 26, II; Table 6, Entry 8)** The loss of almost 50% of the $M_{n,SEC}$ value before and after the CTA aminolysis might suggest than **R01** efficiently controlled the polymerization even though in a non-regioselective way, making it subject to quick crosslinking when applied to *star*-shaped CTA. Finally, the control of **R01**

over methyl methacrylate (MMA) polymerization was investigated by its polymerization with 10 mol% AIBN relative to the CTA. After 45 minutes at 80 °C, the solution became viscous and the reaction was interrupted, yielding PMMA **P03** with an estimated $M_{n,SEC}$ value of 213 kg mol^{-1} and a high dispersity of 1.66. **(Scheme 26, III; Table 6, Entry 9)** The obtained polymer $M_{n,SEC}$ value was found to not be corelated to the CTA equivalent but rather to AIBN. Moreover, the yellow RAFT agent was washed away from the polymer by reprecipitation in methanol, yielding **P03** as a white solid. Considering also the high dispersity of 1.66, it was concluded that mostly a free radical polymerization of MMA occurred, indicating that **R01** was not able to interact properly with the propagating radical and therefore remained inactive during the complete polymerization process.

Table 6: Overview of styrene **(Entry 1–6)**, methyl acrylate **(Entry 7–8)** and methyl methacrylate **(Entry 9)** polymerizations obtained *via* linear RAFT agent **R01**, including their respective thiol-terminated polymers obtained by aminolysis.

Entry	Polymer	Polymer type	Polymerization time / min	$M_{n,^1H\text{-}NMR}$ / kg mol^{-1}	$M_{n,SEC/THF}$ / kg mol^{-1}	$Đ_{SEC/THF}$
1	**P01 – 1h**	PS	60	1.8	1.8	1.27
2	**P01 – 2h**	PS	120	2.8	3.1	1.20
3	**P01 – 4h**	PS	240	4.8	4.9	1.17
4	**P01-SH – 1h**	PS	60	*n/a*	1.4	1.28
5	**P01-SH – 2h**	PS	120	*n/a*	2.3	1.21
6	**P01-SH – 4h**	PS	240	*n/a*	3.3	1.16
7	**P02**	PMA	30	16.4	14.0	1.11
8	**P02-SH**	PMA	30	16.2	8.1	1.13
9	**P03**	PMMA	45	*n/a*	213	1.66

4.2.2 Unfunctionalized Three-Arm *Star*-shaped CTA as Model RAFT Agent

Following the successful synthesis of the linear RAFT agent **R01** in good yield and its regioselective control of styrene polymerization, the synthesis of an unfunctionalized three-arms *star*-shaped RAFT agent **R02** was planned to further investigate its capacity to create polymer stars. Its synthesis was directly adapted from **R01** by switching the benzyl bromide to a trivalent 1,3,5-tris(bromomethyl)benzene core. **(Scheme 27)** As expected, the yield remained relatively high at 55% despite the triple S_N2 reaction required per molecule. This 55% yield could also be correlated with the yield of 82% obtained for **R01**, as 0.82^3 is indeed approximately equal to 0.55.

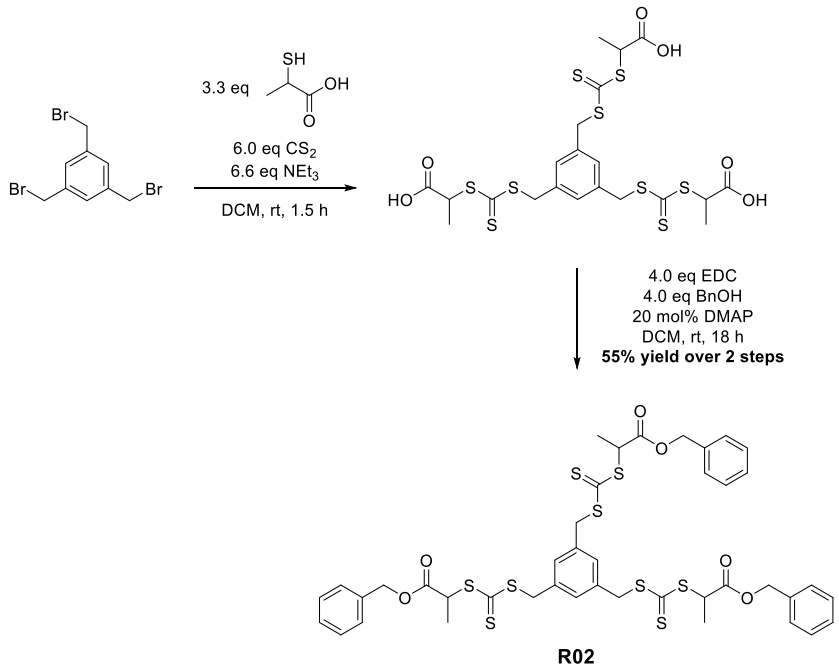

Scheme 27: Two-step synthesis of *star*-shaped RAFT agent **R01** obtained in 55% overall yield.

Once synthetized, the ability of **R02** to regioselectively control the polymerization of styrene and to form *star*-shaped PS was examined. In order to do so, a styrene polymerization **P04** was conducted at 80 °C with 30 mol% AIBN relative to the *star*-shaped RAFT agent **R02** (10 mol% per CTA present on each arm). **(Scheme 28; Table 7, Entry 1–5)** Samples were taken after 30, 60, 90, 120 and 180 minutes in order to carefully follow the occurrence of defects in the *star*-shaped polymer structure. All estimated dispersities from SEC traces were comprised between 1.2 and 1.4. The M_n value of **P04** after 3 hours of polymerization was estimated at 7.1 kg mol^{-1} by SEC and at 11.2 kg mol^{-1} by ^{1}H-NMR analysis. Considering the particular

star-shaped topology of **P04** and its impact on the hydrodynamic volume compared to linear polymers, the underestimation of the size of the polymer in SEC analysis was expected. However, the progressive growth of a high-molecular weight shoulder in the SEC traces, that typically results of side reaction at the CTA positions leading among other to star-star coupling, could also be observed from a DP_{arm} of 20 to 25. **(Figure 2, I)** In consequence, the maximal degree of polymerization of *star*-shaped polymers while keeping a low amount of defect was limited by the occurrence of these side-reactions. Cleavage of each polymer arms by aminolysis led to **P04-SH** with monodisperse SEC traces with dispersity values between 1.2 and 1.4. The DP_{arm} estimated from the $M_{n,SEC}$ data of **P04-SH** were found to be in accordance with the values calculated from the **P04** ^{1}H-NMR data. **(Figure 2, III)** In summary, the regioselectivity of the **R01** and **R02** RAFT agents with styrene was definitively confirmed by all these results. However, in order to keep an end-group fidelity as high as possible and to limit the side-reaction occurrences, a second polymerization with a lower amount of radical initiator equivalent was planned.

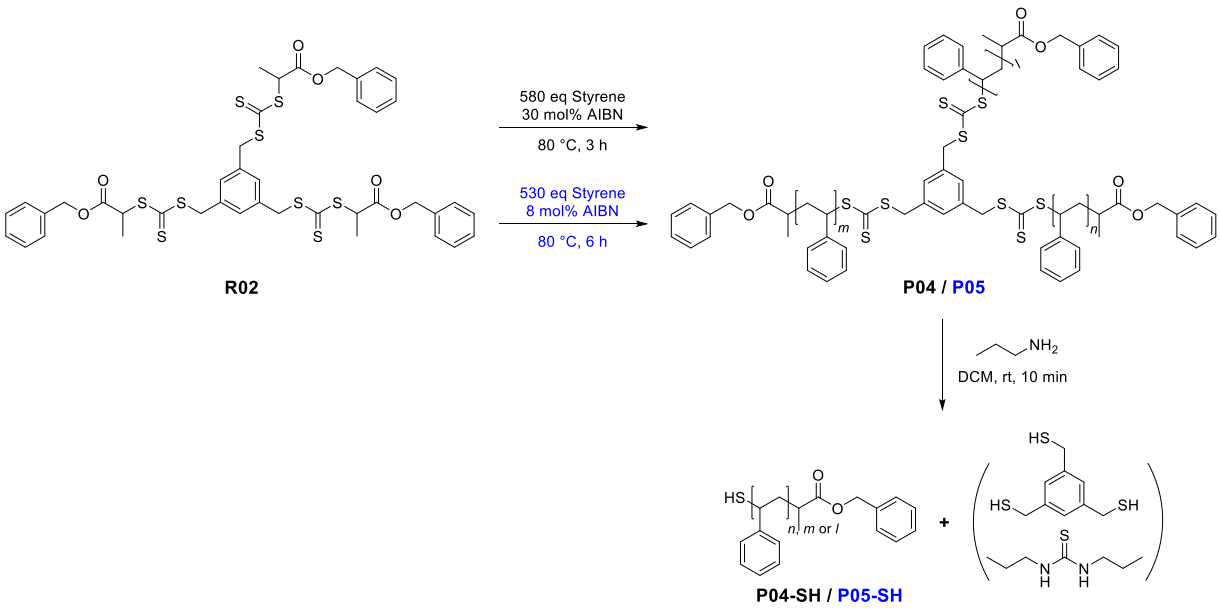

Scheme 28: RAFT polymerizations **P04** and **P05** of styrene by RAFT agent **R02** with 30 mol% and 8 mol% AIBN loading relative to the RAFT agent followed by their aminolysis to obtain thiol end-functionalized **P04-SH** and **P05-SH** PS polymers, respectively.

Thus, a second styrene polymerization **P05** with RAFT agent **R02** and 8 mol% AIBN relative to the *star*-shaped RAFT agent (2.7 mol% per CTA present on each arms) was set up. Due to the slower polymerization kinetics caused by the lower amount of propagating radical chains, samples were taken after 1, 2, 3, 4 and 6 hours. **(Scheme 28; Table 7, Entry 6–10)** After

6 hours of polymerization at 80 °C, the M_n value was estimated to reach 6.0 and 10.5 kg mol^{-1} according to SEC and ^{1}H-NMR analysis, respectively. All dispersities recorded by SEC analysis were between 1.2 and 1.4. Similar to what was already observed for **P04**, a high-molecular shoulder occurred as soon as a DP_{arm} of 20 reached, although high-molecular weight polymers are not mandatory to examine the subsequent topological conversion to *cage*-shaped polymers. **(Figure 2, II)** However, it is still not clear if the origin of the defect came from the increasing bulkiness at the star center, leading to the impossibility for the propagating chains to be efficiently monitored by the CTAs or on the contrary from a minor occurrence of non-regioselective chain exchanges. Finally, the DP_{arm} values of **P05** were compared with the DP_{arm} values from the former **P04** polymerization and in both cases a drop in the polymerization kinetic curve could be noticed once a DP of about 20 was reached. **(Figure 2, III)**

Table 7: Overview of RAFT polymerizations of styrene **P04 (Entry 1-5)** and **P05 (Entry 6-10)** of styrene by RAFT agent **R02** with 30 mol% and 8 mol% AIBN loading relative to the RAFT agent, including their respective thiol-terminated polymers **P04-SH** and **P05-SH** obtained by aminolysis.

Entry	Polymer	$M_{n,^1H\text{-}NMR}$ / kg mol^{-1}	$M_{n,SEC/THF}$ / kg mol^{-1}	$Đ_{SEC/THF}$	Polymer	$M_{n,SEC/THF}$ / kg mol^{-1}	$Đ_{SEC/THF}$
1	**P04 – 30min**	3.3	2.4	1.31	**P04-SH – 30min**	1.0	1.37
2	**P04 – 60min**	5.1	3.4	1.26	**P04-SH – 60min**	1.5	1.31
3	**P04 – 90min**	7.2	4.4	1.25	**P04-SH – 90min**	2.2	1.21
4	**P04 – 120min**	8.6	5.4	1.26	**P04-SH – 120min**	2.8	1.20
5	**P04 – 180min**	11.2	7.1	1.34	**P04-SH – 180min**	3.6	1.19
6	**P05 – 60min**	3.1	2.4	1.32	**P05-SH – 60min**	1.1	1.38
7	**P05 – 120min**	5.0	3.4	1.28	**P05-SH – 120min**	1.5	1.29
8	**P05 – 180min**	7.1	4.2	1.27	**P05-SH – 180min**	2.1	1.24
9	**P05 – 240min**	8.2	4.9	1.29	**P05-SH – 240min**	2.5	1.21
10	**P05 – 360min**	10.5	6.0	1.37	**P05-SH – 360min**	3.1	1.21

At last, in order to verify the non-regioselectivity behavior of **R01** and therefore **R02** during the polymerization with MA, two distinct polymerization **P06** and **P07** were conducted in 1 M MA with toluene and dioxane as solvent, respectively. In both cases, the solution became turbid within 5 min at 80 °C, yielding yellow precipitates. The precipitates were found to be insoluble in THF, DMF and DMAC and were probably most likely the result of the formation of highly crosslinked polymer aggregates by star-star coupling. No further analysis was therefore performed as these results matched the ones obtained for **P02** polymerization with **R01**.

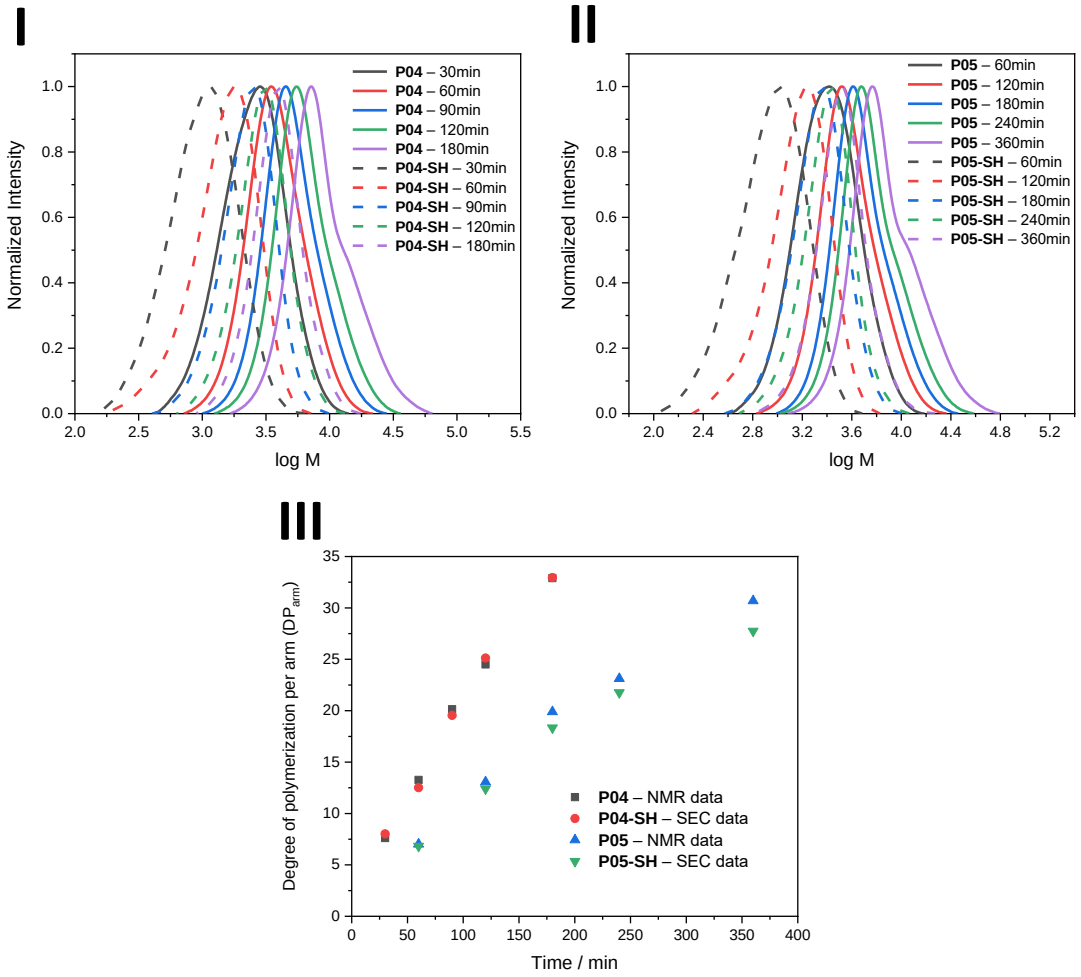

Figure 2: (**I**) SEC traces of **P04** and **P04-SH** polymer samples; (**II**) SEC traces of **P05** and **P05-SH** polymer samples; (**III**) Comparison of the degree of polymerization per arm (DP_{arm}) reached at different polymerization time. DP_{arm} values calculated from **P04**/**P05** $M_{n,^1H\text{-}NMR}$ and **P04-SH**/**P05-SH** $M_{n,SEC/THF}$ data.

4.2.3 Synthesis of First End-functionalized *Star*-shaped RAFT Agent and its Compatibility Towards RAFT Polymerization

As a first end-group candidate to form stable macrocycle for the forthcoming topological conversion to *cage*-shaped polymers, compound **C03** was obtained in a three-steps synthesis from commercially available 3-amino-5-bromobenzoic acid in 37% overall yield. **(Scheme 29, I)** A seven-steps synthesis from 3,5-dinitrobenzoic acid had been previously reported, although being more time consuming.[280,281,282] Starting from the carboxylic acid reduction by lithium aluminum hydride, the benzylic alcohol **C01** was obtained in 61% yield. The reduction suffered from amide group formation as side reaction, leading to the formation of unstable secondary amine in these basic conditions. This first reaction was the followed by a Sonogashira cross-coupling and then direct TMS group deprotection yielding **C02** in 58% yield. At last, a Sandmeyer reaction with azide anions as the nucleophiles was performed, yielding **C03** in an almost quantitative 95% yield. Following the previous procedure already used in **R01** and **R02** syntheses, RAFT agent **R03** was obtained after two chromatography purification steps in a low 16% yield. In order to do so, benzyl alcohol was switched to **C03** at the EDC esterification step of the *star*-shaped tricarboxylic acid precursor. **(Scheme 29, II)** However, compound **C03** showed poor solubility in DCM and therefore DCM was replaced by THF during the esterification step. As the star synthesis is quite sensitive to partial conversion, the final yield might have been impacted by the formation of a floating gel in the reaction medium due to the observed insolubility of the EDC-urea byproducts in pure THF that might have trapped a non-negligible part of the reactants. In consequence, the procedure for the forthcoming EDC esterifications was adapted by using a mixture of DCM and THF as co-solvents. Nevertheless, enough RAFT agent **R03** was isolated to investigate its ability to control styrene polymerization. Thus, the number of AIBN equivalents was fixed at 5 mol% regarding to the *star*-shaped RAFT agent. After 1 hour at 80 °C, the resulting polymer **P08** displayed a polymodal SEC trace including a broad dispersity of 1.82 as well as a low DP_{arm} value. Estimation of the M_n value by SEC and ^{1}H-NMR analysis led to 2.5 kg mol^{-1} and 2.3 kg mol^{-1} values, respectively. Cleaved polymer arms **P08-SH** were further analyzed by SEC and also showed a broad 1.60 dispersity for $M_{n,SEC/THF}$ value of 1.5 kg mol^{-1}. **(Figure 3)** These results implied that end-group **C03** negatively impacted the RAFT polymerization mechanism due to the presence of the azide or terminal alkyne groups. In particular, radical-driven side-reactions

could have occurred at these positions, leading to topological defects by crosslinking and/or CTA decomposition.

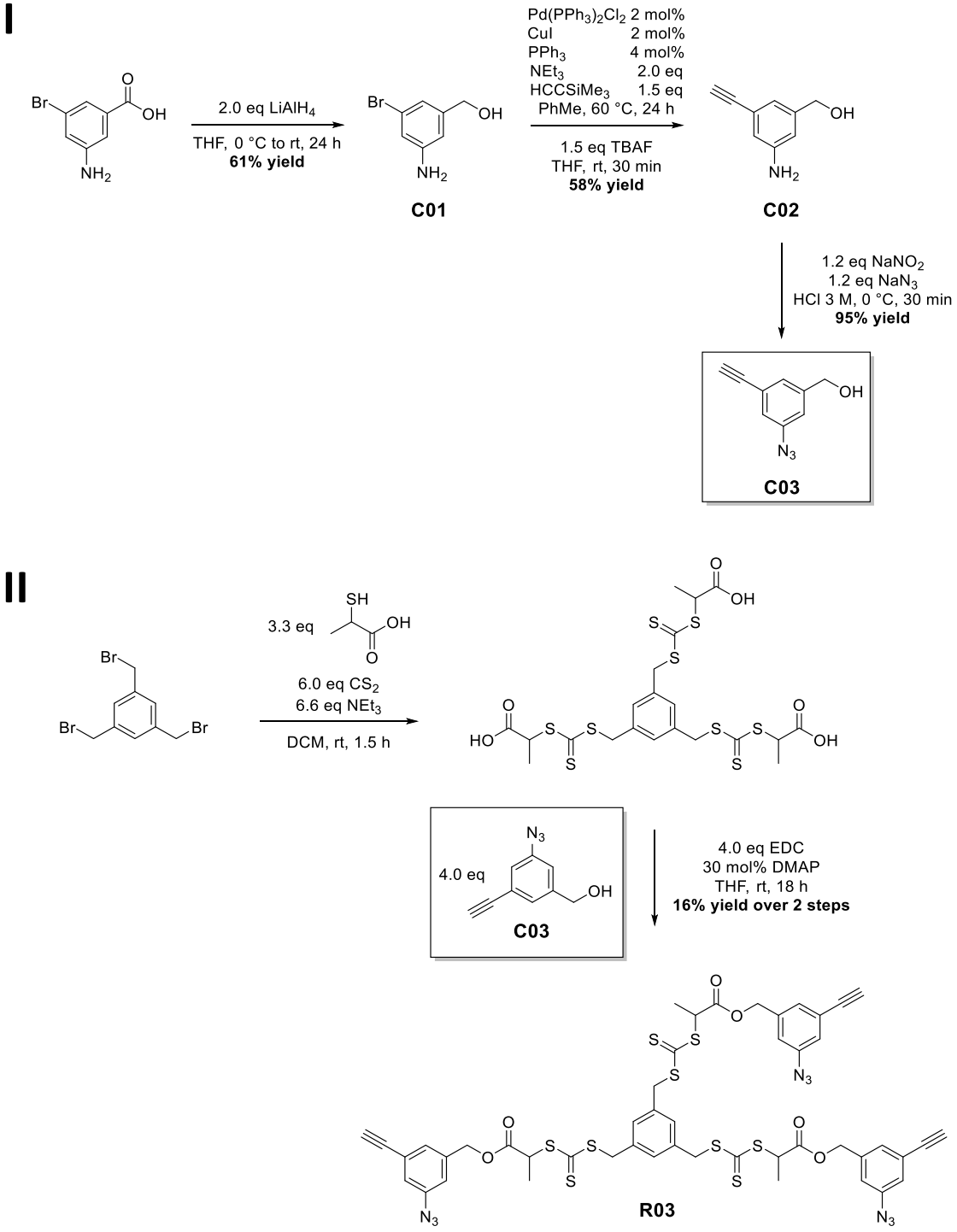

Scheme 29: (**I**) Three-step synthesis of compound **C03** obtained in 37% overall yield; (**II**) Two-step synthesis of *star*-shaped RAFT agent **R03** following the previous synthesis conditions at the exception of the substitution of benzyl alcohol for compound **C03** at each arm extremity.

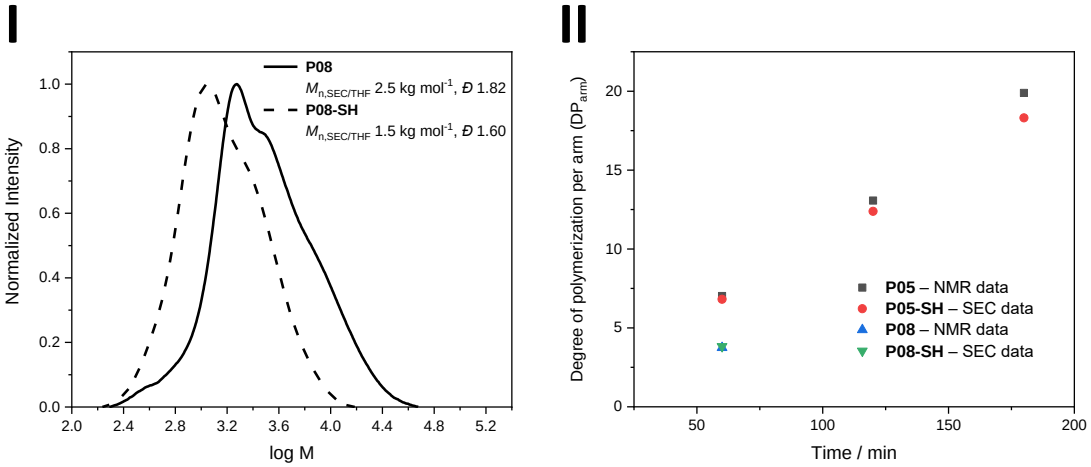

Figure 3: (**I**) SEC traces of **P08** and **P08-SH** obtained after 1 hour polymerization and displaying a high number of topological defects; (**II**) Comparison of the degree of polymerization per arm (DP_{arm}) reached between **P05** and **P08** polymerizations. DP_{arm} values calculated from **P05**/**P08** $M_{n,^1H\text{-}NMR}$ and **P05-SH**/**P08-SH** $M_{n,SEC/THF}$ data.

For instance, aliphatic and aromatic azides were reported to undergo 1,3-dipolar cycloaddition (i.e. [2+3] cyclization) with electro-deficient olefin (like electro-deficient acrylate or acrylamide monomers) at common polymerization temperatures.[283] The resulting heterocyclic product – 1,2,3-triazoline – is however unstable and prompt to follow different decomposition pathways, as it does not benefit from the same aromatic stabilization than triazoles. According to the same authors, monomers that stabilize the propagating radicals without having to resort to strong electron-withdrawing but rather on electron delocalization (i.e. styrenic monomers) possess a higher tolerance towards azide groups at a given temperature. In this regard, based on the catalyzed degradation of benzoyl peroxide (BPO) by *N*,*N*-dimethylaniline (DMA) to generate initiating radicals at room temperature, a few examples of azide-containing monomers polymerized by RAFT were still reported.[284,285] At last, reports of free-radical oligomerization of phenylacetylene were also published and caused by the mesomeric stabilization provided by the phenyl ring.[286] In consequence, avoiding inductive or mesomeric stabilizing group next to the terminal alkyne was also essential to ensure the smooth running of the RAFT polymerization. In summary, the following changes were taken into account for the next experiments: a) a reduction of the radical concentration during the polymerization; b) a reduction of the polymerization temperature; and c) the absence of radical-stabilizing group next to the terminal alkyne.

4.2.4 Investigation regarding Low-temperature RAFT Polymerization

As previously mentioned, the decomposition of benzoyl peroxide triggered by *N*,*N*-dimethylaniline – although suffering from a lower probability to induce propagating radical chain – is known to produce radicals at room temperature and more particularly to allow the RAFT polymerization of azide-bearing monomers. Therefore, starting from linear RAFT agent **R01** present in equimolar ratio with BPO and DMA co-initiators, a RAFT polymerization of styrene **P09** was carried out at room temperature. **(Figure 4, I; Table 8, Entry 1)** However, SEC analysis revealed that only a low $M_{n,SEC}$ value of 1.6 kg mol^{-1} with a dispersity of 1.4 could be reached after 22 hours of polymerization, making this initiator system difficultly viable. Consequently, V-70 (i.e. 2,2'-azobis(4-methoxy-2,4-dimethylvaleronitrile)), a commercially available radical initiator operating at a lower temperature range than most common radical initiators, was instead chosen. More precisely, V-70 has an equivalent degradation rate at 40 °C than AIBN at 80 °C with an estimated half-life slightly below 2 hours in both cases. Styrene polymerization **P10** was conducted for 24 hours at 40 °C with 5 mol% V-70 and RAFT agent **R02**. **(Scheme 30; Table 8, Entry 2–5)** ^{1}H-NMR and SEC data of the *star*-shaped **P10** as well as SEC data from its cleaved arms **P10-SH** suggested the controlled nature of the polymerization while its DP_{arm} values were reduced by a factor of two in comparison to what had been observed for **P05** after 8 hours. **(Figure 4, II–III)** The SEC traces also remained unimodal during the polymerization time with dispersity values tending to 1.3 after 24 hours.

Table 8: Overview of RAFT polymerizations of styrene **P09 (Entry 1-3)** and **P10 (Entry 4-7)** carried out at room temperature with BPO/DMA co-initiator and at 40 °C with V-70 initiator, respectively, as well as thiol-terminated **P10-SH** polymer samples obtained by aminolysis.

Entry	Polymer	$M_{n,^1H\text{-}NMR}$ / kg mol^{-1}	$M_{n,SEC/THF}$ / kg mol^{-1}	$Đ_{SEC/THF}$	Polymer	$M_{n,SEC/THF}$ / kg mol^{-1}	$Đ_{SEC/THF}$
1	**P09 – 1h**	*n/a*	0.8	1.27	*n/a*	*n/a*	*n/a*
2	**P09 – 3h**	*n/a*	1.2	1.32	*n/a*	*n/a*	*n/a*
3	**P09 – 22h**	*n/a*	1.6	1.4	*n/a*	*n/a*	*n/a*
4	**P10 – 2h**	2.5	1.9	1.43	**P10-SH – 2h**	0.6	1.70
5	**P10– 5h**	3.5	2.7	1.35	**P10-SH – 5h**	1.1	1.45
6	**P10 – 8h**	4.5	3.3	1.31	**P10-SH – 8h**	1.4	1.33
7	**P10 – 24h**	5.5	4.3	1.33	**P10-SH – 24h**	2.1	1.30

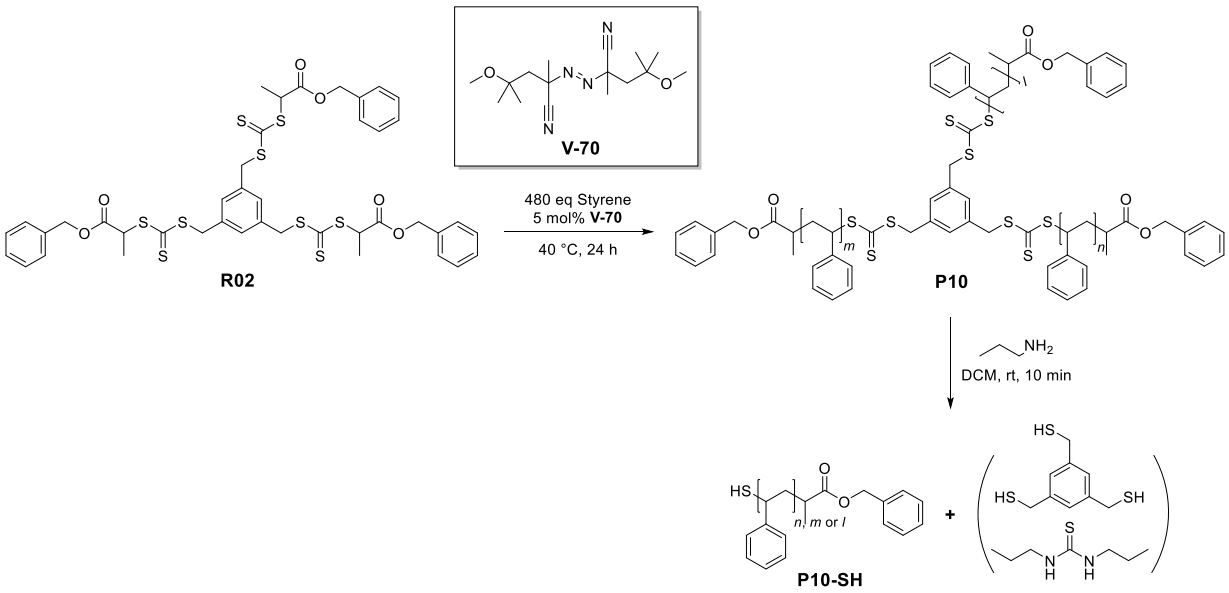

Scheme 30: RAFT polymerizations **P10** of styrene by RAFT agent **R02** with 5 mol% V-70 loading relative to the RAFT agent followed by its aminolysis to obtain thiol end-functionalized PS **P10-SH**.

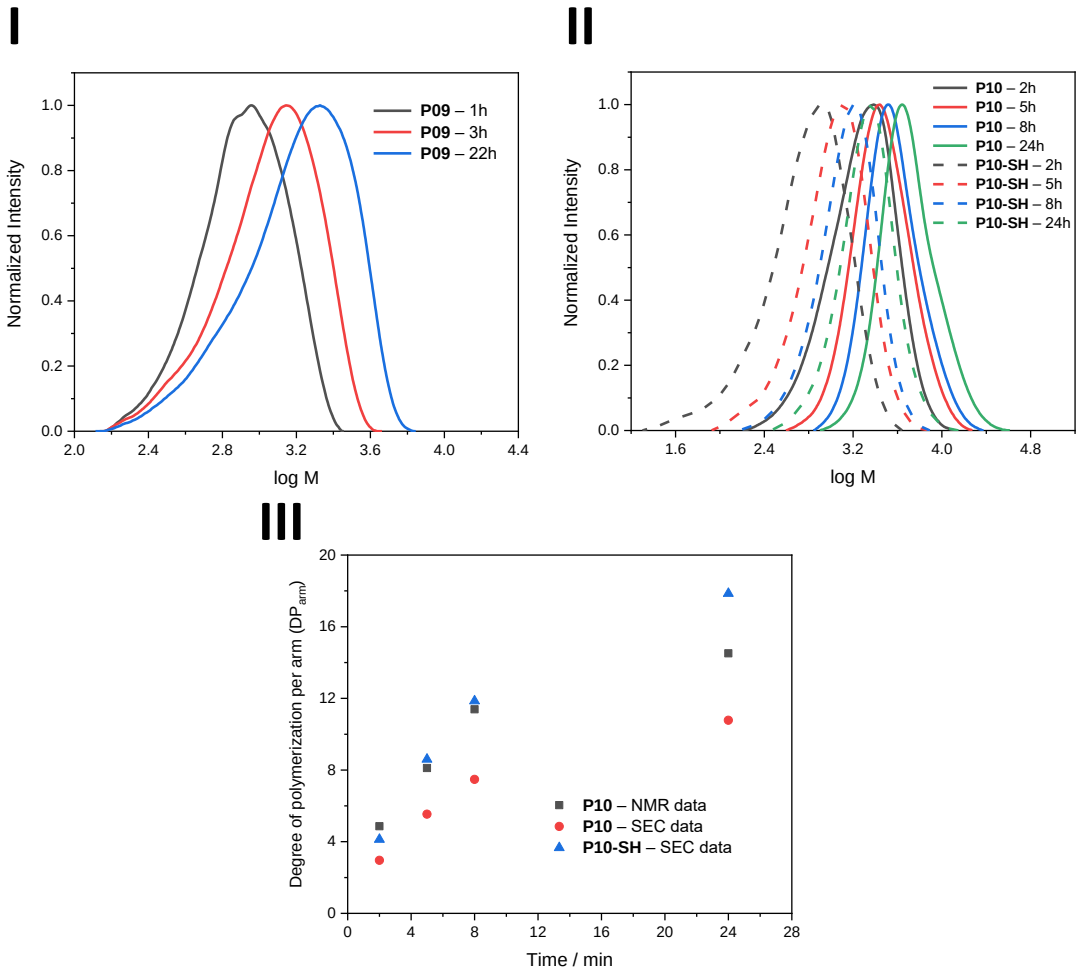

Figure 4: (**I**) SEC traces of **P09** polymer samples taken after 1, 3 and 22 hours; (**II**) SEC traces of **P10** and **P10-SH** polymer samples; (**III**) Degree of polymerization per arm (DP_{arm}) reached at different polymerization time. DP_{arm} values calculated from **P10** and **P10-SH** $M_{n,SEC/THF}$ as well as **P10** $M_{n,^1H\text{-}NMR}$ data.

4.2.5 Synthesis of Second End-functionalized *Star*-shaped RAFT Agent and its Compatibility Towards RAFT Polymerization

Concerning the synthesis of an alternative second end-group, the main concern was to avoid any radical stabilizing group next to the terminal alkyne while keeping a sufficient structural strain to avoid any intramolecular cyclization for the end-group as well as for its dimer. Therefore, the azide group was conserved on the phenyl ring to ensure a minimal rigidity of the molecule while the alkyne group was placed two aliphatic carbons away from the aromatic ring. Furthermore, in order to reduce the number of steps, both alcohol and alkyne groups were planned to be simultaneously incorporated into the end-group structure. Thus, 4-nitrobenzaldehyde was reacted with trimethylsulfonium iodide and potassium hydroxide to obtain the corresponding epoxide **C04** in 52% yield.[287,288] This reaction – known as Johnson-Corey-Chaykovsky reaction[289,290] – consists in the *in situ* formation of a sulfur ylide reagent, which further reacts with carbonyls or imines to ultimately yield epoxide or aziridine products, respectively. Then, the epoxide ring was opened using the lithium acetylide complex in order to incorporate both terminal alkyne and alcohol functional groups in one reaction, according to former reports on primary halide[291] and epoxide[292] substrates. However, the low 8% yield of **C05** suffered from the side-reactions occurring between the nitro groups and the acetylide anions. Nevertheless, the aromatic nitro group was then reduced by metal iron in acidic condition to form **C06** in 60% yield. Finally, a Sandmeyer reaction with sodium azide as nucleophile was used to obtain end-group **C07** in 95% yield. **(Scheme 31, I)** In summary, the low 2.4% yield over four steps coupled to the extended purification required at each step made this synthesis particularly impracticable and therefore not likely to be further considered. Subsequently, RAFT agent **R04** was synthetized from **C07** in a low 17% yield after two successive purifications by column chromatography **(Scheme 31, II)** and only one polymerization was attempted with the isolated amount of RAFT agent **R04**. Based on the polymerization data obtained from **P10** polymerization conducted with RAFT agent **R02** and 5 mol% radical initiator V-70 at 40 °C, the polymerization time for the present **P11** was fixed at 3 hours to target a DP_{arm} close to 5 units. **(Scheme 32, I–II)** However, only a DP_{arm} of 3 was achieved after the 3 hours of polymerization according to both SEC and ^{1}H-NMR data. **(Figure 5, II)** At last, both SEC traces of **P11** and its cleaved arms **P11-SH** possessed bimodal distribution with dispersity of 1.49 and 1.46, implying once again defects in the *star*-shaped polymer topology. **(Figure 5, I)**

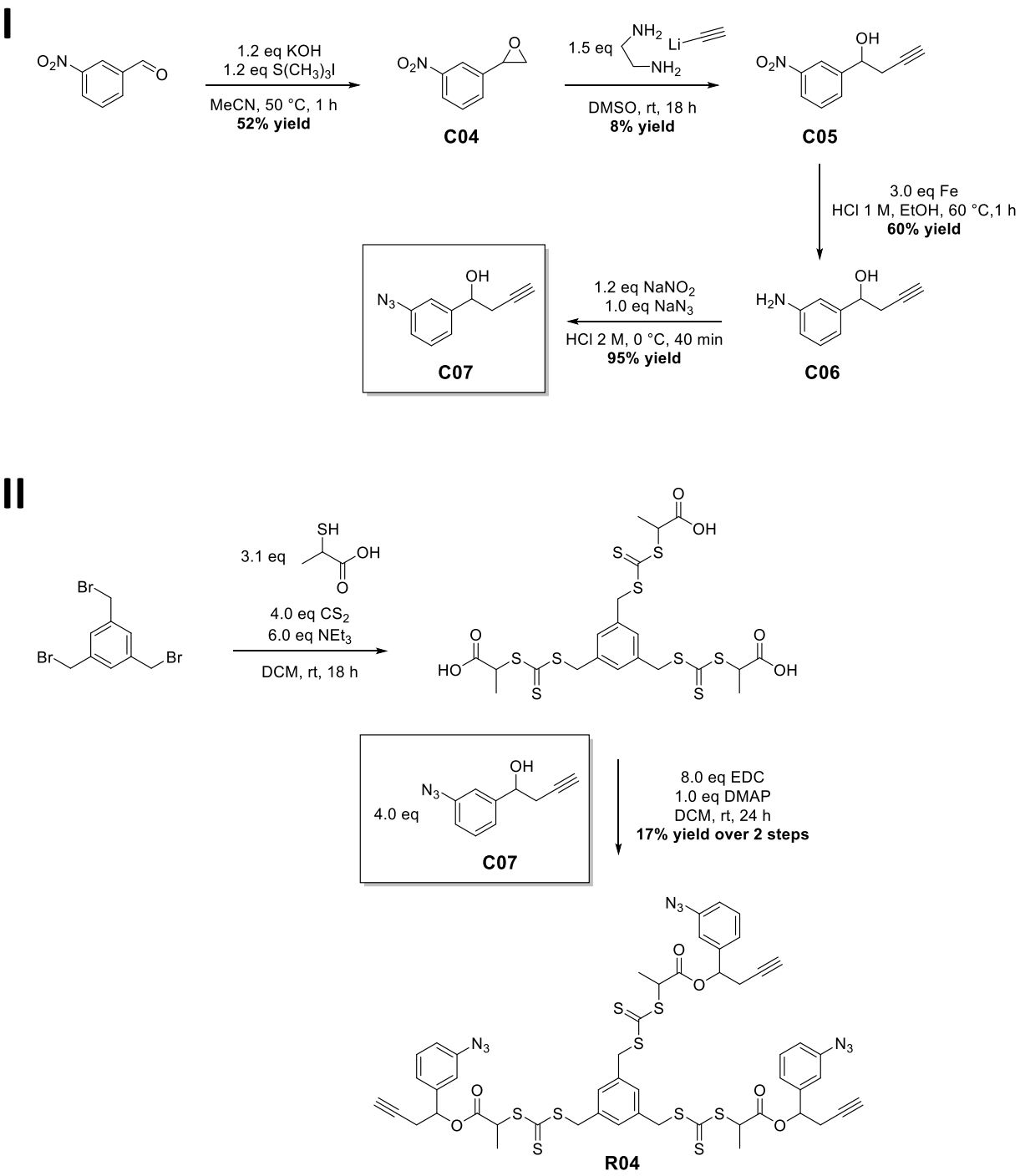

Scheme 31: (**I**) Four-step synthesis of compound **C07** obtained in 2.3% overall yield; (**II**) Two-step synthesis of *star*-shaped RAFT agent **R04** obtained in 17% yield.

At last, **P11** was employed for a single CuAAC closing attempt. To do so, copper(I) iodide was suspended in toluene at 80 °C. Then, 42 mg of **P11** were added over 8 hours *via* a syringe pump before heating the resulting mixture for another 2 hours to obtain **P11-C** as an opaque yellow gel after isolation. **(Scheme 32, III; Figure 5, I)** The syringe filter prior to SEC analysis was found to be quickly obstructed, indicating the presence of a polymer network. Once the

aminolysis of **P11-C** was achieved, the filtration of **P11-C-SH (Scheme 32, IV; Figure 5, I)** before SEC analysis still remained partially obstructed. Also, the intensity of the azide characteristic strong stretching band only partially decreased at 2113 cm^{-1} in the FT-IR spectrum of **P11-C**, indicating a partial conversion despite the apparent high degree of cross-linking. **(Figure 5, III)** At last, considering that topological defects were already present after the **P11**, no clear conclusion could be extrapolated from the experimental data.

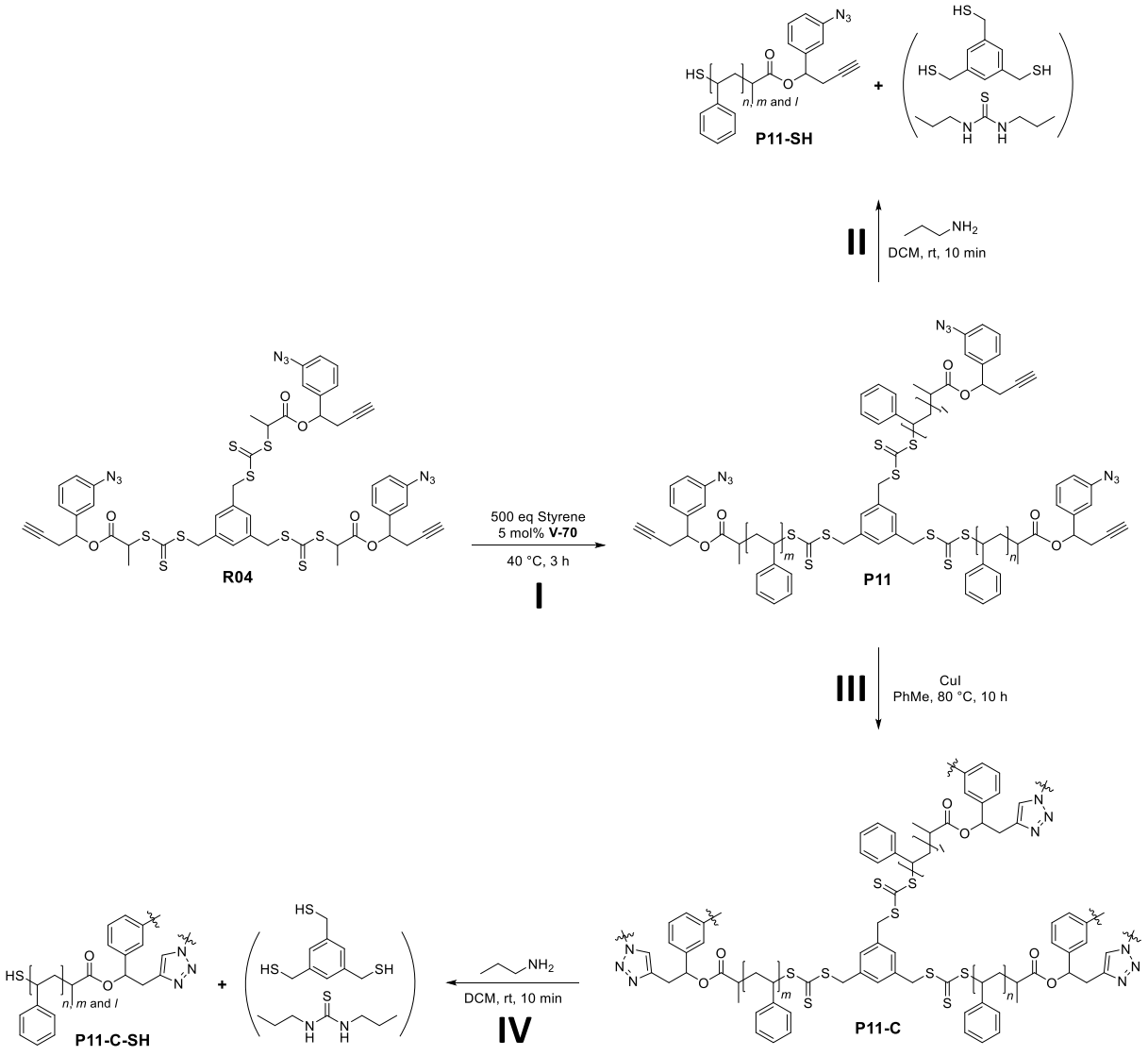

Scheme 32: (**I**) RAFT polymerizations **P11** of styrene by RAFT agent **R04** and with 5 mol% V-70 loading relative to the RAFT agent; (**II**) **P11** aminolysis yielding thiol end-functionalized PS **P10-SH**; (**III**) Topological conversion attempt from *star*-shaped **P11** to *cage*-shaped **P11-C** polymer; (**IV**) **P11** aminolysis yielding **P10-C-SH**.

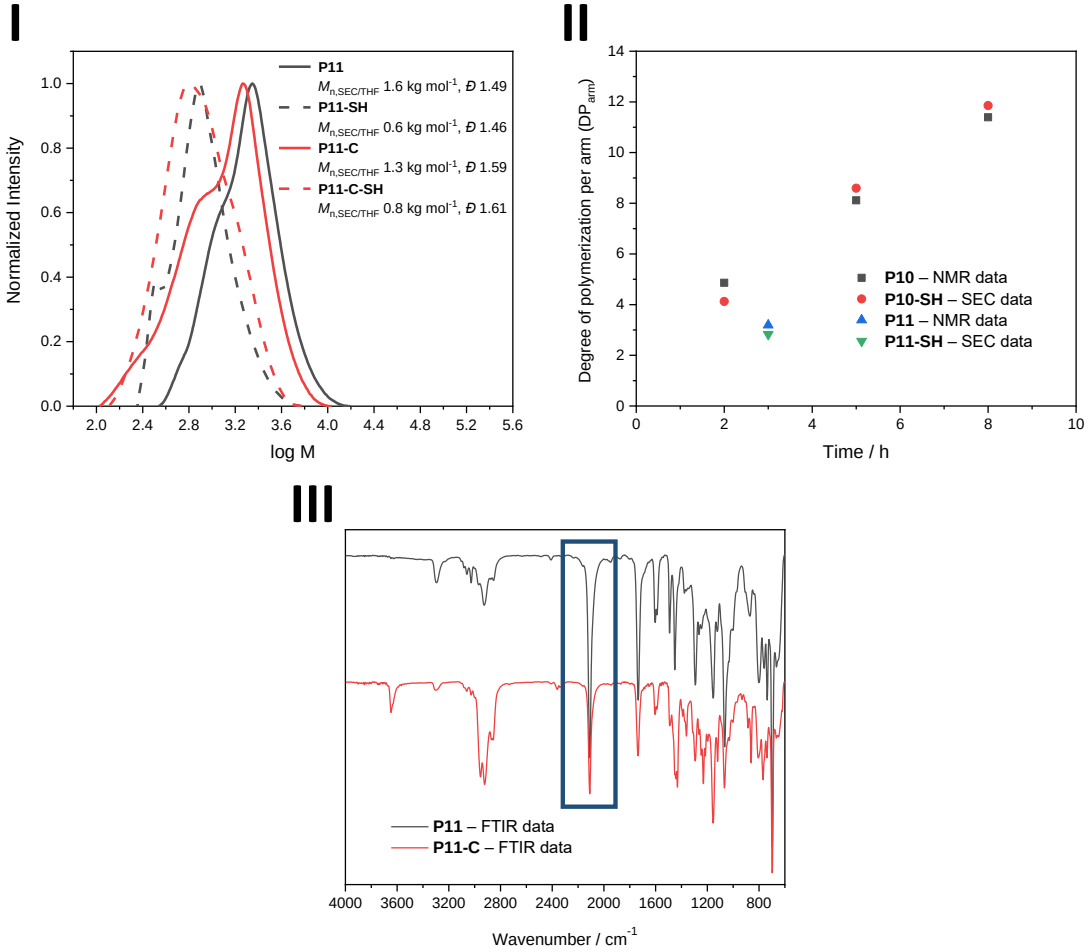

Figure 5: (**I**) SEC traces of **P11** and its cleaved arm **P11-SH** obtained after 3 hours polymerization with V-70 as initiator at 40 °C and displaying a high number of topological defects as well as **P11-C** obtained by CuAAC reaction from **P08** in high dilution and its cleaved arm **P08-SH**; (**II**) Comparison of the degree of polymerization per arm (DP_{arm}) reached between **P10** and **P11** polymerizations. DP_{arm} values calculated from **P10**/**P11** $M_{n,^1H\text{-}NMR}$ and **P10-SH**/**P11-SH** $M_{n,SEC/THF}$ data; (**III**) Comparison of the FT-IR traces from **P11** and **P11-C** obtained after CuAAC reaction in high dilution and in particular the retention of the azide band intensity at 2113 cm^{-1} (**blue rectangle**).

4.2.6 Synthesis of Third End-functionalized *Star*-shaped RAFT Agent and its Compatibility Towards RAFT Polymerization

Considering the difficult synthesis of compound **C07** and the polymerization issues of RAFT agent **R04**, the synthesis of a series of purely aliphatic end-groups with different spacing length between the azide and alkyne functional groups was devised. Foremost, the synthesis of **C09** was achieved in a two steps synthesis from a commercially available 2-methylbut-1-en-3-yne substrate. The alcohol and the azide functionalities were incorporated in a two steps synthesis by mCPBA epoxidation of the alkene[293] followed by the ring-opening reaction with sodium azide to obtain **C09** in 30% yield. **(Scheme 33, I)** Noteworthy, the DCM present from the epoxidation step was completely removed to avoid any risk of explosion resulting from the S_N2 reaction of DCM and sodium azide during the second step by addition of diethylether to a distillation setup including a Vigreux column. The mCPBA epoxidation was estimated to be quantitative by ^{1}H-NMR. However, due to the volatility of intermediate **C08**, no separate yields were recorded for each step as the diethylether– used to remove any trace of DCM prior to the azide addition – could not be totally removed itself. At last, the synthesis of the related RAFT agent failed due to the low reactivity of the tertiary alcohol with carboxylic acids by EDC esterification, probably due to increased steric hindrance. **(Scheme 34, I)** In order to make the alcohol react *via* EDC esterification, the synthesis of an end-group similar to **C09** but without its methyl group was planned. Therefore, the synthesis of **C12** was envisaged from two distinct pathways. The first pathway consisted in a Sonogashira cross-coupling of vinyl bromide with TMS acetylene to obtain but-1-en-3-yne substrate as **C10**, followed by the mCPBA epoxidation of the double bond to yield **C11** and a subsequent epoxide opening with sodium azide. **(Scheme 33, II)** However, due to the missing methyl group, this last step led to a mixture of both regioisomers with a very low overall yield for the expected regioisomers **C12** as the steric hindrance was sufficient to prevent the nucleophilic attack at the secondary carbon position. Furthermore, even if the solvent was never fully removed and even if a distillation aperture with a Vigreux column was used, a large part of the product was lost by evaporation as the synthesis suffered from multiple solvent incompatibilities (i.e. THF/mCPBA and DCM/NaN_3) and therefore, from the need to use cyclohexane in the distillation process to remove the undesired solvents.

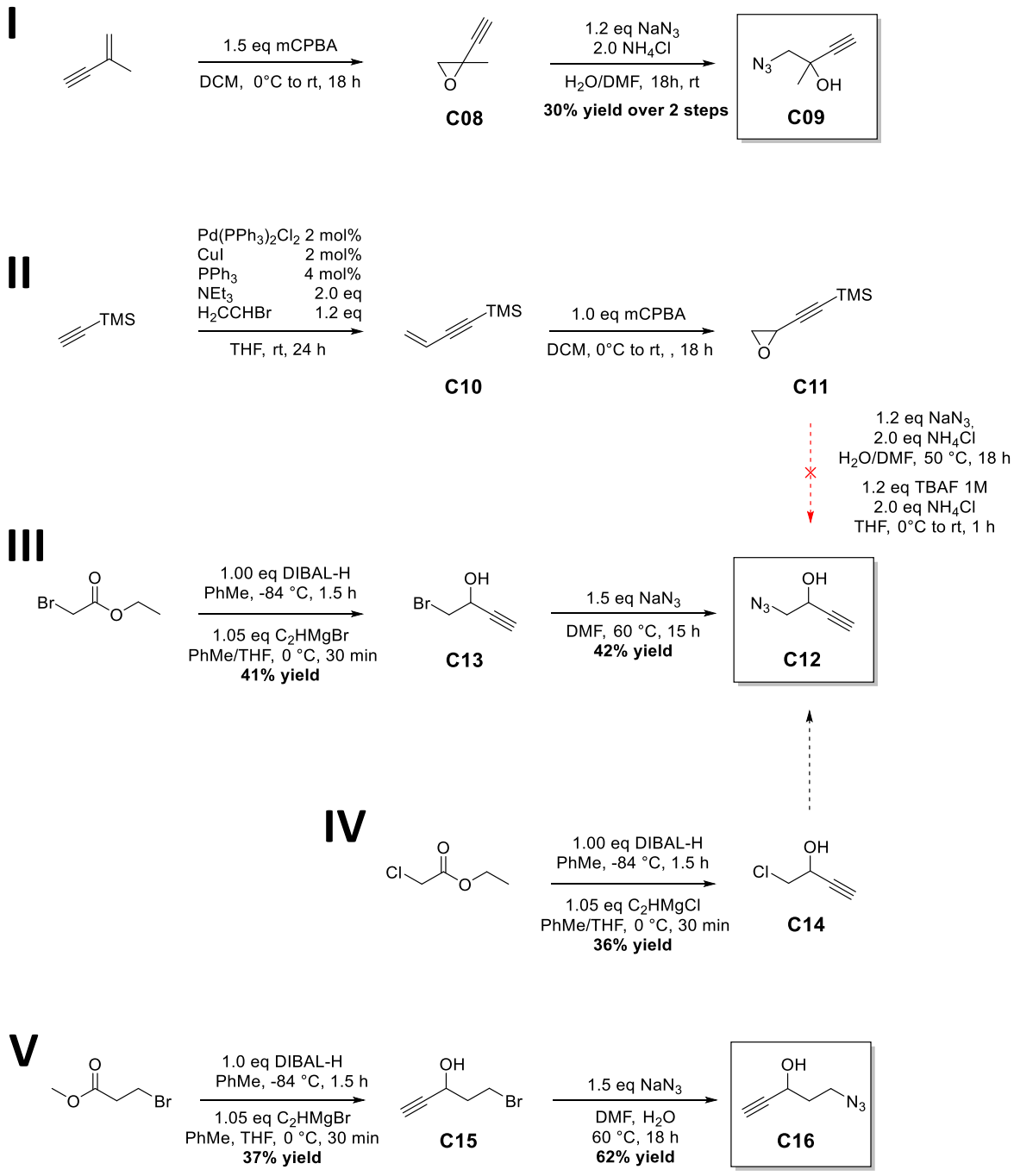

Scheme 33: (**I**) Two-step synthesis of compound **C09** obtained in 30% overall yield; (**II**) There-step synthesis of compound **C12** but without isolation of the final product; (**III**) Two-step synthesis of compound **C12** obtained in 17% overall yield from ethyl bromoacetate; (**IV**) Planned two-step synthesis of compound **C12** from ethyl chloroacetate but which led to lower yield than the one obtained from synthesis pathway (**III**); (**V**) Two-step synthesis of compound **C16** obtained in 23% overall yield.

Considering all the drawbacks of the first synthesis pathways, a second two-steps synthesis of **C12** was investigated. **(Scheme 33, III)** Starting from a one pot reduction of ethyl bromoacetate with DIBAL-H, bromo-acetaldehyde was further reacted *in situ* with commercially available Grignard magnesium acetylene bromide reagent to form **C13** in 41% yield.[294] The forthcoming

step consisting of the S_N2 reaction of bromides by azide anions was achieved in 42% yield after 15 hours at 60 °C, ultimately resulting in a 17% yield of **C12** over two steps. Additionally, the synthesis of **C12** was also examined from ethyl chloroacetate substrate and using magnesium acetylene chloride as Grignard agent to limit the halide exchange and thus the number to different products after the first step. **(Scheme 33, IV)**

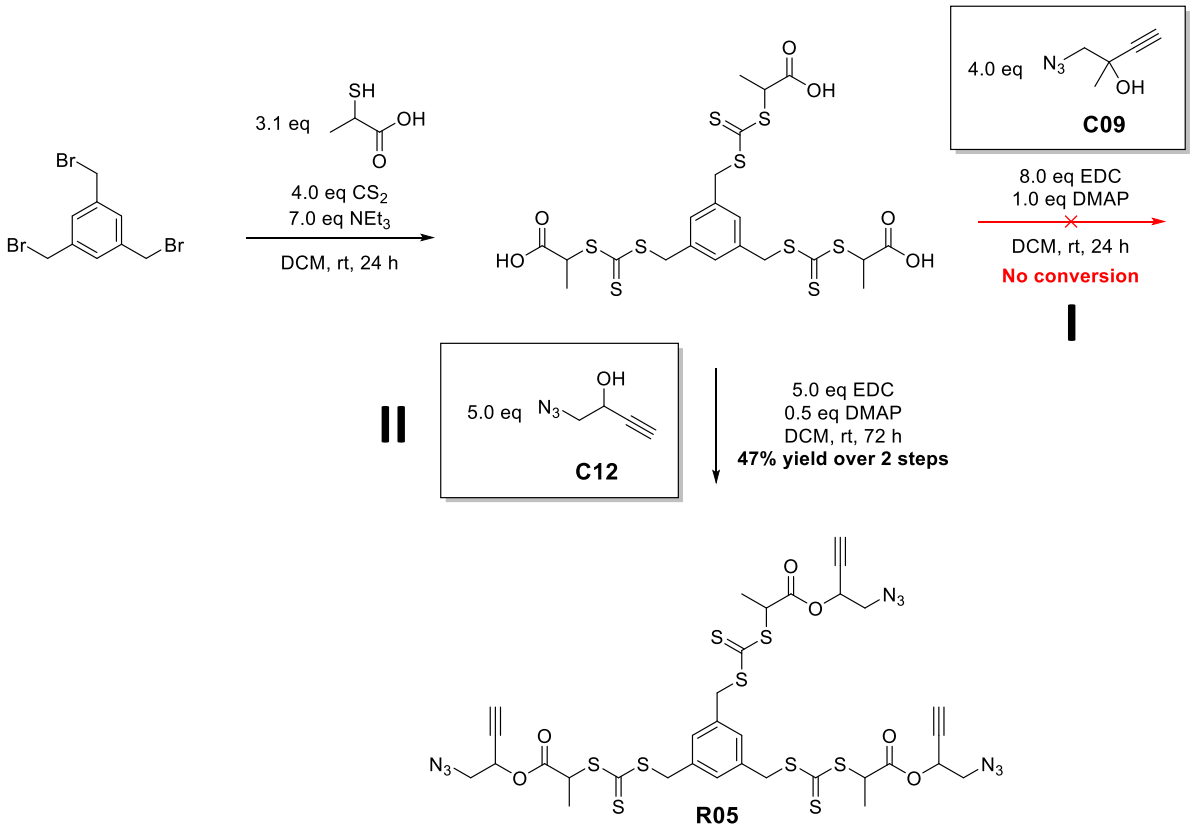

Scheme 34: (**I**) Unsuccessful two-step synthesis of *star*-shaped RAFT bearing **C09** due to the steric hindrance of the tertiary alcohol; (**II**) Two-step synthesis of *star*-shaped RAFT agent **R05** obtained in 47% yield.

However, the yield of the first step to **C14** was similar to the yield of **C13** (i.e. 36% and 41%, respectively) and the azide substitution led to even more degradation products than with the bromide due to the higher temperature needed to achieve the substitution. At last, a synthesis following a similar pathway was achieved from methyl 3-bromopropanotate, resulting in more flexible end-group **C16** in 23% overall yield. **(Scheme 33, V)** However, polymerization **P12** had been done by this time and its negative results due to the functional group incompatibilities made further synthesis of a RAFT agents obsolete.

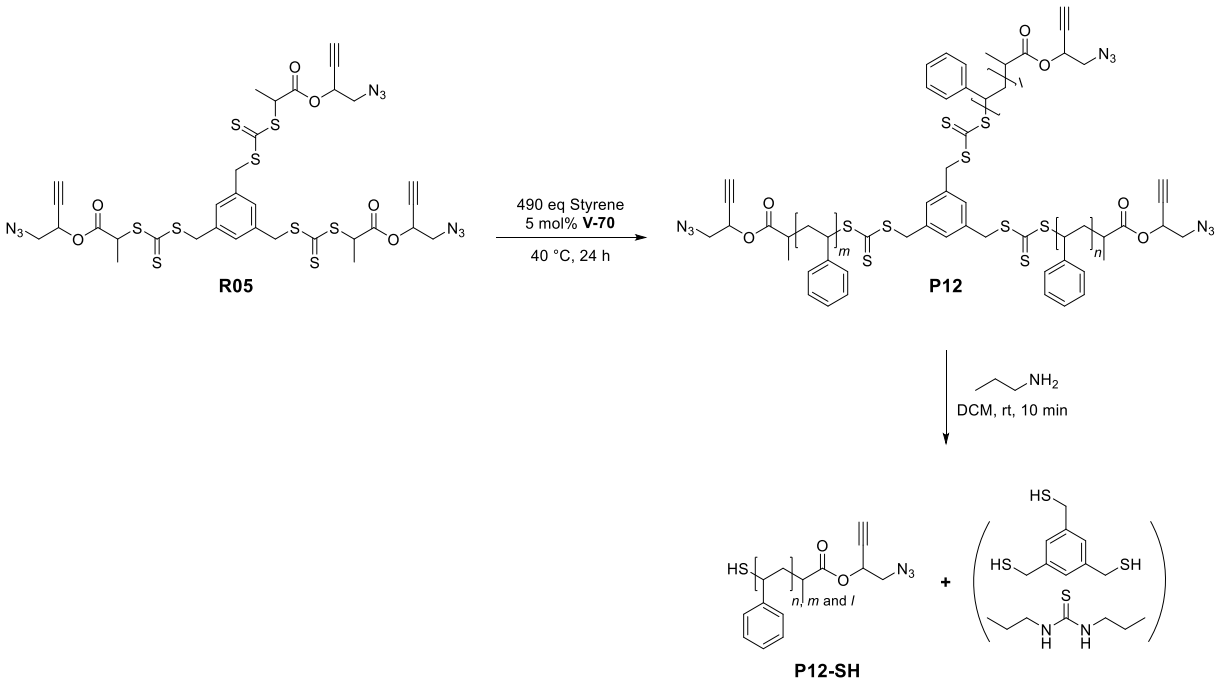

Scheme 35: RAFT polymerizations **P12** of styrene by RAFT agent **R05** and with 5 mol% V-70 loading relative to the RAFT agent followed by its aminolysis yielding thiol end-functionalized PS **P12-SH**.

Star-shaped RAFT agent **R05** was successfully synthesized from the end-group **C13** in a satisfying 47% yield **(Scheme 34, II)**. However, styrene polymerization of RAFT agent **R05** with V-70 as initiator led to polymer **P12**, **(Scheme 35)** which displayed irregular SEC traces with broad dispersity above 1.5. **(Figure 6, I-II; Table 9)** On the contrary, the analysis of **P12-SH** surprisingly led to a $M_{n,SEC}$ of 0.9 kg mol^{-1} after 2 hours to 1.6 kg mol^{-1} after 24 hours while keeping a good gaussian SEC trace with dispersity kept between 1.3 and 1.4. These results seem to indicate that at least some of the arms continued to grow as intended over time despite the presence of side-reactions occurring at the CTA or the end-group sites. As a result, it seems that end-group **C13** has a strong negative effect on the polymerization. Even if the cleaved arms **P12-SH** continue to grow with the expected dispersity of 1.3, the presence of topological defects in the *star*-shaped polymer **P12** made it incompatible with the following topological conversion step to polymer cages.

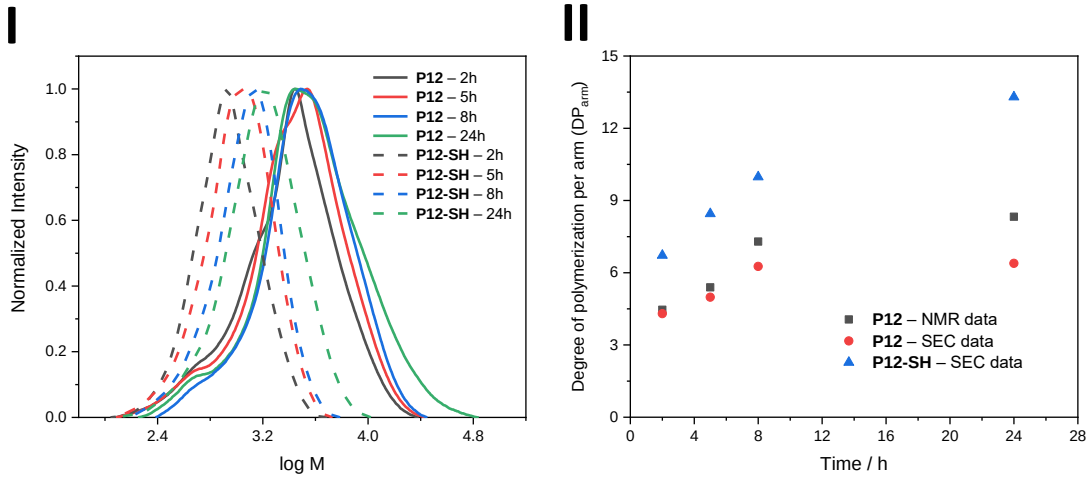

Figure 6: (**I**) SEC traces of **P12** and **P12-SH** polymer samples taken at different polymerization time; (**II**) Degree of polymerization per arm (DP_{arm}) reached at different polymerization time. DP_{arm} values calculated from **P12** and **P12-SH** $M_{n,SEC/THF}$ as well as **P12** $M_{n,^1H\text{-}NMR}$ data.

Table 9: Overview of RAFT polymerization of styrene **P12** carried out at 40 °C with **R05** and V-70 initiator as well as of its thiol-terminated polymers **P12-SH** obtained by **P12** samples aminolysis.

Entry	Polymer	$M_{n,^1H\text{-}NMR}$ / kg mol^{-1}	$M_{n,SEC/THF}$ / kg mol^{-1}	$Đ_{SEC/THF}$	Polymer	$M_{n,SEC/THF}$ / kg mol^{-1}	$Đ_{SEC/THF}$
1	**P12 – 2h**	2.3	2.3	1.64	**P12-SH – 2h**	0.9	1.33
2	**P12 – 5h**	2.6	2.5	1.64	**P12-SH – 5h**	1.1	1.34
3	**P12 – 8h**	3.2	2.9	1.57	**P12-SH – 8h**	1.2	1.30
4	**P12 – 24h**	3.5	2.9	1.83	**P12-SH – 24h**	1.6	1.41

4.2.7 Synthesis of *Star*-shaped RAFT Agent bearing Carboxylic Acid as End- groups and its Compatibility Towards RAFT Polymerization

The initial approach consisting in using an end-functionalized *star*-shaped RAFT agent was not anymore considered viable at this point of the research. Therefore, instead of further being focus on the use of end-functionalized *star*-shaped RAFT agent, the possibility to introduce the end-group by post-polymerization modification was thoroughly considered. Therefore, the polymerization of *star*-shaped RAFT agent **R06** followed by its post-polymerization modification by EDC coupling was envisioned. Thus, **R06** was synthetized and used without further purification as none was found to be efficient due to its three free carboxylic acid groups. **(Scheme 36, I)** The styrene polymerization **P13** was performed from **R06** at 80 °C over 6 hours. **(Scheme 36, II)** As **R06** RAFT agent was not soluble in pure styrene, an additional 25 vol% DMF was used as cosolvent. Furthermore, ACVA was used as radial initiator to conserve as much as possible the carboxylic acid groups at each end-group position. According to ^{1}H-NMR data, DP_{arm} values did not exceed 10 units compared to the 30-40 units obtained from RAFT agent **R02**. Furthermore, the resulting polymer samples showed dispersity values between 1.3 and 1.4 with a $M_{n,SEC/THF}$ of 3.5 kg mol^{-1} and $M_{n,^{1}H\text{-}NMR}$ 4.5 kg mol^{-1} after 6 hours. **(Figure 7; Table 10)**

Table 10: Overview of RAFT polymerization of styrene **P13** carried out at 40 °C with **R06** and ACVA initiator as well as of its thiol-terminated polymers **P13-SH** obtained by **P13** polymer samples aminolysis.

Entry	Polymer	$M_{n,^{1}H\text{-}NMR}$ / kg mol^{-1}	$M_{n,SEC/THF}$ / kg mol^{-1}	$Đ_{SEC/THF}$	Polymer	$M_{n,SEC/THF}$ / kg mol^{-1}	$Đ_{SEC/THF}$
1	**P13 – 1h**	2.2	1.3	1.61	**P13-SH – 1h**	1.1	1.57
2	**P13 – 2h**	2.8	2.1	1.36	**P13-SH – 2h**	1.2	1.50
3	**P13 – 3h**	3.5	2.5	1.35	**P13-SH – 3h**	1.4	1.44
4	**P13 – 4h**	3.9	3.0	1.30	**P13-SH – 4h**	1.6	1.40
5	**P13 – 6h**	4.5	3.5	1.31	**P13-SH – 6h**	1.8	1.27

Although, it is likely that the ionic nature of the end-groups led to unreliable SEC results because of dynamic H-bond dimer formation on the SEC column, it became clear that more radical changes were needed and that the general polymerization approach had to be

reconsidered in order to overcome the challenge of producing defect-free star topologies with high end-group fidelity.

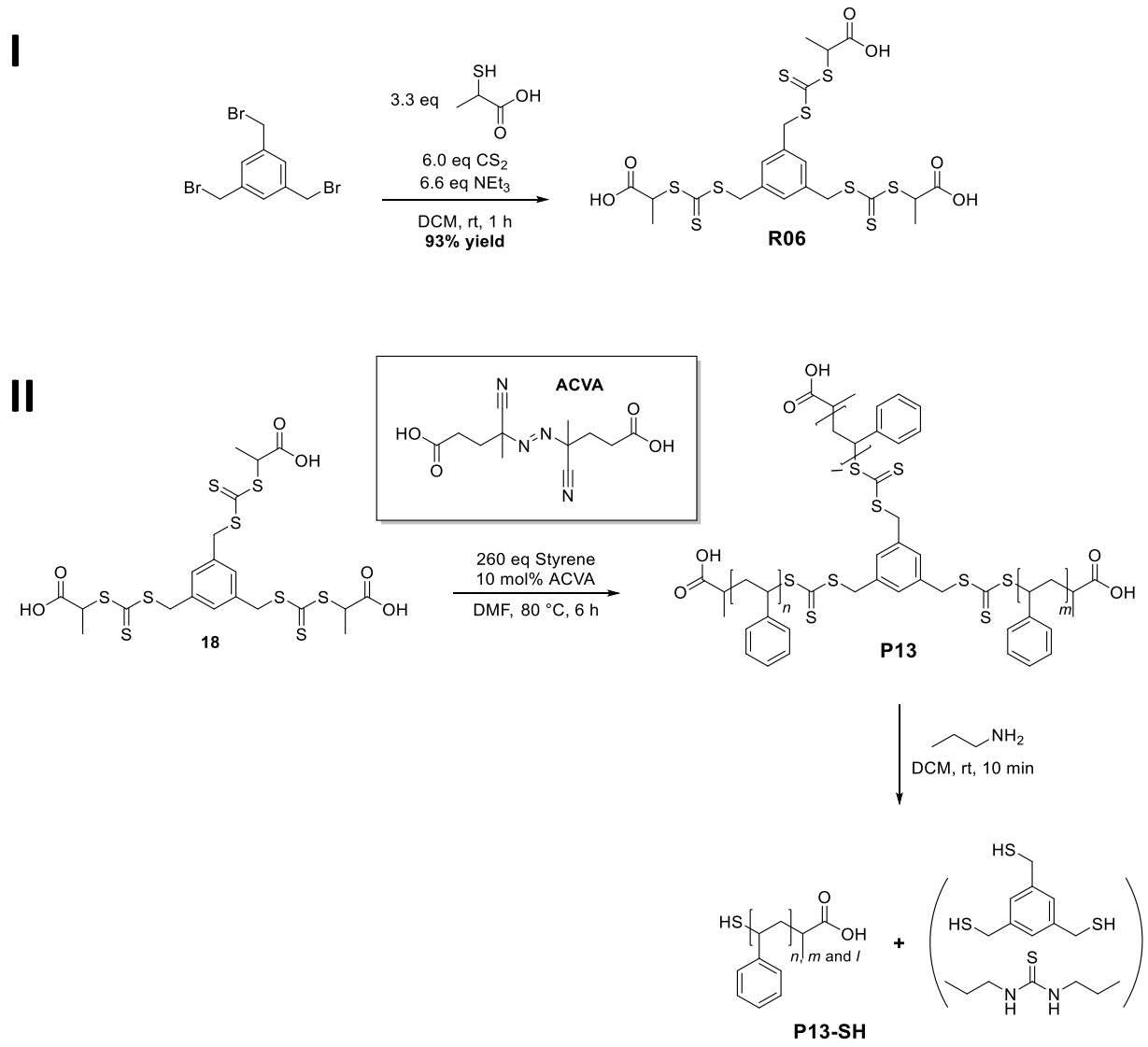

Scheme 36: (**I**) One-step synthesis of *star*-shaped RAFT agent **R06** obtained in 93% yield without purification; (**II**) RAFT polymerizations **P13** of styrene by RAFT agent **R06** and with 5 mol% ACVA loading relative to the RAFT agent followed by its aminolysis yielding thiol end-functionalized PS **P13-SH**.

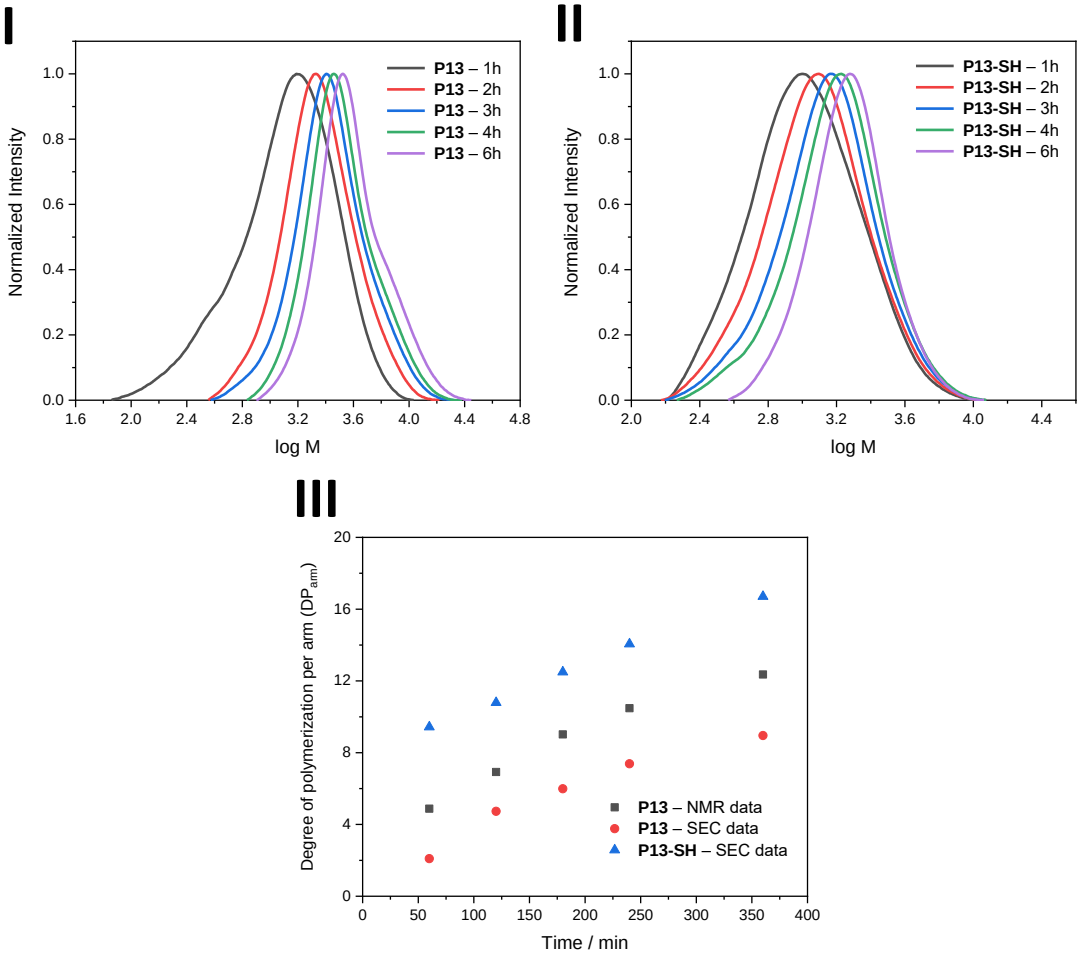

Figure 7: (**I**) SEC traces of **P13** taken at different polymerization times; (II) SEC traces of **P13-SH** polymer samples obtained by **P13** aminolysis; (**III**) Degree of polymerization per arm (DP_{arm}) reached at different polymerization times. DP_{arm} values calculated from **P13** and **P13-SH** $M_{n,SEC/THF}$ as well as **P13** $M_{n,^1H\text{-}NMR}$ data.

4.3 Project Part I – Conclusion

In summary, the first part of the project suffered from a series of major drawbacks. The syntheses of *star*-shaped RAFT agents bearing end-groups proved to be more tedious than expected. Also, the CTAs were found to be incompatible with both functional groups incorporated within the RAFT agent structure. The modification of the end-groups from aromatic to aliphatic alkyne and azide did not suppress the side-reactions. In the same manner, the lowering of the polymerization temperature did not substantially impact these results. Worst, even for the non-functionalized CTA, the side reactions leading to star-star coupling or loss of arms could never be sufficiently prevented once a low DP was reached to ensure a sufficient quality of the *star*-shaped polymer prior to its topological conversion. Moreover, the presence of functional groups like the trithiocarbonates directly incorporated in the polymer structure may have constituted, in retrospect, an issue for the chemical stability of the produced polymer topologies towards degradation and nucleophilic attacks. At last, despite no evidence of successful topological conversion by $(AB)_3$ trimerization had been provided so far, the project implementation flaws were clearly identified and with the help of scientific literature, some major corrections were incorporated, as shown in the next two chapters.

5 Project Part II – Milligram-scaled Synthesis of *Cage*-shaped Polymers

5.1 Project Part II – Introduction

As summarized in the previous section, the application of the initial idea utilizing RAFT *star*-shaped polymers was not optimal and two major changes were therefore necessary to ensure the continuity of the project. First, the synthesis of the *star*-shaped polymer substrate was reoriented to ring-opening polymerization (ROP) from multifunctional alcohol cores to obtain defect-free *star*-shaped polymers with more ease. In this regard, poly(ε-caprolactone) was chosen for its straightforward synthesis as well as for its great solubility, non-hydroscopic and suitable thermo-mechanical properties. Thus, diphenyl phosphate (DPP)-catalyzed cationic ROP of ε-caprolactone[295] – which does not require any metal or toxic catalysts – was selected to produce the four-arm *star*-shaped polymer substrates that are suited for any further topological conversion investigations to *cage*-shaped ε-PCL. **(Scheme 37)**

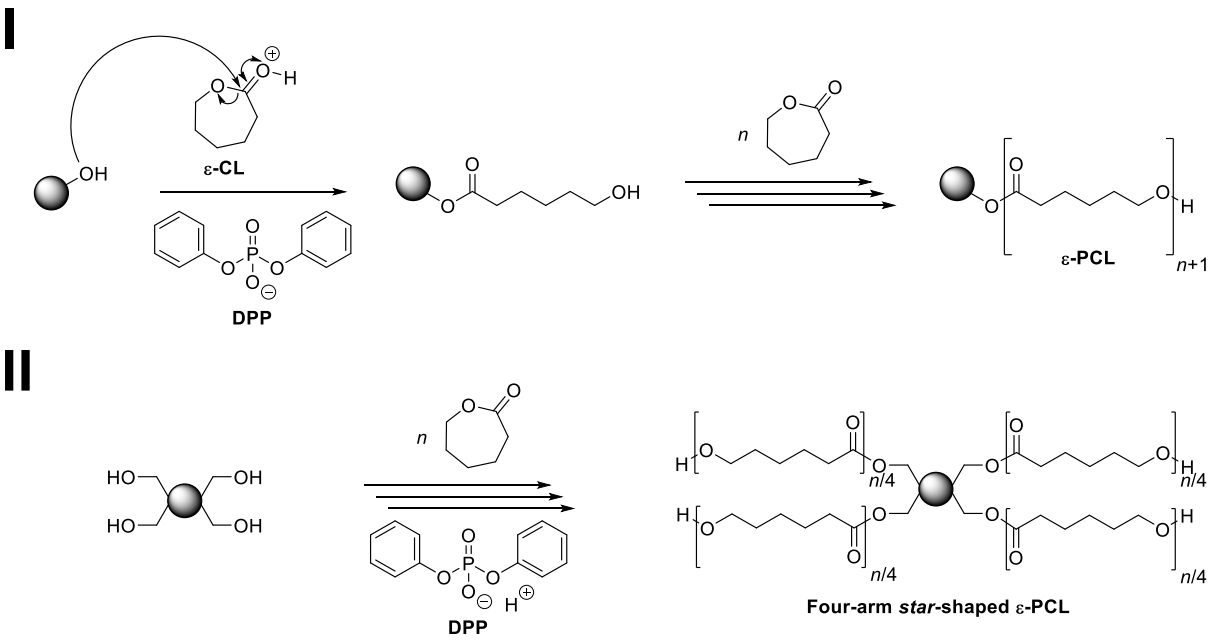

Scheme 37: (**I**) Mechanism of diphenyl phosphate-catalyzed cationic ring-opening polymerization (CROP) of ε-caprolactone; (**II**) Four-arm *star*-shaped poly(ε-caprolactone) synthesis conducted from a multifunctional initiator.

Secondly, despite the extended efforts to find suitable macrocyclic structures that could be obtained by $(AB)_n$ *n*-oligomerization, no candidate had been identified in the literature so far. In this context, the work of Amar H. Flood on the formation of rigid D_{2h}-[3*4*]triazolophane macrocycles allowed the present work to continue on a solid scientific basis. In a few words, these D_{2h}-[3*4*]triazolophane macrocycles were used as size-selective chelating ligands for halide anion recognition.[296,297,298] More specifically, they were reported to own great chelation values with middle-sized halides and in particular a high pairing equilibrium constant of $4.7 \pm 2.1 \cdot 10^6$ mol L^{-1} for chloride anions in DCM.[299] Weaker equilibrium constants were also reported for fluoride and iodine anions, respectively too small and too massive to be stabilized inside the macrocycle cavity estimated to be 3.8 Å wide.[300,301] In addition, it is important to emphasize that while both D_{2h}-[3*4*]triazolophane and D_{4h}-[3*4*]triazolophane regioisomers share a same general structural motif, they fundamentally differ by their point group symmetry. Thus, although all reported D_{2h}-[3*4*]triazolophanes were obtained through multi-step syntheses consisting in a series of CuAAC, Sonogashira cross-coupling and TMS deprotections from two distinct building blocks, **(Scheme 38, I)** their reports constituted a good hint that a more symmetrical D_{4h}-[3*4*]triazolophane regioisomer could be obtained from the tetramerization of *m*-azidoethynylbenzene units. Considering at last that a *m*-azidoethynylbenzene derivative had already been synthetized at the very beginning of the project (i.e. **C01** to **C03**), the topological conversion of four-arm *star*-shaped polymers into polymer cages by intramolecular D_{4h}-[3*4*]triazolophane formation was investigated in detail, as shown in the following chapter. **(Scheme 38, II)**

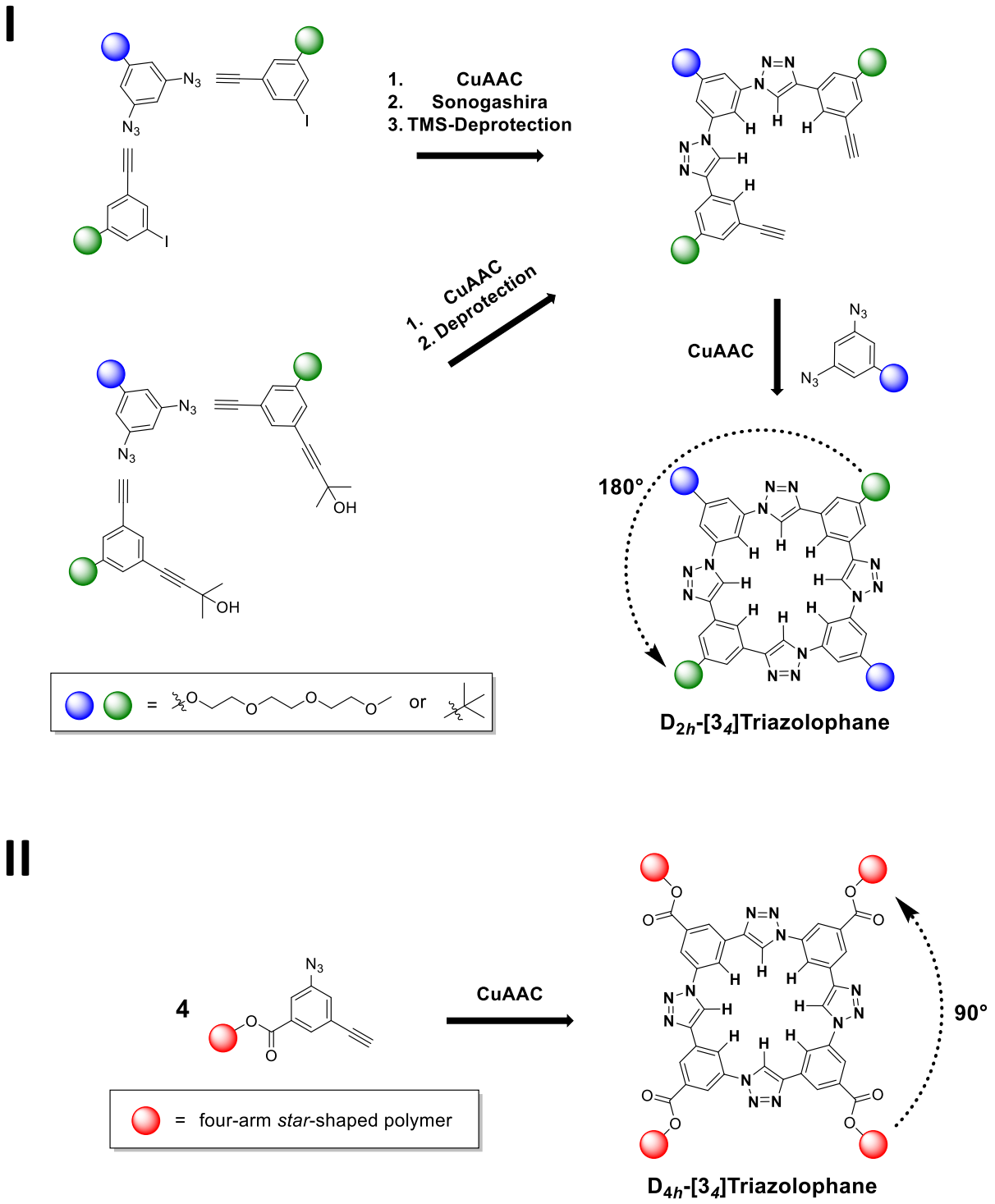

Scheme 38: (**I**) Previously reported multi-step D_{2h}-[3_4]triazolophane synthesis by Amar. H. Flood owning an 180° symmetry in the horizontal plane (D_{2h} point group symmetry); (**II**) Unreported one pot intramolecular D_{4h}-[3_4]triazolophane synthesis from end-functionalized *star*-shaped four-arm polymer owning an 90° symmetry in the horizonal plane (D_{4h} point group symmetry).

5.2 Project Part II – Results and Discussion

5.2.1 Synthesis of 3-Azido-5-ethynylbenzoic Acid End-group

The synthesis of the new *m*-azidoethynylbenzene derivative was adapted from the former three-step synthesis of compound **C03**. To do so, the benzyl alcohol group was substituted by a free carboxylic acid, allowing it to end-functionalize poly(ε-caprolactone)s by simple EDC esterification. Although a similar synthesis was also previously reported starting from inexpensive 3,5-dinitrobenzoic acid, the former seven-step synthesis did constitute a major drawback to the present one.[302] Thus, the synthesis of 3-azido-5-ethynylbenzoic acid **C20** was achieved in 61% yield over four steps. **(Scheme 39)** Starting from a commercially available 3-amino-5-bromobenzoic acid, the carboxylic acid first underwent a Fisher esterification in ethanol to obtain ethyl ester **C17**. Then, TMS-acetylene was placed at the bromide position *via* a Sonogashira cross-coupling, before being deprotected under basic conditions to yield compound **C19**. Finally, the azide functionality was introduced *via* Sandmeyer reaction, yielding the desired end-group molecule **C20**. All steps were followed by ^{1}H-NMR, ^{13}C-NMR and HSQC analyses.

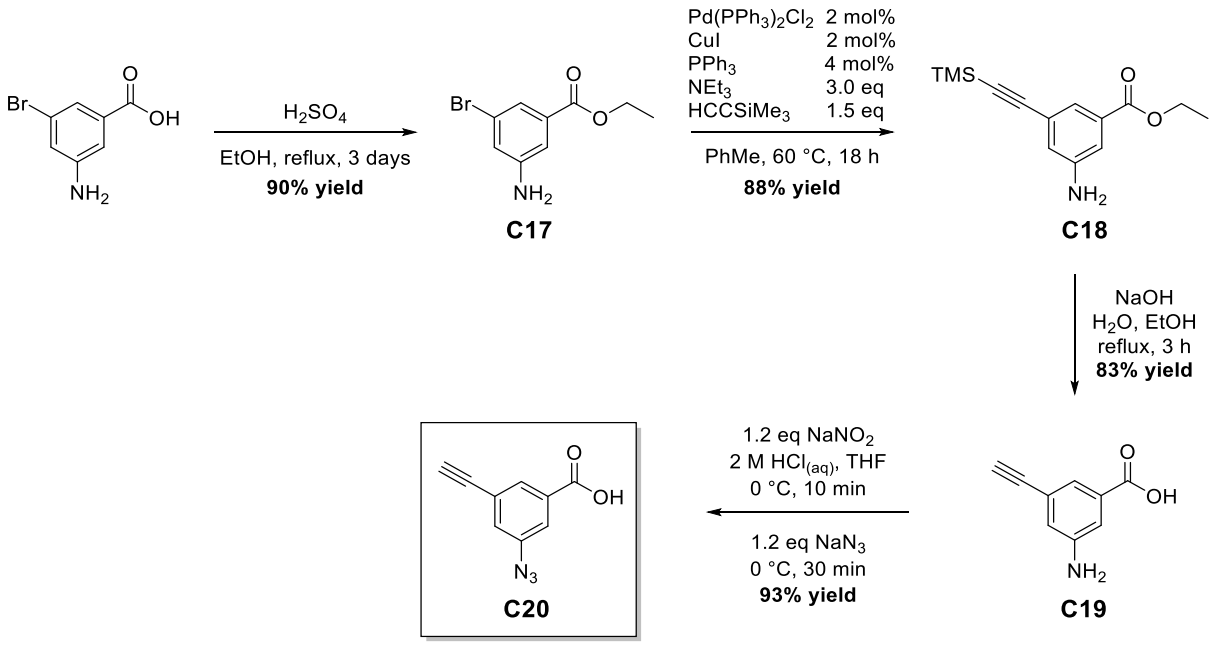

Scheme 39: Four-step synthesis of compound **C20** obtained in an overall yield of 61%.

5.2.2 Synthesis and End-functionalization of *Star*-shaped Poly(ε-caprolactone)s

Polymerization of ε-caprolactone (ε-CL) was conducted in bulk with 5 mol% diphenylphosphate (DDP) as proton exchange catalyst for cationic ring opening polymerization (CROP) from a commercially available triol initiator (2-ethyl-2-(hydroxymethyl) propane-1,3-diol). The polymerization was stopped after 2 hours at 80 °C as the medium viscosity had increased noticeably. After simple precipitation in cold methanol, the three-arm *star*-shaped polymer **P14** was successfully isolated in high purity and characterized. **(Scheme 40, I; Table 11, Entry 1)** According to the ^{1}H-NMR analysis, the conversion was estimated at 94% for a $M_{n,^{1}H\text{-}NMR}$ value of 5.5 kg mol^{-1} and a good end-group fidelity. Furthermore, SEC analysis showed a narrow dispersity of 1.11 with no evidence of structural defects. From this first bulk polymerization, a second attempt was conducted with toluene as solvent to aim for a full monomer conversion. Consequently, the resulting ε-PCL **P15** displayed full conversion according to ^{1}H-NMR analysis after 4 hours at 80 °C. **(Scheme 40, I; Table 11, Entry 2)** However, SEC analysis revealed a slightly broader dispersity (i.e. 1.17) than previously observed for **P14**. As defect-free topologies with narrow dispersity were strictly preferred to polymers with precisely targeted $M_{n,^{1}H\text{-}NMR}$ values, the succeeding polymerizations were conducted in bulk.

Table 11: Overview of *star*-shaped three-arm polymers achieved in bulk **(Entry 1)** and in solution **(Entry 2)** from a trifunctional alcohol core as well as four-arm. **(Entry 3)** ε-PCL achieved in bulk from a pentaerythritol core and its end-functionalized polymer with **C20**.

Entry	Polymer	Reaction time / h	$M_{n,^{1}H\text{-}NMR}$ / kg mol^{-1}	$M_{n,SEC/THF}$ / kg mol^{-1}	$Đ_{SEC/THF}$	Yield / %	Conversion / %
1	**P14**	2	5.5	8.0	1.11	59	85
2	**P15**	4	6.3	9.9	1.17	85	108
3	**P16**	1	4.4	6.9	1.10	53	134
4	**P16-F**	72	5.1	7.9	1.13	95	quantitative

At that point, the synthesis of a four-arm *star*-shaped ε-PCL was planned and the synthesis of four-arm *star*-(ε-PCL-OH)$_4$ polymer **P16** was achieved from pentaerythritol cores with a good 1.10 dispersity and $M_{n,^{1}H\text{-}NMR}$ estimated at 5.1 kg mol^{-1}. **(Scheme 40, II; Table 11, Entry 3)** However, due to its poor solubility, a part of the pentaerythritol crystals were not able to dissolve during the polymerization, resulting in higher conversion (i.e. 134%) than intended

and the necessity to remove the remaining pentaerythritol crystals from the polymer by filtration after polymerization. To overcome this issue and obtain a better control on the polymerization, a more soluble core was later selected for the subsequent four-arm *star*-shaped ε-PCL syntheses. **(See Chapter 5.2.4 – Investigation on the Correlation between Polymer Size and Properties)**

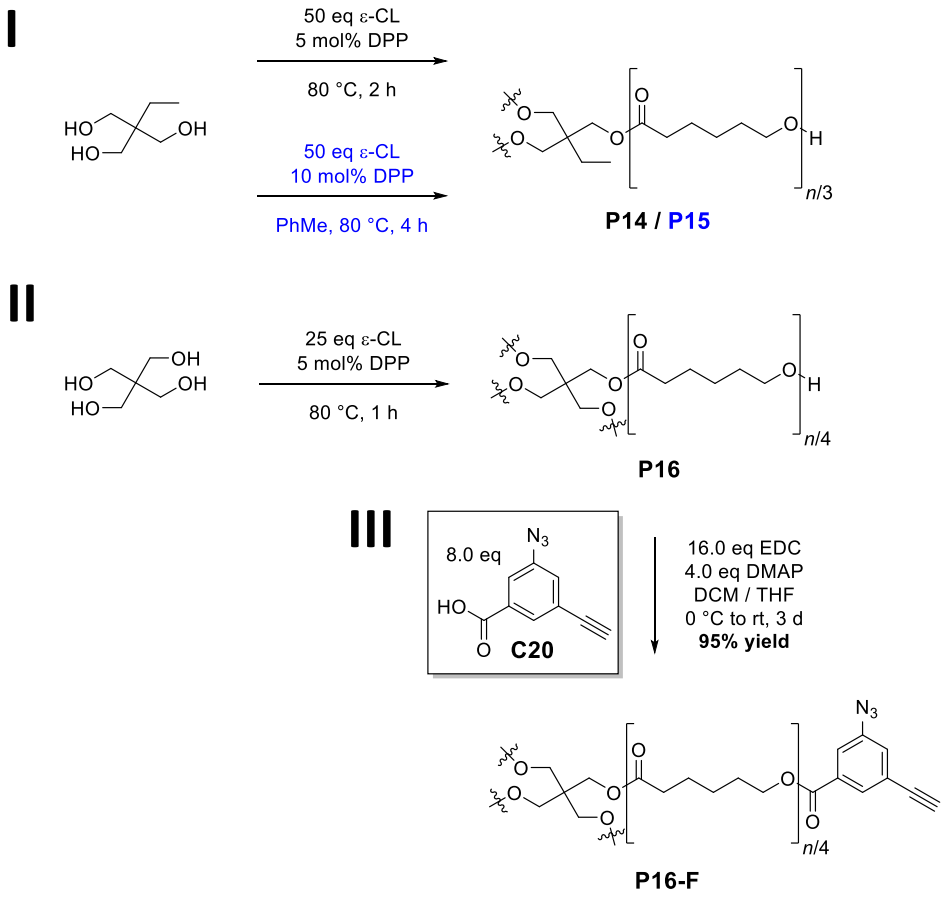

Scheme 40: (**I**) Synthesis of *star*-shaped three-arm ε-PCL achieved from a trifunctional alcohol core in bulk (**P14**) or in solution (**P15**); (**II**) Synthesis of *star*-shaped four-arm ε-PCL **P16** in bulk achieved from a pentaerythritol core; (**III**) End-functionalization of **P16** with **C20** by EDC coupling, yielding **P16-F** polymer as precursor to upcoming topological conversion attempts.

Nevertheless, in a first attempt **P16** was used as obtained and end-functionalized with the *m*-azidoethynylbenzene carboxylic acid derivative **C20** *via* EDC coupling to yield **P16-F**. The functionalization was estimated quantitative according to ^{1}H-NMR analysis, as the triplet resonance attributed to the CH_2 signal next to the terminal alcohol was downfield shifted from 3.64 to 4.32 ppm. Furthermore, its SEC analysis revealed a small high-molecular weight shoulder and a slightly broader dispersity value of 1.13 due to a small number of topological defects by undesired crosslinking. **(Scheme 40, III; Table 11, Entry 4)** At last, FT-IR analysis

of **P16-F** showed a strong and characteristic band located at 2114 cm^{-1} in accordance with the presence of aromatic azide within the polymer structure.

5.2.3 *Cage*-shaped Poly(ε-caprolactone) Synthesis by Topological Conversion

Starting from the CuAAC conditions reported by Amar H. Flood for the synthesis of D_{2h}-[3$_4$]triazolophane macrocycles *via* CuAAC the topological conversion step was conducted in toluene with DBU as the ligand for copper(I). For practical and comparative reasons, a constant solvent volume was fixed at 500 mL and the reaction temperature at 70 °C. Furthermore, copper(I) iodide and DBU loadings were left at 100 mg and 0.5 mL respectively to ensure a sufficient catalyst loading despite the high solvent volume employed. At last, the amount of polymer was set to 50 mg to minimize its concentration – and therefore the intermolecular reaction – as much as possible while obtaining a sufficient amount of product to be fully characterized.

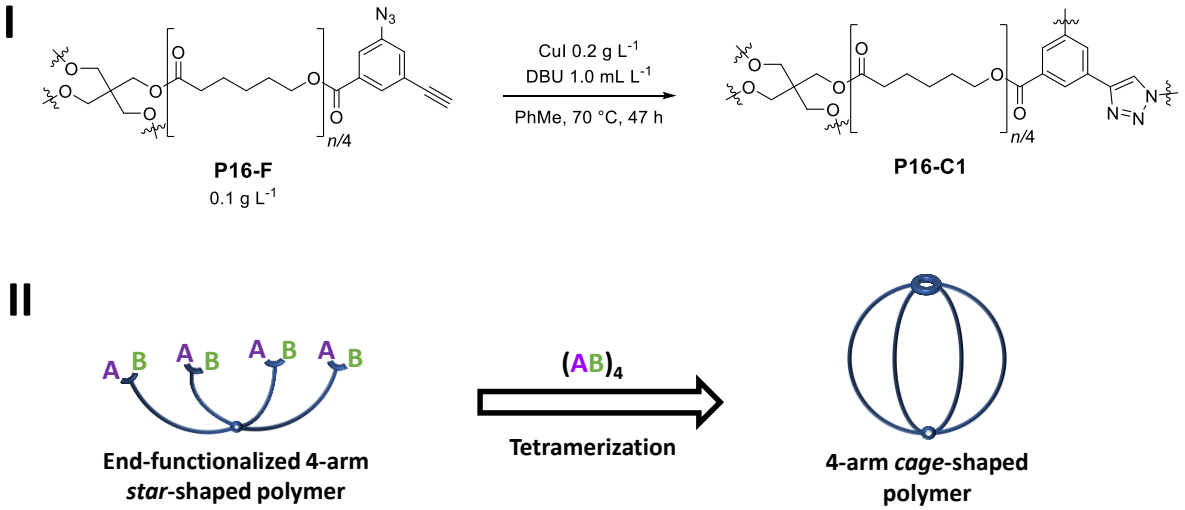

Scheme 41: (**I**) Successful topological conversion of *star*-shaped **P16-F** to *cage*-shaped **P16-C1** polymer by CuAAC; (**II**) Schematic representation of the topological conversion by $(AB)_4$ tetramerization of the end-groups.

Thus, following the aforementioned conditions, end-functionalized polymer **P16-F** was reacted over 47 hours, yielding **P16-C1** as a brown gel after isolation. **(Scheme 41; Table 12, Entry 3)** While the extended reaction time at 70 °C led to a non-negligible amount of DBU degradation byproducts, the extended washing of the polymer over silica gel with DCM as eluent considerably reduced their presence in the final product.

Table 12: Overview of the polymers obtained from four-arm *star*-shaped ε-PCLs **(Entry 1)**, including end-functionalized *star*-shaped polymer **(Entry 2)**, *cage*-shaped polymers obtained by varying the reaction time **(Entry 3**–**7)** as well as by varying the polymer concentration **(Entry 8**–**9)** with a fixed reaction time of 1 hour.

Entry	Polymer	Reaction time / h	Reaction concentration / mg mL^{-1}	$M_{n,SEC/DMAC}$ / kg mol^{-1}	$Đ_{SEC/DMAC}$	Yield / %
1	**P16**	*n/a*	*n/a*	7.2	1.06	53
2	**P16-F**	*n/a*	*n/a*	7.7	1.14	95
3	**P16-C1**	**47**	0.10	10.0	1.06	96
4	**P16-C2**	**23**	0.10	10.5	1.08	94
5	**P16-C3**	**8**	0.10	10.7	1.14	92
6	**P16-C4**	**4**	0.10	10.3	1.12	68
7	**P16-C5**	**2**	0.10	10.0	1.08	74
8	**P16-C6**	**1**	0.10	10.5	1.11	70
9	**P16-C7**	**0.5**	0.10	10.4	1.14	50
10	**P16-C8**	1	**0.25**	11.6	1.21	64
11	**P16-C9**	1	**0.50**	12.9	1.31	62

Concerning the characterization by the ^{1}H-NMR analysis, the three aromatic and the terminal alkyne resonances in the **P16-F** spectrum disappeared in favor of four broad aromatic signals within the 10–8 ppm range. Furthermore, a strong reduction of the azide band intensity located at 2113 cm^{-1} was noticed in the corresponding FT-IR spectrum. At last, SEC analysis of **P16-C1** with THF as eluent revealed a shift to lower $M_{n,SEC/THF}$ values although with a signal intensity close to the detector noise level. Suspecting an interaction between the rigid D_{4h}-[3$_4$]triazolophane structure and the SEC_{THF} column, **P16**, **P16-F** and **P16-C1** polymers were investigated by SEC analysis using DMAC with 0.03 weight% lithium bromide as eluent. In addition to the more polar character of the eluent, the addition of lithium bromide may have also greatly reduced the interaction of the macrocycle with the column packing by saturating the macrocycle with bromide anions. As a result, **P16-C1** chromatogram was greatly shifted to higher molecular masses and therefore to larger hydrodynamic volumes. This result was in total contradiction to the expected topological shift from a *star*- to a *cage*-shaped polymer. Additionally, the dispersity recorded in SEC_{DMAC} remained at a very low value of 1.06, discrediting any simple cross-linking explanation.

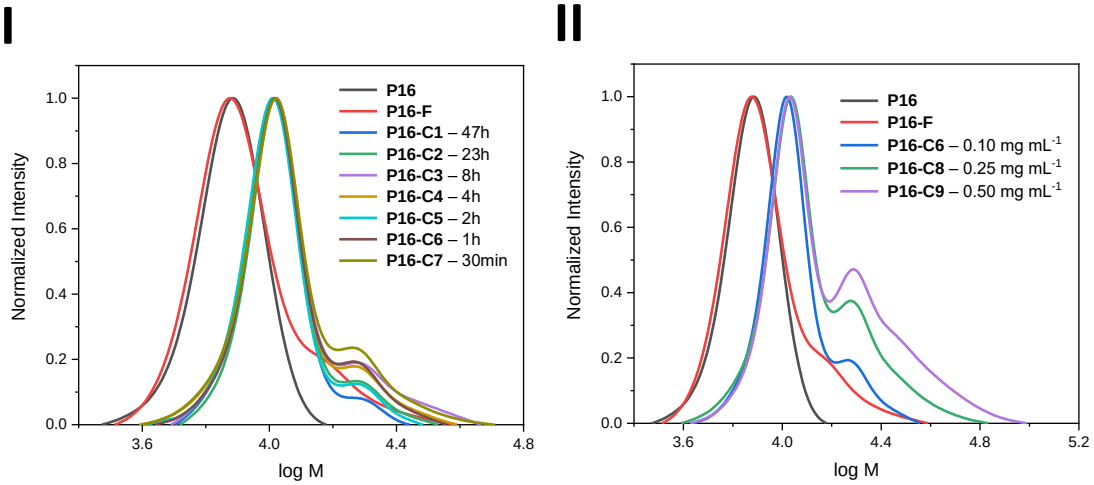

Figure 8: (**I**) Comparison of the SEC_{DMAC} traces of four-arm *star*-shaped **P16**, end-functionalized **P16-F** and seven *cage*-shaped **P16-C** polymer batches obtained with reaction times varying from 47 hours to 30 minutes; (**II**) Comparison of the SEC traces of four-arm *star*-shaped **P16**, end-functionalized **P16-F** and three *cage*-shaped **P16-C** obtained a with reaction time fixed at 1 hour and varying polymer concentration from 0.10 to 0.50 mg mL^{-1}.

In order to reproduce these unexpected results as well as investigate the topological conversion kinetics by progressively reducing the reaction time, a series of six other reactions with reaction time ranging from 23 hours to 30 minutes (i.e. **P16-C2** to **P16-C7**) was conducted. **(Table 12, Entry 4–9)** While the ^{1}H-NMR and FT-IR analyses remained consistent with each other, it is the constancy of the SEC_{DMAC} traces which was found to be particularly remarkable. **(Figure 8, I)** Finally, the impact of the reaction time on the isolated yield was investigated. However, no clear trend could be drawn from the lowering of reaction time above 1 hour, considering the challenge for each iteration to remain consistent throughout all the purification process and the low amount of polymer involved. On the contrary, a significant drop of about 20% yield was observed for **P16-C7** after a short reaction time of 30 minutes at 70 °C. **(Table 12, Entry 9)** Nevertheless, the amount of DBU degradation byproducts was almost totally prevented by the reduction of the reaction time to 1 hour, allowing a more straightforward isolation process and therefore this reaction time was fixed for the next iterations of the topological conversion.

Now that a rough idea of the intramolecular reaction kinetic taking place during the topological conversion to *cage*-shaped polymers was established, the effect of the polymer concentration on the intermolecular kinetic (i.e. undesired star-star crosslinking) was investigated in more detail. Using the same conditions as for **P16-C6**, **(Table 12, Entry 8)** additionally **P16-C8** and **P16-C9** were reacted while varying the polymer concentration to 0.25 mg mL^{-1} and

0.5 mg mL^{-1}, respectively. **(Table 12, Entry 10–11)** While no clear decline in yield was observed between the three samples, a clear increase of high molecular weight shoulders in their SEC_{DMAC} traces was noticed, indicating an increase of polymer oligomers within the samples. **(Figure 8, II)**

5.2.4 Investigation on the Correlation between Polymer Size and Properties†

After the above-mentioned preliminary investigations, a more ambitious study was initiated in order to investigate the influence of the arm lengths on the properties of the respective *cage*-shaped polymers. The synthesis of a series of *cage*-shaped polymers varying in their molecular weight was therefore planned. To do so, four *star*-shaped ε-PCLs polymers **(Table 13, Entry 1–4)** with $M_{n,^1H\text{-}NMR}$ values going from 4.6 to 13.9 kg mol^{-1} were synthetized from commercially available di(trimethylolpropane) cores.

Table 13: Overview of a series of four four-arm *star*-shaped ε-PCLs varying in molecular weight **(Entry 1–4)**, their end-functionalized polymers with end-group **C20 (Entry 5–8)**, as well as the respective *cage*-shaped polymers. **(Entry 9–12)**

Entry	Polymer	$M_{n,^1H\text{-}NMR}$ / kg mol^{-1}	$M_{n,SEC/DMAC}$ / kg mol^{-1}	$Đ_{SEC/DMAC}$	$D_{h,Volume}$ / nm	Yield / %
1	**P17**	4.6	8.0	1.06	3.11 ± 0.75	65
2	**P18**	6.6	11.8	1.06	3.80 ± 0.81	64
3	**P19**	9.8	17.0	1.05	4.71 ± 1.32	69
4	**P20**	13.9	24.3	1.05	6.20 ± 1.95	56
5	**P17-F**	5.3	8.8	1.08	4.78 ± 1.06	95
6	**P18-F**	7.3	12.5	1.07	5.27 ± 1.18	97
7	**P19-F**	10.5	18.6	1.08	6.43 ± 1.61	85
8	**P20-F**	14.6	25.4	1.08	7.93 ± 1.94	88
9	**P17-C**	5.3	9.9	1.08	4.16 ± 0.98	78
10	**P18-C**	7.3	12.3	1.06	4.47 ± 1.13	72
11	**P19-C**	10.5	16.2	1.08	4.81 ± 1.32	64
12	**P20-C**	14.6	20.2	1.07	6.60 ± 1.80	36

† Parts of this subchapter and the associated parts in the experimental section were previously reported within in the following publication: M. Gauthier-Jaques, P. Theato, Synergy of Macrocycles and Macromolecular Topologies: An Efficient [3_4] Triazolophane-Based Synthesis of *Cage*-Shaped Polymers. *ACS Macro Lett.* **2020**, *9*, 700–705.

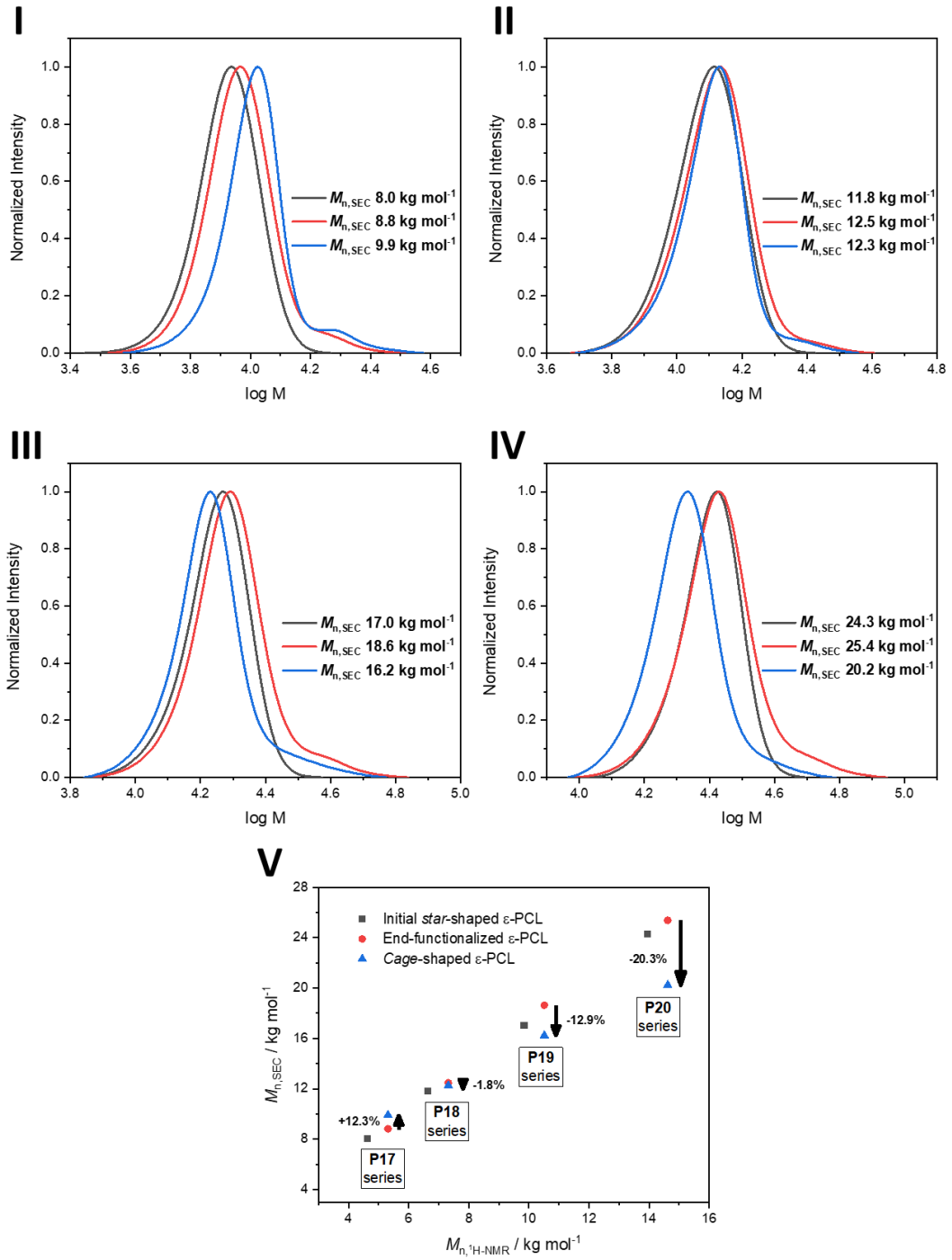

Figure 9: SEC chromatograms of (**I**) **P17**, (**II**) **P18**, (**III**) **P19** and (**IV**) **P20** polymer series, including *star*-shaped ε-PCLs varying in molecular weight (**black traces**), the respective end-functionalized (**red traces**), and *cage*-shaped polymers (**blue traces**); (**V**) Plot of $M_{n,SEC}$ and $M_{n,^1H\ NMR}$ of all four polymer series, featuring a linear deviation of the *cage*-shaped polymers compared to their two *star*-shaped precursors.

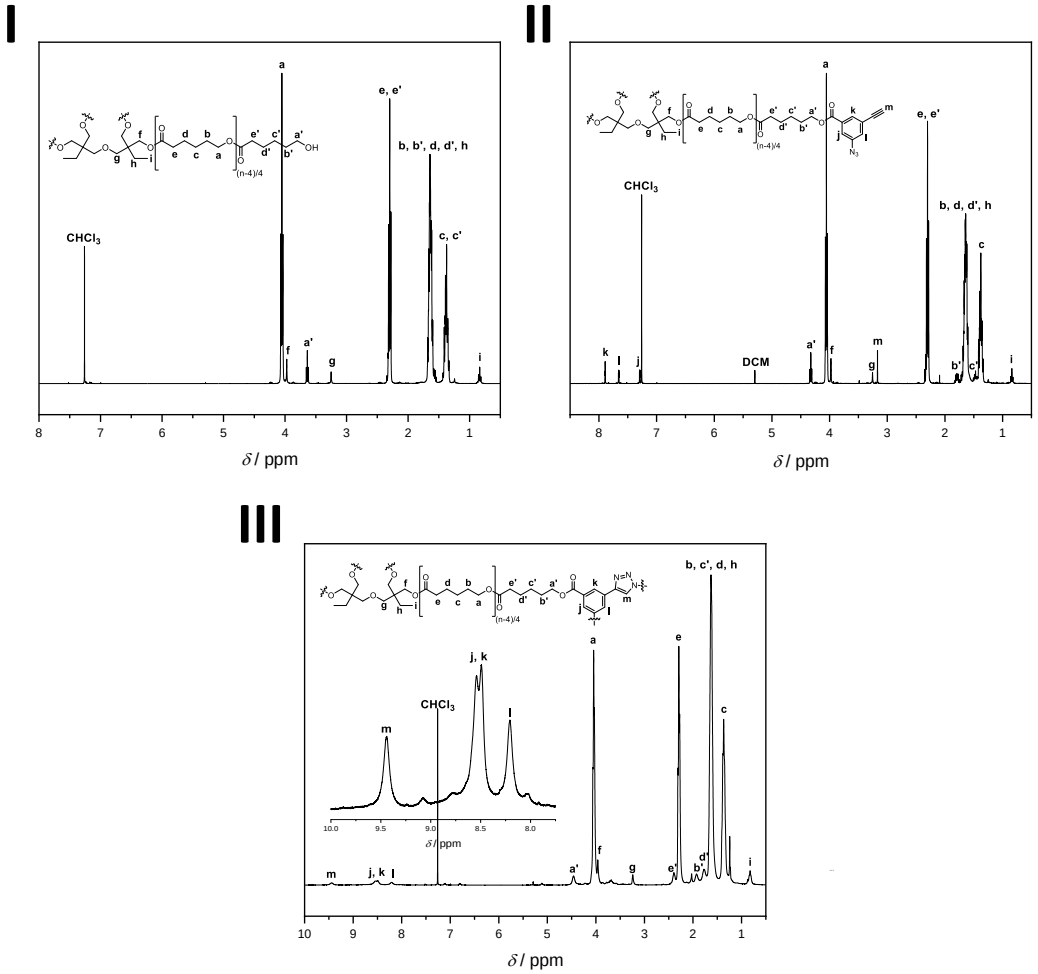

Figure 10: ^{1}H-NMR spectra with peak assignment of (**I**) *star*-shaped ε-PCL **P18**, (**II**) end-functionalized **P18-F**, and (**III**) *cage*-shaped **P18-C** polymers.

All *star*-shaped ε-PCLs were characterized by SEC_{DMAC} and featured narrow dispersities ($1.06 \geq Đ \geq 1.05$). The end-functionalization with **C20** as the end-group was achieved by EDC coupling. **(Table 13, Entry 5–8)** For all four *star*-shaped polymers, the full conversion was confirmed by ^{1}H-NMR **(Figure 10, II)** and the low amount of topological defects was ensured by their narrow dispersity values ($1.08 \geq Đ \geq 1.07$) and the absence of high molecular weight shoulders in their respective SEC_{DMAC} traces. **(Figure 9, I–IV)** At last, the appearance of a strong absorption band assigned to the azide groups stretching at 2113 cm^{-1} was constantly observed by FT-IR analysis. **(Figure 11, II)**

Following the reaction conditions applied to the synthesis of **P16-C6**, (i.e. reaction time fixed at one hour, polymer concentration kept at 0.1 mg mL^{-1}), the four *cage*-shaped ε-PCLs were obtained. **(Table 13, Entry 9–12)** First of all, SEC_{DMAC} analysis ensured that all *cage*-shaped

polymers featured unimodal distribution and narrow dispersity ($1.08 \geq Đ \geq 1.06$). **(Figure 9, I-IV)** However, $M_{n,SEC/DMAC}$ values were not systematically shifted to the lower molecular weights and therefore to lower hydrodynamic volume values, as it would be expected for this type of topological conversion. Thus, while the $M_{n,SEC/DMAC}$ value of **P17-C** – the smallest of the polymer cages – increased (+12.3%) compared to its *star*-shaped precursor, this unexpected result was progressively compensated by the increase of the arm lengths and ultimately overcome, as shown for **P18-C** (-1.8%), for **P18-C** (-12.9%) and for **P18-C** (-20.3%) polymers. **(Figure 9, V)** This exotic effect is most likely caused by the intrinsically rigid macromolecular structure (i.e. D_{4h}-[3_4]triazolophane) within the *cage*-shaped polymer structure.

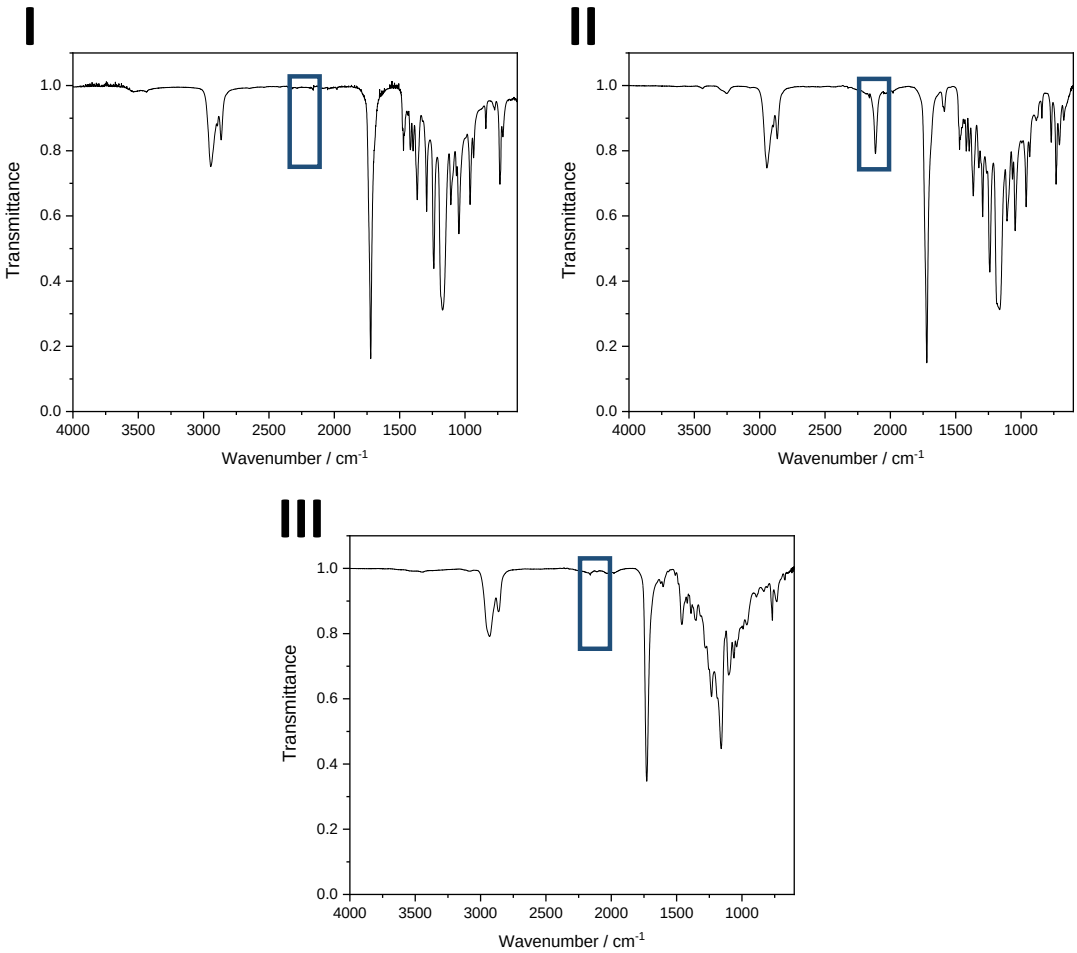

Figure 11: FT-IR spectra of (**I**) *star*-shaped ε-PCL **P18**, (**II**) end-functionalized **P18-F**, and (**III**) *cage*-shaped **P18-C** polymers, featuring the appearance and disappearance of the azide stretching band located at 2113 cm^{-1} (**blue square**).

As previously observed for the **P16-C** iterations, the presence of the triazole rings were also confirmed by the complete disappearance of the azide stretching band located at 2113 cm^{-1} in

the FT-IR spectrum. **(Figure 11, III)** Likewise, the resonance signals assigned to the CH_2-groups located next to the D_{4h}-[3_4]triazolophane were downfield shifted in the ^{1}H-NMR spectra. Additionally, the singlet signal attributed to the alkyne at 3.17 ppm and the three sharp aromatic signals of the phenyl rings disappeared in favor of four broad signals located in the 10–8 ppm region. **(Figure 10, III)** These four signals were particularly broadened in the case of the two smallest cages **P17-C** and **P18-C**. The origin of this broadening was attributed to a strong D_{4h}-[3_4]triazolophane – chloride host-guest interaction originated from the use of 1 M HCl during the reaction workup. Similar reports about the ability for D_{2h}-[3_4]triazolophanes to coordinate medium-sized halides are reported in the preexisting scientific literature. **(See Project Part II – Introduction)** At last, the ε-PCL backbone signals in the ^{1}H-NMR spectra were found to broaden as the cage size decreased, presumably indicating a faster ^{1}H spin-spin relaxation time (T_2) at the NMR timescale due to a decrease of the polymer arms freedom.

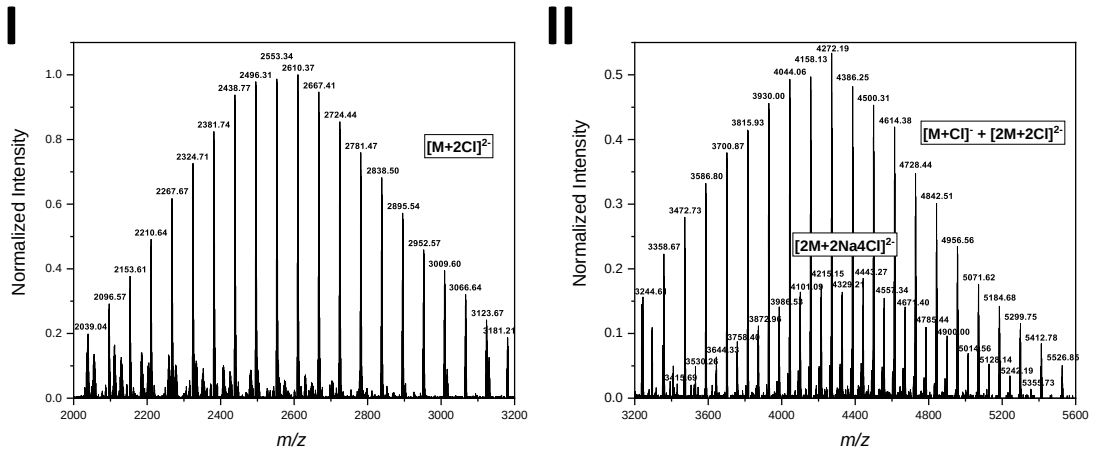

Figure 12: ESI-MS spectrum of the smallest *cage*-shaped ε-PCL **P17-C** recorded in the negative mode, including: (**I**) the main distribution corresponding to $[M+2Cl]^{2-}$ pattern, featuring peak intervals of 57.034 *m/z*; (**II**) smaller distributions corresponding to superimposed $[M+Cl]^-$ and $[2M+2Cl]^{2-}$ patterns as well as a $[2M+2Na4Cl]^{2-}$ pattern, all featuring peak intervals of 114.068 *m/z*.

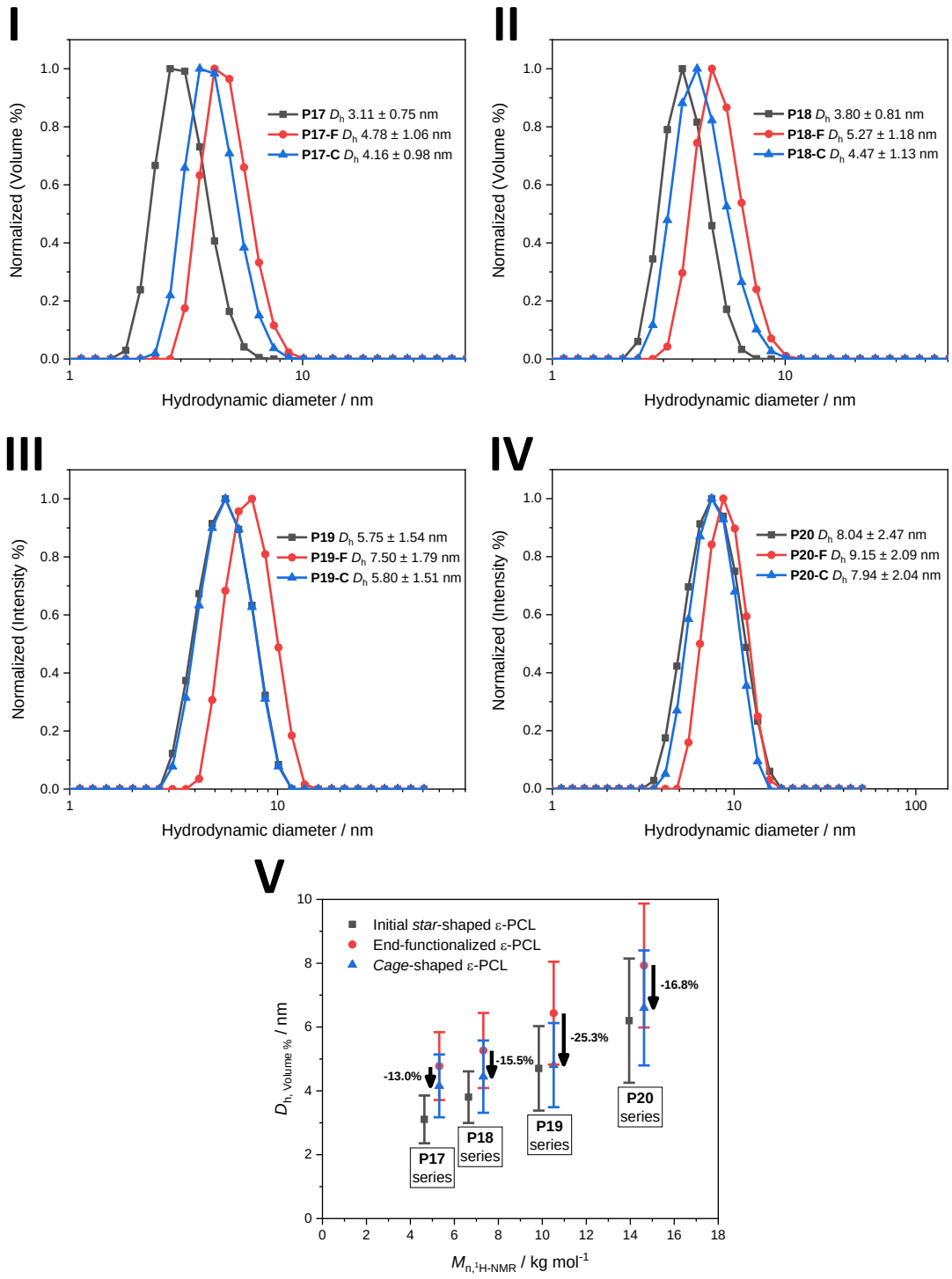

Figure 13: Estimation of the hydrodynamic diameter $D_{h,vol\%}$ of (**I**) **P17**, (**II**) **P18**, (**III**) **P19** and (**IV**) **P20** polymer series carried out by DLS analysis, including *star*-shaped ε-PCLs varying in molecular weight (**black traces**), the end-functionalized (**red traces**), and *cage*-shaped polymers (**blue traces**); (**V**) Plot of all four polymer series $D_{h,vol\%}$ values to their respective $M_{n,^1H\ NMR}$ values.

Additionally, the smallest polymer cage **P17-C** was characterized by ESI-MS analysis. Although no mass distribution was distinguishable in positive mode with sodium cation buffer,

clear distributions with chlorides were recorded in negative mode corresponding to the reported high binding constant reported for D_{2h}-[3$_4$]triazolophanes for chloride anions **(See Project Part II – Introduction)**. Therefore, the most intense distribution was attributed to $[M+2Cl]^{2-}$, **(Figure 12, I)** followed by decreasing intensity to a mixed pattern of $[M+Cl]^{-}$ and $[2M+2Cl]^{2-}$ distributions as well as a minor distribution attributed to a $[2M+2Na4Cl]^{2-}$ cluster. **(Figure 12, II)** The mass intervals of all distributions were corresponding to the ε-PCL repeating unit with 57.034 *m/z* and 114.068 *m/z*, respectively. Moreover, an estimation of the hydrodynamic diameter $D_{h,vol\%}$ of the polymers in solution was carried out by DLS analysis. **(Figure 13)** According to these data, a clear increase of the hydrodynamic diameter was observed between the initial and the end-functionalized *star*-shaped ε-PCL, which was most likely caused by the interference of the large aromatic end-groups with a proper packing of the ε-PCL units, yielding significantly larger D_h values. Although this effect was partially compensated by the topological conversion of the polymers, the hydrodynamic diameter of the *cage*-shaped polymers remained larger than their initial *star*-shaped polymers, preventing any shrinking to occur.

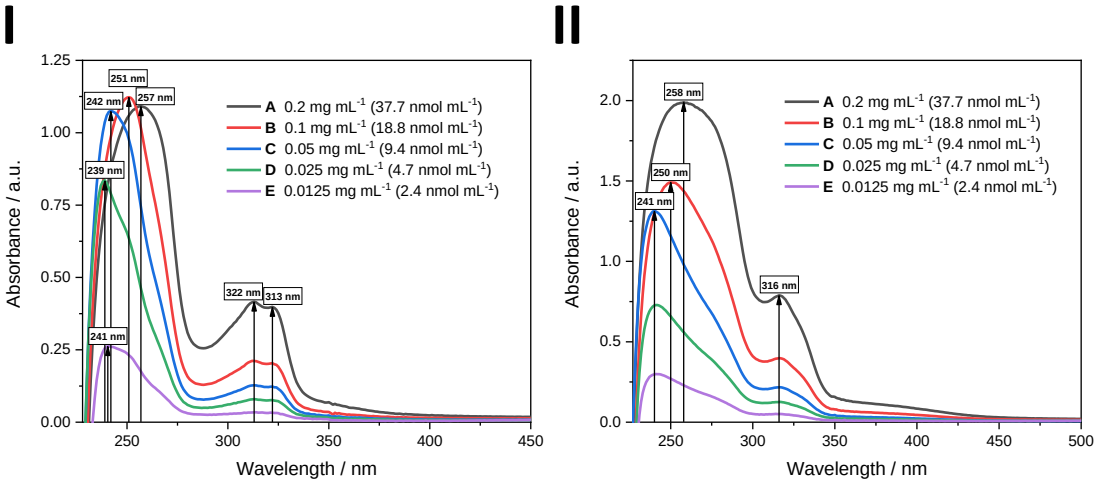

Figure 14: UV-Vis spectra of (**I**) the smallest end-functionalized *star*-shaped ε-PCL **P17-F** and (**II**) its *cage*-shaped polymer **P17-C**, featuring the formation of D_{4h}-[3$_4$]triazolophane macrocycles from the tetramerization of *m*-azidoethynylbenzene units by triazole formation.

Both **P17-F** and **P17-C** polymers were further analyzed by UV-Vis spectroscopy. **(Figure 14)** The two polymers were differentiated by their UV-Vis spectra because of the presence of D_{4h}-[3$_4$]triazolophane macrocycles within the **P17-C** structure. In this regard, the two noticeable absorption maxima at 322 and 313 nm in the **P17-F** spectrum merged into a single

absorption maximum located at 316 nm for **P17-C**. At last, a shift of the main absorption maximum from 241 nm to the 250–260 nm range was observed for higher concentrations in both cases and may be the result of π–π stacking occurring between the aromatic rings.

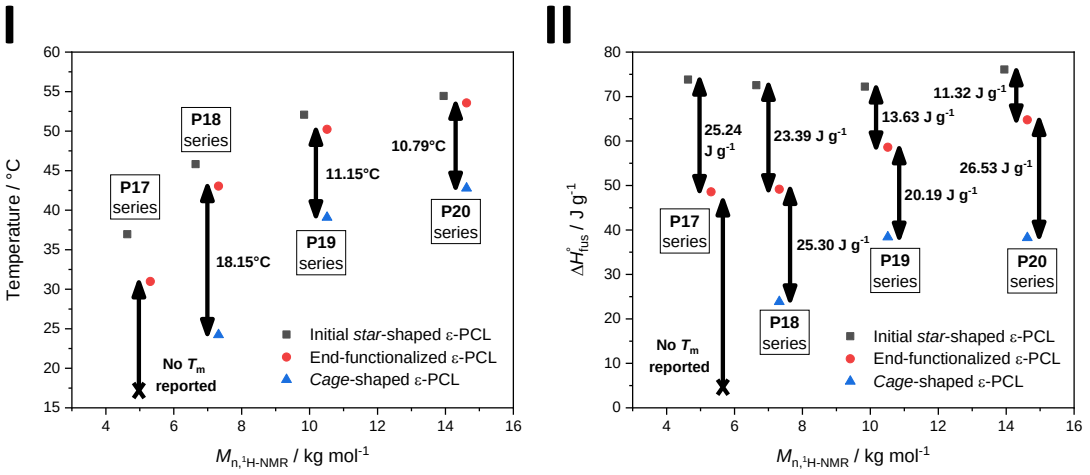

Figure 15: (**I**) Plot of the melting point temperatures T_m of each polymer series to their respective $M_{n,^1H\text{-}NMR}$ values. (**II**) Plot of the latent heats of fusion ΔH°_{fus} of each polymer series to their respective $M_{n,^1H\text{-}NMR}$ values.

Finally, DSC analysis of the different topological structures revealed surprising results in many aspects. **(Figure 15, Table 14)** Thus, no melting temperature could be recorded in the case of **P17-C**, unlike its precursors. Furthermore, **P18-C** was only able to crystallize during the heating ramp with a melting temperature 18 °C below the one recorded for **P18-F** while the **P19-C** and **P20-C** melting point values were 11 °C lower than their respective end-functionalized precursors. In addition, the latent heat of fusions of the *cage*-shaped polymers were observed to decrease by 20 to 27 J g^{-1} in comparison to their respective end-functionalized precursors. A glass transition temperature was recorded between -53 °C and -43 °C for each *cage*-shaped polymer. Finally, the transition from crystalline to amorphous nature of *cage*-shaped polymer by simple decrease of their molecular mass was highlighted by the progressive reduction and disappearance of the latent heat of fusion in their DSC thermograms. In this regard, the additional presence of a rigid D_{4h}-[3$_4$]triazolophane within the polymer structure might have induced a spatial constraint between the polymer arms and created some disorder in the polymer chain stacking. Considering all of the aforementioned effects hindered the crystallization process, their combined effects ultimately led to complete amorphous polymer below a critical polymer size.

Table 14: Overview of the thermal properties of the series of four four-arm *star*-shaped ε-PCLs varying in molecular weight **(Entry 1–4)**, their end-functionalized polymers with end-group **C20 (Entry 5–8)**, as well as their respective *cage*-shaped polymer obtained by topological conversion. **(Entry 9–12).** All thermal values were extrapolated from the second heating ramp (10 K min^{-1}) by DSC analysis.

Entry	Polymer name	T_g / °C	T_m / °C	$\Delta H°_{fus}$ / J g^{-1}	T_{cris} / °C	$\Delta H°_{cris}$ / J g^{-1}
1	**P17**	*n/a*	36.96	73.81	*n/a*	*n/a*
2	**P18**	*n/a*	45.83	72.56	*n/a*	*n/a*
3	**P19**	*n/a*	52.08	72.23	*n/a*	*n/a*
4	**P20**	*n/a*	54.45	76.09	*n/a*	*n/a*
5	**P17-F**	-44.05	30.99	48.57	*n/a*	*n/a*
6	**P18-F**	*n/a*	43.05	49.17	*n/a*	*n/a*
7	**P19-F**	*n/a*	50.23	58.60	*n/a*	*n/a*
8	**P20-F**	*n/a*	53.57	64.77	*n/a*	*n/a*
9	**P17-C**	-47.05	*n/a*	*n/a*	*n/a*	*n/a*
10	**P18-C**	-53.41	24.23	23.87	-23.90	-15.97
11	**P19-C**	-42.61	39.08	38.41	*n/a*	*n/a*
12	**P20-C**	*n/a*	42.78	38.24	*n/a*	*n/a*

5.2.5 Attempts for a Three-arm *Cage*-shaped Polymer Synthesis by Tricarbazolo Triazolophane Macrocycle Formation‡

Following his initial work on the synthesis of D_{2h}-[3*4*]triazolophanes, Amar H. Flood reported a similar macrocyclic structure known as tricarbazolo triazolophane in 2016.[303] **(Scheme 42)** While his former work on D_{2h}-[3*4*]triazolophanes was based on the combination of two pairs of benzene subunits **(See Project Part II – Introduction)**, this new macrocyclic structure was obtained by trimerization of three 3-azido-9-decyl-6-ethynylcarbazole subunits.

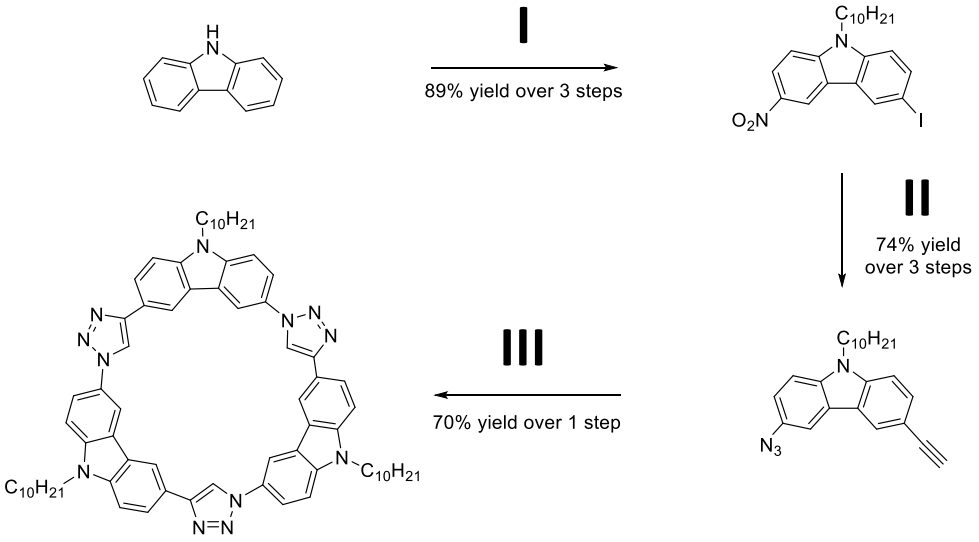

Scheme 42: Seven-step synthesis of tricarbazolo triazolophane macrocycle reported by Amar H. Flood and coworkers.

Starting from carbazole, the seven-step synthesis was initiated by a S_N2 reaction with 1-bromodecane to ensure a good solubility of the rigid macrocyclic product as well as to avoid side-reactions on the following synthesis steps. Then, the *N*-substituted carbazole successively underwent two electrophilic aromatic substitutions at its para positions to yield 9-decyl-3-iodo-6-nitrocarbazole. **(Scheme 42, I)** Afterwards, the nitro group was first reduced to the respective amine before undergoing a Sandmeyer reaction with sodium azide as the nucleophile. Subsequently, a Sonogashira cross-coupling with TMS-acetylene was conducted at the iodide

‡ This subchapter constitutes a summary of the work achieved by M. Sc. Susanne Moser in the context of her Master Thesis.

position, resulting after TMS deprotection, in 3-azido-9-decyl-6-ethynylcarbazole in a 66% yield over six steps. **(Scheme 42, II)** At last, the tricarbazolo triazolophane macrocycle was obtained in gram-scale by a semi-batch reaction in 70% yield. **(Scheme 42, III)** Inspired by the results published on the synthesis of four-arm *cage*-shaped polymers by $(AB)_4$ tetramerization of four 3-azido-5-ethynylbenzyl subunits, a Master Thesis work was accordingly planned to investigate how tricarbazolo triazolophane macrocyclic structures could be similarly used to obtain three-arm polymer cages. The synthesis of the carbazole subunits was based on the Amar H. Flood synthesis from 2016. However, the decyl group was planned to be replaced by an ester group that could later be cleaved into free carboxylic acid and serve to end-functionalize a three-arm *star*-shaped ε-PCL. **(Scheme 43)**

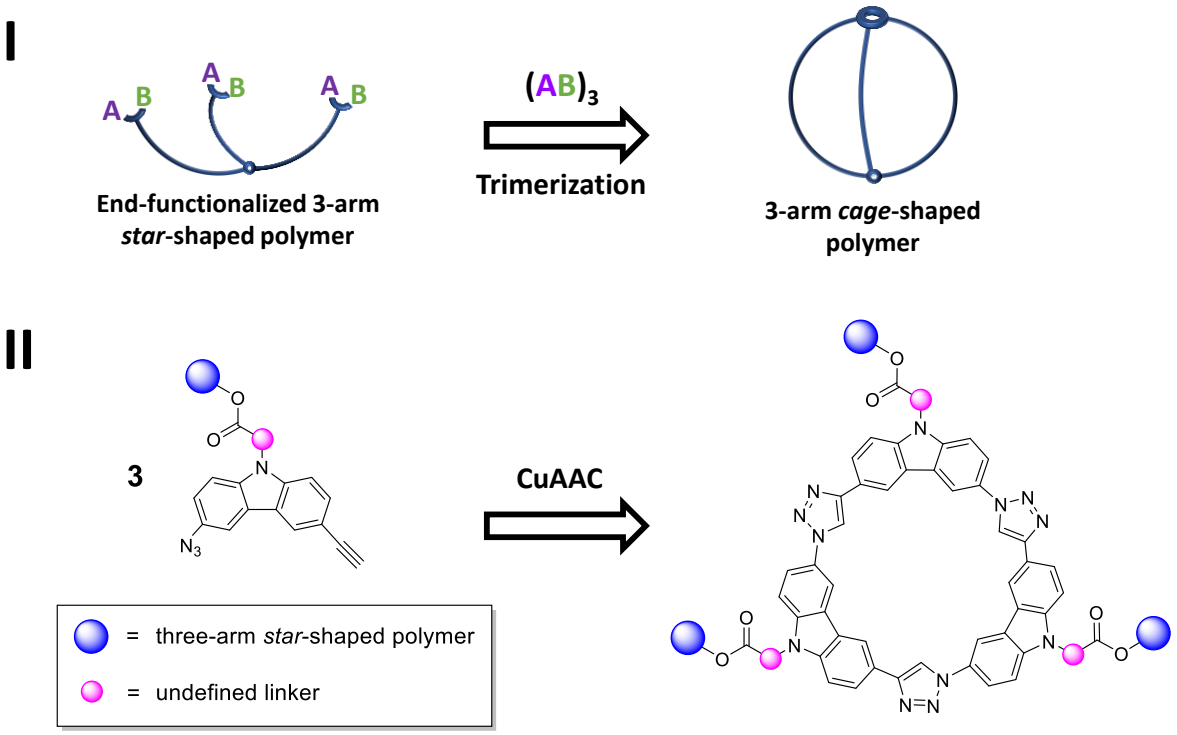

Scheme 43: (**I**) Schematic representation of the topological conversion of a *star*-shaped polymer into *cage*-shaped polymer by $(AB)_3$ trimerization of the three end-groups; (**II**) Specific example of a $(AB)_3$ trimerization by tricarbazolo triazolophane macrocycle synthesis.

Without entering into the details, several synthesis pathways including the use of different esters were investigated. However, none of the routes gave the desired product in an acceptable yield. Beside the incompatibility issues directly caused by the presence of the ester group in the molecular structure, the poor solubility of the carbazole products as well as the extended number of steps impeded the finalization of the project.

5.3 Project Part II – Conclusion

In conclusion, the modifications made at the transition from the first to the second part of this work allowed the successful and reproductible synthesis of four-arm *cage*-shaped poly(ε-caprolactone)s in competitive yields relative to former reports of polymer cage syntheses at the milligram scale. **(See Theoretical Background – Part III)** First, the synthesis of *star*-shaped ε-PCLs by cationic ROP with diphenyl phosphate as proton exchange catalyst was carried out. Additionally, the work of Amar H. Flood on D_{2h}-[3_4]triazolophane macrocycles served as an inspiration for the practical development of the $(AB)_n$ *n*-oligomerization as a tool for the topological conversion of *star*-shaped polymers to polymer cages by $(AB)_4$ tetramerization of *m*-azidoethynylbenzene units into D_{4h}-[3_4]triazolophane macrocycles. To do so, a *m*-azidoethynylbenzene carboxylic acid derivative was obtained in 61% yield over four steps before being used to quantitively end-functionalize four-arm *star*-shaped ε-PCLs by EDC coupling. Subsequently, a first successful topological conversion was achieved and the influence of the reaction time as well as the polymer concentration were successively investigated in order to optimize the reaction conditions. While the reaction time variation provided valuable hints on the intramolecular reaction kinetics, varying the polymer concentration demonstrated its critical impact on undesired intermolecular reactions and therefore on the topological purity of the produced *cage*-shaped polymers. Inspired by these preliminary results, the research was further focused on investigating the impact of the polymer size on the cage synthesis yield and properties. Thus, a series of four different well-defined polymer cages varying in size was synthetized. The four *cage*-shaped ε-PCLs were isolated in 36% to 78% yields and thoroughly characterized by ^{1}H-NMR, SEC, FT-IR, DSC, DLS, UV-Vis and ESI-MS analyses. At last, a Master Thesis project was focused on investigating the topological conversion of three-arm *star*-shaped polymers end-functionalized with carbazole derivatives into three-arm *cage*-shaped polymers by formation of tricarbazolo triazolophane macrocycles. However, the synthesis of the 3-azido-9-decyl-6-ethynylcarbazole derivative including a carboxylic acid group suffered from several issues and the synthesis could not be carried out to the end. As a result, no three-arm *cage*-shaped polymers could be produced by this method.

6 Project Part III – Gram-scaled Synthesis of *Cage*-shaped Polymers

6.1 Project Part III – Introduction

As described in the previous chapter, the methodology for the synthesis of poly(ε-caprolactone) cages with molecular masses up to 15 kg mol^{-1} had been optimized and the obtained materials featured interesting characteristics compared to previously reported cage polymers. **(See Project – Part II)** However, a last question still remained about its upscalability as the production of *cage*-shaped polymers to this point was only focused on milligram scale syntheses. **(See Theoretical Background – Part III)**

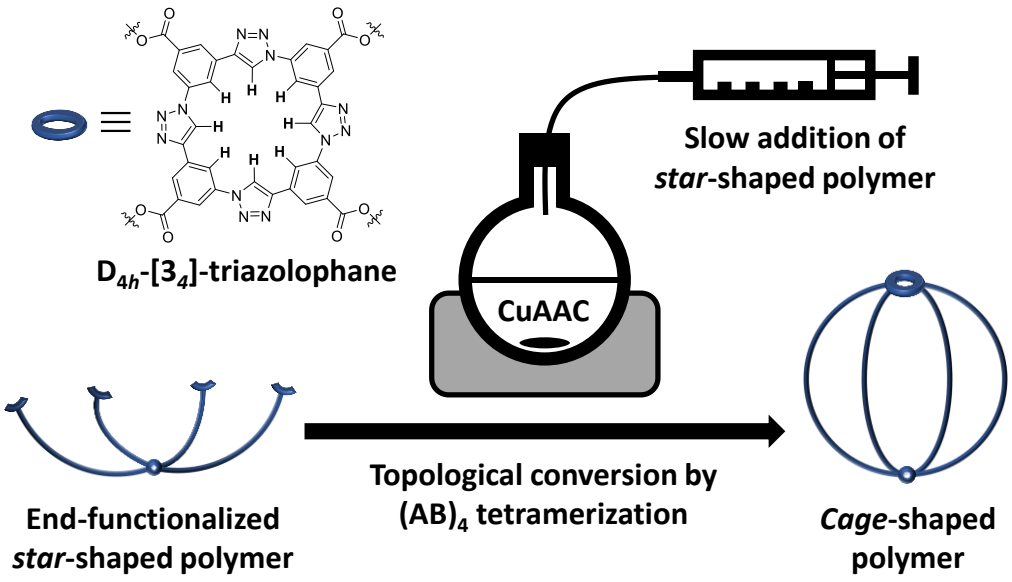

Scheme 44: Schematic representation of a gram-scale synthesis of cage-shaped polymer by a semi-batch reaction, ensuring a low steady-state concentration of reactants through the reaction time.

Indeed, while the $(AB)_4$ tetramerization is worth of interest for the production of polymer cages at the milligram scale, its true potential may fully arise from its capacity to produce them at the gram-scale. Furthermore, being able to produce a sufficient quantity of material may pave the way for further possible applications, such as exploiting the usual reduction of crystallinity reported for similar topological conversions. In this regard, the synthesis of polymer cages can be adapted to a semi-batch process by taking advantage of the *in-situ* formation of chemically inert D_{4h}-[3_4]triazolophane structures, guaranteeing a steady-state concentration of the reactive

species throughout the reaction duration and thus preventing polymer cages to further crosslink intermolecularly once formed. **(Scheme 44)** To do so, the upscaling was first intended to start as a semi-batch synthesis of a known ε-PCL in order to compare the results with previous syntheses. Then, the nature of the polymer was planned to be shifted from ε-PCL to poly(ethylene oxide) (PEO) to provide an insight on the robustness of the procedure as well as to expand the range of potential applications offered by the versatility of PEO-based materials.

6.2 Project Part III – Results and Discussion

6.2.1 Upscaled Synthesis of *Cage*-shaped Poly(ε-caprolactone)s

As noted in the introduction, the synthesis of *cage*-shaped poly(ε-caprolactone)s was envisioned to be extended to the gram-scale by a semi-batch process. To do so, end-functionalized polymer **P19-F** was chosen for four main reasons: a) The to-be formed cage polymer was already synthesized at the milligram scale; b) Its topological conversion can be easily followed by a clear shift of its SEC_{DMAC} trace to lower molecular weight values; c) Its 64% yield still remains relatively high considering its molecular size; and d) Maximizing the polymer size allows the production of a higher amount of end-functionalized polymer for a given amount of end-group **C20**. However, renewed SEC_{DMAC} analyzes of stored **P19-F** polymer reveled a high degree of cross-linking within its polymer structure. These topological defects occurred despite the storage of the solid samples at 2 °C and in absence of direct contact with sunlight. Considering the instability of azide groups over time, these functional groups may have slowly decomposed into radical species and resulted in subsequent hydrogen abstraction of nearby polymer chains. In consequence, a fresh multi-gram batch of end-functionalized **P19-F** (i.e. **P19-F$_{bis}$**) was produced from a remaining part of the *star*-shaped **P19** ε-PCL and a freshly made batch of end-group **C20**. **(Table 15, Entry 1–2)**

Table 15: Overview of the characteristics of the starting *star*-shaped ε-PCL **(Entry 1)**, its new batch of end-functionalized polymer **(Entry 2)**, a milligram-scale synthesis of *cage*-shaped polymer with a reduced reaction temperature **(Entry 3)**, as well as two upscaled semi-batch cage syntheses **(Entry 4-5)**.

Entry	Polymer	$M_{n,^1H\text{-}NMR}$ / kg mol^{-1}	$M_{n,SEC/DMAC2}$ / kg mol^{-1}	$Đ_{SEC/DMAC2}$	$M_{n,SEC/THF}$ / kg mol^{-1}	$Đ_{SEC/THF}$	Yield / %	Yield / g
1	**P19**	9.8	13.6	1.18	15.4	1.07	69	6.10
2	**P19-Fbis**	10.5	15.3	1.24	17.4	1.14	97	2.344
3	**P19-C1$_{bis}$**	10.5	11.1	1.20	11.4	1.33	46	0.023
4	**P19-C2$_{bis}$**	10.5	11.3	1.24	12.7	1.24	61	0.305
5	**P19-C3$_{bis}$**	10.5	10.9	1.32	13.2	1.29	50	0.874

At this point, a last experiment at the 50 milligram-scale was planned with a reaction temperature lowered from 70 °C to 40 °C in order to suppress the DBU degradation occurring over the extended period of time at high temperatures and later facilitate the polymer isolation

at the condition to not significantly impact the reaction yield. While the DBU degradation was indeed mostly prevented, the *cage*-shaped polymer **P19-C1$_{bis}$** was obtained in 46% yield, therefore staying substantially below its former milligram-scaled **P19-C1** yield of 64%. **(Figure 16; Table 15, Entry 3)** As a result, the yield gap was judged to be too significant to be approved and the subsequent up-scaled reactions were accordingly kept at 70 °C.

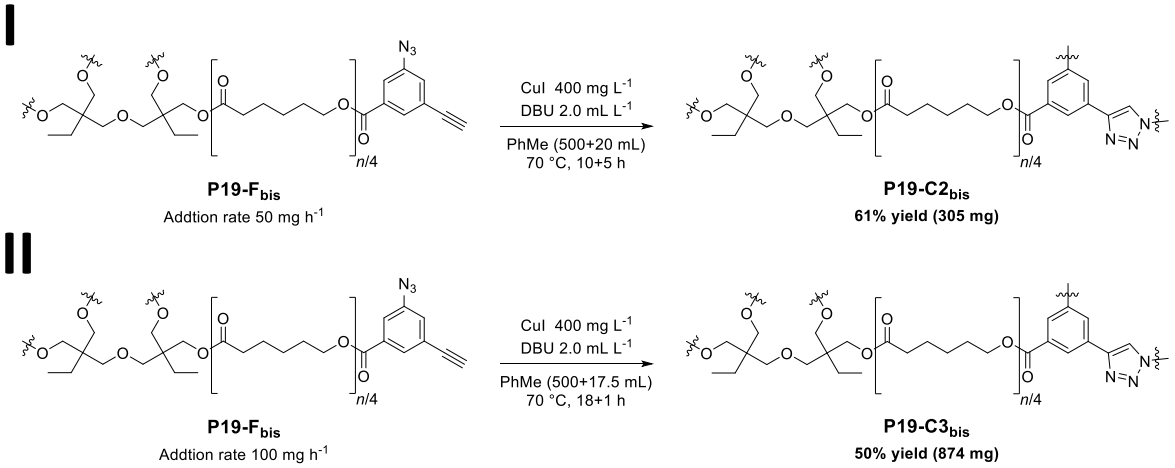

Scheme 45: (**I**) Scheme of upscaled synthesis of *cage*-shaped polymer **P19-C2$_{bis}$**, yielding 305 mg material; (**II**) Scheme of upscaled synthesis of *cage*-shaped polymer **P19-C3$_{bis}$**, yielding 874 mg material.

Before anything else, it should be noted that a second SEC_{DMAC} (i.e. SEC_{DMAC2}) system was used for the last experiments on ε-PCLs as the former SEC_{DMAC} system went out of order. This second DMAC system was used as temporary solution and seemed to suffer from several issues related to its column packing. On the contrary, the polymers were also examined by SEC_{THF} and unlike what had been observed for the **P16** series of *cage*-shaped ε-PCLs, the SEC traces did not feature the same issues. This contrast of behavior during the SEC_{THF} analyses is most likely due to the size gap of a factor above two between both polymer series (i.e. $M_{n,^1H\text{-}NMR}$ 4.4 kg mol^{-1} for **P16**; $M_{n,^1H\text{-}NMR}$ 9.8 kg mol^{-1} for **P19**). Thus, in the case of *star*-shaped ε-PCLs, all polymers displayed a low molecular weight shoulder even if none were either visible on the previous SEC_{DMAC} or on the SEC_{THF} systems. Because of these concerns, the very existence of the low molecular shoulders observed in the following ε-PCL SEC_{DMAC2} traces is questionable. Nevertheless, a first simplified method to conceptualize the transition from batch to semi-batch procedures consisted in looking at a semi-batch synthesis as a juxtaposed series of distinct batch reactions. In this regard, a first semi-batch reaction consisting of 500 mg **P19-F$_{bis}$** added *via* a syringe pump over 10 hours at a polymer addition rate of 50 mg h^{-1} was conducted. **(Scheme**

45, I) After purification, **P19-C2$_{bis}$** was isolated in 61% yield (i.e. 305 mg) in accordance with the former 64% yield obtained for **P19-C1** made at the 50 milligram-scale in similar reaction conditions. **(Figure 16; Table 15, Entry 4)**

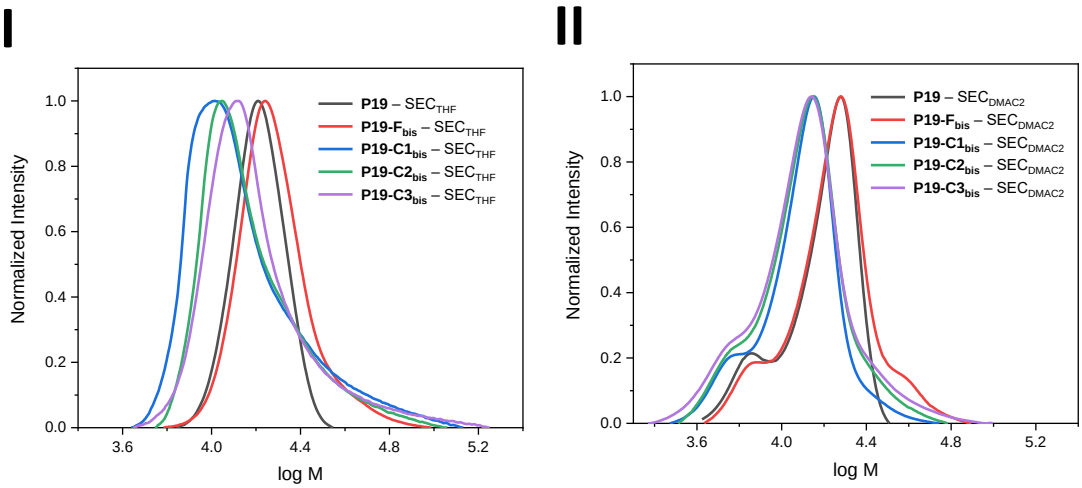

Figure 16: SEC traces of four-arm *star*-shaped **P19**, its end-functionalized polymer **P19-F$_{bis}$,** a *cage*-shaped polymer **P19-C1$_{bis}$** obtained at milligram-scale at reduced reaction temperature, as well as two upscaled gram-scale syntheses of *cage*-shaped polymers **P19-C1$_{bis}$** and **P19-C1$_{bis}$,** characterized by (**I**) SEC with THF as eluent (SEC$_{THF}$); and (**II**) the second SEC with DMAC as eluent (SEC$_{DMAC2}$).

Encouraged by these preliminary results, a second semi-batch reaction starting from 1750 mg of **P19-F$_{bis}$** was planned in order to obtain about 1.0 gram of *cage*-shaped polymer by assuming a theoretical yield of about 60% and therefore confirming the ability of this method to reach the gram scale. **(Scheme 45, II)** For this second try the polymer addition rate was increased to 100 mg h^{-1} to limit the reaction time and therefore the amount of DBU degradation products forming during the reaction. Considering that the constant addition of **P19-F$_{bis}$** contributes to the formation of a steady-state concentration of unreacted end-groups remaining far below the 0.1 mg mL^{-1} value previously used for batch syntheses, the increase of the polymer addition rate to 100 mg h^{-1} was assumed to not impact the yield in a substantial manner. The resulting *cage*-shaped polymer **P19-C3$_{bis}$** was isolated in 50% yield (874 mg). **(Figure 16; Table 15, Entry 5)** Although the 1000 mg threshold was not reached due to a 10% yield loss, which was probably due to the increase of the addition rate to 100 mg h^{-1}, these results clearly show the potential of this method to obtain *cage*-shaped polymer above the milligram scale.

6.2.2 Gram-scale Synthesis of *Cage*-shaped Poly(ethylene oxide)s[§]

Although ε-PCL polymers can be easily obtained with narrow dispersity values below 1.1, their scope of potential applications remains relatively limited in comparison to other polymer compositions. In this regard, the transition from ε-PCL to PEO substrates was made to provide a broader range of applications to the produced *cage*-shaped polymers. **(See Project Part III – Introduction)** However, the synthesis of PEO by ring-opening polymerization requires a high level of safety precautions because of the high toxicity of its gaseous monomer (i.e. ethylene oxide). Therefore, a commercially available four-arm *star*-shaped PEO polymer **P21**, claiming a number average molar mass of 5.0 kg mol^{-1} and a dispersity below 1.05, was purchased as the starting material and carefully characterized prior to its end-functionalization. While SEC_{THF} analysis confirmed the presence of a single gaussian distribution with a low dispersity of 1.04, **(Figure 17)** ^{1}H-NMR **(Figure 18, I)** and FT-IR analyses **(Figure 19, I)** ensured the chemical purity of the material. In addition, ^{1}H-NMR spectroscopy allowed to determine a molecular weight $M_{n,^{1}H\text{-}NMR}$ of 5.7 kg mol^{-1} in accordance with the SEC_{THF} results. **(Table 16, Entry 1)**

Table 16: Overview of the characteristics of the commercial *star*-shaped PEO **(Entry 1)**, its end-functionalized polymer **(Entry 2)**, an upscaled semi-batch topological conversion **(Entry 3)**, as well as a second end-functionalization batch **(Entry 4)** and the first *cage*-shaped synthesis featuring a yield above the gram-scale (i.e. 1.548 g) **(Entry 5)**.

Entry	Polymer	$M_{n,^{1}H\text{-}NMR}$ / kg mol^{-1}	$M_{n,SEC/THF}$ / kg mol^{-1}	$Đ_{SEC/THF}$	Yield / %	Yield / g	T_g / °C	T_m / °C	$\Delta H°_{fus}$ / J g^{-1}
1	**P21**	5.7	7.2	1.04	*n/a*	*n/a*	*n/a*	47.47	121.0
2	**P21-F**	6.4	8.0	1.05	98	1.554	*n/a*	*n/a*	*n/a*
3	**P21-C**	6.4	5.9	1.08	43	0.515	*n/a*	*n/a*	*n/a*
4	**P21-F$_{bis}$**	6.4	8.0	1.05	94	3.62	*n/a*	32.30	63.42
5	**P21-C$_{bis}$**	6.4	4.7	1.14	43	1.548	-45.9	30.34	51.58

§ Parts of this subchapter and the associated parts in the experimental section were previously reported within in the following publication: A. J. Butzelaar, M. Gauthier-Jaques, K. L. Liu, G. Brunklaus, M. Winter, P. Theato, The Power of Architecture – *Cage*-shaped PEO and its Application as Polymer Electrolyte. *Polym. Chem.* **2021**, *12*, 4326–4331.

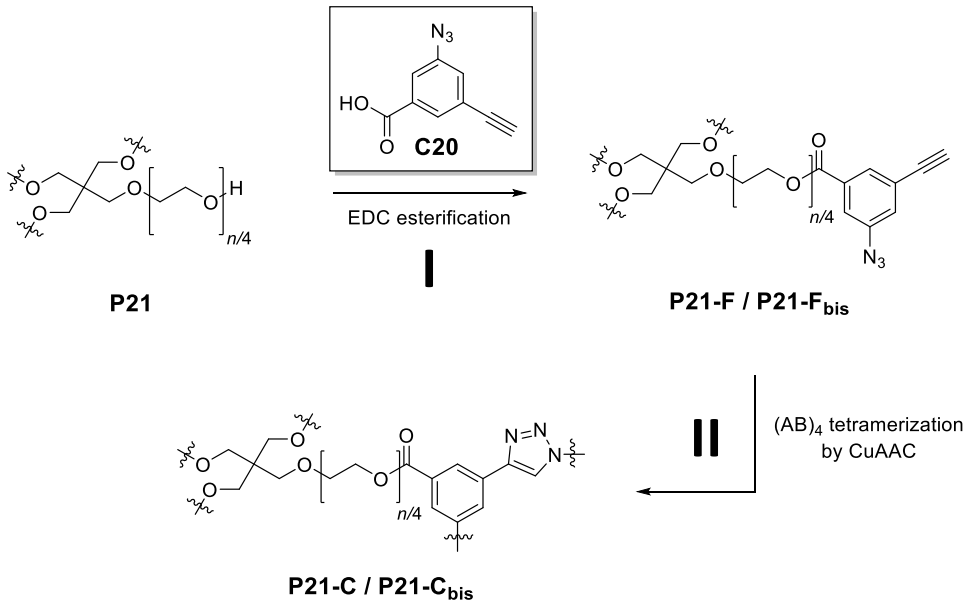

Scheme 46: (**I**) Two end-functionalization batches of *star*-shaped PEO with compound **C20**, yielding **P21-F** and **P21-F**$_{bis}$; (**II**) Gram-scale topological conversion to *cage*-shaped polymers by D_{4h}-[3_4]triazolophane formation, yielding **P21-C** and **P21-C**$_{bis}$.

P21 esterification with end-group **C20** was once again successfully conducted under mild conditions by EDC coupling. **(Scheme 46, I; Table 16, Entry 2)** However, unlike for the previous ε-PCL end-functionalizations, the purification by reprecipitation in cold methanol was compromised by the good solubility of PEO polymers in this solvent. While no other solvent mixture was found suitable for its isolation by reprecipitation, the use of 1.0 kg mol^{-1} dialysis membranes in methanol was hindered by the partial crosslinking of the polymers through the extended dialysis time. In consequence, a purification procedure by silica gel filtration consisting of an initial washing of all impurities with a polar eluent (i.e. chloroform or DCM) followed by the subsequent addition of methanol – typically 10% – to the eluent mixture to recover the PEO material from the silica gel was considered. Although the purification by silica gel filtration was first considered challenging due to the strong affinity of PEO polymers for polar silica, end-functionalized *star*-shaped **P21-F** was ultimately isolated in an excellent 98% yield. The quantitative end-functionalization and the polymer purity were ensured by ^{1}H-NMR analysis, as shown later for the **P21-F**$_{bis}$ sample. **(Figure 18, II)** In this regard, the three aromatic protons, the terminal alkyne proton at 3.18 ppm, as well as the four protons of the terminal ethylene oxide repeating units located between 4.51 and 3.79 ppm could be successfully assigned. Furthermore, a $M_{n,SEC}$ shift to higher molar mass (from 7.2 to 8.0 kg mol^{-1}) as well as a monomodal distribution and a low dispersity of 1.05 were observed by SEC$_{THF}$ analysis. **(Figure 17, I)** Furthermore, the introduction of the end-group

functionalities was also proven by FT-IR though the appearance of the azide double bond stretching and alkyne proton stretching bands located at 1725 cm^{-1} and 2882 cm^{-1}, respectively, as well as the introduction of aromatic hydrogen stretching signals, as shown later for the **P21-F$_{bis}$** sample. **(Figure 19, II)**

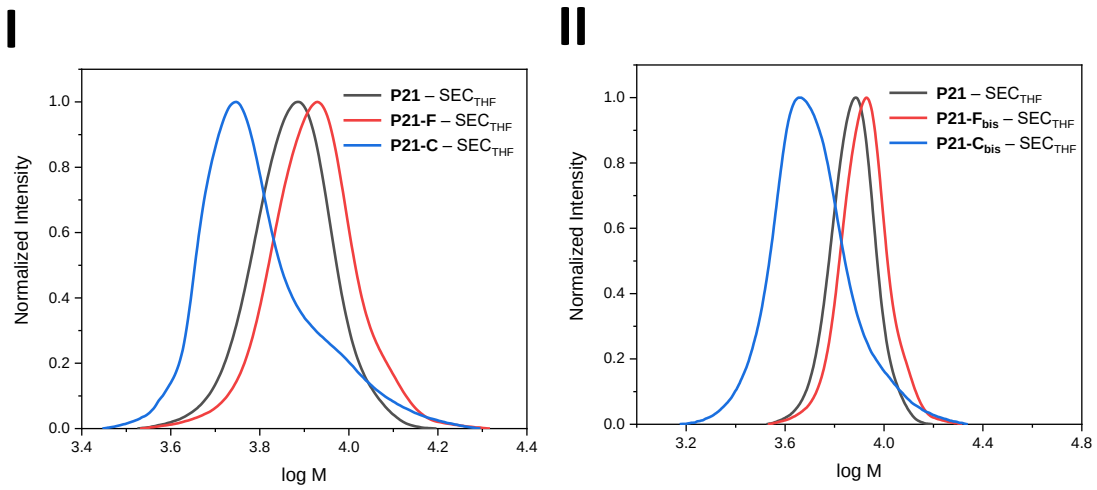

Figure 17: (**I**) SEC$_{THF}$ traces of four-arm *star*-shaped PEO **P21**, its end-functionalized polymer **P21-F**, and **P19-C**, its *cage*-shaped polymer synthesis, yielding 0.515 grams of material; (**II**) A second batch of its end-functionalized polymer **P21-F$_{bis}$**, and **P19-Cbis**, its *cage*-shaped polymer synthesis featuring yield above the gram-scale (i.e. 1.548 g).

Starting from the reaction conditions developed for the gram-scaled synthesis of *cage*-shaped ε-PCLs, a first topological conversion consisting in 1.2 g of *star*-shaped PEO **P21-F** as starting material was achieved by a semi-batch procedure. Although the PEO purification was found to be more tedious than for the ε-PCL cages due to its higher affinity for silica gel, a 43% yield (i.e. 515 mg) of *cage*-shaped PEO **P21-C** was achieved. **(Scheme 46, II; Table 16, Entry 3)** The topological transformation was first followed by SEC$_{THF}$ analysis with a clear shift to the lower molecular weight (i.e. $M_{n,SEC/THF}$ 8.0 to 5.9 kg mol^{-1}) while keeping a relatively low 1.08 dispersity. **(Figure 17, I)** Unlike former *cage*-shaped ε-PCLs, no column interaction was observed during the SEC$_{THF}$ analysis of the *cage*-shaped PEOs. Once again, the formation of the D_{4h}-[3_4]triazolophane structure was confirmed by ^{1}H-NMR spectroscopy and the complete disappearance of the alkyne proton signal previously located at 3.19 ppm, the appearance of the triazole proton signal at 10.31 ppm as well as the downfield shifting and broadening of the three aromatic proton signals from 7.29–7.92 ppm to 8.91–8.98 ppm, as shown later for the **P21-C$_{bis}$** sample. **(Figure 18, III)** Concerning the characterization by FT-IR analysis, a strong attenuation of the azide stretching band located at 1725 cm^{-1}, the suppression of the

alkyne-hydrogen stretching band located at 3236 cm^{-1} as well as the broadening of the aromatic protons stretching bands were clearly observed, as shown later for the **P21-C$_{bis}$** sample. **(Figure 19, III)**

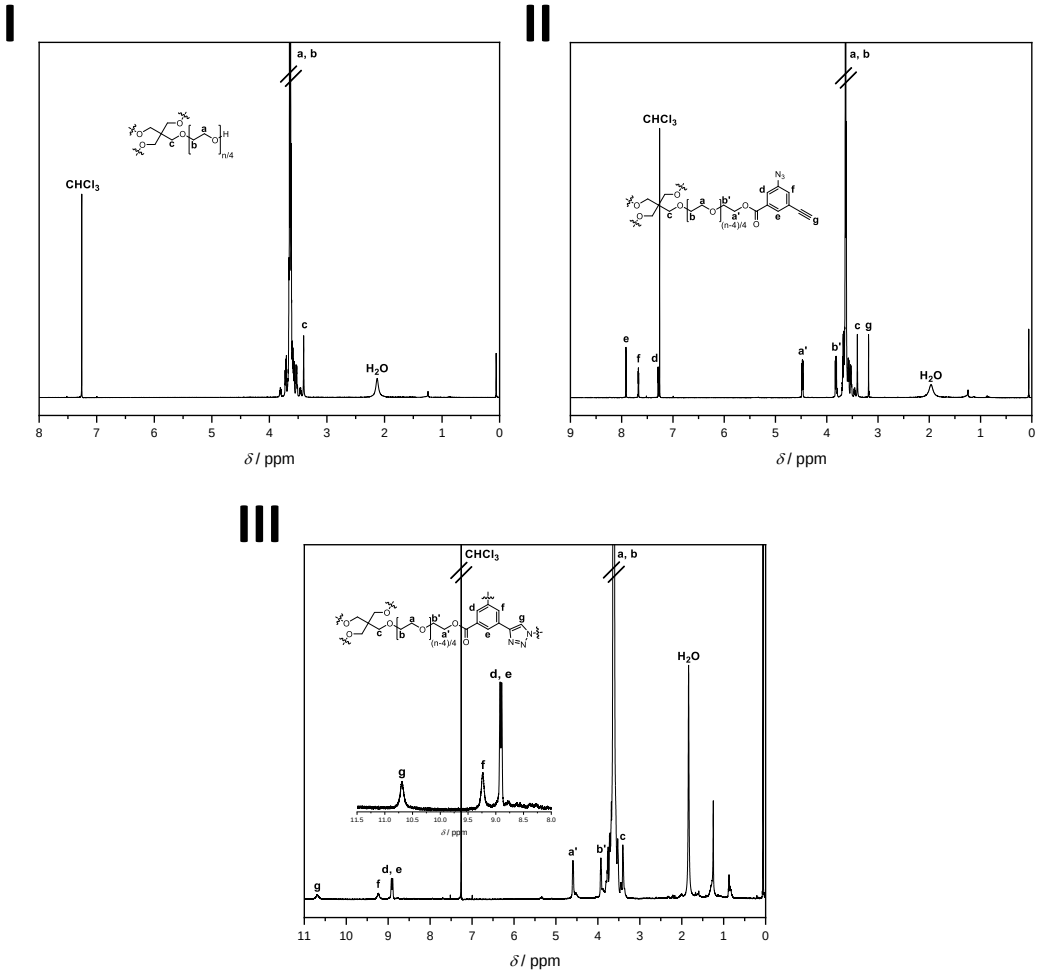

Figure 18: ^{1}H-NMR spectra with peak assignment of (**I**) *star*-shaped PEO **P21**; (**II**) its end-functionalized polymer **P21-F$_{bis}$**; and (**III**) its *cage*-shaped polymer **P21-C$_{bis}$**.

From this point, a second gram-scaled topological conversion of *star*-shaped PEO was planned. To do so, a multigram batch of end-functionalized *star*-shaped PEO **P21-F$_{bis}$** was obtained in 94% yield by following the former procedures. **(Scheme 46, I; Table 16, Entry 4)** Starting from 3.6 g of starting material, **P21-F$_{bis}$** was added once again at a rate of 100 mg h^{-1} to the reaction mixture and *cage*-shaped **P21-C$_{bis}$** was isolated in 43% yield (i.e. 1.548 g). **(Scheme 46, II; Table 16, Entry 5)** According to the SEC_{THF} analysis, the monodisperse gaussian curve was retained with a with a slightly higher dispersity of 1.14 while its $M_{n,SEC}$ value was shifted from 8.0 to 4.7 kg mol^{-1}. **(Figure 17, II)** The divergences of both $Đ$ and $M_{n,SEC}$ values observed

between **P21-C** and **P21-C$_{bis}$** polymers are likely to be a consequence of the variable ion content present in the materials considering the natural propensity of PEO materials to stabilize numerous ionic species. In this regard, increasing the amount of polymer might have allowed a higher retention of the chloride anions coming from the acidic extraction step taking place during the isolation process.

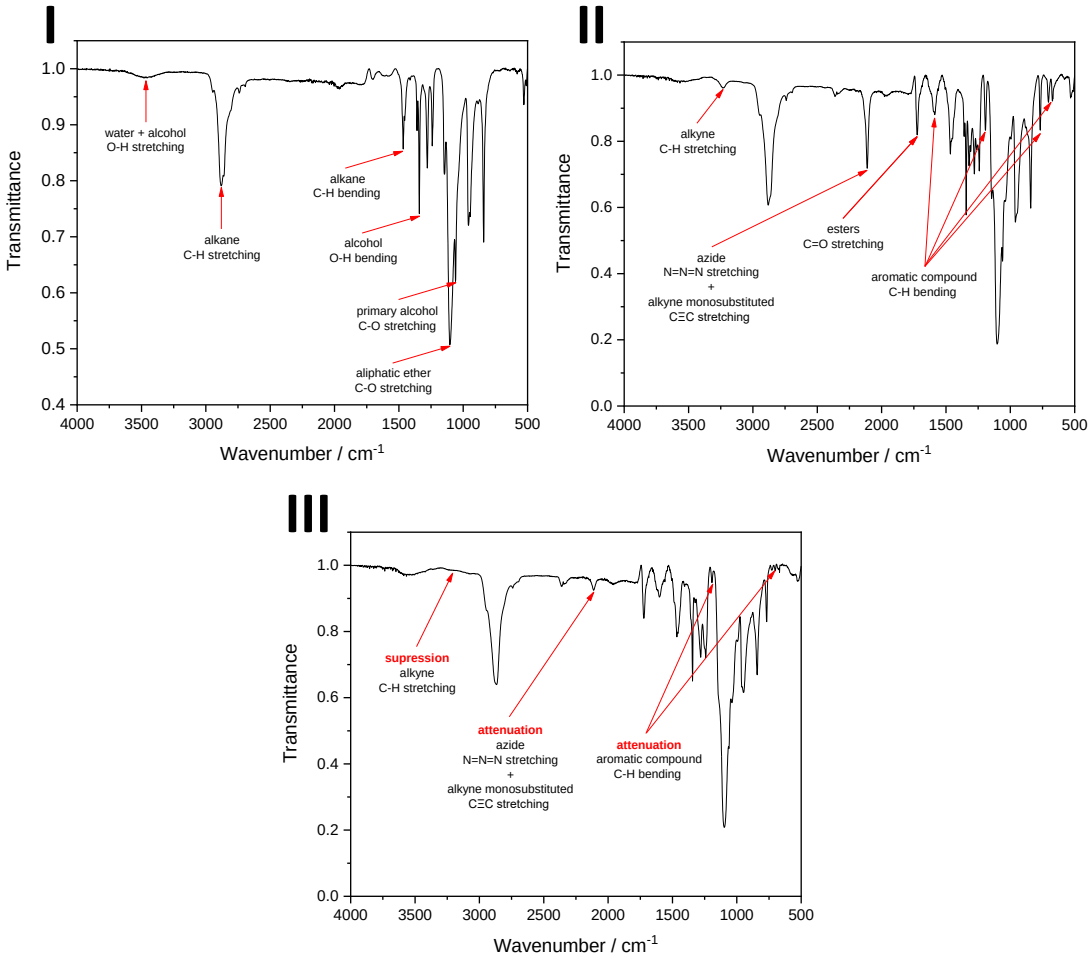

Figure 19: FT-IR spectra of (**I**) *star*-shaped PEO **P21**; (**II**) end-functionalized **P21-F$_{bis}$**; and (**III**) *cage*-shaped **P21-C$_{bis}$** polymers, featuring the appearance and disappearance of the azide stretching band located at 2113 cm^{-1} and of the alkyne-hydrogen stretching band located at 3236 cm^{-1}.

In addition, **P21-C$_{bis}$** was characterized by ESI-MS analysis. **(Figure 20)** Similarly to the analysis of the ε-PCL polymer cages, no clean polymer distribution could be recorded in positive mode. Instead, several distributions were acquired in negative mode with a mixture of chloride anions and sodium cations as ionic buffers. Considering the high affinity of [3$_4$]triazolophane macrocycles and PEO towards chloride anions, the previously discussed $Đ$ and $M_{n,SEC}$ values divergences observed between **P21-C** and **P21-C$_{bis}$**, and the mass

spectroscopy data previously obtained for the *cage*-shaped ε-PCL **P17-C**, the main $[M+2Cl]^{2-}$ distribution featuring peak intervals of 22.014 *m/z* as well as the four minor distributions with additional sodium chloride content are plausible.

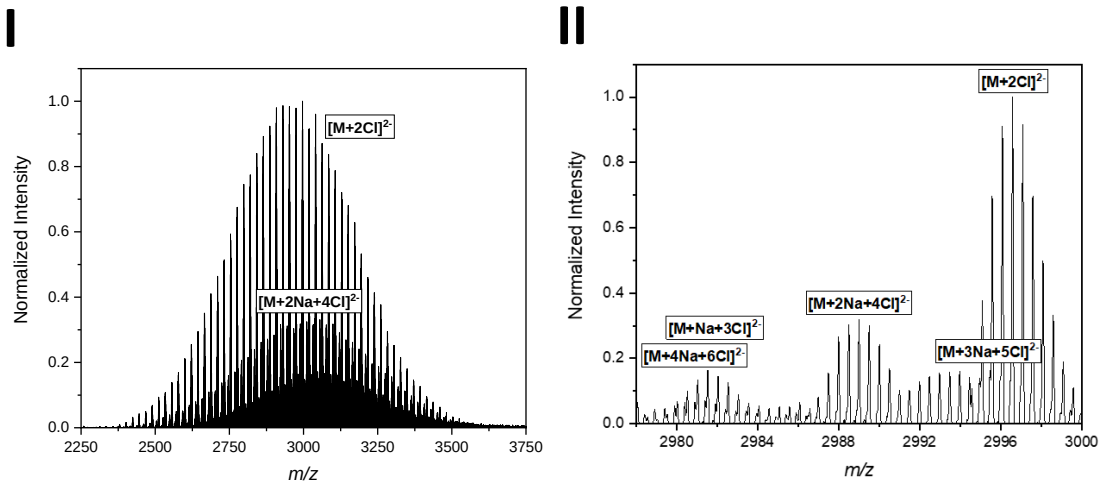

Figure 20: (**I**) ESI-MS spectrum of *cage*-shaped PEO **P21-C$_{bis}$** recorded in the negative mode; (**II**) The spectrum includes a main distribution corresponding to a $[M+2Cl]^{2-}$ pattern as well as four minor distributions corresponding to additional NaCl units present in the polymer matrix. All distributions feature peak intervals of 22.014 *m/z* as expected for PEO polymers.

The thermal properties of **P21**, **P21-F$_{bis}$** and **P21-C$_{bis}$** were examined by DSC analysis. **(Figure 21, I–III; Table 16, Entry 3–5)** Like ε-PCL polymers, the PEO polymers feature a semi-crystalline structure comprised of crystalline and amorphous domains in variable ratios. Thus, the predominant crystalline nature of the unfunctionalized *star*-shaped **P21** was highlighted by its considerable latent heats of fusion $\Delta H°_{fus}$ of 121.0 J g^{-1} located at 47.47 °C and the absence of any noticeable glass transition temperature. As already observed for the end-functionalized ε-PCLs **(See Project – Part II)**, a substantial suppression of the crystalline domains was noticed for **P21-F$_{bis}$** with a $\Delta H°_{fus}$ value divided by a factor of almost two to 63.42 J g^{-1} and a reduced T_m value to 32.30 °C. Those values were further reduced after topological conversion to 51.58 J g^{-1} and 30.34 °C, respectively, and a T_g was noticed at -45.9 °C. In addition, the thermal stability of **P21-C$_{bis}$** was further investigated by TGA analysis. **(Figure 21, IV)** The *cage*-shaped polymer exhibited a typical degradation curve for PEO materials, although no chain-end favoring the polymer thermal degradation by unzipping mechanism was initially present in its structure. As a result, the TGA analysis revealed a good thermal stability up to 300 °C of the polymer, quickly followed by a fast weight% loss above

these temperature values. Interestingly, the remaining 13 weight% around 500 °C could be correlated to the estimated 11.8 weight% of the D_{4h}-[3_4]triazolophane content.

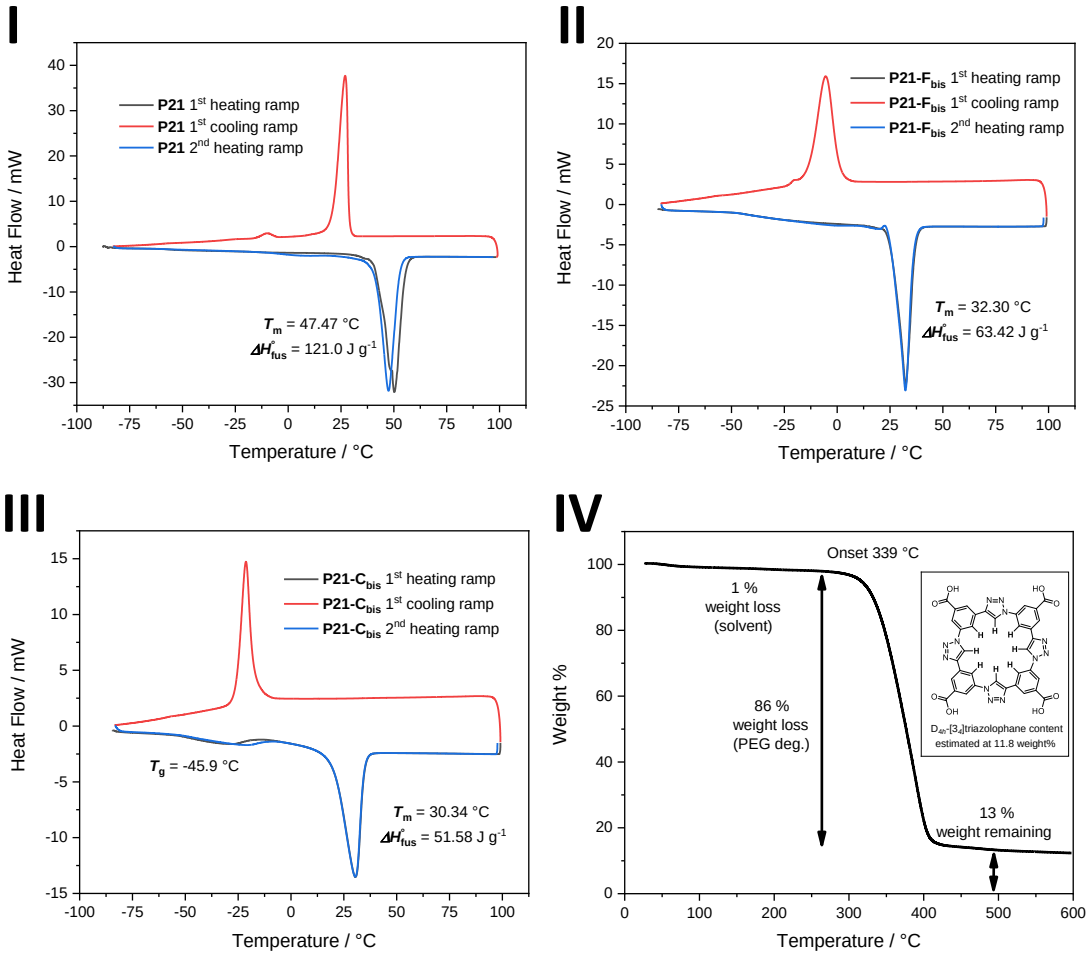

Figure 21: DSC thermograms of (**I**) *star*-shaped PEO **P21**; (**II**) end-functionalized **P21-F$_{bis}$**; and (**III**) *cage*-shaped **P21-C$_{bis}$** polymers, featuring a progressive reduction of the melting point temperatures T_m as well as latent heats of fusion $\Delta H°_{fus}$ between each samples; (**IV**) TGA thermogram of *cage*-shaped PEO **P21-C$_{bis}$,** featuring the degradation of the polymer over 300 °C and the remaining weight content corelated to the theoretical content of D_{4h}-[3_4]triazolophane within the polymer.

6.2.3 *Cage*-shaped PEO as Lithium-Ion Polymer Electrolyte**

With sufficient material in hands, the scope of the research was shifted to the identification of potential applications for *cage*-shaped PEO polymers. Considering the strong interest of the Theato research group within the ‘’FestBatt Project’’ in partnership with the University of Münster for the development of the next generations of lithium-ion polymer electrolytes, an internal collaboration was initiated with one of my colleagues – Andreas J. Butzelaar – involved in the project.[304,305] Taking advantage of both the novelty of the material and his knowledge about lithium-ion polymer electrolytes, the impact of the *cage*-shaped topology on the ionic conductivity of PEO-based polymer electrolytes was examined. While pure PEO materials are known to be mostly crystalline, the DSC analysis of both *cage*-shaped ε-PCL and PEO polymers revealed a strong decrease or even total disappearance of the crystalline phases indicated by the reduction of the melting temperature T_m as well as the latent heats of fusion $\Delta H°_{fus}$ values. **(See Project Part II – III)**

Table 17: Overview of the thermal characteristics obtained by DSC analysis of the polymer precursors **(Entry 1–2)**, as well as the polymer electrolytes made from *star*-shaped **P21 (Entry 2–3)** and from *cage*-shaped **P21-C$_{bis}$ (Entry 5–6)**, featuring among other the total suppression of the crystalline domains within the *cage*-shaped polymer electrolyte samples.

Entry	Polymer (electrolyte) names	[Li+]:[EO] Ratio	T_g / °C	T_m / °C	$\Delta H°_{fus}$ / J g^{-1}
1	**P21**	*n/a*	*n/a*	47.47	121.0
2	**P21-Li$_{1:20}$**	1:20	-42.5	35.0	38.6
3	**P21-Li$_{1:25}$**	1:25	-44.2	39.0	61.6
4	**P21-C$_{bis}$**	*n/a*	-45.9	30.3	51.6
5	**P21-C$_{bis}$-Li$_{1:20}$**	1:20	-40.8	*n/a*	*n/a*
6	**P21-C$_{bis}$-Li$_{1:25}$**	1:25	-41.3	*n/a*	*n/a*

** Parts of this subchapter and the associated parts in the experimental section were previously reported within in the following publication: A. J. Butzelaar, M. Gauthier-Jaques, K. L. Liu, G. Brunklaus, M. Winter, P. Theato, The Power of Architecture – *Cage*-shaped PEO and its Application as Polymer Electrolyte. *Polym. Chem.* **2021**, *12*, 4326–4331.

As the ionic conductivity strongly depends of the existence of free volumes located within the polymer electrolyte material, the presence of a high content of amorphous phases is essential for an efficient ion transport. Moreover, the mobility of the polymer chains also plays an important role to promote a maximal ion transport by segmental motion and can also be estimated by DSC analysis, as a low glass transition temperature T_g tends to indicate a high chain mobility. The largest batch of *cage*-shaped PEO **P21-C$_{bis}$** (i.e. 1.548 g) was chosen to be mixed with lithium bis(trifluoromethanesulfonyl)imide (LiTFSI) salt in [Li^+]:[EO] 1:20 and 1:25 ratios (i.e. **P21-C$_{bis}$-Li$_{1:20}$** and **P21-C$_{bis}$-Li$_{1:25}$**). It is known that LiTFSI tends to reduce the polymer crystallinity due to its plasticizing character. However, unlike what was observed for comparable *star*-shaped PEO electrolytes prepared accordingly from **P21** (i.e. **P21-Li$_{1:20}$** and **P21-Li$_{1:25}$**) the complete crystallization suppression was already achieved at these low lithium-salt loading values for both *cage*-shaped PEO electrolytes. **(Table 17)**

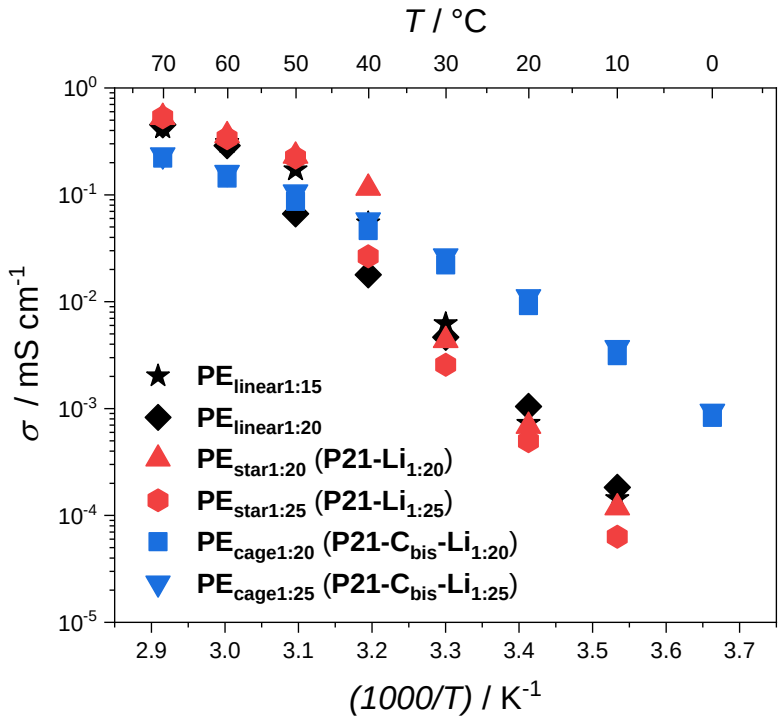

Figure 22: Temperature-dependent ionic conductivity of polymer electrolytes varying in polymer topology and LiTFSI loading ratios.

Considering the determination of the ionic conductivity itself, both polymer electrolyte series obtained from **P21** and **P21-C$_{bis}$** as well as two polymer electrolytes prepared from linear 5 Mg mol^{-1} PEO with [Li^+]:[EO] 1:15 and 1:20 LiTFSI loading ratios were conditioned and sealed into cell coins. Then, the cell coins were analyzed within a temperature range of 70 °C

to 0 °C by Electrochemical Impedance Spectroscopy (EIS) at the University of Münster. **(Figure 22)** Unlike what could be observed for the linear and *star*-shaped PEO samples, no abrupt drop of ionic conductivity was recorded around 40 °C for both *cage*-shaped polymer electrolytes because of their inability to crystallize. As a result, the ionic conductivities of both *cage*-shaped polymer electrolytes outperformed the other linear and *star*-shaped polymer electrolytes below their respective melting points but were surpassed above them due to the lower chain mobility granted by their specific topology. At last, the ionic conductivity values recorded for the polymer electrolytes with the lowest LiTFSI loading ratios always tended to outperform the ionic conductivity of the ones with the highest lithium content due to lower degree of ionic coordination hindering the polymer chain motion.

6.3 Project Part III – Conclusion

Following the syntheses of *cage*-shaped poly(e-caprolactone) at the milligram-scale, **(See Project Part II)** the topological conversion was first upscaled for a known ε-PCL. Although the change of SEC system made the comparison with previous data challenging, the semi-batch reaction resulted in up to 874 mg yield of *cage*-shaped polymer. The feasibility of the upscaling being now established, the robustness of the procedure was then examined by varying the polymer nature, achieving yields beyond the gram-scale, as well as determine possible applications specifically suiting the polymer topology. Hence, starting from a commercially available *star*-shaped PEO, a semi-batch reaction yielded 515 mg of *cage*-shaped PEO and was followed by a second synthesis resulting in 1.548 g yield (i.e. 43% yield in both cases), far above the symbolic gram-threshold. Following the extended characterization of the *cage*-shaped PEO by ^{1}H-NMR, SEC_{THF}, FT-IR, DSC, TGA and ESI-MS analyses, a collaboration with one of my colleagues – Andreas J. Butzelaar – working on the synthesis of PEO-based polymer electrolyte for lithium-ion battery was initiated. Interestingly, the combination of the plasticizing effects resulting from the topological conversion and the lithium-salt addition were sufficient to yield purely amorphous polymer electrolytes at low loading ratios (i.e. $[Li^+]$:[EO] 1:20 and 1:25). While the ionic conductivities of the *cage*-shaped polymer electrolytes were outperformed by the linear and star-shaped samples due to a hindrance in chain motion, the *cage*-shaped polymer electrolytes outperformed them below their crystallization temperature (i.e. 40 °C). Thus, ionic conductivities of 0.011 mS cm^{-1} were obtained for both *cage*-shaped polymer electrolytes at 20 °C while all other crystalized samples exhibited values already below 10^{-3} mS cm^{-1} at the same temperature. Although *cage*-shaped polymer electrolytes might never be considered as a viable alternative for practical applications due to their demanding synthesis, the strong causal link between topology and polymer properties was once again emphasized.

7 Conclusion and Outlook

In conclusion, a novel procedure for the synthesis of *cage*-shaped polymers by topological conversion was successfully conceptualized and developed. Thus, for the first time since their initial report more than 20 years ago, *cage*-shaped polymers were synthetized in gram-scale, yielding a substantial amount of material *per* reaction batch. Beyond this achievement, the present work opens the door to future applications and developments for *cage*-shaped polymer-based materials.

In a more general manner, generations of organic and polymer chemists focused their efforts during the last century on the synthesis of macrocyclic structures featuring a unique set of properties. **(See Theoretical Background, Part II)** Regardless of the nature of the final product, their concerted works constituted a solid basis allowing *inter alia* the synthesis of even more sophisticated cyclic polymer architectures. In this context, the first example of a *cage*-shaped polymer was reported in the early 2000s. Beyond the simple challenge of their synthesis, polymer cages quickly became a subject of interest because of the effect that their multicyclic polymer topology associated with their low hydrodynamic radius could have on the thermo-mechanical properties of these materials. Hence, several synthesis protocols for polymer cages were proposed through several strategies over the past two decades, resulting in a series of polymer cages varying in yield, composition, molecular weight and arm number. **(See Theoretical Background, Part III)** However, despite these renewed efforts, the synthesis of *cage*-shaped polymers remained, in the vast majority of cases, below the 50-miligram-scale and no example of a synthesis approaching the gram-scale was ever published due to either the tedious synthesis of the precursors or the limitations induced by their synthesis procedure.

In order to address this challenge, the pursuit of a more efficient synthesis of *cage*-shaped polymers was launched and its practical development constituted the starting point of this work. Thus, a new synthesis procedure for the synthesis of *cage*-shaped polymers by topological conversion of *star*-shaped polymers was envisioned. For this purpose, *n*-arm *star*-shaped polymers bearing AB bifunctional groups at each chain-end were planned to react intramolecularly into a chemically-inert macrocyclic structure by $(AB)_n$ *n*-oligomerization. **(See Motivation)** By this means, the symmetrical nature of the *star*-shaped precursor not only

limits the complexity of its synthesis, but also ensures a maximal probability for the chain end-groups to react with each other. Additionally, the use of a purely intramolecular reaction allows the topological conversion to be conducted in high-dilution conditions without any impact on its kinetic. At last, the formation of a chemically inert macrocyclic structure opens the opportunity to upscale the reaction in a semi-batch process without risk of further intermolecular reactions between the finalized *cage*-shaped polymers. Consequently, the chemistry involved in the $(AB)_n$ *n*-oligomerization was thoroughly chosen to suit a series of criteria such as: high orthogonality, irreversibility, ability to be triggered by a physical stimulus or a catalyst, and ability to reach high conversion in a minimal timeframe. Additionally, the synthesis of the bifunctional end-group had to be accessible enough to be viable. While other chemistries were concurrently considered, the use of CuAAC click chemistry was quickly favored and the synthesis of a suitable azido-alkyne bifunctional end-group thoroughly investigated. Regarding the synthesis of the end-functionalized *star*-shaped polymers, RDRP methods were quickly considered as promising due to their ability to produce a great diversity of well-defined polymers. Among them, the RAFT polymerization was chosen *inter alia* for the opportunity to directly include the bifunctional end-groups in the *star*-shaped RAFT agent structure and therefore to avoid any superfluous post-polymerization modifications prior to the final topological conversion step. However, the syntheses of the end-functionalized *star*-shaped RAFT agents and of their polymerizations proved to suffer from multiple side-reactions and functional incompatibilities, which durably compromised the initially envisioned synthetic route. **(See Project Part I – Early Attempts of *Cage*-shaped Polymer Synthesis)**

Nevertheless, the encountered obstacles were overcome by realigning the synthetic route. First, the synthesis of defect-free *star*-shaped polymers was ensured by employing ring-opening polymerization of ε-caprolactone from multifunctional initiators. Secondly, the topological conversion was focused on the synthesis of [3_4]triazolophane macrocycles. Based on in-depth literature research these structural motifs were identified as suitable candidates that could be obtained by means of CuAAC $(AB)_n$ *n*-oligomerization. Indeed, while only the D_{2h}-[3_4]triazolophane regioisomer had been synthetized, its report implied the existence of a more symmetrical D_{4h}-[3_4]triazolophane regioisomer, which could be synthetized by $(AB)_4$ tetramerization of *m*-azidoethynylbenzene derivatives. Therefore, 3-azido-5-ethynyl benzoic acid – a *m*-azidoethynylbenzene derivative including a carboxylic acid group – was synthetized in 61% yield over four steps. Moreover, once the well-defined four-arm *cage*-shaped poly(ε-caprolactone)s were obtained, the polymers were quantitively end-functionalized under

mild conditions *via* EDC coupling and a first 50-milligram-scale synthesis of *cage*-shaped polymer quickly followed by the $(AB)_4$ tetramerization of the four bifunctional chain end-groups into a single D_{4h}-[3_4]triazolophane macrocycle. Then, the reaction time was gradually minimized from two days to 30 minutes in order to obtain an estimation of the intramolecular topological conversion kinetic despite the impossibility to follow the reaction conversion *in situ* due to high-dilution conditions (i.e. 0.1 mg mL^{-1}). Therefore, the reaction time for the subsequent topological conversions was systematically fixed at 1 hour and the impact of the polymer concentration on the occurrence of undesired intermolecular cross-linking reaction was examined by progressively increasing the polymer concentration from 0.1 mg mL^{-1} to 0.5 mg mL^{-1}. However, an raising high-molecular weight shoulder was observed in the polymer SEC traces as the polymer concentration increased and therefore polymer concentrations were kept at 0.1 mg mL^{-1} for the following batch iterations. Finally, the impact of the polymer size on its synthesis yield and thermo-mechanical properties was investigated. To do so, a series of four *cage*-shaped poly(ε-caprolactone)s with $M_{n,^1H\text{-}NMR}$ values varying from 5.3 to 14.6 kg mol^{-1} was prepared at the 50-milligram-scale in 36% to 78% yield and meticulously characterized. In particular, a strong reduction of the crystallinity degree for all polymer cages in comparison to their respective *star*-shaped polymer precursors was observed and even resulted in pure amorphous poly(ε-caprolactone) material in the case of the smallest polymer cage. **(See Project Part II – *Cage*-shaped Polymer Synthesis at the Milligram-scale)**

At this point of the project, the 50-milligram-scale syntheses of four-arm *cage*-shaped poly(ε-caprolactone) polymers were considered robust enough to be adapted to the gram-scale. Thus, the topological conversion protocol was switched to a semi-batch procedure employing a low steady-state concentration of the *star*-shaped polymer precursor throughout the reaction time. Consequently, a semi-batch synthesis of a known *cage*-shaped poly(ε-caprolactone) featuring a $M_{n,^1H\text{-}NMR}$ value of 10.5 kg mol^{-1} led to up to 874 mg in 50% yield. By taking into consideration that its former 50-miligram-scale synthesis resulted in only a slightly higher 64% yield, these first results motivated the determination of suitable applications for *cage*-shaped polymer materials. In particular, applications benefiting from the reduction of crystallinity that was noted after every topological conversion were privileged. Accordingly, as part of a collaboration, the gram-scale synthesis of *cage*-shaped poly(ethylene oxide)s was envisioned to be used for the production of an unusual poly(ethylene oxide)-based polymer electrolyte for lithium-ion batteries. Therefore, two successive semi-batch syntheses of

cage-shaped poly(ethylene oxide) polymers featuring a $M_{n,^1H\text{-}NMR}$ value of 6.4 kg mol^{-1} were conducted and resulted in 515 mg and 1.548 g of material, respectively. While the cage topology was not sufficient to fully suppress every crystalline domain by itself, the crystallinity of the poly(ethylene oxide) was greatly reduced. As a result, low loading ratios of lithium salt (i.e. [Li^+]:[EO] 1:20 and 1:25) were sufficient to yield fully amorphous polymer electrolyte. As a result, the absence of crystalline domains within the polymer electrolyte lattice led to remarkable electric conductivities in comparison to *star*-shaped and linear poly(ethylene oxide) electrolytes once brought below their melting point temperature (i.e. < 40 °C). Thus, great electric conductivities were noted at room temperature for both lithium loading ratios. (i.e. 0.011 mS cm^{-1} at 20°C). **(See Project Part II – *Cage*-shaped Polymer Synthesis at the Gram-scale)**

While the synthetical complexity of the *cage*-shaped polymer electrolytes might constitute a non-negligible barrier for any major breakthrough in this domain of application, the perspectives of this thesis do not limit themselves to it, nor to the synthesis of polymer cages by formation of D_{4h}-[3_4]triazolophane units. Thus, neither the D_{4h}-[3_4]triazolophanes, nor the CuAAC reaction are likely to remain the only suitable options to fulfil the topological conversion by $(AB)_n$ *n*-oligomerization, especially since a first structural motif for the synthesis of three-arm cages by $(AB)_3$ trimerization was already identified. **(See Project Part II – Chapter 5.2.5)** Consequently, future work needs to be addressed on the formation of polymer cages with three, five or more arms by further varying the nature of the $(AB)_n$ *n*-oligomerization chemistry. And whatever the upcoming advances will concern the development of novel synthetical methods or simply the optimization of former procedures with enhanced accessibility or upscability, the number of potential applications related to *cage*-shaped polymers will accordingly keep expanding in the upcoming years.

8 Experimental Section

8.1 General Methods

8.1.1 Reagents and Solvents

All chemicals were purchased from commercial suppliers and were used without further purification. All chiral chemicals were purchased as racemic mixture. 3-Amino-5-bromobenzoic acid (Merck, 97%); ammonium chloride (NH_4Cl, Carl Roth, ≥99.5%); 4,4-azobis(4-cyanovaleric acid) (ACVA, FUJIFILM Wako, 95%); 2,2'-azobis(4-methoxy-2,4-dimethylvaleronitrile) (V-70, FUJIFILM Wako, 96%); 2,2′-azobis(2-methylpropionitrile) (AIBN, Merck, 98%); benzoyl peroxide 75 wt.% (BPO, Merck, 75 wt.%); bis(triphenylphosphine) palladium(II) dichloride ($Pd(PPh_3)_2Cl_2$, Acros Organics, 98%); 2,2-bis(hydroxymethyl)propane-1,3-diol (Merck, 99%);(bromomethyl)benzene (Alfa Aesar, 99%); ε-caprolactone (ε-CL, Alfa Aesar, 99%); carbon disulfide (CS_2, Acros Organics, 99.9%); 3-chloroperoxybenzoic acid (mCPBA, Merck,70 wt.%); copper(I) iodide (CuI, Acros Organics, 98%); 1,8-diazabicyclo[5.4.0]undec-7-ene (DBU, Merck, ≥99%); diisobutylaluminum hydride (DIBAL-H, Merck, 1 M in PhMe); *N*-(3-dimethylaminopropyl)-*N*′-ethylcarbodiimide hydrochloride (EDC, Carl Roth, ≥99%); 4-dimethylaminopyridine (DMAP, Acros Organics, 99%); *N*,*N*-dimethylaniline (DMA, Merck, 99%); diphenyl phosphate (DPP, Acros Organics, 99%); di(trimethylolpropane) (TCI, >98%); ethyl 2-bromoacetate (Merck, 98%); ethyl 2-chloroacetate (Alfa Aesar, 98%); 2-ethyl-2-(hydroxymethyl) propane-1,3-diol (Acros Organics, 98%); ethynyl magnesium bromide (Merck, 0.5 M in THF); ethynyl magnesium chloride (Acros Organics, 0.5 M in THF/PhMe); ethynyltrimethylsilane (TMS-acetylene, TCI, >98%); hydrochloric acid ($HCl_{(aq)}$, Carl Roth, 37 wt.%); iron powder (Fe, Merck, ≥99%); lithium acetylide, ethylenediamine complex (Alfa Aesar, 90%); lithium aluminum hydride ($LiAlH_4$, Merck, 95%); magnesium sulfate ($MgSO_4$, Carl Roth, ≥99%); 2-mercaptopropanoic acid (TCI, >97%); methyl acrylate (MA, TCI, >99%); methyl 3-bromopropanoate (Merck, 98%); 2-methylbut-1-en-3-yne (Alfa Aesar, 97%); methyl methacrylate (MMA, Alfa Aesar, 99%); 3-nitrobenzaldehyde (Acros Organics, 99%); phenylmethanol (TCI, >98%); potassium hydroxide (KOH, Carl Roth, ≥85%); propyl-1-amine (Alfa Aesar, ≥99%); sodium azide (NaN_3, Acros Organics, 99%); sodium hydroxide (NaOH, Carl Roth, ≥98%); sodium nitrite ($NaNO_2$, Fluka, ≥99%); *star*-shaped PEG 5000 g mol^{-1} (JenKem Technology®, ≥95%); styrene (Alfa

Aesar, 99%); sulfuric acid (H_2SO_4, Carl Roth, 96%); tetra-*N*-butylammonium fluoride (TBAF, Merck, 1 M in THF); triethylamine (NEt_3, Acros Organics, 99%); trimethylsulfonium iodide (Alfa Aesar, ≥98%); triphenylphosphine (PPh_3, Alfa Aesar, ≥99%); 1,3,5-tris(bromomethyl)benzene (Merck, 97%); vinyl bromide (Acros Organics, 1 M in THF). All solvents were purchased from VWR Chemicals with AnalaR NORMAPUR purity grade and were used without preliminary distillation. Deuterated solvents were obtained from Eurisotop, a subsidiary of Cambridge Isotope Laboratories, Inc. Flash column chromatography was carried out using silica gel (40-63 µm mesh, Geduran® Si 60 from Merck Millipore).

8.1.2 Nuclear Magnetic Resonance Spectroscopy (NMR)

All ^{1}H-NMR, ^{13}C-NMR and two-dimensional ^{1}H-^{13}C-HSQC (Heteronuclear Single Quantum Correlation) spectra were recorded at a temperature of 293 K on a Bruker Ascend III 400 MHz spectrometer (^{1}H-NMR 400 MHz, ^{13}C-NMR 101 MHz) using chloroform-*d* or DMSO-*d6* as deuterated solvents. Chemical shifts were reported in ppm (δ), relative to the solvent residual peak as internal standards. chloroform-*d* (δ 7.26 for ^{1}H-NMR, δ 77.16 for ^{13}C-NMR) and DMSO (δ 2.50 for ^{1}H-NMR, δ 39.52 for ^{13}C-NMR). The coupling constants (J) are given in Hz. Splitting patterns are designated as s (singlet), d (doublet), dd (double doublet), t (triplet), q (quartet) and m (multiplet).

8.1.3 Size Exclusion Chromatography (SEC)

Size Exclusion Chromatography (SEC) analysis with tetrahydrofuran (THF) as eluent were performed on a PL-SEC 50 Plus Integrated System, comprising an autosampler, a differential Refractive Index (RI) detector, a PLgel 5 µm bead-size guard column (50 ×7.5 mm) followed by three PLgel 5 µm Mixed C column (300 × 7.5 mm) and a PLgel 3 µm Mixed E column (300 × 7. mm). THF was used at an operating temperature of 35 °C and a flow rate of 1.0 mL min^{-1}. Size Exclusion Chromatography (SEC) analysis with *N*,*N*-dimethylacetamide (DMAC) as eluent were performed on two distinct SEC systems as the first one went out of service during the research time lapse. The first DMAC SEC system (DMAC) was constituted of a PL-SEC 50 Plus Integrated System, comprising an autosampler, a PLgel 5 µm bead-size guard column (50 × 7.5 mm) followed by three PLgel 5 µm Mixed C column (300 × 7.5 mm) and a differential Refractive Index (RI) detector. Lithium bromide (LiBr) 0.03 wt% enriched DMAC was used at an operating temperature of 50 °C and a flow rate of 1.0 mL min^{-1}. The

second DMAC SEC system (DMAC2) was constituted of a PSS SECcurity SEC System, comprising an autosampler, a PLgel 5 μm bead-size guard column (50 × 7.5 mm) followed by two PLgel 5 μm Mixed C column (300 × 7.5 mm) and a differential Refractive Index (RI) detector. Lithium bromide (LiBr) 0.03 wt% enriched DMAC was used at an operating temperature of 50 °C and a flow rate of 0.5 mL min^{-1}. All samples were prepared with a polymer concentration of 2.0 mg ml^{-1} and 100 μL were typically injected to the columns. All number average molar mass M_n, mass average molar mass M_w and dispersity $Đ$ values were extrapolated from a range of linear polystyrene standard between 370 and $6 \cdot 10^6$ g mol^{-1}.

8.1.4 Fourier-Transform Infrared Spectroscopy (FT-IR)

FT-IR measurements were first performed on a Bruker Vertex 70 FT-IR/NIR spectrometer equipped with an ATR unit (FT-IR). All FT-IR spectra were measured though 32 scans from 4000 to 600 cm^{-1} at a resolution of 1 cm^{-1}. A second FT-IR analytical device (FT-IR2), consisting in a Bruker ALPHA FT-IR spectrometer equipped with an ATR unit was additionally employed as the first one was momentarily defective at the end of the research time lapse. All FT-IR2 spectra were measured though 32 scans from 4000 to 500 cm^{-1} at a resolution of 1 cm^{-1}.

8.1.5 Electrospray Ionization Mass Spectrometry (ESI-MS)

ESI-MS measurements were achieved on a Thermo Fisher Q-Exactive Orbitrap Mass Spectrometer. As sample preparation, a small molecule concentration of 0.03 mg mL^{-1} or a polymer concentration of 0.05 mg mL^{-1} was prepared in a mixture of THF/MeOH 3:2 or DCM/MeOH 3:1 enriched with 100 μmol sodium trifluoroacetate as cation source.

8.1.6 Ultraviolet–visible Spectroscopy (UV-Vis)

UV-Vis measurements were carried out by a Varian Cary 300 Spectrometer at 22 °C from 800 to 200 nm. The measurements were recorded at 22 °C in DCM for concentration values from 0.0125 to 0.2 mg ml^{-1}.

8.1.7 Dynamic Light Scattering (DLS)

DLS measurements were performed on Zetasizer Nano S from Malvern Panalytical with a sample concentration of 2.0 mg ml^{-1} in THF and at a temperature of 25 °C.

8.1.8 Differential Scanning Calorimetry (DSC)

DSC measurements were performed by a from TA Instruments Q200 incorporating a RCS90 cooling system. All samples weighing between 10.0 and 14.0 mg were heated from -90 °C to 100 °C twice with a heating ramp of 10.0 K min^{-1}. All reported temperature and enthalpy values were given from the second heating ramp curves.

8.1.9 Thermal Gravimetric Analysis (TGA)

Thermal Gravimetric Analysis (TGA) was carried out by a TGA 5500 from TA Instruments at a heating rate of 10.0 K min^{-1} and under nitrogen atmosphere up to 600 °C. Typically, about 10 mg material were weighted on a palladium pan prior to the measurements.

8.1.10 Syringe Pump

All experiments involving a syringe pump were conducted with a Landgraf HLL LA-30 syringe pump system.

8.1.11 Polymer Electrolyte (PE) Preparation††

Prior to the preparation, each polymer was dried at 80 °C under vacuum overnight. Each polymer was dissolved in acetone and mixed with a predefined ratio of LiTFSI to yield a homogenous mixture. Then, acetone was slowly removed under reduced pressure at 50 °C, before being dried under reduced pressure (10^{-3} mbar) at 80 °C for 24 hours.

8.1.12 Coin Cell Preparation††

The coin cells (CR2032) were assembled by sandwiching the previously prepared polymer electrolytes between two stainless steel electrodes using a Mylar foil spacer ring (thickness l = 100 µm, inner diameter = 8 mm).

8.1.13 Electrochemical Impedance Spectroscopy (EIS)‡‡

Each coin cell was preconditioned in a temperature chamber (Binder MK53, controlled with the Autolab Software Nova 2.1.3) with a gradual increase of temperature from 20 °C – 70 °C

†† Preparations conducted at the Karlsruhe Institute of Technology (KIT) by Andreas J. Butzelaar
‡‡ Analyses conducted at the University of Münster by Kun L. Liu.

in 10 °C steps while maintaining each temperature for 2 hours. 1 hour after the preconditioning was finished, measurements were carried out by gradually increasing the temperature in 10 °C steps from 0 °C to 70 °C with each temperature being maintained for 2 h to attain a thermal equilibrium. The measurements were performed using a PGSTAT302N potentiostat / galvanostat (Autolab) over a frequency range of 1 MHz – 1 Hz with an amplitude of 10 mV. The ionic conductivity σ was calculated according to the following equation: $\sigma = (1/R_b)\cdot(l\ A^{-1})$; R_b being the bulk resistance that can be accessed from the Nyquist plot, l is the film thickness ($l = 100\ \mu m$) and A is the film area ($A = 5.03 \times 10^{-5}\ m^2$). Three successive coin cells were prepared and measured for each SPE. Subsequently, the mean average ionic conductivity was derived from these three separated measurements.

8.2 Small Molecules Synthesis – Project Part I

8.2.1 **(C01)** (3-Amino-5-bromophenyl)methanol

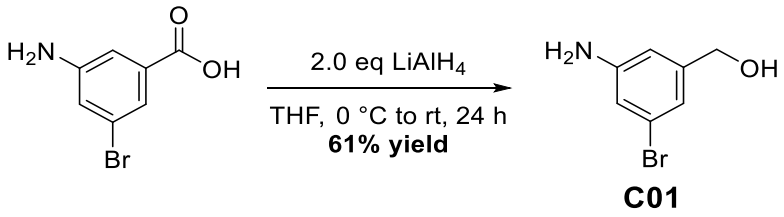

Lithium aluminum hydride (1.75 g, 46.2 mmol, 2.0 eq) was added carefully to dry THF (20 mL) at 0 °C. 3-Amino-5-bromobenzoic acid (5.00 g, 23.1 mmol, 1.0 eq) in dry THF (50 mL) was added dropwise over 30 min at 0 °C. The mixture was left stirring overnight at room temperature. Afterwards, the mixture was again cooled to 0 °C and cold water (100 mL) was carefully added. The solid deposit was filtered off and most THF was removed under reduced pressure. The resulting THF-aqueous mixture was extracted with DCM (3 × 30 mL). The organic fractions were collected, dried over magnesium sulfate and the solvent was removed under reduced pressure. The crude material was purified by flash chromatography (silica, MeOH / DCM, 1:10) in order to give **C01** as a yellow solid. **(2.85 g, 14.1 mmol, 61% yield)**

^{1}H NMR (400 MHz, DMSO) ***δ*** 6.60 – 6.55 (m, 2H), 6.51 – 6.46 (m, 1H), 5.33 (s, 2H), 5.12 (t, J = 5.9 Hz, 1H), 4.32 (d, J = 5.8 Hz, 2H).

^{13}C NMR (101 MHz, DMSO) ***δ*** 150.32 (s), 145.64 (s), 121.79 (s), 115.91 (s), 114.17 (s), 110.61 (s), 62.44 (s).

ESI-HRMS (*m/z*) calculated for $[M+H]^+$ 201.9868 found 201.9866.

ESI-HRMS (*m/z*) calculated for $[M+H]^+$ 203.9847 found 203.9845.

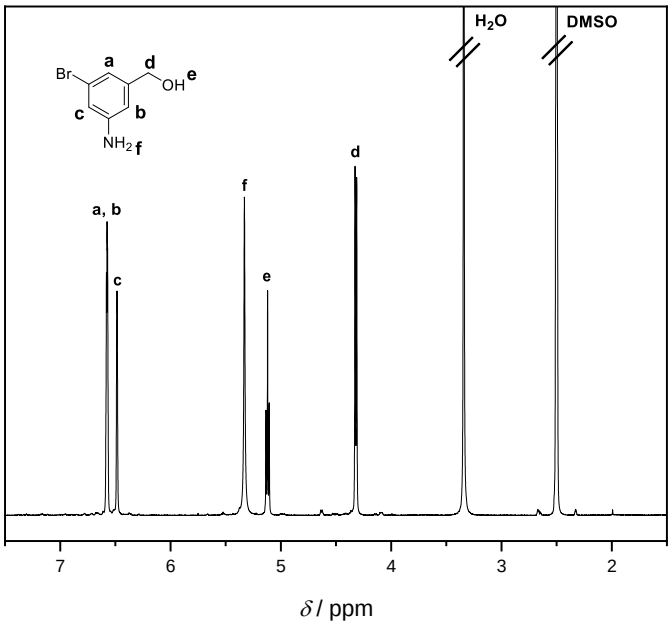

Figure S1: ^{1}H-NMR spectrum of **C01**, **^{1}H NMR (400 MHz, DMSO)** δ 6.60 – 6.55 (m, 2H), 6.51 – 6.46 (m, 1H), 5.33 (s, 2H), 5.12 (t, J = 5.9 Hz, 1H), 4.32 (d, J = 5.8 Hz, 2H).

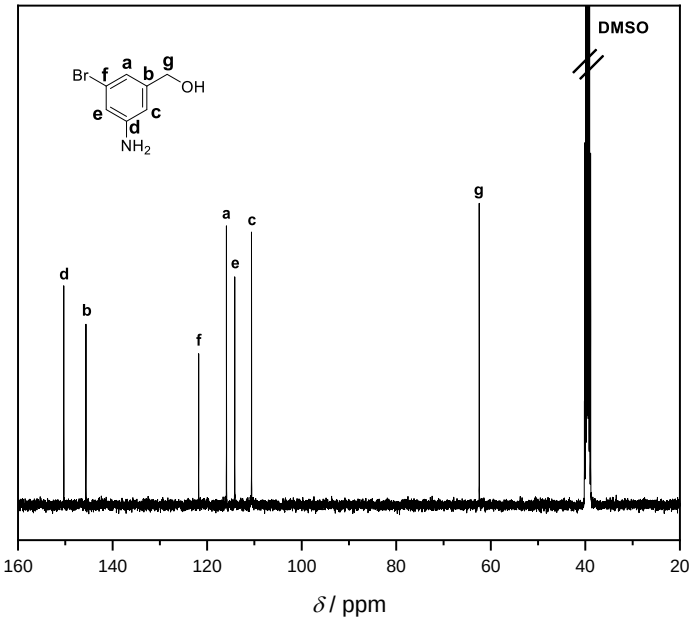

Figure S2: ^{13}C-NMR spectrum of **C01**, **^{13}C NMR (101 MHz, DMSO)** δ 150.32 (s), 145.64 (s), 121.79 (s), 115.91 (s), 114.17 (s), 110.61 (s), 62.44 (s).

8.2.2 **(C02)** (3-Amino-5-ethynylphenyl)methanol

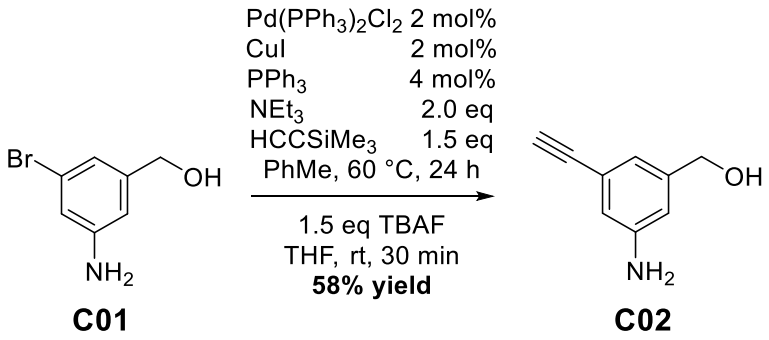

(3-Amino-5-bromophenyl)methanol **C01** (14.1 mmol, 2.85 g, 1.0 eq), bis(triphenylphosphine) palladium(II) dichloride (0.28 mmol, 196 mg, 0.02 eq), copper(I) iodide (0.28 mmol, 53 mg, 0.02 eq), triphenylphosphine (0.56 mmol, 147 mg, 0.04 eq), toluene (60 mL), triethylamine (28.2 mmol, 3.9 mL, 2.0 eq) and ethynyltrimethylsilane (21.1 mmol, 2.9 mL, 1.5 eq) were added to a round flask with stirring bar and water condenser under argon atmosphere. The mixture was then heated at 60 °C for 24 hours. Afterwards, the reaction mixture was allowed to cool down to room temperature and water (200 mL) was added. The aqueous phase was extracted with DCM (3 × 50 mL). The organic fractions were collected, dried over magnesium sulfate and the solvent was removed under reduced pressure. The crude material was purified by two consecutive flash chromatography runs (silica, MeOH / DCM, 1:10) and (silica, EtOAc / *c*-Hex, 1:1). In order to remove the TMS protecting group, the yellow solid was dissolved in THF (10 mL) and 1 M TBAF in THF (14 mL, 14 mmol, 1.5 eq) was added. The mixture was stirred at room temperature for 30 min. Water (50 mL) was added and the aqueous mixture was extracted with DCM (3 × 50 mL). The organic fractions were collected, dried over magnesium sulfate and the solvent was removed under reduced pressure. The crude material was purified by flash chromatography (silica, EtOAc) order to give **C02** as a brown solid. **(1.20 g, 8.15 mmol, 58% yield)**

^{1}H NMR (400 MHz, DMSO) δ 6.60 – 6.49 (m, 3H), 5.18 (s, 2H), 5.07 (t, J = 5.8 Hz, 1H), 4.33 (d, J = 5.6 Hz, 2H), 3.93 (s, 1H).

^{13}C NMR (101 MHz, DMSO) δ 148.62 (s), 143.72 (s), 121.58 (s), 117.28 (s), 115.01 (s), 112.79 (s), 84.59 (s), 78.71 (s), 62.65 (s).

ESI-HRMS (*m/z*) calculated for $[M+H]^+$ 148.0757 found 148.0757.

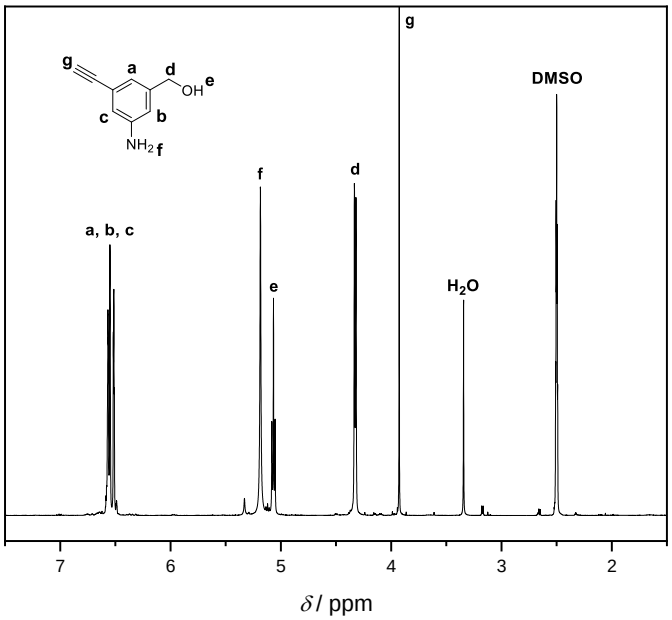

Figure S3: ^{1}H-NMR spectrum of **C02**, **^{1}H NMR (400 MHz, DMSO)** δ 6.60 – 6.49 (m, 3H), 5.18 (s, 2H), 5.07 (t, J = 5.8 Hz, 1H), 4.33 (d, J = 5.6 Hz, 2H), 3.93 (s, 1H).

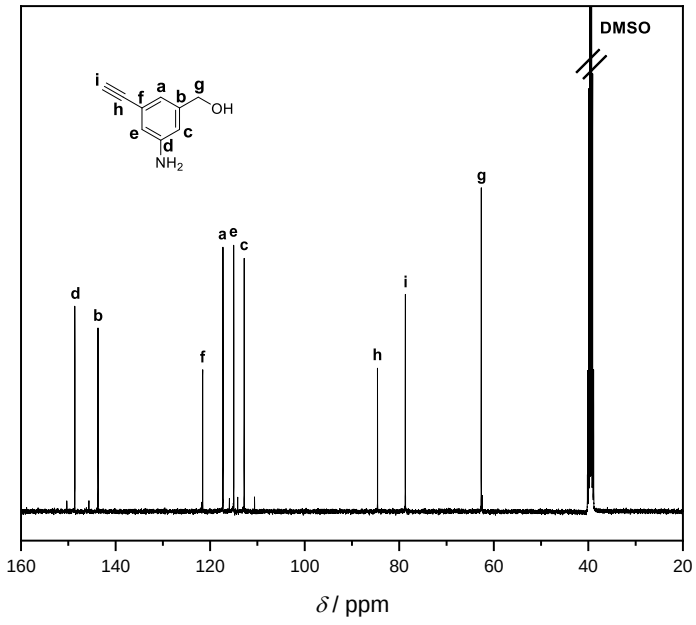

Figure S4: ^{13}C-NMR spectrum of **C02**, **^{13}C NMR (101 MHz, DMSO)** δ 148.62 (s), 143.72 (s), 121.58 (s), 117.28 (s), 115.01 (s), 112.79 (s), 84.59 (s), 78.71 (s), 62.65 (s).

8.2.3 **(C03)** (3-Azido-5-ethynylphenyl)methanol

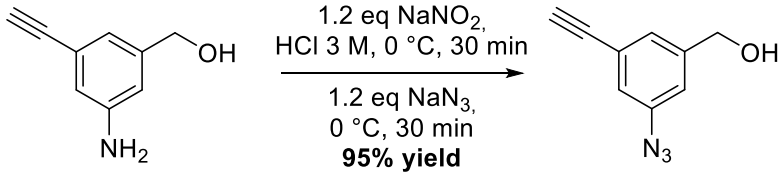

C02 **C03**

(3-Amino-5-ethynylphenyl)methanol **C02** (1.36 mmol, 200 mg, 1.0 eq) was dissolved in 3 M HCl (4 mL) at 0 °C. Sodium nitrite (112 mg, 1.63 mmol, 1.2 eq) was dissolved in water (1 mL) and was added dropwise over 5 min and the resulting aqueous solution was stirred for 10 min at 0 °C. Then, sodium azide (106 mg, 1.63 mmol, 1.2 eq.) was added over 20 min and the solution was stirred for another 20 min at 0 °C. Afterwards, the pH was neutralized by sodium bicarbonate addition and the mixture was extracted with EtOAc (3 × 20 mL). The crude material was purified by flash chromatography (silica, MeOH / DCM, 1:20) in order to give **C03** as a brown solid. **(225 mg, 1.30 mmol, 96% yield)**

^{1}H NMR (400 MHz, DMSO) δ 7.24 – 7.21 (m, 1H), 7.14 – 7.08 (m, 1H), 7.06 – 7.01 (m, 1H), 5.36 (t, J = 5.8 Hz, 1H), 4.49 (d, J = 5.8 Hz, 2H), 4.26 (s, 1H).

^{13}C NMR (101 MHz, DMSO) δ 145.50 (s), 139.76 (s), 126.13 (s), 122.99 (s), 120.19 (s), 117.39 (s), 82.61 (s), 81.42 (s), 61.81 (s).

ESI-HRMS (*m/z*) calculated for $[M]^+$ 173.0589 found 173.0589.

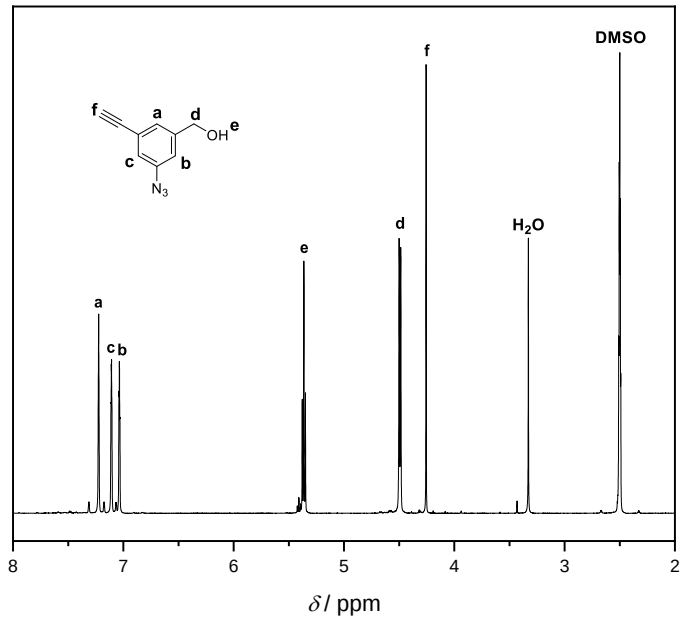

Figure S5: ^{1}H-NMR spectrum of **C03**, **^{1}H NMR (400 MHz, DMSO)** δ 7.24 – 7.21 (m, 1H), 7.14 – 7.08 (m, 1H), 7.06 – 7.01 (m, 1H), 5.36 (t, J = 5.8 Hz, 1H), 4.49 (d, J = 5.8 Hz, 2H), 4.26 (s, 1H).

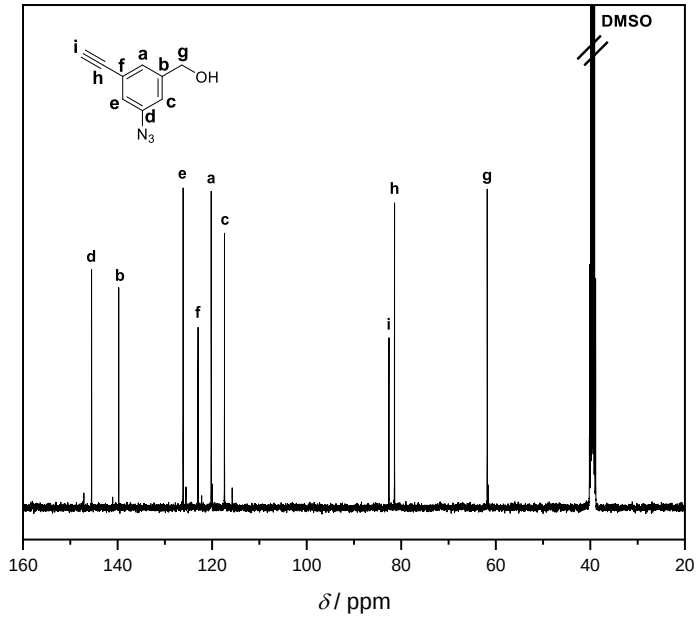

Figure S6: ^{13}C-NMR spectrum of **C03**, **^{13}C NMR (101 MHz, DMSO)** δ 145.50 (s), 139.76 (s), 126.13 (s), 122.99 (s), 120.19 (s), 117.39 (s), 82.61 (s), 81.42 (s), 61.81 (s).

8.2.4 **(C04)** 2-(3-Nitrophenyl)oxirane

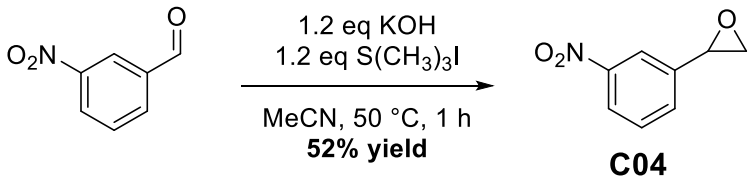

Potassium hydroxide 85 weight% (2.23 g, 39.7 mmol, 1.2 eq) and trimethylsulfonium iodide (8.10 g, 39.7 mmol, 1.2 eq) were dissolved in dry acetonitrile (40 mL). The mixture was heated for 20 min under argon atmosphere at 50 °C. 3-Nitrobenzaldehyde (5.00 g, 33.1 mmol, 1.0 eq) dissolved in acetonitrile (20 mL) was purged with argon and added over 5 min to the first mixture. The reaction was quenched with water (10 mL) after 60 minutes. The aqueous phase was then extracted with DCM (3 × 50 mL). The organic fractions were collected, dried over magnesium sulfate and the solvent was removed under reduced pressure. The crude material was purified by flash chromatography (silica, EtOAc / *c*-Hex, 1:4) in order to give **C04** as a yellowish solid. **(2.87 g, 17.3 mmol, 52% yield)**

^{1}H NMR (400 MHz, $CDCl_3$) δ 8.20 – 8.12 (m, 2H), 7.62 (dt, *J* = 7.7, 1.3 Hz, 1H), 7.57 – 7.50 (m, 1H), 3.97 (dd, *J* = 4.0, 2.5 Hz, 1H), 3.22 (dd, *J* = 5.4, 4.1 Hz, 1H), 2.81 (dd, *J* = 5.4, 2.5 Hz, 1H).

^{13}C NMR (101 MHz, $CDCl_3$) δ 148.67 (s), 140.24 (s), 131.59 (s), 129.71 (s), 123.24 (s), 120.72 (s), 51.55 (s), 51.53 (s).

ESI-HRMS (*m/z*) calculated for $[M+Na]^+$ 188.0318 found 188.0315.

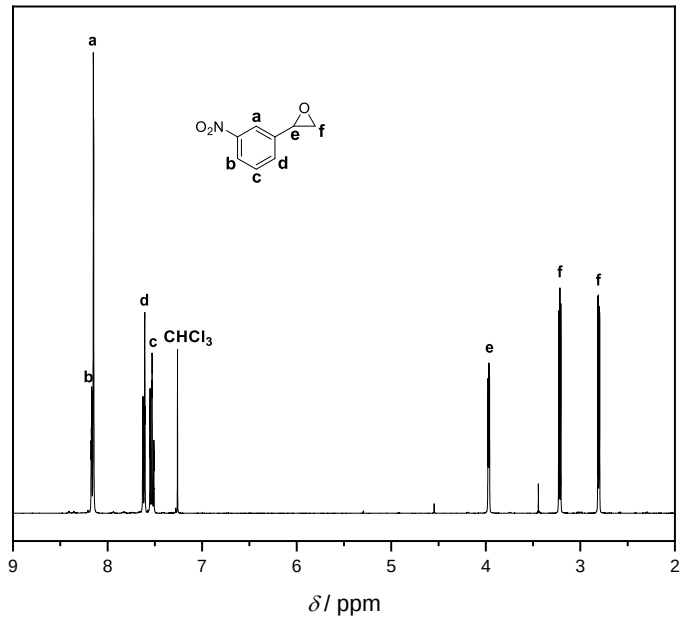

Figure S7: ^{1}H-NMR spectrum of **C04**, **^{1}H NMR (400 MHz, $CDCl_3$) δ** 8.20 – 8.12 (m, 2H), 7.62 (dt, *J* = 7.7, 1.3 Hz, 1H), 7.57 – 7.50 (m, 1H), 3.97 (dd, *J* = 4.0, 2.5 Hz, 1H), 3.22 (dd, *J* = 5.4, 4.1 Hz, 1H), 2.81 (dd, *J* = 5.4, 2.5 Hz, 1H).

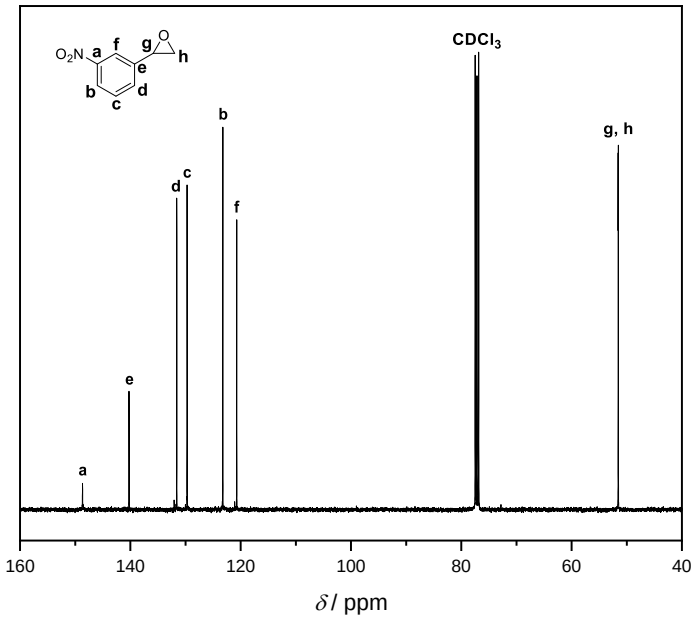

Figure S8: ^{13}C-NMR spectrum of **C04**, **^{13}C NMR (101 MHz, $CDCl_3$) δ** 148.67 (s), 140.24 (s), 131.59 (s), 129.71 (s), 123.24 (s), 120.72 (s), 51.55 (s), 51.53 (s).

8.2.5 **(C05)** 1-(3-Nitrophenyl)but-3-yn-1-ol

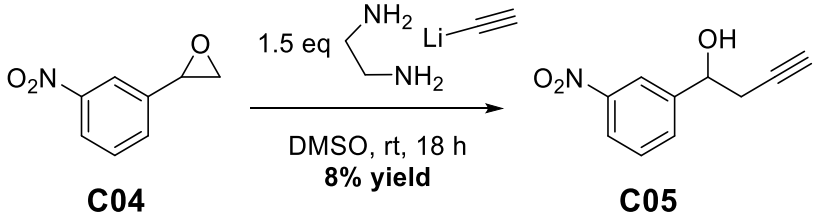

Lithium acetylide, ethylenediamine complex 90 weight% (2.66 g, 26.0 mmol, 1.5 eq) was added portionwise to dry DMSO (20 mL) and the mixture was placed under argon atmosphere. **C04** (2.87 g, 17.3 mmol, 1.0 eq) was dissolved in dry DMSO (10 mL) and placed under argon atmosphere. The second solution was added dropwise to the acetylide solution at room temperature and the resulting mixture was stirred for 18 hours. Afterwards, the reaction was quenched with water (500 mL). The aqueous phase was then extracted with Et_2O (3 × 200 mL) and EtOH as co-solvent (3 × 20 mL). The organic fractions were collected, dried over magnesium sulfate and the solvent was removed under reduced pressure. The crude material was purified by flash chromatography (silica, EtOAc / *c*-Hex, 1:4) in order to give **C05** as a yellow solid. **(0.268 g, 1.40 mmol, 8% yield)**

^{1}H NMR (400 MHz, $CDCl_3$) ***δ*** 8.29 (t, *J* = 1.9 Hz, 1H), 8.16 (ddd, *J* = 8.2, 2.2, 1.0 Hz, 1H), 7.75 (d, *J* = 7.7 Hz, 1H), 7.54 (t, *J* = 7.9 Hz, 1H), 5.04 – 4.95 (m, 1H), 2.76 – 2.61 (m, 2H), 2.57 (s, 1H), 2.11 (t, *J* = 2.6 Hz, 1H).
^{13}C NMR (101 MHz, $CDCl_3$) ***δ*** 148.48 (s), 144.55 (s), 132.07 (s), 129.56 (s), 123.06 (s), 121.11 (s), 79.53 (s), 72.15 (s), 71.34 (s), 29.68 (s).
ESI-HRMS (*m/z*) calculated for $[M+Na]^+$ 214.0470 found 214.0480.

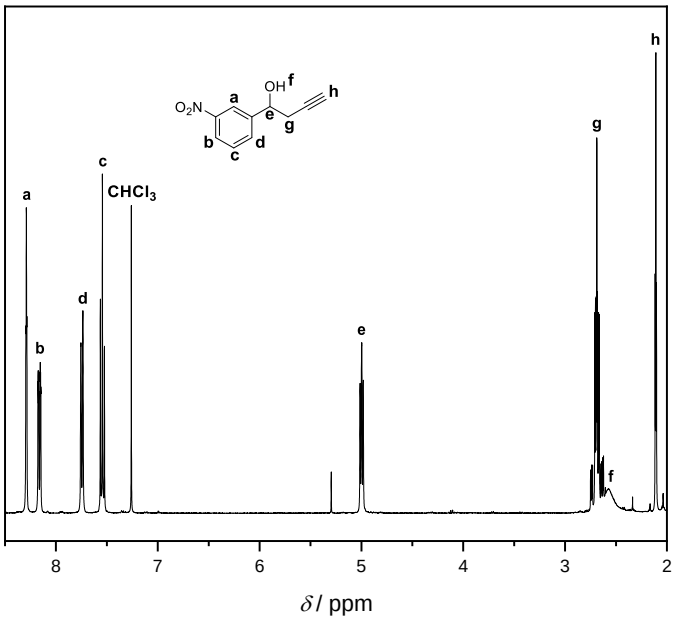

Figure S9: ^{1}H-NMR spectrum of **C05**, **^{1}H NMR (400 MHz, $CDCl_3$) δ** 8.29 (t, *J* = 1.9 Hz, 1H), 8.16 (ddd, *J* = 8.2, 2.2, 1.0 Hz, 1H), 7.75 (d, *J* = 7.7 Hz, 1H), 7.54 (t, *J* = 7.9 Hz, 1H), 5.04 – 4.95 (m, 1H), 2.76 – 2.61 (m, 2H), 2.57 (s, 1H), 2.11 (t, *J* = 2.6 Hz, 1H).

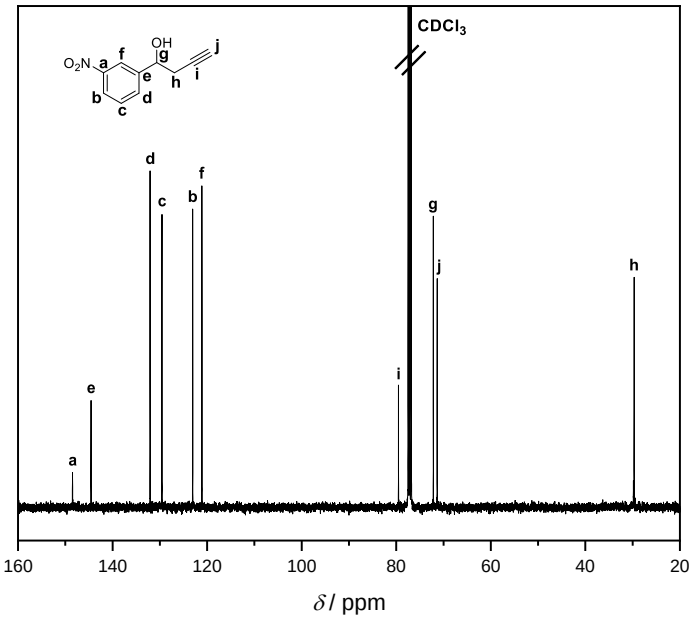

Figure S10: ^{13}C-NMR spectrum of **C05**, **^{13}C NMR (101 MHz, $CDCl_3$) δ** 148.48 (s), 144.55 (s), 132.07 (s), 129.56 (s), 123.06 (s), 121.11 (s), 79.53 (s), 72.15 (s), 71.34 (s), 29.68 (s).

8.2.6 **(C06)** 1-(3-Aminophenyl)but-3-yn-1-ol

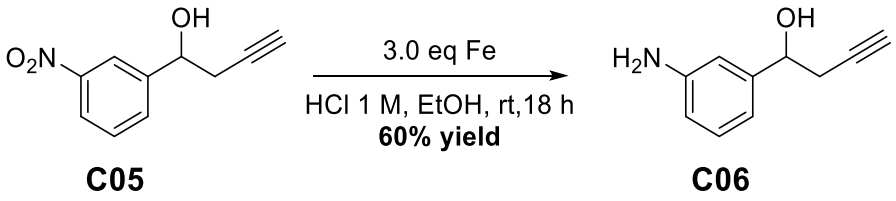

C05 **C06**

Iron powder (0.235 g, 4.20 mmol, 3.0 eq) and **C05** (0.268 g, 1.40 mmol, 1.0 eq) were dissolved in a mixture of aqueous 1 M HCl (6 mL) and EtOH (4 mL). The mixture was placed under argon atmosphere and heated for 60 minutes at 60 °C. Afterwards, the reaction was quenched with an aqueous solution of 1 M NaOH until reaching a pH > 10 and the mixture was stirred under standard atmosphere until total oxidation of the soluble iron(II) into iron(III) hydroxide precipitate. Then the solid was filtered off and washed with MeCN (10 mL). The aqueous phase was then extracted with DCM (3 × 30 mL). The organic fractions were collected, dried over magnesium sulfate and the solvent was removed under reduced pressure. The crude material was purified by flash chromatography (silica, EtOAc) in order to give **C06** as a yellow solid. **(0.135 g, 0.84 mmol, 60% yield)**

^{1}H NMR (400 MHz, DMSO) δ 6.94 (t, J = 7.7 Hz, 1H), 6.58 (t, J = 1.9 Hz, 1H), 6.49 (d, J = 7.5 Hz, 1H), 6.43 (ddd, J = 7.9, 2.3, 1.0 Hz, 1H), 5.31 (d, J = 4.3 Hz, 1H), 4.97 (s, 2H), 4.49 (td, J = 6.4, 4.5 Hz, 1H), 2.70 (t, J = 2.6 Hz, 1H), 2.48 – 2.36 (m, 2H).

^{13}C NMR (101 MHz, DMSO) δ 148.26 (s), 145.14 (s), 128.30 (s), 113.67 (s), 112.73 (s), 111.60 (s), 82.23 (s), 72.15 (s), 71.47 (s), 28.95 (s).

ESI-HRMS (*m/z*) calculated for $[M+Na]^+$ 184.0738 found 184.0730.

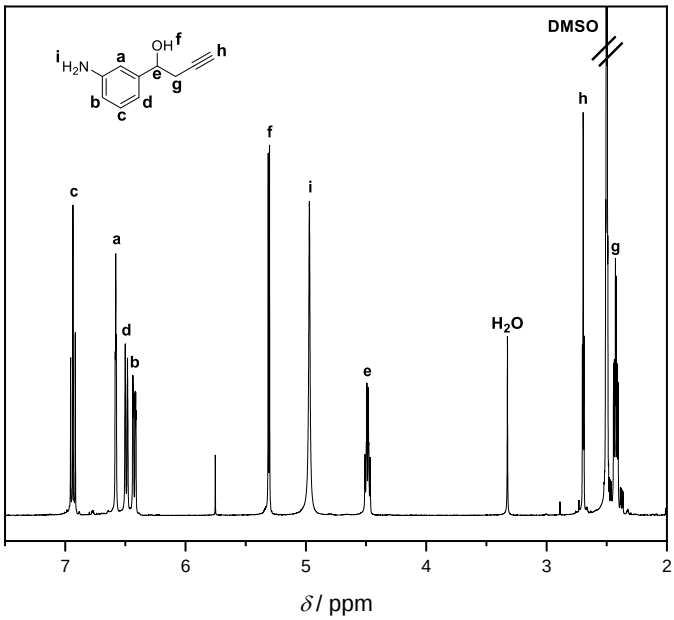

Figure S11: ^{1}H-NMR spectrum of **C06**, **^{1}H NMR (400 MHz, DMSO) δ** 6.94 (t, *J* = 7.7 Hz, 1H), 6.58 (t, *J* = 1.9 Hz, 1H), 6.49 (d, *J* = 7.5 Hz, 1H), 6.43 (ddd, *J* = 7.9, 2.3, 1.0 Hz, 1H), 5.31 (d, *J* = 4.3 Hz, 1H), 4.97 (s, 2H), 4.49 (td, *J* = 6.4, 4.5 Hz, 1H), 2.70 (t, *J* = 2.6 Hz, 1H), 2.48 – 2.36 (m, 2H).

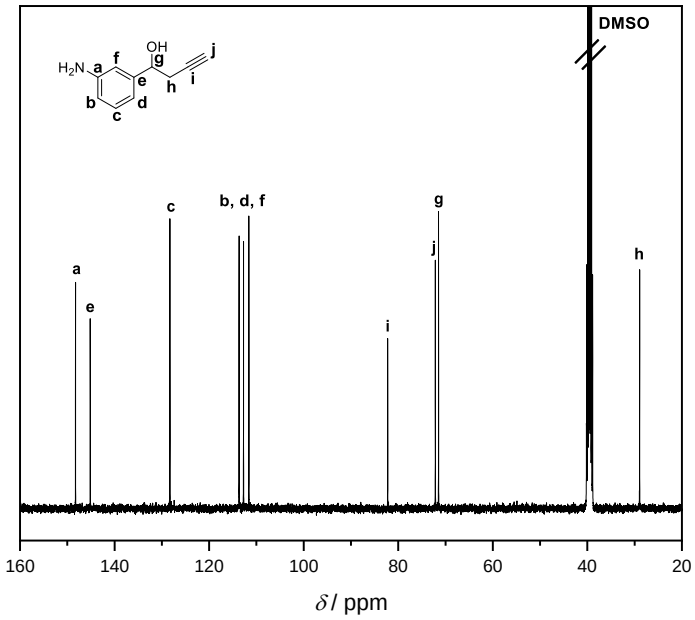

Figure S12: ^{13}C-NMR spectrum of **C06**, **^{13}C NMR (101 MHz, DMSO) δ** 148.26 (s), 145.14 (s), 128.30 (s), 113.67 (s), 112.73 (s), 111.60 (s), 82.23 (s), 72.15 (s), 71.47 (s), 28.95 (s).

8.2.7 **(C07)** 1-(3-Azidophenyl)but-3-yn-1-ol

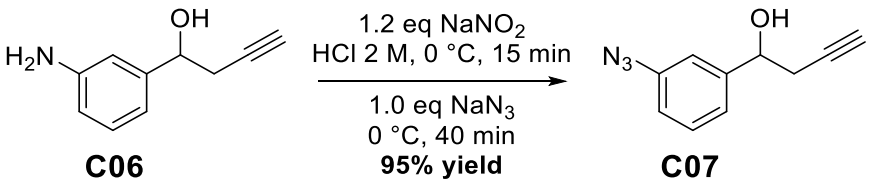

C06 **C07**

C06 (126 mg, 0.78 mmol, 1.0 eq) was dissolved in a solution de 2 M HCl (6 mL) at 0 °C. Sodium nitrite (65 mg, 0.94 mmol, 1.2 eq) was dissolved in water (1 mL) and added dropwise over 5 min and the resulting aqueous solution was stirred for 10 min at 0 °C. Then, sodium azide (61 mg, 0.94 mmol, 1.2 eq) was added over 20 min and the solution was stirred for another 20 min at 0 °C. Afterwards, the pH was neutralized by sodium bicarbonate addition and the mixture was extracted with EtOAc (3 × 20 mL). The organic fractions were collected, dried over magnesium sulfate and the solvent was removed under reduced pressure. No further purification was needed in order to give **C07** as a brown solid. **(116 mg, 0.62 mmol, 79% yield)**

^{1}H NMR (400 MHz, $CDCl_3$) δ 7.34 (t, *J* = 7.8 Hz, 1H), 7.15 (d, *J* = 7.7 Hz, 1H), 7.09 (t, *J* = 1.9 Hz, 1H), 6.97 (ddd, *J* = 8.0, 2.3, 0.9 Hz, 1H), 4.99 – 4.78 (m, 1H), 2.72 – 2.55 (m, 2H), 2.42 (s, 1H), 2.09 (t, *J* = 2.6 Hz, 1H).
^{13}C NMR (101 MHz, $CDCl_3$) δ 144.64 (s), 140.46 (s), 130.01 (s), 122.44 (s), 118.71 (s), 116.53 (s), 80.30 (s), 71.95 (s), 71.54 (s), 29.65 (s).
ESI-HRMS (*m/z*) no molecular peak could be recorded.

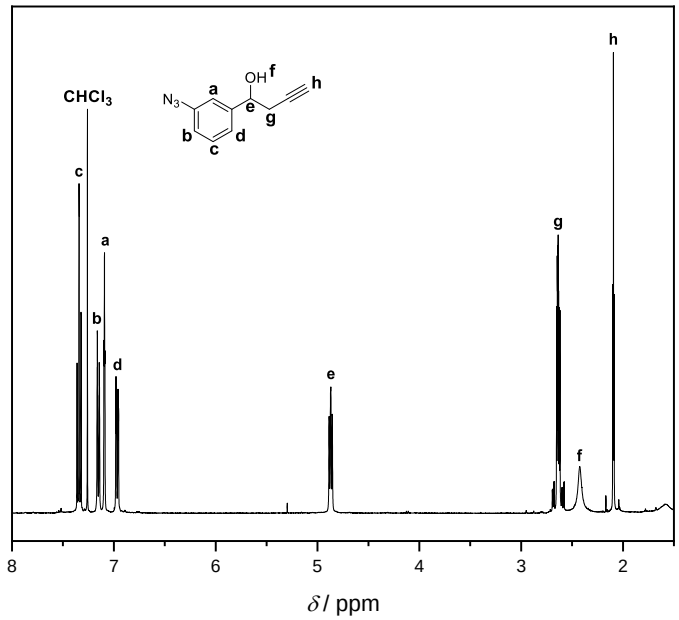

Figure S13: ^{1}H-NMR spectrum of **C07**, **^{1}H NMR (400 MHz, $CDCl_3$) δ** 7.34 (t, *J* = 7.8 Hz, 1H), 7.15 (d, *J* = 7.7 Hz, 1H), 7.09 (t, *J* = 1.9 Hz, 1H), 6.97 (ddd, *J* = 8.0, 2.3, 0.9 Hz, 1H), 4.99 – 4.78 (m, 1H), 2.72 – 2.55 (m, 2H), 2.42 (s, 1H), 2.09 (t, *J* = 2.6 Hz, 1H).

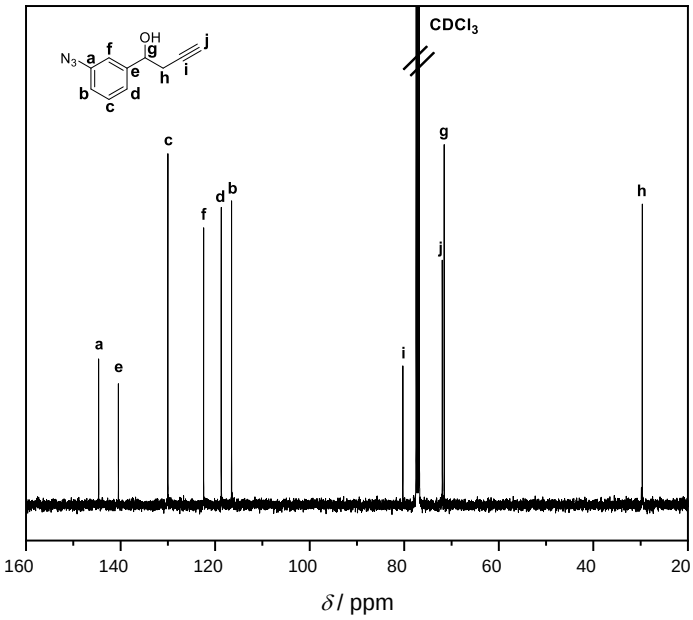

Figure S14: ^{13}C-NMR spectrum of **C07**, **^{13}C NMR (101 MHz, $CDCl_3$) δ** 144.64 (s), 140.46 (s), 130.01 (s), 122.44 (s), 118.71 (s), 116.53 (s), 80.30 (s), 71.95 (s), 71.54 (s), 29.65 (s).

8.2.8 **(C08)** 2-Ethynyl-2-methyloxirane

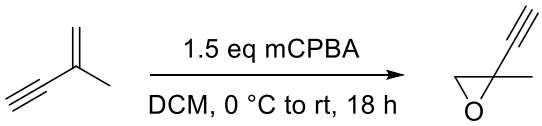

C08

2-Methylbut-1-en-3-yne (3.00 mL, 31.8 mmol, 1.0 eq) was diluted in DCM (30 mL) and the mixture was cooled down to 0 °C. 3-Chloroperoxybenzoic acid 70 weight% (11.8 g, 47.7 mmol, 1.5 eq) was added to the mixture and the reaction was left stirring at room temperature for 18 hours. Afterwards, the reaction was quenched with a 1 M NaOH solution (30 mL) and sodium thiosulfate was added in large excess. The aqueous phase was then extracted with DCM (3 × 20 mL). The organic fractions were collected, dried over magnesium sulfate and the solvent was removed by distillation with a Vigreux column (1 atm, 70 °C). Diethylether (2 × 100 mL) was then added during the distillation to remove the remaining amount of DCM. No more purification was needed to give **C08** as a transparent solution in diethylether. **(No yield reported for this step)**

^{1}H NMR (400 MHz, $CDCl_3$) *δ* 3.01 (dd, *J* = 5.6, 0.6 Hz, 1H), 2.73 (d, *J* = 5.6 Hz, 1H), 2.28 (s, 1H), 1.61 – 1.50 (m, 3H).

^{13}C NMR (101 MHz, $CDCl_3$) *δ* 83.23 (s), 70.39 (s), 55.24 (s), 46.97 (s), 22.74 (s).

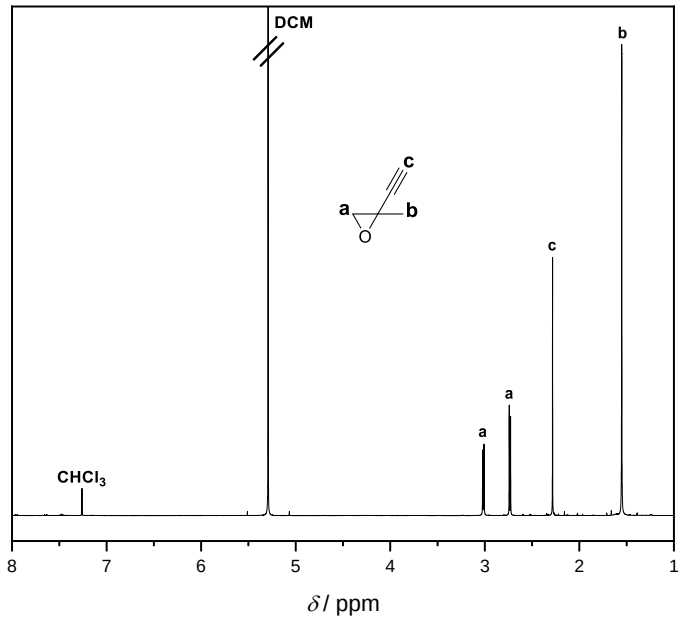

Figure S15: ^{1}H-NMR spectrum of **C08**, **^{1}H NMR (400 MHz, $CDCl_3$) *δ*** 3.01 (dd, *J* = 5.6, 0.6 Hz, 1H), 2.73 (d, *J* = 5.6 Hz, 1H), 2.28 (s, 1H), 1.61 – 1.50 (m, 3H).

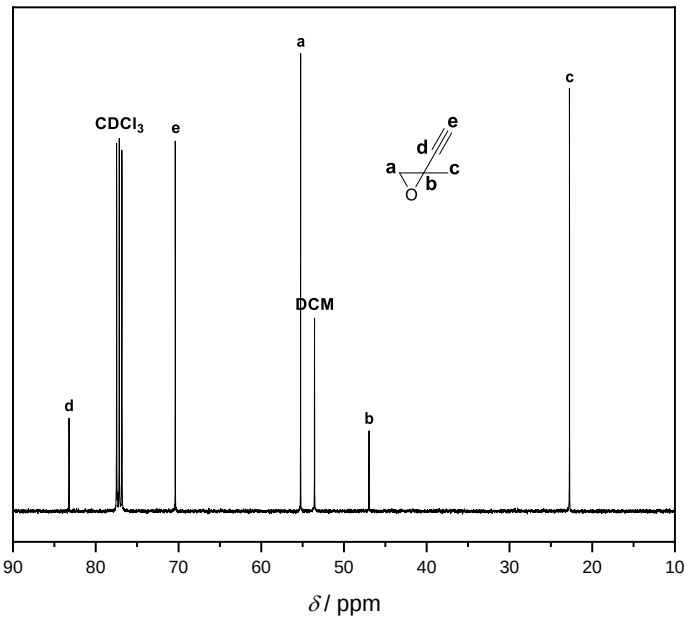

Figure S16: ^{13}C-NMR spectrum of **C08**, **^{13}C NMR (101 MHz, $CDCl_3$) *δ*** 83.23 (s), 70.39 (s), 55.24 (s), 46.97 (s), 22.74 (s).

8.2.9 **(C09)** 1-Azido-2-methylbut-3-yn-2-ol

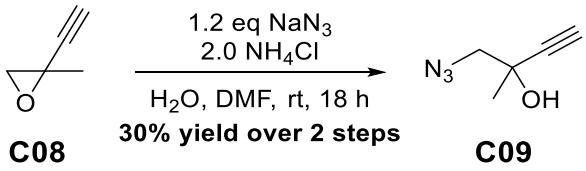

C08 **C09**

Previously prepared 2-ethynyl-2-methyloxirane **C08** (31.8 mmol, 1.0 eq) was diluted in water (10 mL) and DMF (10 mL). Ammonium chloride (3.4 g, 64 mmol, 2.0 eq) and sodium azide (2.48 g, 38.2 mmol, 1.2 eq) were added and the reaction was stirred at room temperature for 18 hours. Afterwards, water (200 mL) was added and the aqueous phase was extracted with DCM (3 × 50 mL). The organic fractions were collected, dried over magnesium sulfate and the solvent was removed under reduced pressure. The crude material was purified by flash chromatography (silica, Et_2O / PE, 1:3) in order to give **C09** as a transparent liquid. **(1.18 g, 9.43 mmol, 30% yield over two steps)**

^{1}H NMR (400 MHz, DMSO) δ 5.85 (s, 1H), 3.39 (s, 1H), 3.27 (q, J = 12.3 Hz, 2H), 1.35 (s, 3H).

^{13}C NMR (101 MHz, DMSO) δ 87.02 (s), 74.39 (s), 66.76 (s), 60.09 (s), 27.21 (s).

ESI-HRMS (*m/z*) calculated for $[M+Na]^+$ 148.0481 found 148.0478.

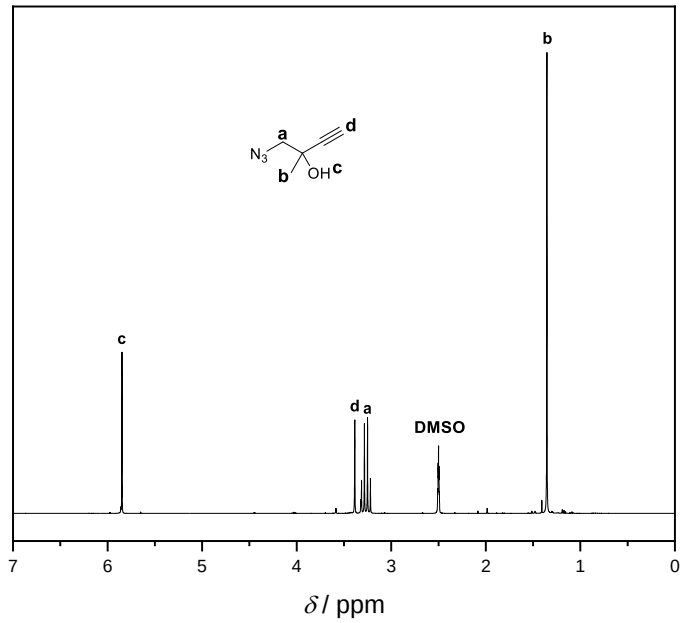

Figure S17: ^{1}H-NMR spectrum of **C09**, **^{1}H NMR (400 MHz, DMSO) δ** 5.85 (s, 1H), 3.39 (s, 1H), 3.27 (q, J = 12.3 Hz, 2H), 1.35 (s, 3H).

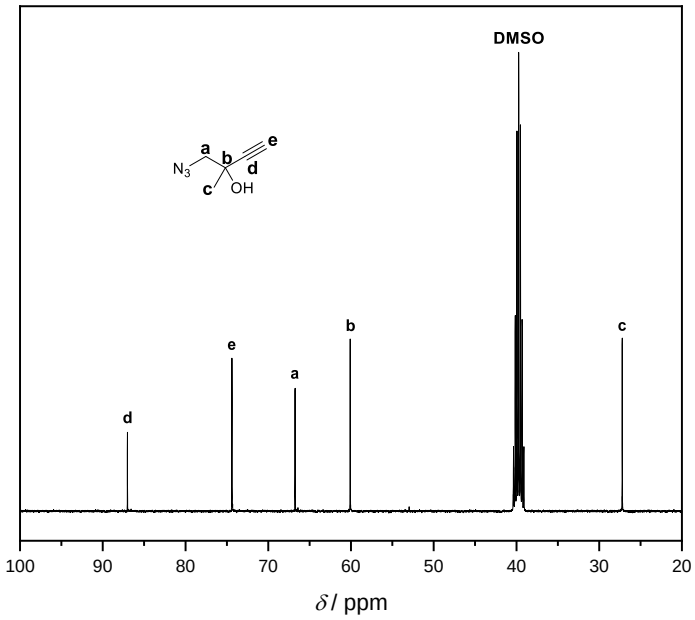

Figure S18: ^{13}C-NMR spectrum of **C09**, **^{13}C NMR (101 MHz, DMSO) δ** 87.02 (s), 74.39 (s), 66.76 (s), 60.09 (s), 27.21 (s).

8.2.10 **(C10)** But-3-en-1-yn-1-yltrimethylsilane

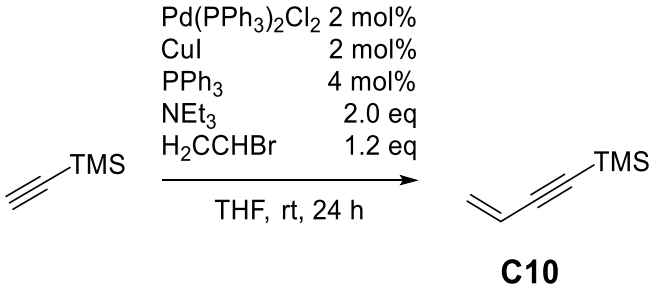

C10

Bis(triphenylphosphine) palladium(II) dichloride (505 mg, 0.72 mmol, 0.02 eq), copper(I) iodide (274 mg, 1.44 mmol, 0.04 eq) and triphenylphosphine (378 mg, 1.44 mmol, 0.04 eq) were added to a 250 mL round flask. The flask was purged with argon for 5 min and triethylamine (10.1 mL, 72.2 mmol, 2.0 eq), ethynyltrimethylsilane (5.00 mL, 36.1 mmol, 1.0 eq) and finally a 1 M solution of vinyl bromide in THF (47.0 mL, 46.9 mmol, 1.2 eq) were added. The reaction mixture was purged with argon for another 20 min and then stirred at room temperature for 18 hours. Afterwards, the reaction was quenched with water (200 mL) and a 1 M HCl solution was added until pH < 2 was reached. The aqueous phase was then extracted with DCM (3 × 50 mL). The organic fractions were collected, dried over magnesium sulfate and the solvents were removed by distillation with a Vigreux column (DCM, 1 atm, 70 °C), (THF, 1 atm, 100 °C). The crude material was purified by flash chromatography (silica, *c*-Hex) and the solvent was removed by distillation with a Vigreux column (*c*-Hex, 1 atm, 110 °C) in order to give **C10** as a transparent solution in cyclohexane. **(No yield reported for this step)**

^{1}H NMR (400 MHz, $CDCl_3$) δ 5.82 (dd, *J* = 17.6, 11.0 Hz, 1H), 5.69 (dd, *J* = 17.6, 2.4 Hz, 1H), 5.49 (dd, *J* = 11.0, 2.4 Hz, 1H), 0.37 – 0.02 (m, 9H).

^{13}C NMR (101 MHz, $CDCl_3$) δ 128.19 (s), 117.57 (s), 104.03 (s), 95.37 (s), 0.13 (s).

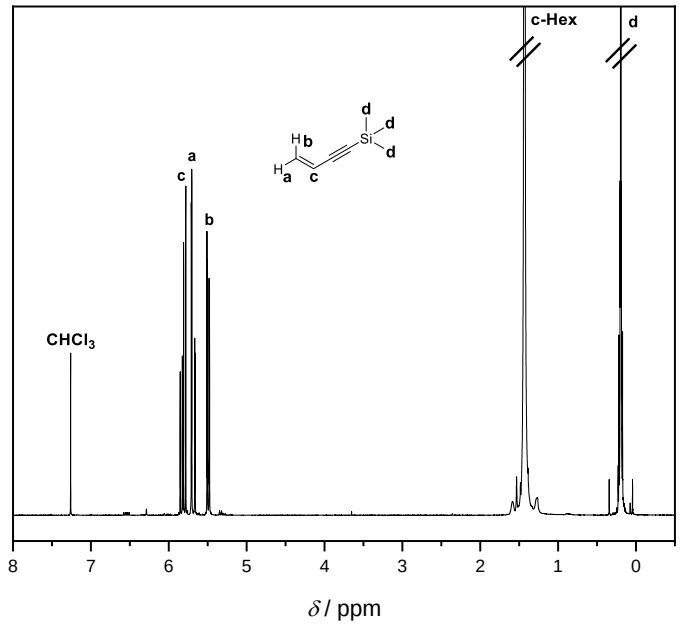

Figure S19: ^{1}H-NMR spectrum of **C10**, **^{1}H NMR (400 MHz, $CDCl_3$) δ** 5.82 (dd, *J* = 17.6, 11.0 Hz, 1H), 5.69 (dd, *J* = 17.6, 2.4 Hz, 1H), 5.49 (dd, *J* = 11.0, 2.4 Hz, 1H), 0.37 – 0.02 (m, 9H).

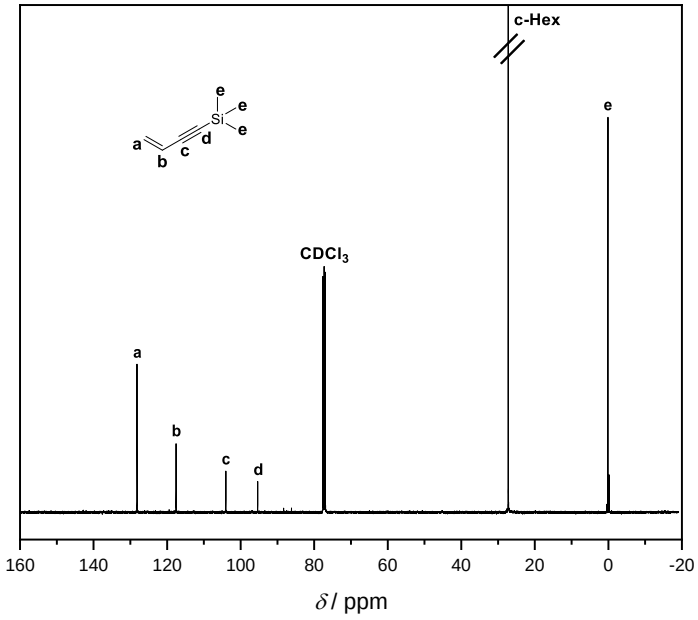

Figure S20: ^{13}C-NMR spectrum of **C10**, **^{13}C NMR (101 MHz, $CDCl_3$) δ** 128.19 (s), 117.57 (s), 104.03 (s), 95.37 (s), 0.13 (s).

8.2.11 **(C11)** Trimethyl(oxiran-2-ylethynyl)silane

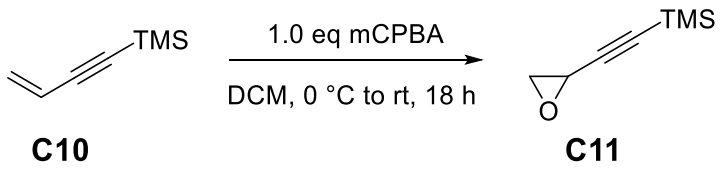

But-3-en-1-yn-1-yltrimethylsilane **C10** (36.1 mmol, 1.0 eq) was prepared directly from the previous step. The liquid was diluted with DCM (80 mL) and cooled down to 0 °C. 3-Chloroperoxybenzoic acid 70 weight% (8.1 g, 36.1 mmol, 1.0 eq) was added portionwise to the solution and the reaction was left stirring at room temperature for 18 hours. Afterwards, the reaction was quenched with a 1 M NaOH solution (50 mL) and sodium thiosulfate was added until no more peroxide was detected. The aqueous phase was then extracted with DCM (3 × 30 mL). The organic fractions were collected, dried over magnesium sulfate and the solvent was removed by distillation with a Vigreux column (1 atm, 70 °C). *c*-Hex (50 mL) was then added during the distillation to remove the remaining amount of DCM (*c*-Hex, 1 atm, 110 °C). No more purification was needed to give **C11** as a transparent solution in cyclohexane. **(No yield reported for this step)**

^{1}H NMR (400 MHz, $CDCl_3$) δ 3.35 (t, J = 3.4 Hz, 1H), 2.90 (d, J = 3.4 Hz, 2H), 0.18 (s, 9H).
^{13}C NMR (101 MHz, $CDCl_3$) δ 101.96 (s), 89.43 (s), 49.06 (s), 40.03 (s), -0.21 (s).

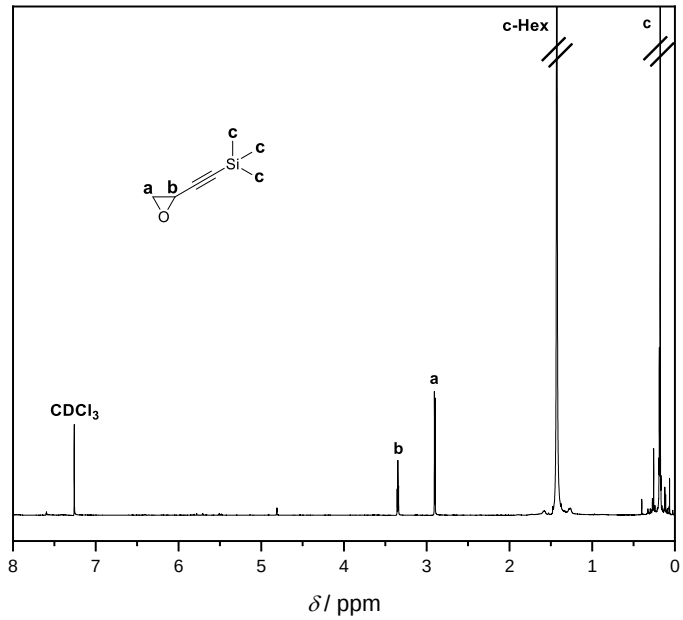

Figure S21: ^{1}H-NMR spectrum of **C11**, **^{1}H NMR (400 MHz, $CDCl_3$) δ** 3.35 (t, *J* = 3.4 Hz, 1H), 2.90 (d, *J* = 3.4 Hz, 2H), 0.18 (s, 9H).

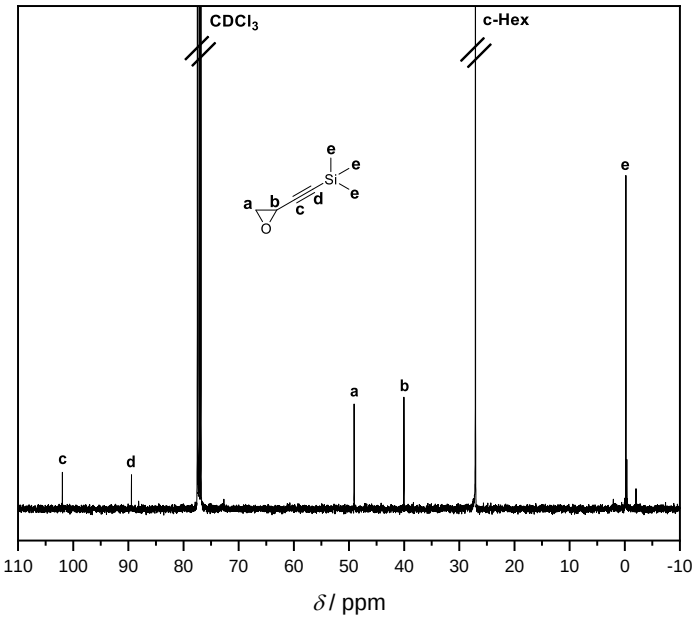

Figure S22: ^{13}C-NMR spectrum of **C11**, **^{13}C NMR (101 MHz, $CDCl_3$) δ** 101.96 (s), 89.43 (s), 49.06 (s), 40.03 (s), -0.21 (s).

8.2.12 **(C12)** 1-Azidobut-3-yn-2-ol

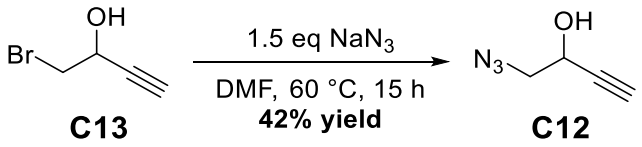

1-Bromobut-3-yn-2-ol **C13** (340 mg, 2.28 mmol, 1.0 eq) was diluted in DMF (10 mL). Sodium azide (602 mg, 9.27 mmol, 1.5 eq) was added and the mixture was heated for 15 hours at 60 °C under argon atmosphere. Afterwards, water (500 mL) and brine (50 mL) were added and the aqueous phase was extracted with DCM (3 × 50 mL). The organic fractions were collected, dried over magnesium sulfate and the solvent was removed under reduced pressure. The crude material was purified by flash chromatography (silica, Et_2O / PE, 1:3) in order to give **C12** as a transparent liquid. **(286 mg, 2.57 mmol, 42% yield)**

^{1}H NMR (400 MHz, $CDCl_3$) δ 4.53 (ddd, J = 6.1, 4.5, 2.2 Hz, 1H), 3.54 – 3.42 (m, 2H), 2.56 (d, J = 2.2 Hz, 1H), 2.19 (s, 1H).

^{13}C NMR (101 MHz, $CDCl_3$) δ 81.51 (s), 75.01 (s), 61.82 (s), 56.38 (s).

ESI-HRMS (*m/z*) calculated for $[M+Na]^+$ 134.0325 found 134.0323.

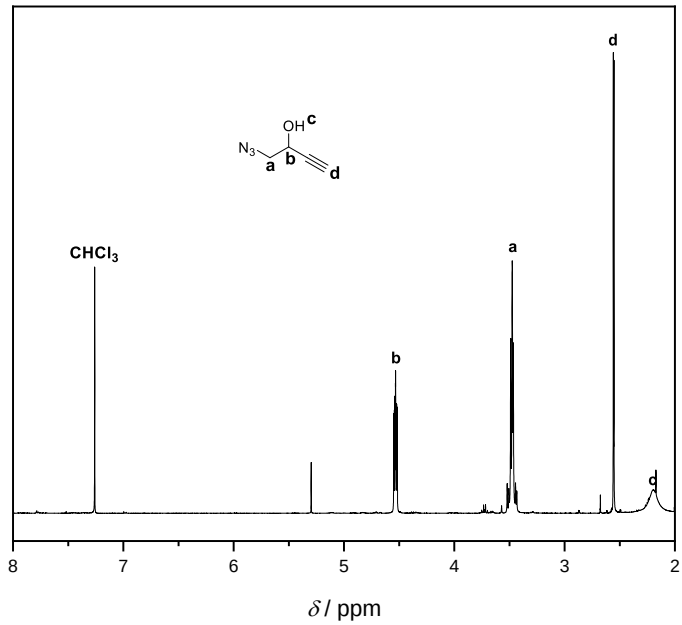

Figure S23: ^{1}H-NMR spectrum of **C12**, **^{1}H NMR (400 MHz, $CDCl_3$)** δ 4.53 (ddd, J = 6.1, 4.5, 2.2 Hz, 1H), 3.54 – 3.42 (m, 2H), 2.56 (d, J = 2.2 Hz, 1H), 2.19 (s, 1H).

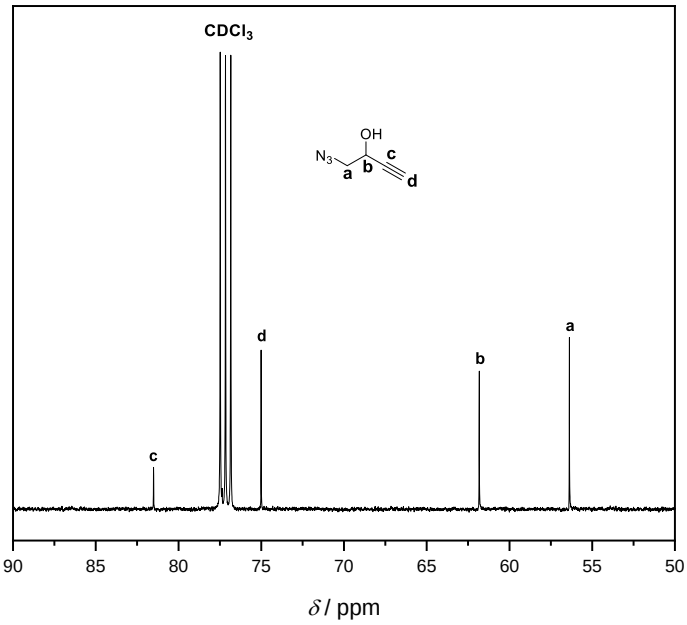

Figure S24: ^{13}C-NMR spectrum of **C12**, **^{13}C NMR (101 MHz, $CDCl_3$)** δ 81.51 (s), 75.01 (s), 61.82 (s), 56.38 (s).

8.2.13 **(C13)** 1-Bromobut-3-yn-2-ol

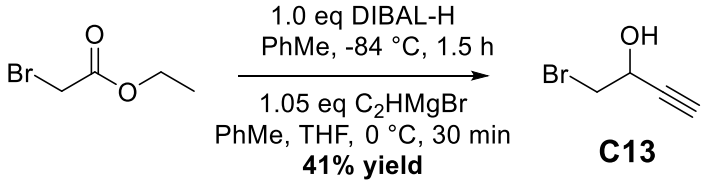

Ethyl 2-bromoacetate (1.66 mL, 15.0 mmol, 1.0 eq) was dissolved in dry toluene (15 mL) under argon atmosphere and the solution was cooled down to -84 °C (ethyl acetate / liquid nitrogen bath). 1 M DIBAL-H solution in toluene (15.0 mL, 15.0 mmol, 1.0 eq) was added over 30 min. The resulting mixture was stirred for 1 hour at -84 °C before being heated up to 0 °C. 0.5 M ethynyl magnesium bromide solution in THF (32.0 mL, 16.0 mmol, 1.05 eq) was added over 15 min and the mixture was stirred another 15 min at 0 °C. Afterwards, the reaction was quenched at 0 °C by addition of a saturated ammonium chloride solution (20 mL) and the aqueous phase was extracted with ethyl acetate (3 × 50 mL). The organic fractions were collected, dried over magnesium sulfate and the solvent was removed under reduced pressure. The crude material was purified by flash chromatography (silica, Et_2O / PE, 1:4) in order to give **C13** as a slightly yellowish liquid. **(920 mg, 6.18 mmol, 41% yield)**

^{1}H NMR (400 MHz, DMSO) δ 5.99 (d, J = 4.2 Hz, 1H), 4.45 (m, 1H), 3.54 – 3.46 (m, 2H), 3.42 (d, J = 2.1 Hz, 1H).

^{13}C NMR (101 MHz, DMSO) δ 83.66 (s), 75.51 (s), 60.74 (s), 37.54 (s).

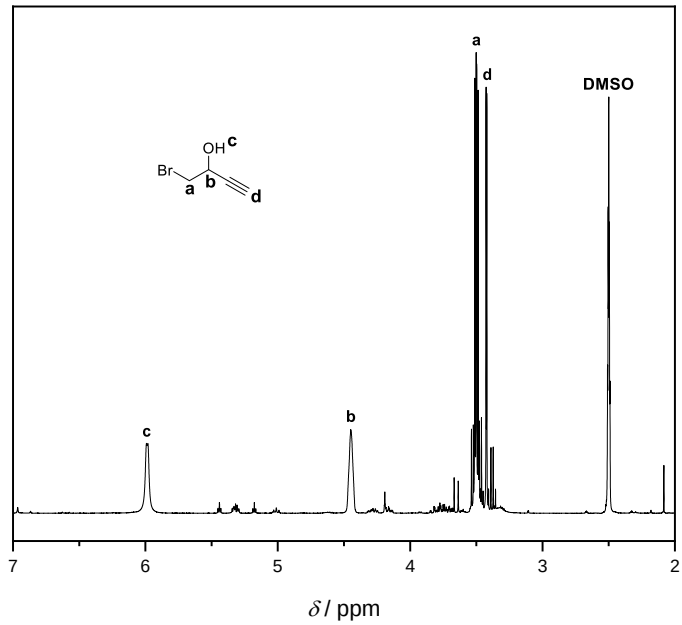

Figure S25: ^{1}H-NMR spectrum of **C13**, **^{1}H NMR (400 MHz, DMSO) δ** 5.99 (d, *J* = 4.2 Hz, 1H), 4.45 (m, 1H), 3.54 – 3.46 (m, 2H), 3.42 (d, *J* = 2.1 Hz, 1H).

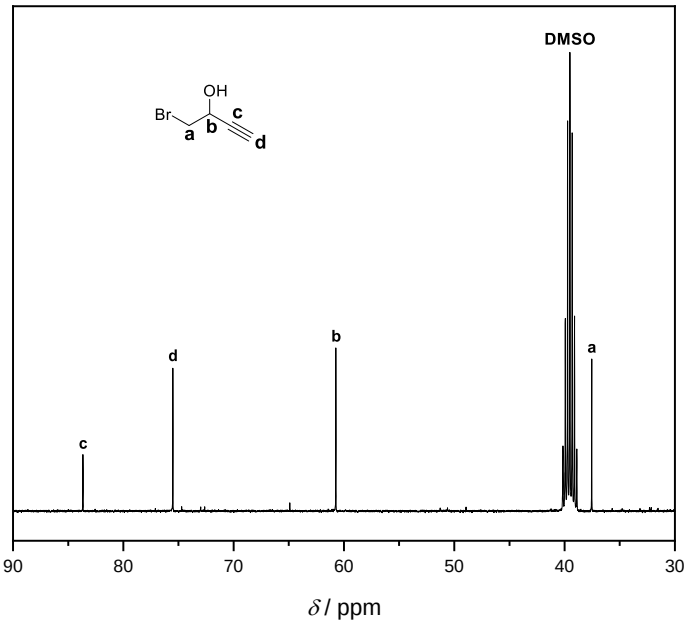

Figure S26: ^{13}C-NMR spectrum of **C13**, **^{13}C NMR (101 MHz, DMSO) δ** 83.66 (s), 75.51 (s), 60.74 (s), 37.54 (s).

8.2.14 **(C14)** 1-Chlorobut-3-yn-2-ol

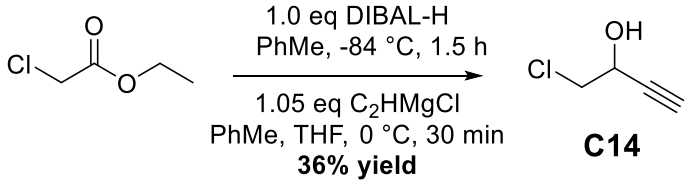

Ethyl 2-chloroacetate (1.53 mL, 14.3 mmol, 1.00 eq) was dissolved in dry toluene (10 mL) under argon atmosphere and the solution was cooled down to -84 °C (ethyl acetate / liquid nitrogen bath). 1.0 M DIBAL-H solution in toluene (15.0 mL, 15.0 mmol, 1.05 eq) was added over 30 min. The resulting mixture was stirred for 1 hour at -84 °C before being heated up to 0 °C. 0.5 M ethynyl magnesium chloride solution in THF/toluene (30.0 mL, 15.0 mmol, 1.05 eq) was added over 15 min and the mixture was stirred another 15 min at 0 °C. Afterwards, the reaction was directly quenched at 0 °C by addition of a saturated ammonium chloride solution (20 mL) and the aqueous phase was extracted with DCM (3 × 50 mL). The organic fractions were collected, dried over magnesium sulfate and the solvent was removed under reduced pressure. The crude material was purified by flash chromatography (silica, Et_2O / PE, 1:4) in order to give **C14** as a yellowish liquid. **(538 mg, 5.15 mmol, 36% yield)**

^{1}H NMR (400 MHz, $CDCl_3$) δ 4.61 (ddd, *J* = 6.3, 4.2, 2.2 Hz, 1H), 3.70 (ddd, *J* = 17.4, 11.2, 5.2 Hz, 2H), 2.55 (d, *J* = 2.2 Hz, 1H), 2.49 (s, 1H).

^{13}C NMR (101 MHz, $CDCl_3$) δ 81.04 (s), 74.76 (s), 62.43 (s), 48.87 (s).

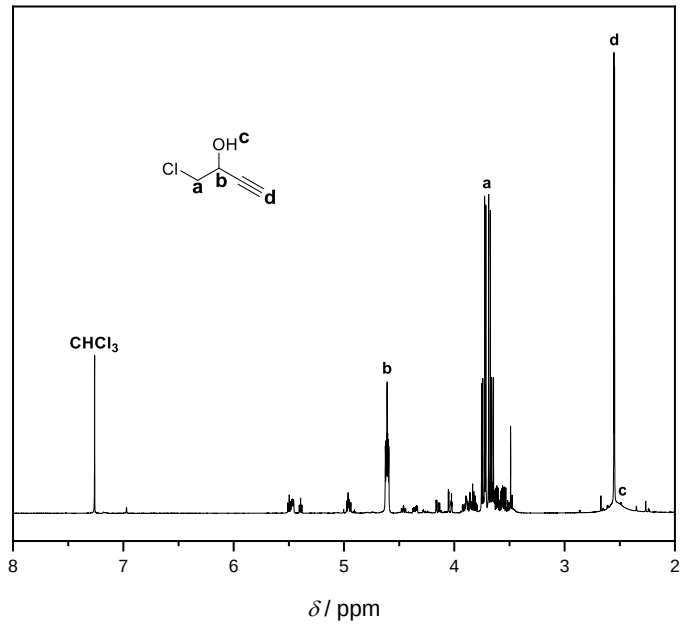

Figure S27: ^{1}H-NMR spectrum of **C14**, **^{1}H NMR (400 MHz, $CDCl_3$)** δ 4.61 (ddd, J = 6.3, 4.2, 2.2 Hz, 1H), 3.70 (ddd, J = 17.4, 11.2, 5.2 Hz, 2H), 2.55 (d, J = 2.2 Hz, 1H), 2.49 (s, 1H).

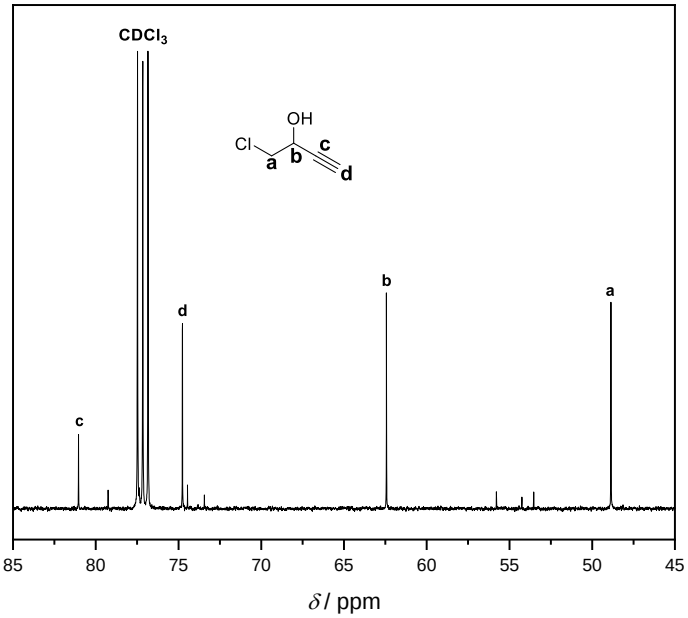

Figure S28: ^{13}C-NMR spectrum of **C14**, **^{13}C NMR (101 MHz, $CDCl_3$)** δ 81.04 (s), 74.76 (s), 62.43 (s), 48.87 (s).

8.2.15 **(C15)** 5-Bromopent-1-yn-3-ol

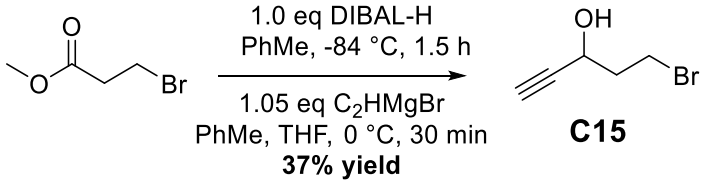

Methyl 3-bromopropanoate (1.56 mL, 14.3 mmol, 1.00 eq) was dissolved in dry toluene (10 mL) under argon atmosphere and the solution was cooled down to -84 °C (ethyl acetate / liquid nitrogen bath). 1.0 M DIBAL-H solution in toluene (15.0 mL, 15.0 mmol, 1.05 eq) was added over 30 min. The resulting mixture was stirred for 1 hour at -84 °C before being heated up to 0 °C. 0.5 M ethynyl magnesium bromide solution in THF (30.0 mL, 15.0 mmol, 1.05 eq) was added over 15 min and the mixture was stirred another 15 min at 0 °C. Afterwards, the reaction was directly quenched at 0 °C by addition of a saturated ammonium chloride solution (20 mL) and the aqueous phase was extracted with DCM (3 × 50 mL). The organic fractions were collected, dried over magnesium sulfate and the solvent was removed under reduced pressure. The crude material was purified by flash chromatography (silica, Et_2O / PE, 1:4) in order to give **C15** as a transparent liquid. **(873 mg, 5.36 mmol, 37% yield)**

^{1}H NMR (400 MHz, $CDCl_3$) ***δ*** 4.62 (ddd, *J* = 7.6, 5.7, 2.1 Hz, 1H), 3.56 (tdt, *J* = 12.6, 10.2, 6.3 Hz, 2H), 2.52 (d, *J* = 2.1 Hz, 1H), 2.35 – 2.16 (m, 2H), 2.11 (s, 1H).

^{13}C NMR (101 MHz, $CDCl_3$) ***δ*** 83.67 (s), 74.02 (s), 60.57 (s), 40.09 (s), 28.76 (s).

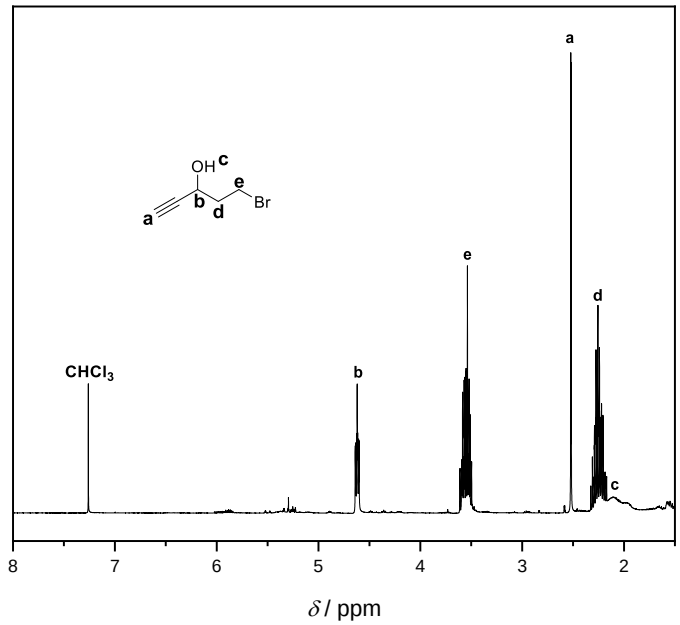

Figure S29: ^{1}H-NMR spectrum of **C15**, **^{1}H NMR (400 MHz, $CDCl_3$) δ** 4.62 (ddd, *J* = 7.6, 5.7, 2.1 Hz, 1H), 3.56 (tdt, *J* = 12.6, 10.2, 6.3 Hz, 2H), 2.52 (d, *J* = 2.1 Hz, 1H), 2.35 – 2.16 (m, 2H), 2.11 (s, 1H).

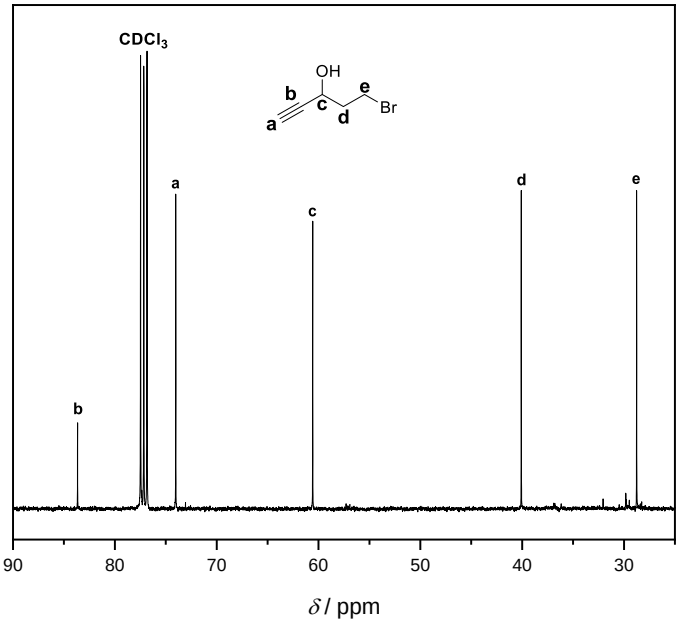

Figure S30: ^{13}C-NMR spectrum of **C15**, **^{13}C NMR (101 MHz, $CDCl_3$) δ** 83.67 (s), 74.02 (s), 60.57 (s), 40.09 (s), 28.76 (s).

8.2.16 **(C16)** 5-Azidopent-1-yn-3-ol

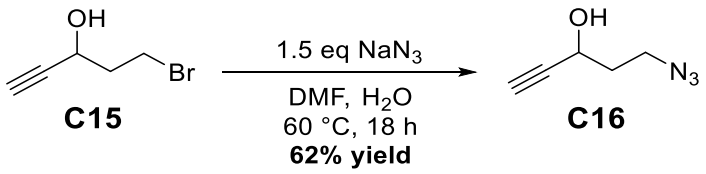

5-Bromopent-1-yn-3-ol **C15** (873 mg, 5.36 mmol, 1.0 eq) was diluted in DMF (10 mL) and water (2 mL). Sodium azide (523 mg, 8.04 mmol, 1.5 eq) was added and the mixture was heated for 18 hours at 60 °C under argon atmosphere. Afterwards, water (500 mL) and brine (50 mL) were added and the aqueous phase was extracted with DCM (3 × 50 mL). The organic fractions were collected, dried over magnesium sulfate and the solvent was removed under reduced pressure. The crude material was purified by flash chromatography (silica, Et_2O / PE, 1:3) in order to give **C16** as a transparent liquid. **(414 mg, 3.31 mmol, 62% yield)**

^{1}H NMR (400 MHz, $CDCl_3$) ***δ*** 4.53 (td, *J* = 6.3, 2.1 Hz, 1H), 3.63 – 3.42 (m, 2H), 2.51 (d, *J* = 2.2 Hz, 1H), 2.06 (s, 1H), 1.96 (dd, *J* = 13.1, 6.4 Hz, 2H).

^{13}C NMR (101 MHz, $CDCl_3$) ***δ*** 83.76 (s), 74.00 (s), 59.89 (s), 47.73 (s), 36.36 (s).

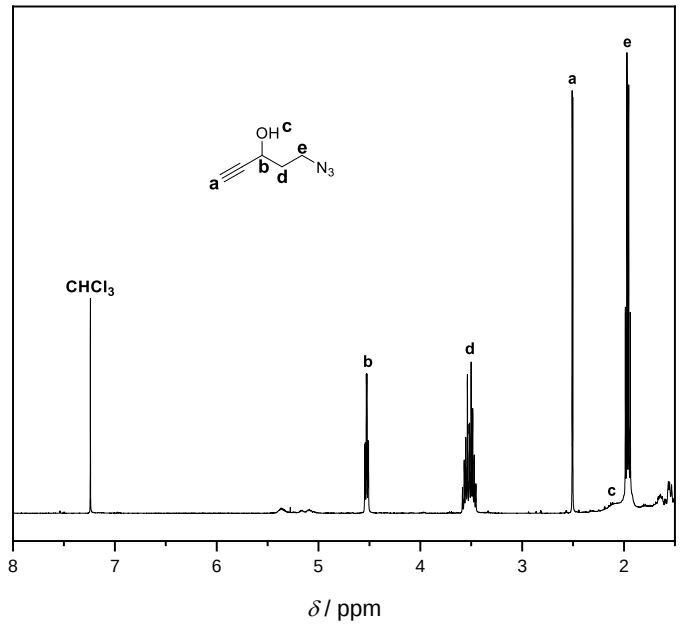

Figure S31: ^{1}H-NMR spectrum of **C16**, **^{1}H NMR (400 MHz, $CDCl_3$) δ** 4.53 (td, *J* = 6.3, 2.1 Hz, 1H), 3.63 – 3.42 (m, 2H), 2.51 (d, *J* = 2.2 Hz, 1H), 2.06 (s, 1H), 1.96 (dd, *J* = 13.1, 6.4 Hz, 2H).

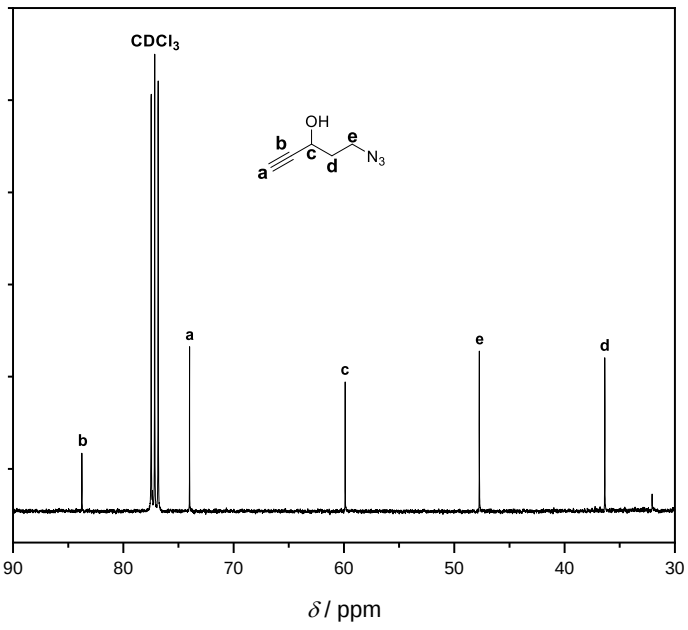

Figure S32: ^{13}C-NMR spectrum of **C16**, **^{13}C NMR (101 MHz, $CDCl_3$) δ** 83.76 (s), 74.00 (s), 59.89 (s), 47.73 (s), 36.36 (s).

8.3 RAFT Agents Synthesis – Project Part I

8.3.1 **(R01)** Benzyl 2-(((benzylthio)carbonothioyl)thio) propanoate

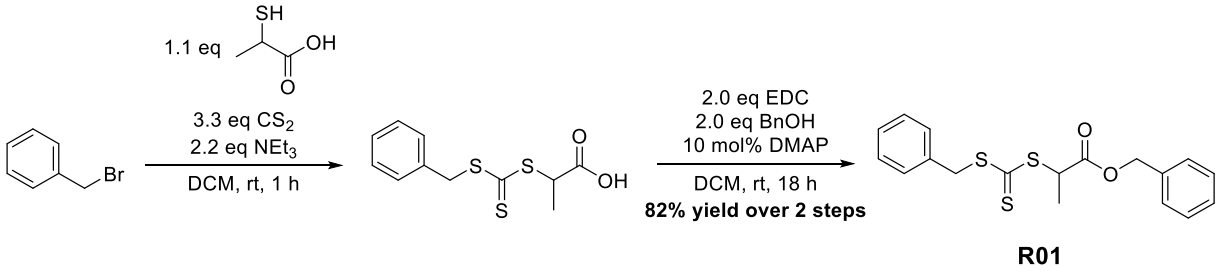

2-Mercaptopropanoic acid (0.83 mL, 9.25 mmol, 1.1 eq) and triethylamine (2.58 mL, 18.5 mmol, 2.2 eq) were dissolved in dry DCM (2 mL) The mixture was cooled down to 0 °C and carbon disulfide (1.67 mL, 27.8 mmol, 3.3 eq) was added. After 5 min, (bromomethyl)benzene (1.00 mL, 8.41 mmol, 1.0 eq) was added and the reaction was left stirring at room temperature for 60 min. Afterwards, water (10 mL) was added to the reaction mixture and 1 M HCl was added until pH < 2 was reached. The aqueous phase was then extracted with DCM (3 × 30 mL). The organic fractions were collected, dried over magnesium sulfate and the solvent was removed under reduced pressure in order to obtain a yellow oil. The freshly obtained yellow oil was dissolved in dry DCM (20 mL) without further purification. DMAP (114 mg, 0.93 mmol, 0.1 eq), phenylmethanol (1.91 mL, 18.5 mmol, 2.0 eq) were added and the mixture was cooled down to 0 °C. EDC (3.55 g, 18.5 mmol, 2.0 eq) was added and the reaction was left stirring at room temperature for 18 hours. Afterwards, water (20 mL) was added to the reaction mixture and 1 M HCl was added until pH < 2 was reached. The aqueous phase was then extracted with DCM (3 × 30 mL). The organic fractions were collected, dried over magnesium sulfate and the solvent was removed under reduced pressure. The crude material was purified by flash chromatography (silica, PhMe / *c*-Hex, 1:1) in order to give **R01** as a yellow oil. **(2.75 g, 7.59 mmol, 82% yield)**

^{1}H NMR (400 MHz, $CDCl_3$) δ 7.41 – 7.27 (m, 10H), 5.18 (d, J = 1.2 Hz, 2H), 4.87 (q, J = 7.4 Hz, 1H), 4.59 (s, 2H), 1.62 (d, J = 7.4 Hz, 3H).

^{13}C NMR (101 MHz, $CDCl_3$) δ 221.16 (s), 171.04 (s), 135.46 (s), 134.79 (s), 129.41 (s), 128.88 (s), 128.72 (s), 128.52 (s), 128.30 (s), 128.01 (s), 67.67 (s), 48.29 (s), 41.88 (s), 16.95 (s).

ESI-HRMS (*m/z*) calculated for $[M+Na]^+$ 385.0361 found 385.0351.

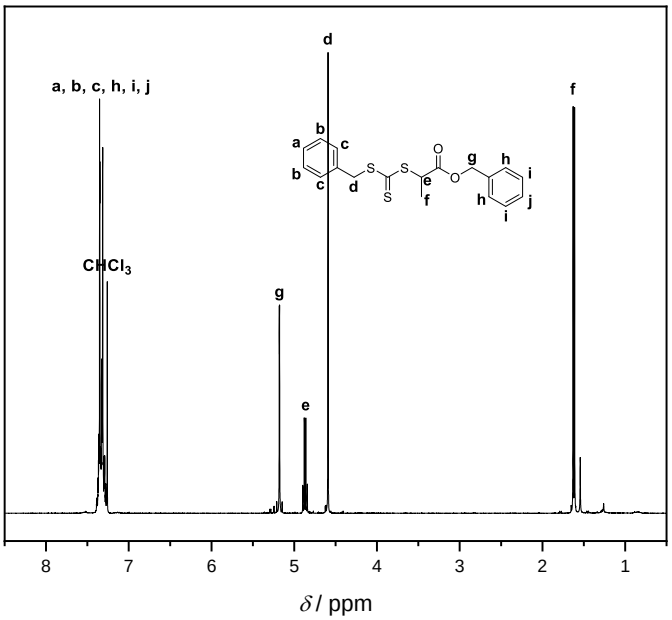

Figure S33: ^{1}H-NMR spectrum of **R01**, **^{1}H NMR (400 MHz, $CDCl_3$)** δ 7.41 – 7.27 (m, 10H), 5.18 (d, J = 1.2 Hz, 2H), 4.87 (q, J = 7.4 Hz, 1H), 4.59 (s, 2H), 1.62 (d, J = 7.4 Hz, 3H).

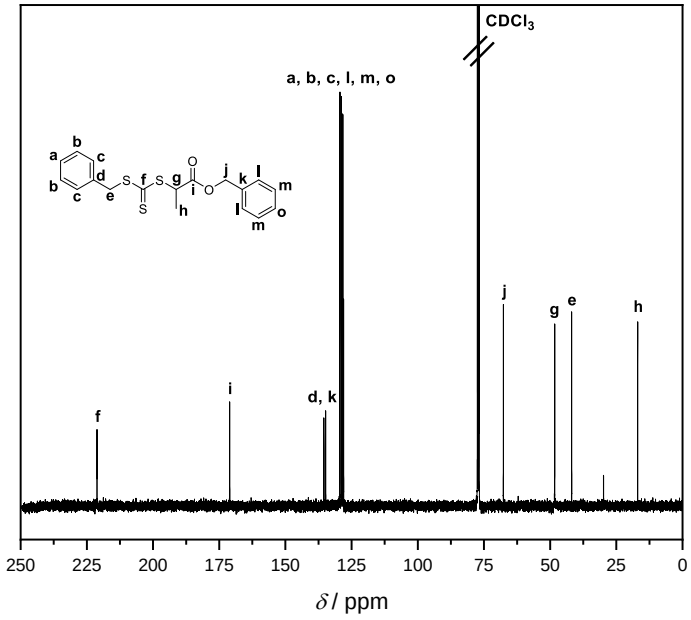

Figure S34: ^{13}C-NMR spectrum of **R01**, **^{13}C NMR (101 MHz, $CDCl_3$)** δ 221.16 (s), 171.04 (s), 135.46 (s), 134.79 (s), 129.41 (s), 128.88 (s), 128.72 (s), 128.52 (s), 128.30 (s), 128.01 (s), 67.67 (s), 48.29 (s), 41.88 (s), 16.95 (s).

8.3.2 **(R02)** Tribenzyl2,2',2''-((((benzene-1,3,5-triyltris (methylene))tris(sulfanediyl))tris(carbonothioyl)) tris(sulfanediyl))tripropionate

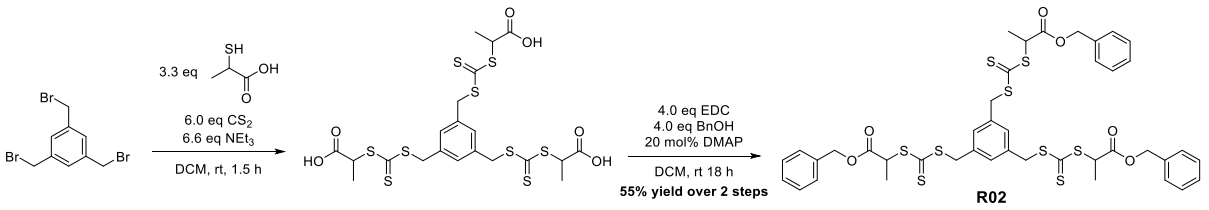

2-Mercaptopropanoic acid (0.413 mL, 4.62 mmol, 3.3 eq) and triethylamine (1.29 mL, 9.24 mmol, 6.6 eq) were dissolved in dry DCM (5 mL) The mixture was cooled down to 0 °C and carbon disulfide (0.505 mL, 8.40 mmol, 6.0 eq) was added. After 5 min, 1,3,5-tris(bromomethyl)benzene (0.50 g, 1.40 mmol, 1.0 eq) was added and the reaction was stirred at room temperature for 1.5 hours. Afterwards, water (10 mL) was added to the reaction mixture and a 1 M HCl solution was added until pH < 2 was reached. The aqueous phase was then extracted with DCM (3 × 30 mL). The organic fractions were collected, dried over magnesium sulfate and the solvent was removed under reduced pressure in order to obtain a yellow oil.

The freshly obtained yellow oil was dissolved in dry DCM (20 mL) without further purification. DMAP (112 mg, 0.92 mmol, 0.2 eq), phenylmethanol (1.90 mL, 18.4 mmol, 4.0 eq) were added and the mixture was cooled down to 0 °C. EDC (3.53 g, 18.4 mmol, 4.0 eq) was added and the reaction was left under stirring at room temperature for 18 hours. Afterwards, water (20 mL) was added to the reaction mixture and a 1 M HCl solution was added until pH < 2 was reached. The aqueous phase was then extracted with DCM (3 × 30 mL). The organic fractions were collected, dried over magnesium sulfate and the solvent was removed under reduced pressure. The crude material was purified by flash chromatography (silica, PhMe) in order to give **R02** as a yellow oil. **(0.716 g, 0.77 mmol, 55% yield)**

^{1}H NMR (400 MHz, $CDCl_3$) δ 7.42 – 7.29 (m, 15H), 7.19 (s, 3H), 5.22 – 5.13 (m, 6H), 4.86 (q, J = 7.4 Hz, 3H), 4.51 (q, J = 13.6 Hz, 6H), 1.62 (d, J = 7.4 Hz, 9H).

^{13}C NMR (101 MHz, $CDCl_3$) δ 220.63 (s), 170.93 (s), 136.23 (s), 135.44 (s), 129.70 (s), 128.72 (s), 128.54 (s), 128.29 (s), 67.68 (s), 48.43 (s), 41.10 (s), 16.96 (s).

ESI-HRMS (*m/z*) calculated for $[M+Na]^+$ 953,0360 found 953.0353.

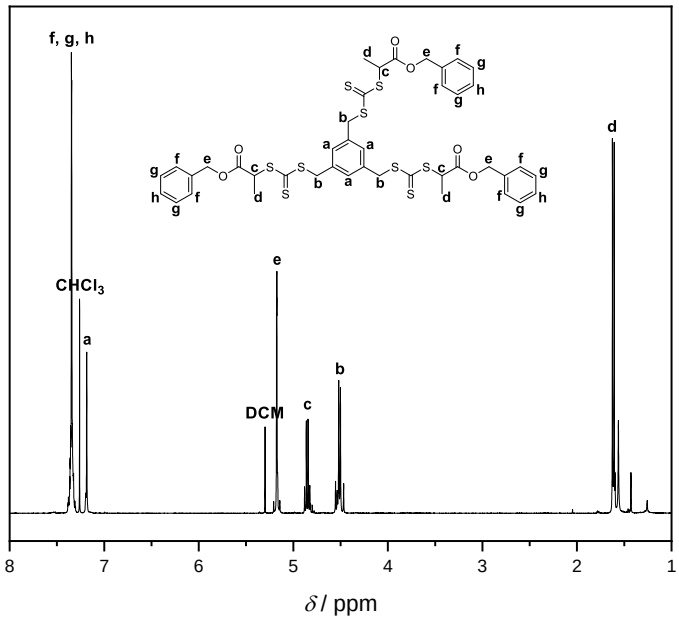

Figure S35: ^{1}H-NMR spectrum of **R02**, **^{1}H NMR (400 MHz, $CDCl_3$) δ** 7.42 – 7.29 (m, 15H), 7.19 (s, 3H), 5.22 – 5.13 (m, 6H), 4.86 (q, J = 7.4 Hz, 3H), 4.51 (q, J = 13.6 Hz, 6H), 1.62 (d, J = 7.4 Hz, 9H).

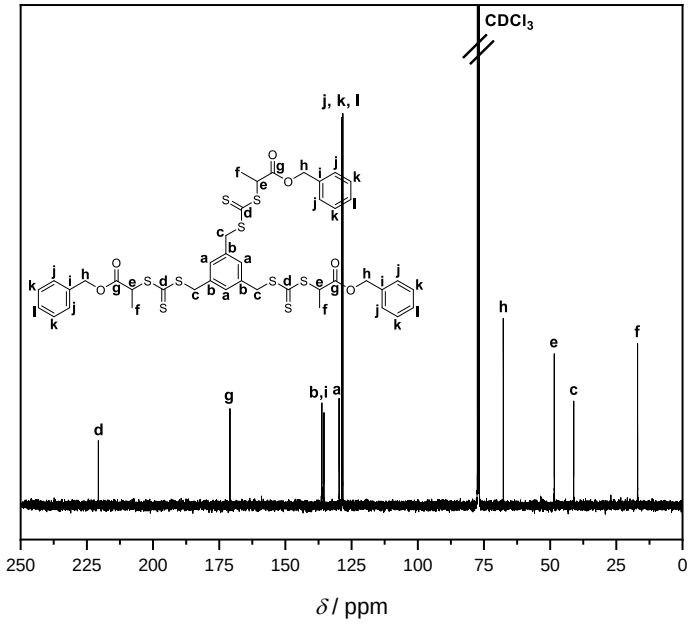

Figure S36: ^{13}C-NMR spectrum of **R02**, **^{13}C NMR (101 MHz, $CDCl_3$) δ** 220.63 (s), 170.93 (s), 136.23 (s), 135.44 (s), 129.70 (s), 128.72 (s), 128.54 (s), 128.29 (s), 67.68 (s), 48.43 (s), 41.10 (s), 16.96 (s).

8.3.3 **(R03)** Tris(3-azido-5-ethynylbenzyl)2,2',2''-((((benzene-1,3,5triyltris(methylene))tris(sulfanediyl))tris(carbonothioyl))tris(sulfanediyl))tripropionate

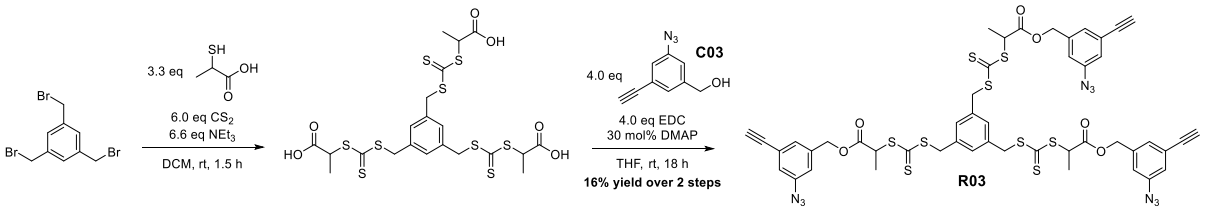

2-Mercaptopropanoic acid (0.082 mL, 0.92 mmol, 3.3 eq) and triethylamine (0.260 mL, 1.85 mmol, 6.6 eq) were dissolved in dry DCM (1 mL) The mixture was cooled down to 0 °C and carbon disulfide (0.101 mL, 1.68 mmol, 6.0 eq) was added. After 5 min, 1,3,5-tris(bromomethyl)benzene (0.100 g, 0.28 mmol, 1.0 eq) was added and the reaction was stirred at room temperature for 1.5 hours. Afterwards, water (10 mL) was added to the reaction mixture and 1 M HCl was added until pH < 2 was reached. The aqueous phase was then extracted with DCM (3 × 30 mL) and THF (3 × 5 mL) as extraction cosolvent. The organic fractions were collected, dried over magnesium sulfate and the solvent was removed under reduced pressure in order to obtain a yellow oil.

The freshly obtained yellow oil was dissolved in dry THF (6 mL) without further purification. DMAP (17 mg, 0.14 mmol, 0.5 eq), (3-azido-5-ethynylphenyl)methanol **C03** (194 mg, 1.12 mmol, 4.0 eq) were added and the mixture was cooled down to 0 °C. EDC (322 mg, 1.68 mmol, 6.0 eq) was added and the reaction was left under stirring at room temperature for 18 hours. Afterwards, water (20 mL) was added to the reaction mixture and 1 M HCl was added until pH < 2 was reached. The aqueous phase was then extracted with DCM (3 × 30 mL). The organic fractions were collected, dried over magnesium sulfate and the solvent was removed under reduced pressure. The crude material was purified by flash chromatography (silica, DCM) followed by a consecutive (silica, PhMe) flash chromatography in order to give **R03** as a yellow oil. **(49 mg, 0.044 mmol, 16% yield)**

^{1}H NMR (400 MHz, $CDCl_3$) δ 7.25 – 7.18 (m, *J* = 12.0 Hz, 6H), 7.12 – 7.06 (m, 3H), 6.98 (s, 3H), 5.17 – 5.07 (m, 6H), 4.86 (q, *J* = 7.4 Hz, 3H), 4.52 (q, *J* = 13.6 Hz, 6H), 3.12 (s, 3H), 1.63 (d, *J* = 7.4 Hz, 9H).

^{13}C NMR (101 MHz, $CDCl_3$) δ 220.54 (s), 170.80 (s), 140.88 (s), 137.77 (s), 136.17 (s), 129.75 (s), 128.00 (s), 124.20 (s), 122.36 (s), 119.03 (s), 82.32 (s), 78.81 (s), 66.30 (s), 48.13 (s), 41.20 (s), 16.75 (s).

ESI-HRMS (*m/z*) calculated for $[M+Na]^+$ 1148,0402 found 1148.0394.

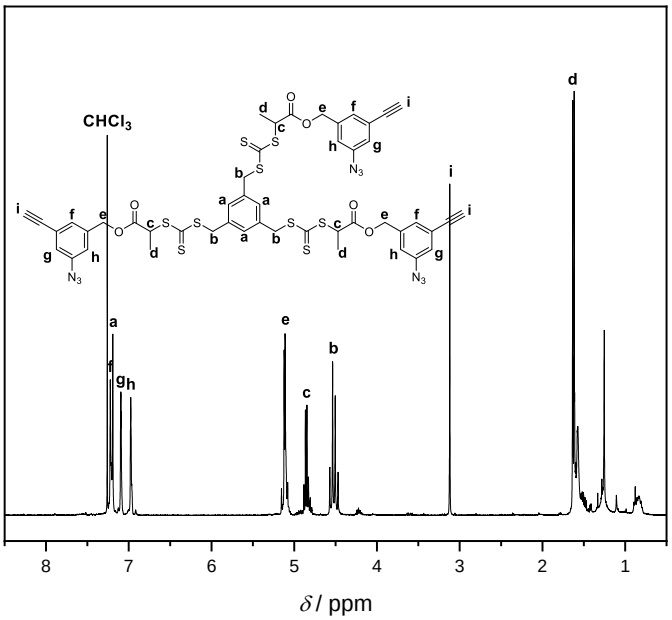

Figure S37: ^{1}H-NMR spectrum of **R03**, **^{1}H NMR (400 MHz, $CDCl_3$)** ***δ*** 7.25 – 7.18 (m, *J* = 12.0 Hz, 6H), 7.12 – 7.06 (m, 3H), 6.98 (s, 3H), 5.17 – 5.07 (m, 6H), 4.86 (q, *J* = 7.4 Hz, 3H), 4.52 (q, *J* = 13.6 Hz, 6H), 3.12 (s, 3H), 1.63 (d, *J* = 7.4 Hz, 9H).

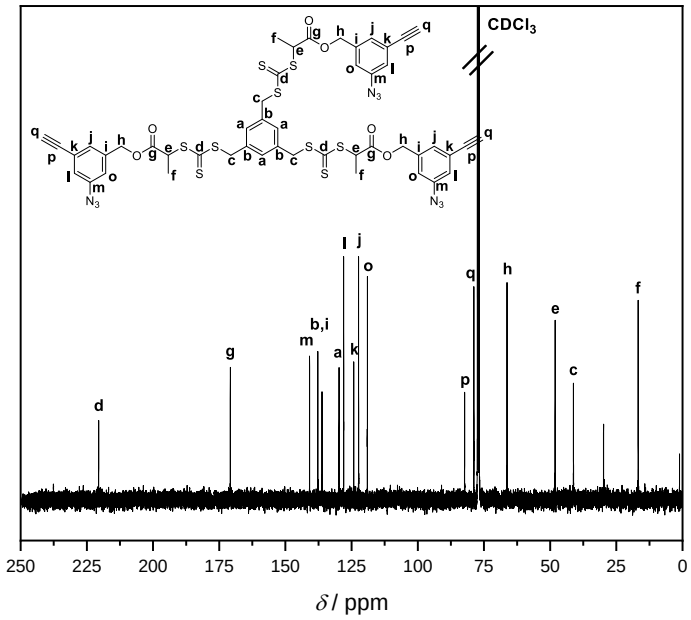

Figure S38: ^{13}C-NMR spectrum of **R03**, **^{13}C NMR (101 MHz, $CDCl_3$)** ***δ*** 220.54 (s), 170.80 (s), 140.88 (s), 137.77 (s), 136.17 (s), 129.75 (s), 128.00 (s), 124.20 (s), 122.36 (s), 119.03 (s), 82.32 (s), 78.81 (s), 66.30 (s), 48.13 (s), 41.20 (s), 16.75 (s).

8.3.4 **(R04)** Tris(1-(3-azidophenyl)but-3-yn-1-yl)2,2',2''-((((benzene-1,3,5-triyltris(methylene))tris(sulfanediyl))tris(carbonothioylsulfanediyl))tripropionate

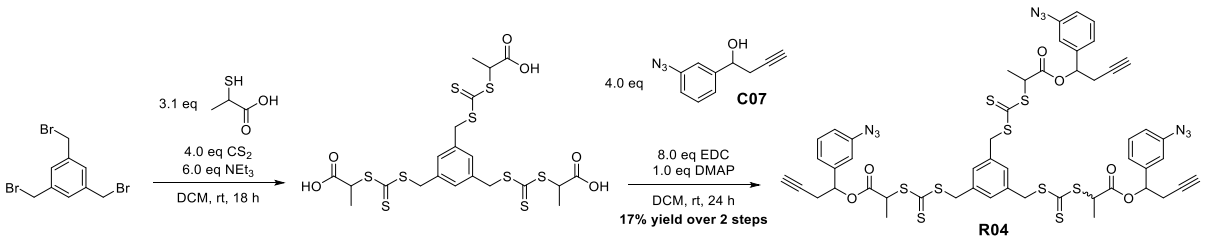

2-Mercaptopropanoic acid (0.042 mL, 0.465 mmol, 3.1 eq) and triethylamine (0.125 mL, 0.90 mmol, 6.0 eq) were dissolved in dry DCM (1 mL) The mixture was cooled down to 0 °C and carbon disulfide (0.036 mL, 0.60 mmol, 4.0 eq) was added. After 5 min, 1,3,5-tris(bromomethyl)benzene (0.053 g, 0.15 mmol, 1.0 eq) was added and the reaction was stirred at room temperature for 18 hours. Afterwards, water (5 mL) was added to the reaction mixture and 1 M HCl was added until pH < 2 was reached. The aqueous phase was then extracted with DCM (3 × 20 mL) and THF (3 × 2 mL) as extraction cosolvent. The organic fractions were collected, dried over magnesium sulfate and the solvent was removed under reduced pressure in order to obtain a yellow oil. The freshly obtained yellow oil was dissolved in dry DCM (1 mL) without further purification. DMAP (18 mg, 0.15 mmol, 1.0 eq), 1-(3-azidophenyl)but-3-yn-1-ol **C07** (110 mg, 0.59 mmol, 4.0 eq) were added and the mixture was cooled down to 0 °C. EDC (230 mg, 1.20 mmol, 8.0 eq) was added and the reaction was left stirring at room temperature for 48 hours. Afterwards, water (20 mL) was added to the reaction mixture and 1 M HCl was added until pH < 2 was reached. The aqueous phase was then extracted with DCM (3 × 20 mL). The organic fractions were collected, dried over magnesium sulfate and the solvent was removed under reduced pressure. The crude material was purified by flash chromatography (silica, PhMe) and (silica, DCM) in order to give **R04** as a yellow oil. **(29 mg, 0.025 mmol, 17% yield)**

^{1}H NMR (400 MHz, $CDCl_3$) δ 7.33 (t, *J* = 7.7 Hz, 3H), 7.19 (dd, *J* = 7.8, 4.0 Hz, 3H), 7.13 (dd, *J* = 7.7, 3.9 Hz, 3H), 7.08 – 6.95 (m, 6H), 5.85 (t, *J* = 6.6 Hz, 3H), 4.87 (dq, *J* = 14.9, 7.4 Hz, 3H), 4.62 – 4.39 (m, 6H), 2.85 – 2.62 (m, 6H), 1.99 (dd, *J* = 3.9, 2.5 Hz, 3H), 1.63 (dd, *J* = 13.7, 7.4 Hz, 9H).**^{13}C NMR (101 MHz, $CDCl_3$)** δ 220.45 (s), 170.04 (s), 169.94 (s), 140.48 (s), 140.46 (s), 140.45 (s), 140.42 (s), 136.20 (s), 130.07 (s), 129.73 (s), 123.12 (s), 123.08 (s), 119.26 (s), 117.20 (s), 117.15 (s), 78.89 (s), 78.77 (s), 74.45 (s), 71.51 (s), 71.36 (s), 48.27 (s), 41.14 (s), 26.57 (s), 26.54 (s), 16.73 (s), 16.67 (s).**ESI-HRMS (*m/z*)** calculated for $[M+Na]^+$ 1190.0871 found 1190.0906.

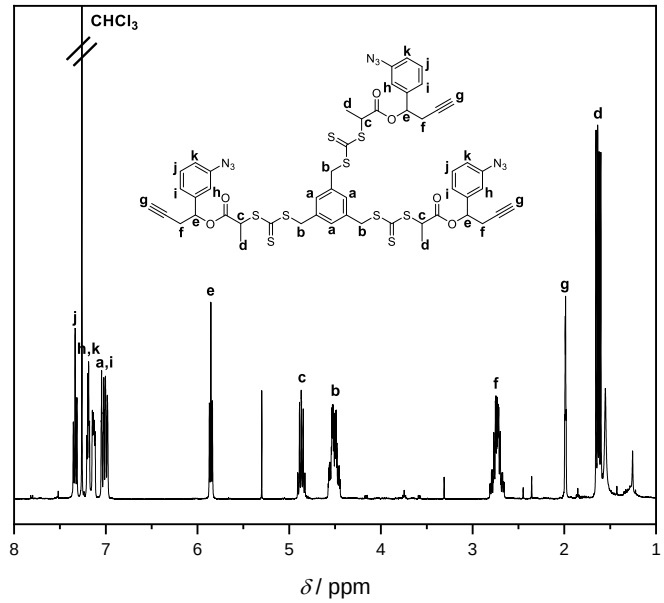

Figure S39: ^{1}H-NMR spectrum of **R04**, **^{1}H NMR (400 MHz, $CDCl_3$) δ** 7.33 (t, *J* = 7.7 Hz, 3H), 7.19 (dd, *J* = 7.8, 4.0 Hz, 3H), 7.13 (dd, *J* = 7.7, 3.9 Hz, 3H), 7.08 – 6.95 (m, 6H), 5.85 (t, *J* = 6.6 Hz, 3H), 4.87 (dq, *J* = 14.9, 7.4 Hz, 3H), 4.62 – 4.39 (m, 6H), 2.85 – 2.62 (m, 6H), 1.99 (dd, *J* = 3.9, 2.5 Hz, 3H), 1.63 (dd, *J* = 13.7, 7.4 Hz, 9H).

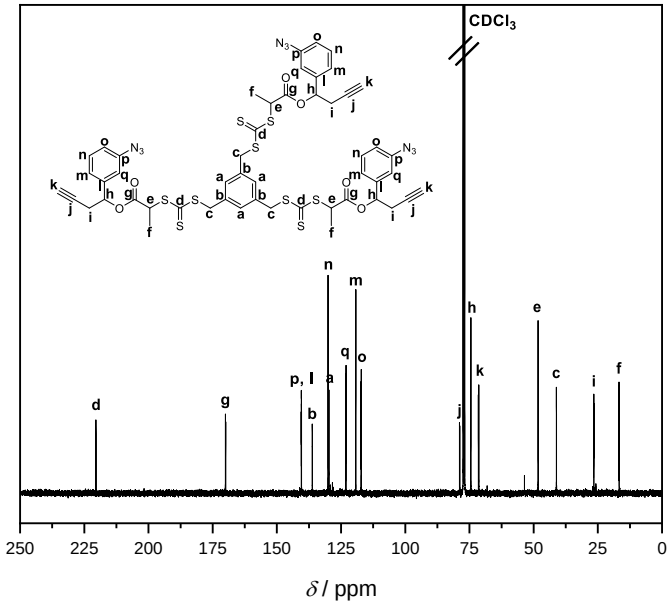

Figure S40: ^{13}C-NMR spectrum of **R04**, **^{13}C NMR (101 MHz, $CDCl_3$) δ** 220.45 (s), 170.04 (s), 169.94 (s), 140.48 (s), 140.46 (s), 140.45 (s), 140.42 (s), 136.20 (s), 130.07 (s), 129.73 (s), 123.12 (s), 123.08 (s), 119.26 (s), 117.20 (s), 117.15 (s), 78.89 (s), 78.77 (s), 74.45 (s), 71.51 (s), 71.36 (s), 48.27 (s), 41.14 (s), 26.57 (s), 26.54 (s), 16.73 (s), 16.67 (s).

8.3.5 **(R05)** Tris(1-azidobut-3-yn-2-yl)2,2',2'' ((((benzene-1,3,5triyltris(methylene)) tris(sulfanediyl))tris(carbonothioyl)) tris(sulfanediyl))tripropionate

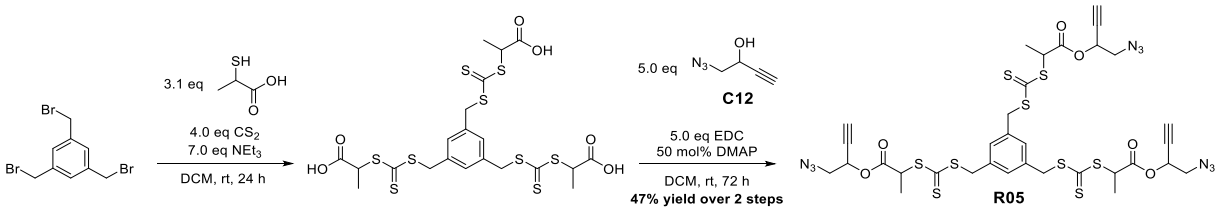

2-Mercaptopropanoic acid (0.141 mL, 1.58 mmol, 3.1 eq) and triethylamine (0.50 mL, 3.6 mmol, 7.0 eq) were dissolved in dry DCM (3 mL) The mixture was cooled down to 0 °C and carbon disulfide (0.120 mL, 2.0 mmol, 4.0 eq) was added. After 5 min, 1,3,5-tris(bromomethyl)benzene (182 mg, 0.51 mmol, 1.0 eq) was added and the reaction was stirred at room temperature for 24 hours. Afterwards, water (20 mL) was added to the reaction mixture and 1 M HCl was added until pH < 2 was reached. The aqueous phase was then extracted with DCM (3 × 20 mL) and THF (3 × 2 mL) as extraction cosolvent. The organic fractions were collected, dried over magnesium sulfate and the solvent was removed under reduced pressure in order to obtain a yellow oil. The freshly obtained yellow oil was dissolved in dry DCM (5 mL) without further purification. DMAP (32 mg, 0.26 mmol, 0.5 eq), 1-(3-azidophenyl)but-3-yn-1-ol **C12** (278 mg, 2.55 mmol, 5.0 eq) were added and the mixture was cooled down to 0 °C. EDC (489 mg, 2.55 mmol, 5.0 eq) was added and the reaction was left under stirring at room temperature for 72 hours. Afterwards, water (20 mL) was added to the reaction mixture and 1 M HCl was added until pH < 2 was reached. The aqueous phase was then extracted with DCM (3 × 20 mL). The organic fractions were collected, dried over magnesium sulfate and the solvent was removed under reduced pressure. The crude material was purified by flash chromatography columns (silica, PhMe) and (silica, DCM) in order to give **R05** as a yellow oil. **(228 mg, 0.242 mmol, 47% yield)**

^{1}H NMR (400 MHz, $CDCl_3$) δ 7.20 (s, 3H), 5.62 – 5.34 (m, 3H), 4.82 (qd, *J* = 7.4, 1.2 Hz, 3H), 4.58 – 4.47 (m, 6H), 3.62 – 3.47 (m, 6H), 2.58 (dd, *J* = 5.1, 2.2 Hz, 3H), 1.65 (dd, *J* = 7.4, 0.9 Hz, 9H).

^{13}C NMR (101 MHz, $CDCl_3$) δ 220.38 (s), 220.36 (s), 169.89 (s), 169.85 (s), 136.20 (s), 136.18 (s), 129.76 (s), 77.56 (s), 77.36 (s), 76.33 (s), 76.24 (s), 64.26 (s), 53.56 (s), 53.54 (s), 48.16 (s), 48.02 (s), 41.18 (s), 16.55 (s), 16.46 (s).

ESI-HRMS (*m/z*) calculated for $[M+Na]^+$ 961.9932 found 961.9926.

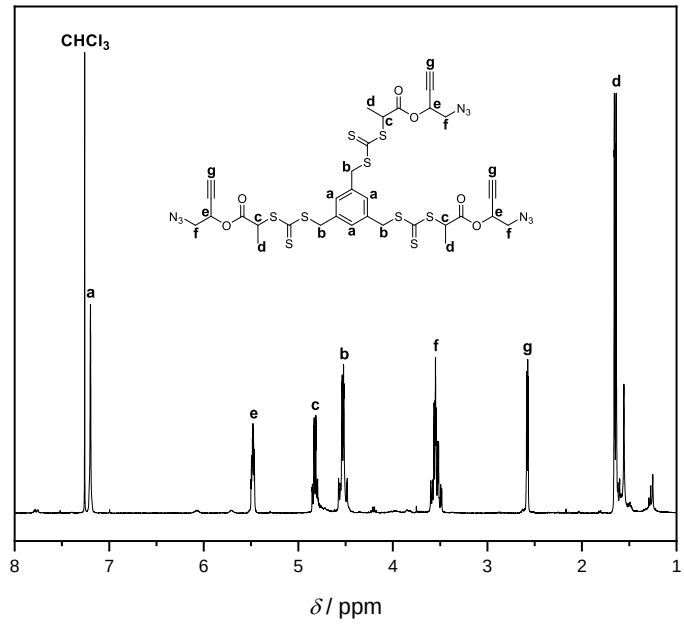

Figure S41: ^{1}H-NMR spectrum of **R05**, **^{1}H NMR (400 MHz, $CDCl_3$)** ***δ*** 7.20 (s, 3H), 5.62 – 5.34 (m, 3H), 4.82 (qd, *J* = 7.4, 1.2 Hz, 3H), 4.58 – 4.47 (m, 6H), 3.62 – 3.47 (m, 6H), 2.58 (dd, *J* = 5.1, 2.2 Hz, 3H), 1.65 (dd, *J* = 7.4, 0.9 Hz, 9H).

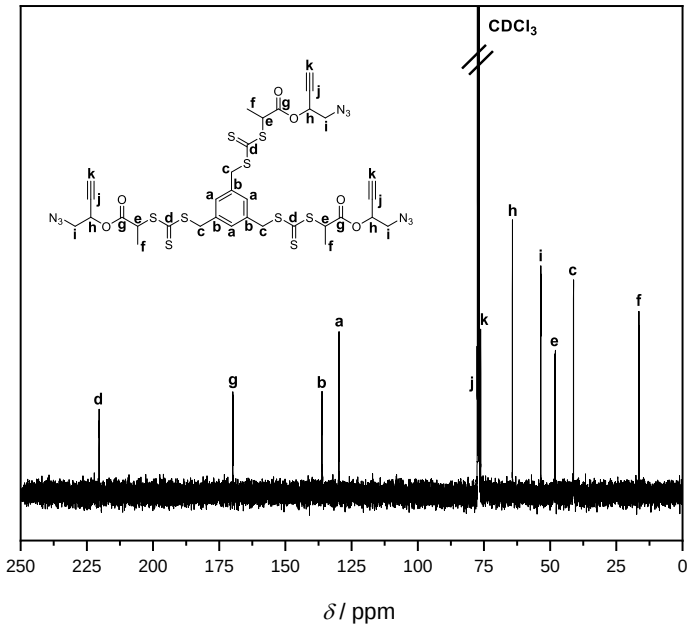

Figure S42: ^{13}C-NMR spectrum of **R05**, **^{13}C NMR (101 MHz, $CDCl_3$)** ***δ*** 220.38 (s), 220.36 (s), 169.89 (s), 169.85 (s), 136.20 (s), 136.18 (s), 129.76 (s), 77.56 (s), 77.36 (s), 76.33 (s), 76.24 (s), 64.26 (s), 53.56 (s), 53.54 (s), 48.16 (s), 48.02 (s), 41.18 (s), 16.55 (s), 16.46 (s).

8.3.6 **(R06)** 2,2',2''-((((Benzene-1,3,5-triyltris (methylene))tris(sulfanediyl))tris(carbonothioyl)) tris(sulfanediyl))tripropionic acid

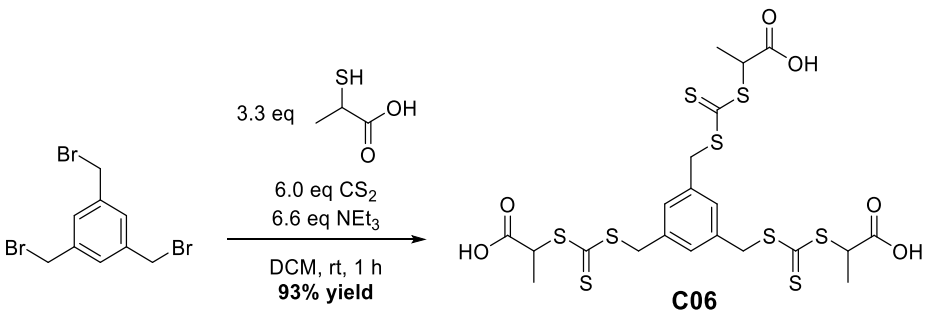

2-Mercaptopropanoic acid (0.413 mL, 4.62 mmol, 3.3 eq) and triethylamine (1.29 mL, 9.24 mmol, 6.6 eq) were dissolved in dry DCM (5 mL) The mixture was cooled down to 0 °C and carbon disulfide (0.505 mL, 8.40 mmol, 6.0 eq) was added. After 5 min, 1,3,5-tris(bromomethyl)benzene (0.500 g, 1.40 mmol, 1.0 eq) was added and the reaction was stirred at room temperature for 1 hour. Afterwards, water (20 mL) was added to the reaction mixture and 1 M HCl solution was added until pH < 2 was reached. The aqueous phase was then extracted with DCM (3 × 30 mL) and THF (3 × 5 mL) as extraction cosolvent. The organic fractions were collected, dried over magnesium sulfate and the solvent was removed under reduced pressure in order to obtain **R06** as a yellow oil. **(0.86 g, 1.30 mmol, 93% yield)**

^{1}H NMR (400 MHz, DMSO) δ 13.20 (s, 3H), 7.34 (s, 3H), 4.72 – 4.58 (m, 9H), 1.52 (d, J = 7.3 Hz, 9H).

^{13}C NMR (101 MHz, DMSO) δ 221.05 (s), 171.47 (s), 136.11 (s), 129.49 (s), 48.44 (s), 30.43 (s), 16.79 (s).

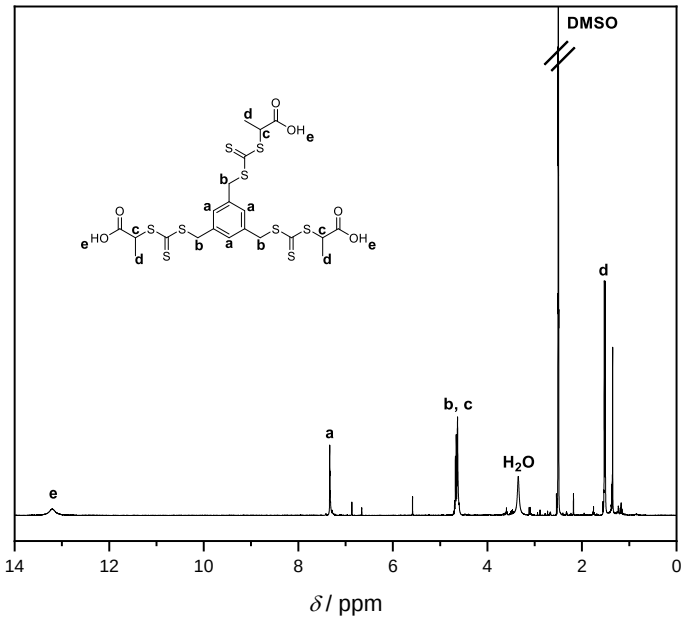

Figure S43: ^{1}H-NMR spectrum of **R06**, **^{1}H NMR (400 MHz, DMSO)** δ 13.20 (s, 3H), 7.34 (s, 3H), 4.72 – 4.58 (m, 9H), 1.52 (d, J = 7.3 Hz, 9H).

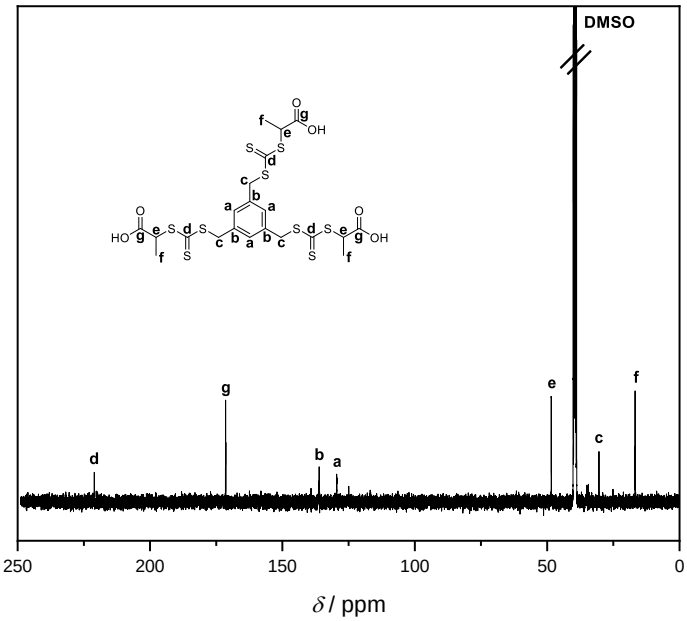

Figure S44: ^{13}C-NMR spectrum of **R06**, **^{13}C NMR (101 MHz, DMSO)** δ 221.05 (s), 171.47 (s), 136.11 (s), 129.49 (s), 48.44 (s), 30.43 (s), 16.79 (s).

8.4 Polymer Synthesis and Post-Polymerization Modifications – Project Part I

8.4.1 **(P01)** Polymerization of Styrene by RAFT agent R01

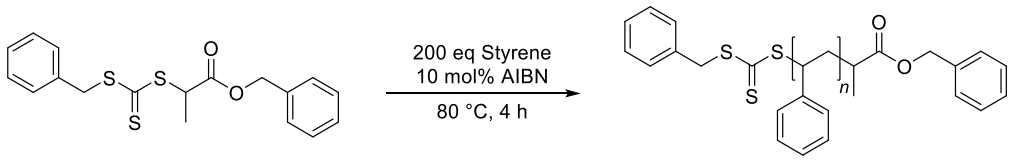

R01 **P01**

2,2′-Azobis(2-methylpropionitrile) (1.6 mg, 0.01 mmol, 0.1 eq) and RAFT agent **R01** (36 mg, 0.1 mmol, 1.0 eq) were added to disinhibited styrene (2.30 mL, 20 mmol, 200 eq). The homogeneous mixture was sealed under argon atmosphere before being stirred at 80 °C for 4 hours. Samples (0.5 mL) were taken from the reaction after 1, 2 and 4 hours and reprecipitated in cold MeOH in order to follow **P01** polymerization by SEC_{THF} and ^{1}H-NMR analyses.

Table S1: Overview of polymer **P01** data.

Entry	Polymer name	Time / h	$M_{n,^1H\text{-}NMR}$ / kg mol^{-1}	$M_{n,SEC/THF}$ / kg mol^{-1}	$M_{w,SEC/THF}$ / kg mol^{-1}	$Đ_{THF}$
1	P01	1	1.8	1.8	2.3	1.27
2	P01	2	2.8	3.1	3.7	1.20
3	P01	4	4.8	4.9	5.7	1.17

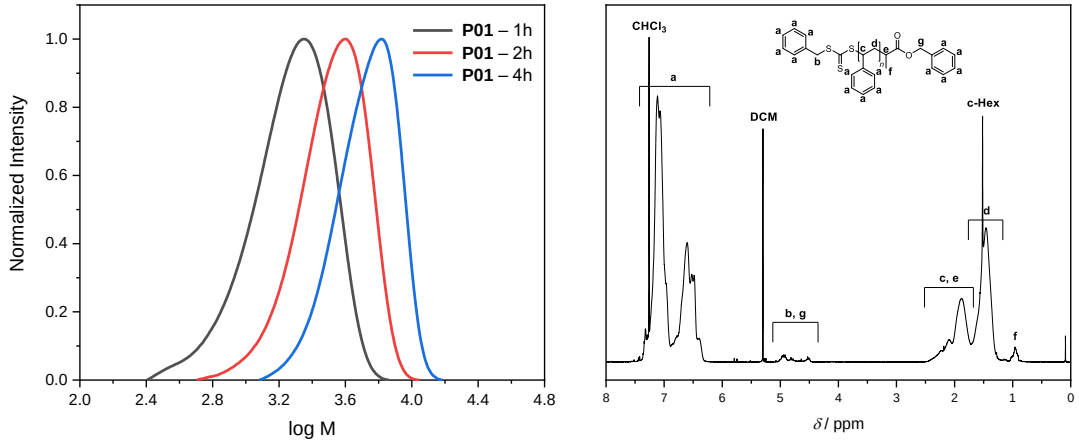

Figure S45: SEC_{THF} traces of polymer **P01** (*left*); ^{1}H-NMR spectrum of polymer **P01–4h** (*right*).

8.4.2 **(P01-SH)** Trithiocarbonate Aminolysis of P01

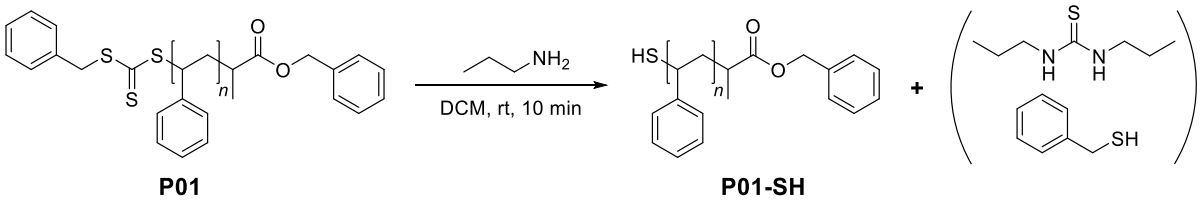

Typical procedure for each **P01** sample. A polymer sample (4.0 mg) was dissolved in DCM (0.5 mL). A large excess of *n*-propylamine (0.1 mL) was added to the yellow solution. After 10 minutes, the remaining *n*-propylamine and solvent were evaporated and the corresponding transparent solid **P01-SH** was characterized by SEC_{THF} analysis.

Table S2: Overview of polymer **P01-SH** data.

Entry	Polymer name	Time / h	$M_{n,^1H\text{-}NMR}$ / kg mol^{-1}	$M_{n,SEC/THF}$ / kg mol^{-1}	$M_{w,SEC/THF}$ / kg mol^{-1}	$Đ_{THF}$
1	P01-SH	1	1.6	1.4	1.7	1.28
2	P01-SH	2	2.6	2.3	2.7	1.21
3	P01-SH	4	4.6	3.3	3.9	1.16

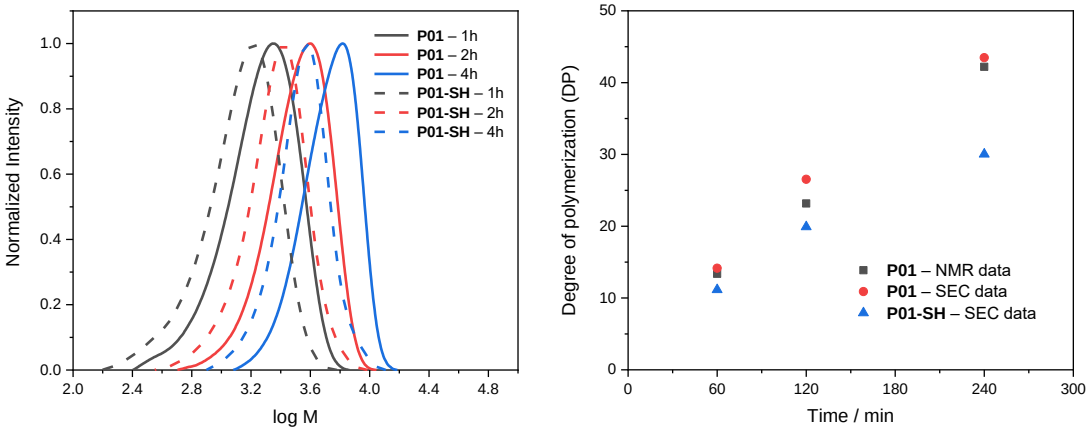

Figure S46: SEC_{THF} traces of polymers **P01** and **P01-SH** (*left*); Plot of DP vs Time for **P01** polymerization (*right*).

8.4.3 **(P02)** Polymerization of Methyl Acrylate by RAFT Agent R01

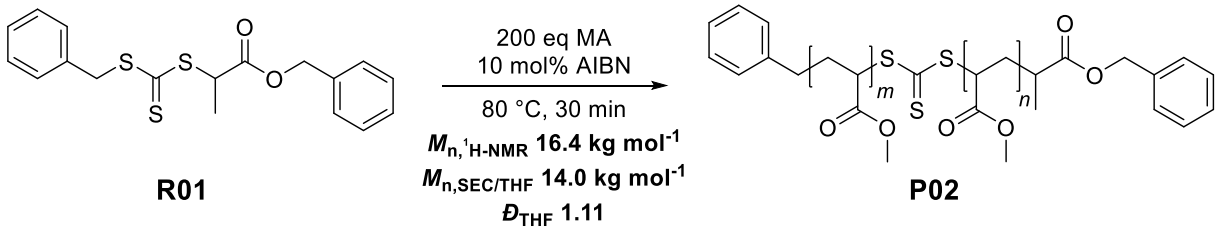

2,2′-Azobis(2-methylpropionitrile) (1.6 mg, 0.01 mmol, 0.1 eq) and RAFT agent **R01** (36 mg, 0.1 mmol, 1.0 eq) were added to disinhibited methyl acrylate (1.80 mL, 20 mmol, 200 eq). The homogeneous mixture was sealed under argon atmosphere before being stirred at 80 °C. After 30 min, the reaction mixture started to became too viscous to be properly stirred and was therefore cooled down to room temperature. The resulting polymer was reprecipitated in cold MeOH in order to obtain **P02** as a yellow solid and was subsequently characterized by SEC_{THF} and ^{1}H-NMR analyses.

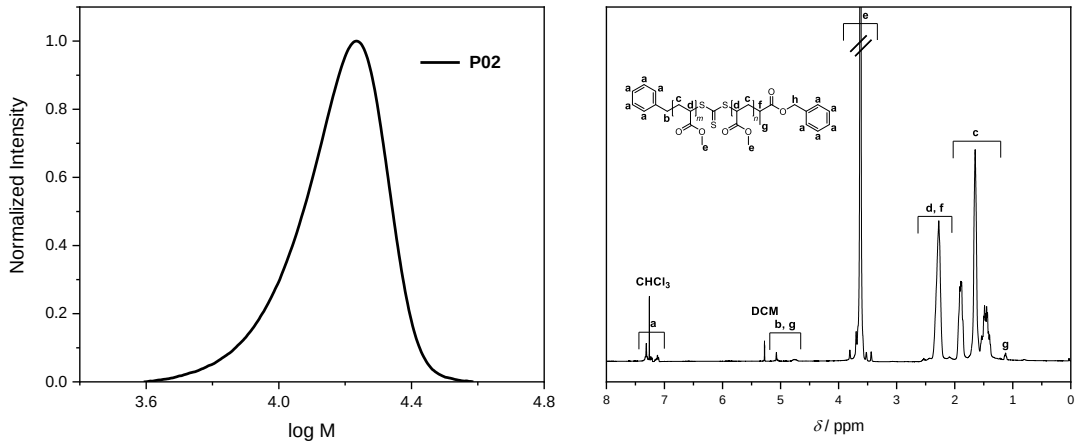

Figure S47: SEC_{THF} trace of polymer **P02** (*left*); ^{1}H-NMR spectrum of polymer **P02** (*right*).

8.4.4 **(P02-SH)** Trithiocarbonate Aminolysis of P02

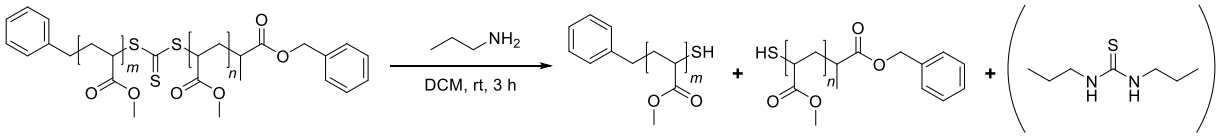

P02
$M_{n,^1H\text{-}NMR}$ 16.4 kg mol^{-1}
$M_{n,SEC/THF}$ 14.0 kg mol^{-1}
$Đ_{THF}$ 1.11

P02-SH
$M_{n,^1H\text{-}NMR}$ 16.2 kg mol^{-1}
$M_{n,SEC/THF}$ 8.1 kg mol^{-1}
$Đ_{THF}$ 1.13

P02 (4.0 mg) was dissolved in DCM (0.5 mL). A large excess of *n*-propylamine (0.1 mL) was added to the yellow solution. After 3 hours, the remaining *n*-propylamine and solvent were evaporated and the resulting transparent solid **P02-SH** was characterized by SEC_{THF} analysis.

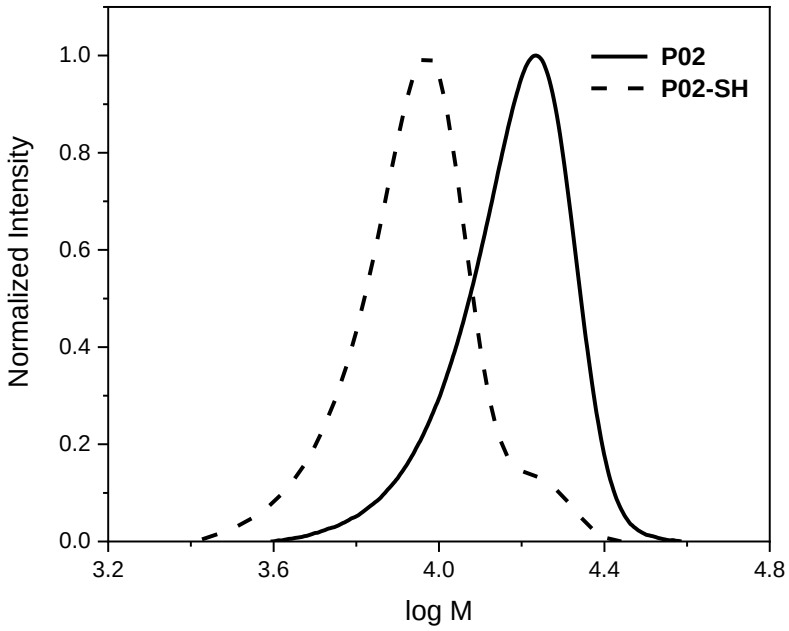

Figure S48: SEC_{THF} traces of polymers **P02** and **P02-SH**.

8.4.5 **(P03)** Polymerization of Methyl Methacrylate by RAFT Agent R01

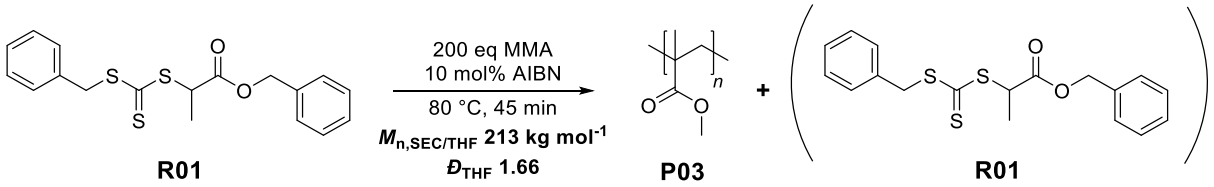

2,2′-Azobis(2-methylpropionitrile) (1.6 mg, 0.01 mmol, 0.1 eq) and RAFT agent **R01** (36 mg, 0.1 mmol, 1.0 eq) were added to disinhibited methyl methacrylate (2.14 mL, 20 mmol, 200 eq). The homogeneous mixture was sealed under argon atmosphere before being stirred at 80 °C. After 45 min, the reaction mixture started to become too viscous to be properly stirred and was therefore cooled down to room temperature. The resulting yellow polymer was reprecipitated in cold MeOH in order to obtain **P03** as a white solid and was subsequently characterized by SEC_{THF} and ^{1}H-NMR analyses.

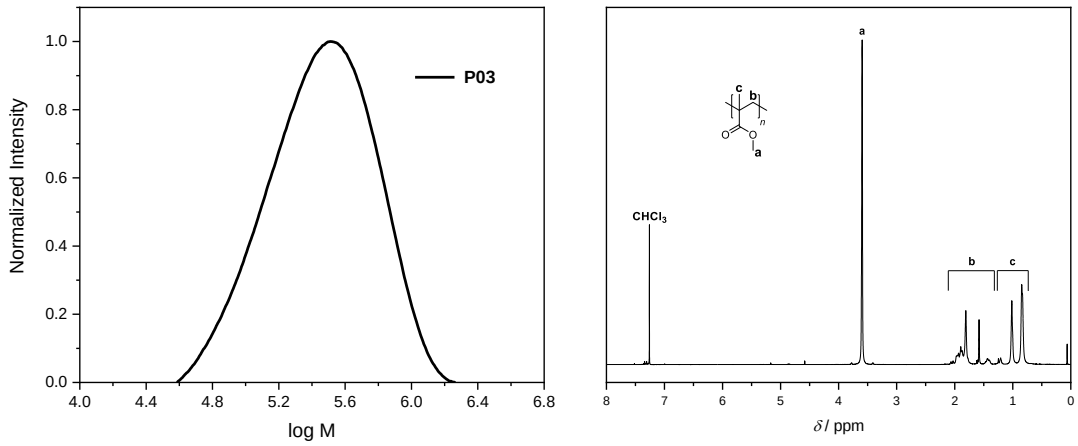

Figure S49: SEC_{THF} trace of polymer **P03** (*left*); ^{1}H-NMR spectrum of polymer **P03** (*right*).

8.4.6 **(P04)** Polymerization of Styrene by RAFT Agent R02

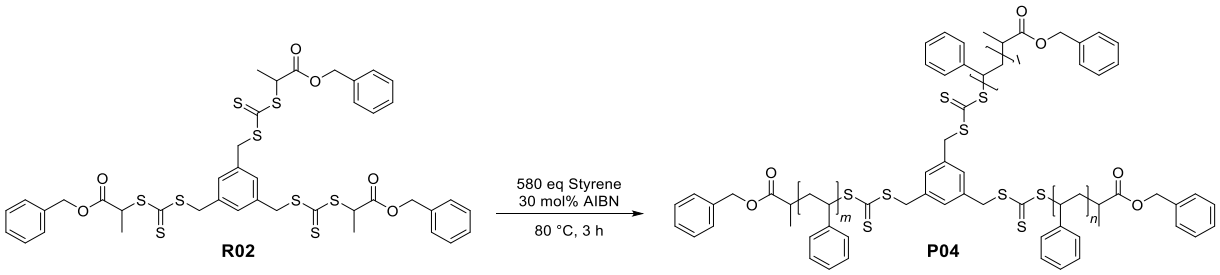

2,2′-Azobis(2-methylpropionitrile) (1.5 mg, 0.009 mmol, 0.3 eq) and RAFT agent **R02** (28 mg, 0.03 mmol, 1.0 eq) were added to disinhibited styrene (2.0 mL, 17.4 mmol, 580 eq). The homogeneous mixture was sealed under argon atmosphere before being stirred at 80 °C. Samples (0.3 mL) were taken from the reaction after 30, 60, 90, 120 and 180 minutes and reprecipitated in cold MeOH in order to follow **P04** polymerization by SEC_{THF} and ^{1}H-NMR analyses.

Table S3: Overview of polymer **P04** data.

Entry	Polymer	Time / min	$M_{n,^1H\text{-}NMR}$ / kg mol^{-1}	$M_{n,SEC/THF}$ / kg mol^{-1}	$M_{w,SEC/THF}$ / kg mol^{-1}	$Đ_{THF}$
1	P04	30	3.3	2.4	3.1	1.31
2	P04	60	5.1	3.4	4.3	1.26
3	P04	90	7.2	4.4	5.5	1.25
4	P04	120	8.6	5.4	6.8	1.26
5	P04	180	11.2	7.1	9.5	1.37

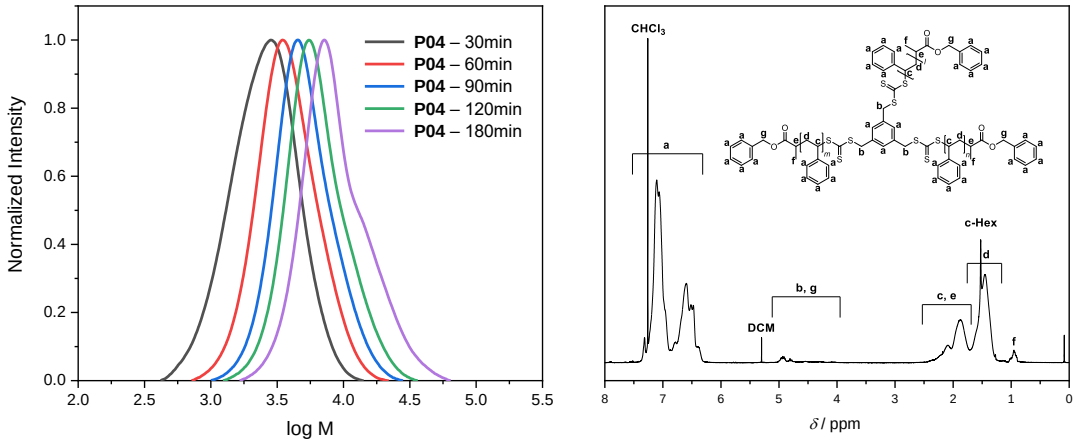

Figure S50: SEC_{THF} trace of polymer **P04** (*left*); ^{1}H-NMR spectrum of polymer **P04–180min** (*right*).

8.4.7 **(P04-SH)** Trithiocarbonate Aminolysis of P04

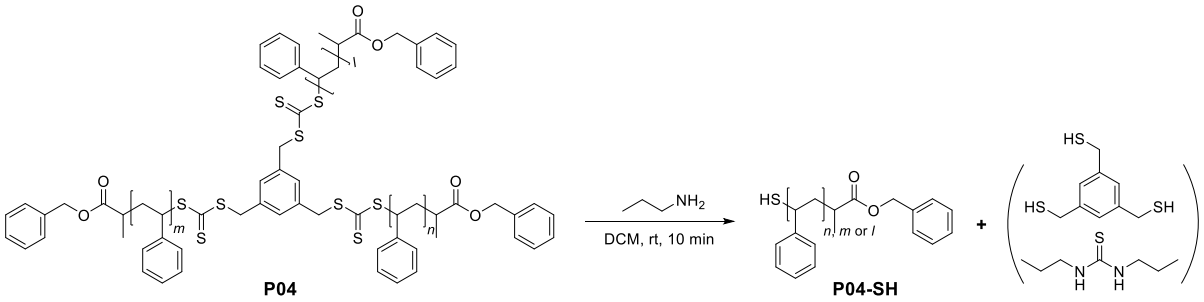

Typical procedure for each **P04** sample. A polymer sample (4.0 mg) was dissolved in DCM (0.5 mL). A large excess of *n*-propylamine (0.1 mL) was added to the yellow solution. After 10 minutes, the remaining *n*-propylamine and solvent were evaporated and the corresponding transparent solid **P04-SH** was characterized by SEC_{THF} analysis.

Table S4: Overview of polymer **P04-SH** data.

Entry	Polymer	Time / min	$M_{n,^1H\text{-}NMR}$ / kg mol^{-1}	$M_{n,SEC/THF}$ / kg mol^{-1}	$M_{w,SEC/THF}$ / kg mol^{-1}	$Đ_{THF}$
1	P04-SH	30	1.0	1.0	1.4	1.37
2	P04-SH	60	1.6	1.5	2.0	1.31
3	P04-SH	90	2.3	2.2	2.7	1.21
4	P04-SH	120	2.7	2.8	3.4	1.20
5	P04-SH	180	3.6	3.6	4.3	1.19

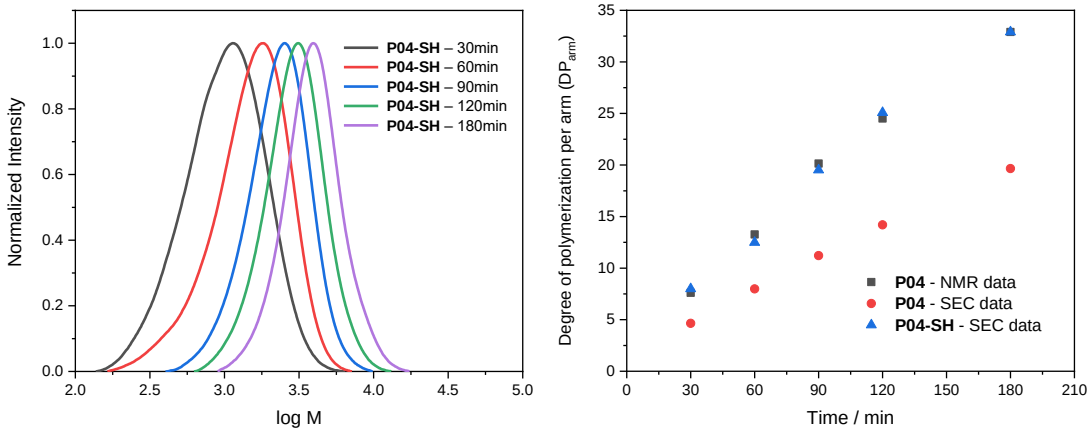

Figure S51: SEC_{THF} traces of polymer and **P04-SH** (*left*); Plot of DP_{arm} vs Time for **P04** polymerization (*right*).

8.4.8 **(P05)** Polymerization of Styrene by RAFT Agent R02

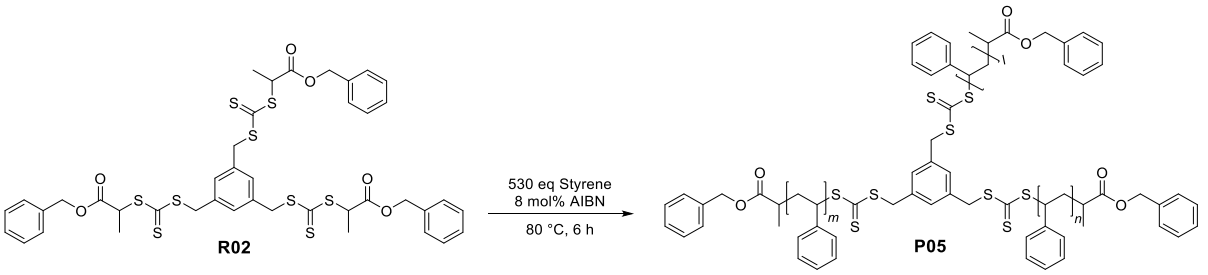

A stock solution of 2,2′-azobis(2-methylpropionitrile) (2.2 mg, 0.013 mmol) in disinhibited styrene (10.0 mL, 87 mmol) was prepared. 2.0 mL of the stock solution including styrene (2.0 mL, 17.4 mmol, 530 eq) and 2,2′-azobis(2-methylpropionitrile) (0.43 mg, 0.0026 mmol, 0.08 eq) were added to RAFT agent **R02** (31 mg, 0.033 mmol, 1.0 eq). The homogeneous mixture was sealed under argon atmosphere before being stirred at 80 °C. Samples (0.3 mL) were taken from the reaction after 1, 2, 3, 4 and 6 hours and reprecipitated in cold MeOH in order to follow **P05** polymerization by SEC_{THF} and ^{1}H-NMR analyses.

Table S5: Overview of polymer **P05** data.

Entry	Polymer	Time / h	$M_{n,^{1}H\text{-}NMR}$ / kg mol^{-1}	$M_{n,SEC/THF}$ / kg mol^{-1}	$M_{w,SEC/THF}$ / kg mol^{-1}	$Đ_{THF}$
1	P05	1	3.1	2.4	3.2	1.32
2	P05	2	5.0	3.4	4.3	1.28
3	P05	3	7.1	4.2	5.3	1.27
4	P05	4	8.2	4.9	6.3	1.29
5	P05	6	10.5	6.0	8.3	1.37

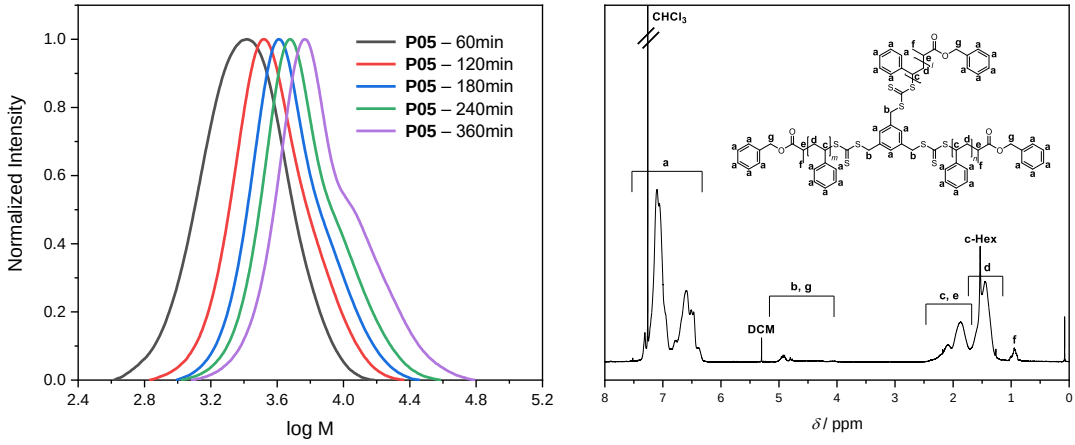

Figure S52: SEC_{THF} trace of polymer **P05** (*left*); ^{1}H-NMR spectrum of polymer **P05–6h** (*right*).

8.4.9 **(P05-SH)** Trithiocarbonate Aminolysis of P05

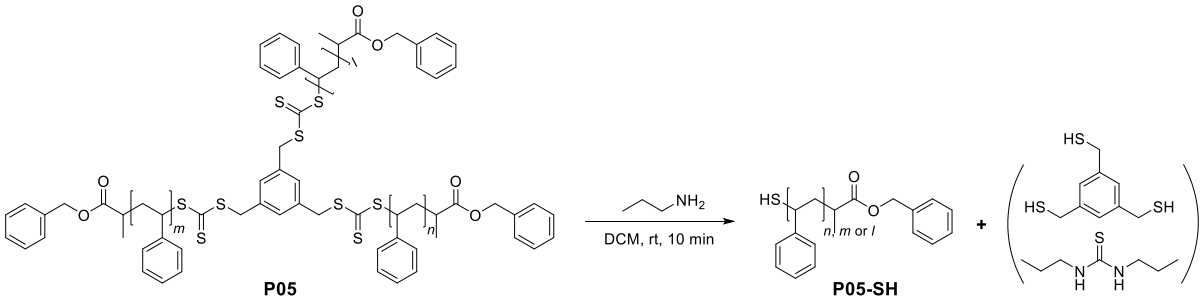

Typical procedure for each **P05** sample. A polymer sample (4.0 mg) was dissolved in DCM (0.5 mL). A large excess of *n*-propylamine (0.1 mL) was added to the yellow solution. After 10 minutes, the remaining *n*-propylamine and solvent were evaporated and the corresponding transparent solid **P05-SH** was characterized by SEC_{THF} and analysis.

Table S6: Overview of polymer **P05-SH** data.

Entry	Polymer	Time / h	$M_{n,^1H\text{-}NMR/THF}$ / kg mol^{-1}	$M_{n,SEC/THF}$ / kg mol^{-1}	$M_{w,SEC/THF}$ / kg mol^{-1}	$Đ_{THF}$
1	P05-SH	1	0.9	0.9	1.3	1.38
2	P05-SH	2	1.6	1.5	1.9	1.29
3	P05-SH	3	2.3	2.1	2.6	1.24
4	P05-SH	4	2.6	2.5	3.0	1.21
5	P05-SH	6	3.4	3.1	3.7	1.21

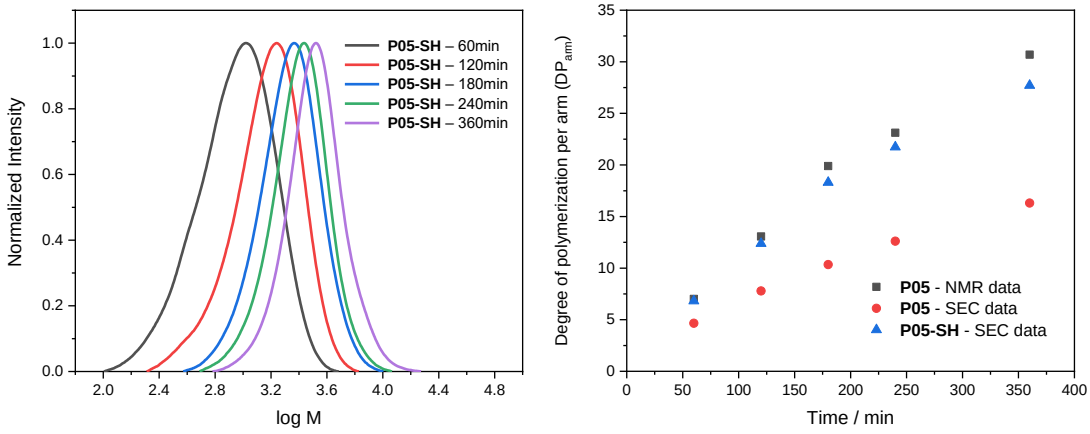

Figure S53: SEC_{THF} traces of polymer **P05-SH** (*left*); Plot of DP_{arm} vs Time for **P05** polymerization (*right*).

8.4.10 **(P06)** Polymerization of Methyl Acrylate by RAFT Agent R02

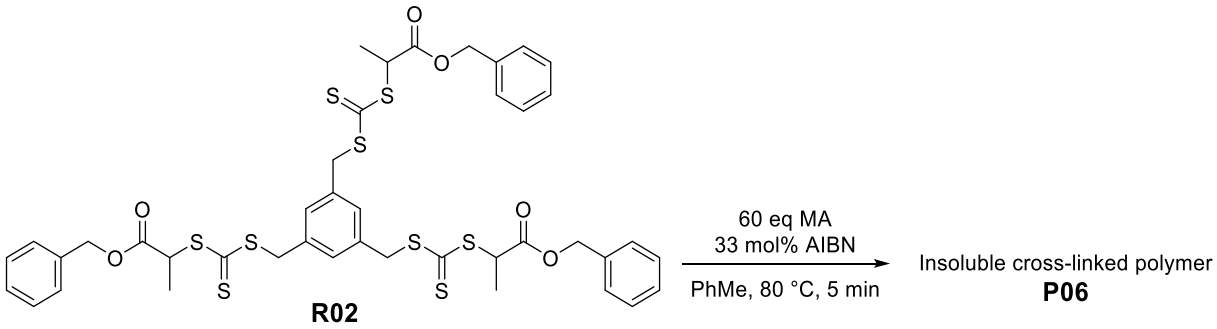

2,2′-Azobis(2-methylpropionitrile) (1.6 mg, 0.01 mmol, 0.33 eq) and RAFT agent **R02** (31 mg, 0.033 mmol, 1.0 eq) were added to 1 M disinhibited methyl acrylate (0.18 mL, 2.0 mmol, 60 eq) in toluene (0.82 mL). The homogeneous mixture was sealed under argon atmosphere before being stirred at 80 °C. After 5 minutes, the mixture became turbid and a yellow solid precipitated. The resulting cross-linked polymer **P06** was found to be totally insoluble in organic solvents and therefore no SEC_{THF} nor ^{1}H-NMR analysis was performed.

8.4.11 **(P07)** Polymerization of Methyl Acrylate by RAFT Agent R02

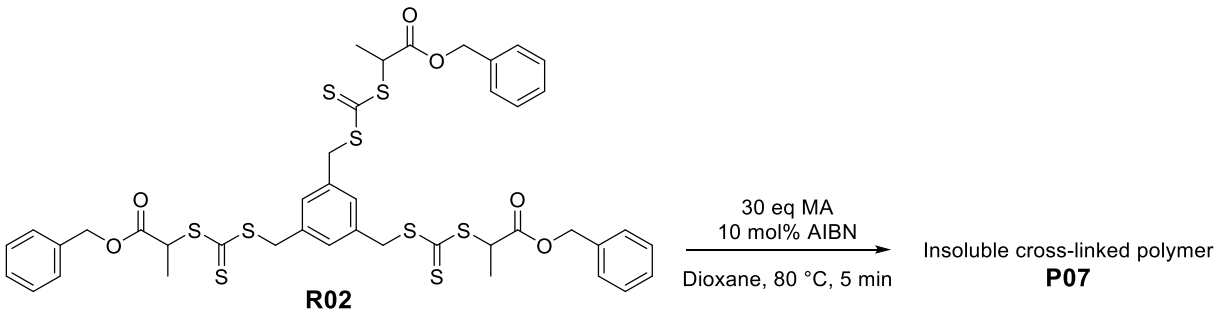

2,2′-Azobis(2-methylpropionitrile) (0.5 mg, 0.0033 mmol, 0.1 eq) and RAFT agent **R02** (31 mg, 0.033 mmol, 1.0 eq) were added to 1 M disinhibited methyl acrylate (0.09 mL, 1.0 mmol, 30 eq) in dioxane (0.82 mL). The homogeneous mixture was sealed under argon atmosphere before being stirred at 80 °C. After 5 minutes, the mixture became turbid and a yellow solid precipitated. The resulting cross-linked polymer **P07** was found to be totally insoluble in organic solvents and therefore no SEC_{THF} nor ^{1}H-NMR analysis was performed.

8.4.12 **(P08)** Polymerization of styrene by RAFT Agent R03

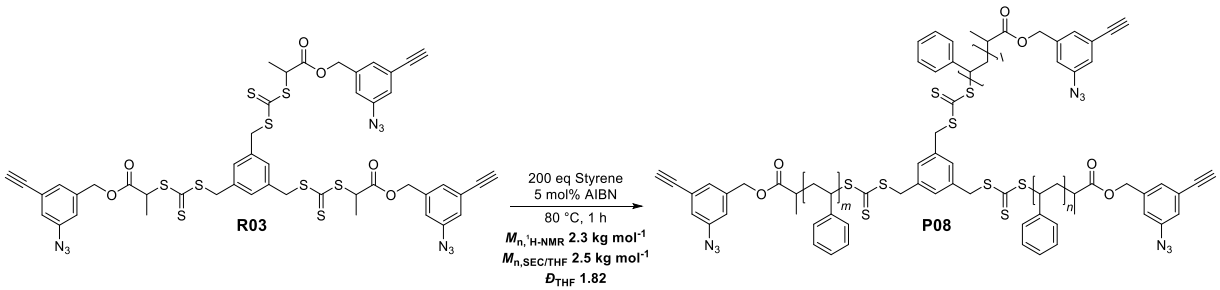

A stock solution of 2,2′-azobis(2-methylpropionitrile) (3.6 mg, 0.022 mmol) in disinhibited styrene (10.0 mL, 87 mmol) was prepared. 1.0 mL of the stock solution including styrene (1.0 mL, 8.7 mmol, 200 eq) and 2,2′-azobis(2-methylpropionitrile) (0.36 mg, 0.0022 mmol, 0.05 eq) were added to RAFT agent **R03** (49 mg, 0.0435 mmol, 1.0 eq). The homogeneous mixture was sealed under argon atmosphere before being stirred at 80 °C for 1 hour. Afterwards, the mixture was cooled down to room temperature, the remaining monomers were evaporated and the resulting polymer **P08** was characterized by SEC_{THF} analysis.

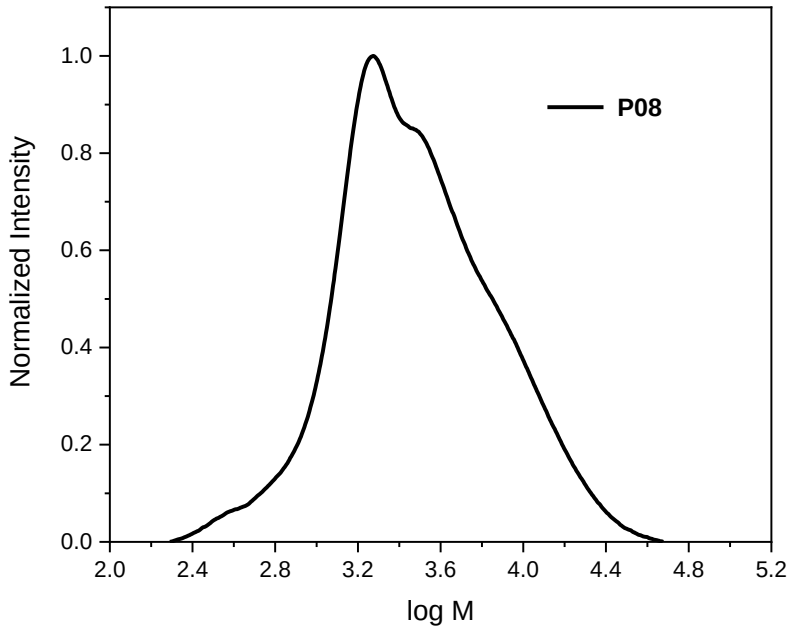

Figure S54: SEC_{THF} trace of polymer **P08**.

8.4.13 **(P08-SH)** Trithiocarbonate Aminolysis of P08

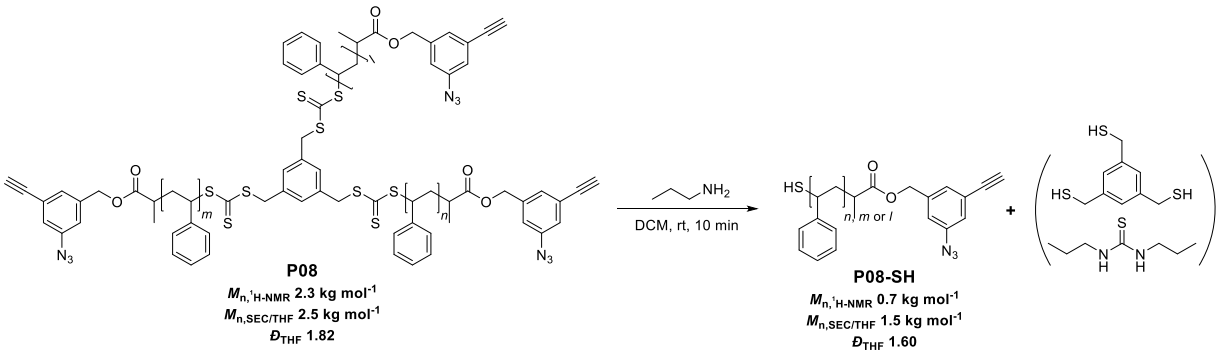

P08 (4.0 mg) was dissolved in DCM (0.5 mL). A large excess of *n*-propylamine (0.1 mL) was added to the yellow solution. After 10 minutes, the remaining *n*-propylamine and solvent were evaporated and the resulting transparent solid **P08-SH** was characterized by SEC_{THF} analysis.

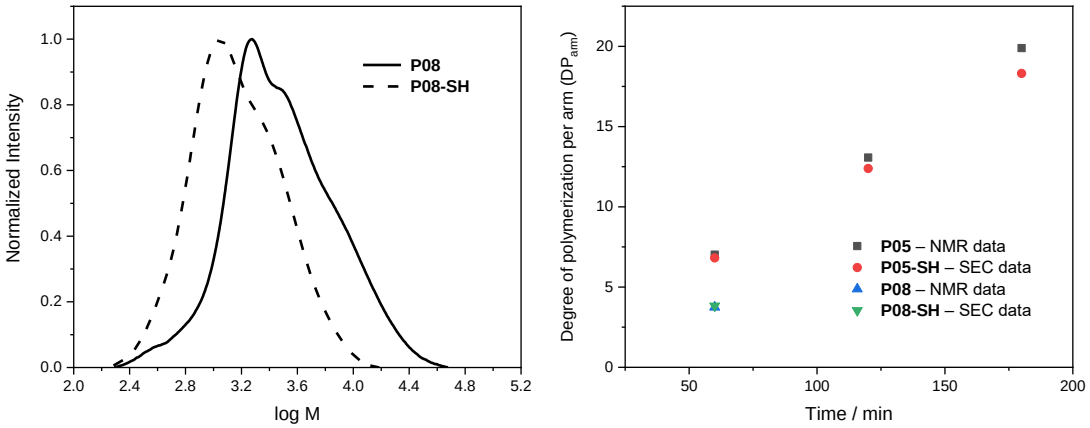

Figure S55: SEC_{THF} trace of polymers **P08** and **P08-SH** (*left*); Plot of DP_{arm} vs Time for **P08** polymerization and its comparison with **P05** values (*right*).

8.4.14 **(P09)** Polymerization of Styrene by RAFT Agent R01 and BPO/DMA as Co-initiators

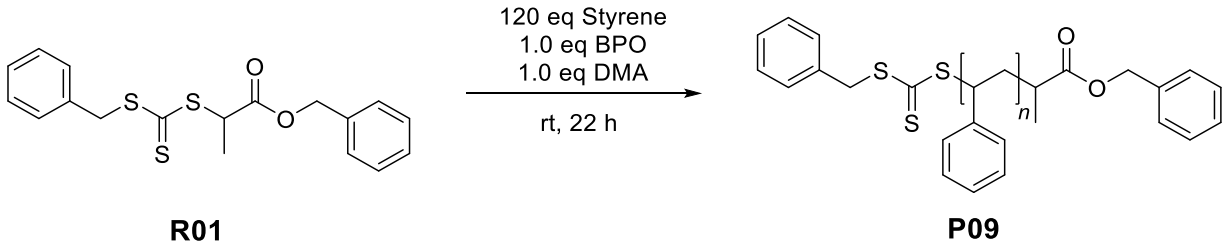

Benzoyl peroxide 75 weight% (45 mg, 0.14 mmol, 1.0 eq), *N*,*N*-dimethylaniline (17 mg, 0.14 mmol, 1.0 eq) and RAFT agent **R01** (50 mg, 0.14 mmol, 1.0 eq) were added to disinhibited styrene (2.0 mL, 17.4 mmol, 120 eq). The homogeneous mixture was sealed under argon atmosphere before being stirred at room temperature. Samples (0.3 mL) were taken from the reaction after 1, 3 and 22 hours in order to follow **P09** polymerization by SEC_{THF} analysis.

Table S7: Overview of polymer **P09** data.

Entry	Polymer name	Time / h	$M_{n,SEC/THF}$ / kg mol^{-1}	$M_{w,SEC/THF}$ / kg mol^{-1}	$Đ_{THF}$
1	P09	1	0.8	1.1	1.27
2	P09	3	1.2	1.5	1.32
3	P09	22	1.6	2.2	1.39

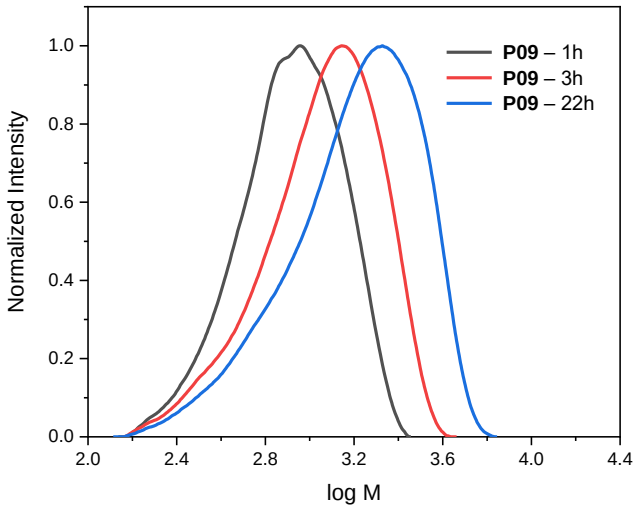

Figure S56: SEC_{THF} traces of polymer **P09**.

8.4.15 **(P10)** Polymerization of Styrene by RAFT Agent R02 and V-70 as Initiator

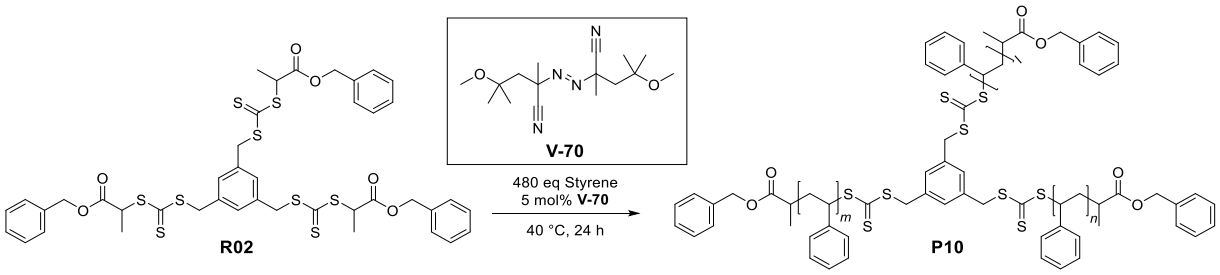

A stock solution of 2,2'-azobis(4-methoxy-2,4-dimethylvaleronitrile) (2.5 mg, 0.0081 mmol) in disinhibited styrene (9.0 mL, 78 mmol) was prepared. 3.0 mL of the stock solution including styrene (3.0 mL, 26 mmol, 480 eq) and 2,2'-azobis(4-methoxy-2,4-dimethylvaleronitrile) (0.83 mg, 0.0027 mmol, 0.05 eq) were added to RAFT agent **R02** (50 mg, 0.054 mmol, 1.0 eq). The homogeneous mixture was sealed under argon atmosphere before being stirred at 40 °C. Samples (0.3 mL) were taken from the reaction after 2, 5, 8 and 24 hours and reprecipitated in cold MeOH in order to follow **P10** polymerization by SEC_{THF} and ^{1}H-NMR analyses.

Table S8: Overview of polymer **P10** data.

Entry	Polymer	Time / h	$M_{n,^1H\text{-}NMR}$ / kg mol^{-1}	$M_{n,SEC/THF}$ / kg mol^{-1}	$M_{w,SEC/THF}$ / kg mol^{-1}	$Đ_{THF}$
1	P10	2	2.5	1.9	2.6	1.43
2	P10	5	3.5	2.7	3.6	1.35
3	P10	8	4.5	3.3	4.3	1.31
4	P10	24	5.5	4.3	5.7	1.33

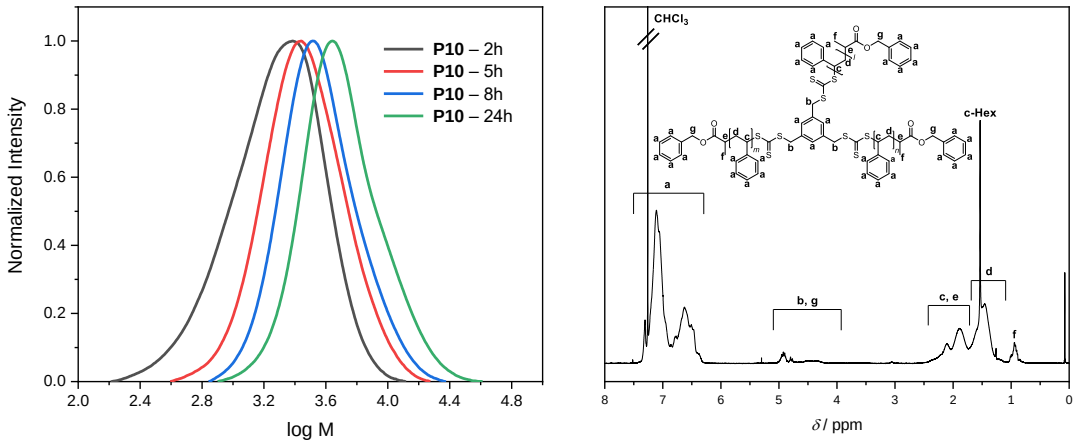

Figure S57: SEC_{THF} traces of polymer **P10** (*left*); ^{1}H-NMR spectrum of polymer **P10–24h** (*right*).

8.4.16 **(P10-SH)** Trithiocarbonate Aminolysis of P10

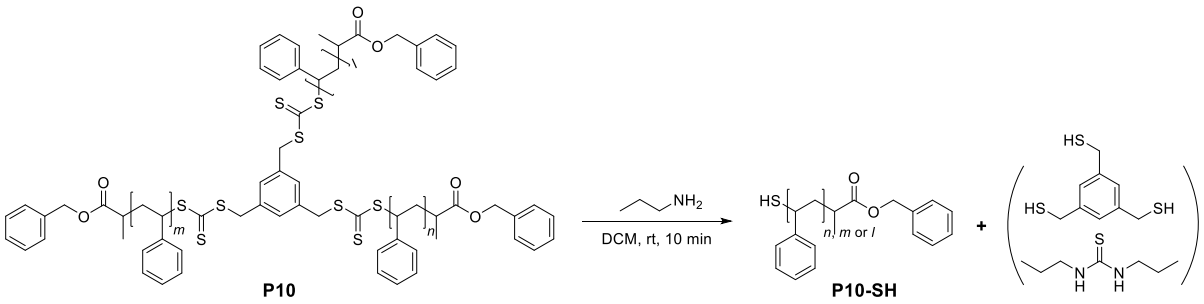

Typical procedure for each **P10** sample. A polymer sample (4.0 mg) was dissolved in DCM (0.5 mL). A large excess of *n*-propylamine (0.1 mL) was added to the yellow solution. After 10 minutes, the remaining *n*-propylamine and solvent were evaporated and the corresponding transparent solid **P10-SH** was characterized by SEC_{THF} analysis.

Table S9: Overview of polymer **P10 -SH** data.

Entry	Polymer	Time / h	$M_{n,^1H\text{-}NMR}$ / kg mol^{-1}	$M_{n,SEC/THF}$ / kg mol^{-1}	$M_{w,SEC/THF}$ / kg mol^{-1}	$Đ_{THF}$
1	P10-SH	2	0.7	0.6	1.1	1.70
2	P10-SH	5	1.0	1.1	1.6	1.45
3	P10-SH	8	1.4	1.4	1.9	1.33
4	P10-SH	24	1.7	2.1	2.7	1.30

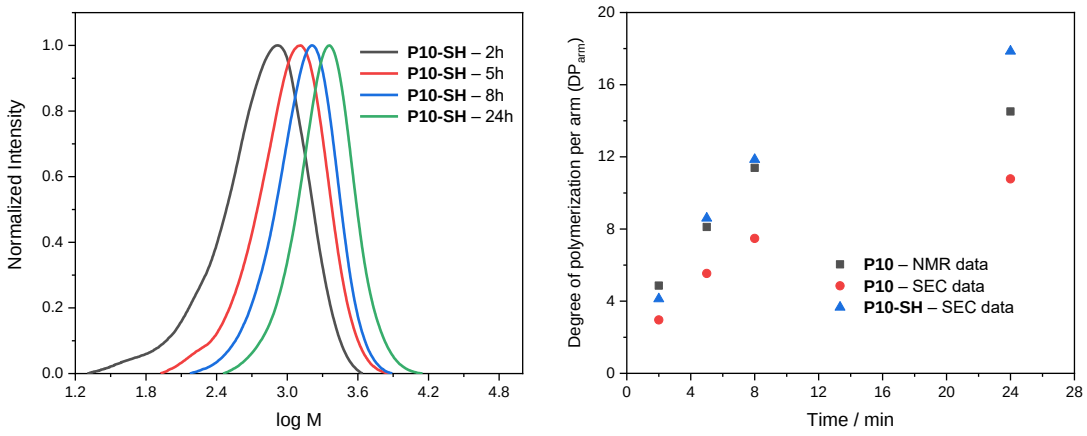

Figure S58: SEC_{THF} traces of polymer **P10-SH** (*left*); Plot of DP_{arm} vs Time for **P10** polymerization (*right*).

8.4.17 **(P11)** Polymerization of Styrene by RAFT Agent R04 and V-70 as Initiator

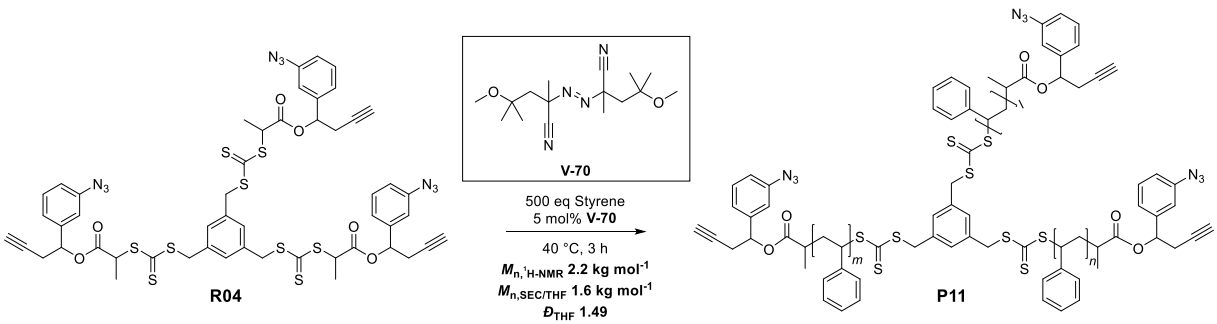

A stock solution of 2,2'-azobis(4-methoxy-2,4-dimethylvaleronitrile) (3.4 mg, 0.0081 mmol) in disinhibited styrene (12.8 mL, 111 mmol) was prepared. 1.28 mL of the stock solution including styrene (1.28 mL, 11.1 mmol, 500 eq) and 2,2'-azobis(4-methoxy-2,4-dimethylvaleronitrile) (0.34 mg, 0.0011 mmol, 0.05 eq) were added to RAFT agent **R04** (26 mg, 0.022 mmol, 1.0 eq). The homogeneous mixture was sealed under argon atmosphere before being stirred at 40 °C for 3 hours. Afterwards, the mixture was cooled down to room temperature, the remaining monomers were evaporated and the resulting polymer **P11** (47 mg) was characterized by SEC_{THF} and FT-IR analyses.

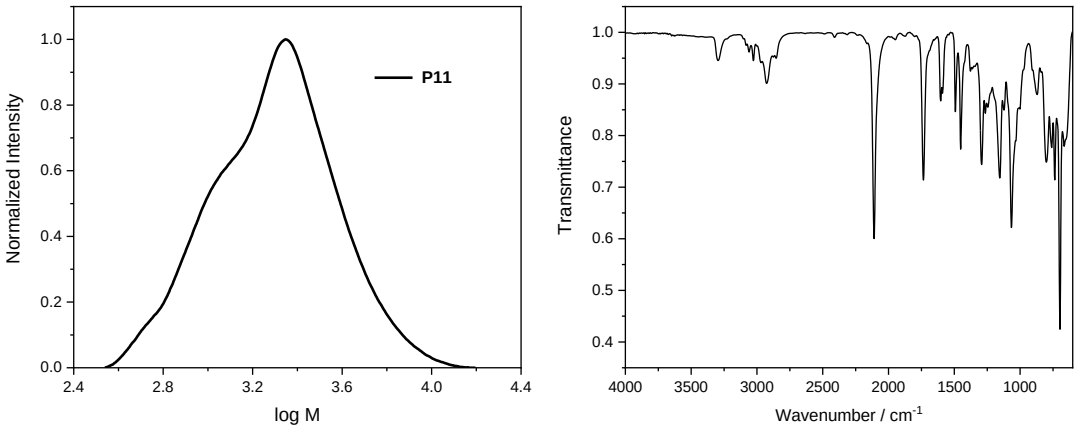

Figure S59: SEC_{THF} trace of polymer **P11** (*left*); FT-IR spectra of polymer **P11** (*right*), **IR (ATR, cm^{-1})** 3296, 2926, 2110, 1735, 1603, 1590, 1492, 1452, 1378, 1292, 1264, 1245, 1154, 1122, 1066, 870, 800, 760, 737, 697, 665.

8.4.18 **(P11-SH)** Trithiocarbonate Aminolysis of P11

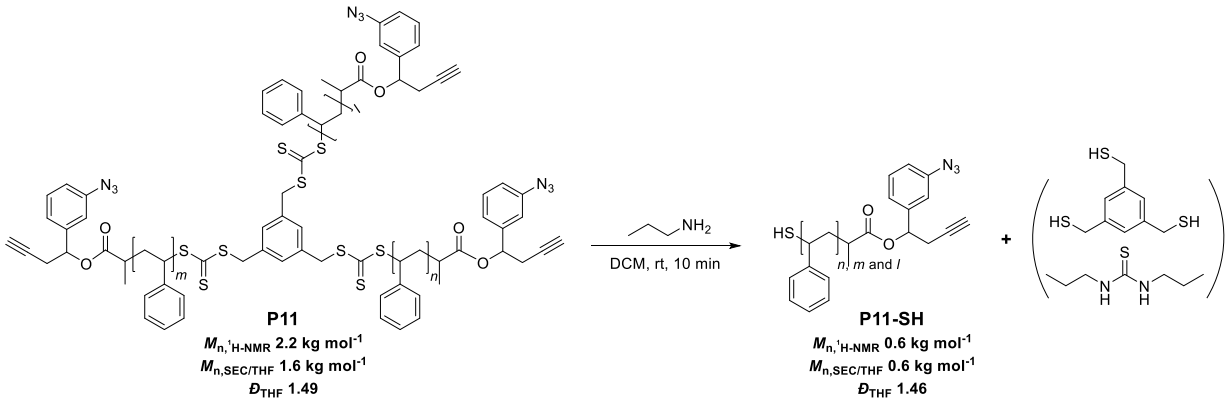

P11 (4.0 mg) was dissolved in DCM (0.5 mL). A large excess of *n*-propylamine (0.1 mL) was added to the yellow solution. After 10 minutes, the remaining *n*-propylamine and solvent were evaporated and the resulting transparent solid **P11-SH** was characterized by SEC_{THF} analysis.

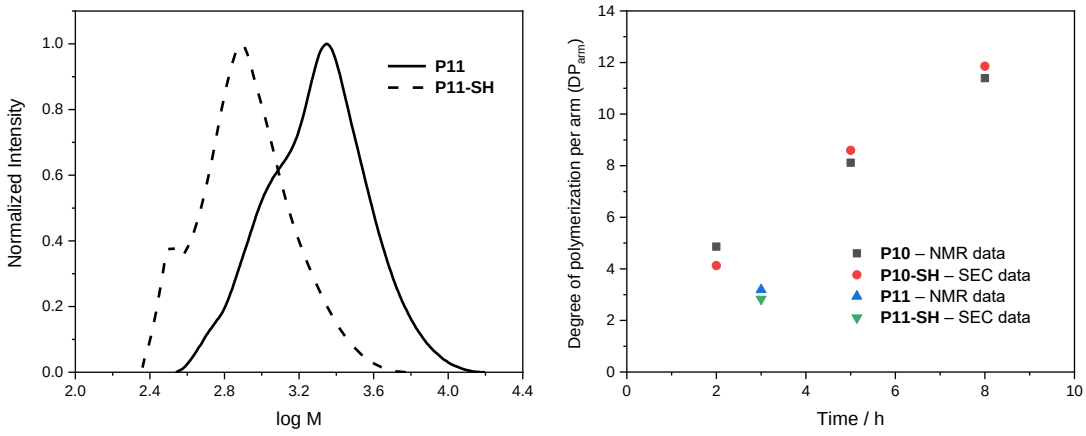

Figure S60: SEC_{THF} traces of polymers **P11** and **P11-SH** (*left*); Plot of DP_{arm} vs Time for **P11** polymerization (*right*).

8.4.19 **(P11-C)** *Cage*-shaped Polymer Synthesis *via* CuAAC Reaction from P11

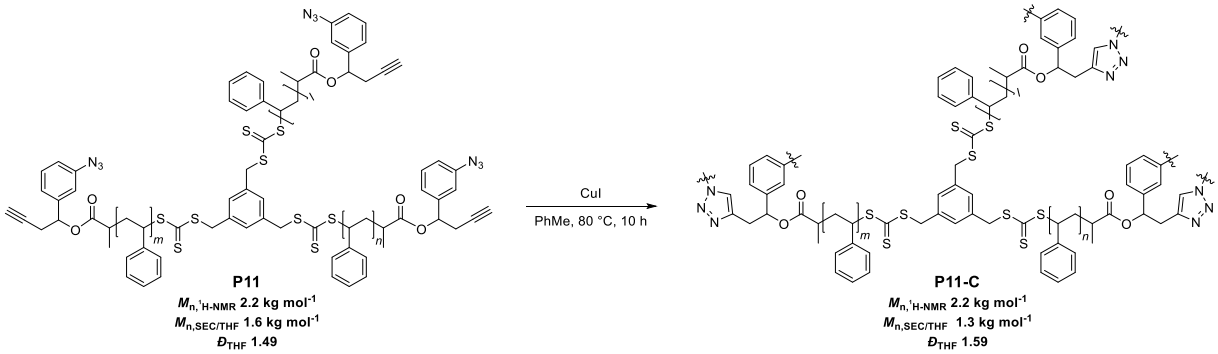

Copper(I) iodide (2.0 g, 10.0 g L^{-1}, 53 mmol L^{-1}) and redistilled toluene (200 mL) were added to a 500 mL round flask. The suspension was sealed under argon atmosphere before being preheated at 80 °C. A solution of **P11** (42 mg) in redistilled toluene (20 mL) was added to the heated mixture over 8 hours (2.5 mL h^{-1}) *via* a syringe pump. Then, the solution was stirred for another 2 hours at 80 °C. Afterwards, the solvent was removed under reduced pressure and the crude material was filtered off over neutral aluminum oxide with THF as eluent. The resulting yellow polymer **P11-C** (62 mg) was characterized by SEC$_{THF}$ and FT-IR analyses.

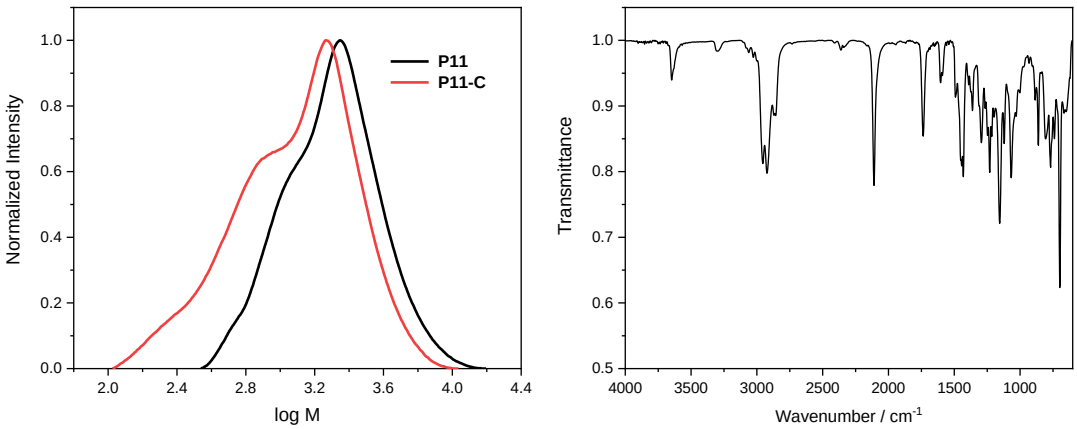

Figure S61: SEC$_{THF}$ trace of polymers **P11** and **P11-C** (*left*); FT-IR spectra of polymer **P11-C** (*right*), **IR (ATR, cm^{-1})** 3647, 3298, 2955, 2923, 2857, 2110, 1736, 1443, 1431, 1361, 1294, 1231, 1215, 1155, 1120, 1068, 861, 806, 768, 739, 698, 666.

8.4.20 **(P11-C-SH)** Trithiocarbonate Aminolysis of P11-C

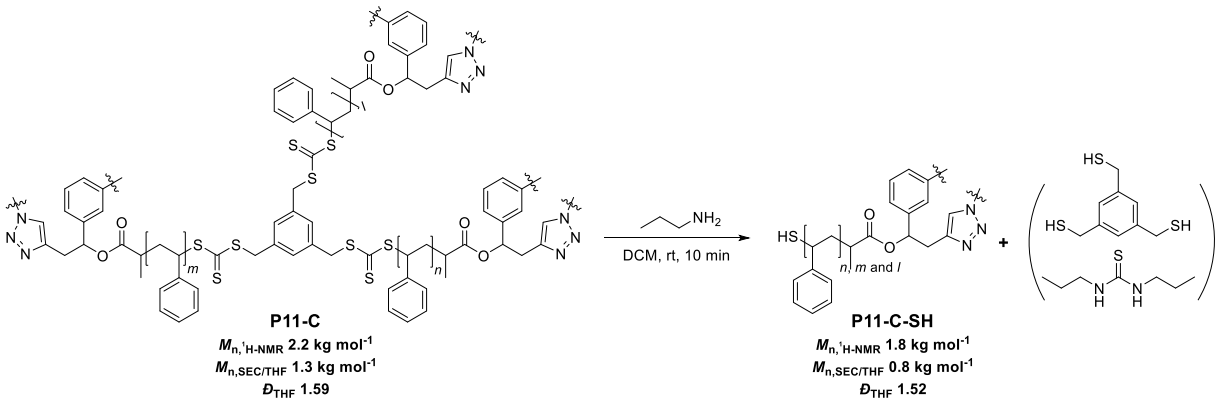

P11-C (4.0 mg) was dissolved in DCM (0.5 mL). A large excess of *n*-propylamine (0.1 mL) was added to the yellow solution. After 10 minutes, the remaining *n*-propylamine and solvent were evaporated and the resulting transparent solid **P11-C-SH** was characterized by SEC_{THF} analysis.

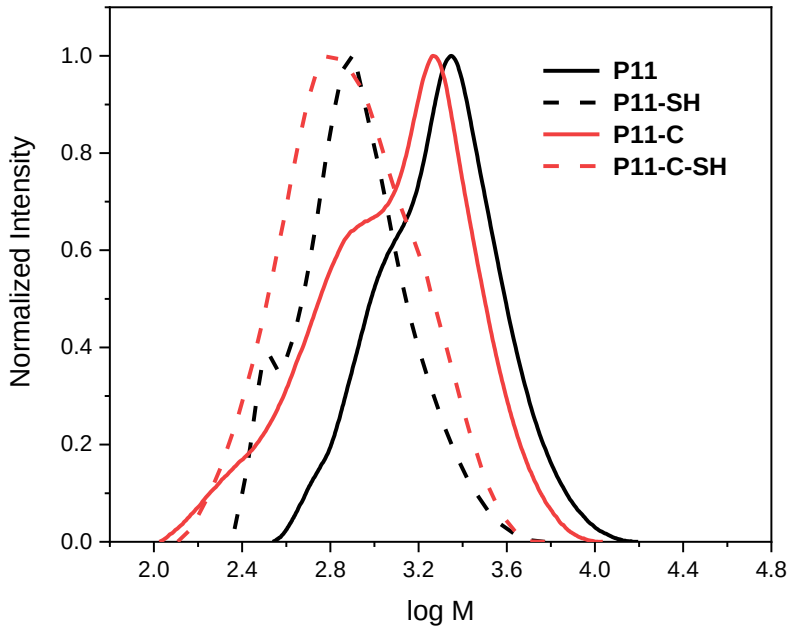

Figure S62: SEC_{THF} traces of polymers **P11**, **P11-SH**, **P11-C** and **P11-C-SH**.

8.4.21 **(P12)** Polymerization of Styrene by RAFT Agent R05 and V-70 as Initiator

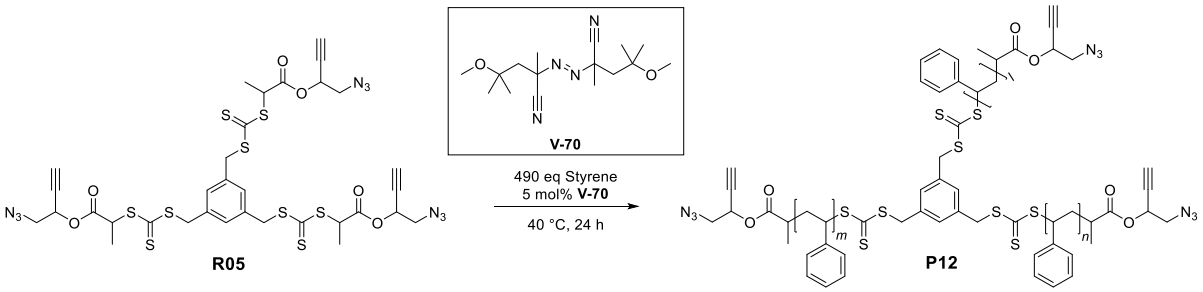

A stock solution of 2,2'-azobis(4-methoxy-2,4-dimethylvaleronitrile) (2.7 mg, 0.0088 mmol) in disinhibited styrene (10.0 mL, 87 mmol) was prepared. 1.8 mL of the stock solution including styrene (1.8 mL, 15.7 mmol, 490 eq) and 2,2'-azobis(4-methoxy-2,4-dimethylvaleronitrile) (0.49 mg, 0.0016 mmol, 0.05 eq) were added to RAFT agent **R05** (30 mg, 0.032 mmol, 1.0 eq). The homogeneous mixture was sealed under argon atmosphere before being stirred at 40 °C. Samples (0.3 mL) were taken from the reaction after 2, 5, 8 and 24 hours and reprecipitated in cold MeOH in order to follow **P12** polymerization by SEC_{THF} analysis.

Table S10: Overview of polymer **P12** data.

Entry	Polymer	Time / h	$M_{n,^1H\text{-}NMR}$ / kg mol^{-1}	$M_{n,SEC/THF}$ / kg mol^{-1}	$M_{w,SEC/THF}$ / kg mol^{-1}	$Đ_{THF}$
1	P12	2	2.3	2.3	3.8	1.64
2	P12	5	2.6	2.5	4.1	1.64
3	P12	8	3.2	2.9	4.5	1.57
4	P12	24	3.5	2.9	5.4	1.83

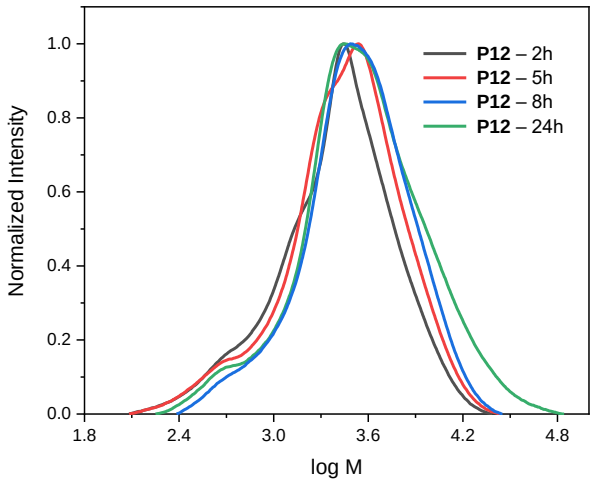

Figure S63: SEC_{THF} traces of polymer **P12**.

8.4.22 **(P12-SH)** Trithiocarbonate Aminolysis of P12

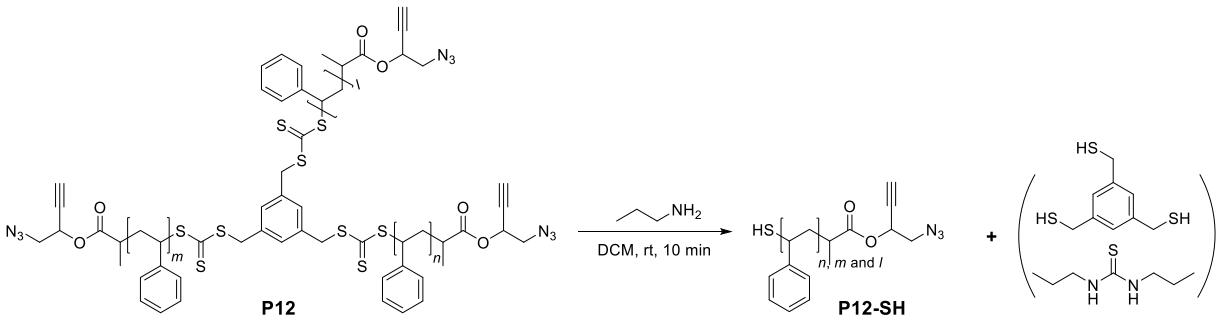

Typical procedure for each **P12** sample. A polymer sample (4.0 mg) was dissolved in DCM (0.5 mL). A large excess of *n*-propylamine (0.1 mL) was added to the yellow solution. After 10 minutes, the remaining *n*-propylamine and solvent were evaporated and the corresponding transparent solid **P12-SH** was characterized by SEC_{THF} analysis.

Table S11: Overview of polymer **P12** data.

Entry	Polymer	Time / h	$M_{n,^1H\text{-}NMR}$ / kg mol^{-1}	$M_{n,SEC/THF}$ / kg mol^{-1}	$M_{w,SEC/THF}$ / kg mol^{-1}	$Đ_{THF}$
1	P12-SH	2	0.7	0.9	1.2	1.33
2	P12-SH	5	0.8	1.1	1.4	1.34
3	P12-SH	8	1.0	1.2	1.6	1.30
4	P12-SH	24	1.1	1.6	2.2	1.41

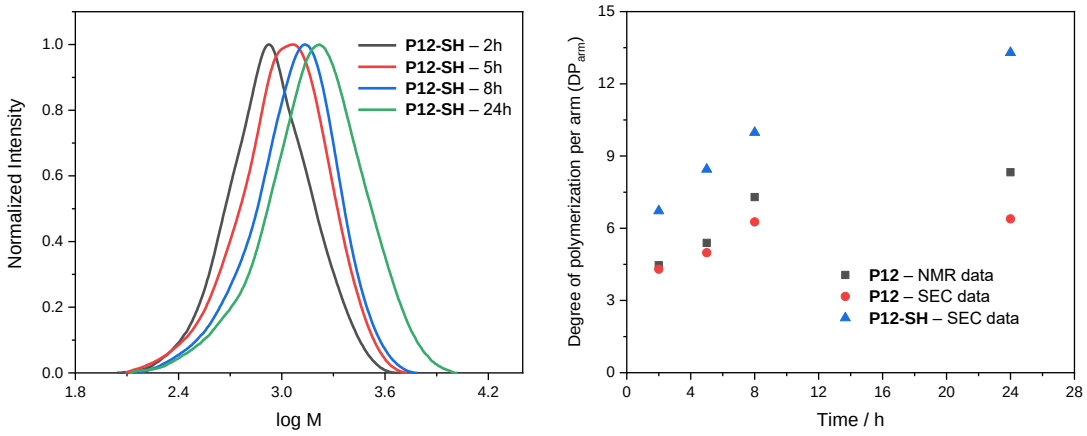

Figure S64: SEC_{THF} traces of polymer **P12-SH** (*left*); Plot of DP_{arm} vs Time for **P12** polymerization (*right*).

8.4.23 **(P13)** Polymerization of Styrene by RAFT Agent R06 and ACVA as Initiator

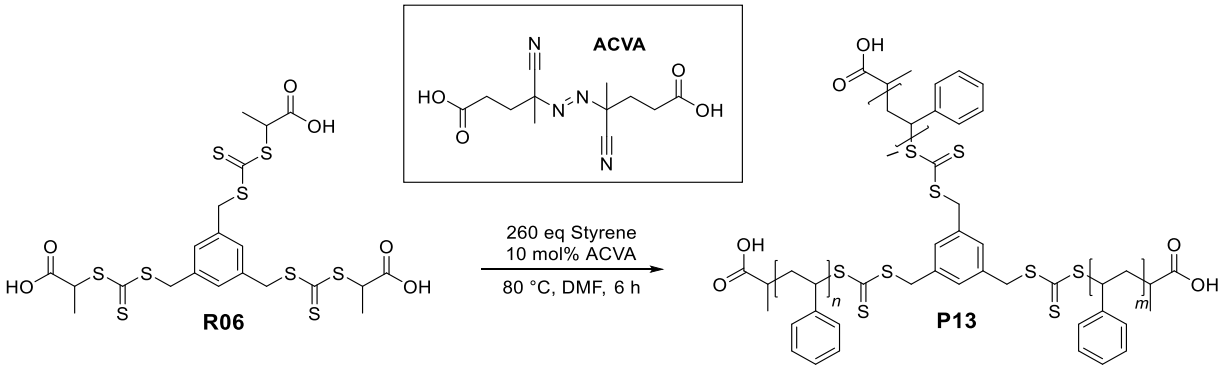

4,4-Azobis(4-cyanovaleric acid) (1.4 mg, 0.005 mmol, 0.1 eq) and RAFT agent **R06** (33 mg, 0.05 mmol, 1.0 eq) were added to disinhibited styrene (1.5 mL, 13.0 mmol, 260 eq) and DMF (0.5 mL). The homogeneous mixture was sealed under argon atmosphere before being stirred at 80 °C. Samples (0.3 mL) were taken from the reaction after 1, 2, 3, 4 and 6 hours and reprecipitated in cold MeOH in order to follow **P13** polymerization by SEC_{THF} and ^{1}H-NMR analyses.

Table S12: Overview of polymer **P13** data.

Entry	Polymer	Time / h	$M_{n,^{1}H\text{-}NMR}$ / kg mol^{-1}	$M_{n,SEC/THF}$ / kg mol^{-1}	$M_{w,SEC/THF}$ / kg mol^{-1}	$Đ_{THF}$
1	P13	1	2.2	1.3	1.6	1.61
2	P13	2	2.8	2.1	2.9	1.36
3	P13	3	3.5	2.5	3.4	1.35
4	P13	4	3.9	3.0	3.9	1.30
5	P13	6	4.5	3.5	4.5	1.31

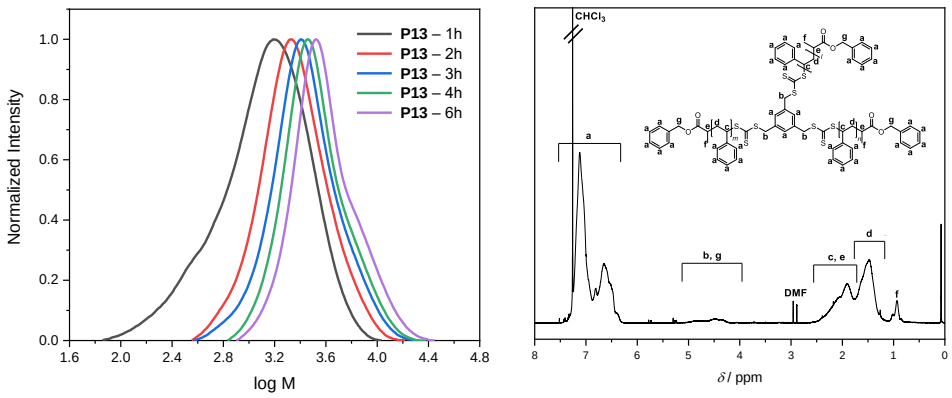

Figure S65: SEC_{THF} traces of polymer **P13** (*left*); ^{1}H-NMR spectrum of polymer **P13–6h** (*right*).

8.4.24 **(P13-SH)** Trithiocarbonate Aminolysis of P13

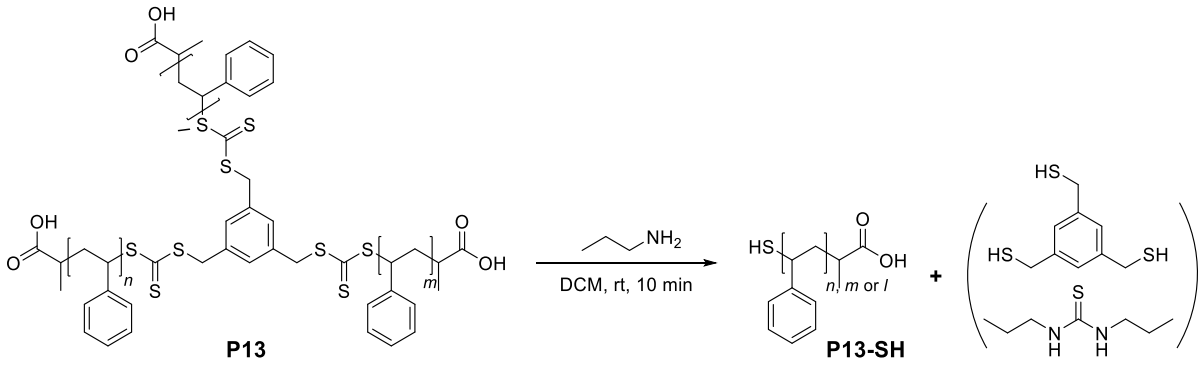

Typical procedure for each **P13** sample. A polymer sample (4.0 mg) was dissolved in DCM (0.5 mL). A large excess of *n*-propylamine (0.1 mL) was added to the yellow solution. After 10 minutes, the remaining *n*-propylamine and solvent were evaporated and the corresponding transparent solid **P13-SH** was characterized by SEC_{THF} analysis.

Table S13: Overview of polymer **P13-SH** data.

Entry	Polymer	Time / h	$M_{n,^1H\text{-}NMR}$ / kg mol^{-1}	$M_{n,SEC/THF}$ / kg mol^{-1}	$M_{w,SEC/THF}$ / kg mol^{-1}	$Đ_{THF}$
1	P13-SH	1	0.6	1.1	1.7	1.57
2	P13-SH	2	0.8	1.2	1.8	1.50
3	P13-SH	3	1.0	1.4	2.0	1.44
4	P13-SH	4	1.2	1.6	2.2	1.40
5	P13-SH	6	1.4	1.8	2.3	1.27

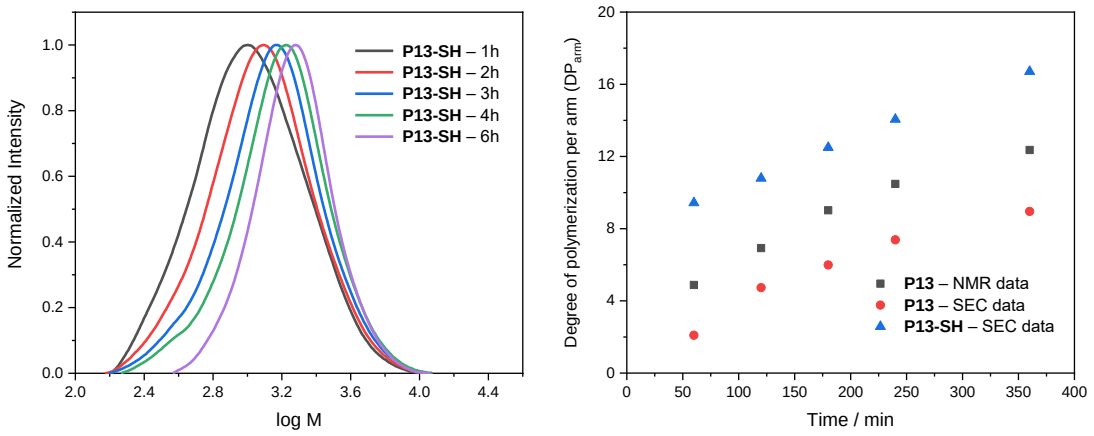

Figure S66: SEC_{THF} traces of polymer **P13-SH** (*left*); Plot of DP_{arm} vs Time for **P13** polymerization (*right*).

8.5 Small Molecules Synthesis – Project Part II

8.5.1 **(C17)** Ethyl 3-Amino-5-bromobenzoate

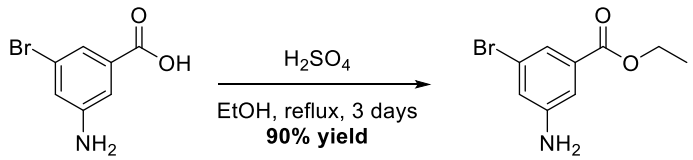

C17

3-Amino-5-bromobenzoic acid (5.00 g, 23.15 mmol, 1.0 eq) was dissolved in EtOH (100 mL) and sulfuric acid (2 mL). The mixture was heated at reflux temperature for 3 days. Afterwards, the resulting mixture was quenched with 1 M NaOH 50 mL) and brine (20 mL). The aqueous phase was then extracted with DCM (3 × 50 mL). The organic fractions were collected, dried over $MgSO_4$ and the solvent was removed under reduced pressure in order to give without further purification **C17** as a yellow solid. **(5.09 g, 20.85 mmol, 90% yield)**

^{1}H NMR (400 MHz, DMSO) δ 7.16 (dd, J = 2.1, 1.5 Hz, 1H), 7.13 – 7.12 (m, 1H), 6.95 (t, J = 2.0 Hz, 1H), 5.73 (s, 2H), 4.26 (q, J = 7.1 Hz, 2H), 1.29 (t, J = 7.1 Hz, 3H).
^{13}C NMR (101 MHz, DMSO) δ 164.96 (s), 150.75 (s), 132.31 (s), 122.01 (s), 119.68 (s), 117.90 (s), 113.21 (s), 60.85 (s), 14.09 (s).

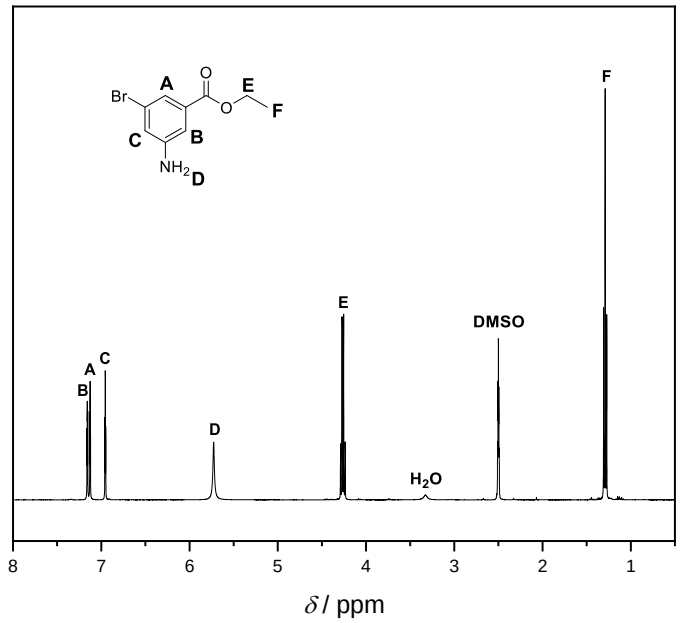

Figure S67: ^{1}H-NMR spectrum of **C17**, **^{1}H NMR (400 MHz, DMSO)** δ 7.16 (dd, J = 2.1, 1.5 Hz, 1H), 7.13 – 7.12 (m, 1H), 6.95 (t, J = 2.0 Hz, 1H), 5.73 (s, 2H), 4.26 (q, J = 7.1 Hz, 2H), 1.29 (t, J = 7.1 Hz, 3H).

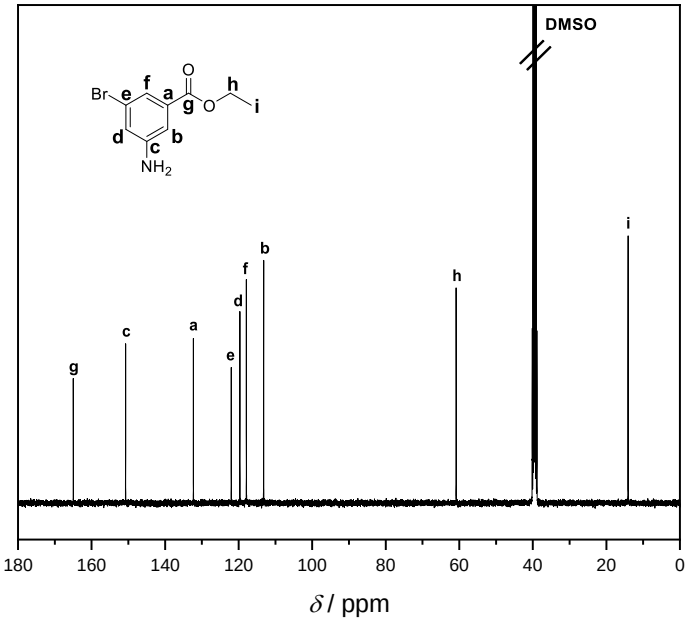

Figure S68: ^{13}C-NMR spectrum of **C17**, **^{13}C NMR (101 MHz, DMSO)** δ 164.96 (s), 150.75 (s), 132.31 (s), 122.01 (s), 119.68 (s), 117.90 (s), 113.21 (s), 60.85 (s), 14.09 (s).

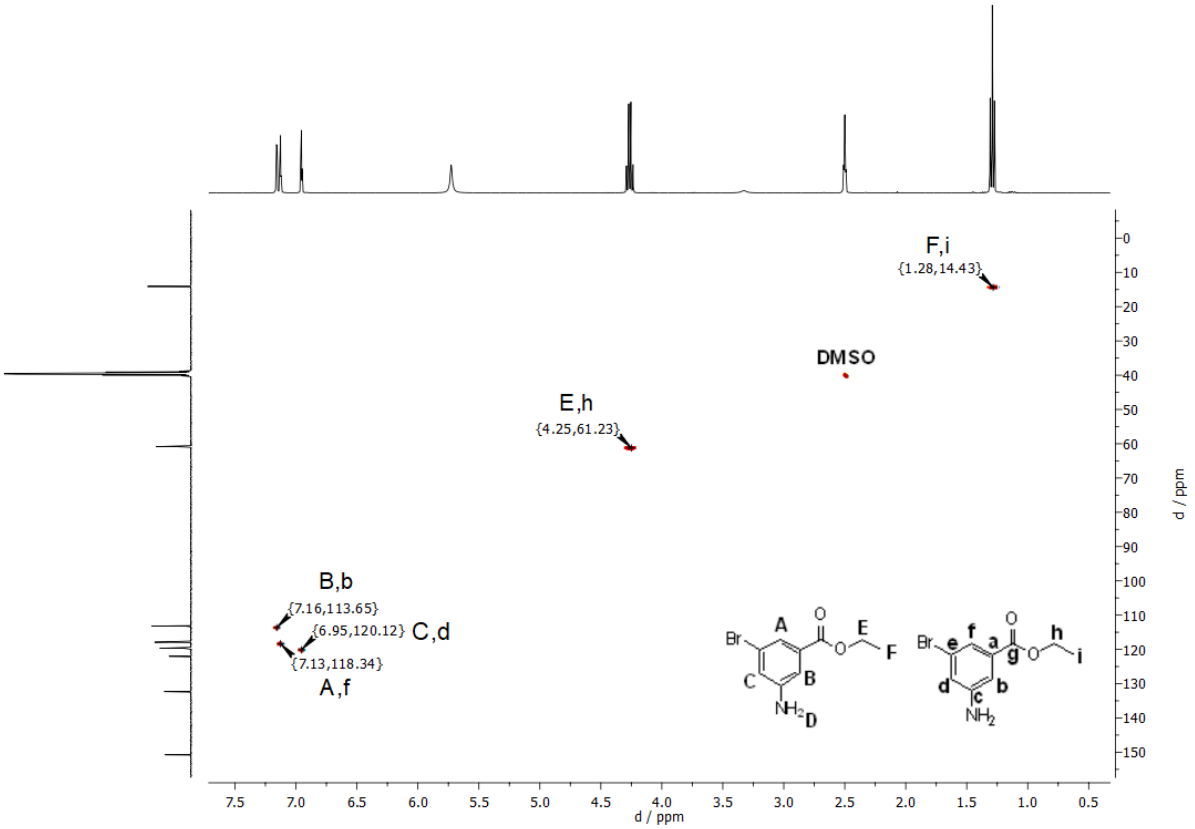

Figure S69: ^{1}H-^{13}C HSQC spectrum of **C17**, **^{1}H NMR 400 MHz, ^{13}C NMR 101 MHz, DMSO *δ***

8.5.2 **(C18)** Ethyl 3-Amino-5-((trimethylsilyl)ethynyl) benzoate

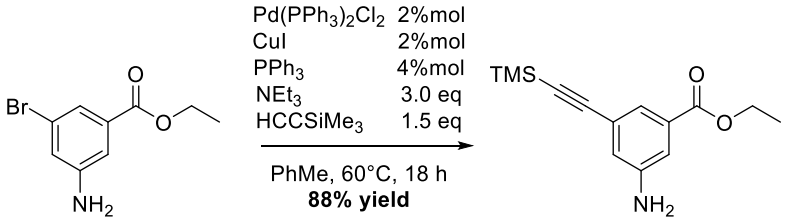

C17 **C18**

Ethyl 3-amino-5-bromobenzoate **C17** (5.09 g, 20.85 mmol, 1.0 eq), bis(triphenylphosphine) palladium(II) dichloride (295 mg, 0.42 mmol, 0.02 eq), copper(I) iodide (80 mg, 0.42 mmol, 0.02 eq), triphenylphosphine (220 mg, 0.84 mmol, 0.04 eq) were dissolved in dry toluene (20 mL), triethylamine (8.8 mL, 63 mmol, 3.0 eq) and ethynyltrimethylsilane (4.3 mL, 31.3 mmol, 1.5 eq) under argon atmosphere. Then, the mixture was heated for 18 hours at 60 °C. Afterwards, the reaction mixture was cooled down to room temperature and quenched with water (50 mL). The aqueous phase was extracted with DCM (3 × 50 mL). The organic fractions were collected, dried over magnesium sulfate and the solvent was removed under reduced pressure. The crude material was purified by flash chromatography (silica, EtOAc / *c*-Hex, 1:10) to (silica, MeOH / EtOAc / *c*-Hex, 1:4:5) in order to obtain **C18** as an orange solid. **(4.80 g, 18.36 mmol, 88% yield)**

^{1}H NMR (400 MHz, DMSO) ***δ*** 7.19 (dd, *J* = 2.3, 1.6 Hz, 1H), 7.09 (t, *J* = 1.5 Hz, 1H), 6.85 (dd, *J* = 2.3, 1.5 Hz, 1H), 5.57 (s, 2H), 4.26 (q, *J* = 7.1 Hz, 2H), 1.29 (t, *J* = 7.1 Hz, 3H), 0.26 – 0.17 (m, 9H).
^{13}C NMR (101 MHz, DMSO) ***δ*** 165.41 (s), 149.23 (s), 130.97 (s), 122.78 (s), 120.18 (s), 119.14 (s), 114.78 (s), 104.94 (s), 93.44 (s), 60.68 (s), 14.11 (s), -0.15 (s).

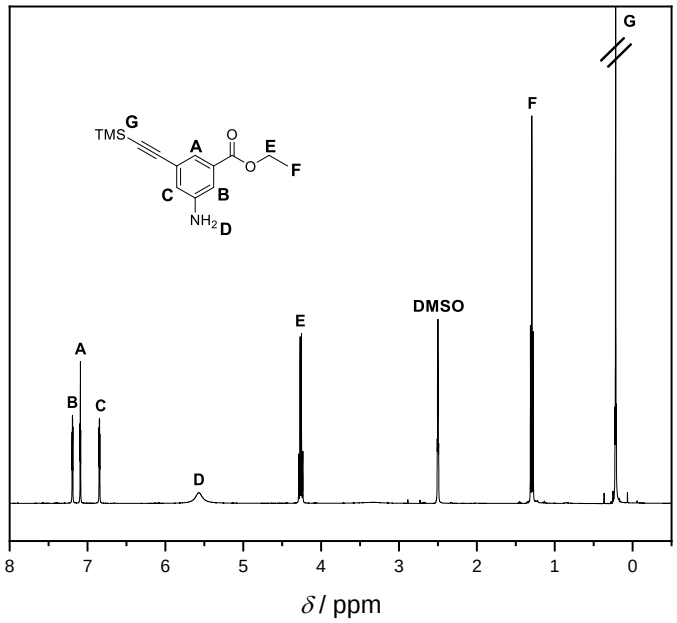

Figure S70: ^{1}H-NMR spectrum of **C18**, **^{1}H NMR (400 MHz, DMSO)** δ 7.19 (dd, J = 2.3, 1.6 Hz, 1H), 7.09 (t, J = 1.5 Hz, 1H), 6.85 (dd, J = 2.3, 1.5 Hz, 1H), 5.57 (s, 2H), 4.26 (q, J = 7.1 Hz, 2H), 1.29 (t, J = 7.1 Hz, 3H), 0.26 – 0.17 (m, 9H).

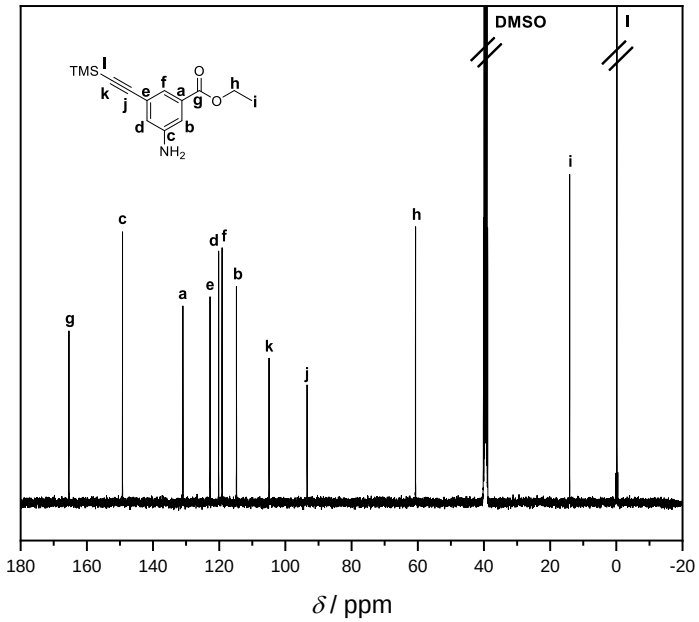

Figure S71: ^{13}C-NMR spectrum of **C18**, **^{13}C NMR (101 MHz, DMSO)** δ 165.41 (s), 149.23 (s), 130.97 (s), 122.78 (s), 120.18 (s), 119.14 (s), 114.78 (s), 104.94 (s), 93.44 (s), 60.68 (s), 14.11 (s), -0.15 (s).

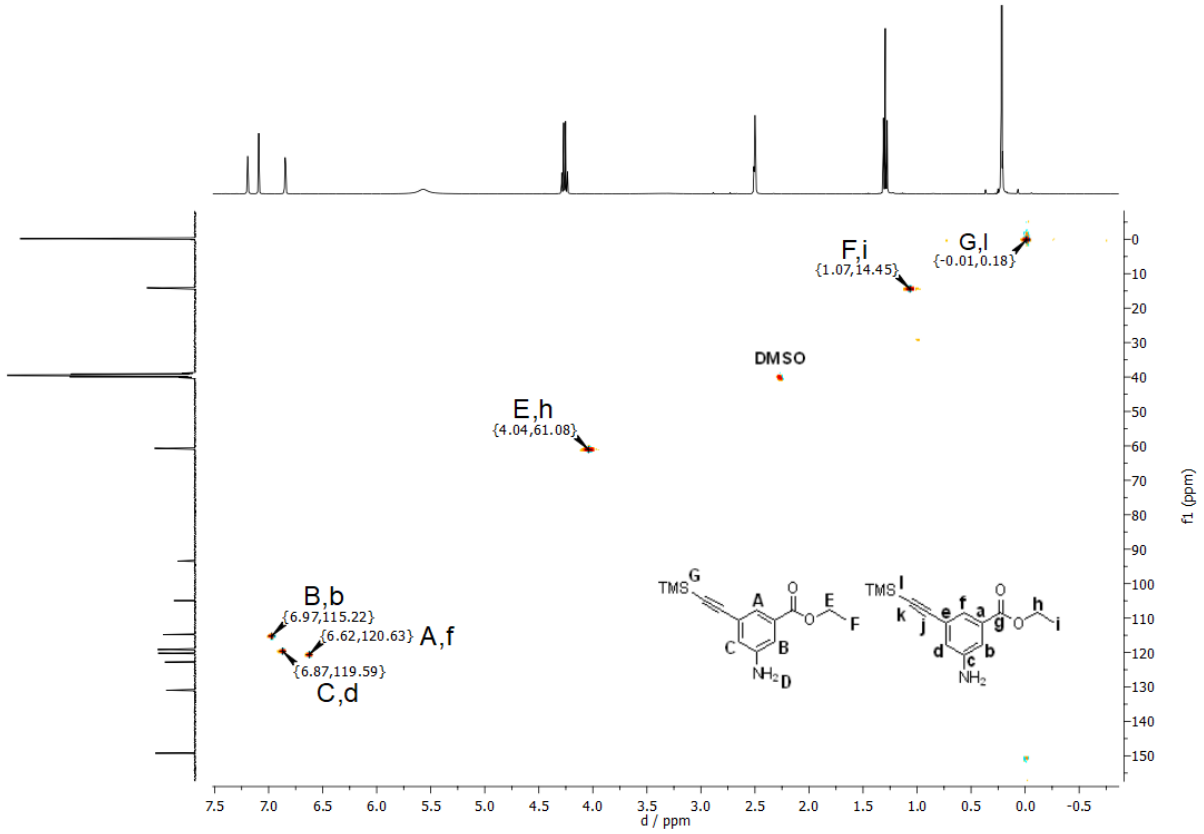

Figure S72: ^{1}H-^{13}C HSQC spectrum of **C18**, **^{1}H NMR 400 MHz, ^{13}C NMR 101 MHz, DMSO δ**

8.5.3 **(C19)** 3-Amino-5-ethynylbenzoic Acid

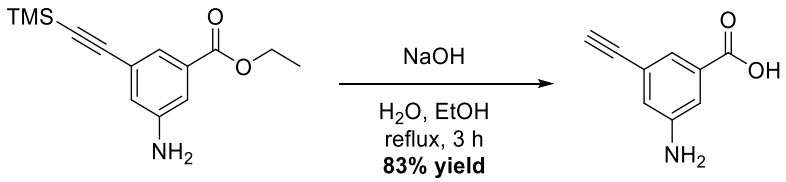

C18 **C19**

Ethyl 3-amino-5-((trimethylsilyl)ethynyl)benzoate **C18** (4.80 g, 18.36 mmol, 1.0 eq) was dissolved in 3 M NaOH (40 mL) and EtOH (10 mL). The mixture was heated at reflux temperature for 3 hours. Afterwards, the resulting mixture was quenched with 1 M HCl until a pH < 2 was reached and the aqueous phase was extracted with MeOH / EtOAc (1:1) (6 x 50 mL). The organic fractions were collected, dried over $MgSO_4$ and the solvents were removed under reduced pressure in order to obtain without further purification **C19** as a brown solid. **(2.42 g, 15.02 mmol, 83% yield)**

^{1}H NMR (400 MHz, DMSO) δ 12.80 (s, 1H), 7.19 (dd, *J* = 2.2, 1.6 Hz, 1H), 7.10 (t, *J* = 1.5 Hz, 1H), 6.84 (dd, *J* = 2.2, 1.5 Hz, 1H), 5.54 (s, 2H), 4.08 (s, 1H).

^{13}C NMR (101 MHz, DMSO) δ 167.02 (s), 148.54 (s), 131.97 (s), 122.29 (s), 120.54 (s), 120.14 (s), 115.58 (s), 83.39 (s), 80.04 (s).

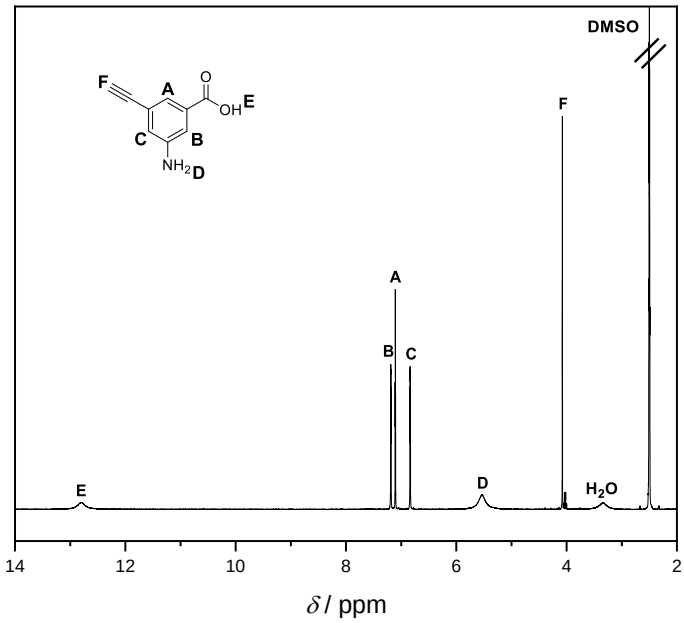

Figure S73: ^{1}H-NMR spectrum of **C19**, **^{1}H NMR (400 MHz, DMSO)** δ 12.80 (s, 1H), 7.19 (dd, J = 2.2, 1.6 Hz, 1H), 7.10 (t, J = 1.5 Hz, 1H), 6.84 (dd, J = 2.2, 1.5 Hz, 1H), 5.54 (s, 2H), 4.08 (s, 1H).

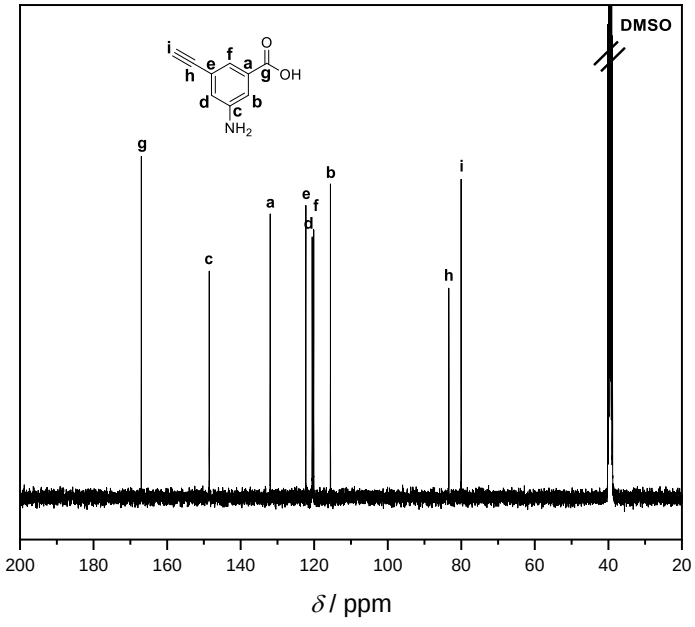

Figure S74: ^{13}C-NMR spectrum of **C19**, **^{13}C NMR (101 MHz, DMSO)** δ 167.02 (s), 148.54 (s), 131.97 (s), 122.29 (s), 120.54 (s), 120.14 (s), 115.58 (s), 83.39 (s), 80.04 (s).

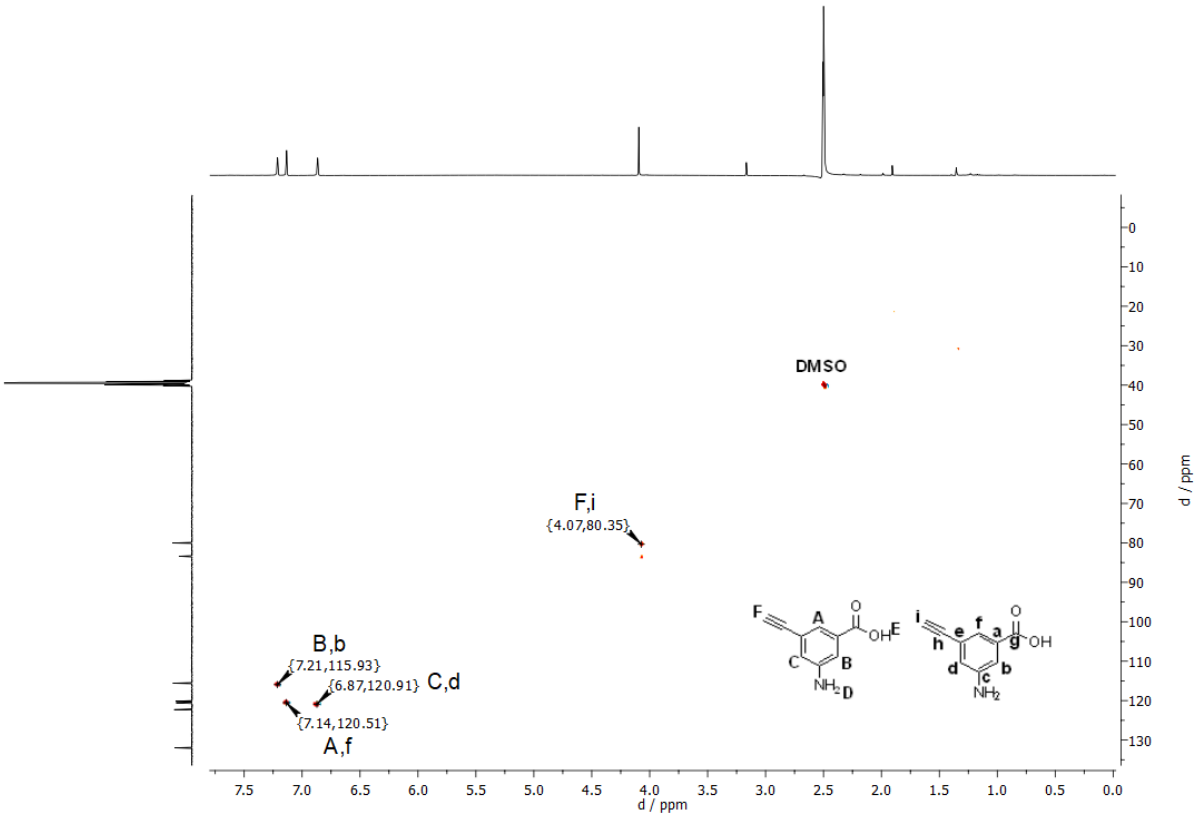

Figure S75: ^{1}H-^{13}C HSQC spectrum of **C19**, **^{1}H NMR 400 MHz, ^{13}C NMR 101 MHz, DMSO δ**

8.5.4 **(C20)** 3-Azido-5-ethynylbenzoic Acid

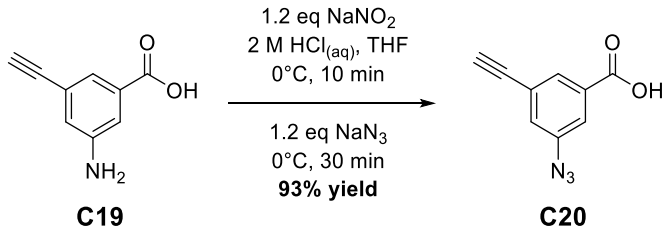

C19 **C20**

3-Amino-5-ethynylbenzoic acid **C19** (400 mg, 2.48 mmol, 1.0 eq) was dissolved in 2 M HCl (6 mL) and THF (2 mL). The mixture was cooled at 0 °C and sodium nitrite (206 mg, 2.98 mmol, 1.2 eq) was added portionwise over 5 min at 0 °C. After 5 min of subsequent stirring at 0 °C, sodium azide (194 mg, 2.98 mmol, 1.2 eq) was added portionwise over 15 min. Finally, the resulting mixture was stirred for another 15 min at 0 °C before being extracted with DCM (3 × 50 mL). The organic fractions were collected, dried over magnesium sulfate and the solvent was removed under reduced pressure. The crude material was purified by flash chromatography (silica, EtOAc) in order to obtain **C20** as a white solid. **(431 mg, 2.30 mmol, 93% yield)**

^{1}H NMR (400 MHz, DMSO) ***δ*** 13.48 (s, 1H), 7.73 (t, *J* = 1.4 Hz, 1H), 7.56 (dd, *J* = 2.2, 1.4 Hz, 1H), 7.43 (dd, *J* = 2.2, 1.5 Hz, 1H), 4.40 (s, 1H).

^{13}C NMR (101 MHz, DMSO) ***δ*** 165.67 (s), 140.70 (s), 133.03 (s), 128.62 (s), 125.98 (s), 123.66 (s), 120.04 (s), 82.68 (s), 81.60 (s).

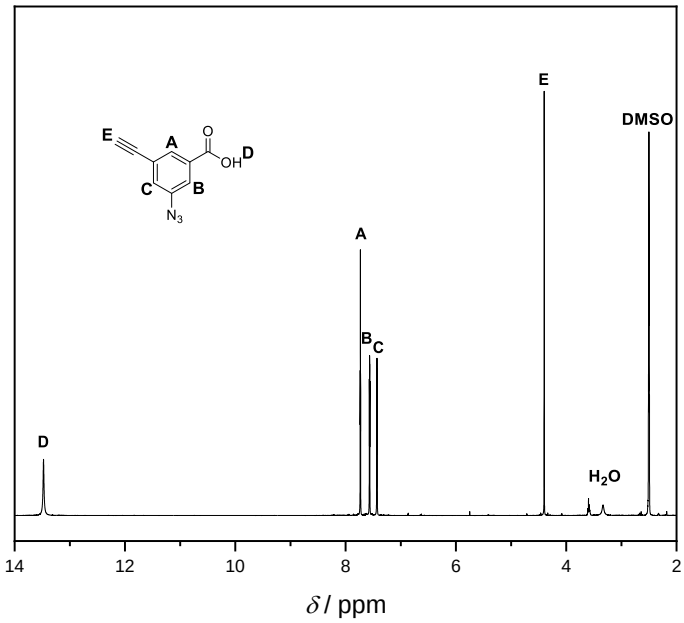

Figure S76: ^{1}H-NMR spectrum of **C20**, **^{1}H NMR (400 MHz, DMSO) δ** 13.48 (s, 1H), 7.73 (t, *J* = 1.4 Hz, 1H), 7.56 (dd, *J* = 2.2, 1.4 Hz, 1H), 7.43 (dd, *J* = 2.2, 1.5 Hz, 1H), 4.40 (s, 1H).

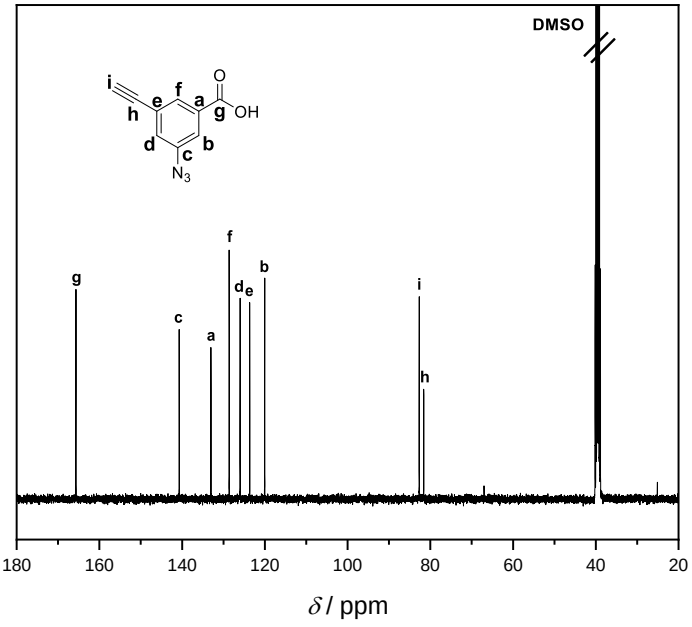

Figure S77: ^{13}C-NMR spectrum of **C20**, **^{13}C NMR (101 MHz, DMSO) δ** 165.67 (s), 140.70 (s), 133.03 (s), 128.62 (s), 125.98 (s), 123.66 (s), 120.04 (s), 82.68 (s), 81.60 (s).

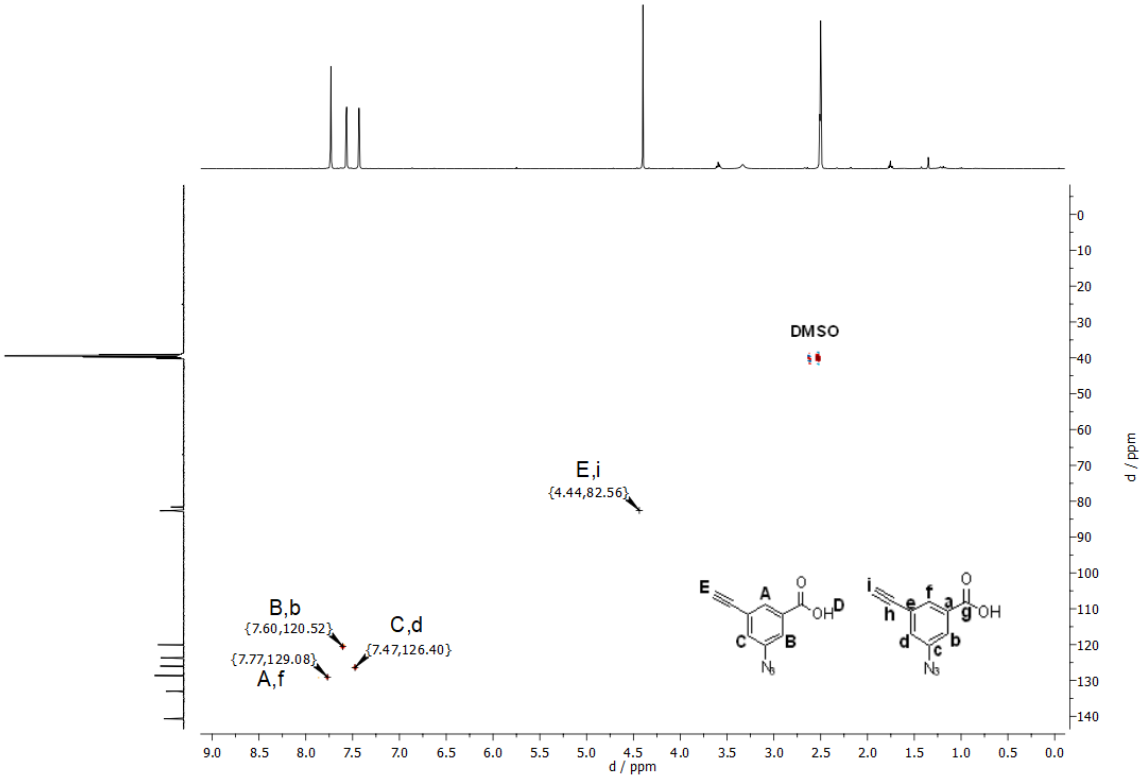

Figure S78: ^{1}H-^{13}C HSQC spectrum of **C20**, **^{1}H NMR 400 MHz, ^{13}C NMR 101 MHz, DMSO δ**

8.6 Polymer Synthesis and Post-Polymerization Modifications – Project Part II

8.6.1 **(P14)** Cationic Ring Opening Polymerization (CROP) of ε-Caprolactone

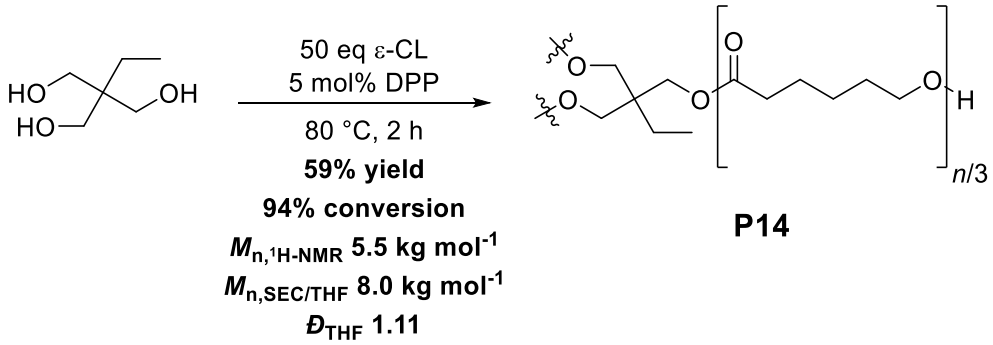

ε-Caprolactone (5.0 mL, 46.9 mmol, 50 eq), 2-ethyl-2-(hydroxymethyl) propane-1,3-diol (126 mg, 0.94 mmol, 1.00 eq) and diphenyl phosphate (12 mg, 0.047 mmol, 0,05 eq) were homogenized under argon atmosphere. The mixture was then heated at 80 °C for 2 hours. Afterwards, the viscous liquid was cooled down to room temperature and precipitated in cold MeOH (80 mL, -20 °C) The white precipitate was then redissolved in DCM (2 mL) and reprecipitated in cold MeOH (80 mL, -20 °C) two more times in order to obtain the desired polymer **P14** as a white solid. **(3.22 g, 0.58 mmol, 59% yield)**

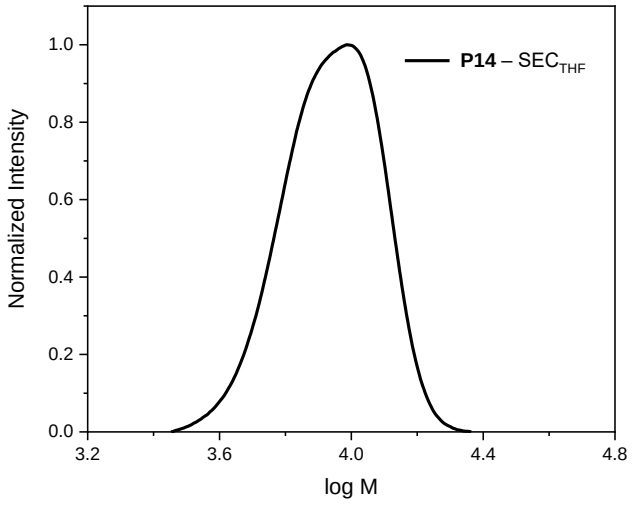

Figure S79: SEC_{THF} trace of polymer **P14**.

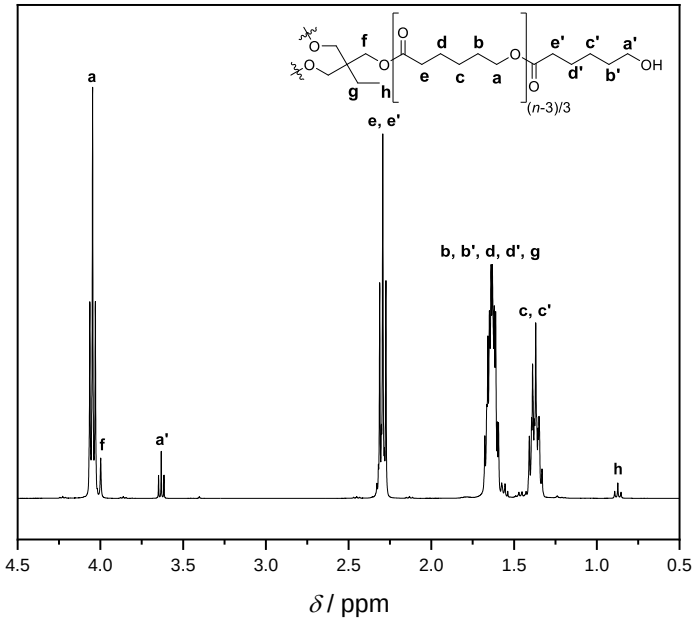

Figure S80: ^{1}H-NMR spectrum of **P14**, **^{1}H NMR (400 MHz, $CDCl_3$)** δ 4.28 – 3.84 (m), 3.63 (t, J = 6.5 Hz), 2.50 – 2.10 (m), 1.73 – 1.53 (m), 1.46 – 1.30 (m), 0.87 (t, J = 7.6 Hz).

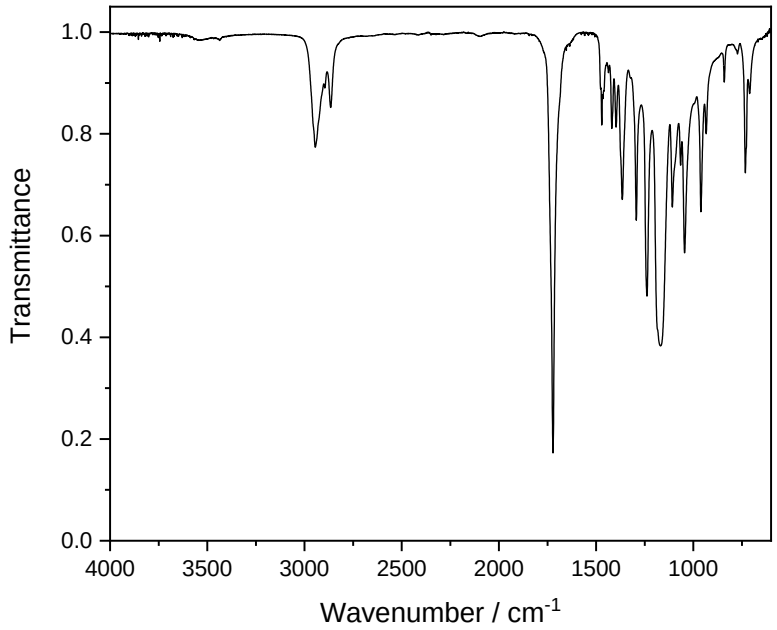

Figure S81: FT-IR spectrum of **P14**, **IR (ATR, cm^{-1})** 2945, 2865, 1721, 1471, 1419, 1397, 1365, 1293, 1238, 1168, 1108, 1065, 1045, 961, 934, 841, 732.

8.6.2 **(P15)** Cationic Ring Opening Polymerization (CROP) of ε-Caprolactone

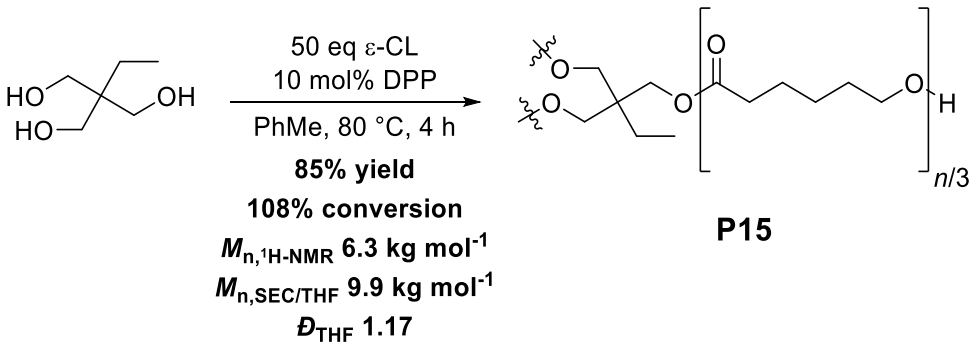

ε-Caprolactone (6.0 mL, 56.3 mmol, 50 eq), 2-ethyl-2-(hydroxymethyl) propane-1,3-diol (151 mg, 1.13 mmol, 1.00 eq) and diphenyl phosphate (28 mg, 0.047 mmol, 0.10 eq) were homogenized under argon atmosphere. The mixture was then heated at 80 °C for 4 hours. Afterwards, the mixture was cooled down to room temperature and precipitated in cold MeOH (80 mL, -20 °C) The white precipitate was then redissolved in DCM (2 mL) and reprecipitated in cold MeOH (80 mL, -20 °C) two more times in order to obtain the desired polymer **P15** as a white solid. **(5.56 g, 0.88 mmol, 85% yield)**

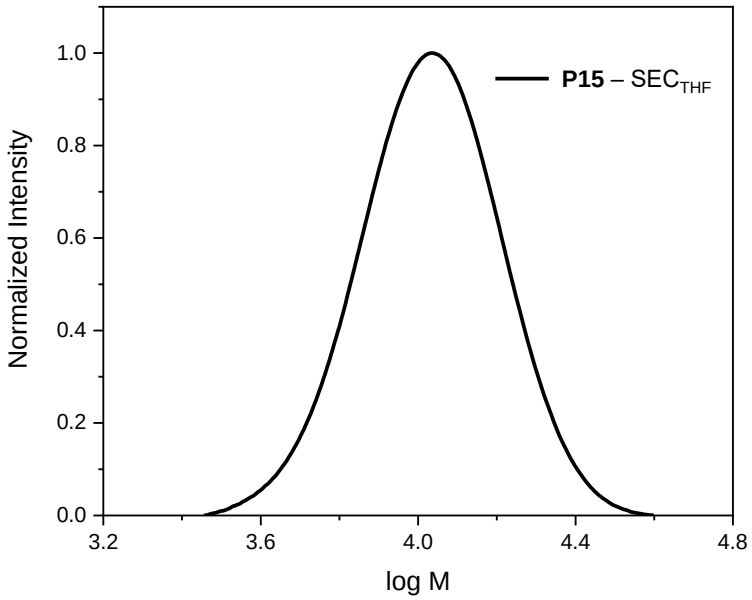

Figure S82: SEC_{THF} trace of polymer **P15**.

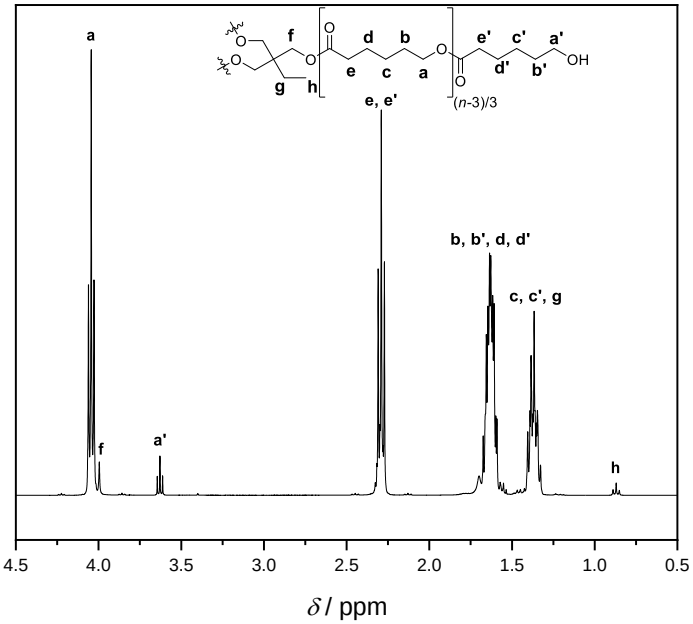

Figure S83: ^{1}H-NMR spectrum of **P15**, **^{1}H NMR (400 MHz, $CDCl_3$)** ***δ*** 4.29 – 3.79 (m), 3.63 (t, *J* = 6.5 Hz), 2.50 – 2.08 (m), 1.75 – 1.52 (m), 1.49 – 1.28 (m), 0.87 (t, *J* = 7.6 Hz).

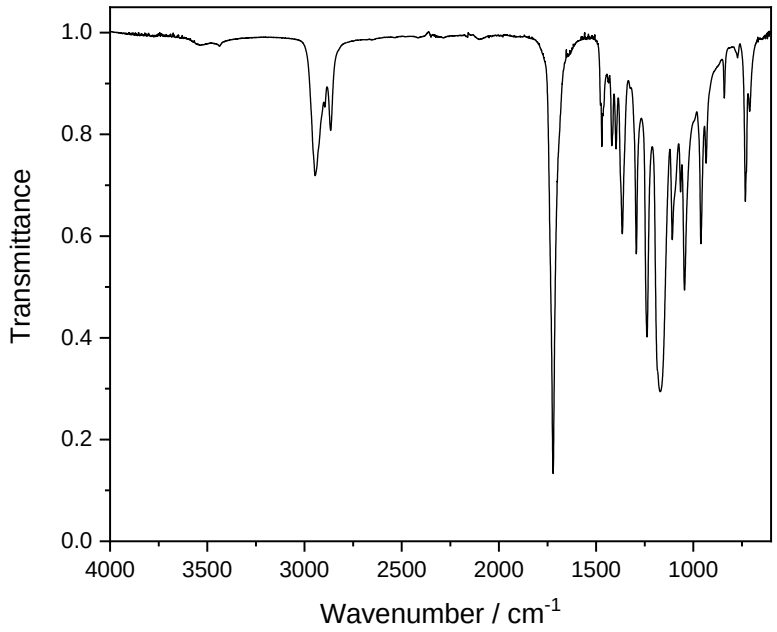

Figure S84: FT-IR spectrum of **P15**, **IR (ATR, cm^{-1})** 2945, 2865, 1720, 1471, 1419, 1397, 1365, 1293, 1238, 1170, 1108, 1066, 1045, 961, 934, 840, 732, 710.

8.6.3 **(P16)** Cationic Ring Opening Polymerization (CROP) of ε-Caprolactone

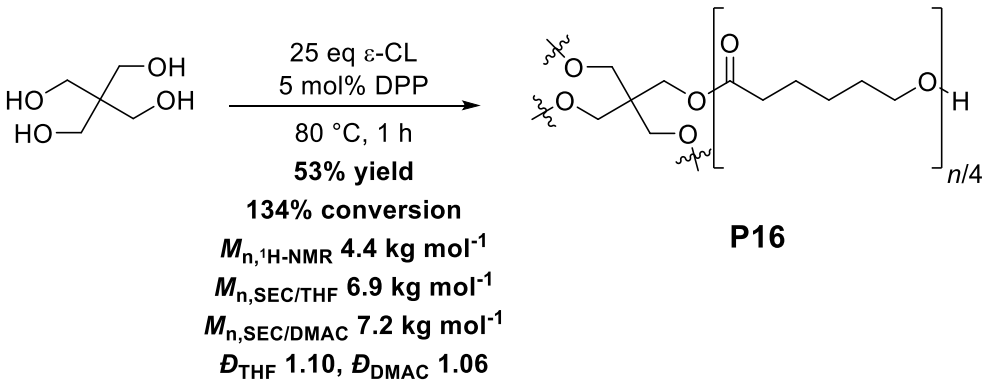

ε-Caprolactone (8.0 mL, 75.0 mmol, 28 eq), 2,2-bis(hydroxymethyl) propane-1,3-diol (365 mg, 2.68 mmol, 1.00 eq) and diphenyl phosphate (34 mg, 0.134 mmol, 0,05 eq) were mixed under argon atmosphere. The mixture was then heated at 80 °C for 1 hour. Afterwards, the viscous liquid was cooled down to room temperature, filtered off the remaining insoluble 2,2-bis(hydroxymethyl) propane-1,3-diol and precipitated in cold MeOH (80 mL, -20 °C). The white precipitate was then redissolved in DCM (2 mL) and reprecipitated in cold MeOH (80 mL, -20 °C) two more times in order to obtain the desired polymer **P16** as a white solid. **(4.63 g, 1.05 mmol, 53% yield)**

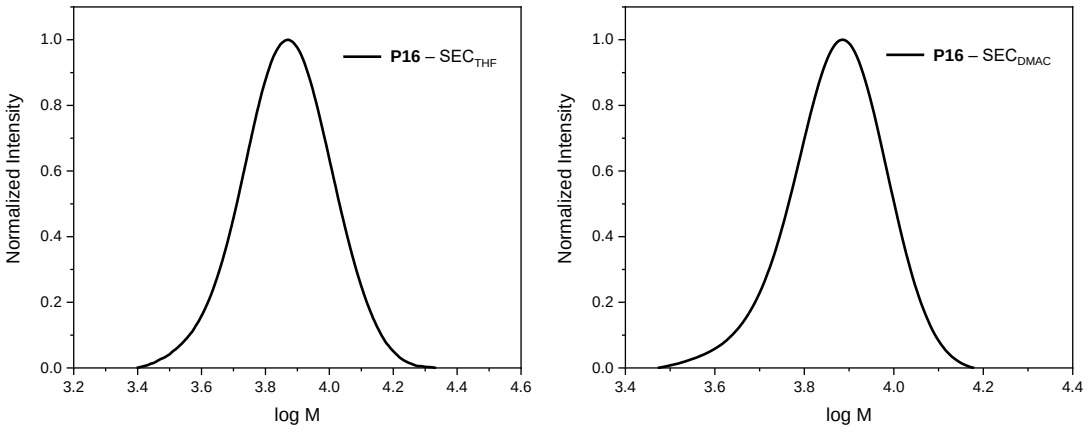

Figure S85: SEC$_{THF}$ (*left*) and SEC$_{DMAC}$ (*right*) traces of polymer **P16**.

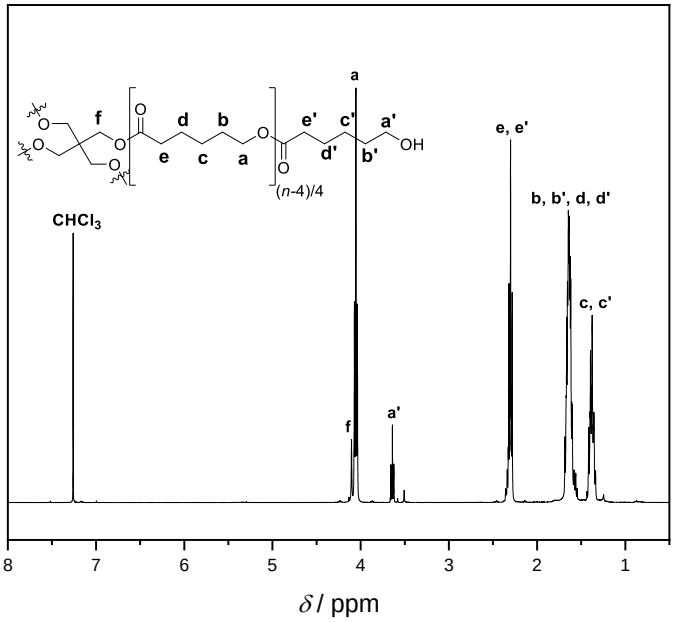

Figure S86: ^{1}H-NMR spectrum of **P16**, **^{1}H NMR (400 MHz, $CDCl_3$)** ***δ*** 4.10 (s), 4.09 – 4.01 (m), 3.64 (t, *J* = 6.5 Hz), 2.51 – 2.09 (m), 1.76 – 1.50 (m), 1.48 – 1.26 (m).

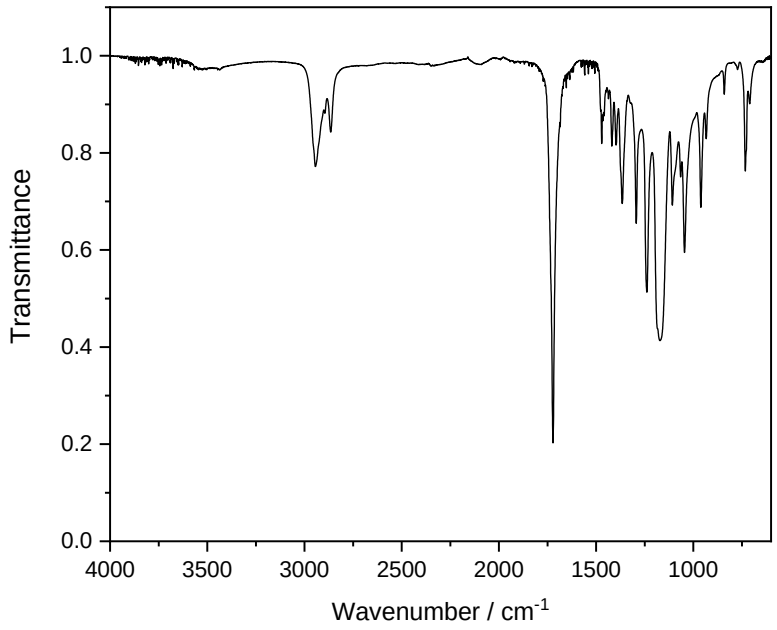

Figure S87: FT-IR spectrum of **P16**, **IR (ATR, cm^{-1})** 2944, 2865, 1721, 1471, 1419, 1397, 1366, 1293, 1239, 1172, 1108, 1065, 1045, 961, 934, 841, 732, 710.

8.6.4 **(P16-F)** End-functionalization of P16 with End-group C20

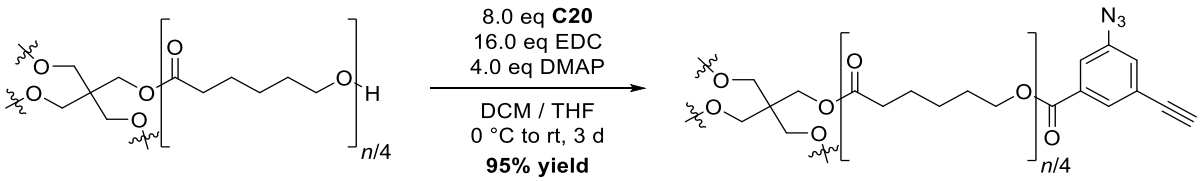

P16
$M_{n,^1H\text{-}NMR}$ 4.4 kg mol^{-1}
$M_{n,SEC/THF}$ 6.9 kg mol^{-1}
$M_{n,SEC/DMAC}$ 7.2 kg mol^{-1}
$Đ_{THF}$ 1.10, $Đ_{DMAC}$ 1.06

P16-F
$M_{n,^1H\text{-}NMR}$ 5.1 kg mol^{-1}
$M_{n,SEC/THF}$ 7.9 kg mol^{-1}
$M_{n,SEC/DMAC}$ 7.7 kg mol^{-1}
$Đ_{THF}$ 1.13, $Đ_{DMAC}$ 1.14

Previously synthetized *star*-(ε-PCL-OH)$_4$ **P16** (1.236 g, 0.280 mmol, 1.0 eq), 3-azido-5-ethynylbenzoic acid **C20** (419 mg, 2.24 mmol, 8.0 eq) and 4-dimethylaminopyridine (137 mg, 1.12 mmol, 4.0 eq) were dissolved in dry DCM (8 mL) and dry THF (2 mL). The solution was cooled down to 0 °C and *N*-(3-dimethylaminopropyl)-*N*′-ethylcarbodiimide hydrochloride (859 mg, 4.48 mmol, 16.0 eq) was added portionwise. The mixture was then stirred for 3 days at room temperature. Afterwards, the resulting mixture was quenched with 1 M HCl and the aqueous phase was extracted with DCM (3 × 20 mL). The organic fractions were collected, dried over magnesium sulfate and the solvents were removed under reduced pressure. The crude polymer was then reprecipitated three times in cold MeOH (80 mL, -20 °C) in order to give **P16-F** as a dark brown solid. **(1.35 g, 0.265 mmol, 95% yield)**

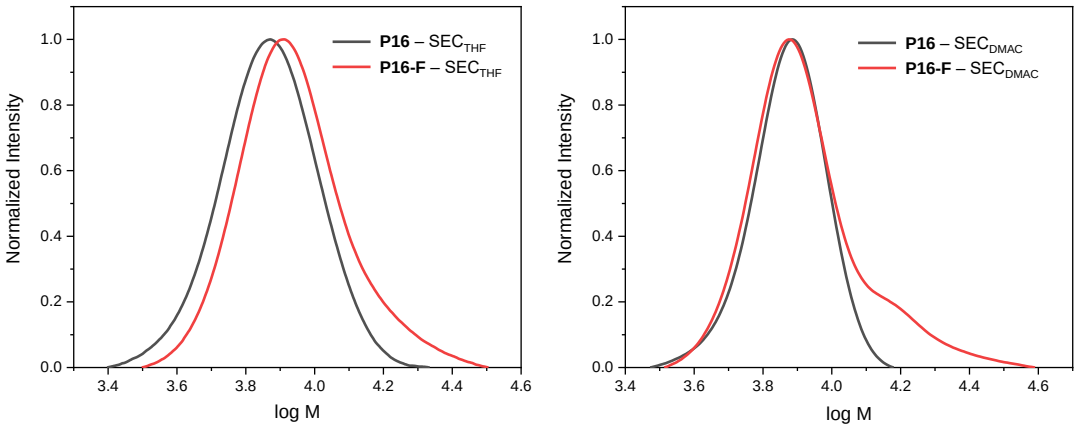

Figure S88: SEC_{THF} (*left*) and SEC_{DMAC} (*right*) traces of polymers **P16** and **P16-F**.

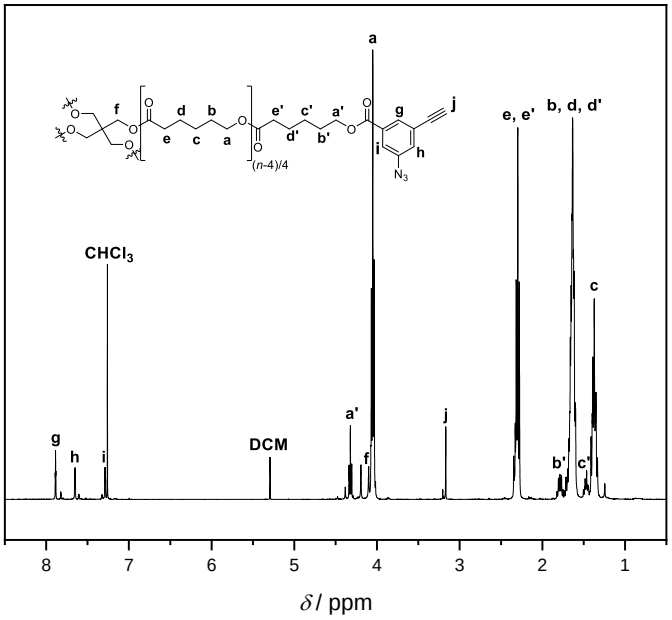

Figure S89: ^{1}H-NMR spectrum of **P16-F**, **^{1}H NMR (400 MHz, $CDCl_3$)** δ 7.89 (t, J = 1.4 Hz), 7.65 (dd, J = 2.1, 1.5 Hz), 7.29 (dd, J = 2.2, 1.5 Hz), 4.32 (t, J = 6.6 Hz), 4.32 (t, J = 6.6 Hz), 4.10 (s), 4.09 – 4.01 (m), 3.17 (s), 2.39 – 2.21 (m), 1.86 – 1.55 (m), 1.54 – 1.28 (m).

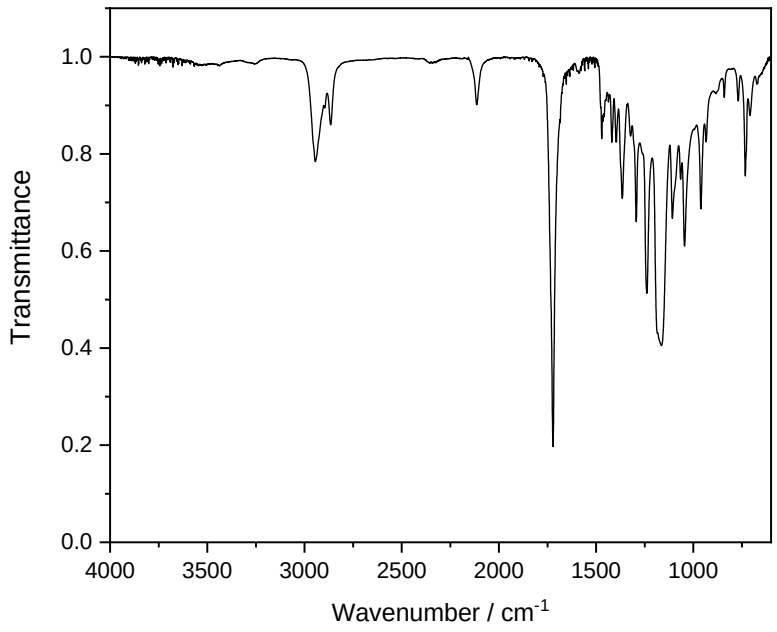

Figure S90: FT-IR spectrum of **P16-F**, **IR (ATR, cm^{-1})** 2945, 2865, 2114, 1721, 1471, 1419, 1397, 1366, 1293, 1239, 1163, 1108, 1065, 1045, 961, 934, 841, 769, 732, 708.

8.6.5 **(P16-C1)** *Cage*-shaped Polymer Synthesis *via* CuAAC Reaction

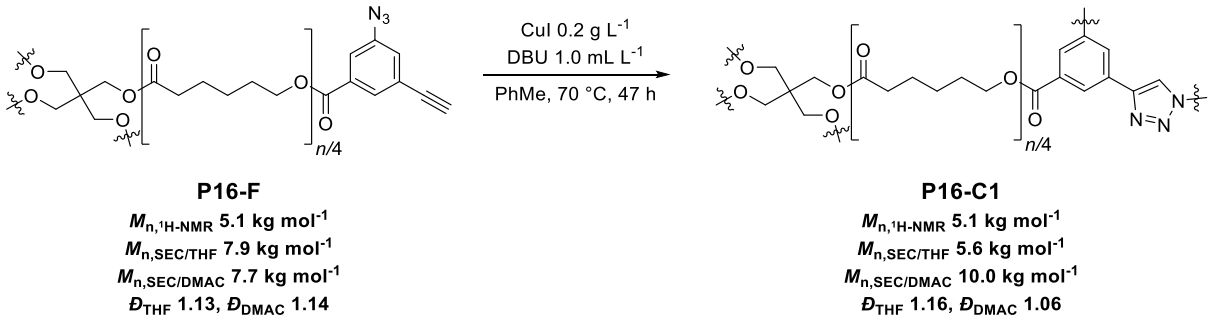

P16-F
$M_{n,^1H\text{-}NMR}$ 5.1 kg mol^{-1}
$M_{n,SEC/THF}$ 7.9 kg mol^{-1}
$M_{n,SEC/DMAC}$ 7.7 kg mol^{-1}
$Đ_{THF}$ 1.13, $Đ_{DMAC}$ 1.14

P16-C1
$M_{n,^1H\text{-}NMR}$ 5.1 kg mol^{-1}
$M_{n,SEC/THF}$ 5.6 kg mol^{-1}
$M_{n,SEC/DMAC}$ 10.0 kg mol^{-1}
$Đ_{THF}$ 1.16, $Đ_{DMAC}$ 1.06

P16-F (50 mg, 0.10 mg mL^{-1}) and DBU (0.5 mL, 1.0 mL L^{-1}) were dissolved in redistilled toluene (500 mL). The mixture was purged with argon for 15 min and CuI (100 mg, 200 mg L^{-1}) was added. The mixture was then purged a second time with argon for another 15 min before being heated at 70 °C for 47 hours. Afterwards, the solvent was removed under reduced pressure, 1 M HCl (50 mL) was added and the crude material was extracted with DCM (3 × 30 mL). The organic fractions were collected, dried over magnesium sulfate and the solvent was removed under reduced pressure. The crude material was then washed on silica gel with DCM, before being recovered by adding 20% MeOH to the eluent in order to obtain **P16-C1** as a brownish gel. **(48 mg, 96% yield)**

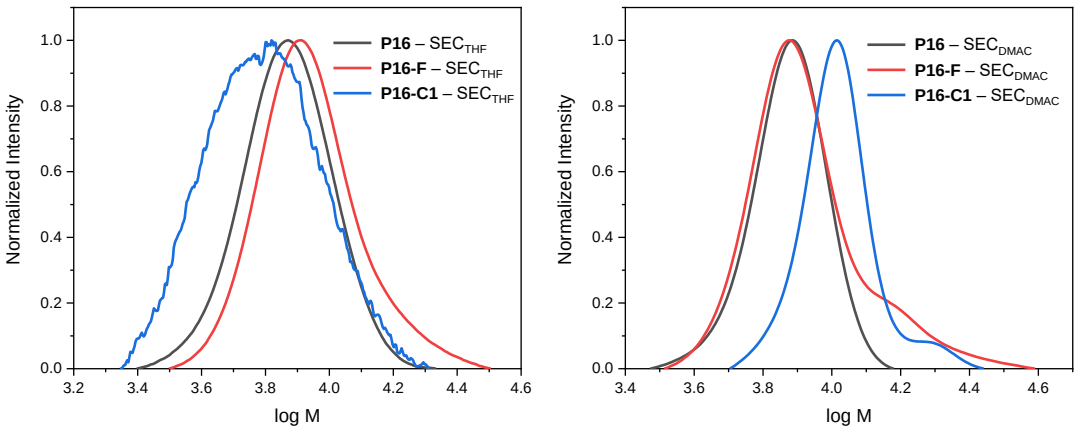

Figure S91: SEC_{THF} (*left*) and SEC_{DMAC} (*right*) traces of polymers **P16**, **P16-F** and **P16-C1**.

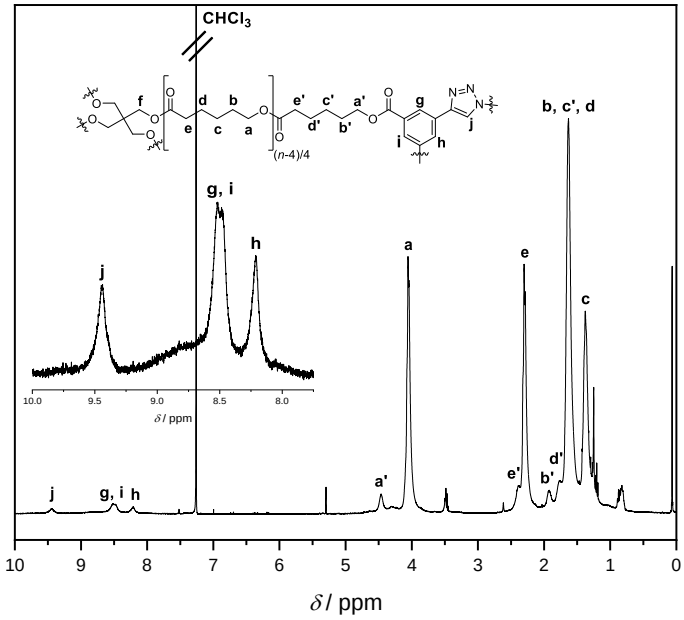

Figure S92: ^{1}H-NMR spectrum of **P16-C1**, **^{1}H NMR (400 MHz, $CDCl_3$)** δ 9.44 (s), 8.52 (s), 8.48 (s), 8.21 (s), 4.58 – 4.35 (m), 4.17 – 3.91 (m), 2.46 – 2.36 (m), 2.36 – 2.17 (m), 1.98 – 1.87 (m), 1.84 – 1.72 (m), 1.73 – 1.49 (m) 1.45 – 1.28 (m).

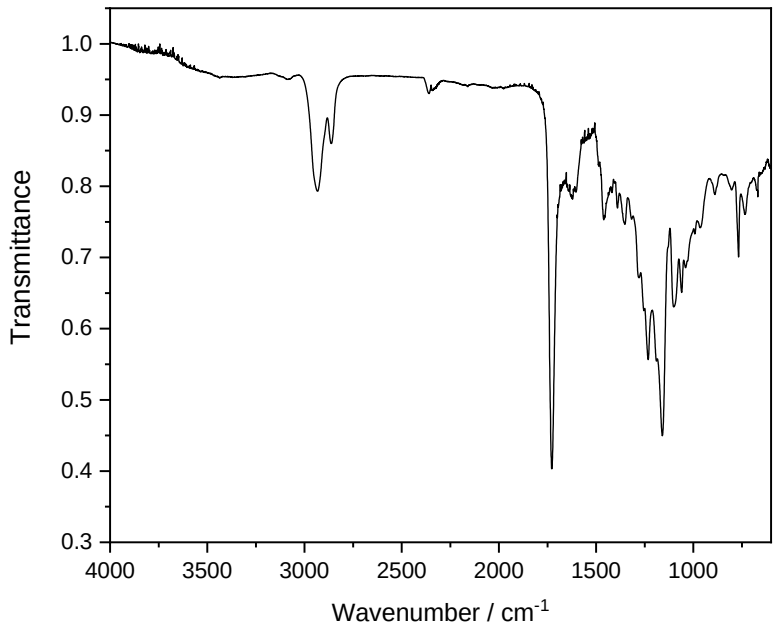

Figure S93: FT-IR spectrum of **P16-C1**, **IR (ATR, cm^{-1})** 2934, 2862, 1728, 1622, 1461, 1390, 1352, 1232, 1159, 1101, 1060, 889, 807, 767, 735, 668.

8.6.6 **(P16-C2)** *Cage*-shaped Polymer Synthesis *via* CuAAC Reaction

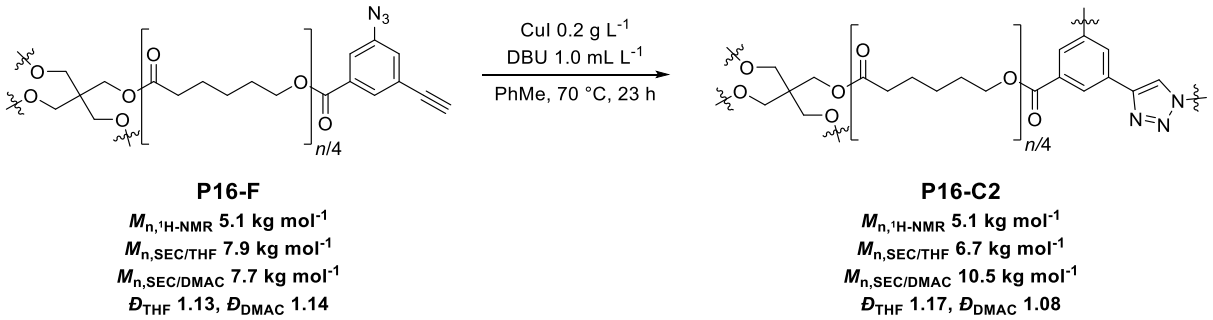

P16-F
$M_{n,^1H\text{-}NMR}$ 5.1 kg mol^{-1}
$M_{n,SEC/THF}$ 7.9 kg mol^{-1}
$M_{n,SEC/DMAC}$ 7.7 kg mol^{-1}
$Đ_{THF}$ 1.13, $Đ_{DMAC}$ 1.14

P16-C2
$M_{n,^1H\text{-}NMR}$ 5.1 kg mol^{-1}
$M_{n,SEC/THF}$ 6.7 kg mol^{-1}
$M_{n,SEC/DMAC}$ 10.5 kg mol^{-1}
$Đ_{THF}$ 1.17, $Đ_{DMAC}$ 1.08

P16 (50 mg, 0.10 mg mL^{-1}) and DBU (0.5 mL, 1.0 mL L^{-1}) were dissolved in redistilled toluene (500 mL). The mixture was purged with argon for 15 min and CuI (100 mg, 200 mg L^{-1}) was added. The mixture was then purged a second time with argon for another 15 min before being heated at 70 °C for 23 hours. Afterwards, the solvent was removed under reduced pressure, 1 M HCl (50 mL) was added and the crude material was extracted with DCM (3 × 30 mL). The organic fractions were collected, dried over magnesium sulfate and the solvent was removed under reduced pressure. The crude material was then washed on silica gel with DCM, before being recovered by adding 20% MeOH to the eluent in order to obtain **P16-C2** as a brownish gel. **(47 mg, 94% yield)**

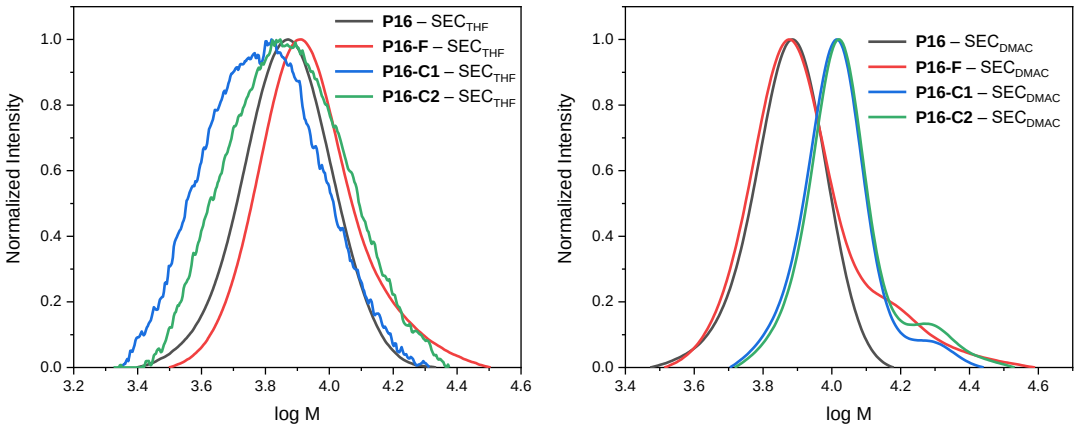

Figure S94: SEC_{THF} (*left*) and SEC_{DMAC} (*right*) traces of polymers **P16**, **P16-F**, **P16-C1** and **P16-C1**.

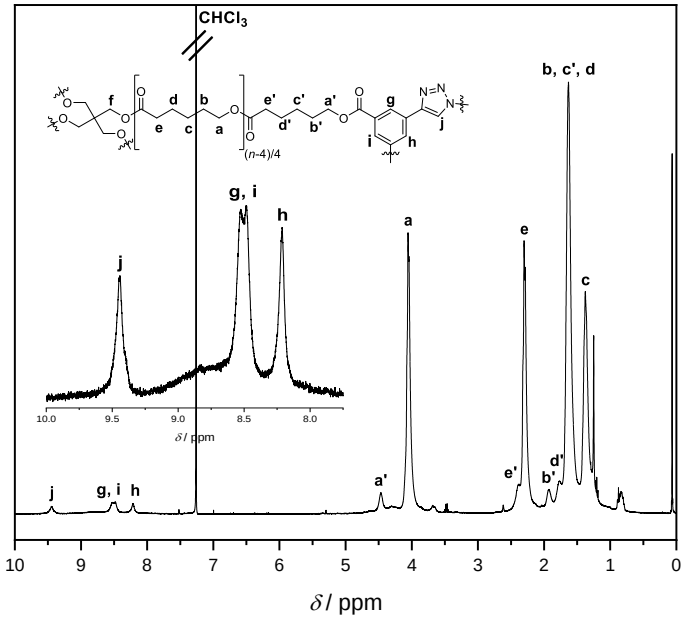

Figure S95: ^{1}H-NMR spectrum of **P16-C2**, **^{1}H NMR (400 MHz, $CDCl_3$) δ** 9.44 (s), 8.53 (s, 8.48 (s), 8.21 (s), 4.56 – 4.37 (m), 4.19 – 3.87 (m), 2.48 – 2.35 (m), 2.36 – 2.12 (m), 2.03 – 1.84 (m), 1.84 – 1.72 (m), 1.72 – 1.48 (m), 1.47 – 1.27 (m).

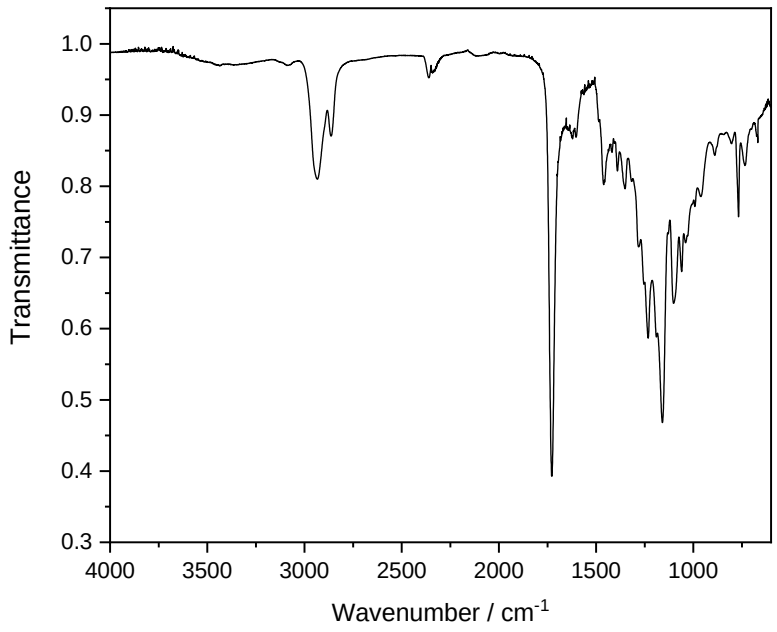

Figure S96: FT-IR spectrum of **P16-C2**, **IR (ATR, cm^{-1})** 2933, 2864, 1728, 1622, 1603, 1461, 1390, 1351, 1232, 1159, 1102, 1060, 1040, 961, 889, 803, 767, 735, 668.

8.6.7 **(P16-C3)** *Cage*-shaped Polymer Synthesis *via* CuAAC Reaction

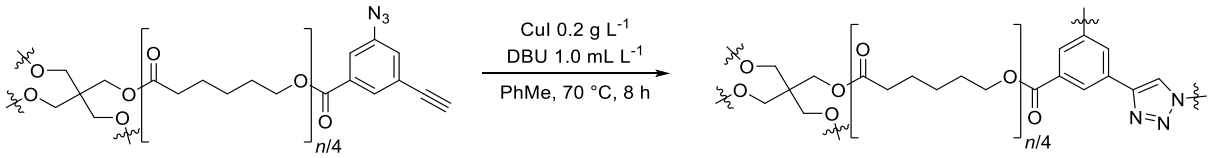

P16-F
$M_{n,^1H\text{-}NMR}$ 5.1 kg mol^{-1}
$M_{n,SEC/DMAC}$ 7.7 kg mol^{-1}
$Đ_{DMAC}$ 1.14

P16-C3
$M_{n,^1H\text{-}NMR}$ 5.1 kg mol^{-1}
$M_{n,SEC/DMAC}$ 10.7 kg mol^{-1}
$Đ_{DMAC}$ 1.14

P16-F (50 mg, 0.10 mg mL^{-1}) and DBU (0.5 mL, 1.0 mL L^{-1}) were dissolved in toluene (500 mL). The mixture was purged with argon for 15 min and CuI (100 mg, 200 mg L^{-1}) was added. The mixture was then purged a second time with argon for another 15 min before being heated at 70 °C for 8 hours. Afterwards, the solvent was removed under reduced pressure, 1 M HCl (50 mL) was added and the crude material was extracted with DCM (3 × 30 mL). The organic fractions were collected, dried over magnesium sulfate and the solvent was removed under reduced pressure. The crude material was then washed on silica gel with DCM, before being recovered by adding 20% MeOH to the eluent in order to obtain **P16-C3** as a brownish gel. **(46 mg, 92% yield)**

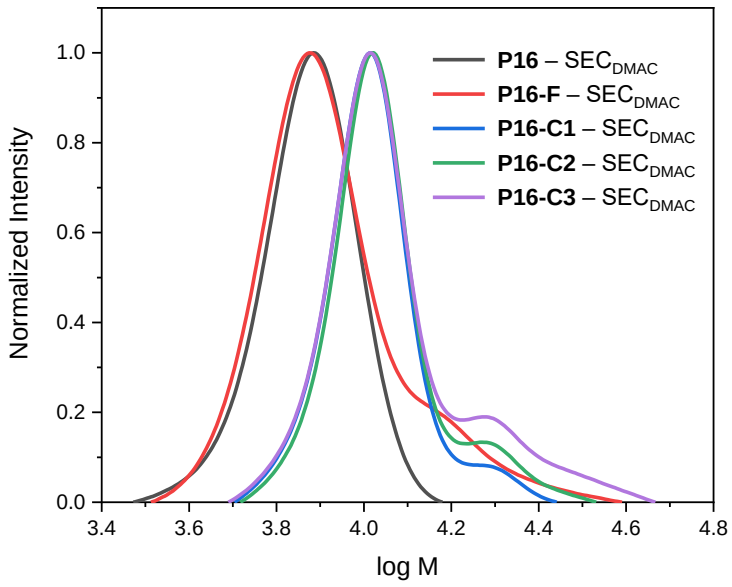

Figure S97: SEC_{DMAC} traces of polymers **P16**, **P16-F**, **P16-C1**, **P16-C2** and **P16-C3**.

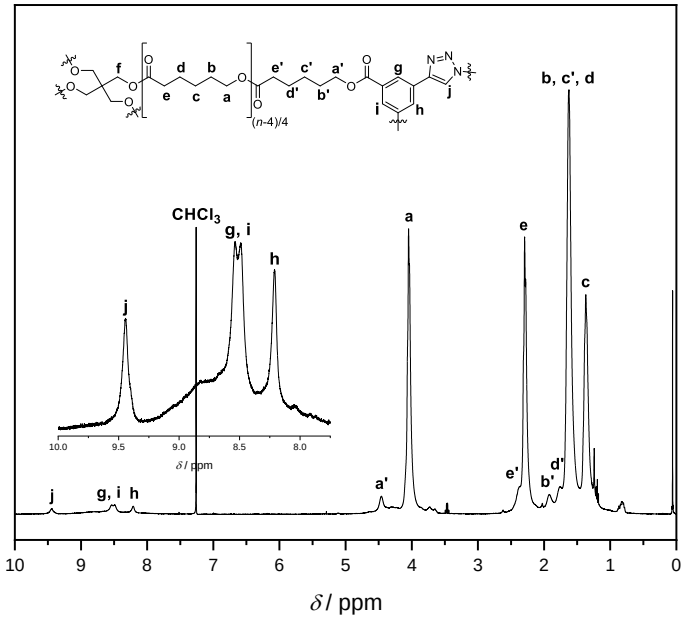

Figure S98: ^{1}H-NMR spectrum of **P16-C3**, **^{1}H NMR (400 MHz, $CDCl_3$)** δ 9.44 (s), 8.55 (s), 8.48 (s), 8.21 (s), 4.56 – 4.37 (m), 4.18 – 3.88 (m), 2.46 – 2.34 (m), 2.35 – 2.17 (m), 1.98 – 1.87 (m), 1.82 – 1.72 (m), 1.72 – 1.48 (m), 1.46 – 1.26 (m).

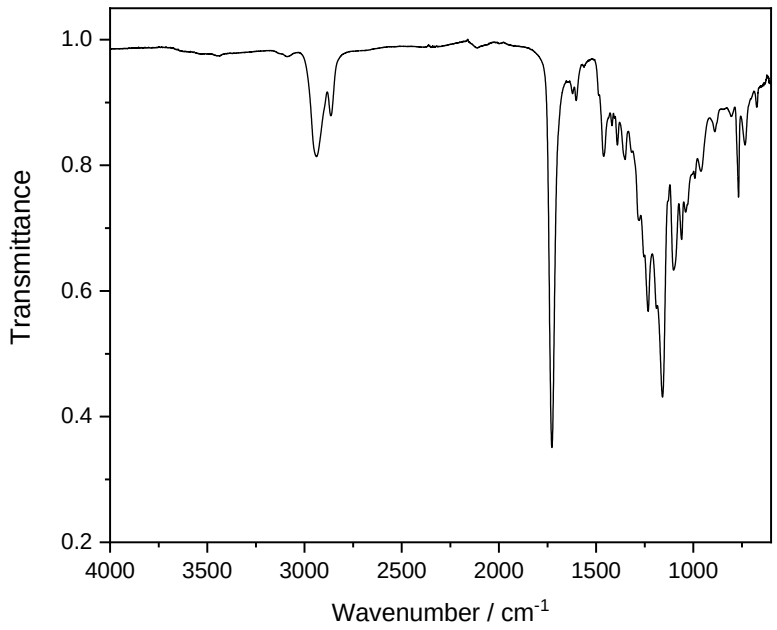

Figure S99: FT-IR spectrum of **P16-C3**, **IR (ATR, cm^{-1})** 2939, 2864, 1727, 1602, 1461, 1418, 1390, 1351, 1232, 1158, 1102, 1060, 1039, 992, 961, 889, 806, 767, 734, 673.

8.6.8 **(P16-C4)** *Cage*-shaped Polymer Synthesis *via* CuAAC Reaction

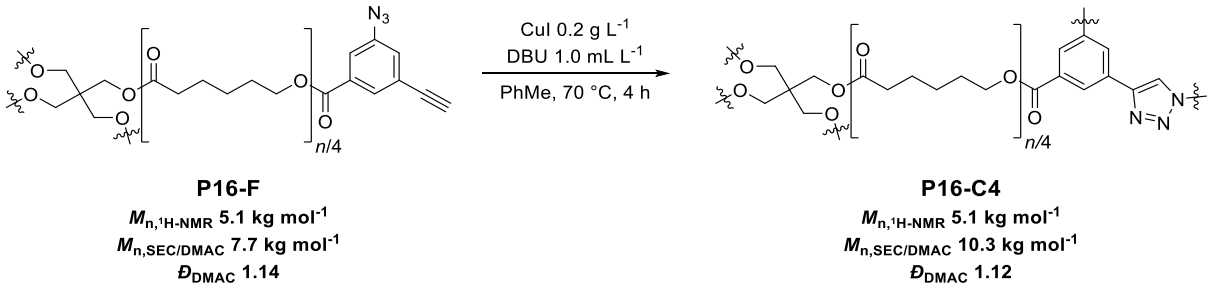

P16-F
$M_{n,^1H\text{-}NMR}$ 5.1 kg mol^{-1}
$M_{n,SEC/DMAC}$ 7.7 kg mol^{-1}
$Đ_{DMAC}$ 1.14

P16-C4
$M_{n,^1H\text{-}NMR}$ 5.1 kg mol^{-1}
$M_{n,SEC/DMAC}$ 10.3 kg mol^{-1}
$Đ_{DMAC}$ 1.12

P16-F (50 mg, 0.10 mg mL^{-1}) and DBU (0.5 mL, 1.0 mL L^{-1}) were dissolved in toluene (500 mL). The mixture was purged with argon for 15 min and CuI (100 mg, 200 mg L^{-1}) was added. The mixture was then purged a second time with argon for another 15 min before being heated at 70 °C for 4 hours. Afterwards, the solvent was removed under reduced pressure, 1 M HCl (50 mL) was added and the crude material was extracted with DCM (3 × 30 mL). The organic fractions were collected, dried over magnesium sulfate and the solvent was removed under reduced pressure. The crude material was then washed on silica gel with DCM, before being recovered by adding 20% MeOH to the eluent in order to obtain **P16-C4** as a brownish gel. **(34 mg, 68% yield)**

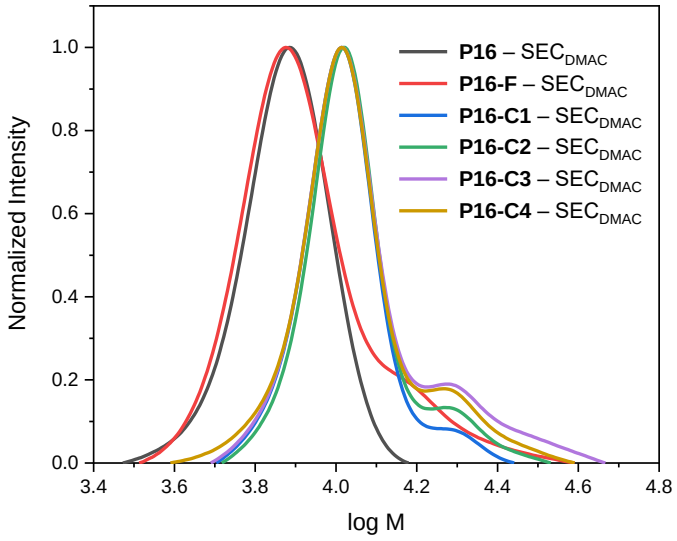

Figure S100: SEC_{DMAC} traces of polymers **P16**, **P16-F**, **P16-C1**, **P16-C2**, **P16-C3** and **P16-C4**.

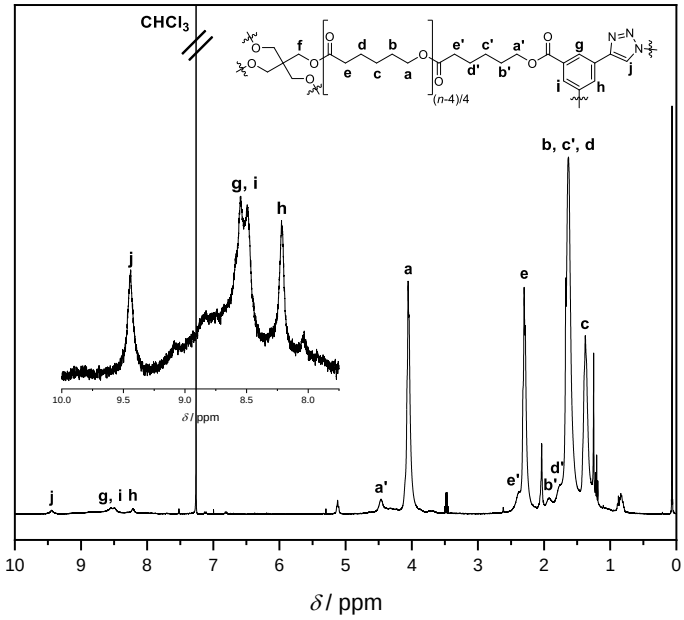

Figure S101: ^{1}H-NMR spectrum of **P16-C4**, **^{1}H NMR (400 MHz, $CDCl_3$) δ** 9.44 (s), 8.55 (s), 8.50 (s), 8.22 (s), 4.58 – 4.38 (m), 4.22 – 3.84 (m), 2.52 – 2.37 (m), 2.35 – 2.11 (m), 1.98 – 1.87 (m), 1.85 – 1.74 (m), 1.74 – 1.47 (m), 1.45 – 1.28 (m).

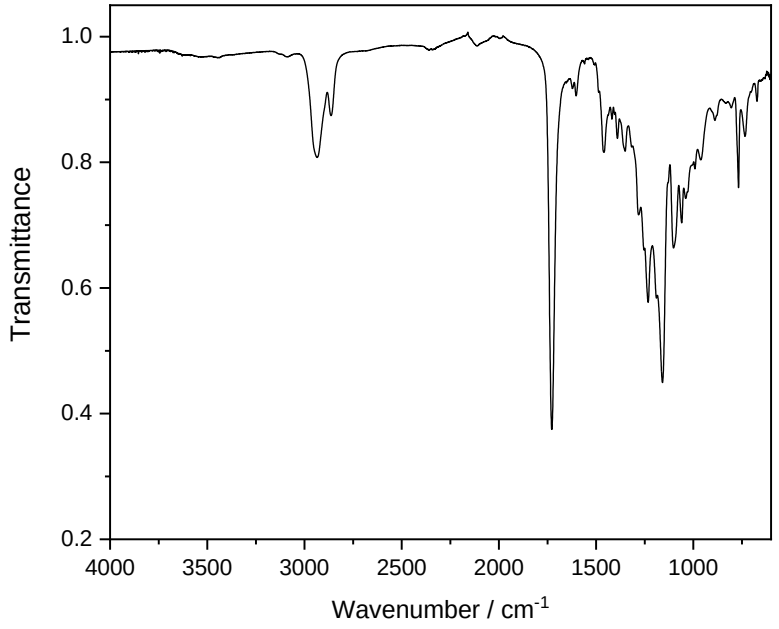

Figure S102: FT-IR spectrum of **P16-C4**, **IR (ATR, cm^{-1})** 2934, 2863, 1728, 1603, 1460, 1419, 1390, 1351, 1232, 1159, 1102, 1060, 1036, 958, 889, 805, 767, 733, 672.

8.6.9 **(P16-C5)** *Cage*-shaped Polymer Synthesis *via* CuAAC Reaction

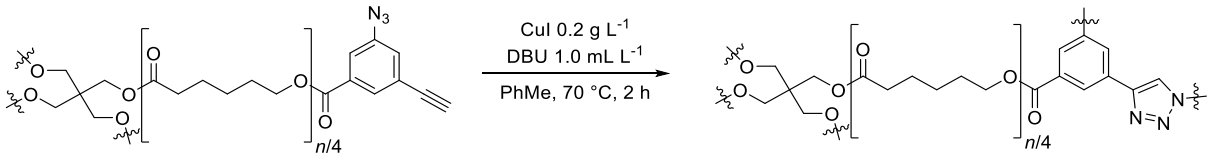

P16-F
$M_{n,^1H\text{-}NMR}$ 5.1 kg mol^{-1}
$M_{n,SEC/DMAC}$ 7.7 kg mol^{-1}
$Đ_{DMAC}$ 1.14

P16-C5
$M_{n,^1H\text{-}NMR}$ 5.1 kg mol^{-1}
$M_{n,SEC/DMAC}$ 10.0 kg mol^{-1}
$Đ_{DMAC}$ 1.08

P16 (50 mg, 0.10 mg mL^{-1}) and DBU (0.5 mL, 1.0 mL L^{-1}) were dissolved in toluene (500 mL). The mixture was purged with argon for 15 min and CuI (100 mg, 200 mg L^{-1}) was added. The mixture was then purged a second time with argon for another 15 min before being heated at 70 °C for 2 hours. Afterwards, the solvent was removed under reduced pressure, 1 M HCl (50 mL) was added and the crude material was extracted with DCM (3 × 30 mL). The organic fractions were collected, dried over magnesium sulfate and the solvent was removed under reduced pressure. The crude material was then washed on silica gel with DCM, before being recovered by adding 20% MeOH to the eluent in order to obtain **P16-C5** as a brownish gel. **(37 mg, 74% yield)**

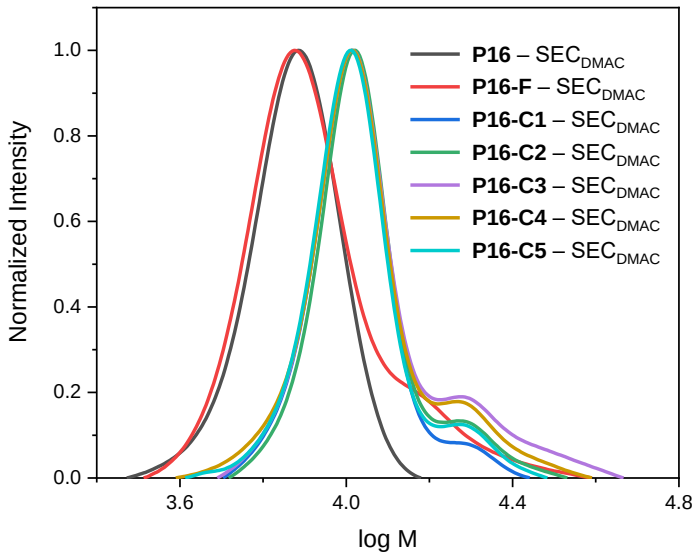

Figure S103: SEC_{DMAC} traces of polymers **P16**, **P16-F**, **P16-C1**, **P16-C2**, **P16-C3**, **P16-C4** and **P16-C5**.

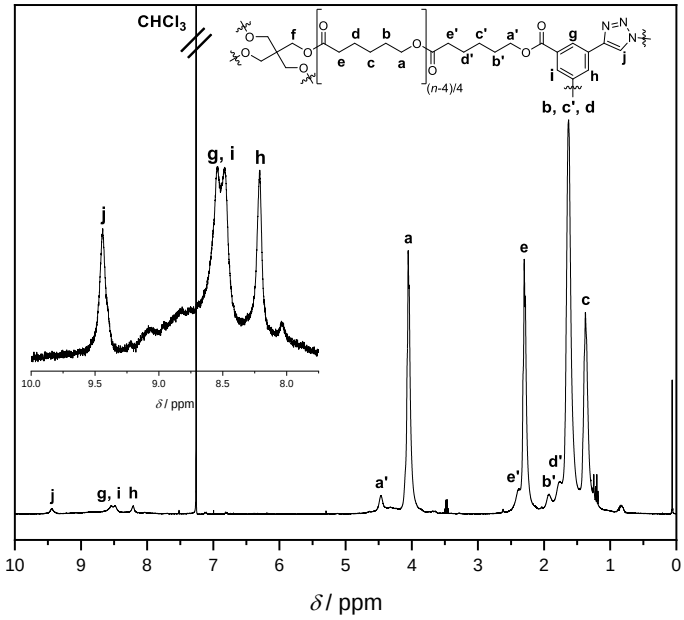

Figure S104: ^{1}H-NMR spectrum of **P16-C5**, **^{1}H NMR (400 MHz, $CDCl_3$) δ** 9.44 (s), 8.54 (s), 8.49 (s), 8.21 (s), 4.57 – 4.38 (m), 4.19 – 3.87 (m), 2.50 – 2.36 (m), 2.36 – 2.12 (m), 2.00 – 1.85 (m), 1.83 – 1.73 (m), 1.73 – 1.46 (m), 1.46 – 1.27 (m).

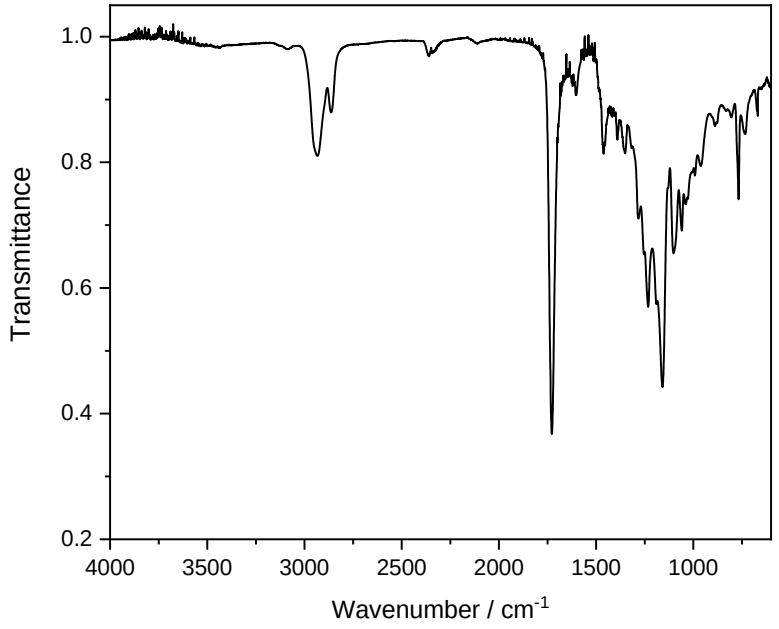

Figure S105: FT-IR spectrum of **P16-C5**, **IR (ATR, cm^{-1})** 2934, 2863, 1728, 1603, 1461, 1420, 1390, 1351, 1232, 1159, 1102, 1059, 1036, 767, 733, 668.

8.6.10 **(P16-C6)** *Cage*-shaped Polymer Synthesis *via* CuAAC Reaction

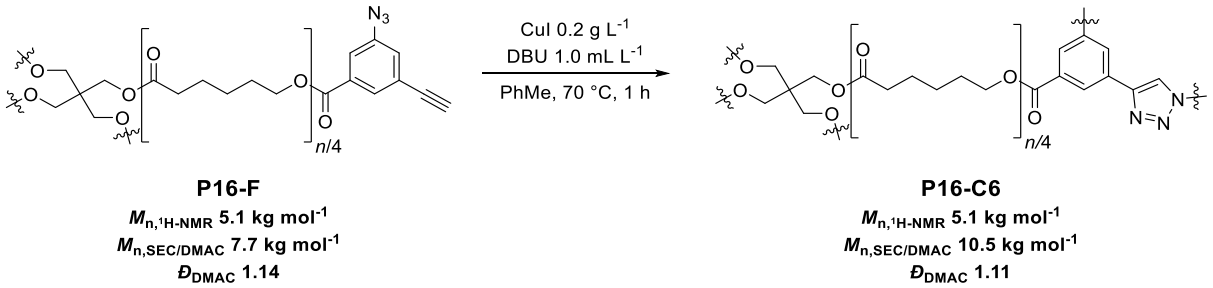

P16-F
$M_{n,^1H\text{-}NMR}$ 5.1 kg mol^{-1}
$M_{n,SEC/DMAC}$ 7.7 kg mol^{-1}
$Đ_{DMAC}$ 1.14

P16-C6
$M_{n,^1H\text{-}NMR}$ 5.1 kg mol^{-1}
$M_{n,SEC/DMAC}$ 10.5 kg mol^{-1}
$Đ_{DMAC}$ 1.11

P16-F (50 mg, 0.10 mg mL^{-1}) and DBU (0.5 mL, 1.0 mL L^{-1}) were dissolved in toluene (500 mL). The mixture was purged with argon for 15 min and CuI (100 mg, 200 mg L^{-1}) was added. The mixture was then purged a second time with argon for another 15 min before being heated at 70 °C for 1 hour. Afterwards, the solvent was removed under reduced pressure, 1 M HCl (50 mL) was added and the crude material was extracted with DCM (3 × 30 mL). The organic fractions were collected, dried over magnesium sulfate and the solvent was removed under reduced pressure. The crude material was then washed on silica gel with DCM, before being recovered by adding 20% MeOH to the eluent in order to obtain **P16-C6** as a brownish gel. **(35 mg, 70% yield)**

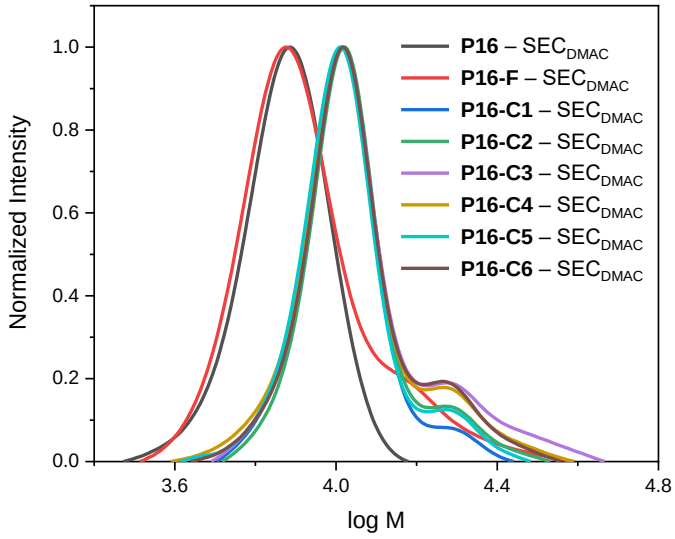

Figure S106: SEC_{DMAC} traces of polymers **P16**, **P16-F**, **P16-C1**, **P16-C2**, **P16-C3**, **P16-C4**, **P16-C5** and **P16-C6**.

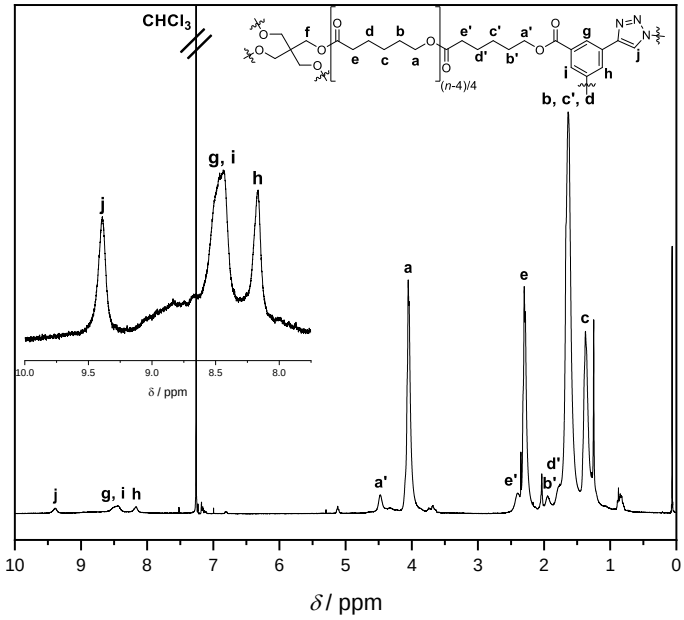

Figure S107: ^{1}H-NMR spectrum of **P16-C6**, **^{1}H NMR (400 MHz, $CDCl_3$)** δ ^{1}H NMR (400 MHz, $CDCl_3$) δ 9.39 (s), 8.60 – 8.35 (m), 8.17 (s), 4.58 – 4.38 (m), 4.20 – 3.85 (m), 2.53 – 2.37 (m), 2.36 – 2.12 (m), 2.00 – 1.86 (m), 1.85 – 1.74 (m), 1.75 – 1.46 (m), 1.46 – 1.29 (m).

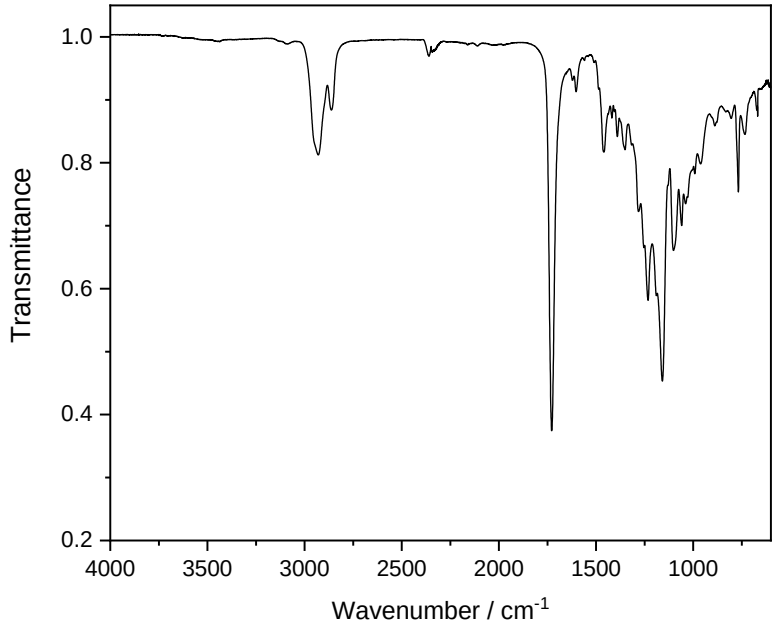

Figure S108: FT-IR spectrum of **P16-C6**, **IR (ATR, cm^{-1})** 2929, 2862, 1728, 1603, 1461, 1390, 1351, 1232, 1159, 1101, 1059, 767, 733, 668.

8.6.11 **(P16-C7)** *Cage*-shaped Polymer Synthesis *via* CuAAC Reaction

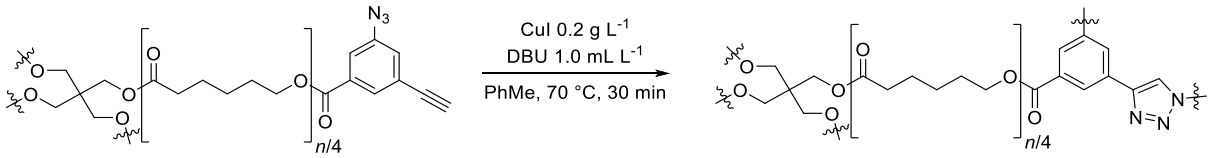

P16-F
$M_{n,^1H\text{-}NMR}$ 5.1 kg mol^{-1}
$M_{n,SEC/DMAC}$ 7.7 kg mol^{-1}
$Đ_{DMAC}$ 1.14

P16-C7
$M_{n,^1H\text{-}NMR}$ 5.1 kg mol^{-1}
$M_{n,SEC/DMAC}$ 10.6 kg mol^{-1}
$Đ_{DMAC}$ 1.14

P16-F (50 mg, 0.10 mg mL^{-1}) and DBU (0.5 mL, 1.0 mL L^{-1}) were dissolved in toluene (500 mL). The mixture was purged with argon for 15 min and CuI (100 mg, 200 mg L^{-1}) was added. The mixture was then purged a second time with argon for another 15 min before being heated at 70 °C for 30 minutes. Afterwards, the solvent was removed under reduced pressure, 1 M HCl (50 mL) was added and the crude material was extracted with DCM (3 × 30 mL). The organic fractions were collected, dried over magnesium sulfate and the solvent was removed under reduced pressure. The crude material was then washed on silica gel with DCM, before being recovered by adding 20% MeOH to the eluent in order to obtain **P16-C7** as a brownish gel. **(25 mg, 50% yield)**

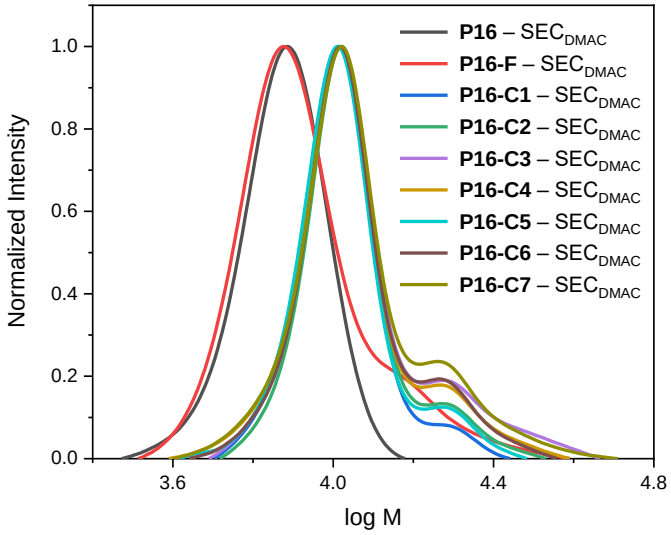

Figure S109: SEC_{DMAC} traces of polymers **P16**, **P16-F**, **P16-C1**, **P16-C2**, **P16-C3**, **P16-C4**, **P16-C5**, **P16-C6** and **P16-C7**.

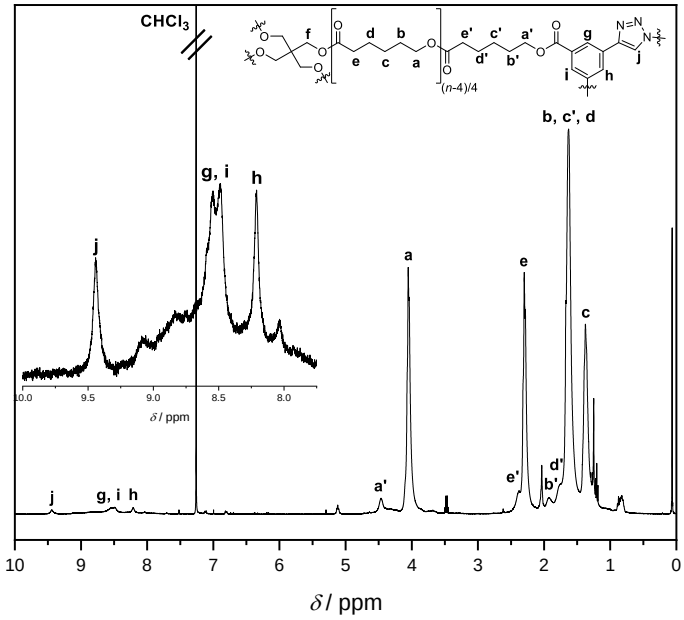

Figure S110: ^{1}H-NMR spectrum of **P16-C7**, **^{1}H NMR (400 MHz, $CDCl_3$) δ** 9.44 (s), 8.55 (s), 8.49 (s), 8.21 (s), 4.56 – 4.37 (m), 4.21 – 3.87 (m), 2.49 – 2.35 (m), 2.36 – 2.13 (m), 1.99 – 1.86 (m), 1.86 – 1.74 (m), 1.74 – 1.45 (m), 1.45 – 1.26 (m).

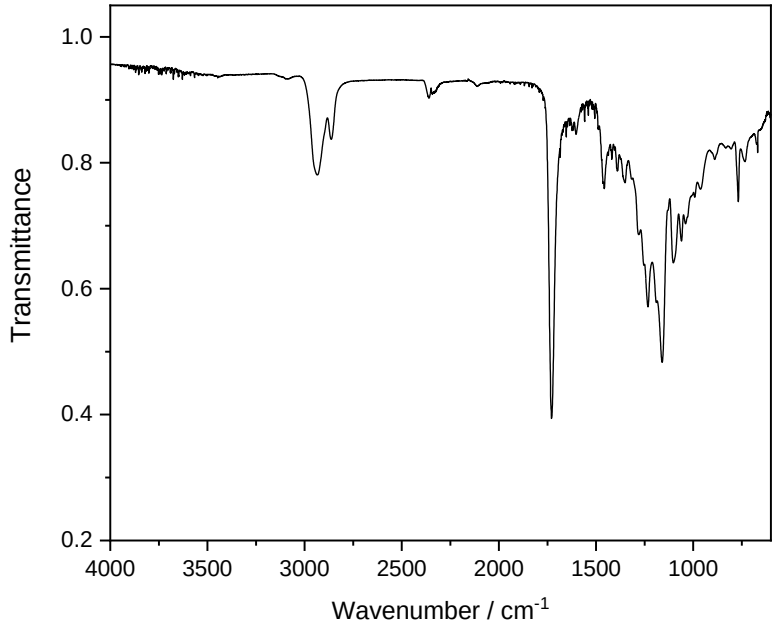

Figure S111: FT-IR spectrum of **P16-C7**, **IR (ATR, cm^{-1})** 2935, 2863, 1729, 1603, 1461, 1419, 1390, 1350, 1233, 1160, 1102, 1060, 768, 668.

8.6.12 **(P16-C8)** *Cage*-shaped Polymer Synthesis *via* CuAAC Reaction

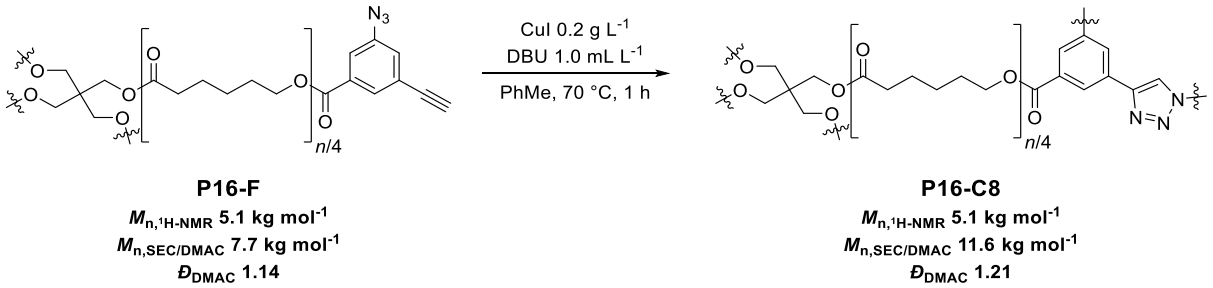

P16-F
$M_{n,^1H\text{-}NMR}$ 5.1 kg mol^{-1}
$M_{n,SEC/DMAC}$ 7.7 kg mol^{-1}
$Đ_{DMAC}$ 1.14

P16-C8
$M_{n,^1H\text{-}NMR}$ 5.1 kg mol^{-1}
$M_{n,SEC/DMAC}$ 11.6 kg mol^{-1}
$Đ_{DMAC}$ 1.21

P16-F (50 mg, 0.25 mg mL^{-1}) and DBU (0.2 mL, 1.0 mL L^{-1}) were dissolved in toluene (200 mL). The mixture was purged with argon for 15 min and CuI (40 mg, 200 mg L^{-1}) was added. The mixture was then purged a second time with argon for another 15 min before being heated at 70 °C for 1 hour. Afterwards, the solvent was removed under reduced pressure, 1 M HCl (50 mL) was added and the crude material was extracted with DCM (3 × 30 mL). The organic fractions were collected, dried over magnesium sulfate and the solvent was removed under reduced pressure. The crude material was then washed on silica gel with DCM, before being recovered by adding 20% MeOH to the eluent in order to obtain **P16-C8** as a brownish gel. **(32 mg, 64% yield)**

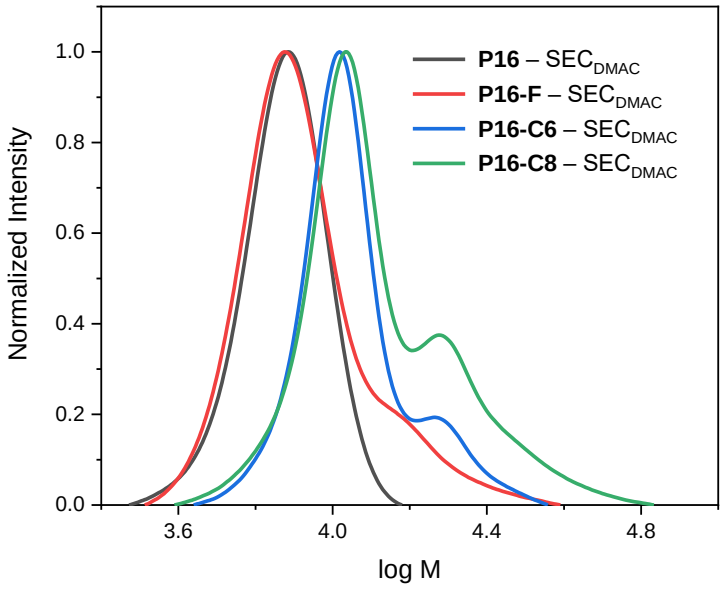

Figure S112: SEC_{DMAC} traces of polymers **P16**, **P16-F**, **P16-C6** and **P16-C8**.

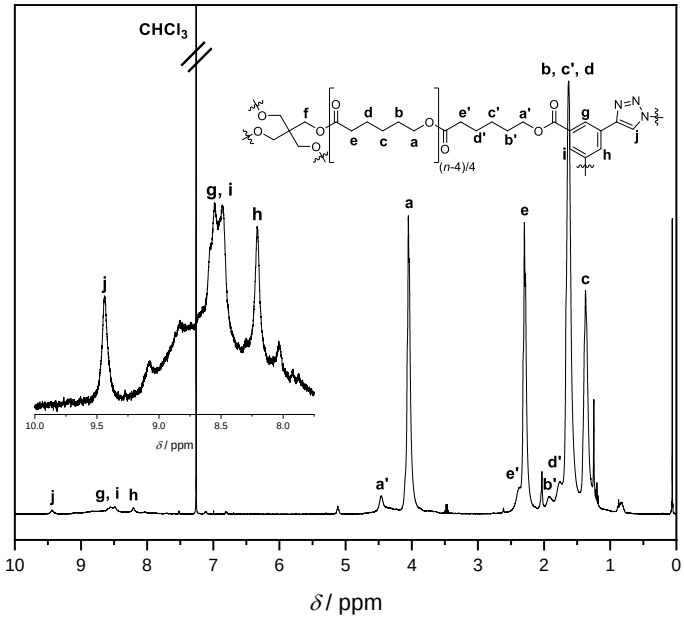

Figure S113: ^{1}H-NMR spectrum of **P16-C8**, **^{1}H NMR (400 MHz, $CDCl_3$)** δ 9.52 – 9.34 (m), 8.61 – 8.52 (m), 8.52 – 8.43 (m), 8.29 – 8.12 (m), 4.55 – 4.38 (m), 4.20 – 3.82 (m), 2.52 – 2.35 (m), 2.35 – 2.11 (m), 1.99 – 1.85 (m), 1.83 – 1.73 (m), 1.72 – 1.46 (m), 1.46 – 1.26 (m).

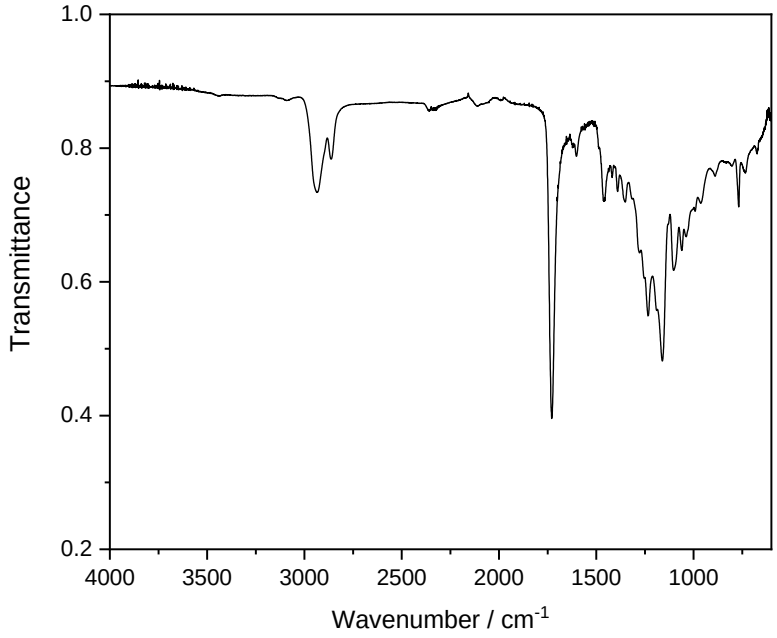

Figure S114: FT-IR spectrum of **P16-C8**, **IR (ATR, cm^{-1})** 2933, 2862, 1729, 1602, 1456, 1390, 1351, 1233, 1160, 1102, 1060, 768, 734, 668.

8.6.13 **(P16-C9)** *Cage*-shaped Polymer Synthesis *via* CuAAC Reaction

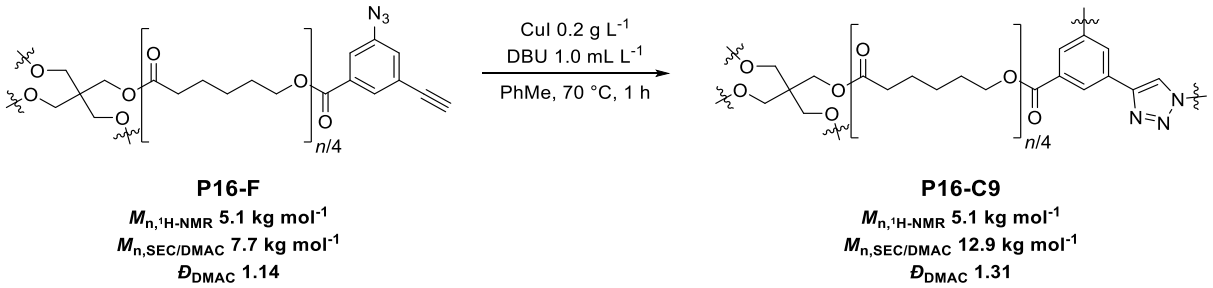

P16-F
$M_{n,^1H\text{-}NMR}$ 5.1 kg mol^{-1}
$M_{n,SEC/DMAC}$ 7.7 kg mol^{-1}
$Đ_{DMAC}$ 1.14

P16-C9
$M_{n,^1H\text{-}NMR}$ 5.1 kg mol^{-1}
$M_{n,SEC/DMAC}$ 12.9 kg mol^{-1}
$Đ_{DMAC}$ 1.31

P16-F (50 mg, 0.50 mg mL^{-1}) and DBU (0.1 mL, 1.0 mL L^{-1}) were dissolved in toluene (100 mL). The mixture was purged with argon for 15 min and CuI (20 mg, 200 mg L^{-1}) was added. The mixture was then purged a second time with argon for another 15 min before being heated at 70 °C for 1 hour. Afterwards, the solvent was removed under reduced pressure, 1 M HCl (50 mL) was added and the crude material was extracted with DCM (3 × 30 mL). The organic fractions were collected, dried over magnesium sulfate and the solvent was removed under reduced pressure. The crude material was then washed on silica gel with DCM, before being recovered by adding 20% MeOH to the eluent in order to obtain **P16-C9** as a brownish gel. **(31 mg, 62% yield)**

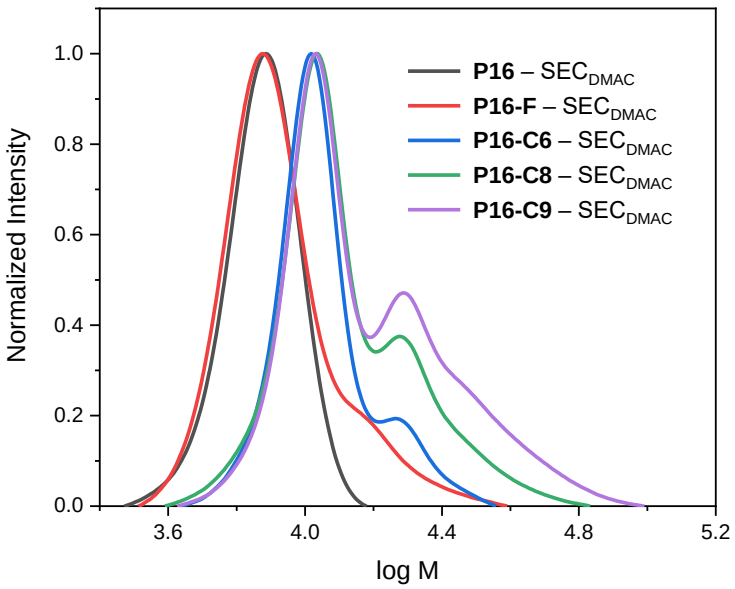

Figure S115: SEC_{DMAC} traces of polymers **P16**, **P16-F**, **P16-C6**, **P16-C8** and **P16-C9**.

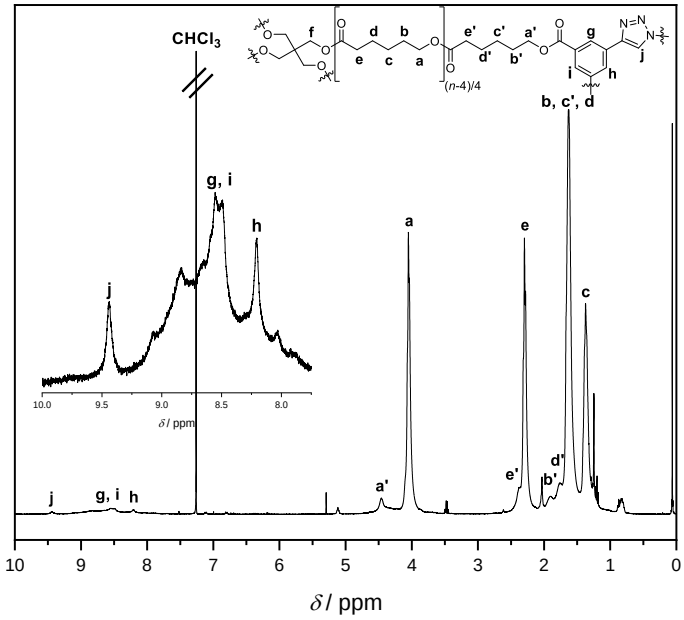

Figure S116: ^{1}H-NMR spectrum of **P16-C9**, **^{1}H NMR (400 MHz, $CDCl_3$) δ** 9.44 (s), 8.93 – 8.38 (m), 8.21 (s), 4.60 – 4.32 (m), 4.22 – 3.83 (m), 2.54 – 2.10 (m), 1.98 – 1.85 (m), 1.84 – 1.71 (m), 1.73 – 1.45 (m), 1.47 – 1.26 (m).

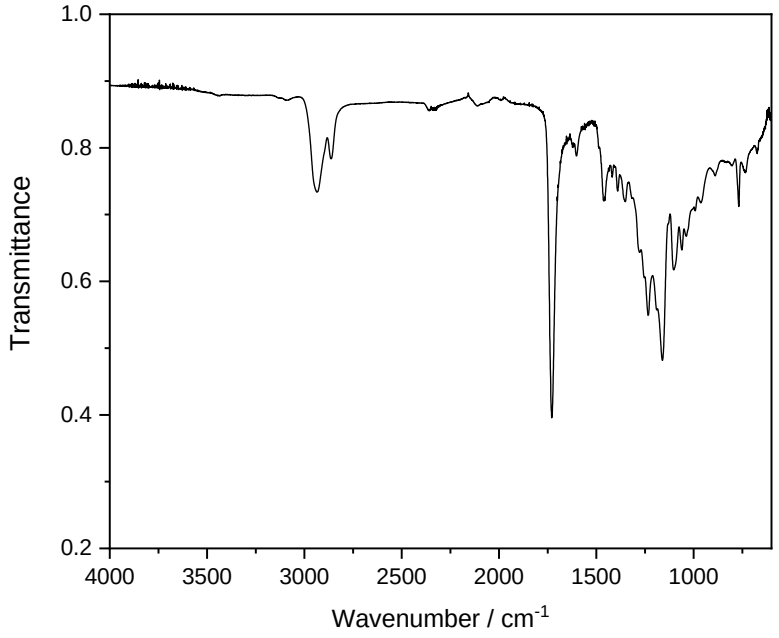

Figure S117: FT-IR spectrum of **P16-C9**, **IR (ATR, cm^{-1})** 2935, 2863, 1729, 1602, 1460, 1390, 1351, 1233, 1160, 1102, 1060, 768.

8.6.14 **(P17)** Cationic Ring Opening Polymerization (CROP) of ε-Caprolactone

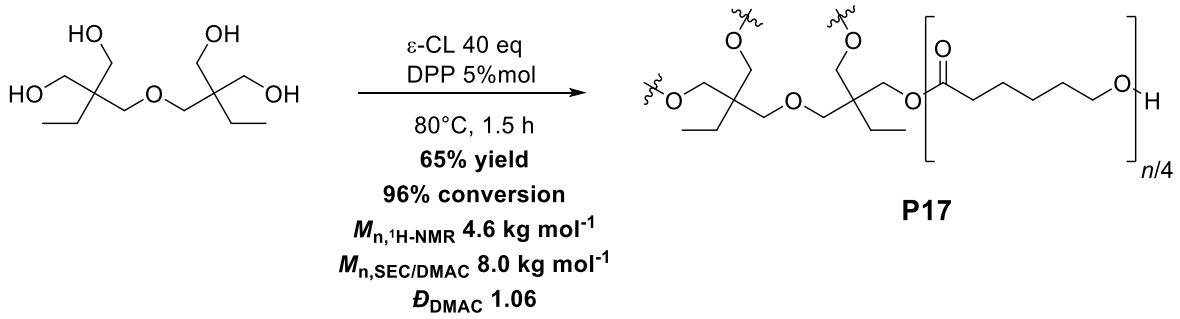

ε-Caprolactone (8.0 mL, 75.0 mmol, 40 eq), di(trimethylolpropane) (471 mg, 1.88 mmol, 1.00 eq) and diphenyl phosphate (23 mg, 0.09 mmol, 0.05 eq) were mixed and heated at 80 °C under stirring for 1.5 hours. Afterwards, the viscous liquid was cooled down to room temperature and precipitated in cold MeOH (80 mL, -20 °C). The white precipitate was then redissolved in DCM and reprecipitated in cold MeOH (80 mL, -20 °C) two more times in order to obtain the desired polymer **P17** as a white solid. **(6.01 g, 1.31 mmol, 65% yield)**

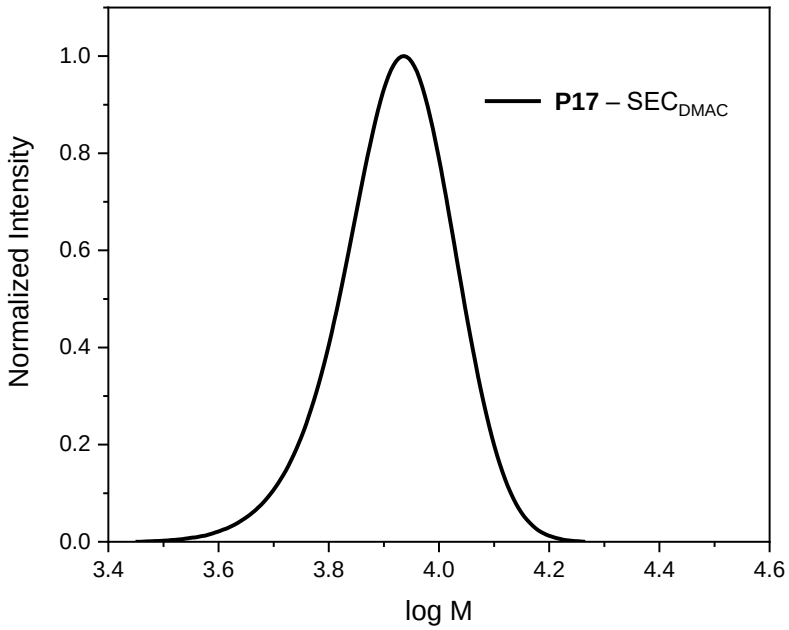

Figure S118: SEC_{DMAC} trace of polymer **P17**.

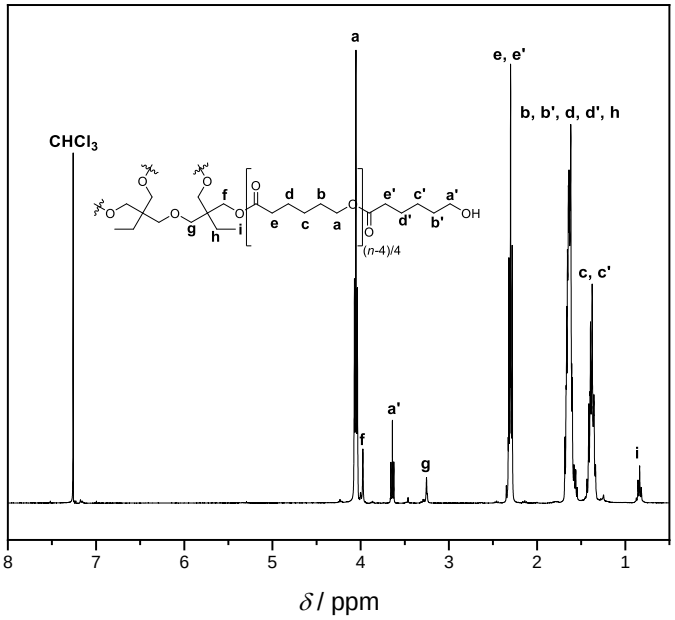

Figure S119: ^{1}H-NMR spectrum of **P17**, **^{1}H NMR (400 MHz, $CDCl_3$)** δ 4.05 (t, J = 6.7 Hz), 3.97 (s), 3.64 (t, J = 6.5 Hz), 3.25 (s), 2.37 – 2.23 (m), 1.69 – 1.53 (m), 1.46 – 1.31 (m), 0.84 (t, J = 7.6 Hz).

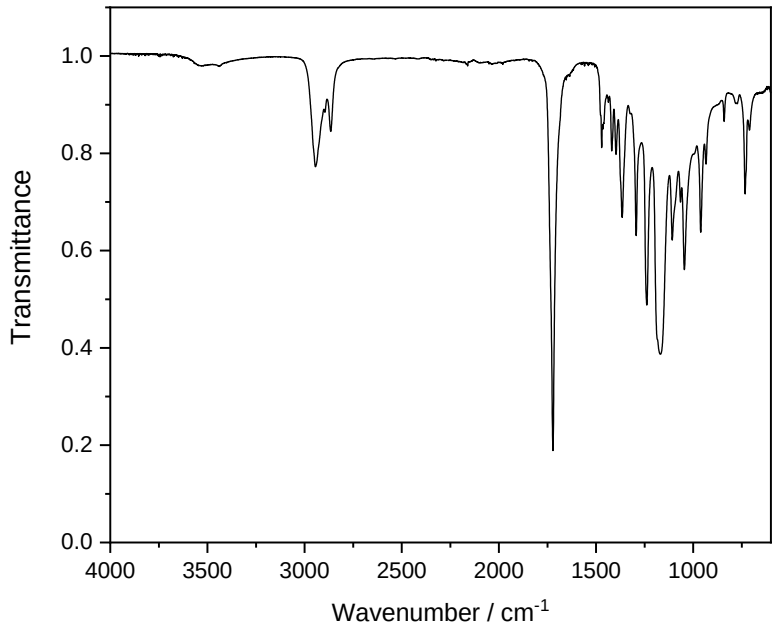

Figure S120: FT-IR spectrum of **P17**, **IR (ATR, cm^{-1})** 2944, 2865, 1721, 1471, 1419, 1397 ,1366, 1293, 1239, 1168, 1108, 1045, 961, 934, 841, 733.

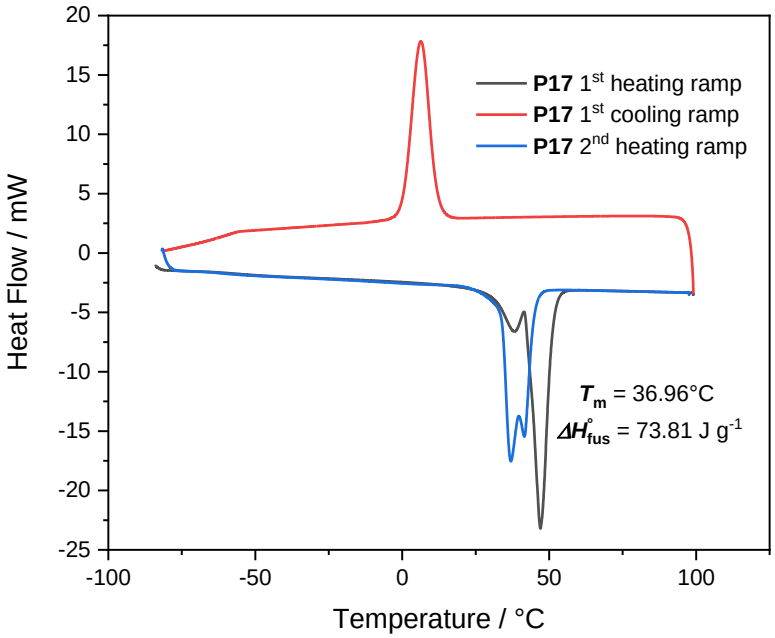

Figure S121: DSC thermogram of **P17**, all thermal values were taken from the second heating ramp.

8.6.15 **(P17-F)** End-functionalization of P17 with End-group C20

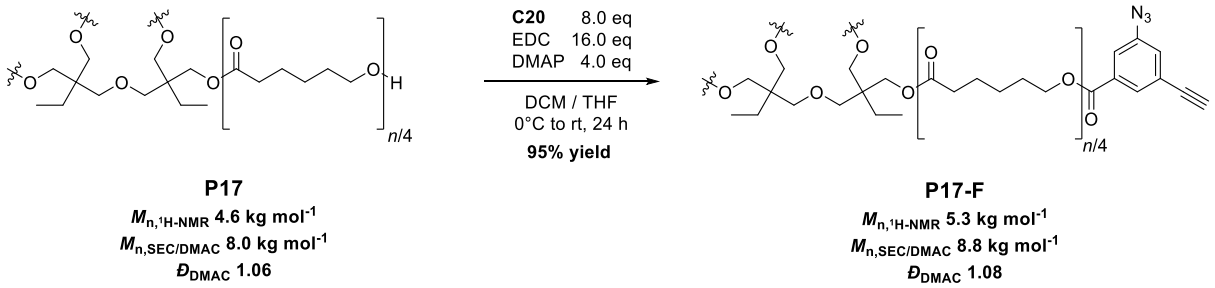

P17
$M_{n,^1H\text{-}NMR}$ 4.6 kg mol^{-1}
$M_{n,SEC/DMAC}$ 8.0 kg mol^{-1}
$Đ_{DMAC}$ 1.06

P17-F
$M_{n,^1H\text{-}NMR}$ 5.3 kg mol^{-1}
$M_{n,SEC/DMAC}$ 8.8 kg mol^{-1}
$Đ_{DMAC}$ 1.08

Previously synthetized *star*-(ε-PCL-OH)$_4$ **P17** (681 mg, 0.148 mmol, 1.0 eq), 3-azido-5-ethynylbenzoic acid **C20** (221 mg, 1.18 mmol, 8.0 eq) and DMAP (72 mg, 0.59 mmol, 4.0 eq) were dissolved in dry DCM (8 mL) and dry THF (2 mL). The solution was cooled down to 0 °C and *N*-(3-dimethylaminopropyl)-*N*′-ethylcarbodiimide hydrochloride (452 mg, 2.36 mmol, 16.0 eq) was added portionwise. The mixture was then stirred for 24 hours from 0 °C to room temperature. Afterwards, the resulting mixture was quenched with 1 M HCl (30 mL) and the aqueous phase was extracted with DCM (3 × 20 mL). The organic fractions were collected, dried over magnesium sulfate and the solvents were removed under reduced pressure. The crude polymer was reprecipitated three times in cold MeOH (80 mL, -20 °C) in order to give **P17-F** as a yellowish solid. **(0.751 g, 0.141 mmol, 95% yield)**

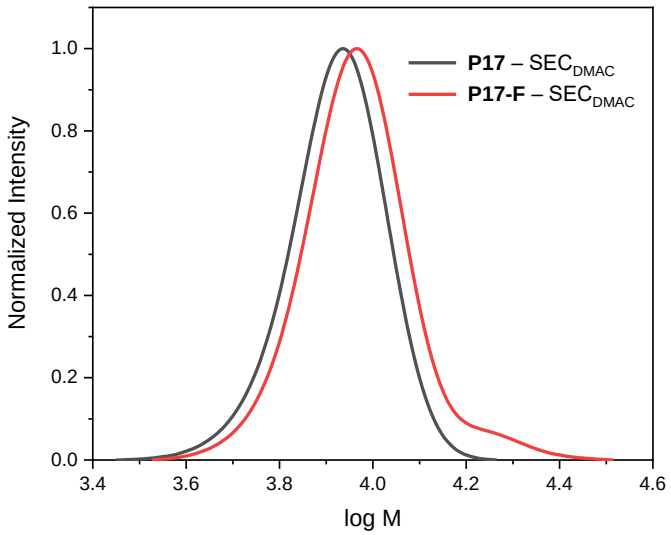

Figure S122: SEC_{DMAC} traces of polymers **P17** and **P17-F**.

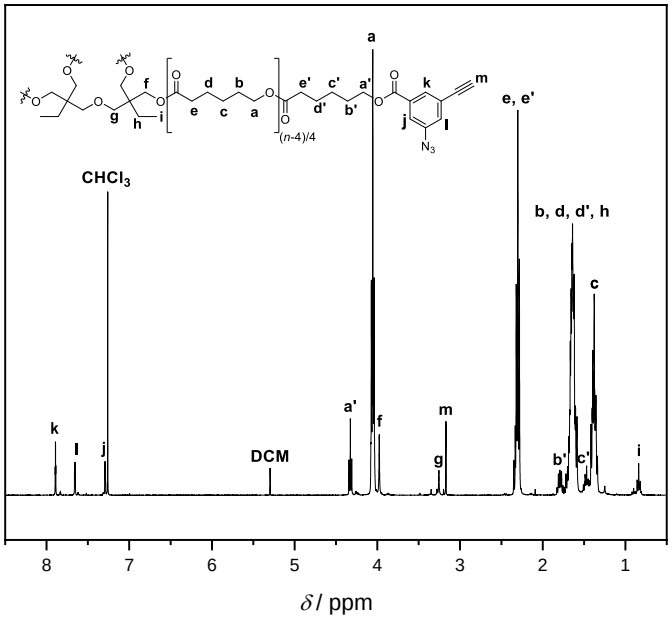

Figure S123: ^{1}H-NMR spectrum of **P17-F**, **^{1}H NMR (400 MHz, $CDCl_3$)** δ 7.89 (t, J = 1.4 Hz), 7.66 (dd, J = 2.2, 1.5 Hz), 7.29 (dd, J = 2.2, 1.4 Hz), 4.33 (t, J = 6.6 Hz), 4.06 (t, J = 6.7 Hz), 3.98 (s), 3.26 (s), 3.17 (s), 2.41 – 2.20 (m), 1.85 – 1.54 (m), 1.52 – 1.30 (m), 0.84 (t, J = 7.5 Hz).

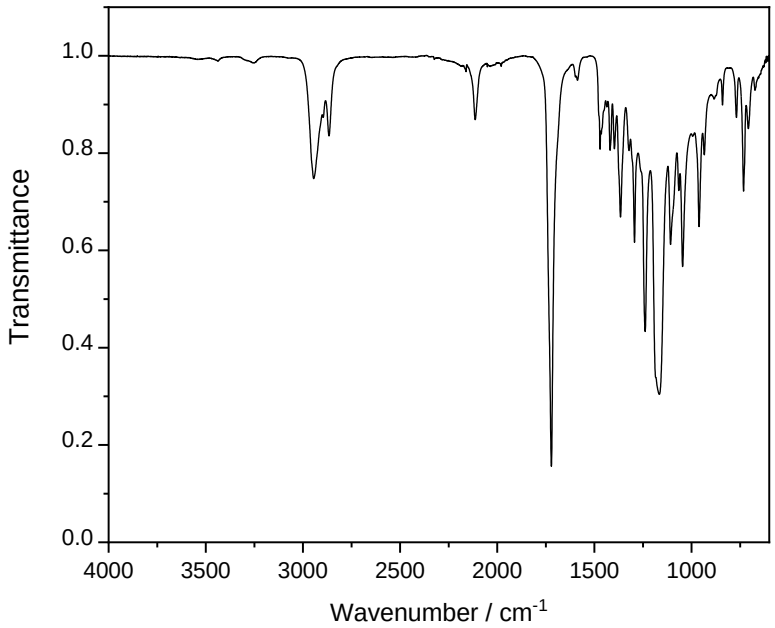

Figure S124: FT-IR spectrum of **P17-F**, **IR (ATR, cm^{-1})** 2945, 2866, 2113, 1721, 1471, 1419, 1397, 1366, 1293, 1239, 1166, 1108, 1066, 1046, 961, 934, 841, 769, 732, 708.

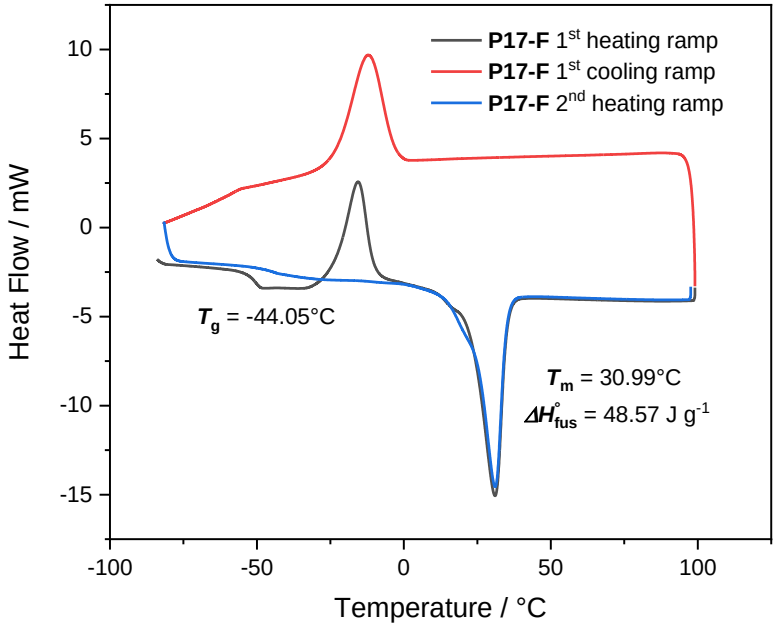

Figure S125: DSC thermogram of **P17-F**, all thermal values were taken from the second heating ramp.

8.6.16 **(P17-C)** *Cage*-shaped Polymer Synthesis *via* CuAAC Reaction

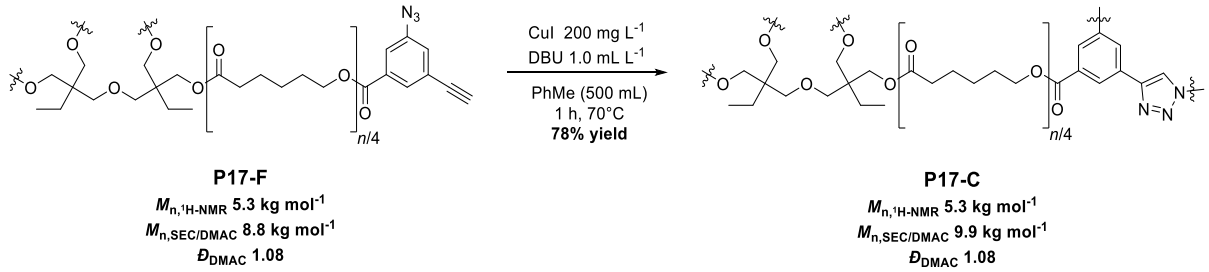

P17-F
$M_{n,^1H\text{-}NMR}$ 5.3 kg mol^{-1}
$M_{n,SEC/DMAC}$ 8.8 kg mol^{-1}
$Đ_{DMAC}$ 1.08

P17-C
$M_{n,^1H\text{-}NMR}$ 5.3 kg mol^{-1}
$M_{n,SEC/DMAC}$ 9.9 kg mol^{-1}
$Đ_{DMAC}$ 1.08

P17-F (50 mg, 0.10 mg mL^{-1}) and DBU (0.5 mL, 1.0 mL L^{-1}) were dissolved in toluene (500 mL). The mixture was purged with argon for 15 min and CuI (100 mg, 200 mg L^{-1}) was added. The mixture was then purged a second time with argon for another 15 min before being heated for 1 hour at 70 °C. Afterwards, the solvent was removed under reduced pressure, 1 M HCl (50 mL) was added and the crude material was extracted with DCM (3 × 30 mL). The organic fractions were collected, dried over magnesium sulfate and the solvent was removed under reduced pressure. The crude material was then washed on silica gel with $CHCl_3$, before being recovered by adding 20% MeOH to the eluent in order to obtain after solvent evaporation and filtration of the remaining silica gel **P17-C** as a brownish gel. **(39 mg, 78% yield)**

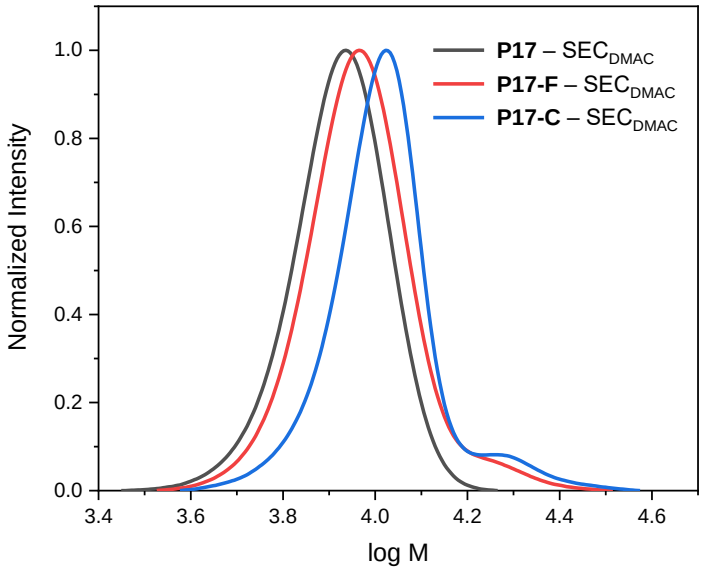

Figure S126: SEC_{DMAC} traces of polymers **P17**, **P17-F** and **P17-C**.

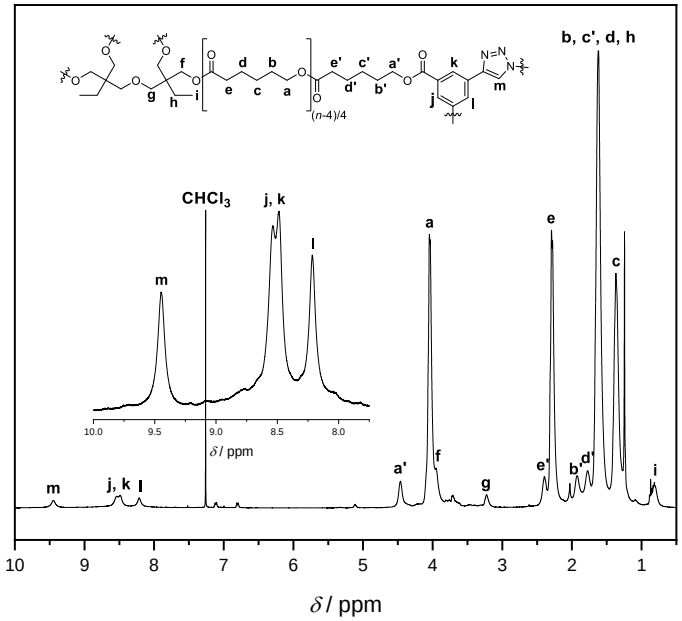

Figure S127: ^{1}H-NMR spectrum of **P17-C**, **^{1}H NMR (400 MHz, $CDCl_3$)** δ 9.44 (s), 8.54 (s), 8.49 (s), 8.21 (s), 4.46 (s), 4.15 – 3.85 (m), 3.23 (s), 2.40 (s), 2.33 – 2.23 (m), 2.03 (s), 1.93 (s), 1.78 (s), 1.62 (s), 1.37 (s), 0.91 – 0.71 (m).

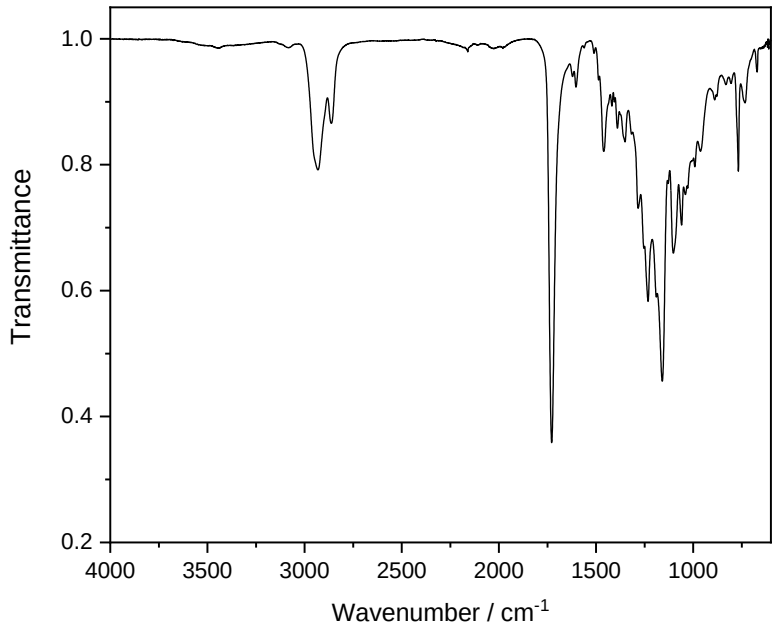

Figure S128: FT-IR spectrum of **P17-C**, **IR (ATR, cm^{-1})** 2931, 2862, 1728, 1603, 1460, 1390, 1351, 1283, 1232, 1159, 1102, 1059, 991, 963, 889, 831, 767, 733, 671.

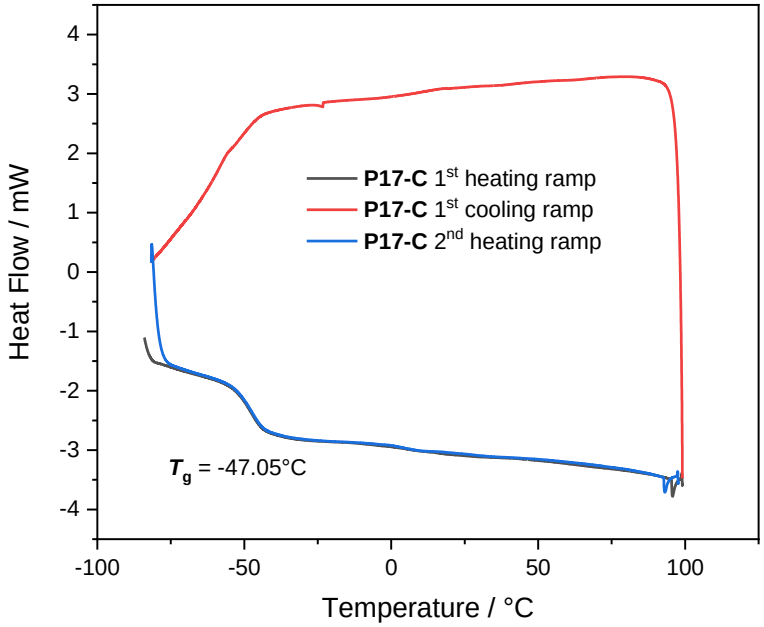

Figure S129: DSC thermogram of **P17-C**, all thermal values were taken from the second heating ramp.

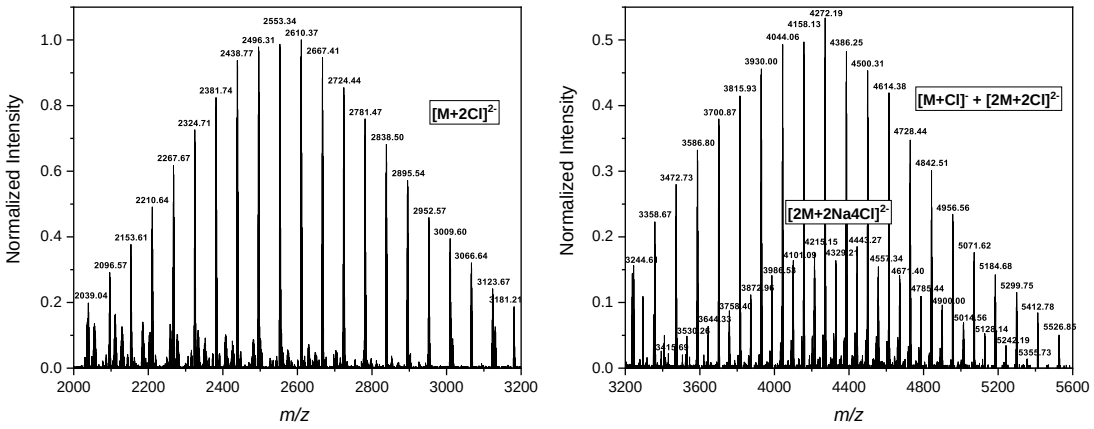

Figure S130: ESI-MS spectra of **P17-C**, featuring all four main distributions obtained in negative mode.

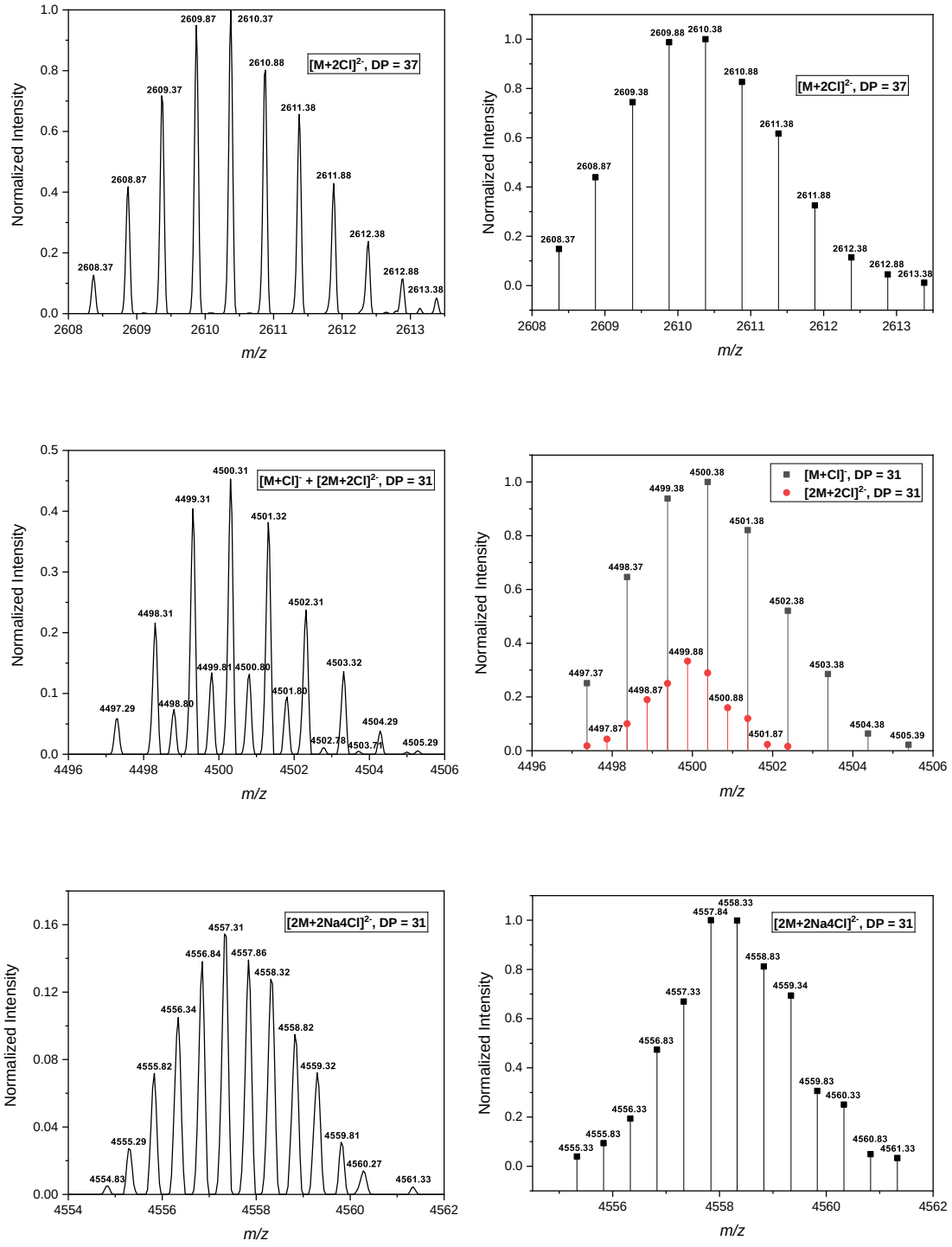

Figure S131: ESI-MS spectra of **P17-C**, experimental (left) and calculated (right) MS patterns obtained for all four main distributions present in negative mode.

8.6.17 **(P18)** Cationic Ring Opening Polymerization (CROP) of ε-Caprolactone

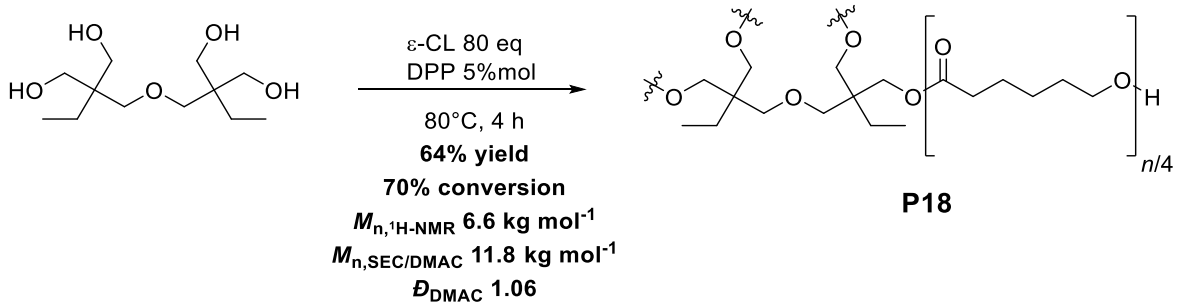

ε-Caprolactone (8.0 mL, 75.0 mmol, 80 eq), di(trimethylolpropane) (235 mg, 0.94 mmol, 1.00 eq) and diphenyl phosphate (13 mg, 0.05 mmol, 0.05 eq) were mixed and heated at 80 °C under stirring for 4 hours. Afterwards, the viscous liquid was cooled down to room temperature and precipitated in cold MeOH (80 mL, -20 °C). The white precipitate was then redissolved in DCM and reprecipitated in cold MeOH (80 mL, -20 °C) two more times in order to obtain the desired polymer **P18** as a white solid. **(5.69 g, 0.86 mmol, 64% yield)**

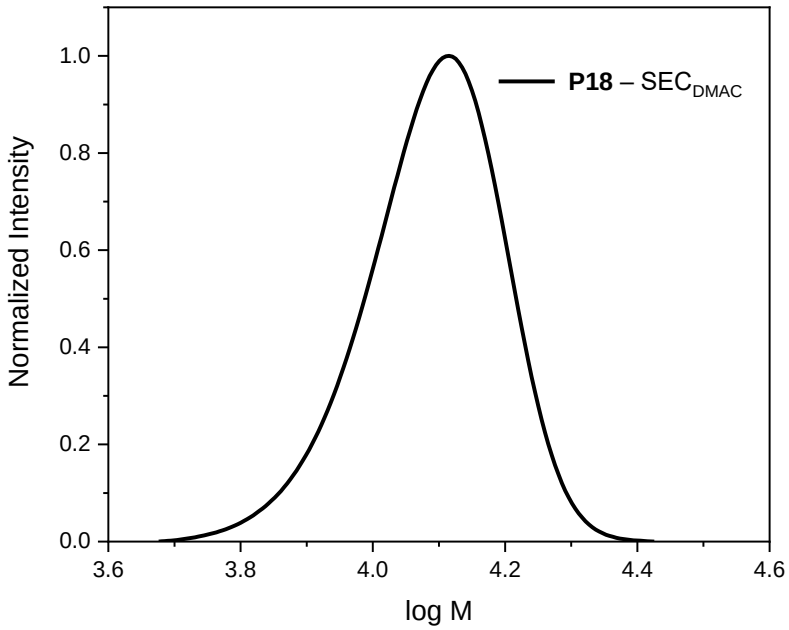

Figure S132: SEC_{DMAC} trace of polymer **P18**.

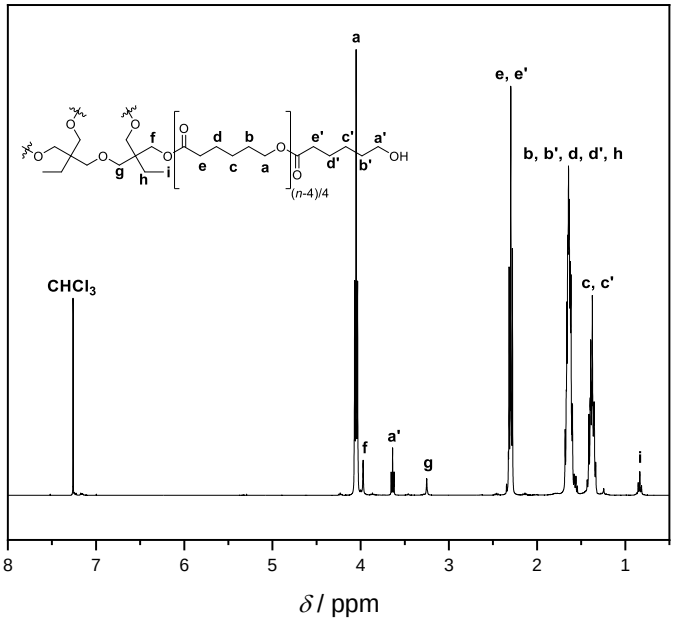

Figure S133: ^{1}H-NMR spectrum of **P18**, **^{1}H NMR (400 MHz, $CDCl_3$)** ***δ*** 4.05 (t, *J* = 6.7 Hz), 3.97 (s), 3.64 (t, *J* = 6.5 Hz), 3.25 (s), 2.37 – 2.23 (m), 1.73 – 1.52 (m), 1.47 – 1.30 (m), 0.83 (t, *J* = 7.6 Hz).

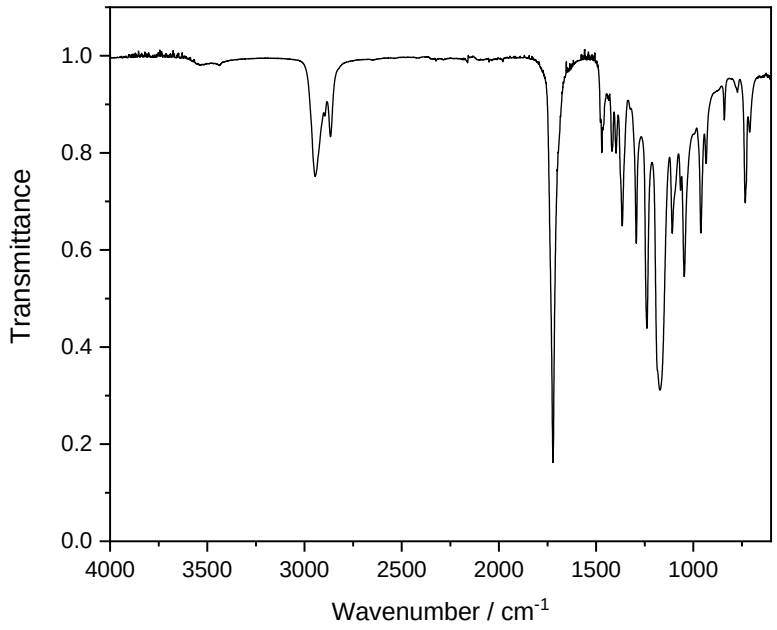

Figure S134: FT-IR spectrum of **P18**, **IR (ATR, cm^{-1})** 2945, 2866. 1721, 1471, 1418, 1397, 1366, 1293, 1239, 1171, 1108, 1047, 961, 934, 840, 73.

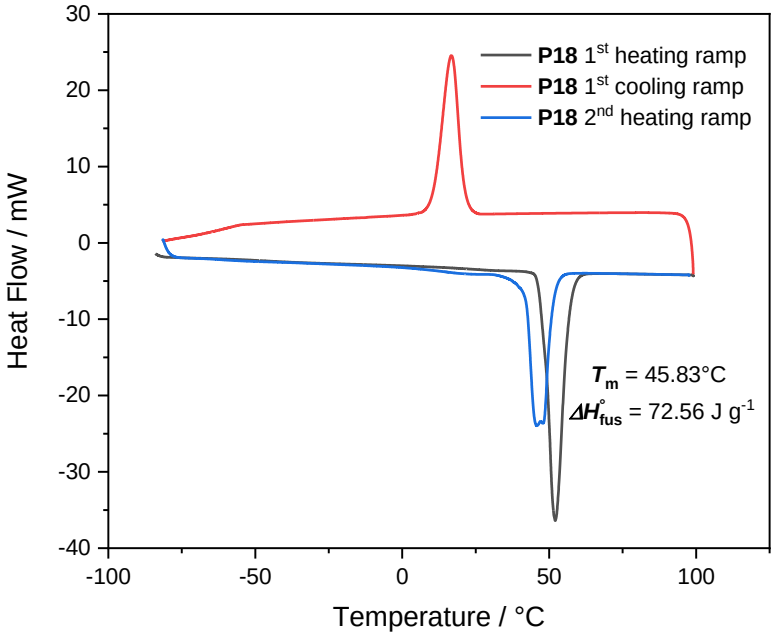

Figure S135: DSC thermogram of **P18**, all thermal values were taken from the second heating ramp.

8.6.18 **(P18-F)** End-functionalization of P18 with End-group C20

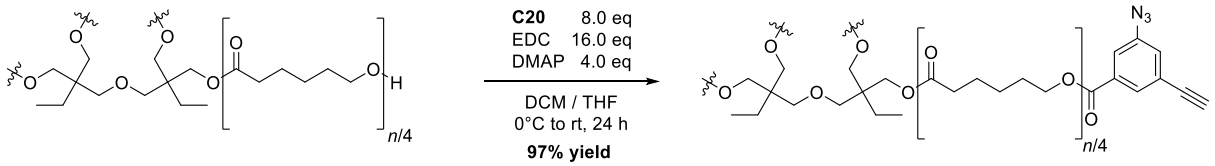

P18
$M_{n,^1H\text{-}NMR}$ 6.6 kg mol^{-1}
$M_{n,SEC/DMAC}$ 11.8 kg mol^{-1}
$Đ_{DMAC}$ 1.06

P18-F
$M_{n,^1H\text{-}NMR}$ 7.3 kg mol^{-1}
$M_{n,SEC/DMAC}$ 12.5 kg mol^{-1}
$Đ_{DMAC}$ 1.07

Previously synthetized *star*-(ε-PCL-OH)$_4$ **P18** (990 mg, 0.150 mmol, 1.0 eq), 3-azido-5-ethynylbenzoic acid **C20** (224 mg, 1.20 mmol, 8.0 eq) and DMAP (73 mg, 0.60 mmol, 4.0 eq) were dissolved in dry DCM (8 mL) and dry THF (2 mL). The solution was cooled down to 0 °C and *N*-(3-dimethylaminopropyl)-*N*′-ethylcarbodiimide hydrochloride (460 mg, 2.40 mmol, 16.0 eq) was added portionwise. The mixture was then stirred for 24 hours from 0 °C to room temperature. Afterwards, the resulting mixture was quenched with 1 M HCl (30 mL) and the aqueous phase was extracted with DCM (3 × 20 mL). The organic fractions were collected, dried over magnesium sulfate and the solvents were removed under reduced pressure. The crude polymer was reprecipitated three times in cold MeOH (80 mL, -20 °C) in order to give **P18-F** as a yellowish solid. **(1.069 g, 0.146 mmol, 97% yield)**

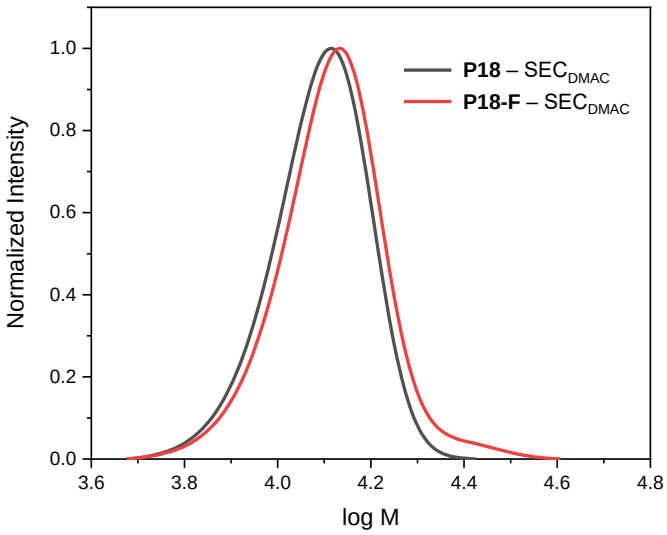

Figure S136: SEC_{DMAC} traces of polymers **P18**, and **P18-F**.

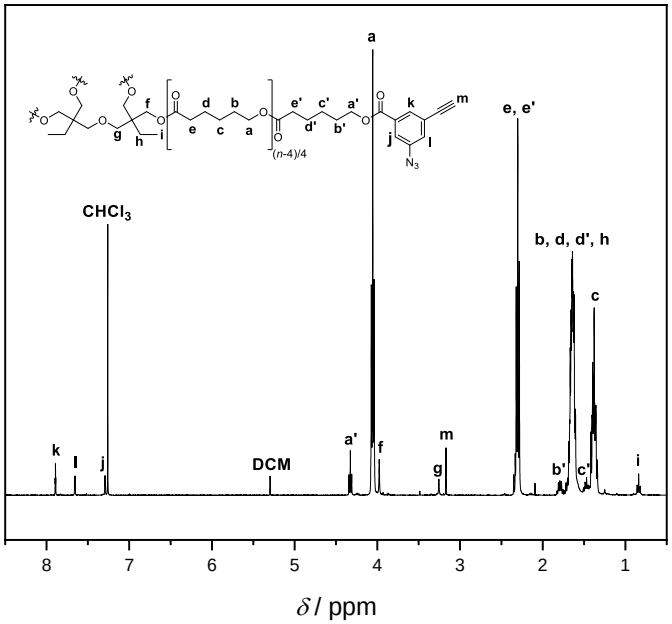

Figure S137: ^{1}H-NMR spectrum of **P18-F**, **^{1}H NMR (400 MHz, $CDCl_3$)** δ 7.89 (t, J = 1.4 Hz), 7.66 (dd, J = 2.2, 1.5 Hz), 7.29 (dd, J = 2.2, 1.4 Hz), 4.33 (t, J = 6.6 Hz), 4.06 (t, J = 6.7 Hz), 3.98 (s), 3.26 (s), 3.17 (s), 2.39 – 2.23 (m), 1.86 – 1.54 (m), 1.53 – 1.30 (m), 0.84 (t, J = 7.5 Hz).

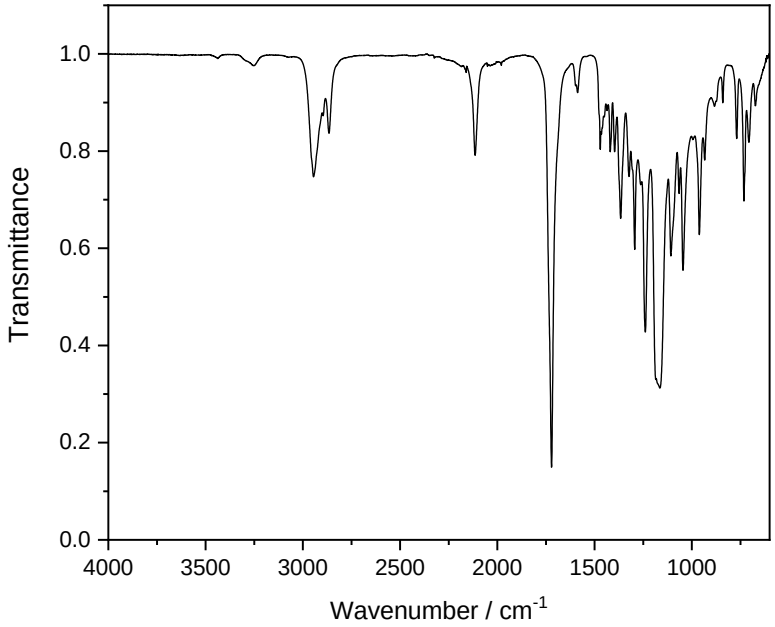

Figure S138: FT-IR spectrum of **P18-F**, **IR (ATR, cm^{-1})** 2945, 2865, 2114, 1721, 1471, 1419, 1397, 1366, 1323, 1294, 1239, 1164, 1108, 1066, 1045, 961, 934, 769, 732, 707.

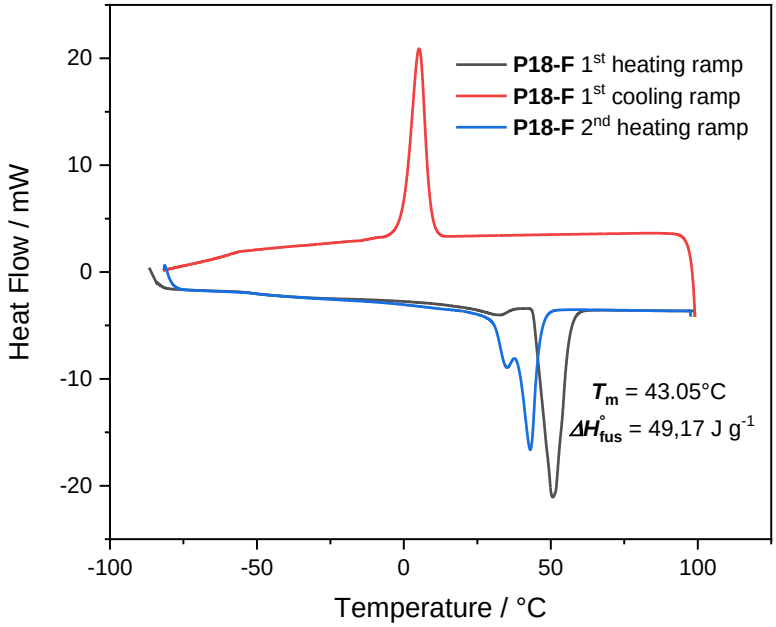

Figure S139: DSC thermogram of **P18-F**, all thermal values were taken from the second heating ramp.

8.6.19 **(P18-C)** *Cage*-shaped Polymer Synthesis *via* CuAAC Reaction

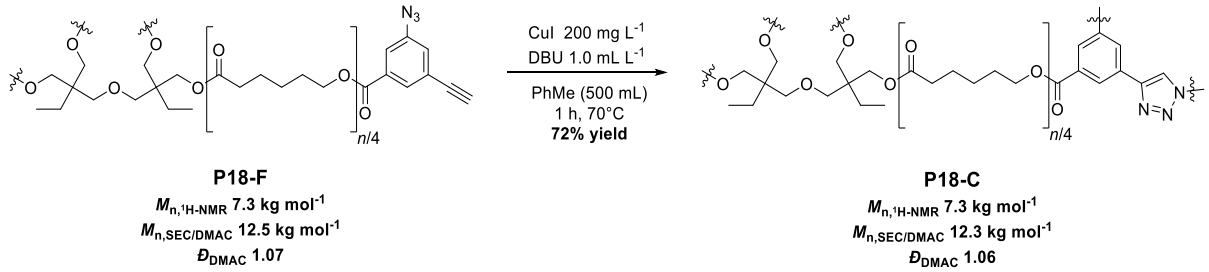

P18-F
$M_{n,^1H\text{-}NMR}$ 7.3 kg mol^{-1}
$M_{n,SEC/DMAC}$ 12.5 kg mol^{-1}
$Đ_{DMAC}$ 1.07

P18-C
$M_{n,^1H\text{-}NMR}$ 7.3 kg mol^{-1}
$M_{n,SEC/DMAC}$ 12.3 kg mol^{-1}
$Đ_{DMAC}$ 1.06

P18-F (50 mg, 0.10 mg mL^{-1}) and DBU (0.5 mL, 1.0 mL L^{-1}) were dissolved in toluene (500 mL). The mixture was purged with argon for 15 min and CuI (100 mg, 200 mg L^{-1}) was added. The mixture was then purged a second time with argon for another 15 min before being heated for 1 hour at 70 °C. Afterwards, the solvent was removed under reduced pressure, 1 M HCl (50 mL) was added and the crude material was extracted with DCM (3 × 30 mL). The organic fractions were collected, dried over magnesium sulfate and the solvent was removed under reduced pressure. The crude material was then washed on silica gel with $CHCl_3$, before being recovered by adding 20% MeOH to the eluent in order to obtain after solvent evaporation and filtration of the remaining silica gel **P18-C** as a brownish gel. **(36 mg, 72% yield)**

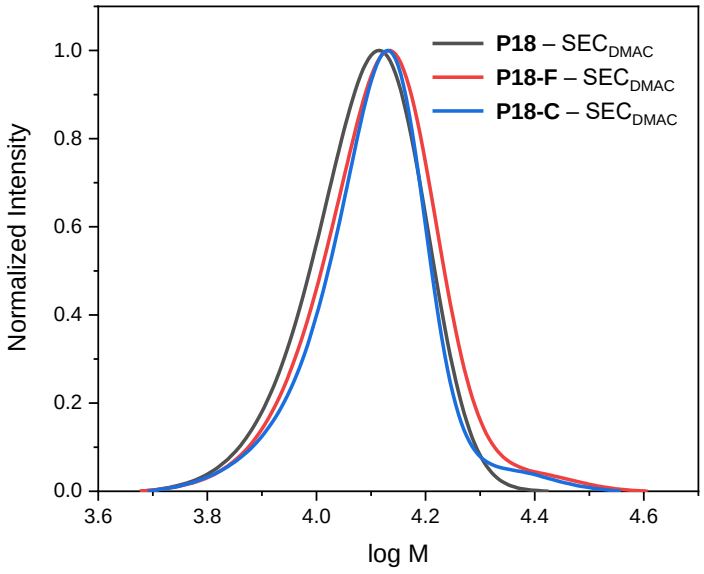

Figure S140: SEC_{DMAC} traces of polymers **P18**, **P18-F** and **P18-C**.

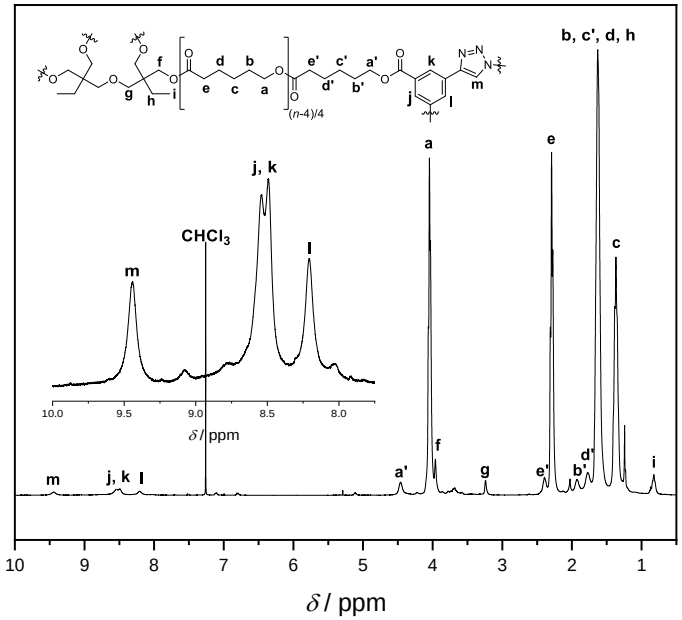

Figure S141: ^{1}H-NMR spectrum of **P18-C**, **^{1}H NMR (400 MHz, $CDCl_3$)** δ 9.44 (s), 8.54 (s), 8.49 (s), 8.20 (s), 4.46 (s), 4.05 (t, J = 5.8 Hz), 3.96 (s), 3.24 (s), 2.39 (s), 2.29 (t, J = 6.9 Hz), 2.03 (s), 1.93 (s), 1.77 (s), 1.63 (s), 1.49 – 1.28 (m), 0.93 – 0.73 (m).

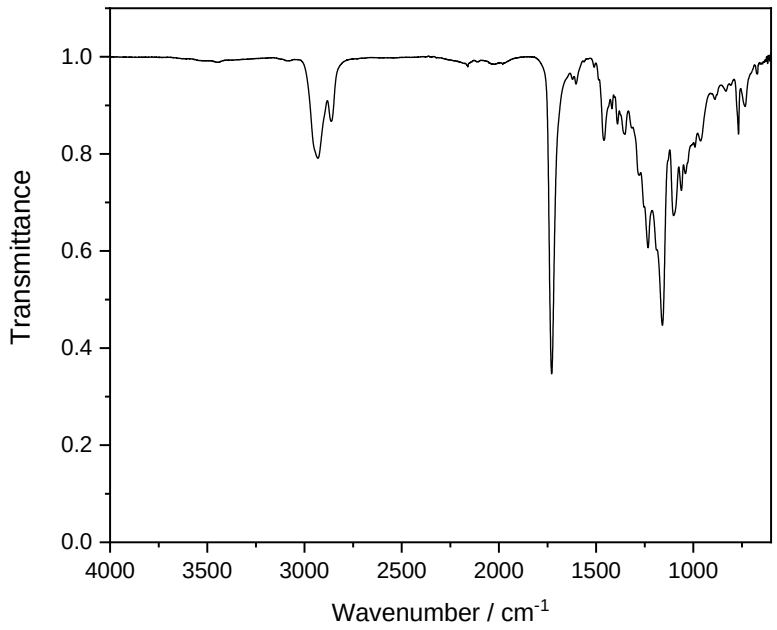

Figure S142: FT-IR spectrum of **P18-C**, **IR (ATR, cm^{-1})** 2931, 2862, 1729, 1603, 1459, 1419, 1390, 1352, 1233, 1159, 1102, 1061, 1041, 962, 889, 833, 767, 733, 671.

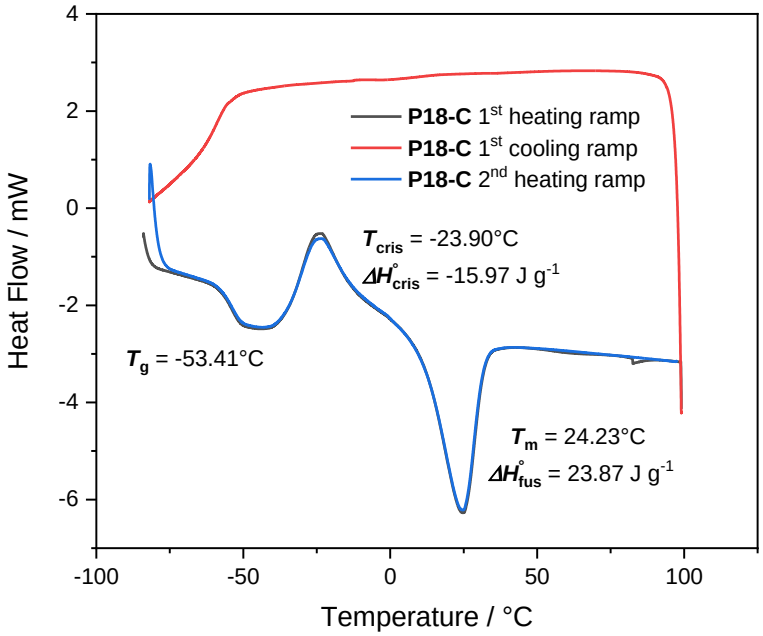

Figure S143: DSC thermogram of **P18-C**, all thermal values were taken from the second heating ramp.

8.6.20 **(P19)** Cationic Ring Opening Polymerization (CROP) of ε-Caprolactone

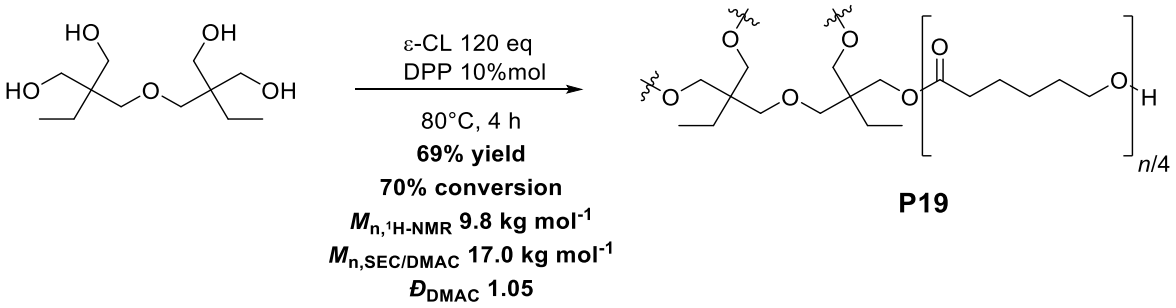

ε-Caprolactone (8.0 mL, 75.0 mmol, 120 eq), di(trimethylolpropane) (158 mg, 0.63 mmol, 1.00 eq) and diphenyl phosphate (15 mg, 0.06 mmol, 0.10 eq) were mixed and heated at 80 °C under stirring for 4 hours. Afterwards, the viscous liquid was cooled down to room temperature and precipitated in cold MeOH (80 mL, -20 °C). The white precipitate was then redissolved in DCM and reprecipitated in cold MeOH (80 mL, -20 °C) two more times in order to obtain the desired polymer **P19** as a white solid. **(6.10 g, 0.62 mmol, 69% yield)**

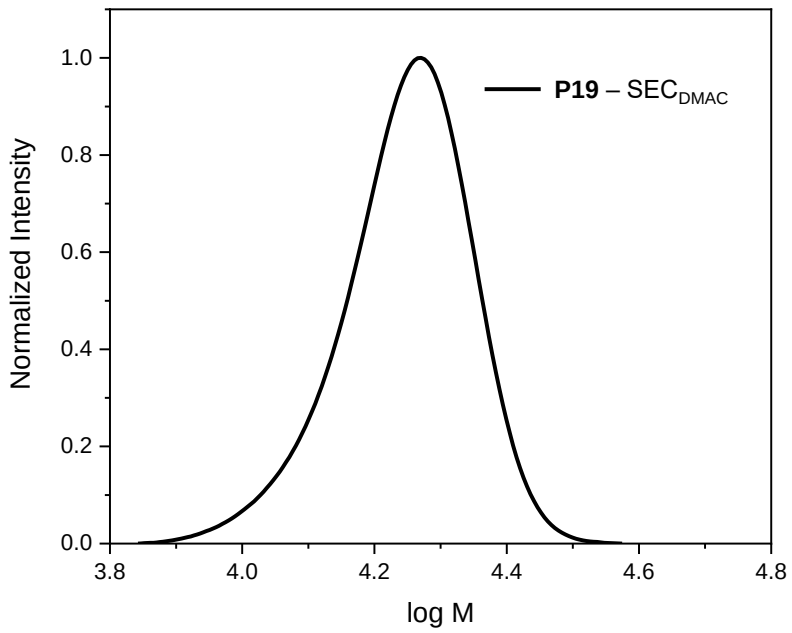

Figure S144: SEC_{DMAC} trace of polymer **P19**.

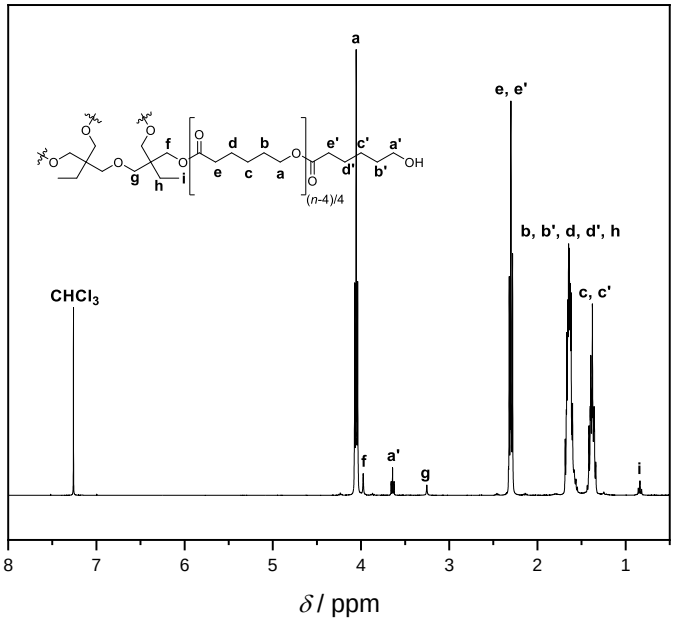

Figure S145: ^{1}H-NMR spectrum of **P19**, **^{1}H NMR (400 MHz, $CDCl_3$) δ** 4.05 (t, *J* = 6.7 Hz), 3.98 (s), 3.64 (t, *J* = 6.5 Hz), 3.25 (s), 2.37 – 2.23 (m), 1.71 – 1.52 (m), 1.48 – 1.28 (m), 0.84 (t, *J* = 7.6 Hz).

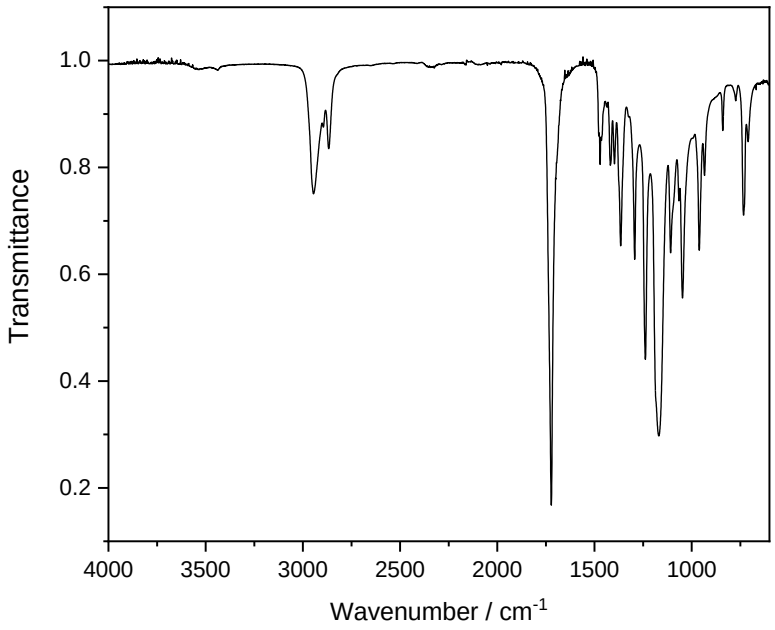

Figure S146: FT-IR spectrum of **P19**, **IR (ATR, cm^{-1})** 2945, 2867, 1722, 1471, 1418, 1397, 1365, 1293, 1238, 1169, 1108, 1047, 961, 934, 840, 733.

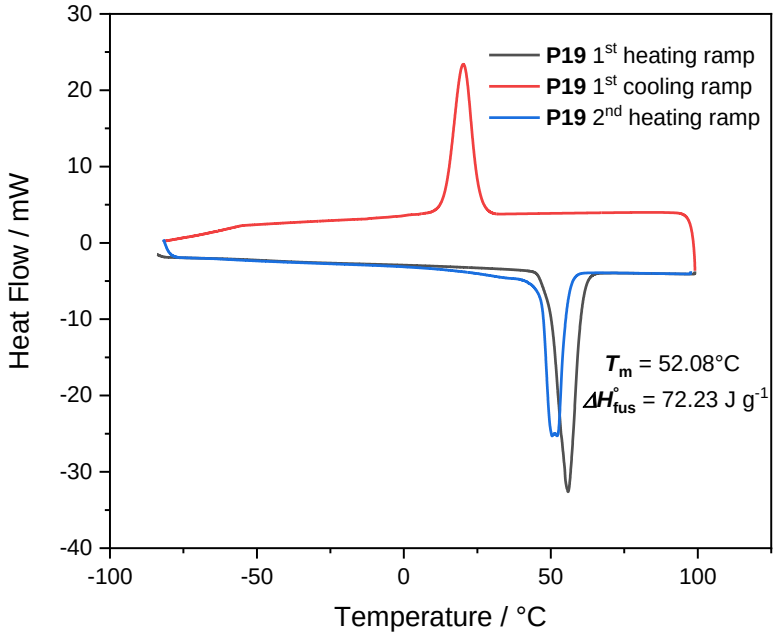

Figure S147: DSC thermogram of **P19**, all thermal values were taken from the second heating ramp.

8.6.21 **(P19-F)** End-functionalization of P19 with End-group C20

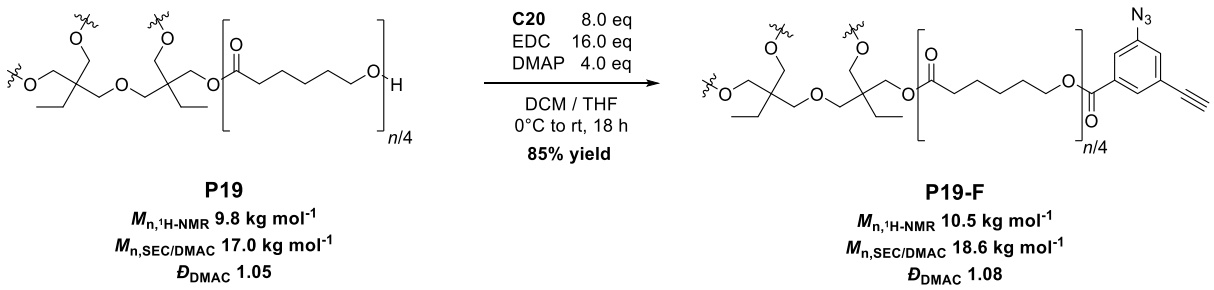

P19
$M_{n,^1H\text{-}NMR}$ 9.8 kg mol^{-1}
$M_{n,SEC/DMAC}$ 17.0 kg mol^{-1}
$Đ_{DMAC}$ 1.05

P19-F
$M_{n,^1H\text{-}NMR}$ 10.5 kg mol^{-1}
$M_{n,SEC/DMAC}$ 18.6 kg mol^{-1}
$Đ_{DMAC}$ 1.08

Previously synthetized *star*-(ε-PCL-OH)$_4$ **P19** (1.11 g, 0.113 mmol, 1.0 eq), 3-azido-5-ethynylbenzoic acid **C20** (169 mg, 0.903 mmol, 8.0 eq) and DMAP (55 mg, 0.45 mmol, 4.0 eq) were dissolved in dry DCM (5 mL) and dry THF (2 mL). The solution was cooled down to 0 °C and *N*-(3-dimethylaminopropyl)-*N*′-ethylcarbodiimide hydrochloride (346 mg, 1.81 mmol, 16.0 eq) was added portionwise. The mixture was then stirred for 18 hours from 0 °C to room temperature. Afterwards, the resulting mixture was quenched with 1 M HCl (30 mL) and the aqueous phase was extracted with DCM (3 × 20 mL). The organic fractions were collected, dried over magnesium sulfate and the solvents were removed under reduced pressure. The crude polymer was reprecipitated three times in cold MeOH (80 mL, -20 °C) in order to give **P19-F** as a light brownish solid. **(1.01 g, 0.096 mmol, 85% yield)**

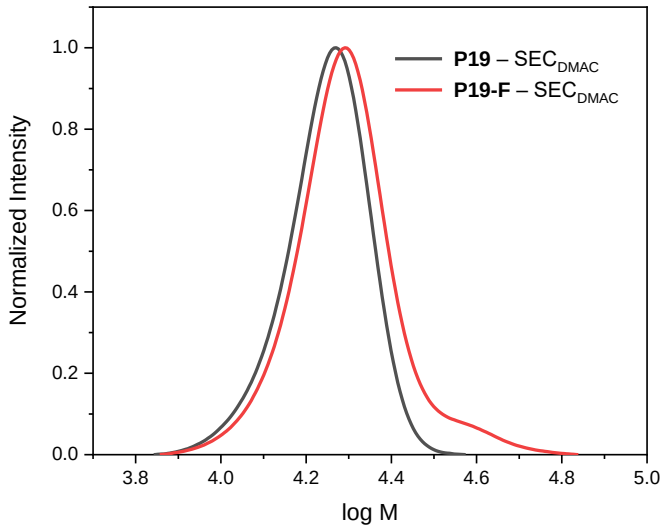

Figure S148: SEC$_{DMAC}$ traces of polymers **P19** and **P19-F**.

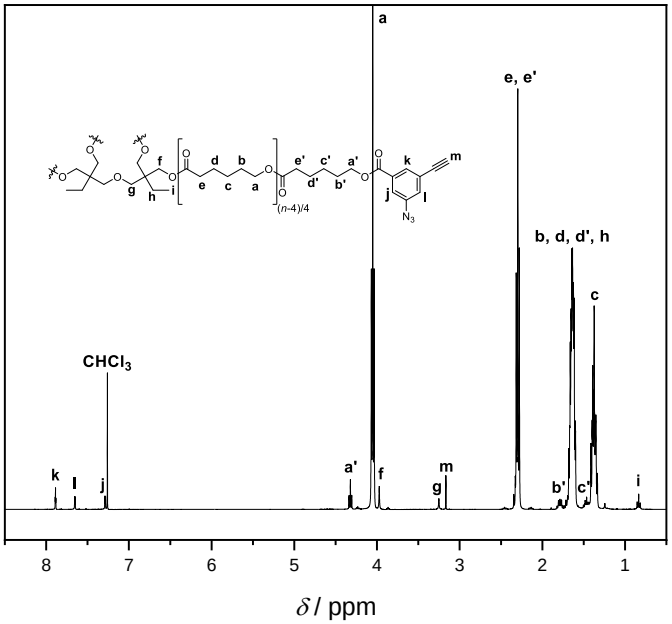

Figure S149: ^{1}H-NMR spectrum of **P19-F**, **^{1}H NMR (400 MHz, $CDCl_3$) δ** 7.89 (t, *J* = 1.4 Hz), 7.65 (dd, *J* = 2.2, 1.5 Hz), 7.29 (dd, *J* = 2.3, 1.4 Hz), 4.32 (t, *J* = 6.6 Hz), 4.05 (t, *J* = 6.7 Hz), 3.97 (s), 3.25 (s), 3.17 (s), 2.39 – 2.20 (m), 1.85 – 1.54 (m), 1.53 – 1.28 (m), 0.83 (t, *J* = 7.5 Hz).

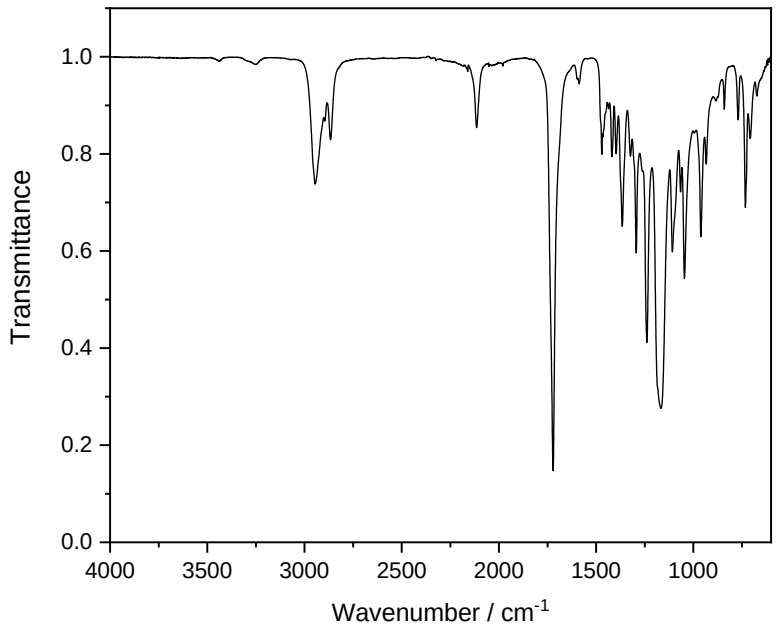

Figure S150: FT-IR spectrum of **P19-F**, **IR (ATR, cm^{-1})** 2945, 2866, 2115, 1721, 1471, 1419, 1397, 1366, 1323, 1294, 1239, 1166, 1108, 1066, 1046, 961, 934, 769, 732, 708.

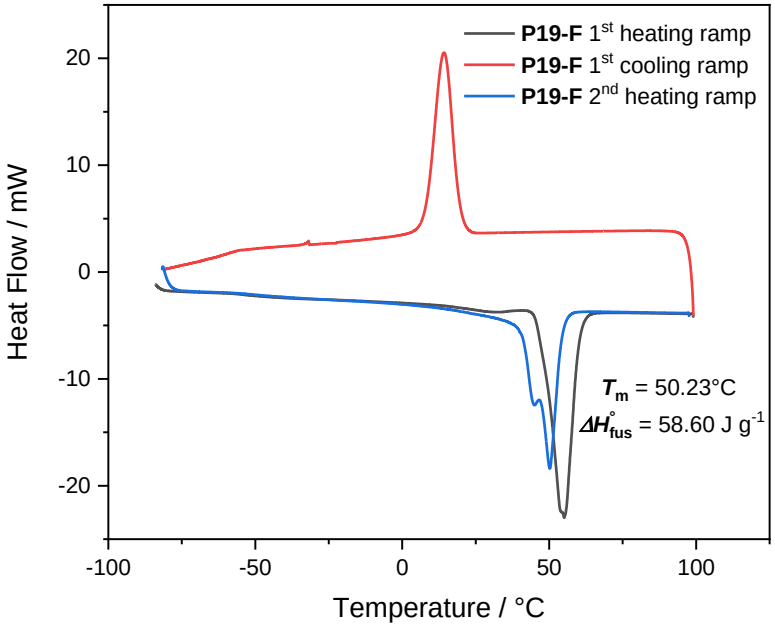

Figure S151: DSC thermogram of **P19-F**, all thermal values were taken from the second heating ramp.

8.6.22 **(P19-C)** *Cage*-shaped Polymer Synthesis *via* CuAAC Reaction

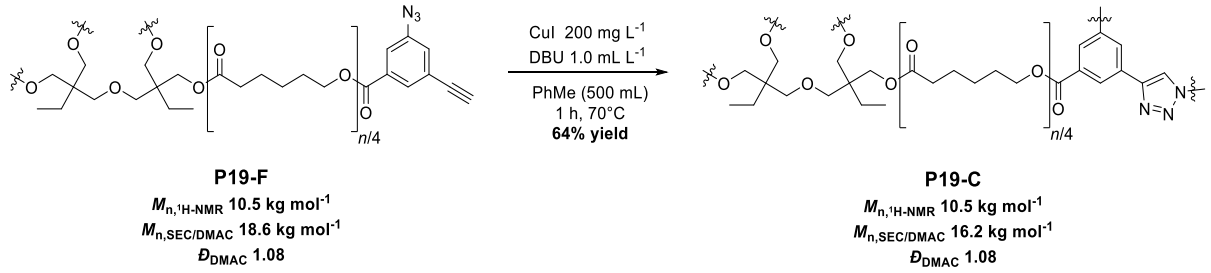

P19-F
$M_{n,^1H\text{-}NMR}$ 10.5 kg mol^{-1}
$M_{n,SEC/DMAC}$ 18.6 kg mol^{-1}
$Đ_{DMAC}$ 1.08

P19-C
$M_{n,^1H\text{-}NMR}$ 10.5 kg mol^{-1}
$M_{n,SEC/DMAC}$ 16.2 kg mol^{-1}
$Đ_{DMAC}$ 1.08

P19-F (50 mg, 0.10 mg mL^{-1}) and DBU (0.5 mL, 1.0 mL L^{-1}) were dissolved in toluene (500 mL). The mixture was purged with argon for 15 min and CuI (100 mg, 200 mg L^{-1}) was added. The mixture was then purged a second time with argon for another 15 min before being heated for 1 hour at 70 °C. Afterwards, the solvent was removed under reduced pressure, 1 M HCl (50 mL) was added and the crude material was extracted with DCM (3 × 30 mL). The organic fractions were collected, dried over magnesium sulfate and the solvent was removed under reduced pressure. The crude material was then washed on silica gel with $CHCl_3$, before being recovered by adding 20% MeOH to the eluent in order to obtain after solvent evaporation and filtration of the remaining silica gel **P19-C** as a brownish solid. **(32 mg, 64%)**

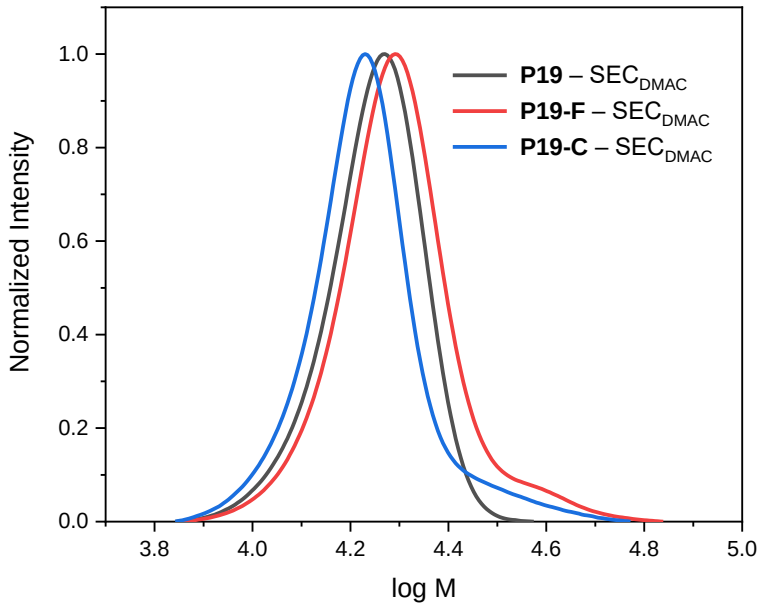

Figure S152: SEC_{DMAC} traces of polymers **P19**, **P19-F** and **P19-C**.

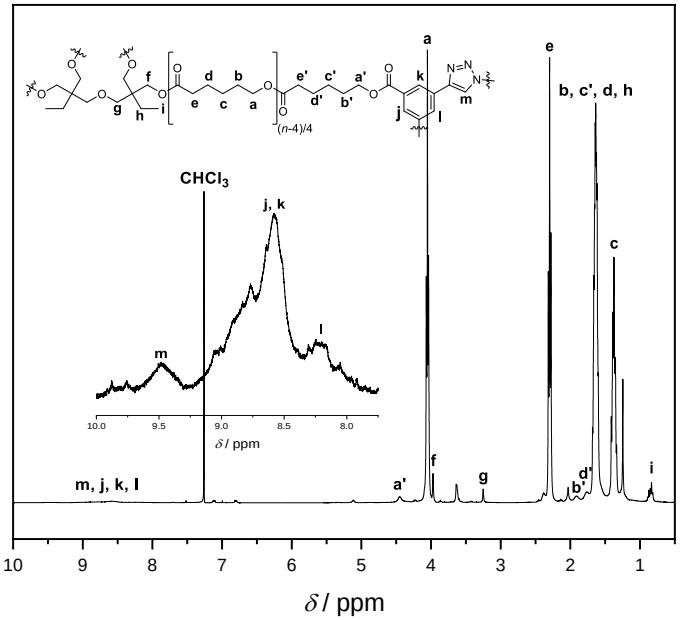

Figure S153: ^{1}H-NMR spectrum of **P19-C**, **^{1}H NMR (400 MHz, $CDCl_3$)** δ 9.48 (s), 9.19 – 8.03 (m), 4.45 (s), 4.05 (t, J = 6.6 Hz), 3.97 (s), 3.25 (s), 2.42 – 2.36 (m), 2.30 (t, J = 7.5 Hz), 2.03 (s), 1.92 (s), 1.84 – 1.72 (m), 1.71 – 1.48 (m), 1.46 – 1.30 (m), 0.83 (t, J = 7.4 Hz).

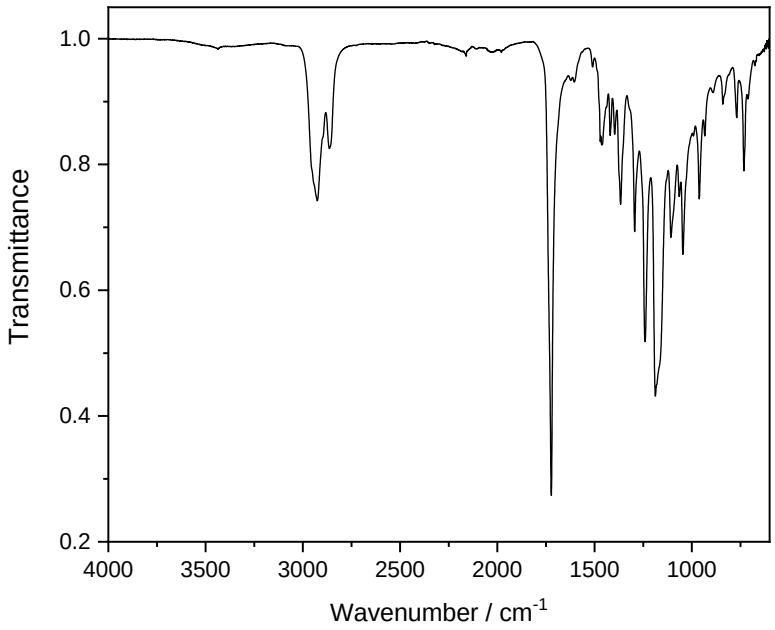

Figure S154: FT-IR spectrum of **P19-C**, **IR (ATR, cm^{-1})** 2925, 2864, 1722, 1605, 1510, 1464, 1420, 1397, 1366, 1294, 1240, 1187, 1107, 1065, 1046, 962, 933, 840, 769, 732.

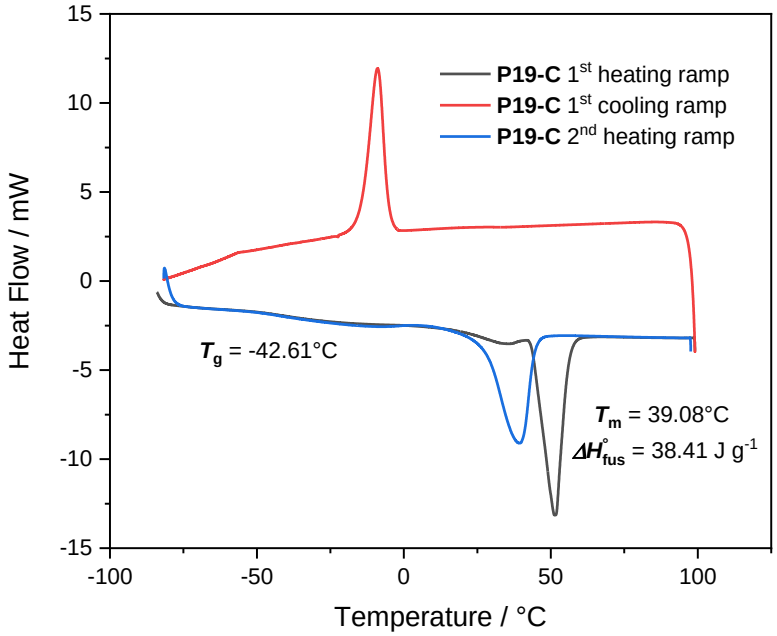

Figure S155: DSC thermogram of **P19-C,** all thermal values were taken from the second heating ramp.

8.6.23 **(P20)** Cationic Ring Opening Polymerization (CROP) of ε-Caprolactone

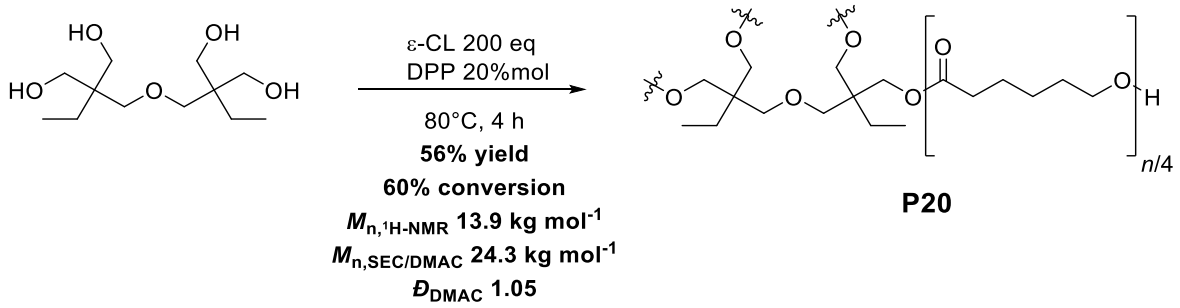

ε-Caprolactone (8.0 mL, 75.0 mmol, 200 eq), di(trimethylolpropane) (94 mg, 0.375 mmol, 1.00 eq) and diphenyl phosphate (19 mg, 0.075 mmol, 0.2 eq) were mixed and heated at 80 °C under stirring for 4 hours. Afterwards, the viscous liquid was cooled down to room temperature and precipitated in cold MeOH (80 mL, -20 °C). The white precipitate was then redissolved in DCM and reprecipitated in cold MeOH (80 mL, -20 °C) two more times in order to obtain the desired polymer **P20** as a white solid. **(5.33 g, 0.38 mmol, 56% yield)**

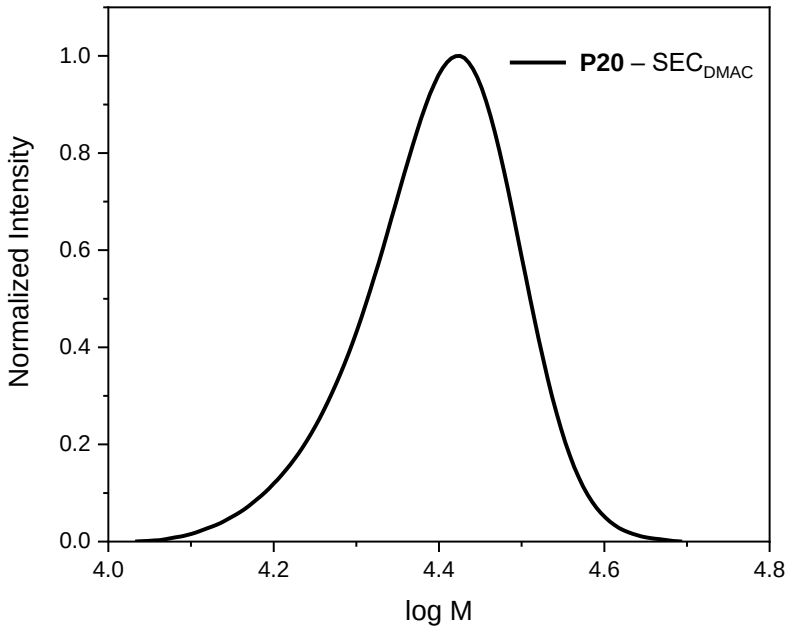

Figure S156: SEC_{DMAC} trace of polymer **P20**.

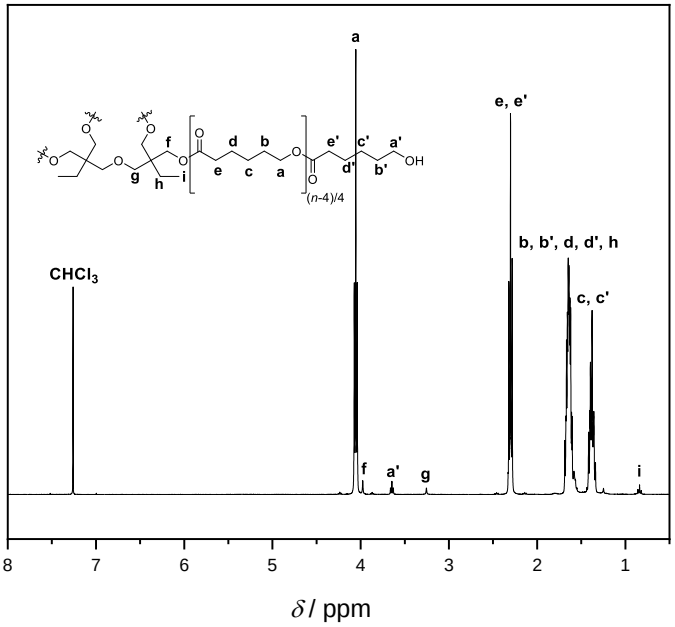

Figure S157: ^{1}H-NMR spectrum of **P20**, **^{1}H NMR (400 MHz, $CDCl_3$)** ***δ*** 4.06 (t, *J* = 6.7 Hz), 3.98 (s), 3.65 (t, *J* = 6.5 Hz), 3.25 (s), 2.37 – 2.23 (m), 1.71 – 1.52 (m), 1.46 – 1.31 (m), 0.84 (t, *J* = 7.6 Hz).

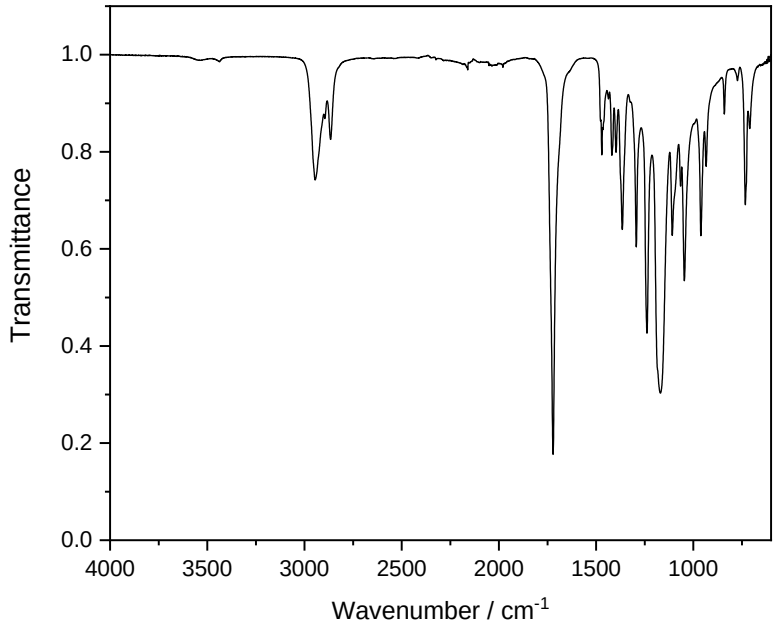

Figure S158: FT-IR spectrum of **P20**, **IR (ATR, cm^{-1})** 2945, 2866, 1721, 1471, 1419, 1397, 1365, 1293, 1238, 1169, 1108, 1066, 1046, 961, 934, 840, 732, 710.

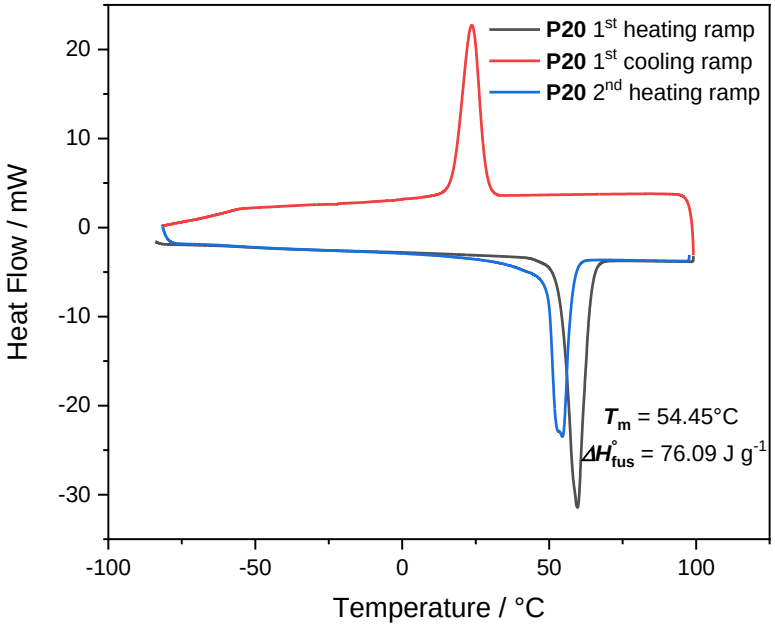

Figure S159: DSC thermogram of **P20**, all thermal values were taken from the second heating ramp.

8.6.24 **(P20-F)** End-functionalization of P20 with End-group C20

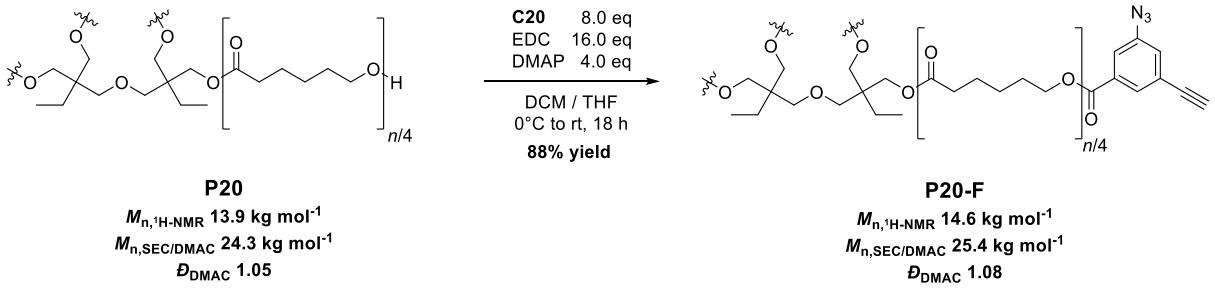

P20
$M_{n,^1H\text{-}NMR}$ 13.9 kg mol^{-1}
$M_{n,SEC/DMAC}$ 24.3 kg mol^{-1}
$Đ_{DMAC}$ 1.05

P20-F
$M_{n,^1H\text{-}NMR}$ 14.6 kg mol^{-1}
$M_{n,SEC/DMAC}$ 25.4 kg mol^{-1}
$Đ_{DMAC}$ 1.08

Previously synthetized *star*-(ε-PCL-OH)$_4$ **P20** (1.043 g, 0.0748 mmol, 1.0 eq), 3-azido-5-ethynylbenzoic acid **C20** (112 mg, 0.598 mmol, 8.0 eq) and DMAP (37 mg, 0.300 mmol, 4.0 eq) were dissolved in dry DCM (5 mL) and dry THF (2 mL). The solution was cooled down to 0 °C and *N*-(3-dimethylaminopropyl)-*N*′-ethylcarbodiimide hydrochloride (229 mg, 1.20 mmol, 16.0 eq) was added portionwise. The mixture was then stirred for 18 hours from 0 °C to room temperature. Afterwards, the resulting mixture was quenched with 1 M HCl (30 mL) and the aqueous phase was extracted with DCM (3 × 20 mL). The organic fractions were collected, dried over magnesium sulfate and the solvents were removed under reduced pressure. The crude polymer was reprecipitated three times in cold MeOH (80 mL, -20 °C) in order to give **P20-F** as a light brownish solid. **(0.961 g, 0.0657 mmol, 88% yield)**

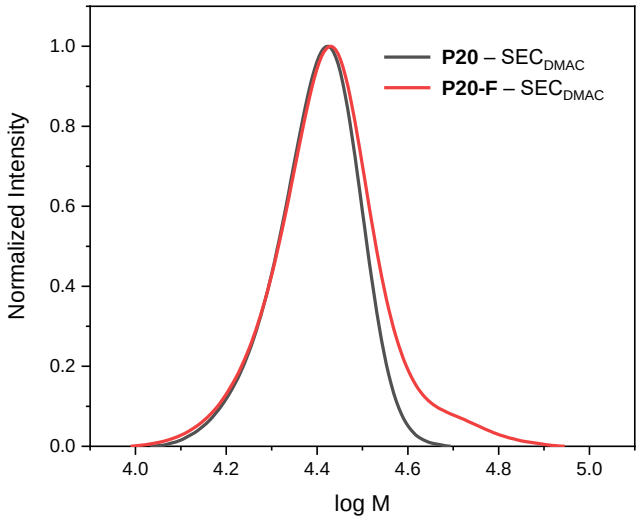

Figure S160: SEC_{DMAC} traces of polymers **P20,** and **P20-F**.

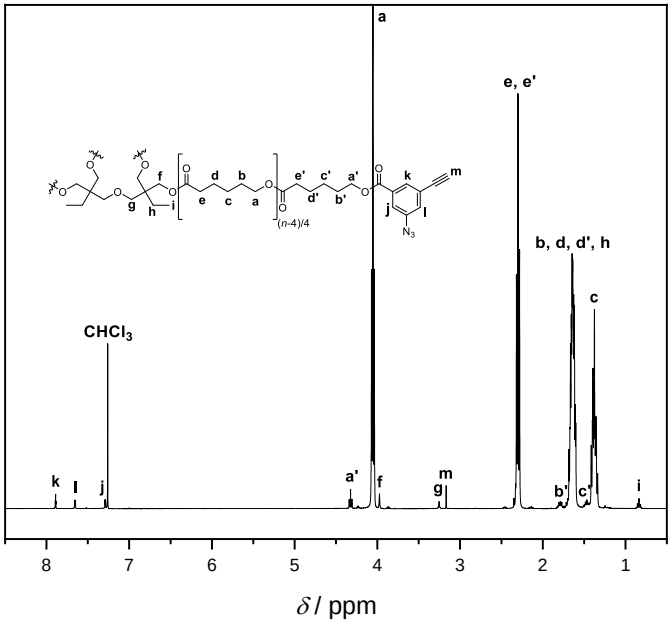

Figure S161: ^{1}H-NMR spectrum of **P20-F**, **^{1}H NMR (400 MHz, $CDCl_3$)** δ 7.89 (t, *J* = 1.4 Hz), 7.65 (dd, *J* = 2.2, 1.5 Hz), 7.29 (dd, *J* = 2.3, 1.4 Hz), 4.32 (t, *J* = 6.6 Hz), 4.05 (t, *J* = 6.7 Hz), 3.97 (s), 3.25 (s), 3.17 (s), 2.38 – 2.25 (m), 1.85 – 1.53 (m), 1.52 – 1.28 (m), 0.84 (t, *J* = 7.5 Hz).

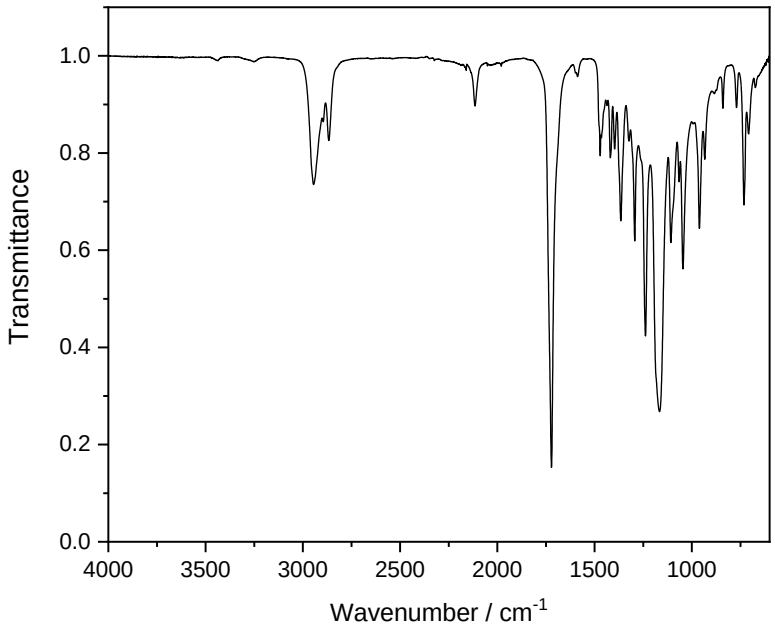

Figure S162: FT-IR spectrum of **P20**, **IR (ATR, cm^{-1})** 2945, 2866, 1721, 1471, 1419, 1397, 1365, 1323, 1293, 1238, 1169, 1108, 1066, 1046, 961, 933, 840, 770, 732, 708.

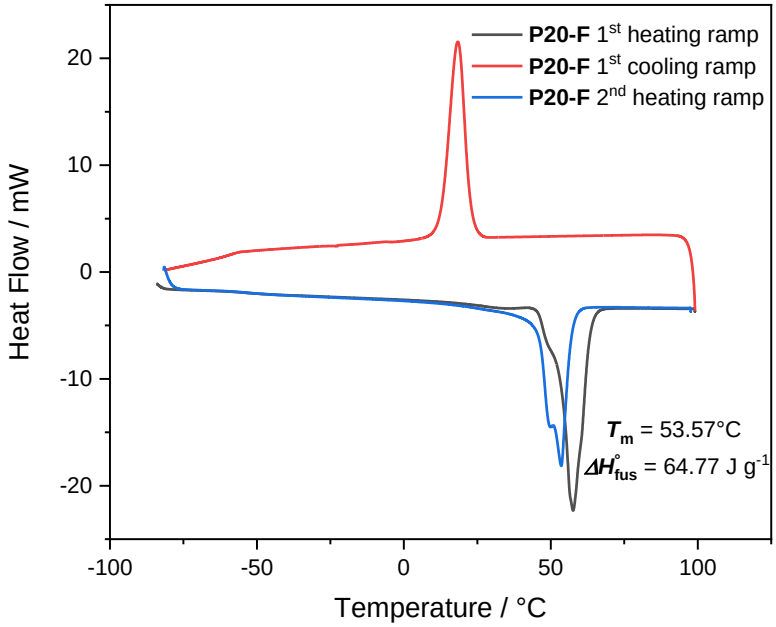

Figure S163: DSC thermogram of **P20-F**, all thermal values were taken from the second heating ramp.

8.6.25 **(P20-C)** Cage-shaped Polymer Synthesis *via* CuAAC Reaction

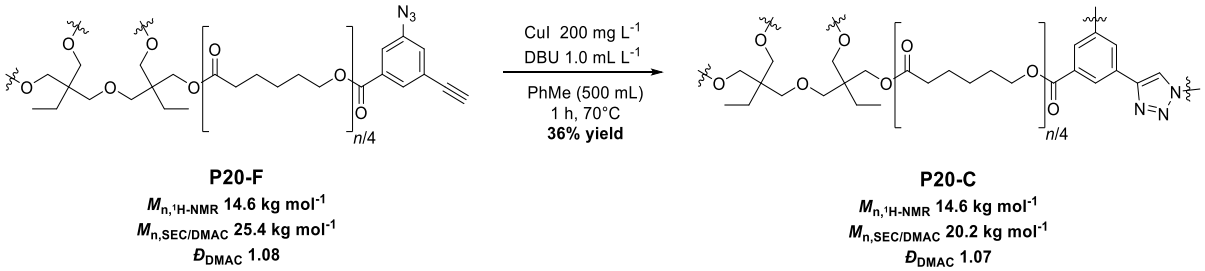

P20-F
$M_{n,^1H\text{-}NMR}$ 14.6 kg mol^{-1}
$M_{n,SEC/DMAC}$ 25.4 kg mol^{-1}
$Đ_{DMAC}$ 1.08

P20-C
$M_{n,^1H\text{-}NMR}$ 14.6 kg mol^{-1}
$M_{n,SEC/DMAC}$ 20.2 kg mol^{-1}
$Đ_{DMAC}$ 1.07

P20-F (50 mg, 0.10 mg mL^{-1}) and DBU (0.5 mL, 1.0 mL L^{-1}) were dissolved in toluene (500 mL). The mixture was purged with argon for 15 min and CuI (100 mg, 200 mg L^{-1}) was added. The mixture was then purged a second time with argon for another 15 min before being heated for 1 hour at 70 °C. Afterwards, the solvent was removed under reduced pressure, 1 M HCl (50 mL) was added and the crude material was extracted with DCM (3 × 30 mL). The organic fractions were collected, dried over magnesium sulfate and the solvent was removed under reduced pressure. The crude material was then washed on silica gel with $CHCl_3$, before being recovered by adding 20% MeOH to the eluent in order to obtain after solvent evaporation and filtration of the remaining silica gel **P20-C** as a brownish solid. **(18 mg, 36% yield)**

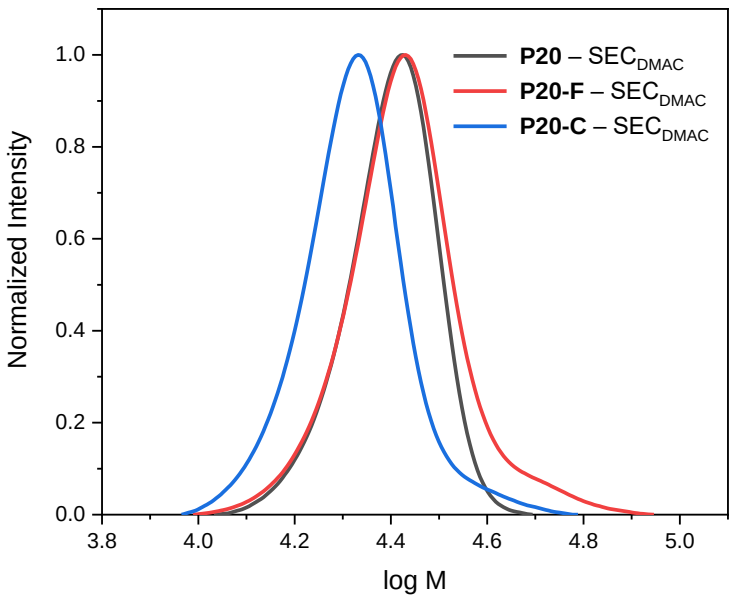

Figure S164: SEC_{DMAC} traces of polymers **P20, P20-F** and **P20-C**.

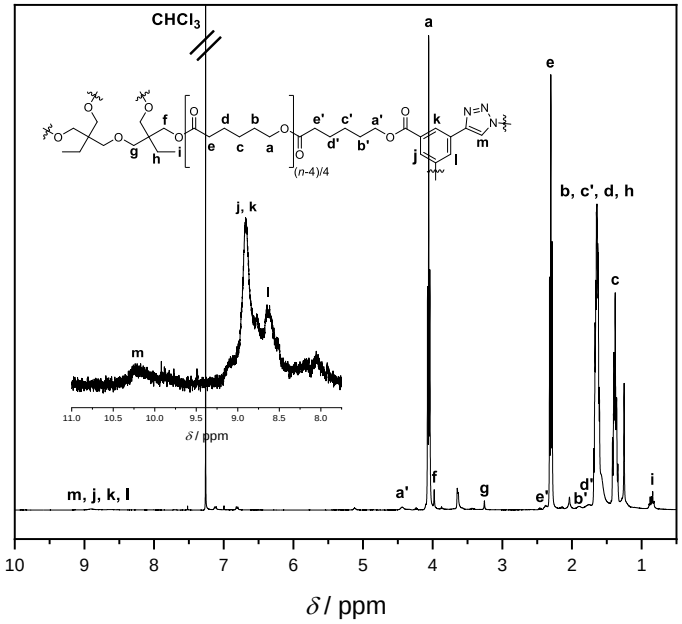

Figure S165: ^{1}H-NMR spectrum of **P20-C**, **^{1}H NMR (400 MHz, $CDCl_3$) δ** 9.22 – 8.40 (m), 4.44 (s), 4.06 (t, *J* = 6.7 Hz), 3.98 (s), 3.26 (s), 2.30 (t, *J* = 7.5 Hz), 2.10 – 1.98 (m), 1.90 (s), 1.82 – 1.52 (m), 1.50 – 1.30 (m), 0.84 (t, *J* = 7.4 Hz).

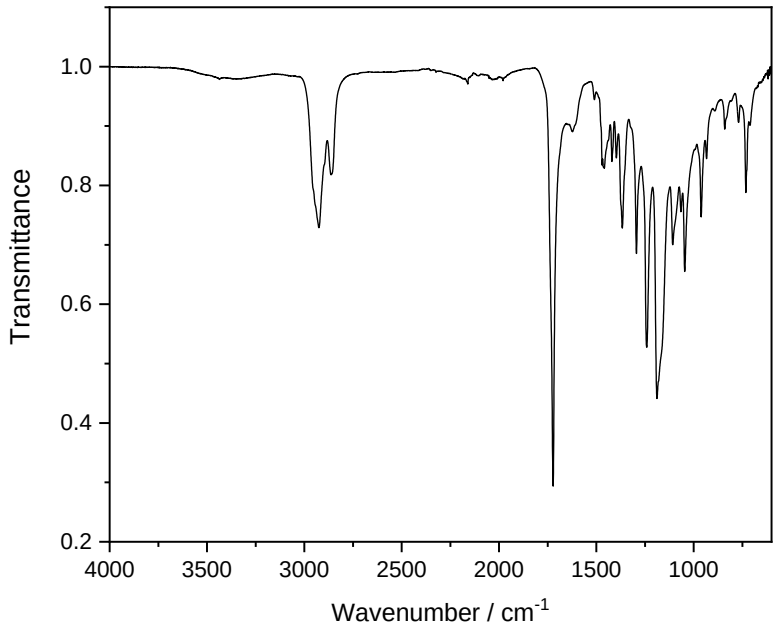

Figure S166: FT-IR spectrum of **P20-C**, **IR (ATR, cm^{-1})** 2925, 2862, 1722, 1623, 1510, 1459, 1420, 1397, 1367, 1294, 1241, 1188, 1108, 1065, 1046, 962, 934, 840, 769, 732.

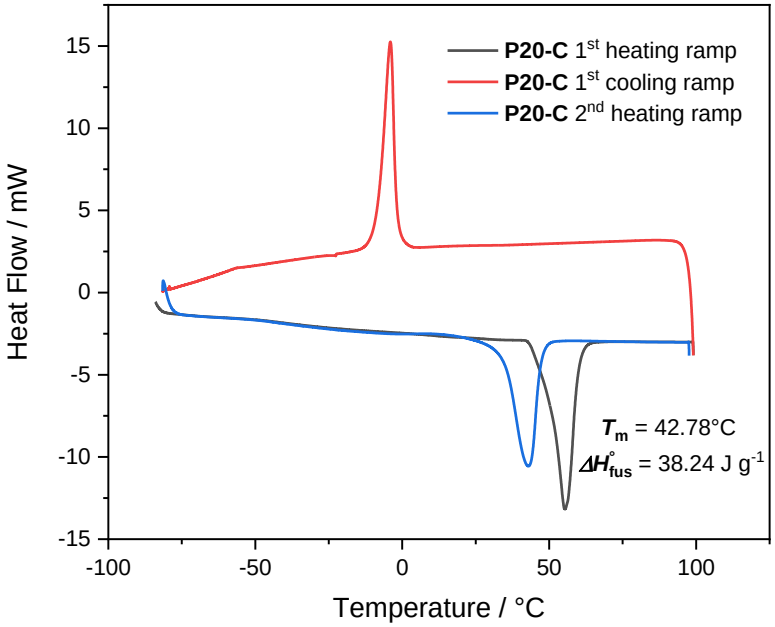

Figure S167: DSC thermogram of **P20-C**, all thermal values were taken from the second heating ramp.

8.7 Polymer Synthesis and Post-Polymerization Modifications – Project Part III

8.7.1 **(P19-F$_{bis}$)** End-functionalization of P19 with End-group C20

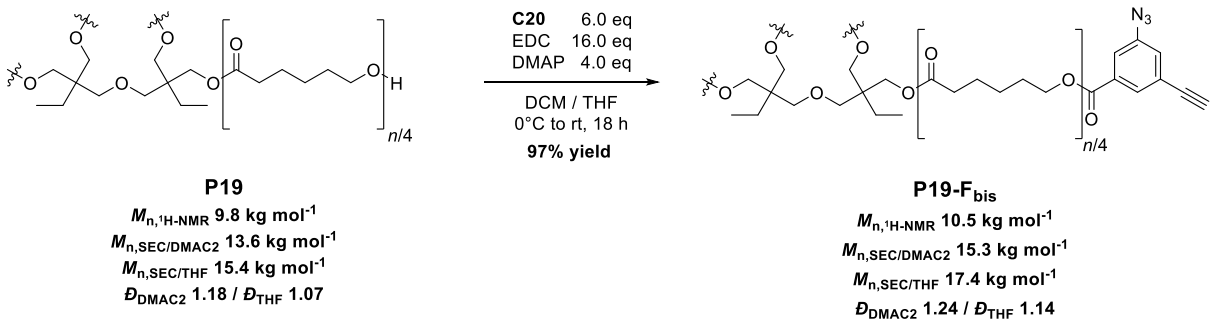

P19
$M_{n,^1H\text{-}NMR}$ 9.8 kg mol^{-1}
$M_{n,SEC/DMAC2}$ 13.6 kg mol^{-1}
$M_{n,SEC/THF}$ 15.4 kg mol^{-1}
$Đ_{DMAC2}$ 1.18 / $Đ_{THF}$ 1.07

P19-F$_{bis}$
$M_{n,^1H\text{-}NMR}$ 10.5 kg mol^{-1}
$M_{n,SEC/DMAC2}$ 15.3 kg mol^{-1}
$M_{n,SEC/THF}$ 17.4 kg mol^{-1}
$Đ_{DMAC2}$ 1.24 / $Đ_{THF}$ 1.14

Previously synthetized *star*-(ε-PCL-OH)$_4$ **P19** (2.26 g, 0.230 mmol, 1.0 eq), 3-azido-5-ethynylbenzoic acid **C20** (260 mg, 1.39 mmol, 6.0 eq) and 4-dimethylaminopyridine (112 mg, 0.92 mmol, 4.0 eq) were dissolved in dry DCM (6 mL) and dry THF (4 mL). The solution was cooled down to 0 °C and *N*-(3-dimethylaminopropyl)-*N*′-ethylcarbodiimide hydrochloride (705 mg, 3.68 mmol, 16.0 eq) was added portionwise. The mixture was then stirred for 18 hours from 0 °C to room temperature. Afterwards, the resulting mixture was quenched with 1 M HCl and the aqueous phase was extracted with DCM (3 × 20 mL). The organic fractions were collected, dried over magnesium sulfate and the solvents were removed under reduced pressure. The crude polymer was reprecipitated three times in cold MeOH (80 mL, -20 °C) in order to give **P19-F$_{bis}$** as a light brownish solid. **(2.34 g, 0.223 mmol, 97% yield)**

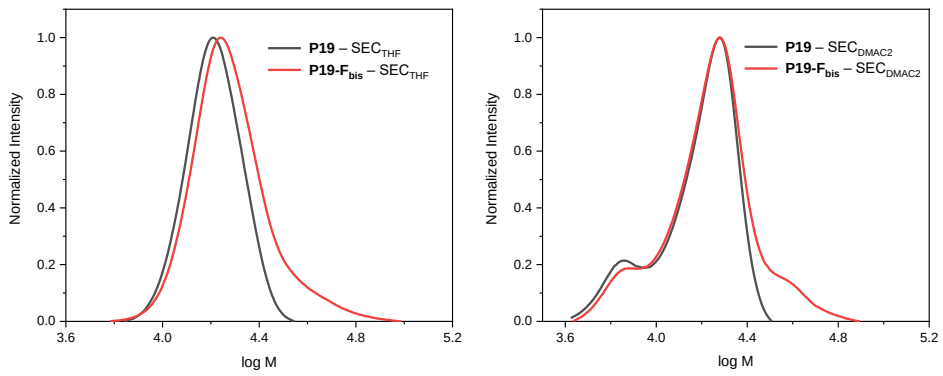

Figure S168: SEC$_{THF}$ (*left*) and SEC$_{DMAC2}$ (*right*) traces of polymers **P19** and **P19-F$_{bis}$**.

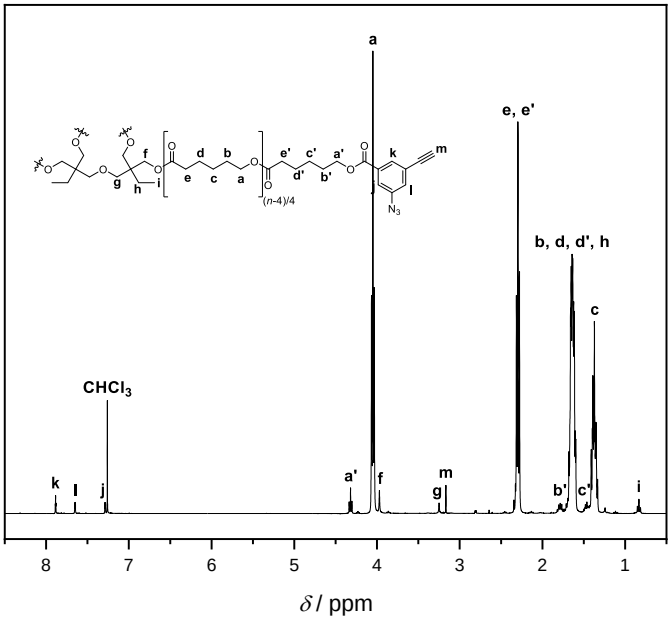

Figure S169: ^{1}H-NMR spectrum of **P19-F$_{bis}$, ^{1}H NMR (400 MHz, CDCl$_3$)** δ 7.89 (t, J = 1.4 Hz), 7.65 (dd, J = 2.3, 1.5 Hz), 7.29 (dd, J = 2.3, 1.4 Hz), 4.32 (t, J = 6.6 Hz), 4.05 (t, J = 6.7 Hz), 3.97 (s), 3.25 (s), 3.17 (s), 2.56 – 2.07 (m), 1.89 – 1.53 (m), 1.52 – 1.30 (m), 0.83 (t, J = 7.5 Hz).

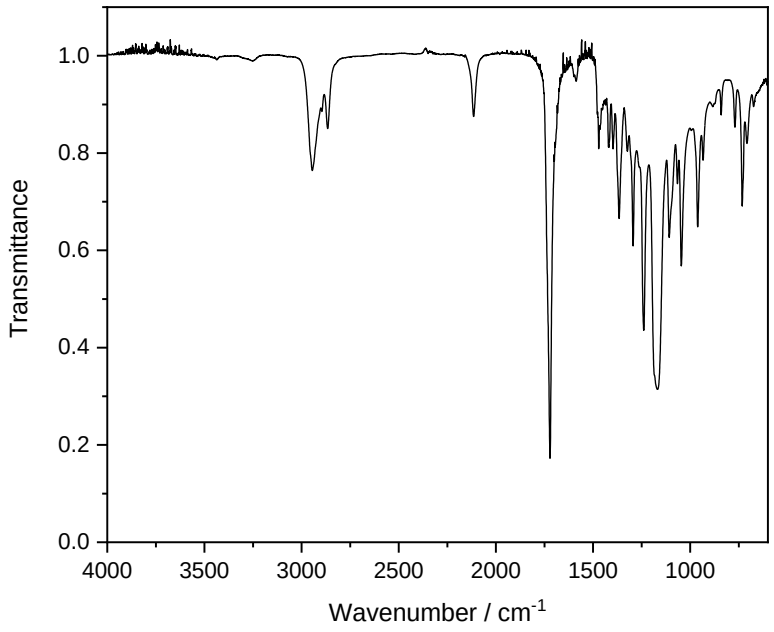

Figure S170: FT-IR spectrum of **P19-F$_{bis}$, IR (ATR, cm^{-1})** 2945, 2866, 2114, 1721, 1471, 1419, 1397, 1366, 1294, 1239, 1168, 1108, 1066, 1046, 961, 934, 841, 770, 732, 708.

8.7.2 **(P19-C1$_{bis}$)** *Cage*-shaped Polymer Synthesis *via* CuAAC Reaction

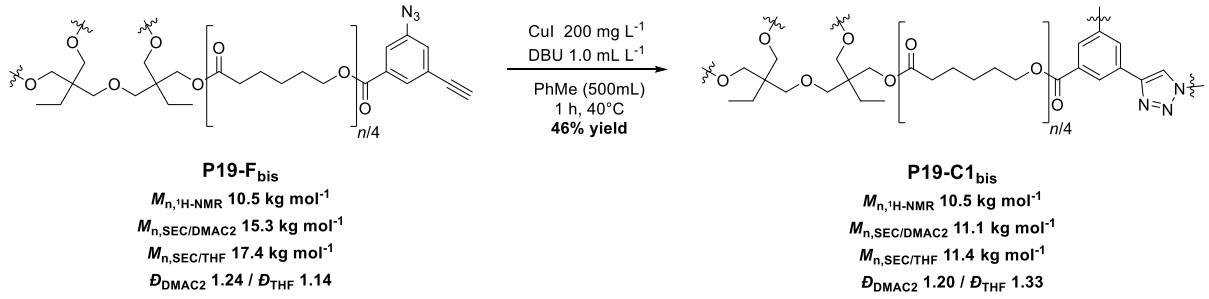

P19-F$_{bis}$
$M_{n,^1H\text{-}NMR}$ 10.5 kg mol^{-1}
$M_{n,SEC/DMAC2}$ 15.3 kg mol^{-1}
$M_{n,SEC/THF}$ 17.4 kg mol^{-1}
$Đ_{DMAC2}$ 1.24 / $Đ_{THF}$ 1.14

P19-C1$_{bis}$
$M_{n,^1H\text{-}NMR}$ 10.5 kg mol^{-1}
$M_{n,SEC/DMAC2}$ 11.1 kg mol^{-1}
$M_{n,SEC/THF}$ 11.4 kg mol^{-1}
$Đ_{DMAC2}$ 1.20 / $Đ_{THF}$ 1.33

P19-F$_{bis}$ (50 mg, 0.10 mg mL^{-1}) and DBU (0.5 mL, 1.0 mL L^{-1}) were dissolved in toluene (500 mL). The mixture was purged with argon for 15 min and CuI (100 mg, 200 mg L^{-1}) was added. The mixture was then purged a second time with argon for another 15 min before being heated for 1 hour at 40 °C. Afterwards, the solvent was removed under reduced pressure, 1 M HCl (50 mL) was added and the crude material was extracted with DCM (3 × 30 mL). The organic fractions were collected, dried over magnesium sulfate and the solvent was removed under reduced pressure. The crude material was then washed on silica gel with $CHCl_3$, before being recovered by adding 20% MeOH to the eluent in order to obtain after solvent evaporation and filtration of the remaining silica gel **P19-C1$_{bis}$** as a brownish solid. **(23 mg, 46% yield)**

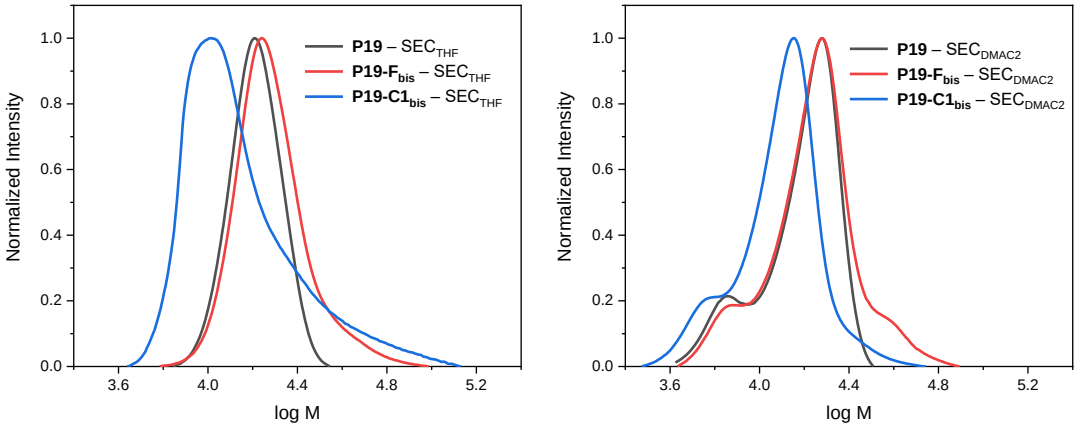

Figure S171: SEC$_{THF}$ (*left*) and SEC$_{DMAC2}$ (*right*) traces of polymers **P19**, **P19-F$_{bis}$** and **P19-C1$_{bis}$**.

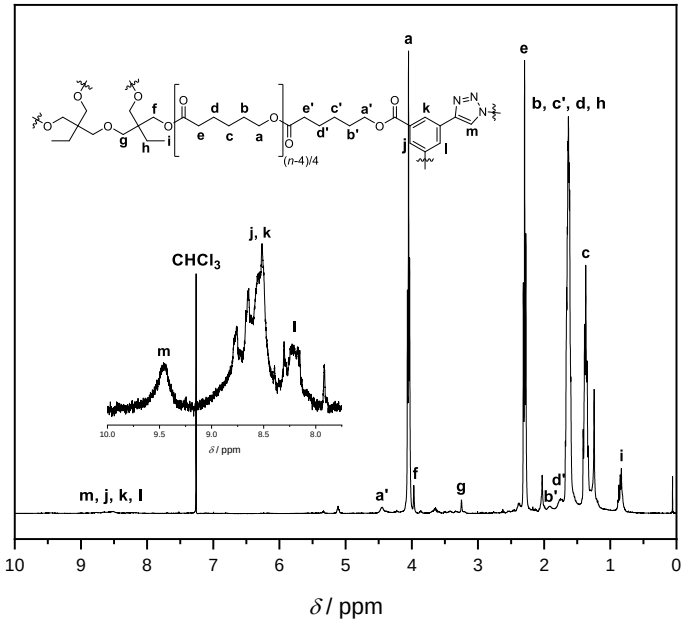

Figure S172: ^{1}H-NMR spectrum of **P19-C1$_{bis}$, ^{1}H NMR (400 MHz, CDCl$_3$) δ** 9.63 – 8.07 (m), 4.46 (s), 4.05 (t, *J* = 6.7 Hz), 3.97 (s, 1H), 3.25 (s), 2.30 (t, *J* = 7.5 Hz), 1.96 – 1.47 (m), 1.47 – 1.28 (m), 0.88 – 0.82 (m).

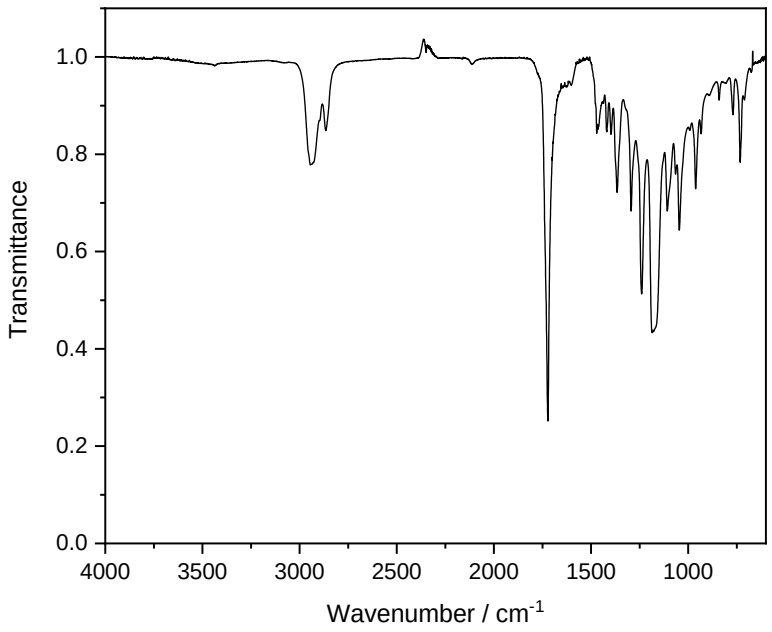

Figure S173: FT-IR spectrum of **P19-C1$_{bis}$, IR (ATR, cm^{-1})** 2944, 2865, 1722, 1471, 1419, 1397, 1366, 1294, 1239, 1186, 1108, 1065, 1046, 961, 934, 841, 770, 732, 666.

8.7.3 **(P19-C2$_{bis}$)** *Cage*-shaped Polymer Synthesis *via* CuAAC Reaction

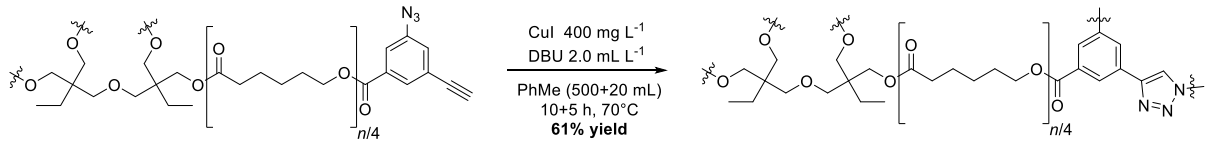

P19-F$_{bis}$
$M_{n,^1H\text{-}NMR}$ 10.5 kg mol^{-1}
$M_{n,SEC/DMAC2}$ 15.3 kg mol^{-1}
$M_{n,SEC/THF}$ 17.4 kg mol^{-1}
$Đ_{DMAC2}$ 1.24 / $Đ_{THF}$ 1.14

P19-C2$_{bis}$
$M_{n,^1H\text{-}NMR}$ 10.5 kg mol^{-1}
$M_{n,SEC/DMAC2}$ 11.3 kg mol^{-1}
$M_{n,SEC/THF}$ 12.7 kg mol^{-1}
$Đ_{DMAC2}$ 1.24 / $Đ_{THF}$ 1.24

DBU (1.0 mL, 2.0 mL L^{-1}) was dissolved in toluene (500 mL). The mixture was purged with argon for 15 min and CuI (200 mg, 400 mg L^{-1}) was added. The mixture was then purged a second time with argon for another 15 min before being heated at 70 °C. **P19-F$_{bis}$** (500 mg, 0.048 mmol) was dissolved in toluene (20 mL) and purged with argon for 15 min before being placed in a 20 mL syringe. The syringe mixture was injected to the first mixture at a regular rate (50 mg h^{-1} polymer, 2.0 mL h^{-1}) over 10 hours. Then, the resulting mixture was heated for 5 more hours at 70 °C before being cooled down to room temperature. Afterwards, the solvent was removed under reduced pressure, 1 M HCl (50 mL) was added and the crude material was extracted with DCM (3 × 30 mL). The organic fractions were collected, dried over magnesium sulfate and the solvent was removed under reduced pressure. The crude material was then washed on silica gel with $CHCl_3$, before being recovered by adding 20% MeOH to the eluent in order to obtain after solvent evaporation and filtration of the remaining silica gel **P19-C2$_{bis}$** as a brownish solid. **(305 mg, 61% yield)**

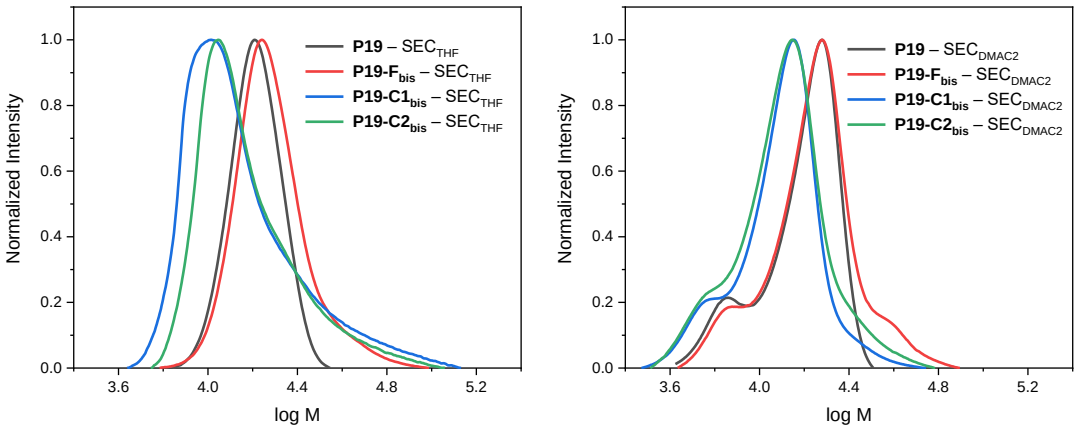

Figure S174: SEC$_{THF}$ (*left*) and SEC$_{DMAC2}$ (*right*) traces of polymers **P19**, **P19-F$_{bis}$**, **P19-C1$_{bis}$** and **P19-C2$_{bis}$**.

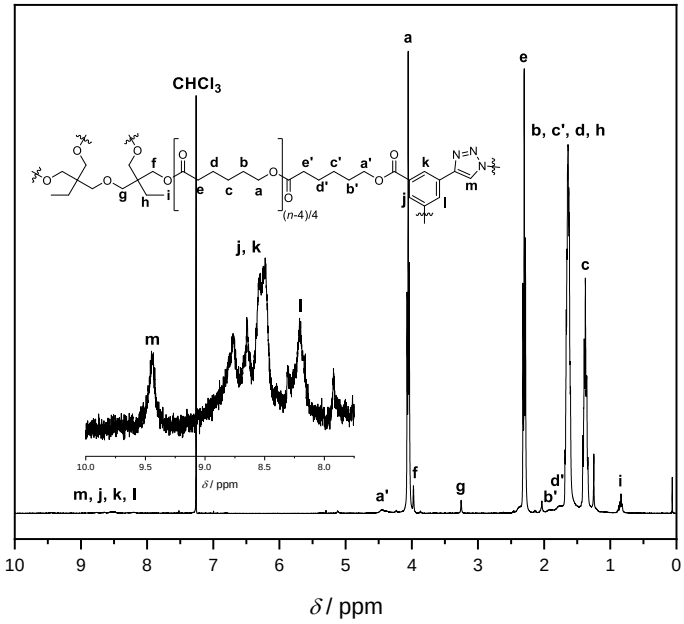

Figure S175: ^{1}H-NMR spectrum of **P19-C2$_{bis}$, ^{1}H NMR (400 MHz, CDCl$_3$) δ** 9.65 – 8.06 (m), 4.45 (s), 4.06 (t, *J* = 6.6 Hz), 3.98 (s), 3.25 (s), 2.30 (t, *J* = 7.5 Hz), 1.96 – 1.50 (m), 1.50 – 1.27 (m), 0.84 (t, *J* = 7.4 Hz).

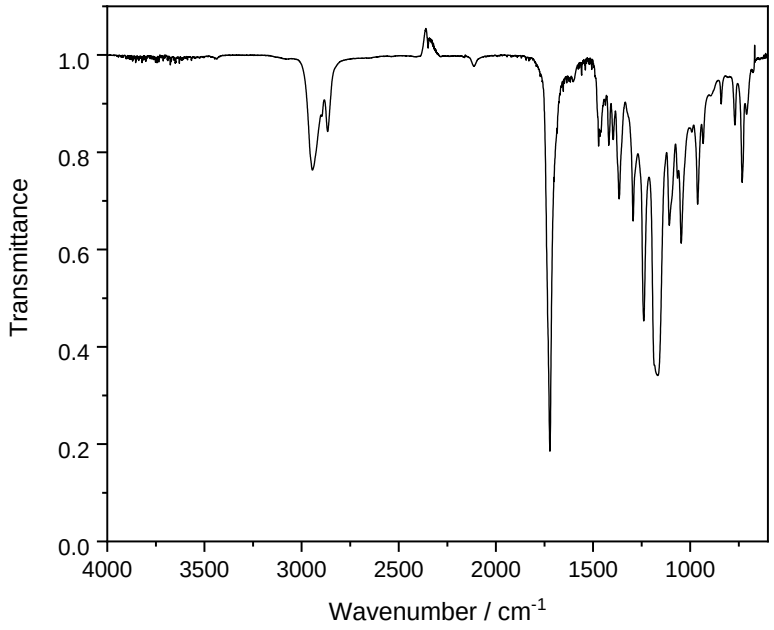

Figure S176: FT-IR spectrum of **P19-C2$_{bis}$, IR (ATR, cm^{-1})** 2944, 2866, 1722, 1471, 1419, 1396, 1366, 1294, 1239, 1167, 1108, 1046, 961, 933, 840, 770, 732.

8.7.4 **(P19-C3$_{bis}$)** *Cage*-shaped Polymer Synthesis *via* CuAAC Reaction

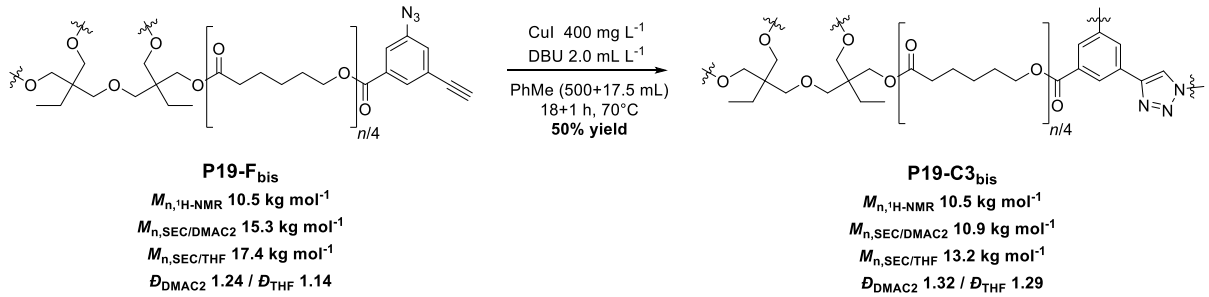

P19-F$_{bis}$
$M_{n,^1H\text{-}NMR}$ 10.5 kg mol^{-1}
$M_{n,SEC/DMAC2}$ 15.3 kg mol^{-1}
$M_{n,SEC/THF}$ 17.4 kg mol^{-1}
$Đ_{DMAC2}$ 1.24 / $Đ_{THF}$ 1.14

P19-C3$_{bis}$
$M_{n,^1H\text{-}NMR}$ 10.5 kg mol^{-1}
$M_{n,SEC/DMAC2}$ 10.9 kg mol^{-1}
$M_{n,SEC/THF}$ 13.2 kg mol^{-1}
$Đ_{DMAC2}$ 1.32 / $Đ_{THF}$ 1.29

DBU (1.0 mL, 2.0 mL L^{-1}) was dissolved in toluene (500 mL). The mixture was purged with argon for 15 min and CuI (200 mg, 400 mg L^{-1}) was added. The mixture was then purged a second time with argon for another 15 min before being heated at 70 °C. **P19-F$_{bis}$** (1750 mg, 0.167 mmol) was dissolved in toluene (17.5 mL) and purged with argon for 15 min before being placed in a 20 mL syringe. The syringe mixture was injected at a regular rate (100 mg h^{-1} polymer, 1.0 mL h^{-1}) to the first mixture over 17.5 hours. Then, the resulting mixture was heated for one more hour at 70 °C before being cooled down to room temperature. Afterwards, the solvent was removed under reduced pressure, 1 M HCl (50 mL) was added and the crude material was extracted with DCM (3 × 30 mL). The organic fractions were collected, dried over magnesium sulfate and the solvent was removed under reduced pressure. The crude material was then washed on silica gel with $CHCl_3$, before being recovered by adding 20% MeOH to the eluent in order to obtain after solvent evaporation and filtration of the remaining silica gel **P19-C3$_{bis}$** as a brownish solid. **(874 mg, 50% yield)**

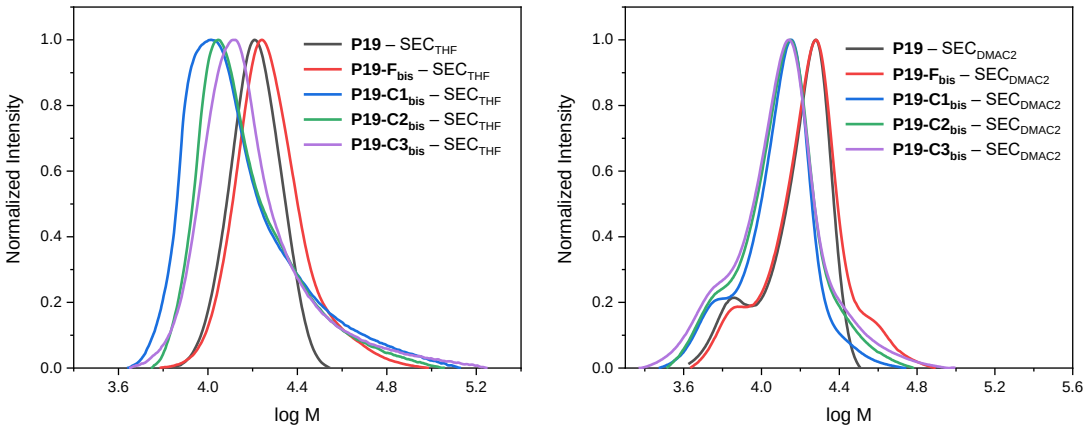

Figure S177: SEC$_{THF}$ (*left*) and SEC$_{DMAC2}$ (*right*) traces of polymers **P19**, **P19-F$_{bis}$**, **P19-C1$_{bis}$**, **P19-C2$_{bis}$** and **P19-C3$_{bis}$**.

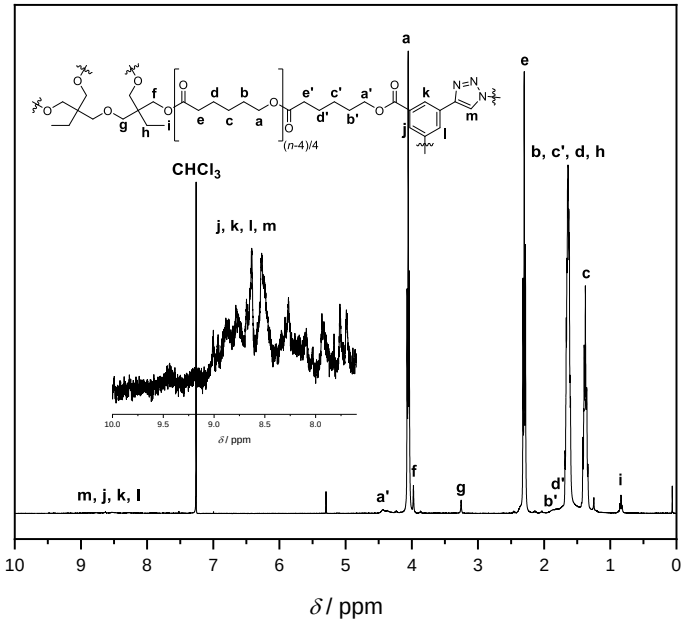

Figure S178: ^{1}H-NMR spectrum of **P19-C3$_{bis}$, ^{1}H NMR (400 MHz, CDCl$_3$) δ** 9.21 – 7.62 (m), 4.43 (s), 4.05 (t, *J* = 6.7 Hz), 3.98 (s), 3.26 (s), 2.30 (t, *J* = 7.5 Hz), 1.98 – 1.50 (m), 1.52 – 1.23 (m), 0.84 (t, *J* = 7.5 Hz).

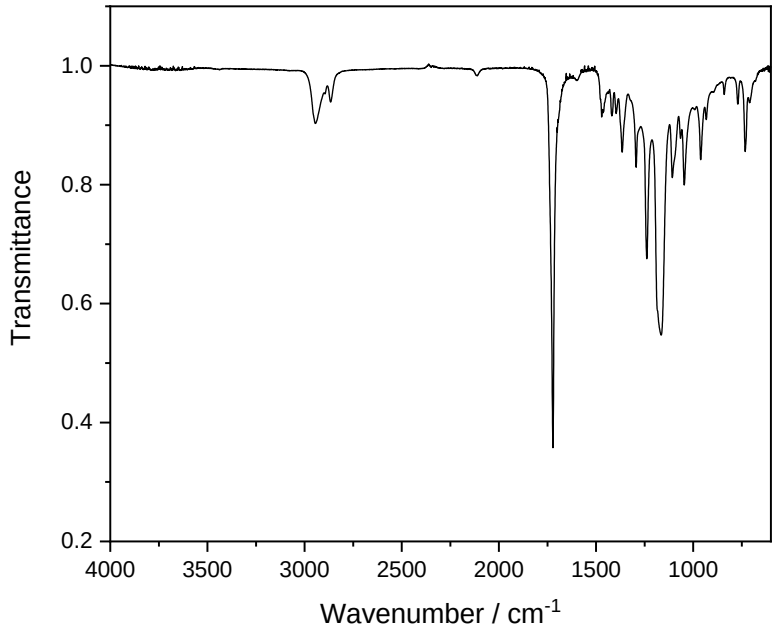

Figure S179: FT-IR spectrum of **P19-C3$_{bis}$, IR (ATR, cm^{-1})** 2945, 2866, 1722, 1471, 1418, 1397, 1365, 1294, 1239, 1164, 1107, 1046, 961, 933, 840, 770, 732.

8.7.5 **(P21)** Analysis of Four-arm *Star*-shaped PEO purchased from JenKem Technology®

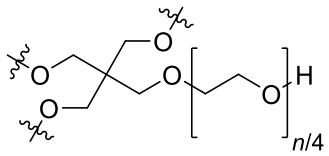

P21

$M_{n,^1H\text{-}NMR}$ 5.7 kg mol^{-1}

$M_{n,SEC/THF}$ 7.2 kg mol^{-1}

$Đ_{THF}$ 1.04

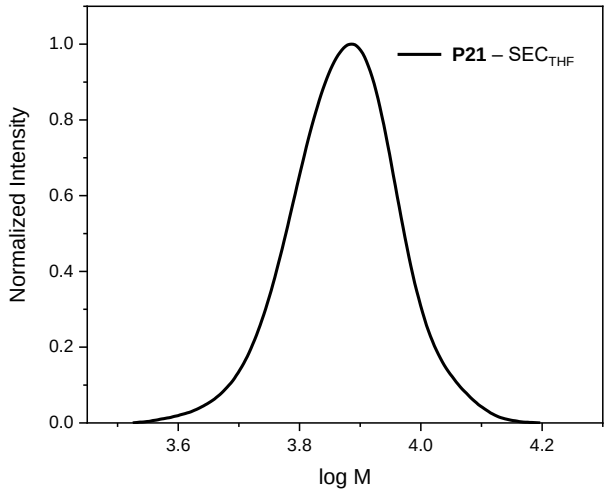

Figure S180: SEC$_{THF}$ trace of polymer **P21**.

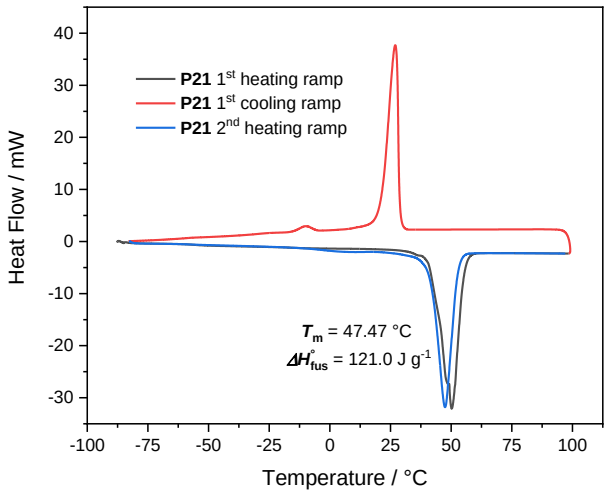

Figure S181: DSC thermogram of **P21**, all thermal values were taken from the second heating ramp.

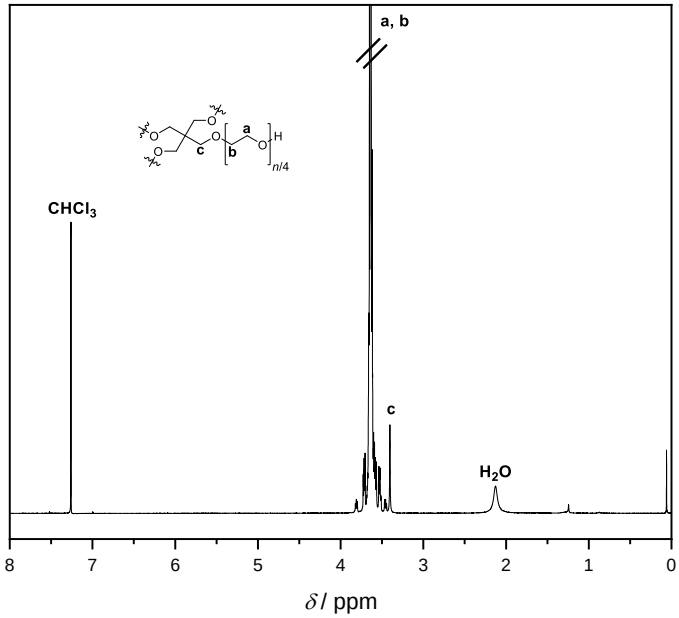

Figure S182: ^{1}H-NMR spectrum of **P21**, **^{1}H NMR (400 MHz, $CDCl_3$)** ***δ*** 3.84 – 3.43 (m), 3.40 (s).

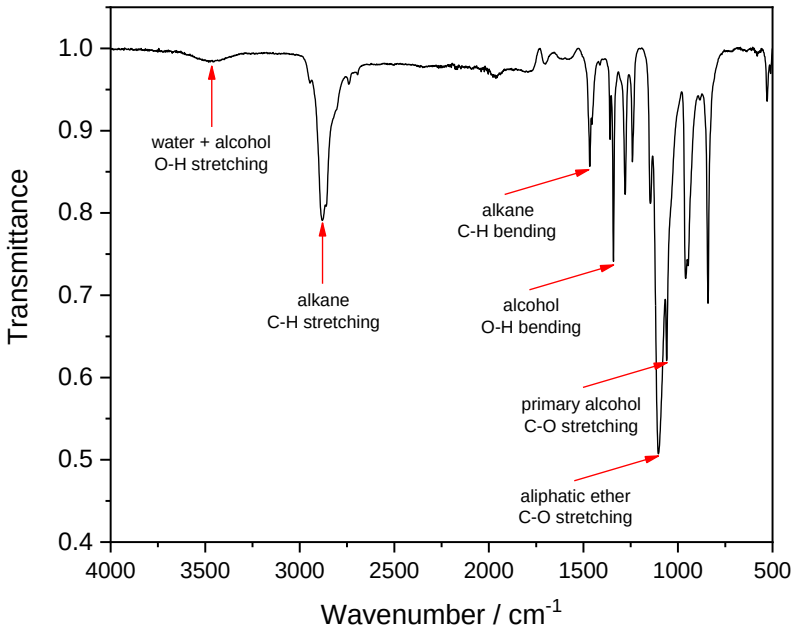

Figure S183: FT-IR spectrum of **P21**, **IR (FT-IR2, ATR, cm^{-1})** 3472, 2883, 1467, 1359, 1341, 1279, 1241, 1145, 1102, 1060, 946, 841.

8.7.6 **(P21-F)** End-functionalization of P21 with End-group C20

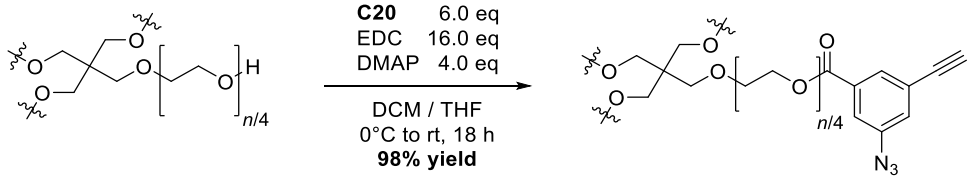

P21
$M_{n,^1H\text{-}NMR}$ 5.7 kg mol^{-1}
$M_{n,SEC/THF}$ 7.2 kg mol^{-1}
$Đ_{THF}$ 1.04

P21-F
$M_{n,^1H\text{-}NMR}$ 6.4 kg mol^{-1}
$M_{n,SEC/THF}$ 8.0 kg mol^{-1}
$Đ_{THF}$ 1.05

Commercial grade *star*-(PEG-OH)$_4$ **P21** (1.422 g, 0.250 mmol, 1.0 eq), 3-azido-5-ethynylbenzoic acid **C20** (281 mg, 1.50 mmol, 6.0 eq) and 4-dimethylaminopyridine (122 mg, 1.00 mmol, 4.0 eq) were dissolved in dry DCM (6 mL) and dry THF (3 mL). The solution was cooled down to 0 °C and *N*-(3-dimethylaminopropyl)-*N*′-ethylcarbodiimide hydrochloride (767 mg, 4.00 mmol, 16.0 eq) was added portionwise. The mixture was then stirred for 18 hours from 0 °C to room temperature. Afterwards, the resulting mixture was quenched with 1 M HCl and the aqueous phase was extracted with DCM (3 × 30 mL). The organic fractions were collected, dried over magnesium sulfate and the solvents were removed under reduced pressure. The crude material was then washed on silica gel with $CHCl_3$, before being recovered by adding 10% MeOH to the eluent in order to obtain, after solvent evaporation and filtration of the remaining silica gel, **P21-F** as a yellow solid. **(1.554 g, 0.244 mmol, 98% yield)**

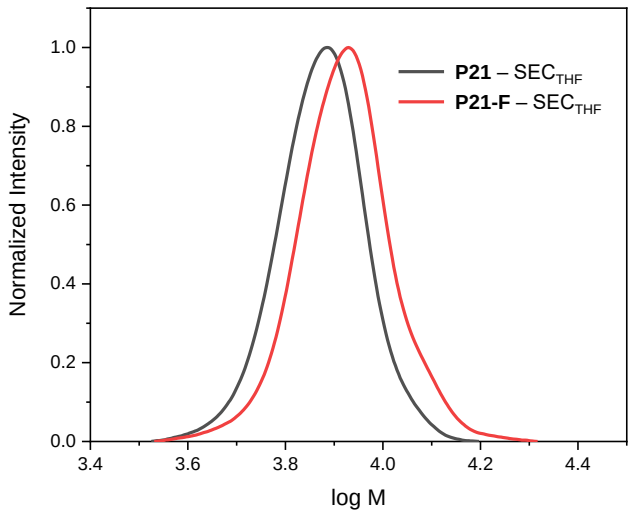

Figure S184: SEC$_{THF}$ traces of polymers **P21** and **P21-F**.

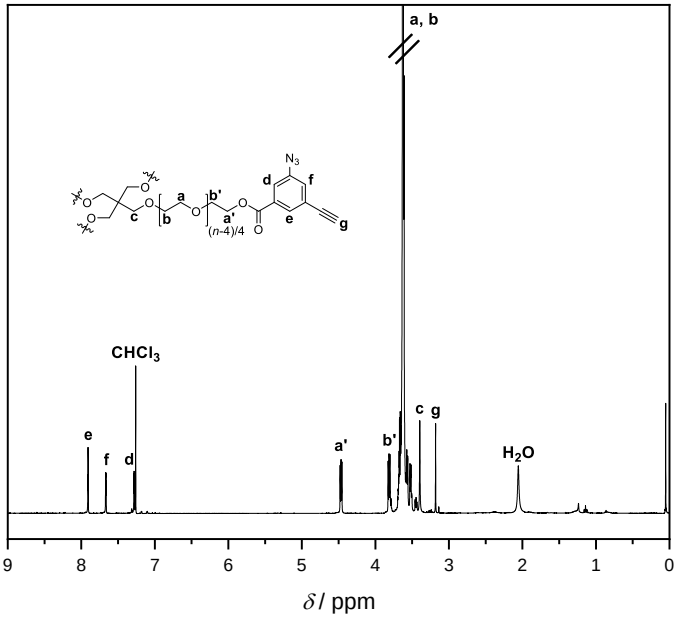

Figure S185: ^{1}H-NMR spectrum of **P21-F**, **^{1}H NMR (400 MHz, $CDCl_3$) δ** 7.91 (t, *J* = 1.4 Hz), 7.67 (dd, *J* = 2.2, 1.5 Hz), 7.28 (dd, *J* = 2.2, 1.4 Hz), 4.51 – 4.43 (m), 3.84 – 3.79 (m), 3.72 – 3.49 (m), 3.40 (s), 3.18 (s).

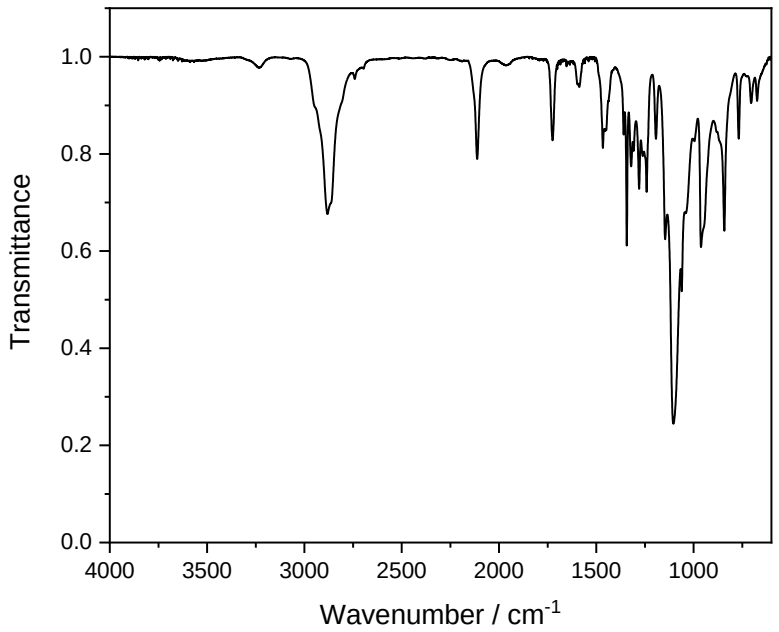

Figure S186: FT-IR spectrum of **P21-F**, **IR (ATR, cm^{-1})** 3224, 2882, 2112, 1725, 1587, 1466, 1359, 1343, 1321, 1308, 1280, 1241, 1193, 1146, 1103, 1061, 962, 842, 768, 704, 674.

8.7.7 **(P21-C)** *Cage*-shaped Polymer Synthesis *via* CuAAC Reaction

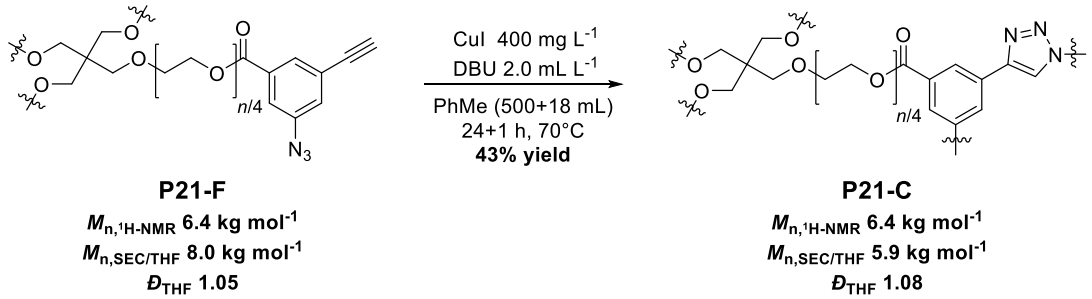

P21-F
$M_{n,^1H\text{-}NMR}$ 6.4 kg mol^{-1}
$M_{n,SEC/THF}$ 8.0 kg mol^{-1}
$Đ_{THF}$ 1.05

P21-C
$M_{n,^1H\text{-}NMR}$ 6.4 kg mol^{-1}
$M_{n,SEC/THF}$ 5.9 kg mol^{-1}
$Đ_{THF}$ 1.08

DBU (1.0 mL, 2.0 mL L^{-1}) was dissolved in toluene (500 mL). The mixture was purged with argon for 15 min and CuI (200 mg, 400 mg L^{-1}) was added. The mixture was then purged with argon for another 15 min before being heated at 70 °C. **P21-F** (1.200 g, 0.188 mmol) was dissolved in toluene (18 mL) and purged with argon for 15 min before being placed in a 20 mL syringe. The syringe mixture was injected at a regular rate (50 mg h^{-1} polymer, 0.75 mL h^{-1}) to the first mixture over 24 hours. Then, the resulting mixture was heated for one more hour at 70 °C before being cooled down to room temperature. Afterwards, the solvent was removed under reduced pressure, 1 M HCl (50 mL) was added and the crude material was extracted with DCM (3 × 50 mL). The organic fractions were collected, dried over magnesium sulfate and the solvent was removed under reduced pressure. The crude material was then washed on silica gel with $CHCl_3$, before being recovered by adding 10% MeOH to the eluent twice before being reprecipitated once in cold Et_2O with EtOH as solubilizing agent in order to obtain after final 0.2 µm PFTE filtration **P21-C** as a brown solid. **(515 mg, 43% yield)**

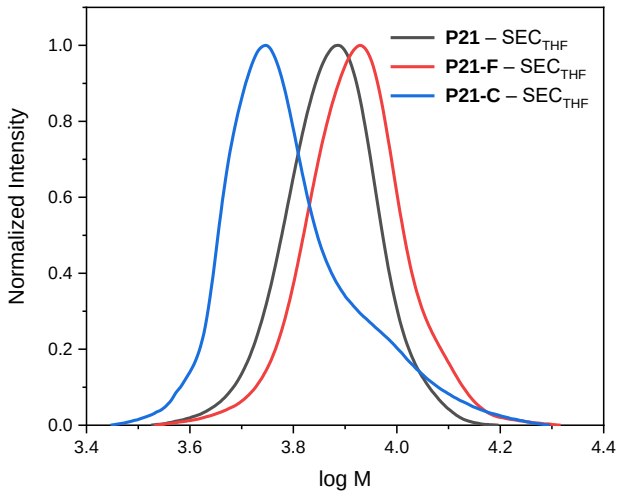

Figure S187: SEC_{THF} traces of polymers **P21, P21-F** and **P21-C**.

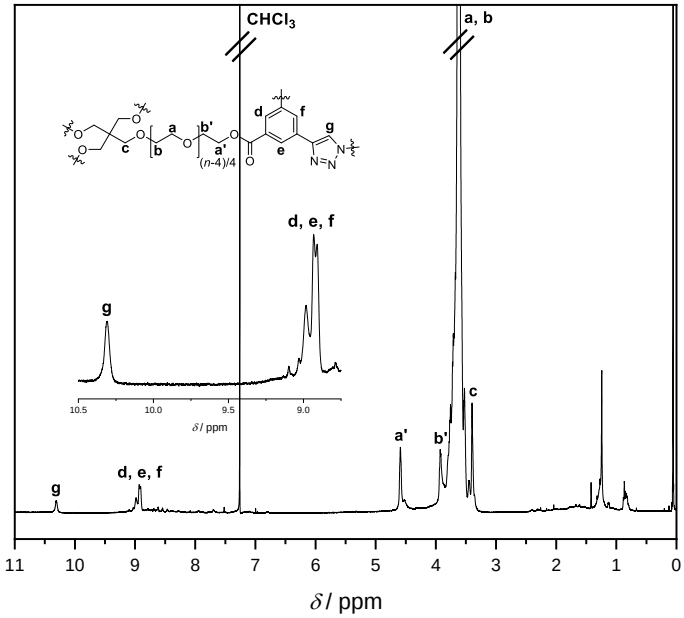

Figure S188: ^{1}H-NMR spectrum of **P21-C**, **^{1}H NMR (400 MHz, $CDCl_3$) δ** 10.31 (s), 8.98 (s), 8.93 (s), 8.91 (s), 4.59 (s), 3.97 – 3.87 (m), 3.83 – 3.43 (m), 3.40 (s).

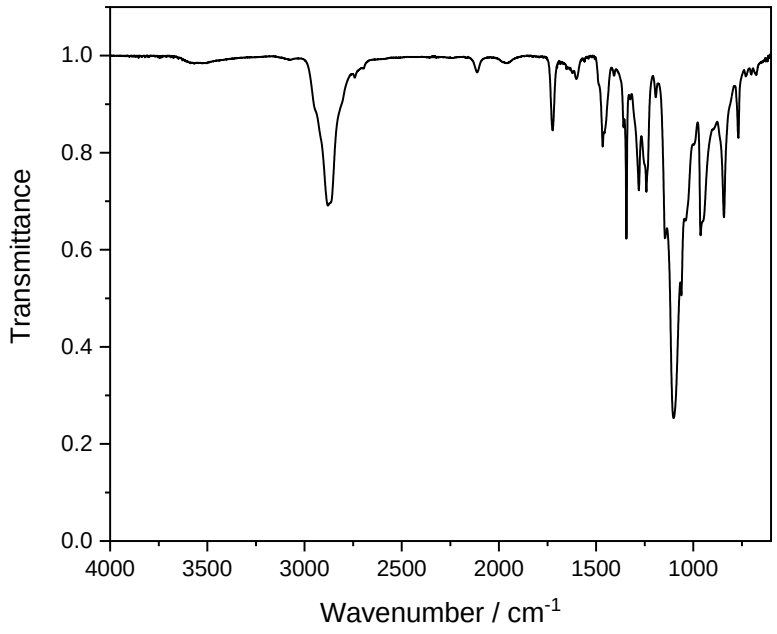

Figure S189: FT-IR spectrum of **P21-C**, **IR (ATR, cm^{-1})** 3566, 2880, 2111, 1724, 1602, 1466, 1359, 1344, 1280, 1241, 1193, 1145, 1101, 1061, 963, 842, 768.

8.7.8 **(P21-F$_{bis}$)** End-functionalization of P21 with End-group C20

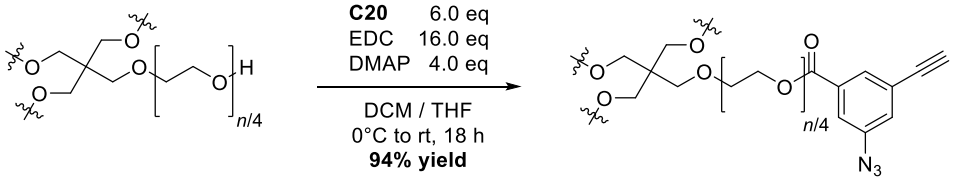

P21
$M_{n,^1H\text{-}NMR}$ 5.7 kg mol^{-1}
$M_{n,SEC/THF}$ 7.2 kg mol^{-1}
$Đ_{THF}$ 1.04

P21-F$_{bis}$
$M_{n,^1H\text{-}NMR}$ 6.4 kg mol^{-1}
$M_{n,SEC/THF}$ 8.0 kg mol^{-1}
$Đ_{THF}$ 1.05

Commercial grade *star*-shaped (PEG-OH)$_4$ **P21** (3.446 g, 0.606 mmol, 5687 g mol^{-1}, 1.0 eq), 3-azido-5-ethynylbenzoic acid **C20** (680 mg, 3.63 mmol, 6.0 eq) and 4-dimethylaminopyridine (296 mg, 2.42 mmol, 4.0 eq) were dissolved in dry DCM (15 mL) and dry THF (10 mL). The solution was cooled down to 0 °C and *N*-(3-dimethylaminopropyl)-*N*′-ethylcarbodiimide hydrochloride (1.86 g, 9.69 mmol, 16.0 eq) was added portionwise. The mixture was then stirred for 18 hours from 0 °C to room temperature. Afterwards, the resulting mixture was quenched with HCl 1 M and the aqueous phase was extracted with DCM (3 × 30 mL). The organic fractions were collected, dried over $MgSO_4$ and the solvents were removed under reduced pressure. The crude material was then washed on silica gel with $CHCl_3$, before being recovered by adding 10% MeOH to the eluent in order to obtain, after solvent evaporation and filtration of the remaining silica gel, **P21-F$_{bis}$** as a yellow solid. **(3.62 g, 0.569 mmol, 94% yield)**

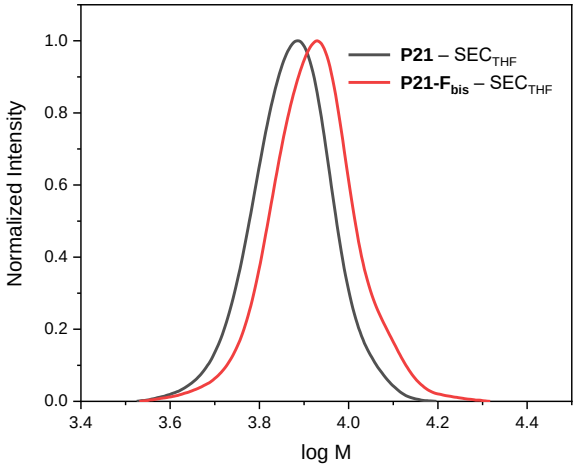

Figure S190: SEC$_{THF}$ traces of polymers **P21** and **P21-F$_{bis}$**.

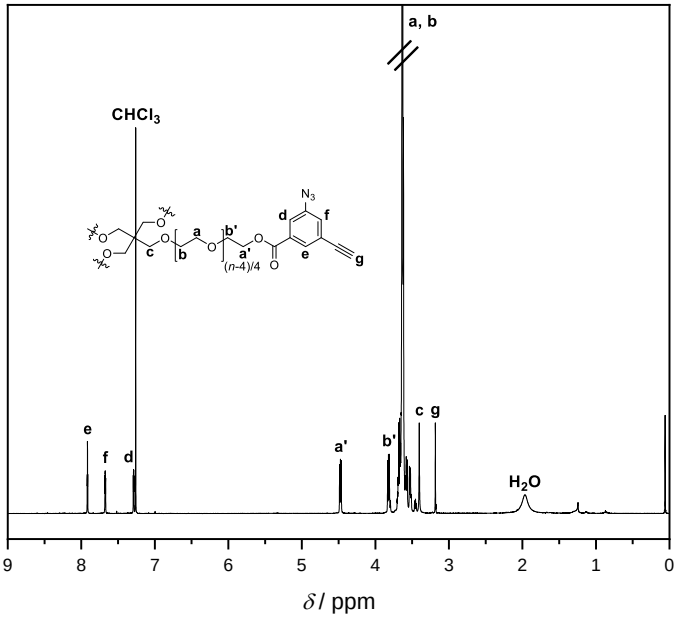

Figure S191: ^{1}H-NMR spectrum of **P21-F$_{bis}$, ^{1}H NMR (400 MHz, CDCl$_3$) δ** 7.92 (t, *J* = 1.4 Hz), 7.67 (dd, *J* = 2.2, 1.5 Hz), 7.29 (dd, *J* = 2.2, 1.4 Hz), 4.52 – 4.43 (m), 3.86 – 3.77 (m), 3.75 – 3.43 (m), 3.40 (s), 3.18 (s).

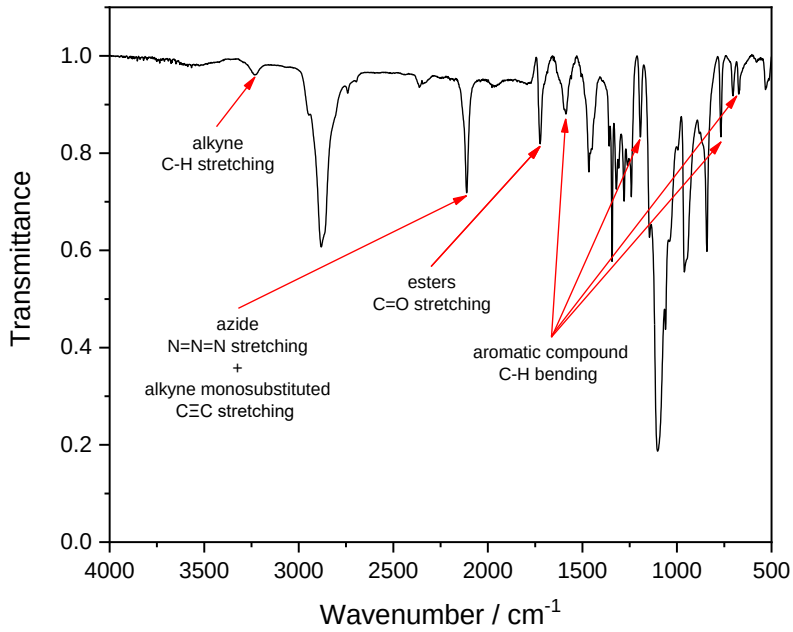

Figure S192: FT-IR spectrum of **P21-F$_{bis}$, IR (FT-IR2, ATR, cm^{-1})** 3236, 2881, 2112, 1724, 1587, 1466, 1359, 1343, 1321, 1280, 1241, 1193, 1102, 1060, 961, 842, 768, 704, 673, 532.

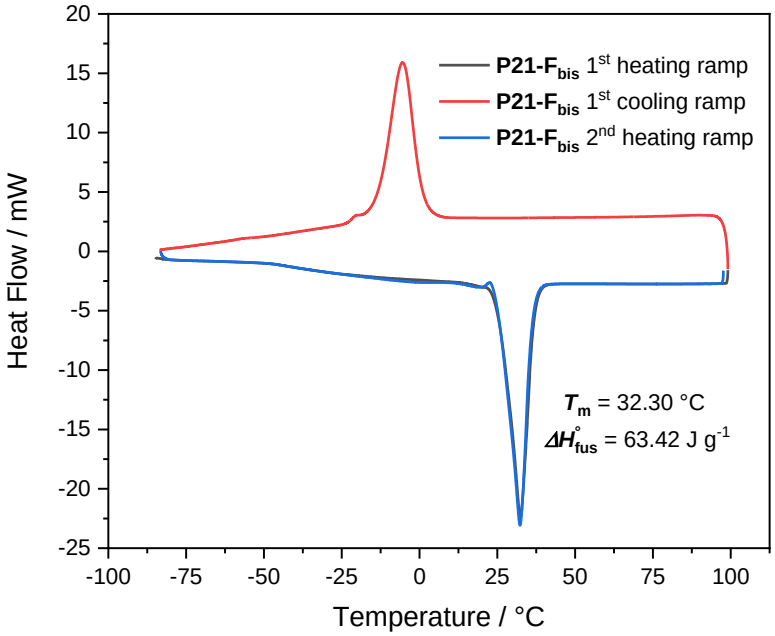

Figure S193: DSC thermogram of **P21-F$_{bis}$,** all thermal values were taken from the second heating ramp.

8.7.9 **(P21-C$_{bis}$)** *Cage*-shaped Polymer Synthesis *via* CuAAC Reaction

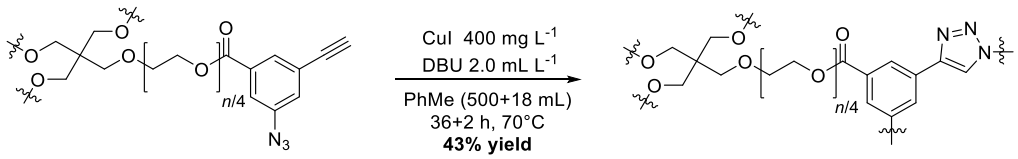

P21-F$_{bis}$
$M_{n,^1H\text{-}NMR}$ 6.4 kg mol^{-1}
$M_{n,SEC/THF}$ 8.0 kg mol^{-1}
$Đ_{THF}$ 1.05

P21-C$_{bis}$
$M_{n,^1H\text{-}NMR}$ 6.4 kg mol^{-1}
$M_{n,SEC/THF}$ 4.7 kg mol^{-1}
$Đ_{THF}$ 1.14

DBU (1.0 mL, 2.0 mL L^{-1}) was dissolved in toluene (500 mL). The mixture was purged with argon for 15 min and CuI (200 mg, 400 mg L^{-1}) was added. The mixture was then purged with argon for another 15 min before being heated at 70 °C. **P21-F$_{bis}$** (3.600 g) was dissolved in toluene (18 mL) and purged with argon for 15 min before being placed in a 20 mL syringe. The syringe mixture was injected at a regular rate (100 mg h^{-1} polymer, 0.50 mL h^{-1}) to the first mixture over 36 hours. Then, the resulting mixture was heated for two more hours at 70 °C before being cooled down to room temperature. Afterwards, the solvent was removed under reduced pressure, 1 M HCl (50 mL) was added and the crude material was extracted with DCM (3 × 50 mL). The organic fractions were collected, dried over magnesium sulfate and the solvent was removed under reduced pressure. The crude material was then washed on silica gel with $CHCl_3$, before being recovered by adding 10% MeOH to the eluent twice. Then, it was reprecipitated once in cold Et_2O with EtOH as solubilizing agent in order to obtain, after final 0.2 µm PFTE filtration, **P21-F$_{cage}$** as a brown solid. **(1.548 g, 43% yield)**

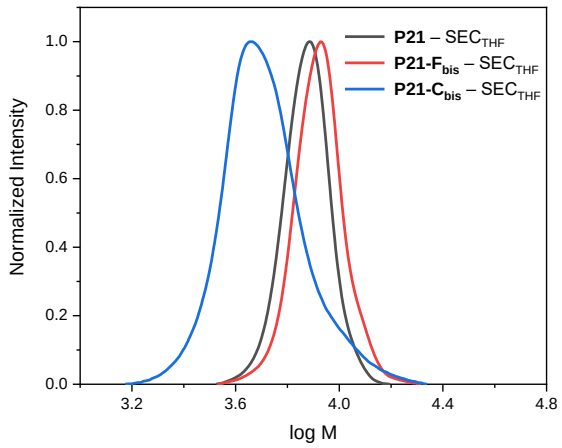

Figure S194: SEC_{THF} traces of polymers **P21, P21-F$_{bis}$** and **P21-C$_{bis}$.**

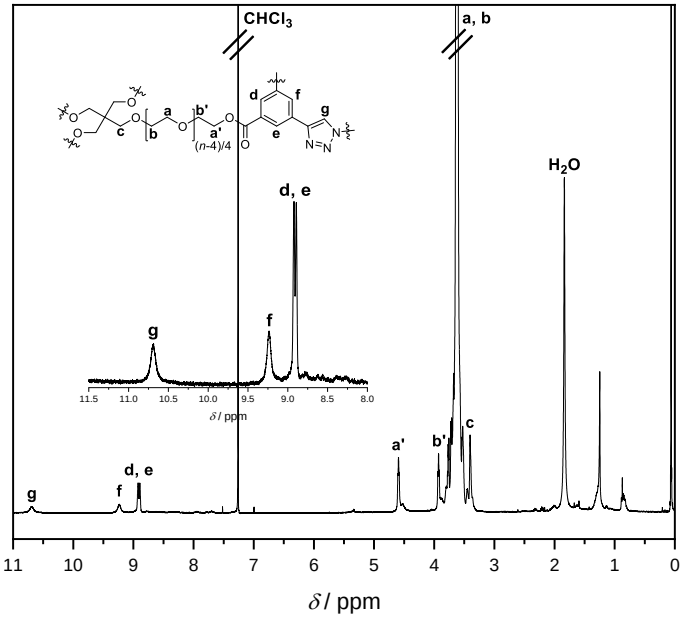

Figure S195: ^{1}H-NMR spectrum of **P21-C$_{bis}$, ^{1}H NMR (400 MHz, CDCl$_3$) δ** 10.69 (s), 9.24 (s), 8.92 (s), 8.89 (s), 4.65 – 4.46 (m), 3.97 – 3.85 (m), 3.83 – 3.33 (m), 3.40 (s).

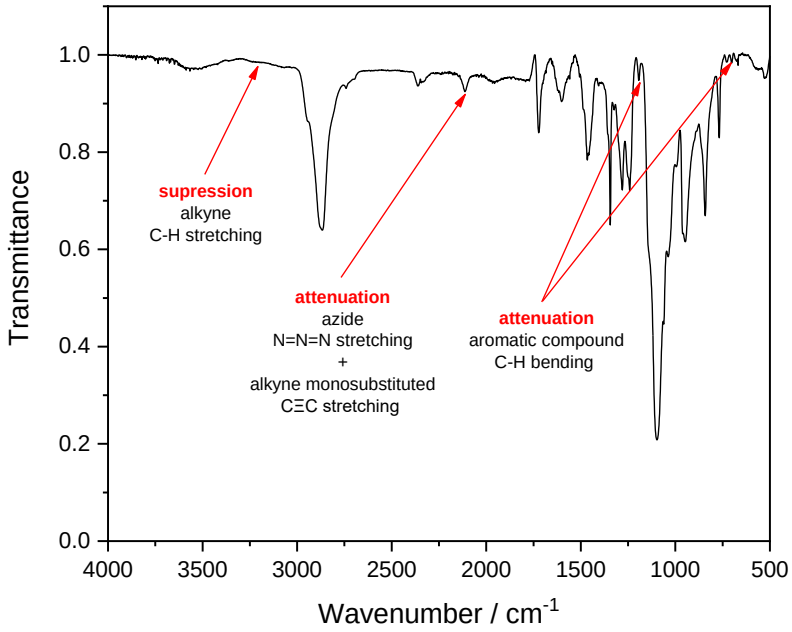

Figure S196: FT-IR spectrum of **P21-C$_{bis}$, IR (FT-IR2, ATR, cm^{-1})** 2867, 1723, 1602, 1466, 1344, 1281, 1242, 1097, 948, 842, 768.

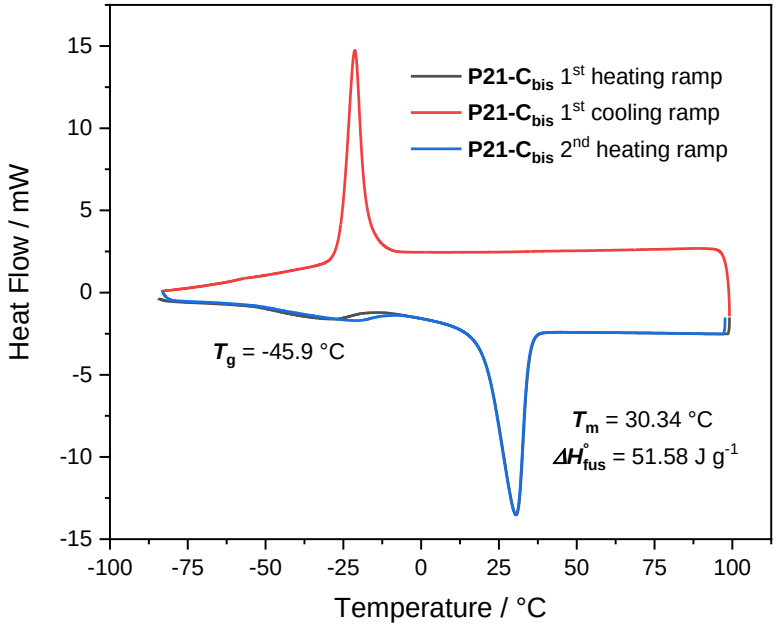

Figure S197: DSC thermogram of **P21-C$_{bis}$,** all thermal values were taken from the second heating ramp.

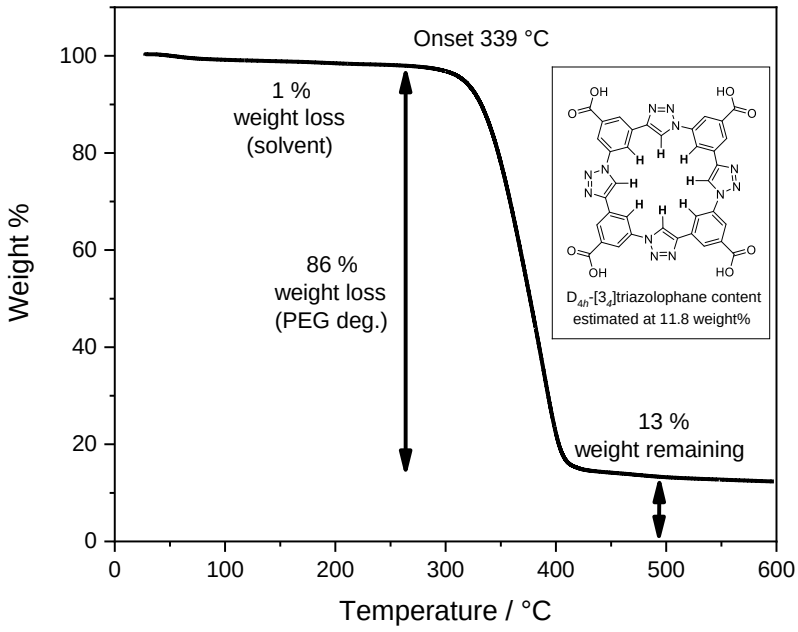

Figure S198: TGA thermogram of **P21-F$_{bis}$.**

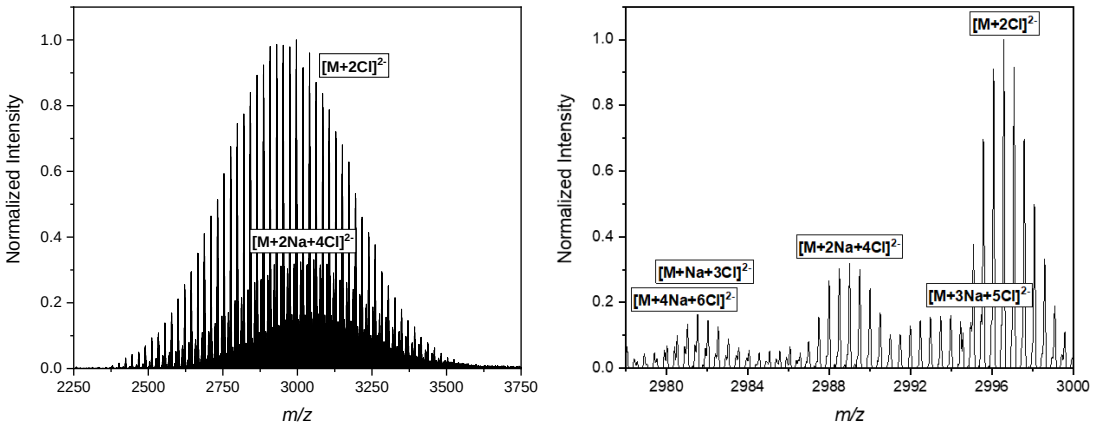

Figure S199: ESI-MS spectra of **P21-C$_{bis}$,** featuring all four main distributions obtained in negative mode.

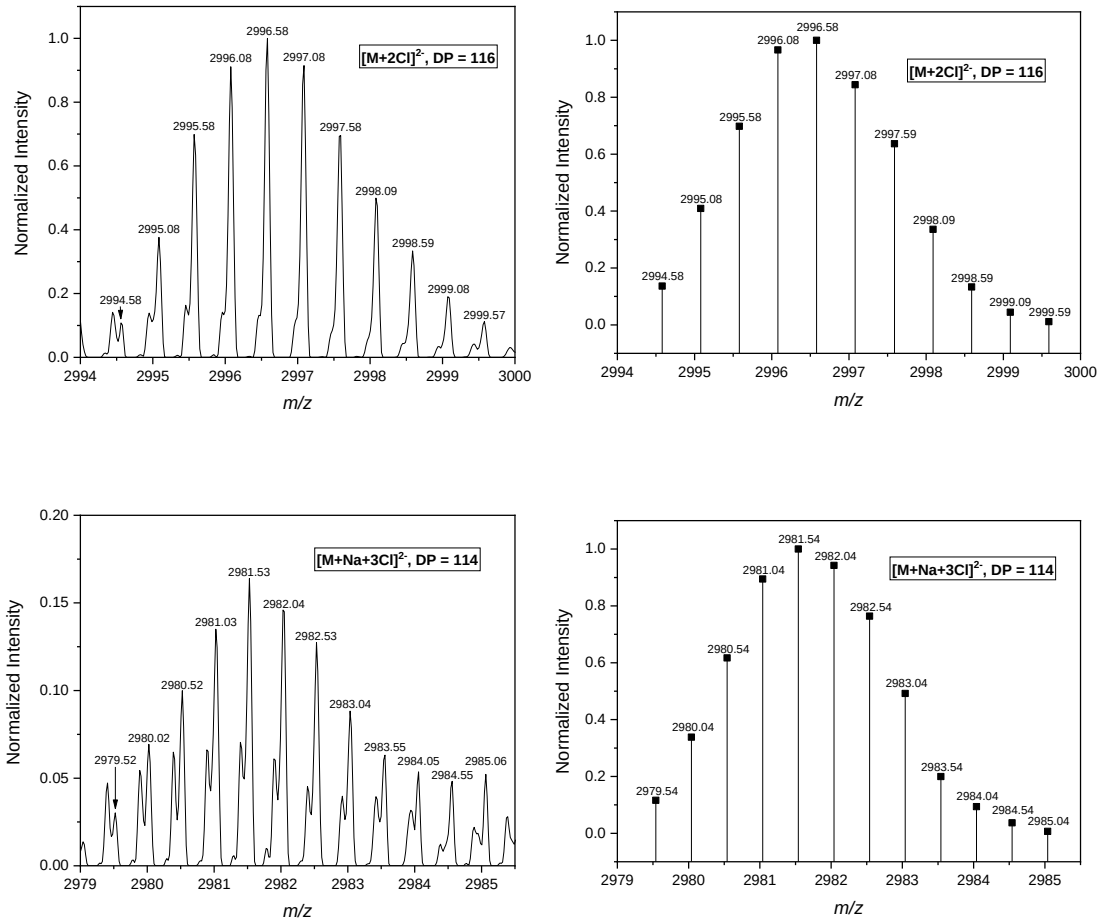

Figure S200: ESI-MS spectra of **P21-C$_{bis}$,** experimental (left) and calculated (right) MS patterns obtained for the first and second main distributions present in negative mode.

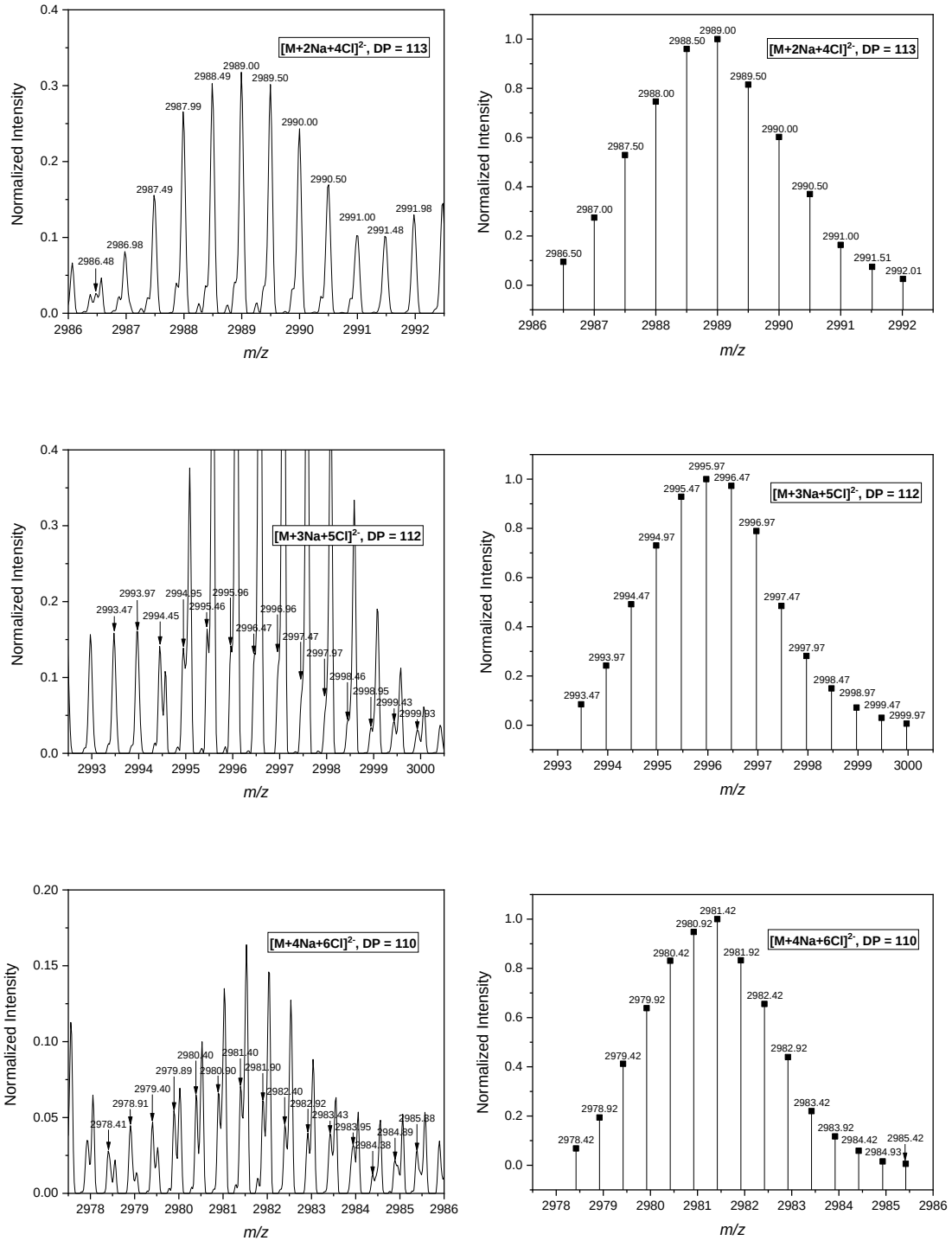

Figure S201: ESI-MS spectra of **P21-C$_{bis}$,** experimental (left) and calculated (right) MS patterns obtained for the third, third, fourth and fifth main distributions present in negative mode.

9 List of Abbreviation

ACVA	4,4′-azobis(4-cyanovaleric acid)
atm	atmospheric pressure
ATR	attenuated total reflection
ATRC	atom transfer radical cross-coupling
ATRP	atom transfer radical polymerization
AIBN	2,2′-azobis(2-methylpropionitrile)
BOP	benzotriazol-1-yloxytris(dimethylamino)phosphonium hexafluorophosphate
BPO	benzoyl peroxide
brine	saturated sodium chloride solution in water
c-Hex	cyclohexane
°C	degree Celsius
ε-CL	ε-caprolactone
CTA	chain transfer agent
CM	cross-metathesis
CuAAC	copper-catalyzed azide-alkyne cycloaddition
^{13}C-NMR	carbon 13 nuclear magnetic resonance
d	day(s)
$Đ$	dispersity (= M_n / M_w)
δ	chemical shift
DBU	1,8-diazabicyclo[5.4.0]undec-7-ene
DCM	dichloromethane
DIBAL-H	diisobutylaluminum hydride
DLS	dynamic light scattering
DMA	dimethylaniline
DMAC	*N*,*N*-dimethylacetamide
DMAP	*N*,*N*-dimethylpyridin-*4*-amine
DMF	*N*,*N*-dimethylformamide
DMSO	dimethyl sulfoxide
DNA	deoxyribonucleic acid

List of Abbreviation

DP	degree of polymerization
DP_{arm}	degree of polymerization per star arm
DPP	diphenyl phosphate
DPPA	diphenylphosphoryl azide
DSC	differential scanning calorimetry
EDC	*N*-(3-dimethylaminopropyl)-*N′*-ethylcarbodiimide hydrochloride
eq	equivalent(s)
ESA-CF	electrostatic self-assembly and covalent fixation process
ESI-MS	electrospray ionization mass spectrometry
ESI-HRMS	high resolution electrospray ionization mass spectrometry
Et_2O	diethyl ether
EtOAc	ethyl acetate
EtOH	ethanol
EZROP	electrophilic zwitterionic ring-opening polymerizations
FT-IR	Fourier-transform infrared
FRP	free radical polymerization
g	gram(s)
h	hour(s)
^{1}H-NMR	hydrogen nuclear magnetic resonance
HOBt	hydroxybenzotriazole
HSQC	heteronuclear single quantum correlation
IUPAC	international union of pure and applied chemistry
K	kelvin(s)
L	liter(s)
LS	light scattering
M	molecular weight distribution
M (unit)	mol L^{-1}
MA	methyl acrylate
mCPBA	3-chloroperoxybenzoic acid
MCR	multicomponent reaction
MeOH	methanol
min	minute(s)
M_n	number average molecular weight

MMA	methyl methacrylate
MOF	metal organic framework
mol	mole(s)
mol%	mole percent
MS	mass spectrometry
M_w	weight average molecular weight
m/z	molecular mass by charge ratio
n/a	(data) not available
N_A	Avogadro's number
NaTFA	sodium trifluoroacetate
NHS	*N*-hydroxysuccinimide
NMR	nuclear magnetic resonance
NMP	nitroxide-mediated radical polymerization
NZROP	nucleophilic zwitterionic ring-opening polymerizations
P_c	probability of intramolecular cyclization
ε-PCL	poly(ε−caprolactone)
PE	poly(ethylene)
PEO	poly(ethylene oxide)
PFP	pentafluorophenol
pH	hydrogen potential
PhMe	toluene
P_L	probability of intermolecular oligomerization
PMA	poly(methyl acrylate)
PMMA	poly(methyl methacrylate)
ppm	part per million
PS	poly(styrene)
PTHF	poly(tetrahydrofuran)
RAFT	reversible addition-fragmentation chain transfer
RDRP	reversible-deactivation radical polymerization
REMP	ring-expansion metathesis polymerization
REP	ring expansion polymerization
ROMO	ring opening metathesis oligomerization
ROP	ring opening polymerization
rt	room temperature

List of Abbreviation

S	siemens (unit)
σ	ionic conductivity
SEC	size exclusion chromatography
S_N2	bimolecular nucleophilic substitution
S_NAr	aromatic nucleophilic substitution
SPAAC	strain-promoted azide-alkyne cycloaddition
St	styrene
TBAF	tetrabutylammonium fluoride
TEMPO	(2,2,6,6-tetramethylpiperidin-1-yl)oxyl
THF	tetrahydrofuran
TLC	thin layer chromatography
T_m	melting temperature
TMS	*tert*-trimethylsilyl
T_g	glass transition temperature
UV-Vis	ultraviolet-visible
V-70	2,2'-azobis(4-methoxy-2,4-dimethylvaleronitrile)
wt.%	weight percent
ZROP	zwitterionic ring-opening polymerizations

10 List of Schemes, Figures, Tables and Equations

10.1 List of Schemes

10.2 List of Figures

10.3 List of Tables

10.4 List of Equations

11 List of Correspondences

LABOR REFERENCE	THESIS REFERENCE	PAPER REFERENCE
MG1	**C01**	
MG2	**C02**	
MG3	**C03**	
MG8	**R01**	
MG13	**R02**	
MG15	**R03**	
MG18	**R06**	
MG24	**C04**	
MG25	**C05**	
MG26	**C06**	
MG27	**C07**	
MG28	**C08**	
MG29	**C09**	
MG31	**R04**	
MG32	**C10**	
MG33	**C11**	
MG34	**C12**	
MG35	**R05**	
MG36	**C13**	
MG38	**C14**	
MG39	**C15**	
MG40	**C16**	
MG44	**C17**	**2**
MG45	**C18**	**3**
MG46	**C19**	**4**
MG47	**C20**	**5 / AEBA**

Labor Reference	Thesis Reference	Paper Reference
P003	**P03**	
P008	**P01**	
P008_SHend	**P01-SH**	
P009	**P02**	
P009_SHend	**P02-SH**	
P010	**P04**	
P010_SHend	**P04-SH**	
P013	**P05**	
P013_SHend	**P05-SH**	
P012	**P06**	
P014	**P07**	
P016	**P08**	
P016_SHend	**P08-SH**	
P020	**P13**	
P020_SHend	**P13-SH**	
P023	**P09**	
P029	**P10**	
P029_SHend	**P10-SH**	
P030	**P11**	
P030_SHend	**P11-SH**	
P030-C	**P11-C**	
P030-C_SHend	**P11-C-SH**	
P032	**P12**	
P032_SHend	**P12-SH**	
P035	**P14**	
P036	**P15**	
P042	**P16**	
P042-47	**P16-F**	
P042-47-C3	**P16-C1**	
P042-47-C4	**P16-C2**	
P042-47-C5	**P16-C3**	
P042-47-C6	**P16-C4**	
P042-47-C7	**P16-C5**	

List of Correspondences

Labor Reference	Thesis Reference	Paper Reference
P042-47-C8	**P16-C6**	
P042-47-C9	**P16-C8**	
P042-47-C10	**P16-C9**	
P042-47-C11	**P16-C7**	
P043	**P17**	**P1**
P043-47	**P17-F**	**P1$_{\text{end-func}}$**
P043-47-C1	**P17-C**	**P1$_{\text{cage}}$**
P044	**P18**	**P2**
P044-47b	**P18-F**	**P2$_{\text{end-func}}$**
P044-47b-C1	**P18-C**	**P2$_{\text{cage}}$**
P045	**P19**	**P3**
P045-47b	**P19-F**	**P3$_{\text{end-func}}$**
P045-47b-C1	**P19-C**	**P3$_{\text{cage}}$**
P046	**P20**	**P4**
P046-47	**P20-F**	**P4$_{\text{end-func}}$**
P046-47-C1	**P20-C**	**P4$_{\text{cage}}$**
P045-47c	**P19-F$_{\text{bis}}$**	
P045-47c-C1	**P19-C1$_{\text{bis}}$**	
P045-47c-C2	**P19-C2$_{\text{bis}}$**	
P045-47c-C3	**P19-C3$_{\text{bis}}$**	
PEG5000	**P21**	**PEO$_{\text{star}}$**
PEG5000-47b	**P21-F**	
PEG5000-47b-C3	**P21-C**	
PEG5000-47c	**P21-F$_{\text{bis}}$**	**PEO$_{\text{end-func}}$**
PEG5000-47c-C1	**P21-C$_{\text{bis}}$**	**PEO$_{\text{cage}}$**
n/a	**P21-Li$_{1:20}$**	**PE$_{\text{cage1:20}}$**
n/a	**P21-Li$_{1:25}$**	**PE$_{\text{cage1:25}}$**
n/a	**P21-C$_{\text{bis}}$-Li$_{1:20}$**	**PE$_{\text{cage1:20}}$**
n/a	**P21-C$_{\text{bis}}$-Li$_{1:25}$**	**PE$_{\text{cage1:25}}$**

12 Acknowledgments

First of all, I am grateful to Prof. Dr. Patrick THÉATO for granting me the opportunity to work in his research group, for taking care of the supervision of my doctoral research, as well as for taking part in the final evaluation of my thesis. In a similar manner, I am also very thankful to Prof. Dr. Stefan BRÄSE for accepting to examinate my doctoral thesis as co-referent, as well as to Prof. Dr. Manfred WILHELM, Prof. Dr. Claus FELDMANN and Prof. Dr. Matthias OLZMANN as third examiner, fourth examiner and chairman, respectively. More generally, I am glad to have been given the chance to carry out my doctoral research in the KARLSRUHE INSTITUTE OF TECHNOLOGY (KIT) and I warmly thank Germany for its hospitality all along these three years and a half spent in Karlsruhe.

Additionally, I would like to thank Dr. Hatice MUTLU for her support and her wise scientific advice based on her extensive experience in the academic world. I wish her a long and successful career in academia. I also thank Prof. Dr. Jonathan G. RUDICK for his fruitful scientific discussion. In a more general manner, I sincerely thank Katharina ELIES for her priceless help and technical instrument expertise as well as Evelyn STÜHRING, Bärbel SEUFERT-DAUSMANN, Vera NOGA, Martina RITTER, Dr. Birgit HUBER, and Dr. Dominik VOLL for their precious administrative and organizational supports.

I also want to thank Edgar MOLLE, Sergej BARABAN, Andreas BUTZELAAR and Stefan FRECH for their friendship and for the moments shared in Laboratory 322, as well as all my colleagues from AKT for the time we spent together. I would especially add that Sergej is a very caring person and that he is truly a great friend to me. I am particularly grateful to him for having taken the time to thoroughly review my entire thesis and I am looking forward to do the same with his own dissertation in the coming months. And above all, how can I not end my acknowledgments without mentioning Edgar again, since we have not only started and finished our PhD together from January 2018 to July 2021, but most importantly, who has been a true friend to me during these decisive years of our lives.

Also, I would infinitely thank and transmit all my love to Eliane, Gilles and Anne as well as to the rest of my family for their flawless support all along my studies. I would have especially loved to share these very special moments of life with you Eliane. Thank you from the bottom

of my heart, thank you for everything you have done for me. Without you and Gilles, I would never have gotten where I stand today, and for that I am eternally grateful to both of you.

At last, I have a small thought for my former colleagues of the UNIVERSITY OF FRIBOURG, in particular Jenny, Joelle and Miriam for our time spent in the Christmas markets and in front of hot chocolates.

13 Bibliography

[1] H. Staudinger, *Chem. Ber.* **1920**, *53*, 1073–1085.

[2] K. Matyjaszewski, *Science* **2011**, *333*, 1068

[3] N. Hadjichristidis, H. Iatrou, M. Pitsikalis, J. Mays, *Prog. Polym. Sci.* **2006**, *31*, 1068–1132.

[4] M. S. Yavuz, Y. Cheng, J. Chen, C. M. Cobley, Q. Zhang, M. Rycenga, J. Xie, C. Kim, K. H. Song, A. G. Schwartz, L. V. Wang, Y. Xia, *Nat. Mater.* **2009**, *8*, 935–939.

[5] D. Lootens, C. Vautrin, H. Van Damme, T. Zemb, *J. Mater. Chem.* **2003**, *13*, 2072–2074.

[6] C. M. Erben, R. P. Goodman, A. J. Turberfield, *Angew. Chem. Int. Ed.* **2006** *45*, 7414–7417.

[7] T. G. Edwardson, K. M. Carneiro, C. K. McLaughlin, C. J. Serpell, H. F. Sleiman, *Nat. Chem.* **2013**, *5*, 868.

[8] N. M. Molino, S. W. Wang, *Curr. Opin. Biotechnol.* **2014**, *28*, 75–82.

[9] Y. T. Lai, D. Cascio, T. O. Yeates, *Science*, **2012**, *336*, 1129–1129.

[10] G. Jutz, P. van Rijn, M. B. Santos, A. Böker, *Chem. Rev.* **2015**, *115*, 1653–1701.

[11] M. Kim, Y. Rho, K. S. Jin, B. Ahn, S. Jung, H. Kim, M. Ree, *Biomacromolecules* **2011**, *12*, 1629–1640.

[12] T. R. Cook, Y. R. Zheng, P. J. Stang, *Chem. Rev.* **2013**, *113*, 734–777.

[13] D. Fujita, Y. Ueda, S. Sato, N. Mizuno, T. Kumasaka, M. Fujita, *Nature* **2016**, *540*, 563–566.

[14] M. Yoshizawa, J. K. Klosterman, M. Fujita, *Angew. Chem. Int. Ed.* **2009**, *48*, 3418–3438.

[15] D. Zhang, A. Martinez, J. P. Dutasta, *Chem. Rev.* **2017**, *117*, 4900–4942.

[16] A. Peacock, Handbook of polyethylene: structures: properties, and applications. *CRC press.* **2000**.

[17] C. Vasile, M. Pascu, Practical guide to polyethylene. *Smithers Rapra Publishing* **2005**.

[18] G. Moad, D. H. Solomon, The chemistry of radical polymerization. *Elsevier* **2006**.

[19] Y. Zheng, S. Li, Z. Weng, C. Gao, *Chem. Soc. Rev.* **2015**, *44*, 4091–4130.

[20] M. A. Gauthier, M. I. Gibson, H. A. Klok, *Angew. Chem. Int. Ed.* **2009**, *48*, 48–58.

[21] C. Feng, Y. Li, D. Yang, J. Hu, X. Zhang, X. Huang, *Chem. Soc. Rev.* **2011**, *40*, 1282–1295.

[22] J. M. Ren, T. G. McKenzie, Q. Fu, E. H. Wong, J. Xu, Z. An, S. Shanmugam, T. P. Davis, C. Boyer, G. G. Qiao, *Chem. Rev.* **2016**, *116*, 6743–6836.

[23] R. B. Grubbs, R. H. Grubbs, *Macromolecules* **2017**, *50*, 6979–6997.

[24] M. Szwarc, *Nature* **1956**, *178*, 1168–1169.

[25] M. Morton, Anionic polymerization: principles and practice. *Elsevier* **2012**.

[26] A. Hirao, R. Goseki, T. Ishizone, *Macromolecules* **2014**, *47*, 1883–1905.

[27] P. Dubois, O. Coulembier, J. M. Raquez, Handbook of ring–opening polymerization. *John Wiley & Sons* **2009**.

[28] S. Aoshima, S. Kanaoka, *Chem. Rev.* **2009**, *109*, 5245–5287.

[29] G. Moad, E. Rizzardo, S. H. Thang, *Acc. Chem. Res.* **2008**, *41*, 1133–1142.

[30] J. Nicolas, Y. Guillaneuf, C. Lefay, D. Bertin, D. Gigmes, B. Charleux, *Prog. Polym. Sci.* **2013**, *38*, 63–235.

[31] D. H. Solomon, E. Rizzardo, P. Cacioli, U.S. Patent No. 4,581,429. Washington, DC: U.S. Patent and Trademark Office. **1986**.

[32] K. Matyjaszewski, *Macromolecules* **2012**, *45*, 4015–4039.

[33] M. Kato, M. Kamigaito, M. Sawamoto, T. Higashimura, *Macromolecules* **1995**, *28*, 1721–1723.

[34] J. S. Wang, K. Matyjaszewski, *J. Am. Chem. Soc.* **1995**, *117*, 5614–5615.

[35] J. Chiefari, Y. K. Chong, F. Ercole, J. Krstina, J. Jeffery, T. P. Le, T. A. Mayadunne, G. F. Meijs, C. L. Moad, G. Moad, E. Rizzardo, S. H. Thang, *Macromolecules* **1998**, *31*, 5559–5562.

[36] G. Moad, E. Rizzardo, S. H. Thang, *Polymer* **2008**, *49*, 1079–1131.

[37] G. Moad, E. Rizzardo, *Polym. Int.* **2020**, *69*, 658–661.

[38] A. Kekulé, *Bull. Soc. Chim. Fr.* **1865**, *3*, 98.

[39] A. Kekulé, *Liebigs Ann.* **1866**, *137*, 129–196.

[40] L. R. MacGillivray, J. L. Atwood, *Angew. Chem. Int. Ed.* **1999**, *38*, 1018–1033.

[41] R. G. Jones, J. Kahovec, R. Stepto, E. S. Wilks, M. Hess, T. Kitayama, W. V. Metanomski, Compendium of Polymer Terminology and Nomenclature IUPAC Recommendations. *RSC Pub.* **2008**.

[42] A. Biwer, G. Antranikian, E. Heinzle, *Appl. Microbiol. Biotechnol.* **2002**, *59*, 609–617.

[43] A. Villiers, *Compt. Rend. Acad. Sci.* **1891**, *112*, 536–538.

[44] K. Freudenberg, F. Cramer, *Z. Naturforsch. B* **1948**, *3*, 464–466.

[45] H. J. Buschmann, E. Schollmeyer, *J. Cosmet. Sci.* **2002**, *53*, 185–192.

[46] J. Szejtli, *Chem. Rev.* **1998**, *98*, 1743–1754.

[47] R. Challa, A. Ahuja, J. Ali, R. K. Khar, *AAPS PharmSciTech* **2005**, *6*, 329–357.

[48] K. Uekama, F. Hirayama, T. Irie, *Chem. Rev.* **1998**, *98*, 2045–2076.

[49] E. M. Del Valle, *Process Biochem.* **2004**, *39*, 1033–1046.

[50] V. Böhmer, *Angew. Chem. Int. Ed.* **1995**, *34*, 713–745.

[51] A. Zinke, E. Ziegler, *Chem. Ber.* **1941**, *74*, 1729–1736.

[52] A. Zinke, E. Ziegler, *Chem. Ber.* **1944**, *77*, 264–272.

[53] D. Crespy, M. Bozonnet, M. Meier, *Angew. Chem. Int. Ed.* **2008**, *47*, 3322–3328.

[54] C. D. Gutsche, B. Dhawan, K. H. No, R. Muthukrishnan, *J. Am. Chem. Soc.* **1981**, *103*, 3782–3792.

[55] J. Rebek Jr, *Chem. Commun.* **2000**, *8*, 637–643.

[56] D. J. Cram, S. Karbach, Y. H. Kim, L. Baczynskyj, K. Marti, R. M. Sampson, G. W. Kalleymeyn, *J. Am. Chem. Soc.* **1988**, *110*, 2554–2560.

[57] R. Warmuth, J. Yoon, *Acc. Chem. Res.* **2001**, *34*, 95–105.

[58] D. J. Cram, G. M. Lein, *J. Am. Chem. Soc.* **1985**, *107*, 3657–3668.

[59] D. J. Cram, *Angew. Chem. Int. Ed.* **1986**, *25*, 1039–1057.

[60] J. R. Moran, S. Karbach, D. J. Cram, *J. Am. Chem. Soc.* **1982**, *104*, 5826–5828.

[61] D. J. Cram, S. Karbach, H. E. Kim, C. B. Knobler, E. F. Maverick, J. L. Ericson, R. C. Helgeson, *J. Am. Chem. Soc.* **1988**, *110*, 2229–2237.

[62] A. S. Lindsey, *J. Chem. Soc.* **1965**, 1685–1692.

[63] A. Collet, *Tetrahedron* **1987**, *43*, 5725–5759.

[64] M. J. Hardie, *Chem. Soc. Rev.* **2010**, *39*, 516–527.

[65] R. Behrend, E. Meyer, F. Rusche, *Liebigs Ann.* **1905**, *339*, 1–37.

[66] W. A. Freeman, W. L. Mock, N. Y. J. Shih, *J. Am. Chem. Soc.* **1981**, *103*, 7367–7368.

[67] E. Masson, X. Ling, R. Joseph, L. Kyeremeh–Mensah, X. Lu, *RSC Adv.* **2012**, *2*, 1213–1247.

[68] Y. Aoyama, Y. Tanaka, H. Toi, H. Ogoshi, *J. Am. Chem. Soc.* **1988**, *110*, 634–635.

[69] A. Shivanyuk, J. Rebek, *Proc. Natl. Acad. Sci. USA* **2001**, *98*, 7662–7665.

[70] J. L. Atwood, L. J. Barbour, A. Jerga, *Proc. Natl. Acad. Sci. USA* **2002**, *99*, 4837–4841.

[71] L. Avram, Y. Cohen, *J. Am. Chem. Soc.* **2004**, 126, 11556–11563.

[72] Q. Zhang, L. Catti, K. Tiefenbacher, *Acc. Chem. Res.* **2018**, *51*, 2107–2114.

[73] C. J. Pedersen, *J. Am. Chem. Soc.* **1967**, *89*, 7017–7036.

[74] H. K. Frensdorff, *J. Am. Chem. Soc.* **1971**, *93*, 600–606.

[75] R. D. Shannon, *Acta Crystallogr. A* **1976**, *32*, 751–767.

[76] R. Reichenbach–Klinke, B. König, *Dalton Trans.* **2002**, *2*, 121–130.

[77] B. Dietrich, J. M. Lehn, J. P. Sauvage, *Tetrahedron Lett.* **1969**, *10*, 2885–2888.

[78] B. Dietrich, J. M. Lehn, J. P. Sauvage, *Tetrahedron Lett.* **1969**, *10*, 2889–2892.

[79] R. M. Izatt, K. Pawlak, J. S. Bradshaw, R. L. Bruening, *Chem. Rev.* **1995**, *95*, 2529–2586.

[80] S. O. Kang, J. M. Llinares, V. W. Day, K. Bowman–James, *Chem. Soc. Rev.* **2010**, *39*, 3980–4003.

[81] R. P. Bonar–Law, J. K. Sanders, *Tetrahedron Lett.* **1992**, *33*, 2071–2074.

[82] D. G. Rivera, L. A. Wessjohann, *Molecules* **2007**, *12*, 1890–1899.

[83] J. Tamminen, E. Kolehmainen, *Molecules* **2001**, *6*, 21–46.

[84] M. Iyoda, J. Yamakawa, M. J. Rahman, *Angew. Chem. Int. Ed.* **2011**, *50*, 10522–10553.

[85] S. Höger, *J. Polym. Sci. Pol. Chem.* **1999**, *37*, 2685–2698.

[86] Y. Yamaguchi, Z. I. Yoshida, *Chem. Eur. J.* **2003**, *9*, 5430–5440.

[87] S. Durot, J. Taesch, V. Heitz, *Chem. Rev.* **2014**, *114*, 8542–8578.

[88] J. M. Lehn, *Science* **1993**, *260*, 1762–1764.

[89] G. C. Ferreira, K. M. Kadish, K. M. Smith, R. Guilard, The Handbook of Porphyrin Science. *World Scientific Publishers: Singapore* **2013**

[90] L. A. Wessjohann, E. Ruijter, D. Garcia–Rivera, W. Brandt, *Mol. Divers.* **2005**, *9*, 171–186.

[91] E. Marsault, M. L. Peterson, *J. Med. Chem.* **2011**, *54*, 1961–2004.

[92] L. A. Wessjohann, C. K. Z. Andrade, O. E. Vercillo, D. G. Rivera, *Targets Heterocycle Systems: Chemistry and Properties* **2006,** *10*, 24–53.

[93] C. Gilon, D. Halle, M. Chorev, Z. Selincer, G. Byk, *Biopolymers* **1991**, *31*, 745–750.

[94] C. Adessi, C. Soto, *Curr. Med. Chem.* **2002**, *9*, 963–978.

[95] E. H. Flynn, M. V. Sigal Jr, P. F. Wiley, K. Gerzon, *J. Am. Chem. Soc.* **1954**, *76*, 3121–3131.

[96] J. Li, S. G. Kim, J. Blenis, *Cell Metab.* **2014**, *19*, 373–379.

[97] D. P. Levine, *Clin. Infect. Dis.* **2006**, *42*, 5–12.

[98] M. E. Falagas, S. K. Kasiakou, L. D. Saravolatz, *Clin. Infect. Dis.* **2005**, *40*, 1333–1341.

[99] K. L. Tedesco, M. J. Rybak, *Pharmacotherapy* **2004**, *24*, 41–57.

[100] J. F. Borel, C. Feurer, H. U. Gubler, H. Stähelin, *Inflamm. Res.* **1994**, *43*, 179–186.

[101] P. Giannakakou, R. Gussio, E. Nogales, K. H. Downing, D. Zaharevitz, B. Bollbuck, G. Poy, D. Sackett, K. C. Nicolaou, T. Fojo, *Proc. Natl. Acad. Sci. USA* **2000**, *97*, 2904–2909.

[102] D. M. Gershenson, L. J. Copeland, J. J. Kavanagh, A. Cangir, G. D. Junco, P. B. Saul, C. A. Stringer, R. S. Freedman, C. L. Edwards, J. T. Wharton, *Cancer* **1985**, *56*, 2756–2761.

[103] V. Letscher–Bru, R. Herbrecht, *J. Antimicrob. Chemother.* **2003**, *51*, 513–521.

[104] D. R. De Figueiredo, U. M. Azeiteiro, S. M. Esteves, F. J. Gonçalves, M. J. Pereira, *Ecotoxicol. Environ. Saf.* **2004**, *59*, 151–163.

[105] K. L. Rinehart, K. Harada, M. Namikoshi, C. Chen, C. A. Harvis, M. H. Munro, J. W. Blunt, P. E. Mulligan, V. R. Beasley, *J. Am. Chem. Soc.* **1988**, *110*, 8557–8558.

[106] S. Merel, D. Walker, R. Chicana, S. Snyder, E. Baurès, O. Thomas, *Environ. Int.* **2013**, *59*, 303–327.

[107] M. S. Butler, *Nat. Prod. Rep.* **2005**, *22*, 162–195.

[108] E. M. Driggers, S. P. Hale, J. Lee, N. K. Terrett, *Nat. Rev. Drug Discov.* **2008**, *7*, 608–624.

[109] S. W. Lamberts, A. J. Van der Lely, W. W. De Herder, L. J. Hofland, *N. Engl. J. Med.* **1996**, *334*, 246–254.

[110] M. E. Caplin, M. Pavel, J. B. Ćwikła, A. T. Phan, M. Raderer, E. Sedláčková, G. Cadiot, E. M. Wolin, J. Capdevila, L. Wall, G. Rindi, A. Langley, S. Martinez, J. Blumberg, P. Ruszniewski, *N. Engl. J. Med.* **2014**, *371*, 224–233.

[111] A. Colao, M. D. Bronstein, P. Freda, F. Gu, C. C. Shen, M. Gadelha, M. Fleseriu, A. J. Van der Lely, A. J. Farrall, K. H. Reséndiz, M. Ruffin, Y. Chen, M. Sheppard, *J. Clin. Endocrinol. Metab.* **2014**, *99*, 791–799.

[112] Y. C. Patel, *Front. Neuroendocrinol.* **1999**, *20*, 157–198.

[113] A. Gradillas, J. Pérez-Castells, *Angew. Chem. Int. Ed.* **2006**, *45*, 6086–6101.

[114] A. Parenty, X. Moreau, J. M. Campagne, *Chem. Rev.* **2006**, *106*, 911–939.

[115] K. X. Chen, F. G. Njoroge, J. Pichardo, A. Prongay, N. Butkiewicz, N. Yao, V. Madison, V. Girijavallabhan, *J. Med. Chem.* **2006**, *49*, 567–574.

[116] D. H. Steinman, M. L. Curtin, R. B. Garland, S. K. Davidsen, H. R. Heyman, J. H. Holms, D. H. Albert, Terry J. Magoc, I. B. Nagy, P. A. Marcotte, J. Li, D. W. Morgan, C. Hutchins, J. B. Summers, *Bioorg. Med. Chem. Lett.* **1998**, *8*, 2087–2092.

[117] R. J. Cherney, L. Wang, D. T. Meyer, C. B. Xue, E. C. Arner, R. A. Copeland, M. B. Covington, K. D. Hardman, Z. R. Wasserman, B. D. Jaffee, C. P. Decicco, *Bioorg. Med. Chem. Lett.* **1999**, *9*, 1279–1284.

[118] G. M. Ksander, R. De Jesus, A. Yuan, R. D. Ghai, A. Trapani, C. Mc Martin, R. Bohacek, *J. Med. Chem.* **1997**, *40*, 495–505.

[119] P. G. Nantermet, J. C. Barrow, C. L. Newton, J. M. Pellicore, M. Young, D. Lewis, B. J. Lucas, J. A. Krueger, D.R. McMasters, Y. Yan, L. C. Kuo, J. P. Vacca, H. G. Selnick, *Bioorg. Med. Chem. Lett.* **2003**, *13*, 2781–2784.

[120] S. Thaisrivongs, J. R. Blinn, D. T. Pals, S. R. Turner, *J. Med. Chem.* **1991**, *34*, 1276–1282.

[121] S. J. Stachel, C. A. Coburn, S. Sankaranarayanan, E. A. Price, B. L. Pietrak, Q. Huang, J. Lineberger, A. S. Espeseth, L. Jin, J. Ellis, M. K. Holloway, S. Munshi, T. Allison, D. Hazuda, A. J. Simon, S. L. Graham, J. P. Vacca, *J. Med. Chem.* **2006**, *49*, 6147–6150.

[122] I. D. Hills, J. P. Vacca, *Curr. Opin. Drug Discov. Dev.* **2007**, *10*, 383–391.

[123] A. E. Weber, M. G. Steiner, P. A. Krieter, A. E. Colletti, J. R. Tata, T. A. Halgren, R. G. Ball, J. J. Doyle, T. W. Schorn, R. A. Stearns, R. R. Miller, P. K. S. Siegl, W. J. Greenlee, A. A. Patchett, *J. Med. Chem.* **1992**, *35*, 3755–3773.

[124] C. F. Dai, F. Cheng, H. C. Xu, Y. P. Ruan, P. Q. Huang, *ACS Comb. Sci.* **2007**, *9*, 386–394.

[125] H. L. Sham, G. Bolis, H. H. Stein, S. W. Fesik, P. A. Marcotte, J. J. Plattner, C. A. Rempel, J. Greer, *J. Med. Chem.* **1988**, *31*, 284–295.

[126] C. Hutchins, J. Greer, D. J. Hoover, *Crit. Rev. Biochem. Mol. Biol.* **1991**, *26*, 77–127.

[127] Y. Huang, E. D. Strobel, C. Y. Ho, C. H. Reynolds, K. A. Conway, J. A. Piesvaux, D. E. Brenneman, G. J. Yohrling, H. M. Arnold, D. Rosenthal, R. S. Alexander, B. A. Tounge, M. Mercken, M. Vandermeeren, M. H. Parker, A. B. Reitz, E. W. Baxter, *Bioorg. Med. Chem. Lett.* **2010**, *20*, 3158–3160.

[128] O. Baudoin, M. P. Teulade–Fichou, J. P. Vigneron, J. P., J. M. Lehn, *J. Org. Chem.* **1997**, *62*, 5458–5470.

[129] D. P. Fairlie, J. D. A. Tyndall, R. C. Reid, A. K. Wong, G. Abbenante, M. J. Scanlon, D. R. March, D. A. Bergman, C. L. L. Chai, B. A. Burkett, *J. Med. Chem.* **2000**, *43*, 1271–1281.

[130] H. Hirai, I. Takahashi-Suziki, T. Shimomura, K. Fukasawa, T. Machida, T. Takaki, M. Kobayashi, T. Eguchi, H. Oki, T. Arai, K. Ichikawa, S. Hasako, T. Kodera, N. Kawanishi, Y. Nakatsuru, H. Kotani, Y. Iwasawa, *Invest. New Drugs* **2011**, *29*, 534–543.

[131] E. De Clercq, N. Yamamoto, R. Pauwels, J. Balzarini, M. Witvrouw, K. De Vreese, Z. Debyser, B. Rosenwirth, P. Peichl, R. Datema, *Antimicrob. Agents Chemother.* **1994**, *38*, 668–674.

[132] C. W. West, D. H. Rich, *Org. Lett.* **1999**, *1*, 1819–1822.

[133] C. P. Decicco, Y. Song, D. A. Evans, *Org. Lett.* **2001**, *3*, 1029–1032.

[134] R. B. Lobell, C. A. Omer, M. T. Abrams, H. G. Bhimnathwala, M. J. Brucker, C. A. Buser, J. P. Davide, S. J. De Solms, C. J. Dinsmore, M. S. Ellis-Hutchings, A. M. Kral, D. Liu, W. C. Lumma, S. V. Machotka, E. Rands, T. M. Williams, S. L. Graham, G. D. Hartman, A. I. Oliff, D. C. Heimbrook, N. E. Kohl, *Cancer Res.* **2001**, *61*, 8758–8768.

[135] A. K. Ghosh, S. Kulkarni, D. D. Anderson, L. Hong, A. I. Baldridge, Y. Wang, A. A. Chumanevich, Andrey Y. Kovalevsky, Y. Tojo, M. Amano, Y. Koh, J. Tang, I. T. Weber, H. Mitsuya, *J. Med. Chem.* **2009**, *52*, 7689–7705.

[136] S. Avolio, V. Summa, *Curr. Top. Med. Chem.* **2010**, *10*, 1403–1422.

[137] F. Velázquez, S. Venkatraman, M. Blackman, P. Pinto, S. Bogen, M. Sannigrahi, K. Chen, J. Pichardo, A. Hart, X. Tong, V. Girijavallabhan, F. G. Njoroge, *J. Med. Chem.* **2009**, *52*, 700–708.

[138] R. Furumai, A. Matsuyama, N. Kobashi, K. H. Lee, M. Nishiyama, H. Nakajima, A. Tanaka, Y. Komatsu, N. Nishino, M. Yoshida, S. Horinouchi, *Cancer Res.* **2002**, *62*, 4916–4921.

[139] T. Pirali, V. Faccio, R. Mossetti, A. A. Grolla, S. Di Micco, G. Bifulco, A. A. Genazzani, G. C. Tron, *Mol. Divers.* **2010**, *14*, 109–121.

[140] A. A. Aimetti, R. K. Shoemaker, C. C. Lin, K. S. Anseth, *Chem. Commun.* **2010**, *46*, 4061–4063.

[141] E. Marsault, P. Deslongchamps, *Org. Lett.* **2000**, *2*, 3317–3320.

[142] S. Phoenix, M. S. Reddy, P. Deslongchamps, *J. Am. Chem. Soc.* **2008**, *130*, 13989–13995.

[143] K. C. Nicolaou, N. Winssinger, J. Pastor, F. Murphy, *Angew. Chem. Int. Ed.* **1998**, *37*, 2534–2537.

[144] V. Balraju, D. S. Reddy, M. Periasamy, J. Iqbal, *J. Org. Chem.* **2005**, *70*, 9626–9628.

[145] K. Akaji, K. Teruya, M. Akaji, S. Aimoto, *Tetrahedron* **2001**, *57*, 2293–2303.

[146] M. Kaiser, C. Siciliano, I. Assfalg–Machleidt, M. Groll, A. G. Milbradt, L. Moroder, *Org. Lett.* **2003**, *5*, 3435–3437.

[147] J. Dufour, L. Neuville, J. Zhu, *Chem. Eur. J.* **2010**, *16*, 10523–10534.

[148] V. Balraju, J. Iqbal, *J. Org. Chem.* **2006**, *71*, 8954–8956.

[149] Q. Wei, S. Harran, P. G. Harran, *Tetrahedron* **2003**, *59*, 8947–8954.

[150] V. Balraju, R. V. Dev, D. S. Reddy, J. Iqbal, *Tetrahedron Lett.* **2006**, *47*, 3569–3571.

[151] L. A. Wessjohann, D. G. Rivera, O. E. Vercillo, *Chem. Rev.* **2009**, *109*, 796–814.

[152] A. Domling, W. Wang, K. Wang, *Chem. Rev.* **2012**, *112*, 3083–3135.

[153] L. A. Wessjohann, E. Ruijter, *Mol. Divers.* **2005**, *9*, 159–169.

[154] L. A. Wessjohann, B. Voigt, D. G. Rivera, *Angew. Chem. Int. Ed.* **2005**, *44*, 4785–4790.

[155] D. G. Rivera, L. A. Wessjohann, *J. Am. Chem. Soc.* **2006**, *128*, 7122–7123.

[156] H. Jacobson, W. H. Stockmayer, *J. Chem. Phys.* **1950**, *18*, 1600.

[157] H. R. Kricheldorf, *Macromolecules* **2003**, *36*, 2302–2308.

[158] B. A. Laurent, S. M. Grayson, *Chem. Soc. Rev.* **2009**, *38*, 2202–2213.

[159] Z. Jia, M. J. Monteiro, *J. Polym. Sci. Pol. Chem.* **2012**, *50*, 2085–2097.

[160] F. M. Haque, S. M. Grayson, *Nat. Chem.* **2020**, *12*, 433–444.

[161] D. Geiser, H. Höcker, *Macromolecules* **1980**, *13*, 653–656.

[162] G. Hild, A. Kohler, P. Rempp, *Eur. Polym. J.* **1980**, *16*, 525–527.

[163] B. Vollmert, J. X. Huang, *Macromol. Rapid Commun.* **1980**, *1*, 333–339.

[164] J. Roovers, P. M. Toporowski, *Macromolecules* **1983**, *16*, 843–849.

[165] N. Hadjichristidis, M. Pitsikalis, S. Pispas, H. Iatrou, *Chem. Rev.* **2001**, *101*, 3747–3792.

[166] K. Ishizu, H. Kanno, *Polymer* **1996**, *37*, 1487–1492.

[167] M. J. Stanford, R. L. Pflughaupt, A. P. Dove, *Macromolecules* **2010**, *43*, 6538–6541.

[168] M. Kubo, H. Yamamoto, T. Uno, T. Itoh, H. Sato, *Polym. Bull.* **2001**, *47*, 25–30.

[169] H. Oike, H. Imaizumi, T. Mouri, Y. Yoshioka, A. Uchibori, Y. Tezuka, *J. Am. Chem. Soc.* **2000**, *122*, 9592–9599.

[170] H. Oike, M. Hamada, S. Eguchi, Y. Danda, Y. Tezuka, *Macromolecules* **2001**, *34*, 2776–2782.

[171] Y. Tezuka, *Acc. Chem. Res.* **2017**, *50*, 2661–2672.

[172] Y. Tezuka, *React. Funct. Polym.* **2020**, *148*, 104489.

[173] M. Schulz, S. Tanner, H. Barqawi, W. H. Binder, *J. Polym. Sci. Pol. Chem.* **2010**, *48*, 671–680.

[174] Y. Tezuka, R. Komiya, *Macromolecules* **2002**, *35*, 8667–8669.

[175] Y. Tezuka, T. Ohtsuka, K. Adachi, R. Komiya, N. Ohno, N. Okui, *Macromol. Rapid Commun.* **2008**, *29*, 1237–1241.

[176] R. P. Quirk, S. F. Wang, M. D. Foster, C. Wesdemiotis, A. M. Yol, *Macromolecules* **2011**, *44*, 7538–7545.

[177] S. Hayashi, K. Adachi, Y. Tezuka, *Chem. Lett.* **2007**, *36*, 982–983.

[178] M. R. Whittaker, Y. K. Goh, H. Gemici, T. M. Legge, S. Perrier, M. J. Monteiro, *Macromolecules* **2006**, *39*, 9028–9034.

[179] E. Q. Rosenthal, J. E. Puskas, C. Wesdemiotis, *Biomacromolecules* **2012**, *13*, 154–164.

[180] Y. Zhang, G. Wang, J. Huang, *Macromolecules* **2010**, *43*, 10343–10347.

[181] M. Schappacher, A. Deffieux, *Macromol. Rapid Commun.* **1991**, *12*, 447–453.

[182] L. Rique–Lurbet, M. Schappacher, A. Deffieux, *Macromolecules* **1994**, *27*, 6318–6324.

[183] M. Schappacher, A. Deffieux, *Macromolecules* **2001**, *34*, 5827–5832.

[184] M. Kubo, T. Hayashi, H. Kobayashi, K. Tsuboi, T. Itoh, *Macromolecules* **1997**, *30*, 2805–2807.

[185] M. Kubo, T. Nishigawa, T. Uno, T. Itoh, H. Sato, *Macromolecules* **2003**, *36*, 9264–9266.

[186] B. Lepoittevin, X. Perrot, M. Masure, P. Hemery, *Macromolecules* **2001**, *34*, 425–429.

[187] B. A. Laurent, S. M. Grayson, *J. Am. Chem. Soc.* **2006**, *128*, 4238–4239.

[188] J. Xu, J. Ye, S. Liu, *Macromolecules* **2007**, *40*, 9103–9110.

[189] D. M. Eugene, S. M. Grayson, *Macromolecules* **2008**, *41*, 5082–5084.

[190] D. E. Lonsdale, C. A. Bell, M. J. Monteiro, *Macromolecules* **2010**, *43*, 3331–3339.

[191] X. P. Qiu, F. Tanaka, F. M. Winnik, *Macromolecules* **2007**, *40*, 7069–7071.

[192] A. S. Goldmann, D. Quémener, P. E. Millard, T. P. Davis, M. H. Stenzel, C. Barner–Kowollik, A. H. Müller, *Polymer* **2008**, *49*, 2274–2281.

[193] G. O'Bryan, N. Ningnuek, R. Braslau, *Polymer* **2008**, *49*, 5241–5248.

[194] P. Sun, Q. Tang, Z. Wang, Y. Zhao, K. Zhang, *Polym. Chem.* **2015**, *6*, 4096–4101.

[195] R. Nicolaÿ, K. Matyjaszewski, *Macromolecules* **2011**, *44*, 240–247.

[196] M. Xie, J. Shi, L. Ding, J. Li, H. Han, Y. Zhang, *J. Polym. Sci. Pol. Chem.* **2009**, *47*, 3022–3033.

[197] T. Sun, G. E. Yu, C. Price, C. Booth, J. Cooke, A. J. Ryan, *Polymer* **1995**, *36*, 3775–3778.

[198] V. Percec, M. Kawasumi, *J. Chem. Soc., Perkin Trans. 1* **1993,** *12*, 1319–1334.

[199] V. Percec, P. J. Turkaly, A. D. Asandei, *Macromolecules* **1997**, *30*, 943–952.

[200] G. E. Yu, P. Sinnathamby, C. Price, C. Booth, *Chem. Commun.* **1996**, *1*, 31–32.

[201] M. Glassner, J. P. Blinco, C. Barner-Kowollik, *Macromol. Rapid Commun.* **2011**, *32*, 724–728.

[202] H. Durmaz, A. Dag, G. Hizal, U. Tunca, *J. Polym. Sci. Pol. Chem.* **2010**, *48*, 5083–5091.

[203] T. Mizawa, K. Takenaka, T. Shiomi, *J. Polym. Sci. Pol. Chem.* **2000**, *38*, 237–246.

[204] T. Josse, O. Altintas, K. K. Oehlenschlaeger, P. Dubois, P. Gerbaux, O. Coulembier, C. Barner–Kowollik, *Chem. Commun.* **2014**, *50*, 2024–2026.

[205] Q. Tang, Y. Wu, P. Sun, Y. Chen, K. Zhang, *Macromolecules* **2014**, *47*, 3775–3781.

[206] Y. A. Chang, R. M. Waymouth, *J. Polym. Sci. Pol. Chem.* **2017**, *55*, 2892–2902.

[207] T. He, G. H. Zheng, C. Y. Pan, *Macromolecules* **2003**, *36*, 5960–5966.

[208] A. Narumi, S. Zeidler, H. Barqawi, C. Enders, W. H. Binder, *J. Polym. Sci. Pol. Chem.* **2010**, *48*, 3402–3416.

[209] C. W. Bielawski, D. Benitez, R. H. Grubbs, *Science* **2002**, *297*, 2041–2044.

[210] C. W. Bielawski, D. Benitez, R. H. Grubbs, *J. Am. Chem. Soc.* **2003**, *125*, 8424–8425.

[211] A. J. Boydston, Y. Xia, J. A. Kornfield, I. A. Gorodetskaya, R. H. Grubbs, *J. Am. Chem. Soc.* **2008**, *130*, 12775–12782.

[212] Y. Xia, A. J. Boydston, Y. Yao, J. A. Kornfield, I. A. Gorodetskaya, H. W. Spiess, R. H. Grubbs, *J. Am. Chem. Soc.* **2009**, *131*, 2670–2677.

[213] C. D. Roland, H. Li, K. A. Abboud, K. B. Wagener, A. S. Veige, *Nat. Chem.* **2016**, *8*, 791.

[214] H. R. Kricheldorf, S. R. Lee, *Macromolecules* **1995**, *28*, 6718–6725.

[215] H. R. Kricheldorf, S. R. Lee, S. Bush, *Macromolecules* **1996**, *29*, 1375–1381.

[216] H. R. Kricheldorf, S. R. Lee, N. Schittenhelm, *Macromol. Chem. Phys.* **1998**, *199*, 273–282.

[217] Z. Wei, L. Liu, M. Qi, *React. Funct. Polym.* **2006**, *66*, 1411–1419.

[218] J. Weil, R. T. Mathers, Y. D. Getzler, *Macromolecules* **2012**, *45*, 1118–1121.

[219] H. R. Kricheldorf, D. Langanke, J. Spickermann, M. Schmidt, *Macromolecules* **1999,** *32*, 3559–3564.

[220] H. R. Kricheldorf, M. Al–Masri, G. Schwarz, *Macromolecules* **2002**, *35*, 8936–8942.

[221] H. Li, A. Debuigne, R. Jérome, P. Lecomte, *Angew. Chem. Int. Ed.* **2006**, *45*, 2264–2267.

[222] H. R. Kricheldorf, S. M. Weidner, F. Scheliga, *Polym. Chem.* **2017**, *8*, 1589–1596.

[223] M. Ouchi, H. Kammiyada, M. Sawamoto, *Polym. Chem.* **2017**, *8*, 4970.

[224] E. Piedra–Arroni, C. Ladavière, A. Amgoune, D. Bourissou, *J. Am. Chem. Soc.* **2013**, *135*, 13306.

[225] D. A. Culkin, W. Jeong, S. Csihony, E. D. Gomez, N. P. Balsara, J. L. Hedrick, R. M. Waymouth, *Angew. Chem. Int. Ed.* **2007**, *119*, 2681–2684.

[226] W. Jeong, J. L. Hedrick, R. M. Waymouth, *J. Am. Chem. Soc.* **2007**, *129*, 8414–8415.

[227] E. J. Shin, H. A. Brown, S. Gonzalez, W. Jeong, J. L. Hedrick, R. M. Waymouth, *Angew. Chem. Int. Ed.* **2011**, *123*, 6512–6515.

[228] W. Jeong, E. J. Shin, D. A. Culkin, J. L. Hedrick, R. M. Waymouth, *J. Am. Chem. Soc.* **2009**, *131*, 4884–4891.

[229] X. Zhang, R. M. Waymouth, *ACS Macro Lett.* **2014**, *3*, 1024–1028.

[230] H. R. Kricheldorf, N. Lomadze, G. Schwarz, *Macromolecules* **2007**, *40*, 4859–4864.

[231] H. R. Kricheldorf, N. Lomadze, G. Schwarz, *Macromolecules* **2008**, *41*, 7812–7816.

[232] I. Asenjo–Sanz, A. Veloso, J. I. Miranda, A. Alegría, J. A. Pomposo, F. Barroso–Bujans, *Macromolecules* **2015**, *48*, 1664.

[233] H. Kudo, S. Makino, A. Kameyama, T. Nishikubo, *Macromolecules* **2005**, *38*, 5964–5969.

[234] H. Kudo, M. Sato, R. Wakai, T. Iwamoto, T. Nishikubo, *Macromolecules* **2008**, *41*, 521–523.

[235] K. J. Shea, S. Y. Lee, B. B. Busch, *J. Org. Chem.* **1998**, *63*, 5746–5747.

[236] S. Matsumura, Y. Suzuki, K. Tsukada, K. Toshima, Y. Doi, K. I. Kasuya, *Macromolecules* **1998**, *31*, 6444–6449.

[237] G. Y. Shi, X. Z. Tang, C. Y. Pan, *J. Polym. Sci. Pol. Chem.* **2008**, *46*, 2390–2401.

[238] Y. Q. Dong, Y. Y. Tong, B. T. Dong, F. S. Du, Z. C. Li, *Macromolecules* **2009**, *42*, 2940–2948.

[239] X. Fan, G. Wang, J. Huang, *J. Polym. Sci. Pol. Chem.* **2011**, *49*, 1361–1367.

[240] B. A. Laurent, S. M. Grayson, *J. Am. Chem. Soc.* **2011**, *133*, 13421–13429.

[241] H. Oike, A. Uchibori, A. Tsuchitani, H. K. Kim, Y. Tezuka, *Macromolecules* **2004**, *37*, 7595–7601.

[242] X. Pang, G. Wang, Z. Jia, C. Liu, J. Huang, *J. Polym. Sci. Pol. Chem.* **2007**, *45*, 5824–5837.

[243] X. Pang, R. Jing, M. Pan, J. Huang, *Sci. China Chem.* **2010**, *53*, 1653–1662.

[244] Z. Jia, Q. Fu, J. Huang, *Macromolecules* **2006**, *39*, 5190–5193.

[245] K. Zhang, M. A. Lackey, Y. Wu, G. N. Tew, *J. Am. Chem. Soc.* **2011**, *133*, 6906–6909.

[246] H. Li, A. Debuigne, R. Jérome, P. Lecomte, *Angew. Chem. Int. Ed.* **2006**, *45*, 2264–2267.

[247] Y. Xia, A. J. Boydston, R. H. Grubbs, *Angew. Chem. Int. Ed.* **2011**, *50*, 5882–5885.

[248] A. J. Boydston, T. W. Holcombe, D. A. Unruh, J. M. Fréchet, R. H. Grubbs, *J. Am. Chem. Soc.* **2009**, *131*, 5388–5389.

[249] S. H. Lahasky, W. K. Serem, L. Guo, J. C. Garno, D. Zhang, *Macromolecules* **2011**, *44*, 9063–9074.

[250] H. R. Kricheldorf, S. R. Lee, *Macromolecules* **1996**, *29*, 8689–8695.

[251] H. R. Kricheldorf, S. Rost, *Polymer* **2004**, *45*, 3205–3213.

[252] Y. Tezuka, R. Komiya, M. Washizuka, *Macromolecules* **2003**, *36*, 12–17.

[253] S. Hayashi, K. Adachi, Y. Tezuka, *Polym. J.* **2008**, 40, 572–576.

[254] G. Y. Shi, L. P. Yang, C. Y. Pan, *J. Polym. Sci. Pol. Chem.* **2008**, *46*, 6496–6508.

[255] G. Y. Shi, C. Y. Pan, *Macromol. Rapid Commun.* **2008**, *29*, 1672–1678.

[256] D. E. Lonsdale, M. J. Monteiro, *Chem. Commun.* **2010**, 46, 7945–7947.

[257] D. E. Lonsdale, M. J. Monteiro, *J. Polym. Sci. Pol. Chem.* **2011**, *49*, 4603–4612.

[258] G. Wang, X. Fan, B. Hu, Y. Zhang, J. Huang, *Macromol. Rapid Commun.* **2011**, *32*, 1658–1663.

[259] M. Kubo, T. Hayashi, H. Kobayashi, T. Itoh, *Macromolecules* **1998**, *31*, 1053–1057.

[260] K. Ishikawa, T. Yamamoto, H. Harada, Y. Tezuka, *Macromolecules* **2010**, *43*, 7062–7067.

[261] N. Sugai, H. Heguri, K. Ohta, Q. Meng, T. Yamamoto, Y. Tezuka, *J. Am. Chem. Soc.* **2010**, *132*, 14790–14802.

[262] Y. Tezuka, F. Ohashi, *Macromol. Rapid Commun.* **2005**, *26*, 608–612.

[263] N. Sugai, H. Heguri, T. Yamamoto, Y. Tezuka, *J. Am. Chem. Soc.* **2011**, *133*, 19694–19697.

[264] M. Igari, H. Heguri, T. Yamamoto, Y. Tezuka, *Macromolecules* **2013**, *46*, 7303–7315.

[265] Y. Tezuka, A. Tsuchitani, Y. Yoshioka, H. Oike, *Macromolecules* **2003**, *36*, 65–70.

[266] T. Noda, Y. Doi, Y. Ohta, S. I. Takata, A. Takano, Y. Matsushita, *J. Polym Sci.* **2020**, *58*, 2098–2107.

[267] J. Jeong, K. Kim, R. Lee, S. Lee, H. Kim, H. Jung, M. A. Kadir, Y. Jang, H. B. Jeon, K. Matyjaszewski, T. Chang, H. J. Paik, *Macromolecules* **2014**, *47*, 3791–3796.

[268] T. Lee, J. Oh, J. Jeong, H. Jung, J. Huh, T. Chang, H. J. Paik, *Macromolecules* **2016**, *49*, 3672–3680.

[269] J. H. Jung, A. K. Mohanty, J. Ye, T. Lee, J. Ahn, Y. G. Lim, T. Chang, H. J. Paik, *J. Polym. Sci. Pol. Chem.* **2017**, *55*, 4020–4026.

[270] A. K. Mohanty, J. Ye, J. Ahn, T. Yun, T. Lee, K. S. Kim, H. B. Jeon T. Chang, H. J. Paik, *Macromolecules* **2018**, *51*, 5313–5322.

[271] G. Y. Shi, C. Y. Pan, *J. Polym. Sci. Pol. Chem.* **2009**, *47*, 2620–2630.

[272] Y. Satoh, H. Matsuno, T. Yamamoto, K. Tajima, T. Isono, T. Satoh, *Macromolecules* **2017**, *50*, 97–106.

[273] B. J. Ree, Y. Satoh, T. Isono, T. Satoh, *Polym. Chem.* **2021**.

[274] Y. Tezuka, K. Fujiyama, *J. Am. Chem. Soc.* **2005**, *127*, 6266–6270.

[275] Y. Mato, K. Honda, K. Tajima, T. Yamamoto, T. Isono, T. Satoh, *Chem. Sci.* **2019**, *10*, 440–446.

[276] B. J. Ree, Y. Mato, L. Xiang, J. Kim, T. Isono, T. Satoh, *Polym. Chem.* **2021**, *12*, 744–758.

[277] C. E. Wagner, J. S. Kim, K. J. Shea, *J. Am. Chem. Soc.* **2003**, *125*, 12179–12195.

[278] J. E. Hein, V. V. Fokin, *Chem. Soc. Rev.* **2010**, *39*, 1302–1315.

[279] C. Barner–Kowollik, T. P. Davis, M. H. Stenzel, *Aust. J. Chem.* **2006**, *59*, 719–727.

[280] T. Hosoya, H. Aoyama, T. Ikemoto, T. Hiramatsu, Y. Kihara, M. Endo, M. Suzuki, *Bioorg. Med. Chem. Lett.* **2002**, *12*, 3263–3265.

[281] T. Hosoya, T. Hiramatsu, T. Ikemoto, H. Aoyama, T. Ohmae, M. Endo, M. Suzuki, *Bioorg. Med. Chem. Lett.* **2005**, *15*, 1289–1294.

[282] Z. Zhang, Z. W. Peng, K. Z. Fan, *Chin. Chem. Lett.* **2011**, *22*, 785–788.

[283] V. Ladmiral, T. M. Legge, Y. Zhao, S. Perrier, *Macromolecules* **2008**, *41*, 6728–6732.

[284] G. Li, H. Zheng, R. Bai, *Macromol. Rapid Commun.* **2009**, *30*, 442–447.

[285] G. Li, H. Wang, H. Zheng, R. Bai, *J. Polym. Sci. Pol. Chem.* **2010**, *48*, 1348–1356.

[286] S. Amdur, A. T. Y. Cheng, C. J. Wong, P. Ehrlich, R. D. Allendoerfer, *J. Polym. Sci. Pol. Chem.* **1978**, *16*, 407–414.

[287] K. Rafizadeh, K. Yates, *Org. Prep. Proced. Int.* **1985**, *17*, 140–142.

[288] L. W. Deady, J. Desneves, *Org. Prep. Proced. Int.* **1995**, *27*, 219–221.

[289] A. W. Johnson, R. B. LaCount, *J. Am. Chem. Soc*. **1961**, *83*, 417–423.

[290] E. J. Corey, M. Chaykovsky, *J. Am. Chem. Soc.* **1965**, *87*, 1353–1364.

[291] E. M. Bassan, C. A. Baxter, G. L. Beutner, K. M. Emerson, F. J. Fleitz, S. Johnson, S. Keen, M. M. Kim, J. T. Kuethe, W. R. Leonard, P. R. Mullens, D. J. Muzzio, C. Roberge, N. Yasuda, *Org. Process Res. Dev.* **2012**, *16*, 87–95.

[292] A. M. Sherwood, S. E. Williamson, S. N. Johnson, A. Yilmaz, V. W. Day, T. E. Prisinzano, *J. Org. Chem.* **2018**, *83*, 980–992.

[293] G. A. Guerrero–Vásquez, N. Chinchilla, J. M. Molinillo, F. A. Macías, *J. Nat. Prod.* **2014**, *77*, 2029–2036.

[294] J. Deska, J. E. Bäckvall, *Org. Biomol. Chem.* **2009**, *7*, 3379–3381.

[295] K. Makiguchi, T. Satoh, T. Kakuchi, *Macromolecules* **2011**, *44*, 1999–2005.

[296] Y. Li, A. H. Flood, *Angew. Chem. Int. Ed.* **2008**, *47*, 2649–2652.

[297] Y. Li, A. H. Flood, *J. Am. Chem. Soc.* **2008**, *130*, 12111–12122.

[298] Y. Li, D. A. V. Griend, A. H. Flood, *Supramol. Chem.* **2009**, *21*, 111–117.

[299] Y. Hua, R. O. Ramabhadran, E. O. Uduehi, J. A. Karty, K. Raghavachari, A. H. Flood, *Chem. Eur. J.* **2011**, *17*, 312–321.

[300] I. Bandyopadhyay, K. Raghavachari, A. H. Flood, *ChemPhysChem* **2009**, *10*, 2535–2540.

[301] Y. Hua, R. O. Ramabhadran, J. A. Karty, K. Raghavachari, A. H. Flood, *Chem. Commun.* **2011**, *47*, 5979–5981.

[302] M. Pošta, V. Soós, P. Beier, *Tetrahedron* **2016**, *72*, 3809–3817.

[303] S. Lee, D. E. Hirsch, Y. Liu, J. R. Dobscha, D. W. Burke, S. L. Tait, A. H. Flood, *Chem. Eur. J.* **2016**, *22*, 560–569.

[304] A. J. Butzelaar, K. L. Liu, P. Röring, G. Brunklaus, M. Winter, P. Theato, *ACS Appl. Polym. Mater.* **2021**, *3*, 1573–1582.

[305] C. H. Krause, A. J. Butzelaar, D. Diddens, D. Dong, P. Théato, D. Bedrov, B. J. Hwang, M. Winter, G. Brunklausac, *J. Power Sources* **2021**, *484*, 229267.